

ISSN 0289-260X
UDC 06.055.8

SPECIAL PUBLICATION OF NATIONAL
AEROSPACE LABORATORY

SP-49T

International Workshop
on Numerical Simulation Technology
for Design of Next Generation
Supersonic Civil Transport

17-19 January 2000, TOKYO

December 2000

NATIONAL AEROSPACE LABORATORY

CHOFU, TOKYO, JAPAN

2nd SST-CFD Workshop

International Workshop on Numerical Simulation Technology for Design of Next Generation Supersonic Civil Transport

17-19 January 2000

PROGRAM

(CONTENTS for the PROCEEDINGS)

===== 17 JAN =====

I. General Lectures

[Opening] Chairperson: Hirotohi Kubota (Univ. of Tokyo)

0930-0950 "Opening Address"
Kan'ichiro Kato (SCJ), Susumu Toda (NAL)

[I-1 Research toward the Next Generation-SST]
Chairperson: Kimio Sakata (NAL)

0950-1020 "Research Activity in Japan toward the Next Generation SST"
Hirotohi Kubota (Univ. of Tokyo) 1

1020-1100 "Progress in Aerodynamic Technology to Support a Second Generation Supersonic
Transport" 7
David Lovell (DERA, U.K.)

1100-1140 "Aerodynamical Designing of the Second Generation Supersonic Transport
(SST-2)" 21
L.E.Vasiliev (TsAGI, Russia)

1140-1220 "ESCT propulsion system integration: Review and Progress " 43
Thierry SURPLY, Damien PRAT (Aerospatiale Matra Airbus)

----- [Lunch] -----

[I-2 NAL's SST Research Project]
Chairperson: Yoshiaki Nakamura (Nagoya Univ.)

1330-1410 "Supersonic Experimental Airplane Program in NAL (NEXST) and its CFD-Design
Research Demand" 53
Kimio Sakata (NAL)

II. General Session

[II-1 Designing SST and Requirement on CFD]
Chairperson: Koji Isogai (Kyushu Univ.)

1430-1510 "Multidisciplinary Optimization Tools Based on Manual Design Exercises" 57
Helmut Sobieczky (DLR, Germany)

1510-1550	"Application of Advanced CFD Methods to the Design of Modern Airplanes"	61
	Fassi Kafyeke (Bombardier, Canada)	
1600-1640	"Sonic Boom Research: TsAGI Approach"	73
	S.L.Chernyshev, L.G.Ivanteeva, V.V.Kovalenko, L.L.Teperin (TsAGI, Russia)	
1640-1720	"Dynamic Systems Approach to Optimization Problems — Optimization through Bifurcation —"	75
	Kazuo Tsuchiya (Kyoto Univ.)	
1720-1800	"Approaches to Simulation and Modeling of Turbulent Flows at High Reynolds Numbers"	
	Kyle Squires (Arizona State Univ., USA)	
1800-1830	Free Discussion	

===== 18 JAN =====

III. Technical Session I

[Opening of Technical Session]

0830-0850 Hideaki Aiso

[III-1 NAL's CFD-Aided Design Research]

Chairperson: Hideaki Aiso(NAL)

0850-0910	"Aerodynamic Design of Supersonic Experimental Airplane"	79
	Toshiyuki Iwamiya, Kenji Yoshida, Yuichi Shimbo, Yoshikazu Makino (NAL), Kisa Matsushima (Fujitsu Ltd.)	
0910-0930	"Boundary Layer Transition Analysis of the Scaled Supersonic Experimental Airplane",	85
	Kenji Yoshida, Toshiyuki Iwamiya, Yoshine Ueda (NAL), Hiroaki Ishikawa (Sankou Software)	
0930-0950	"Inverse Wing Design for the Scaled Supersonic Experimental Airplane with Ensuring Design Constraints" Kisa Matsushima (Fujitsu Ltd.), Toshiyuki Iwamiya, Wanqiu Zhang (NAL)	91
0950-1010	"Developmant of a Preliminary SST Planform Design Tool Using a Numerical Optimization Routine."	97
	Shin Matsumura, John P. Sullivan (Purdue Univ.), Yuichi Shimbo (NAL)	
1010-1035	"NAL's CFD-Aided Design Researches for Propulsion System"	109
	Osamu Nozaki, T. Nishizawa, K. Kikuchi, Y. Matsuo (NAL), Hidekazu Kodama, M. Unno, Y. Ooba (Ishikawajima-Harima Heavy Industries Co.,Ltd.)	
1035-1050	Free Discussion	

[III-2 Numerical Optimization]

1100-1105	"Organizer's Address" Shigeru Obayashi (Tohoku Univ.)	
1105-1135	"Aerodynamic Nacelle Shape Optimization for NAL's Experimental Airplane"	115
	Yoshikazu Makino, Toshiyuki Iwamiya (NAL), Zhong Lei (VINAS Co., Ltd.)	
1135-1205	"Aerodynamic Optimization of Supersonic Wing-Nacelle Configuration Using an Adjoint Method with the Unstructured-Grid Approach"	121
	Hyoung-Jin Kim, Shigeru Obayashi, Kazuhiro Nakahashi (Tohoku Univ.)	

1205-1235	"An Application of Numerical Optimization to a Wing Twist of SST Wing-Nacelle Configuration" Tetsuo Yamazaki, Mitsuru Saito (Fuji Heavy Industries LTD.)131
1235-1250	Free Discussion	
	----- [Lunch] -----	
[III-3 Treatment of Multi-Discipline]		
1350-1355	"Organizer's Address" Toshiyuki Iwamiya (NAL)	
1355-1435	"A Coupled Aero-Structural Optimization Method For Complete Aircraft Configurations" James Reuther (NASA Ames)133
1435-1515	"Supersonic Civil Transport Design Using Collaborative Optimization" Ilan Kroo (Stanford Univ.)153
1525-1555	"Simultaneous Shape and Flight Trajectory Optimization of a Spaceplane using Parallel Optimization Method" Shinji Suzuki, Takeshi Tsuchiya (Univ. of Tokyo)161
1555-1625	"Application of Direct Search Method to Aeroelastic Tailoring of an Arrow Wing Configuration" Koji Isogai (Kyushu Univ.)165
1640-1710	"Multiobjective Evolutionary Computation of Supersonic Wing Geometries" Shigeru Obayashi, Yukihiro Takeguchi, Daisuke Sasaki (Tohoku Univ.)173
1710-1740	"Numerical Flutter Simulation -Application to Structural Design of Main Surface of SST Experimental Aircraft-" Jiro Nakamichi (NAL), Hamid Reza Kheirandish (Research Center of Computational Mechanics, Inc.)179
1740-1810	"CFD Activity for Future Winged Space Transport System" Yukimitsu Yamamoto, Takuji Kurotaki (NAL)183
1810-1840	Free Discussion	
1900-2100	[RECEPTION]	

===== 19 JAN =====

IV. Technical Session II

[IV-1 Next Generation Computer System for Designing (Panel Discussion)]

900-1040	Organizer: Kozo Fujii (ISAS)	
	Yuichi Matsuo(NAL)187
	Kazuomi Yamamoto (NAL),188
	W. Loeve(NLR, The Netherlands)189

[IV-2 Practices in Application Software]

1050-1055	"Organizer's Address" Jiro Nakamichi (NAL)	
-----------	--	--

1055-1125	"CFD Application to Aerodynamic Design of Small Supersonic Experimental Airplane" N. Futatsudera, T.Kaiden (Mitsubishi Heavy Industries Ltd.)	193
1125-1155	"Aerodynamic Design of Natural Laminar Flow Supersonic Aircraft Wings" Hirokage Ogoshi (Kawasaki Heavy Industries Ltd.)	203
1155-1225	"CFD Application to SST Propulsion System" Yoshinori Ooba, H. Kodama (Ishikawajima-Harima Heavy Industries Co. Ltd.) O. Nozaki, K. Kikuchi, T. Nishizawa, Y. Matsuo (NAL)	211
1225-1240	Free Discussion ----- [Lunch] -----	
[IV-3 Fundamental Problems in CFD]		
1340-1345	"Organizer's Address" Kazuhiro Nakahashi (Tohoku Univ.)	
1345-1415	"A Structured Grid Method in Simulating a Flow around Supersonic Transports" Shunji Enomoto (NAL)	213
1415-1445	"Simple Algorithms of CFD for Compressible Flows" Eiji Shima (Kawasaki Heavy Industries Ltd.)	217
1445-1515	"Anisotropic Cartesian Grid Adaptation" P.R. Lahur, Y. Nakamura (Nagoya Univ.)	225
1515-1545	"A Study on Improvement of Aerodynamic Characteristics of Next Generation SST by Active Flow Control" Shigeru Aso (Kyushu Univ.), Keiichi Karashima (Nishinippon Institute of Technology)	233
1545-1615	Free Discussion	
[Closing]		
1615-1630	"Closing Address " Kimio Sakata (NAL), Hirotohi Kubota (Univ. of Tokyo)	

Research Activity in Japan toward the Next Generation SST

Hirotohi Kubota

Department of Aeronautics and Astronautics, University of Tokyo

7-3-1 Hongo, Bunkyo, Tokyo 113-8656, Japan

E-mail kubota@klt.u-tokyo.ac.jp

Abstract: Current status and future perspectives of research and development for the next generation supersonic transport (SST) in Japan are overviewed. At first, status of the research and development for JSRP (Japan Supersonic Transport Program) and the relations with the associate programs and institutions are described. Secondly, the feasibility studies for the next generation SST are presented in the standpoint of aircraft technology accomplishment, market viability and environmental compatibility.

Introduction

A forecast of air traffic demand by JADC (Japan Aircraft Development Corporation) suggests that the annual increase rate of RPK (Revenue Passenger Kilometer) in the world is 5.9 % during the year of 1979 and 1998 and 4.9 % during 1999 and 2018¹⁾. The world RPK in 2018 will be 7.5 trillion which is approximately 2.5 times of the present (see Fig. 1). Especially RPK in the area of Asia-Pacific is higher than average of the world. In order to satisfy these future passenger demands, both the performance of high-speed and large amount of transport is needed.

From the end of 1980's, the research and development of the next generation Supersonic Transport (SST) has been activated in the world for the satisfaction of passenger demand by virtue of high-speed transportation. The technology innovation through lessons learned with the Concorde and other projects in US and Russia is also motivation of those research and development. The HSR (High Speed Research) Program in the US ended in 1999 due to difficulty of solving engine noise problem and small amount of allocation of NASA budget, and ESRP (European Supersonic Research Program) is not yet lifted off. However the HSR Project is followed by UEET (Ultra Efficient Engine Technology) Project and in the age of 2010s the research and development of next generation SST will be surely recovered.

In Japan, SJAC (The Society of Japanese Aircraft Companies, Inc.) has continued a feasibility study of JSRP (Japan Supersonic Transport Program) (Fig. 2)²⁾ under the support of MITI (Ministry of International Trade and Industry) from 1989. In the JSRP, (1) accomplishment of aircraft technologies, (2) viability of market and (3) compatibility to environment are required as the fundamental issues to be resolved. The current status of research and development activities for the next generation SST in Japan associated with JSRP is overviewed in this paper.

Status of Research and Development for the Next Generation SST

The JSRP composes of R & D stages of Phase 1 (1989-1994), Phase 2 (1995-2002) and Phase 3 (2003-) as shown in Fig. 3³⁾. It is associated with ACDMT (Advanced Composite Design and Manufacturing Technology) Program (1998-2002) for light-weighted heat-resistant composite material and HYPR (Supersonic/Hypersonic Transport Propulsion System) Program for combined-cycle jet engine (1989-1998). The ESRP (Research and Development of

Environmentally Compatible Propulsion System for Next-Generation Supersonic Transport) Program started in 1999 as a successor of the HYPR Program.

The Council for Aeronautics, Electronics and other Advanced Technologies of STA (Science and Technology Agency) suggested the necessity of research for the next generation SST in 1994. Following this suggestion, the experimental supersonic aircraft project NEXST (NAL's Experimental Airplane for SST) has started in NAL (National Aerospace Laboratory) in 1997 for accomplishment and demonstration of aerodynamic design technology. Several national research institutes such as Mechanical Engineering Laboratory and National Institute of Material and Chemical Research are in cooperation in innovation of infra-structural technologies. DOT (Department of Transportation) and airlines relates with operational requirement and environmental regulation-making. Academic societies such as JSASS (The Japan Society for Aeronautical and Space Sciences) and universities contribute in the basic research for aircraft technologies, environmental issues and so on. These relations are illustrated in Fig. 4. All these activities will contribute to development of the next generation SST.

Feasibility Studies for the Next Generation SST

1. Aircraft technologies accomplishment

The JSRP reference configuration of airplane is shown in Fig. 5³⁾, having a length of 94.5 m, a span of 43.4 m. The key technologies for the research and development of SST are illustrated in Fig. 6.

(a) Aerodynamics

High lift/drag ratio technologies with wing plan form like a cranked arrow configuration, natural laminarized airfoil, wing warp design and fuselage area rule and airframe/engine integration design technology are studied by the use of low-speed, transonic, and supersonic wind tunnel testings and CFD (Computational Fluid Dynamics) with Euler and Navier-Stokes solvers. Aerodynamic characteristics of high-lift device such as a vortex flap are predicted.

(b) Structure and material

Several structural analyses including FEM (Finite Element Method) are adopted for structural feasibility study. Since light-weighted and heat-resistant characteristics are required, research and development of feasible material including composite and titanium are progressing through ACDMT Program. Aero-elastic tailoring technology is also studied.

(c) Propulsion

The HYPR Program accomplished the combined cycle engine system consisting of turbo-jet and ram-jet up to Mach 5 as a ten-year National Project from 1989 to 1998 as described in Chapter 2. The ESPR Program was started in 1999 having the ecological goals of noise reduction of 3 dB below ICAO Chapter 3 level, NO_x reduction to 1/7 of the current level and CO₂ reductions of 25 % of the current level.

(d) Total Integration System

Researches for cockpit with SVS (Synthetic Vision System), thermal management system with regenerative cooling by fuel and total integrated system are under way.

2. Market viability

According to market research by SJAC including passenger forecast, minimum flight path, operational economy, development / manufacturing cost, passenger stimulation effect, fare flexibility, etc., the most feasible SST in Japan should have seat of 300, cruising Mach number of 2.2, range of 10,200 km (5,500 nm) as shown in Fig. 5³⁾.

Assuming that half of aircraft passengers is carried by SST, the fleet of 500 to 1,000 with reasonable air fare is expected. The expected cruising route is illustrated in Fig. 7⁴⁾. It will have a potential of economical benefit of approximately 3.8 trillion Yen at 1992 prices²⁾.

3. Environmental compatibility

Three issues for environmental compatibility of the next generation SST are recognized as reduction of community noise, suppression of sonic boom and protection of global ozone layer.

(a) Community Noise

The noise issue is studied in two aspects of technology innovation of propulsion system and ICAO assessment. Noise prediction with mixer-ejector nozzle at HYPR Program and noise abatement of flight procedure using engine cut-back, etc. at take-off are studied.

(b) Sonic Boom

Acceptability study with a sonic boom simulator of SJAC and boom propagation study for the planned SST configuration with use of Hayes' Program, etc. are conducted. Development of design technique for low-boom / low-drag configuration is also continued. Figure 8 shows the optimized airplane configuration having ramp-typed sonic boom signature at ground⁵⁾.

(c) Ozone Chemistry

Ozone change prediction with use of 2-D chemistry transport model and its application to NASA AESA (Atmospheric Effect of Stratospheric Aircraft) Scenario IV is studied⁶⁾. Figure 9 is global ozone change due to influence of aircraft cruise, which forecasts decrease of ozone at upper stratosphere (dashed lines), but increase in lower troposphere (solid lines). Technologies for reduction of engine noise, CO₂ and NO_x will be studied in the ESPR Program as described above.

Conclusion

Current status and future perspectives of research and development for the next generation supersonic transport (SST) in Japan including research and development organization, feasibility studies for (1) aircraft technologies accomplishment, (2) market viability and (3) environmental compatibility were overviewed. All activities will contribute to the next generation supersonic transport.

References

- 1) JADC: Internet Home Page, http://www.ijinet.or.jp/jadc/jadc_home.htm, March 1999.
- 2) SJAC: Japan Supersonic Research Program, November 1998.
- 3) SJAC: Study Report on the Next Generation Supersonic Transport, March 1999 (in Japanese).
- 4) Mizuno, H.: Future Aircraft Transportation and Supersonic Transport, Promoting Machine Industry in Japan, Vol. 25, No. 2, pp. 22-26, 1992 (in Japanese)
- 5) Makino, Y., Aoyama, T., Iwamiya, T., Watanuki, T., and Kubota, H.: Numerical optimization of fuselage geometry to modify sonic-boom signature. AIAA Journal of Aircraft, Vol. 36, No. 4, pp.668-674, 1999.

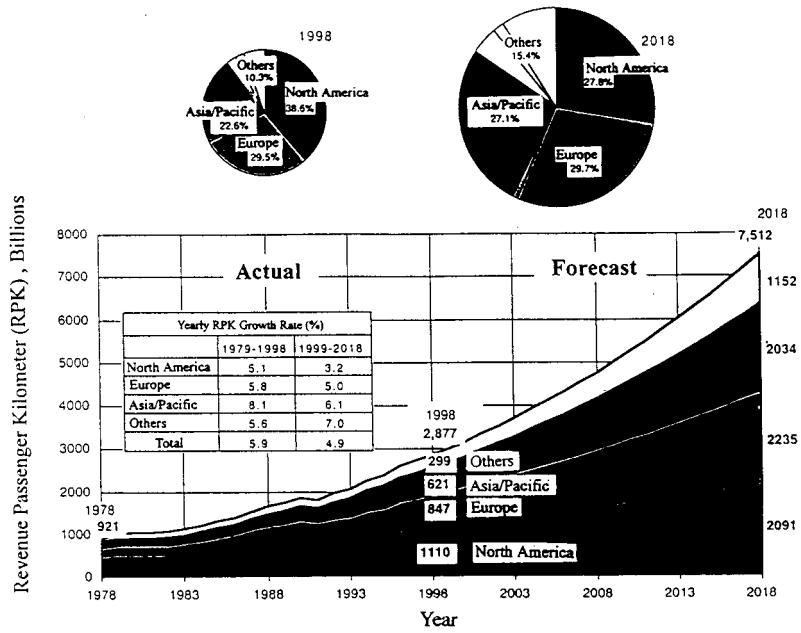


Fig. 1 World air traffic forecast¹⁾

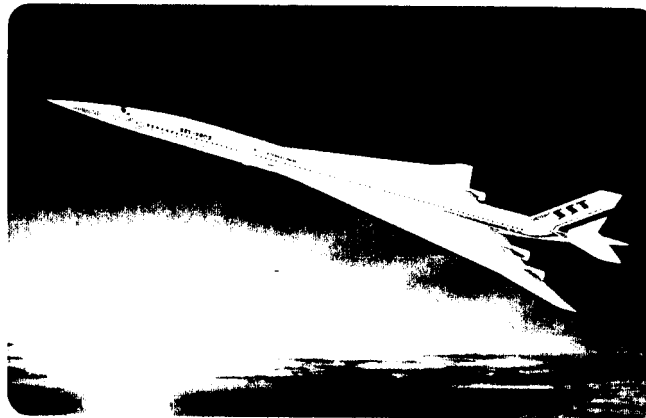


Fig. 2 JSRP airplane image²⁾

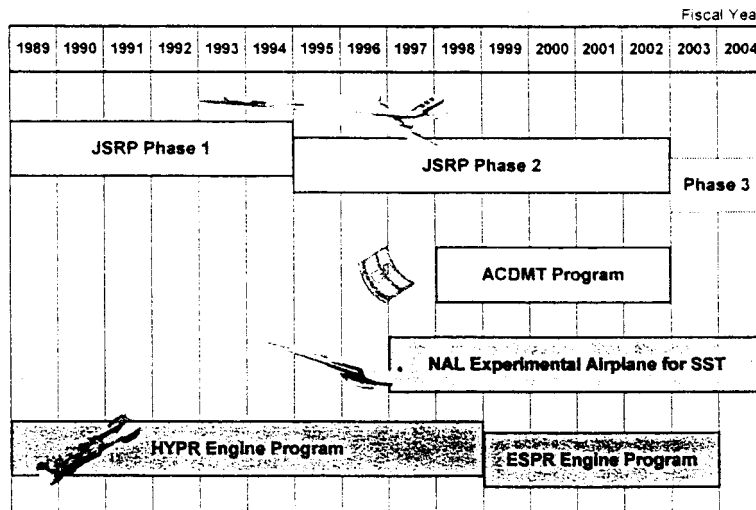


Fig. 3 Program schedule³⁾

Science and Technology Agency/National Aerospace Laboratory

★ Small-size, high-speed experimental aircraft



★ CFD technology



★ Materials evaluation technology

★ Basic theory

Universities/Professional Societies

Airlines, Ministry of Transport (Civil Aviation Bureau)

★ Operational requirements

★ Environmental regulations (ICAO)

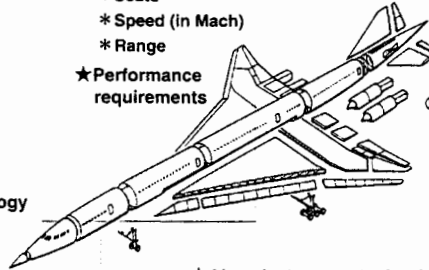
★ Basic aircraft configurations

- * Seats
- * Speed (in Mach)
- * Range

★ Performance requirements

★ Engine research and development

- * HYPR/AMG
- * Next-generation engines



★ Avionics

★ Aircraft structure technology

Aircraft Manufacturers/Ministry of International Trade and Industry/Agency of Industrial Science and Technology

Fig. 4 Relation between institutions for R & D of SST in Japan

Cruise Mach No.	2.2
Range	5500nm
Seat (2 class)	300
Takeoff Thrust	78 kLBS x 4
Max. takeoff weight	880 kLBS
Wing Area	9200 ft ²
Span	142 ft - 5 in
Length	310 ft
Takeoff Field Length	11,000 ft

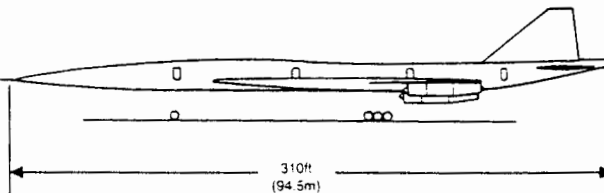
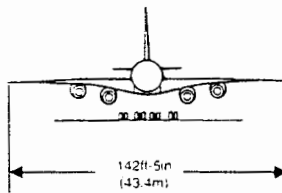
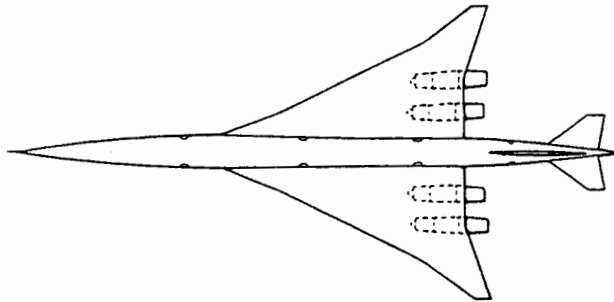


Fig. 5 Airplane configuration³⁾

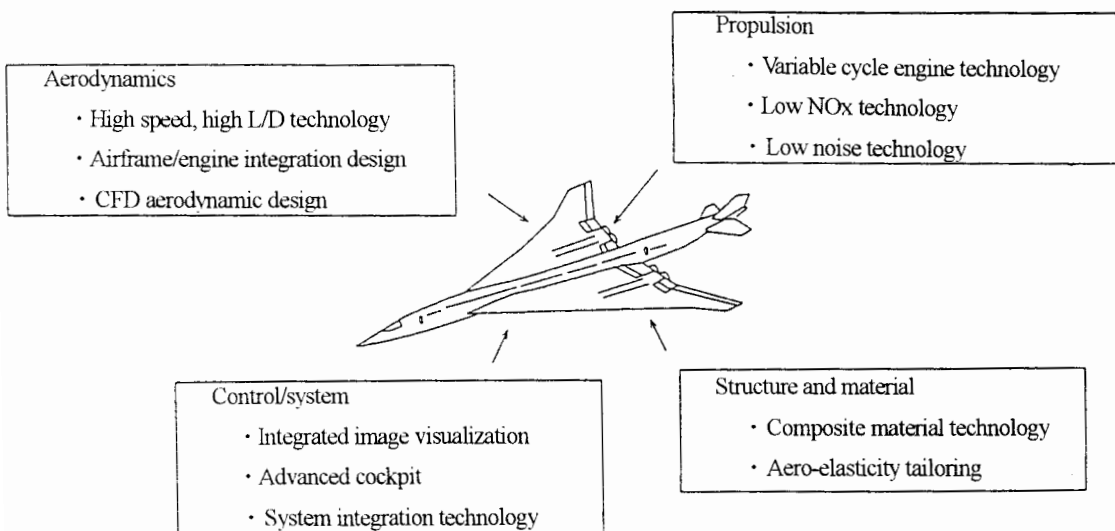


Fig. 6 Key technologies for R & D of SST

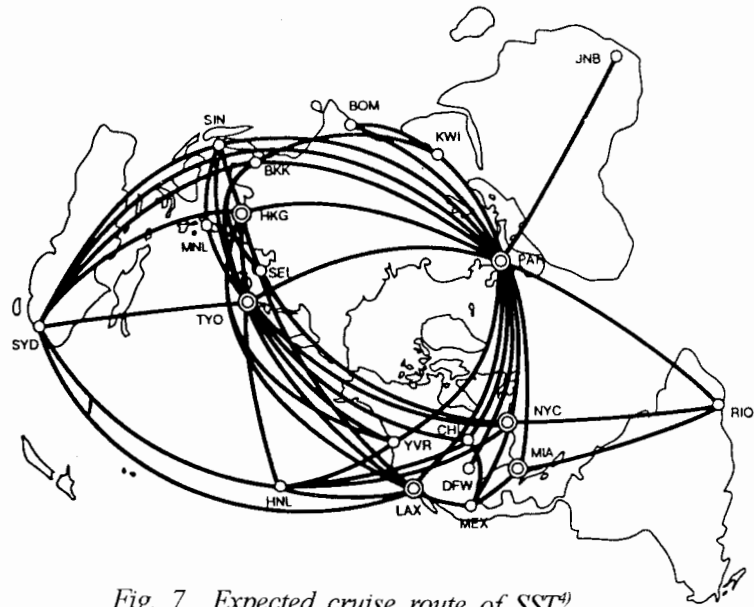
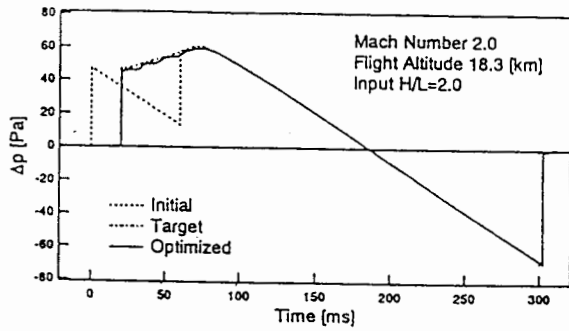
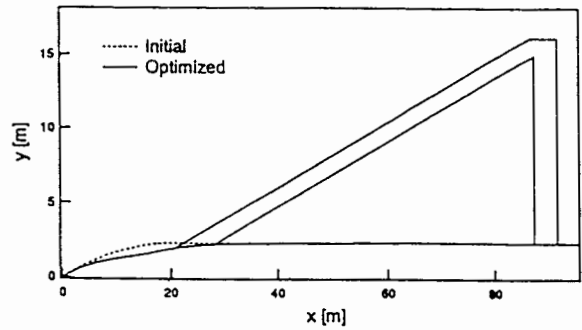


Fig. 7 Expected cruise route of SST⁴⁾



(a) Ground pressure signature



(b) Fuselage configuration

Fig. 8 Optimized airplane Configuration for sonic boom reduction⁵⁾

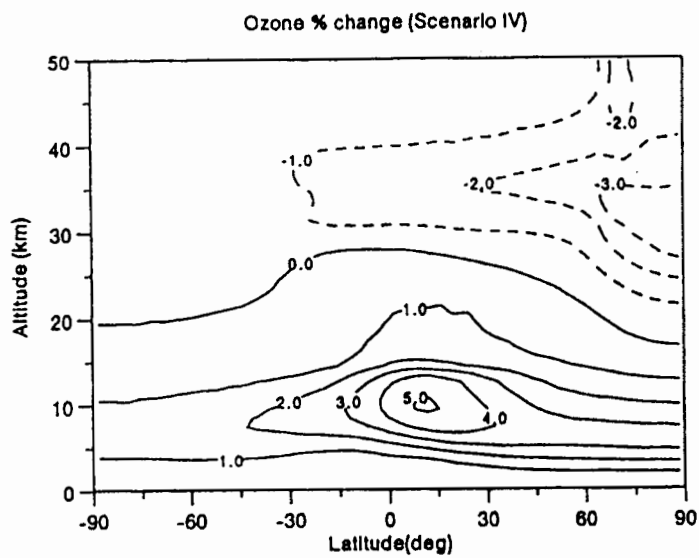


Fig. 9 Predicted ozone change³⁾

PROGRESS IN AERODYNAMIC TECHNOLOGY TO SUPPORT A SECOND-GENERATION SUPERSONIC TRANSPORT

D A Lovell*

Defence Evaluation and Research Agency, Farnborough, Hampshire GU14 0LX, United Kingdom

Abstract

The paper describes some aspects of the development and application within UK and mainland Europe of the aerodynamic technology required for successful design by industry of the next generation of supersonic transport aircraft. The focus is on wing design, but the methods covered are equally applicable to the design of other components and their interaction. Three areas are covered. Firstly a design method for aerodynamic shapes, developed at DERA UK, is summarised and two applications are described: an investigation of dual-point transonic / supersonic aerofoil design using an Euler CFD code, and the dual-point design of a delta-wing / body combination using a multi-block Euler CFD code. Secondly the initial application of the wing shape optimisation method to the dual-point design of a supersonic transport wing is summarised. Finally results from a European research project on the reduction of drag and the assessment of aerodynamic design methods are presented. Two linked wing-design tasks were completed: dual-point transonic/supersonic cruise design and low-speed high-lift design. Three wing configurations were tested at low-speed, transonically and supersonically. Figures showing a selection of the measured forces and pressures indicate the effectiveness of the aerodynamic design.

Introduction

Europe has a firm base of experience, gained in the design and operation of first-generation supersonic transport aircraft, on which to approach the technologies required for a second-generation aircraft. A substantial potential market exists if environmental concerns can be met and fare levels can be maintained close to those for subsonic transport aircraft, by the application of advanced technology. For aerodynamic technology, a major reduction in the level of the drag of a new supersonic transport aircraft is essential to achieve these goals. A supersonic transport aircraft must operate efficiently in three flight regimes: supersonic cruise (typically over sea), transonic cruise (normally over land) and at low speed for airport flyover, take-off and landing. For a viable aircraft the best compromise between these conflicting requirements must be achieved. Modern computational tools for flow simulation, structural analysis and numerical optimisation allow the necessary trade-offs to be performed within an acceptable design cycle time.

Aerodynamic shape design method development

Reduced cycle time for aerodynamic design has been achieved by a range of methods of coupling or integrating flow simulation with optimisation. The classical approach, inverse design, requires the specification of a target pressure distribution. An algorithm is then used to define a change in the surface ordinate derived from the difference in pressure from the target value at that point. Convergence to the shape corresponding to the target pressure distribution can then be obtained. Inverse methods for wing design were developed by applying the aerofoil methods to streamwise sections on the wing⁽¹⁾. More general optimisation may be achieved⁽²⁾ by using a procedure to determine an optimum target pressure distribution. Satisfying constraints on aerodynamic and geometric parameters can be a problem with inverse design methods - the DISC method developed by Campbell⁽³⁾ can handle constraints of this nature and dual-point design.

Direct optimisation design, in which a numerical optimisation procedure controls the geometric shape and derives an objective function from the results of flow analysis, can handle complex constraints and multi-point design. Because of the large computational overhead implicit in this approach (flow solutions are typically required for every change of value of geometric variables, and for the determination of derivatives of the objective and constraint functions) methods employing automatic differentiation and adjoint formulations have been developed⁽⁴⁾. While these methods reduce very considerably the resources required for shape optimisation they require significant additional analyses and problem preparation if design requirements are changed. A further problem with all these methods is the difficulty of determining global optima. Stochastic methods have been developed to overcome this shortcoming but the computational requirements are very high and there remain difficulties in handling complex sets of constraints.

Work at DERA⁽⁵⁾ has focused on developing shape optimisation tools capable of application to continually evolving design problems. For this purpose direct optimisation methods have been found well suited.

* Technical Manager, Applied Aerodynamics

Design Method

The DERA method for the constrained optimisation design of aerodynamic shapes (CODAS) is comprised of the 5 elements shown in figure 1. The optimisation code acts as the main program with the other parts being called as subsidiary programs.

Optimisation Method The constrained optimisation method was developed by Skrobanski⁽⁶⁾, primarily for aircraft design synthesis. Finite difference methods are used to calculate the gradients of the objective and constraint functions with respect to each of the design variables. The objective and constraint functions in the optimisation can be based upon any function for which a value can be extracted from the geometric model, grid or CFD solution. The convergence criterion for termination is typically based on an aerodynamic objective function. In the work reported here convergence to within 1 drag "count" (0.0001 in C_D) has been found to be sufficient. This approach minimises the number of calls to the CFD analysis code.

Geometry Representation In contrast to the general approach of using Base functions and aerofoil libraries, which can restrict the range of shapes that can be designed, CODAS uses geometric variables that reflect the likely aerodynamic influence of a shape change. These variables are related to the local slope/curvature of the camber surface, or the upper or lower surfaces of a section. For the applications described in the present paper the geometry for the whole chord has been designed. For wing design additional variables defining the twist at each design section, relative to the incidence reference axis, are used to complete the definition of the geometry. The overall incidence of the configuration is also treated as a design variable, so that the optimum combination of loading due to incidence, camber and twist can be obtained. The wing geometry between the design sections is defined by fitting bi-cubic patches through the sections. This approach has been found to result in smooth surfaces, both spanwise and chordwise, in all the aerodynamic shape design work completed to date. The geometric representation may be applied to a surface patch on any aircraft component (e.g. fuselage, nacelle, pylon) in addition to wings.

Grid Generation Fast generation of good quality grids is essential. For the applications described here structured grids have been used, as they are typically the most efficient for aerodynamic optimisation, however CODAS can use unstructured grids. For aerofoil design using an Euler code, algebraic grids have been used, with automatic regeneration. For wings a multiblock technique, SAUNA⁽⁷⁾, developed to handle complex configurations was used. To automate this stage of design a Remesh procedure is used. A transfinite interpolation procedure is used to regenerate the field grid in the blocks adjacent to the modified surface, using the new surface grid and the original grids on the adjacent block faces. This process is

very fast and produces good grid quality for geometric changes of the magnitude required.

Flow Simulation A fast robust solution method is required that produces results that are not highly dependent on grid density or quality. While high accuracy is desirable the prime need is for the correct simulation of the incremental effects of changes in the geometry. For inviscid transonic and supersonic flows a cell-vertex Euler method has been used for aerofoil and wing design. A flow-solution restart procedure is used in conjunction with the Euler solver to improve computational efficiency. This restart procedure gives a 50% to 90% time saving relative to starting from free-stream conditions.

Design Method Interface The purpose of this module in fig 1 is to couple the elements described above. The interface controls the input and output of design data, transfers data between the other modules, and provides a means of monitoring the progress of the design process. It acts as a front end to the optimisation algorithm, so that the design problem is properly posed for the optimisation procedure. Having an interface module of this type allows modified or new geometry, grid generation or flow solution procedures to be easily incorporated.

Dual-point Aerofoil Design

The aim was to determine an aerofoil shape that provides a suitable drag compromise at both transonic and supersonic design points. The NACA 64a005 section was chosen for the datum thickness distribution. A cambered aerofoil having this thickness distribution was first designed by conventional means for a transonic point ($M=0.63$, $C_L=0.9$). The supersonic design point was $M=1.2$, $C_L=0.25$. Figure 2 shows the datum aerofoils and their chordwise pressure distributions at the design points. The value of the pressure coefficient at which the transonic flow becomes locally sonic (C_p^*) is plotted as a dashed horizontal line. The cambered datum aerofoil is preferable transonically, while the symmetric datum aerofoil is preferable supersonically. Neither aerofoil is a good compromise for both design points. An aerofoil shape that minimised the drag at the supersonic design point was determined. An optimised camber-line was determined for the datum thickness distribution, and this camber was used as the starting point for design of the upper and lower surfaces (i.e. thickness+camber design). 15 design variables were used; 7 geometric variables for each surface and the angle of incidence. The design was started from the symmetric datum aerofoil. The resulting aerofoil is shown in fig 3 with the convergence history. The shape shows the characteristic double-wedge thickness distribution that might be expected from linear theory. This aerofoil shape is clearly inappropriate for the transonic design point.

Dual-point Camber line design. The transonic drag of the datum symmetrical aerofoil was used as a reference to

define a set of transonic drag constraints for the design of a series of aerofoils having minimum supersonic drag. 10 variables were used in the dual-point camber-line design; 8 geometric variables, and the angles of incidence of the aerofoil at the supersonic and transonic design points, to provide the freedom to match the target C_L .

Dual-point Upper and Lower surface design. 16 variables were used for the dual-point designs; 7 geometric variables for each surface, and 2 for the aerofoil incidence at the supersonic and transonic design points. The corresponding optimised camber-line shape was used as the starting point. Figure 4 shows the optimised aerofoil for the transonic drag constrained not to exceed 0.0333, together with the pressure distributions at the two design points and the convergence history. Compared with the initial thickness distribution (fig 2) the position of maximum thickness has been moved aft and the leading edge radius has been reduced. Figure 5 shows iso-Mach contours for the flow about the datum cambered aerofoil and the aerofoil optimised for zero transonic drag. The optimisation method has reduced the camber to decrease the size of the subcritical flow region, and the strength of the leading- and trailing-edge shocks.

Drag trade-off curves From the results of the aerofoil designs a drag trade-off curve was defined, figure 6. The starting point for the aerofoil design, the symmetric aerofoil, is shown by the asterisk. Camber design without any constraint on transonic drag (the short-dashed line) produces a drag reduction. Constraining the transonic drag to successively lower values in the camber-design set of aerofoils (the circle symbols) produces the upper full line. Repeating this process for the design of the upper and lower surfaces of the aerofoil produces the lowest drag (the long-dashed line) when the transonic drag is not constrained. The lower full line results when the transonic drag is progressively constrained to lower values. The difference in drag between the optimised aerofoil obtained from camber design, and that obtained from upper and lower surface design, is 0.0031 for the single-point supersonic case.

Wing Design

On the basis of the aerofoil work a corresponding dual-point wing design problem was defined i.e. determine a wing shape that provides a suitable drag compromise at both transonic and supersonic design points. The datum 45° sweep delta-wing/body geometry is shown in figure 7, with the multiblock surface grids. The datum wing is untwisted and uncambered and has a constant NACA64a005 section across the span with a constant thickness to chord ratio. The axi-symmetric body was designed using a supersonic area rule method, with a design Mach number of 1.4.

Four sections on the wing were used in the wing design. Each section was twisted relative to the body datum about an axis at 70% of the local chord. For the design of wing camber 21 variables were used; 4 to define the camber line at each section, 4 for the section twist angles and 1 for the

configuration incidence (the angle between the body axis and the free stream). For the design of the wing upper and lower surfaces a total of 45 variables were used; 5 for each surface at the 4 sections, 4 for the section twist angles and 1 for configuration incidence. In addition to constraining the C_L to the design value, geometric constraints were applied to maintain the same wing thickness as the datum and to prevent cross over of the upper and lower wing surfaces at the trailing edge or leading edge of the wing. Drag was used as the objective function. For dual-point design a weighted combination of the drags at the transonic and supersonic design points was used.

The two design points were transonic $M=0.9$, $C_L=0.45$, and supersonic $M=1.6$, $C_L=0.125$. These design points correspond to the aerofoil design points for the flow normal to the wing leading edge. The lower part of figure 8 shows the C_p contours on the upper surface of the datum wing at the transonic design point. The oblique shock starting from the wing root apex joins a weaker normal shock (60% to 70% chord) at 80% span to form a strong normal shock. Single-point design of camber and twist at the transonic point produced a 34% drag reduction after 13 design cycles, requiring 353 CFD analyses. The upper part of figure 8 shows the resulting upper-surface pressure distribution. The nose-down camber and aft camber introduced by CODAS remove the oblique shock almost completely, and move the rear shock aft and reduce its strength. The normal shock near the tip is almost removed. The body drag is reduced by more than half, indicating the much reduced interference effect on the body of the weakened wing shocks.

A series of dual, transonic and supersonic, camber and twist, designs were then completed. For each design two variables controlling incidence in the 2 flow analyses were used; one each for the transonic and supersonic design points, giving a total of 22 variables. Similarly constraints were used to ensure that the design values of C_L were achieved at the two points. The wing shape obtained from either the transonic or the supersonic single point design was used as the starting point for the dual point designs. Between 110 and 160 transonic and supersonic flow calculations were required for each design. The results for 7 designs, covering a range of values for the drag weighting factors, and the datum wing are plotted in figure 9. From this work it is evident that camber design is predominantly of value in reducing transonic drag, as only minor reductions in supersonic drag have been achieved.

Upper and lower surface design Upper and lower wing surfaces, and wing twist were first designed to minimise drag at the transonic design point. This produced a further very small drag reduction. This process was repeated for the supersonic design point, starting from the wing shape obtained by camber design. A drag reduction of 13% relative to the camber design was obtained. A series of dual (transonic and supersonic), upper / lower surface and twist, designs have been completed, covering the same set of

values for the weighting parameters that were used in the dual-point camber design.

Trade-off study Figure 9 shows the results plotted as drag at the supersonic design point versus drag at the transonic design point. The drag of the datum wing with the untwisted, uncambered, NACA 64a005 sections is shown for reference. A very large reduction in transonic drag (29%) was obtained for the same level of supersonic drag as the datum wing. Comparing the results for camber design (the dashed line) with those for upper and lower surface design (the full line), the datum thickness distribution with camber design produces comparable drag to that obtained in upper and lower surface design, when there is no significant requirement for supersonic performance. In contrast, large reductions in supersonic drag are achieved in all other cases from the use of upper and lower surface design, rather than camber design alone. Thus for a similar level of supersonic drag, $C_{D,0.0166}$, upper and lower surface design can reduce transonic drag by 20%.

Conclusions from initial CODAS use

The quality of the results obtained indicated that the method had the capability to give real design improvements. The semi-automatic method maintains the visibility of the relationship between local surface shape and the physical flow characteristics. Because the design method is based upon the SAUNA multiblock CFD system it has the potential to produce results of similar quality for much more complex geometries. Success in multi-point design and comprehensive constraint modelling encouraged further application to practical design tasks.

Initial SCT wing design study

Introduction

One of the early applications of the DERA CODAS method was a brief study of dual-point (transonic - supersonic) design of the wing of a generic supersonic transport⁽⁸⁾. A wing / body / foreplane configuration was chosen, based on layouts published in the open literature in the USA and Europe. Wing planform and location on the fuselage were fixed. The body is slightly waisted in the wing / body junction region but has not been aerodynamically designed. The datum wing geometry was untwisted and uncambered with a constant 2.5% thick NACA66 series section.

Design definition

Two design points were defined; transonic $M = 0.95$, $C_L = 0.19$, and supersonic $M = 2$, $C_L = 0.1$, for an aircraft of 350000kg. take-off mass and 354m² wing area. It was assumed that fuel would be stored in the inboard wing region between 15% and 80% chord. This fuel volume for the datum wing (240m³) was set as a constraint in the shape optimisation (fig 10). For structural reasons a constraint on minimum wing thickness / chord was set at 1.5% over the

whole span. A wing twist axis was defined, based on the likely position of the hinge line for trailing-edge flaps. To prevent the wing leading-edge emerging above the fuselage floor the wing twist at the root was constrained to 1° nose-up.

Wing shape optimisation

The seven sections of the wing shown in fig 11 were used. Geometric shape variables were optimised for the inner five of these and the outer two were derived from the adjacent sections by scaling on wing chord. 26 variables were used for the design of wing twist and camber: 4 to define camber at each section, 5 for section twist angles and 1 for configuration incidence. 46 variables were used for the design of wing twist, camber and thickness: 4 for each surface at the 5 sections, 5 for section twist and 1 for configuration incidence. In addition to the geometric constraints C_L was constrained to the design point value. Drag, calculated as the sum of skin friction and integrated pressure drag from inviscid flow computations, was used as the objective function. Fine grid analyses (549000 cells) of the datum configuration were compared with results for the coarse grid for wing optimisation (78000 cells). There was good agreement on drag levels and the coarse grid adequately captured the important flow features. Wing optimisation was performed with the foreplane removed; subsequent analysis confirmed the validity of this approach.

Camber and twist design Single-point supersonic design produced a 5% improvement in supersonic L/D relative to the datum: the sections are shown in fig 12. L/D at the transonic design point was improved by 14%. Single-point transonic design produced a 33% improvement in transonic L/D, but a reduction of 5% in supersonic L/D relative to the datum.

Upper and lower surface design Single-point supersonic produced a further 3% improvement in supersonic L/D over the camber and twist design. Transonically the L/D improvement was slightly lower. The resulting wing sections are shown in fig 12. These are very similar in shape but wing volume has been shifted inboard while satisfying the thickness constraints.

Trade-off study The single-point designs represent the two extremes of a transonic / supersonic L/D trade off (fig 13). To define the intermediate region of the trade-off a series of wing geometries were defined from the single-point design shapes and analysed on the coarse design grid. The results are shown in fig 13. From this the Dupt_2 geometry was selected as offering a good compromise; relative to the single-point supersonic design it gives a 6% improvement in transonic L/D for a 1% loss in supersonic L/D. Analysis of this geometry on the fine grid gave very good agreement. The corresponding wing / body / foreplane configuration was analysed on the fine grid, and showed very similar performance increments to those obtained with the datum configuration. Fig 14 shows the

change in upper-surface Mach number variation from the datum to the dual-point geometry. The leading-edge shock strength has been reduced considerably, particularly in the tip region where it would probably generate flow separation for the datum configuration. Fig 15 shows spanwise cross-sections of the wing and body. Note that while all the design variables were defined in the chordwise direction a smooth spanwise camber shape has been obtained. Fig 16 shows the resulting spanwise variation of wing thickness compared to the datum and Concorde.

Conclusions from the initial SCT wing design study

The CODAS shape optimisation method produced significant improvements in aerodynamic performance for the transonic and supersonic design points while satisfying realistic geometric constraints. For a wing / body / foreplane configuration L/D values of 9.65 supersonically and 13.8 transonically were predicted. Examination of the wing pressure distributions for the transonic design point suggested that the use of variable geometry (leading and trailing-edge flaps) should lead to further improvements in transonic L/D.

Drag reduction for SCT – the EUROSUP project

Introduction

The EUROSUP project⁽⁹⁾, co-ordinated by DERA, had ten research partners. The project consortium consisted of airframe companies from France (Aerospatiale), Germany (DASA), Italy (Alenia), Sweden (Saab) and UK (British Aerospace Airbus), and research establishments from France (ONERA), Germany (DLR), Italy (CIRA), the Netherlands (NLR) and UK (DERA). The partners completed computational and experimental tasks aimed at reducing the drag of supersonic transport aircraft at low speed and cruise (transonic and supersonic), and assessing relevant aerodynamic design methods. Quantitative targets were set for L/D performance at the three design points to provide a focus for the assessment:

- lift/drag ~ 10 at supersonic cruise ($M = 2.0$)
- lift/drag ~ 15 at transonic speeds ($M = 0.95$)
- lift/drag ~ 8 at low speed ($M \sim 0.3$)

These targets for aerodynamic performance represent improvements of between 20% and 30% relative to that achieved for the first generation of supersonic transport aircraft.

Of equal importance to industry is the rapid completion of a design cycle. Within the design cycle rapid aerodynamic design methods are required to optimise the geometric shape for maximum aerodynamic performance, subject to packaging and off-design performance constraints. Thus another objective for the project was to evaluate the relative merits of alternative aerodynamic shape design methods with respect to speed of execution, ease of use and the ability to incorporate updates to design constraints. Figure

17 shows the time-scales and interrelation of the research tasks.

CFD Evaluation

Several CFD methods, covering a range of fidelity in flow modelling, were evaluated for their accuracy and speed of prediction against an existing set of wind-tunnel data for a generic configuration for a supersonic transport aircraft. The outcome of this work fed into the analysis work in subsequent tasks. This task concluded that linear methods are adequate for supersonic design for the initial design phases. They offer acceptable prediction accuracy for drag and lift, while their high computational efficiency permits the analysis of a much larger number of configurations than Euler and Navier-Stokes codes. It was also concluded that supersonic and two-point supersonic / transonic design could be carried out with optimisation methods based on Euler solutions on less fine grids. The use of medium to coarse grids in three-dimensional shape optimisation, for reasons of cost and speed, is entirely justified in supersonic flow. Computations using Navier-Stokes flow analysis codes are essential to complement Euler calculations as viscous effects are unlikely to be negligible in transonic flow.

Transonic/Supersonic wing design

The European Supersonic Civil Transport (ESCT) configuration formed the basis for the aerodynamic design. The fuselage geometry and the wing planform remained fixed throughout the design work. The untwisted, uncambered wing was used as the datum against which the performance of the new wing designs was assessed. Design variables were the wing twist, camber and thickness distributions, and the overall configuration incidence at each design point. Geometric design constraints were defined for the undercarriage bay, spar depths, wing thickness, and wing/cabin floor relationship (figure 18). Overall lift coefficient was constrained to the design point value. For the later stages of design⁽¹⁰⁾ local Mach number was constrained on the upper surface of the wing.

Design methods Four methods were used for the transonic / supersonic design with the common aim of minimising drag at the high-speed design points. Rolston et al⁽¹¹⁾ have described this work in detail. A linear theory method for manual design was used by Alenia for single-point optimisation of wing twist and camber at the supersonic design point. The Alenia design exceeded the transonic L/D target and came within 4% of the supersonic target (see figure 21). In a parallel activity ONERA used an Euler CFD code for single-point optimisation at the supersonic design point. Wing thickness was first optimised for an untwisted and uncambered wing, and this thickness distribution was then used for wing twist and camber optimisation. This produced improvements in L/D of 1% transonically and 0.5% supersonically (see fig 21),

relative to the Alenia design, but it featured a round leading-edge shape which would be likely to give improved low speed performance.

The ONERA single-point supersonic design was used by DERA for the transonic design⁽¹⁰⁾. For this work it was essential to resolve the wing flow features on a grid coarse enough for design by optimisation. Figure 19 shows that the SAUNA CFD code captured the main features of pressure distributions with a coarse (85000 cells) grid. From initial shape optimisation it was concluded that a fixed geometry could not meet all the design objectives. The basic wing shape was therefore frozen as the single-point supersonic design and DERA defined the optimum deflection angles for segmented leading- and trailing-edge flaps (shown in fig 20) to maximise transonic L/D, with constraints applied on upper surface pressure distributions to ensure attached flow. It was concluded that the transonic / supersonic design problem was closely constrained, so the scope for geometric shape modification was restricted very considerably by geometric constraints.

Low-speed design

Variable leading-edge geometry was examined to reduce drag to meet the airport noise limits for the flyover flight condition of $C_L = 0.4$. It was essential that the low speed design should not compromise unduly the high-speed performance. BAe and DERA investigated hinged leading-edge devices and Alenia slotted leading-edge devices. The same design criteria were used for the high and low speed designs.

Alenia completed 2D and 3D analyses of leading-edge slats. Encouraging results from the 2-D work led to 3D analysis of a slatted wing on the ESCT datum wing without a fuselage. Thin-layer Navier-Stokes calculations indicated that slat deflection delayed flow separation in the outboard region and hence a large L/D increase was achieved at high incidence.

Deflection angles for a hinged leading-edge flap were defined by BAe, using a manual design method based on extensive low-speed wind tunnel results. RANSMB Navier-Stokes calculations were done by BAe and Euler calculations by DERA (on coarse and fine grids). Because of the markedly different solutions obtained it was considered inappropriate to use numerical shape optimisation methods. Figure 22 summarises the work on the hinged devices. The manual design method and the Navier-Stokes computations indicated that the target value of L/D could be achieved at $C_L = 0.4$. It was concluded¹² that further evaluation of the CFD methods is required for this class of flow. Leading-edge flap deflection angles for the 5 flap segments were chosen for the wind tunnel model using the BAe manual design method, and the geometry was supplied to NLR for model design and manufacture.

Experimental Evaluation

The aim of the wind-tunnel model testing was to verify the wing design shapes at the supersonic, transonic and low-speed design points, and to understand the wing flow development to assess the validity of the design approach used. A sting-mounted model (1/80 scale of ESCT) consisting of a fuselage with a cylindrical afterbody and three wings was designed, manufactured and tested by NLR⁽¹³⁾. Three wing configurations were tested: the supersonic twist / camber / thickness design, the supersonic design with LE and TE flaps deflected for transonic cruise, and the supersonic design with LE flaps deflected for low-speed fly over. Overall forces and surface pressures were measured. In addition some flow visualisation was completed to aid the understanding of flow development with incidence on the wing. Because the model was to be tested at high dynamic pressures the manufactured shapes of the transonic and supersonic wings were modified so that in the wind tunnel, under load, the design geometry was approximately recovered.

Flow analysis and comparison with experiment

The three wing configurations were analysed⁽¹⁴⁾ by NLR, CIRA, and DLR using their CFD methods. This provided an independent check on the design computations by Alenia, ONERA, DERA, Saab and BAe.

Analysis methods Linear and Euler methods were used by CIRA to predict the supersonic performance of the upswept-tail full-scale aircraft and wind tunnel model including sting configurations. Skin friction drag was estimated using a flat-plate reference skin friction for a given Mach number, Reynolds number and adiabatic wall temperature, assuming a fully turbulent boundary layer. DLR used a Navier-Stokes method with two turbulence models and three grid densities. NLR used a Navier-Stokes flow solver with two artificial dissipation models and four levels of grid density. NLR performed an initial computation with transition matching the strips applied to the wind tunnel model. Laminar separation was present on the outer wing, in agreement with flow visualisation in the wind tunnel. ONERA performed a computation at the supersonic design case using a viscous-coupled Euler method. In this method a three-dimensional laminar-turbulent boundary layer code is coupled to a structured multi-block Euler solver. The effects of the boundary layer were simulated via transpiration velocities.

Analysis results - surface pressures at supersonic conditions

Predictions by the Navier-Stokes Baldwin-Lomax and Euler solvers were in reasonable agreement. The Euler solution has a higher leading edge peak than the viscous solutions, with slightly lower pressures continuing over the entire chord. The Navier-Stokes and viscous coupled Euler results agree well. A comparison of the predictions of the two Navier-Stokes turbulence models and measurements is shown in Fig 23. Good agreement with experiment was obtained. There is very little change in the Navier-Stokes

solution by moving from the simple Baldwin-Lomax turbulence model to the more complex $k-\omega$ model. This suggests that the flow is not close to separation, so the simple turbulence models prove adequate.

Analysis results - surface pressures at transonic conditions

A comparison of DLR and NLR fine-grid transonic pressure distributions is given in Fig 24, which also includes measured tunnel data and lines of local Mach number ($M_{\text{local}} = 1.3$ for the front half of the chord and 1.1 over the remaining chord). These Mach lines, generated using the approximate Lock theory, represent the flow attachment constraint as applied during the transonic design. The computational results agree very well, the largest differences being over the leading-edge flap surface and around the rear shock. The comparison with the wind-tunnel model data is excellent, including the pressure peak at the flap knuckle, although the rear shock is located too far aft. Both the predicted and measured pressures largely conform to the local Mach number limit imposed during design. Both the Navier-Stokes solutions and model test flow visualisation showed a region of separated flow near the tip, with the remainder of the wing flow being attached. Thus the approach used to design for attached flow at transonic speeds using inviscid Euler methods has been validated. The likelihood of separated flow at the tip was anticipated at the design stage¹¹ but was accepted as a practical wing design would incorporate a swept tip.

Analysis results - surface pressures at subsonic conditions

The comparisons with model measurements in fig 25 are encouraging. The mixed attached / separated flow at the design point is well predicted. The basic vortex structures match those obtained in the wind-tunnel model flow visualisation well, though some of the secondary structures do not appear in the computed results. It should be noted that the flow structure alters rapidly around the design point, changing from an attached to a highly separated character, and is thus very sensitive to small changes in incidence.

Analysis results - overall forces at supersonic conditions

The computed and measured drag polars are plotted in Fig. 26. Overall, including the two DLR Navier-Stokes results, the predicted drags at the design point are within 8 counts and the design lift is reached at similar angles of incidence (within 0.1°). Generally the fine grid results appear to give a good approximation to coefficient values for a grid of vanishing cell size. The Euler drag prediction by CIRA is the closest to the model measurements, with the Navier-Stokes result being some 10 counts higher for both turbulence models. The reasons for the poor Navier-Stokes predictions of C_{D0} are not understood at present and are the subject of further studies, however the Navier-Stokes method gives the closest match to the lift-dependant drag component and the best prediction of the lift curve.

Analysis results - overall forces at transonic conditions

The computed and measured drag polars are plotted in Fig. 27. Two of the predictions are for different implementations

of the Baldwin-Lomax turbulence model (by NLR and DLR) and the third uses the DLR $k-\omega$ turbulence model. The comparison of computed transonic drag shows a difference of over 10 counts for the solutions of NLR and DLR. This is almost entirely due to friction drag differences, pressure drags being within one count of each other. Comparing computations and wind tunnel measurements of the drag polar shows that the DLR Baldwin-Lomax solution over predicts the drag by about 7 counts, the equivalent NLR solution is under by $3\frac{1}{2}$ counts, while the DLR $k-\omega$ prediction is within $1\frac{1}{4}$ counts. This suggests that use of the more complex turbulence model may be justified. Lift-dependent drag computed by the NLR and DLR methods follow the measured polar well.

Analysis results – general There were some significant differences between the measured and computed values for pitching moment. Several potential causes were examined to explain these differences. A grid refinement exercise by NLR showed a strong effect on predicted pitching moment, with lift moving outboard with increasing grid density. Noting the differences between predicted and measured wing twist on the wind-tunnel model, an approximate re-twist of the CFD geometry was carried out by DLR to model more accurately the model shape in the transonic tunnel. Thus the wing C_m would appear to be sensitive to small changes in twist.

Reynolds Number and Configuration Effects

Results for the overall forces on the aircraft configuration at flight Reynolds number are tabulated in Fig 28. For supersonic conditions, tunnel-to-flight aerodynamic effects were examined using CIRA's Linear and Euler methods. The effect of the configuration change (tunnel-model to aircraft) suggests that modelling the former is sufficient to understand what may be expected in terms of pressure distributions on the aircraft. According to the Euler solution the inviscid drag increases by about 5 counts when changing from the tunnel sting geometry to an upswept tail; 3 counts come from the fuselage and the remainder from the wing. There is good agreement between Euler and Navier-Stokes predictions at supersonic conditions, suggesting that scale effects are likely to be small.

Overall Assessment

Performance of CFD methods – supersonic Euler methods are more than adequate for predictions of pressures. Navier-Stokes also perform well, with the algebraic Baldwin-Lomax turbulence model giving similar results to the 2-equation $k-\omega$ model for the attached-flow design case. Part of the difference in prediction of drag could be due to changes in model geometry under load.

Performance of CFD methods – transonic The Navier-Stokes methods give excellent predictions for the transonic pressure distributions. Indicated areas of flow separation agree well with those noted in the wind tunnel flow visualisation.

Performance of CFD methods – low-speed Analysis at the low-speed high lift condition proved challenging. Grid generation was problematic. The final results were extremely encouraging, with the DLR N-S (Baldwin-Lomax) medium grid solutions modelling the changing flow structure with incidence relatively well. The low alpha attached flow condition was well predicted, as was the design condition with mixed attached and separated flow.

Performance of CFD methods for design The use of coarse grids for design might have been expected to have an effect on the ability to predict the flow correctly, but in fact the effect on pressure drag and pitching moment is small in the supersonic case. In the transonic case the DERA coarse grid design shows a 5 counts deviation in C_{Dp} from the NLR N-S results and the DERA fine grid Euler calculation. This is within the variation of the results from the different fine grid analyses.

Dual point optimisation proved too compromising for reasonable aerodynamic performance levels. Leading and trailing edge flaps show considerable potential as a means of achieving acceptable transonic cruise performance without penalising the supersonic performance. The analysis at flight Reynolds number indicates that the supersonic and transonic L/D design targets of 10 and 15 respectively were both achieved with attached flow. The Inverse method was not directly used in the main design exercise. Instead the capabilities were demonstrated in a test case using the datum configuration as starting point and the DERA supersonic design as target. Good results were achieved. The DERA geometry could be quite accurately reproduced over most of the wing, the root section showing the largest deviation, mainly due to the use of a greatly simplified fuselage geometry.

Detailed geometric constraints have been successfully applied in the design process, resulting in a practical wing envelope. Care is also required in applying wing surface-pressure constraints to limit shock induced separation within an inviscid design process using limited grid density. The final analysis indicates that the desired effect was achieved.

For low speed design the Navier-Stokes predictions at the design point showed significant areas of separated flow even with the leading-edge deflected. This gave doubts about the validity of using Euler solutions at this design condition. The manual approach was relatively successful.

General conclusions on the design process Linear methods offer an efficient means of improving supersonic performance in the early stages of design. The use of CFD optimisation coupled to an Euler code has proved to be an effective design process, giving slight improvement over the linear method at supersonic speeds, but offering significant advances at transonic conditions, where linear methods are not applicable. Optimisation techniques can be successfully applied with both geometric and aerodynamic constraints. The design is easier to manage if done in stages, with

thickness, twist and camber design being separated. Aerodynamic constraints should include pitching moment, as well as incidence and surface pressure limits. When applying aerodynamic constraints using inviscid methods, careful grid dependency and flow resolution studies are required for a fully successful design. Leading and trailing edge flap deflections can be included as geometric variables for transonic optimisation.

The need for further evaluation of the CFD methods for the highly complex flow at low speed coupled with a full assessment of the design sensitivities means that it is not possible to propose a design method at this stage. A manual design using a matrix of CFD predictions may be the best approach unless the execution times of acceptability accurate CFD methods for this type of flow can become fast enough for automatic optimisation.

Reynolds number effects on the surface pressures appear to be relatively small at supersonic speeds. At transonic conditions the effect is greater, with the wing rear shock strengthening slightly and moving aft, however this is relatively minor compared with the effect of the upswept tail. Changing from the constant section sting to the actual aircraft geometry significantly increases shock strength across the entire span. Realistic aircraft shape and flight Reynolds number calculations are important in order to gain a full picture of the final design. It is recommended that, as in the EUROSUP project, design should be done on the upswept tail geometry, thus requiring extra CFD computations for comparison with wind tunnel data.

Concluding remarks

The results presented in this paper indicate that considerable progress has been made in the aerodynamic technology to support a second-generation supersonic civil transport. The state of the art aerodynamic analysis and design tools employed have been validated by experiment, and enabled significant improvements to be made in the L/D performance at transonic and supersonic cruise conditions. The situation for the aerodynamic design of the SCT class of configuration is far less satisfactory at low speed - the need for further computational and experimental research in this area has been clearly identified.

Acknowledgements

Work under the EUROSUP project was 50% funded by the Commission of the European Union, under contract BRPR-CT95-0082. The remaining 50% was funded by the industry partners and National governments. The UK DERA research is funded by the Department of Trade and Industry CARAD programme.

References

1. Brandsma, F.J., Fray, J.M.J. "A system for transonic wing design with geometric constraints

- based on an inverse method," AGARD-CP-463 paper 7, 1989
2. van dem Dam, J.A., van Egmond, J.A., Sloof, J.W. "Optimization of target pressure distributions," AGARD-R-780 paper 3, 1990
 3. Campbell, R.L., Smith L.A., "A hybrid algorithm for transonic airfoil and wing design," AIAA-87-2552-CP, 1987
 4. Reuther, J, Alonso, J J, Rimlinger, M J, Jameson, A "Aerodynamic shape optimisation of supersonic aircraft configurations via an adjoint formulation on distributed memory parallel computers" AIAA 96-4045 6th Symposium on MDO, Sept 1996
 5. Lovell D.A., Doherty J.J. "Aerodynamic design of aerofoils and wings using a constrained optimisation method." ICAS-94-2.1.2
 6. Skrobanski, J.J. "Optimisation subject to nonlinear constraints," PhD Thesis, London University, 1986
 7. Shaw, J.A., Peace, A.J., May, N., Pocock, M. "Verification of the CFD simulation system SAUNA for complex aircraft configurations," AIAA paper 94-0393 1994
 8. Doherty J.J., Parker N.T., "Dual-point design of a supersonic transport wing using a constrained optimisation method" Paper 3.21, EAC '94 conference, Toulouse 1994
 9. Lovell D.A., "European research to reduce drag for supersonic transport aircraft", AIAA-99-3100, July 1999
 10. Evans T.P., Doherty J.J., "The aerodynamic design of the EUROSUP configuration" DERA/AS/ASD/CR97620/1 December 1997
 11. Rolston S.C., Doherty J.J., Evans T.P., Grenon R., Averado M.A. "Constrained aerodynamic optimisation of a supersonic transport wing: a European Collaborative Study" AIAA-98-2516, 16th Applied Aerodynamics Conference, 1998
 12. Nicholls K, "EUROSUP Task 4 Overall Report : Low Speed Design", EUROSUP/BAe/T-005/1, Feb 1999
 13. Elsenaar A, "Wind Tunnel Test of the EUROSUP SCT Configuration", EUROSUP/NLR/T017/1
 14. Mann A, "CFD analyses of EUROSUP supersonic, transonic and low-speed configurations.", EUROSUP/BAe/T-003/2, Feb 1999

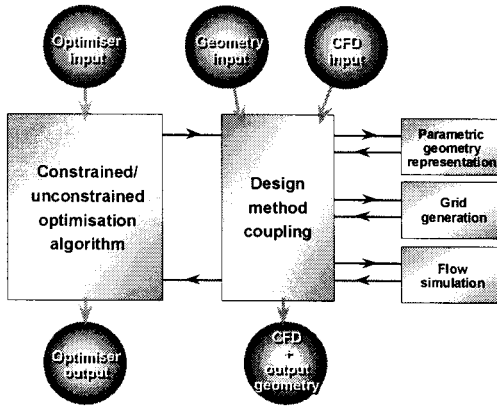


Fig 1 CODAS program structure

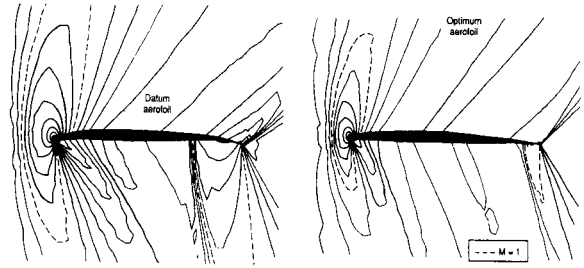


Fig 5 Mach contours for $M = 1.2, C_L = 0.25$

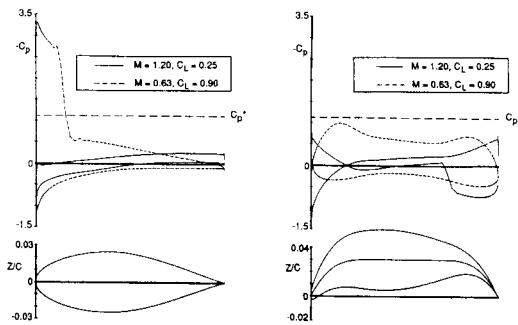


Fig 2 Datum aerofoils

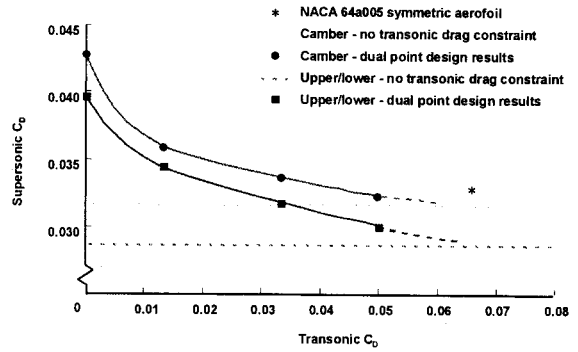


Fig 6 Transonic / supersonic drag trade-off

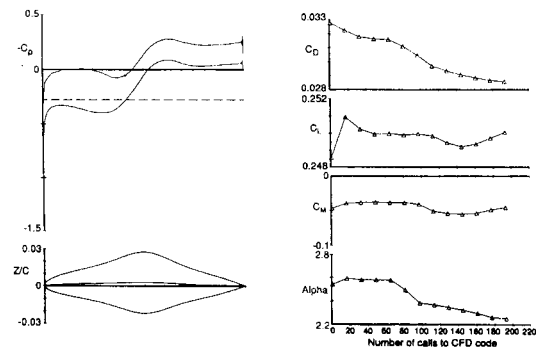


Fig 3 Supersonic upper / lower surface design

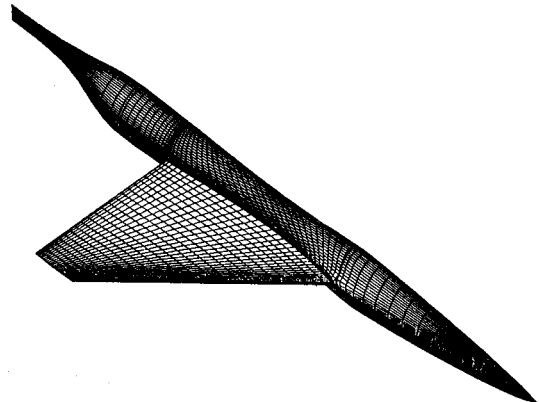


Fig 7 Datum geometry for wing design

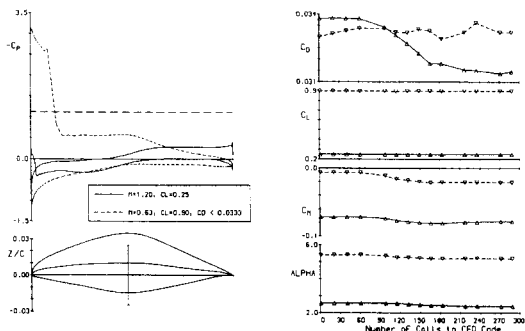


Fig 4 Dual-point upper lower / surface design

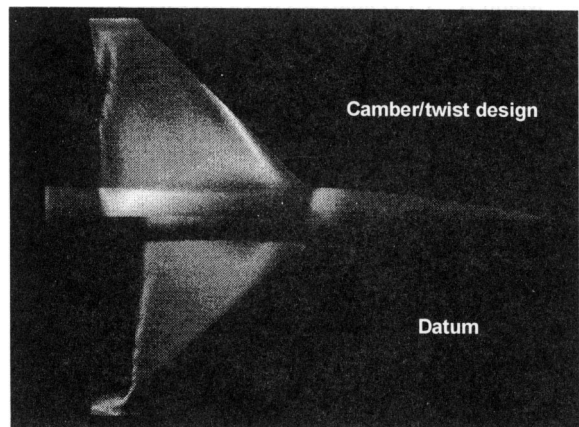


Fig 8 C_p variation at $M = 0.9, C_L = 0.45$

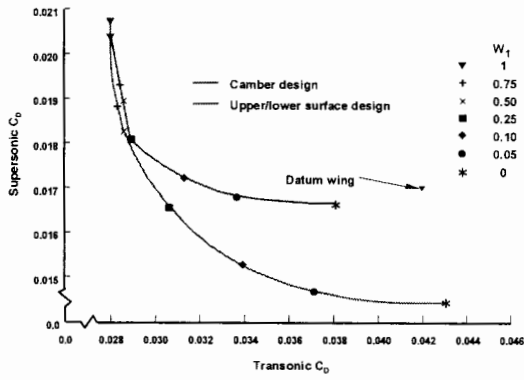


Fig 9 Transonic / supersonic drag trade-off

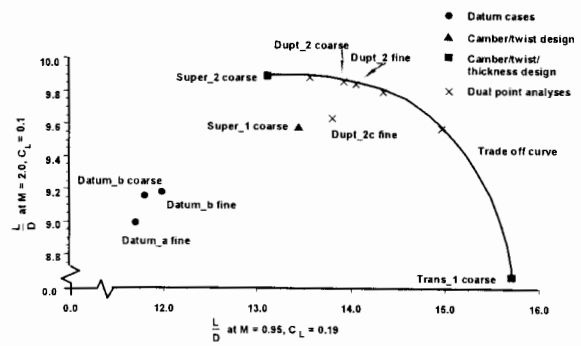


Fig 13 Transonic / supersonic L/D results

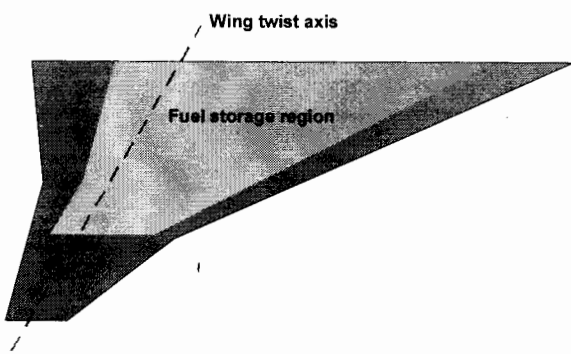


Fig 10 Fuel storage region for wing

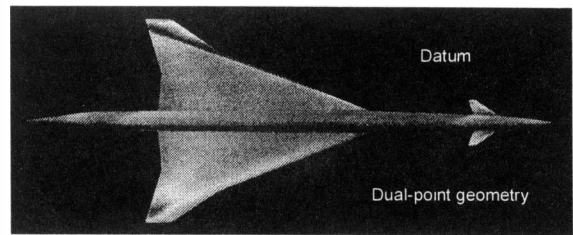


Fig 14 Upper surface Mach number variation at $M = 2, C_L = 0.1$

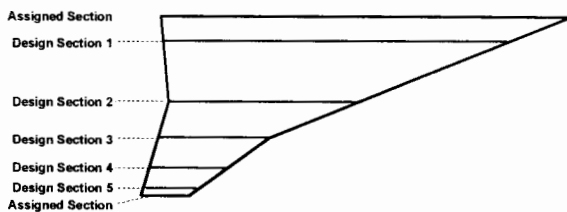


Fig 11 Position of wing design sections

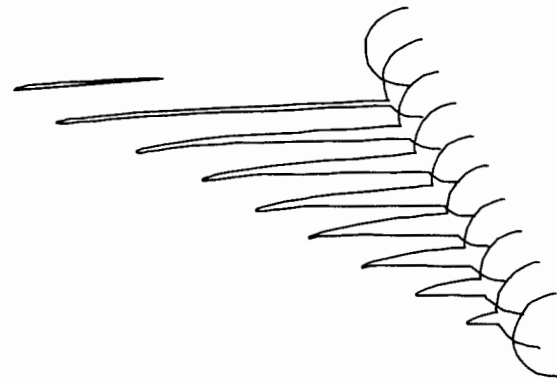


Fig 15 Cross-sections through wing and body for dual-point geometry

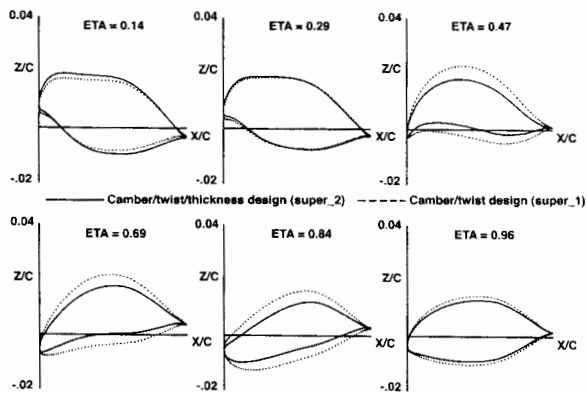


Fig 12 Comparison of wing sections for design at $M = 2, C_L = 0.1$

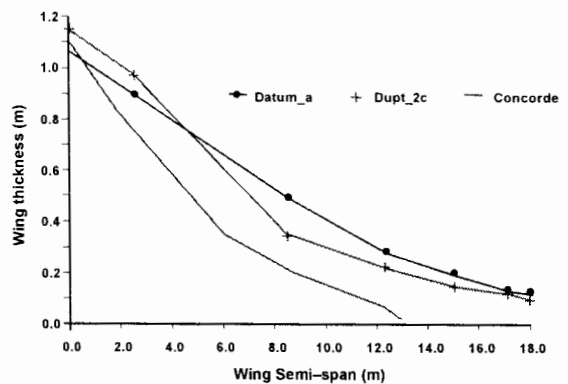


Fig 16 Spanwise variation of wing thickness

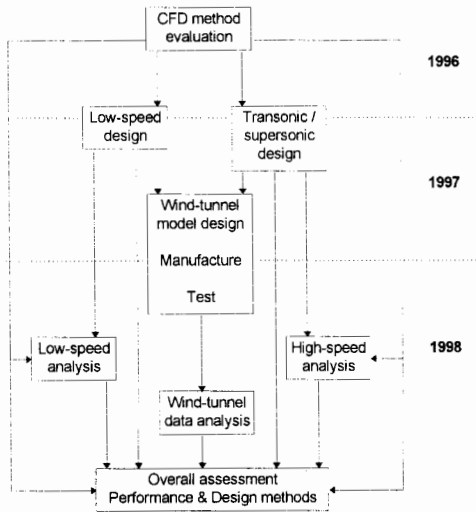


Fig 17 Research tasks and dependencies

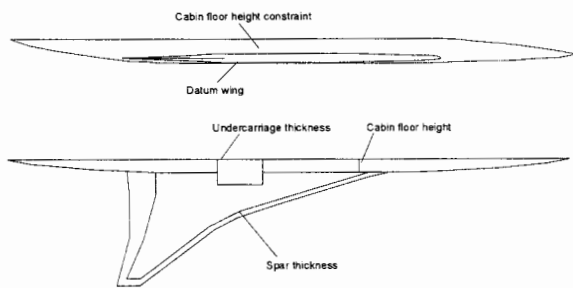


Fig 18 Geometric constraints on the ESCT configuration

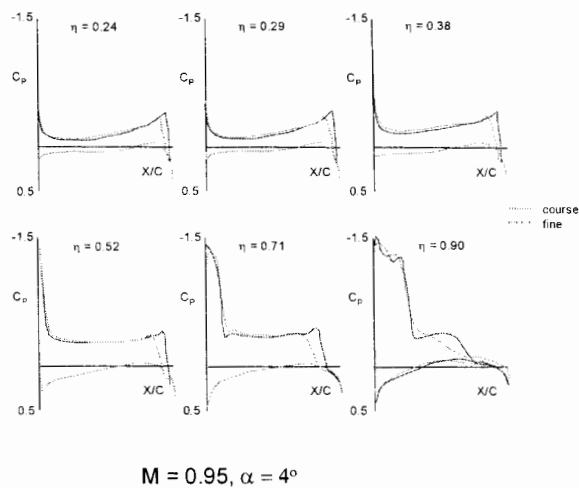


Fig 19 Transonic design – Cp comparison fine and coarse grids

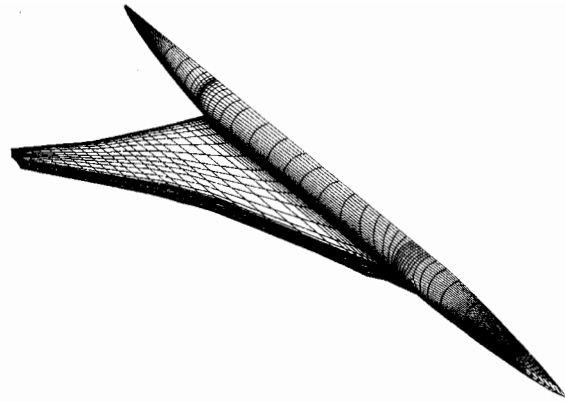


Fig 20 Wing design – deflected leading-edge flaps (coarse grid)

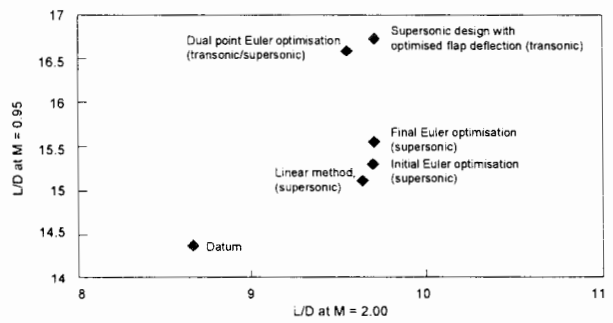


Fig 21 Summary of transonic / supersonic design

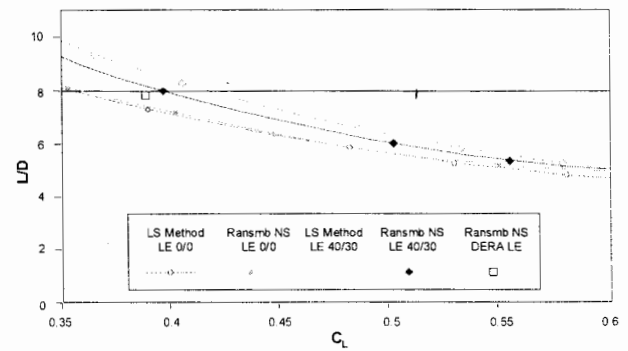


Fig 22 Low speed wing design

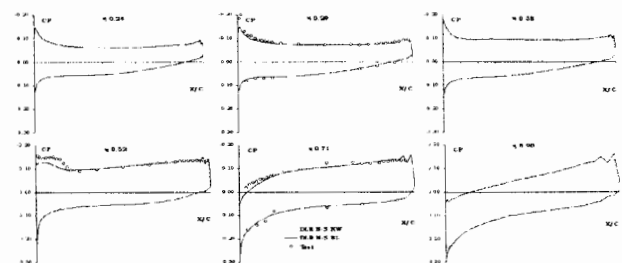


Fig 23 Cp from model and CFD. M = 2

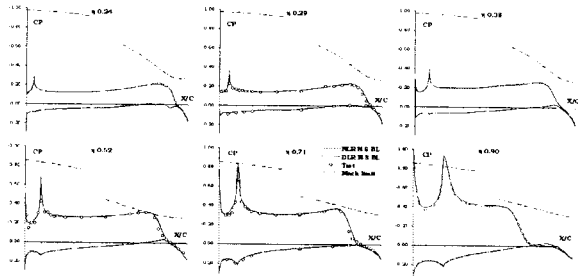


Fig 24 Cp from model and CFD. M = 0.95

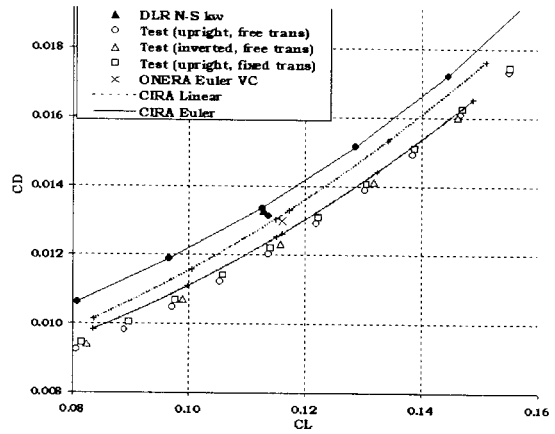


Fig 26 Drag polar at M = 2, wind-tunnel conditions

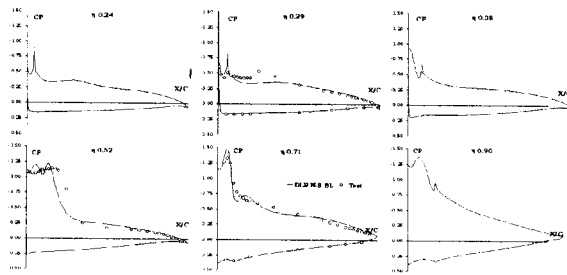


Fig 25 Cp from model and CFD. M = 0.25

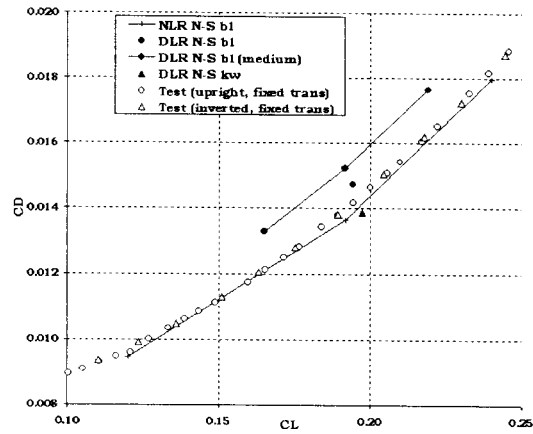


Fig 27 Drag polar at M = 0.95, wind-tunnel conditions

	Mach	Alpha	CL	CD pressure	CD friction	CD total	CM	L/D
Target	2.00	4.0	0.115	~	~	0.0115	-0.0298	10.0
Linear	2.00	4.0200	0.11500	0.00869	0.00348*	0.01217	-0.03293	9.45
Euler	2.00	4.0100	0.11505	0.00798	0.00348*	0.01146	-0.03201	10.04
Target	0.95	4.0	0.192	~	~	0.0128	-0.0553	15.0
N-S bl	0.95	3.8515	0.19200	0.00755	0.00446	0.01201	-0.06335	15.99

* flat-plate skin friction

Fig 28 Aerodynamic performance at aircraft cruise conditions

Aerodynamical designing of the second generation supersonic transport (SST-2)

L.E.Vasiliev, Russia, Zhukowsky town, TsAGI

The aerodynamics of SST-2 with the complex planform wings
(CPW).

The second generation supersonic transport must have the significantly higher effectiveness than the SST-1 had. Besides SST-2 must be the two-regime plane, i.e. it must have the equal range of flight at subsonic and supersonic cruise M numbers. At the take-off and landing SST-2 must satisfy to community noise norms FAR-36, St.3.

The TsAGI investigations had shown that the fulfilment of all these contradictory requirements is possible by use in design the so-called complex planform wings (CPW) like the Tu-144 one. Such wings are the combinations of the base wing of moderate aspect ratio with another wing (strake) of very little aspect ratio disposed immediately in front of the base wing, fig.1. The planforms of base wing and strake may be various. So the strike may have triangular, gothic, rectangular planform.

It was shown that it is possible to design the lifting surfaces with given, including zero, difference between the wing aerodynamic center positions at low subsonic and at supersonic cruise speeds by the appropriate choice of base wing and strake geometrical parameters. The first author's experimental results (1960 year) confirmed the principle of construction of lifting surface with mentioned given difference between a.c. positions are shown on the fig. 2. This principle allowed to solve the problem of longitudinal trim of the tailless vehicles or ones with very small horizontal tail without the significant losses of $(L/D)_{\max}$ -ratios at supersonic speeds.

The further TsAGI computational and experimental investigations have shown that the CPW had the others important properties.

It was established that:

- at subsonic speeds the lifting characteristics of such wings are non-linear favorably and by the adding the strake to base wing the lift increases, fig. 3 (the area of base wing was taken for the coefficient \overline{C}_L calculation);

- due to very big chords in the root sections it is possible to realize practically for CPW the small relative profile thicknesses $\overline{C}_{\max} \sim 2\%$ and therefore to decrease the wave drag and increase L/D-ratios at $M > 1$ and at the same time to provide the big useful volumes for the fuel ;

- CPW with very high angles of strake sweep have the subsonic LE on the significant part of span at the supersonic cruise M numbers and this gives the possibility to gain in the values of $(L/D)_{\max}$ -ratios and receive the

positive increment of C_{mo} by means of optimization of mean wing surface forms, fig. 4;

- the CPW lift is produced on the high length in flow direction and this allows to diminish the sonic boom level;

- at the high subsonic speeds the designs may have the big CPW area and relative small values of drag at zero lift and this compensates the increase of induced drag due to small aspect ratio; besides the beginning of wave crisis moves to the high M numbers, therefore at transonic $M \sim 0,95$ these designs may have higher values of L/D-ratios than designs with conventional high aspect ratio wings;

- at supersonic and hypersonic speeds the use of CPW provides the receipt of high level of aerodynamic perfection;

- CPW have the favorable structure and strength characteristics because it is possible to realize for its the more uniform loading distributions in chord and span directions and diminish the bending moments in root wing sections.

Therefore the CPW give to the constructors the unique possibilities for receiving the good aerodynamic characteristics as at supersonic so at subsonic and transonic speeds. It is no coincidence that the CPW found the wide spreading in Russia and abroad first at all in design of SST Tu-144 which had made its maiden flight on 31. 12. 1968 yr and then in many supersonic manoeuvre and non-maneuvre airplanes up to the aerospace vehicles "Shuttle" and "Buran".

The significant increase in the number of flight regimes and geometrical parameters at aerodynamical designing of SST with CPW demands the wide use of modern computational methods. At choice of these methods it is necessary to take into account the physical flow peculiarities for designs with CPW and in particular the non-linear change of the aerodynamic characteristics at high angles of attack.

The analysis of the wing pressure distributions and flow patterns obtained by the visualization method gives the more full view about the nature of such non-linear peculiarities. At subsonic speeds and high angles of attack the flow separations in the regions of thin leading edges generate above the wing upper surface the strong vortexes wick intensity increases with the angle of attack growth. Under these vortexes on the wing surface the significant pressure reductions take place and this leads to non-linear changes of the CPW lift coefficients.

The flow pattern, fig. 5, gives the visual ideas about the vortex generation above the CPW upper surface.

On the fig. 6 for example the typical pressure distributions are given for the wing-fuselage model ($\chi_{cr}=78^0$; $\chi_0=60^0$; $\bar{z}_{cr}=0,44$; $\lambda=1,4$) tested in the wind tunnel T-102 TsAGI at low subsonic speeds ($V=50$ m/s). These

distributions have the peaks of strong pressure reduction on the upper surface and these peaks are located more back in the chord direction at the transition from the root to tip wing sections. The position of these peaks correspond to the vortex projections on the wing surface.

The changes of the section lift coefficients in the dependence of angle of attack $C_{Lsec}=f(\alpha)$ are shown on the fig. 7. It is seen that the C_{Lsec} values increase non-linear with the rise of angle of attack but in the tip wing sections this rise stops at comparatively small critical angles of attack.

An intensive vortex generation above the upper wing surface takes place not only at subsonic speeds but also at supersonic speeds. The presence of strong vortex may be detected with the high-voltage discharge method [3]. Typical flow pattern is shown on fig. 8. The light discharge lines correspond to the vortex with minimum pressure.

The vortex flow leads to significant non-linear changes of loading on upper wing surface, fig. 9. At the angles of attack $\alpha \geq 8^\circ$ linear theory does not reflect the real characteristics even qualitatively. Therefore for the calculations of CPW aerodynamic characteristics at high angles of attack it is necessary to develop and use the non-linear methods taking into account the detached vortex flow above the upper wing surface. As example of using one of such methods the results of vortex fields calculation are shown on fig. 10 for the SST design with foreplane at $\alpha = 10^\circ$ and $\beta = 10^\circ$ [4].

At the same time there are many cases which may treat on base of linear methods. To this cases it is possible to relate the problems of calculations of the lift derivatives, the positions of wing aerodynamic center and some problem of aerodynamic forms optimization.

For illustration on the fig. 11 the charts of dependencies $C_L^\alpha \beta = f(\sigma_0)$ are given, where $\tilde{h} = h/c_{oo}$, $\beta = \sqrt{M_\infty^2 - 1}$, $\sigma_0 = \beta \text{ctg} \chi_0$ (it is the similarity parameter), $\bar{z}_{cr} = 2z_{cr} / b$ (see fig. 1).

To obtain the CPW with given difference $\Delta \bar{x}_{a.c.}$ in the aerodynamic center positions at low subsonic and cruise supersonic speeds it is necessary to compare the results of corresponding calculations as it is shown on fig. 12-13. With such procedure the dependencies $\bar{h} = f(\bar{z}_{cr})$ were obtained that defines the required values of relative heights of strake $\bar{h} = h / b$ at given $\Delta \bar{x}_{a.c.} = \text{const}$, fig. 14. There are the values of \bar{z}_{cr} for which the condition $\Delta \bar{x}_{a.c.} = \text{const}$ is fulfilled at minimum values \bar{h}_{min} .

Optimization of SST-2 aerodynamical designs.

The SST-1 was designed on the transportation of commercial load $G_{c.1} = 12-15 \text{ t}$ (120-150 passengers) on the range $L = 6000-6500 \text{ kms}$ with cruise $M = 2.2$. The problem of achievement such flight data was

very difficult for that time. The aeroplane had to have the very high levels of aerodynamics, $(L/D)_{\max}=7,8-8$ at $M=2,2$, power plant characteristics and relative fuel weight parameter.

The SST-2 must be more effective than SST-1. It is supposed that SST-2 must be designed on the transportation of $\sim 300-350$ passengers on the range $L=9200$ kms. To solve this more difficult problem it is necessary to refcy the further increase (L/D) -values at all regimes of flight.

The basic ways of improving SST-2 aerodynamic are:

- optimization of wing mean surface shape;
- optimization of volume distribution over wing chord and span,
- optimization of fuselage shape; use of area rules;
- implementation of favorable wing nacelle interference, optimization of boundary layer bleeding system; increase of efficiency of intakes and nozzles,
- decreasing relative areas of fuselage and nacelles mid-sections down to ~ 1 and $\sim 1.5\%$, accordingly, by increasing wing area up to ~ 1000 m²,
- optimization of wing plan form; using base wing of higher aspect ratio to increase $(L/D)_{\max}$ and lifting characteristics at $M < 1$,
- adaptation of nose and rear wing parts for transonic velocities,
- use of static longitudinal instability at take-off and landing flight modes and small stability margins at $M > 1$,
- use of effective take-off wing high-lift devices such as vortex leading edge flaps to reduce required thrust of engines and noise.

The investigations in this directions are actual for SST-2. ' 1

Optimization of wing mean surface forms.

The linear theory methods allowed to solve the inverse problem of definition the optimal wing mean surface forms for increase the lift-to-drag ratio at supersonic cruise speeds. The experimental investigations of the SST-1 Tu-144 model confirmed that the optimised forms of wing mean surface give the significant gains in the lift-to-drag values at $M=2,2$, fig.4.

The computational investigations show that the potential gains in (L/D) increase depend from the wing planform. The key-results of this investigations are represented on fig.15. Its show that the gains in lift-to-drag ratios raise with increasing the sweep angle of strake χ_{st} and reach the maximum values at $\chi_{st} \sim 78^{\circ}-80^{\circ}$. As a consequence the CPW may have significantly higher level of lift-to-drag ratios at cruise supersonic velocities.

The second important result consists that the change of base wing leading edge sweep angle practically does not influence on the lift-to-drag ratios and consequently may be chosen from others considerations fs will

be shown in the next paragraph. As particular the decrease of the base wing sweep angle leads to raise the lift-to-drag values as experimental results of fig.16 show.

Aerodynamical designing of two-regime SST-2

To fulfil the two-regime demands SST-2 must have equal values of range parameter $(L/D)_{cr} M_{cr}/C_{e_{cr}}$ at $M_{cr}<1$ and at $M_{cr}>1$. For given cruising values of specific fuel consumption coefficient $C_{e_{cr}}$ and M_{cr} -number the achievement of equal flight effectiveness is possible for appropriate relations between subsonic and supersonic cruising values of $(L/D)_{cr}$. These relations must be provided by aerodynamic design methods.

It is shown that the most effective aerodynamical means for regulation of $(L/D)_{cr}$ ratios are the choose of the appropriate wing planform and using the adaptive deflections of wing nose flaps and elevons.

The main parameter of complex planform wings by subsonic speeds is aspect ratio of base wing λ_0 , fig. 1. The increase of λ_0 may be reached by decreasing of sweep angle of base wing leading edge χ_0 .

At supersonic cruising M numbers the change of base wing sweep angle does not significant influence on the potential level of $(L/D)_{max}$, fig.15-17. Hence it is possible to vary in wide limits the base wing sweep angle and by this means to regulate the $M(L/D)_{max}/C_e$ values at subsonic cruising M numbers, fig.17.

It is known that downward deflections of wing nose flaps allows to increase the lift-to-drag ratios at subsonic and transonic speeds of flight when the wing leading edge is subsonic one, fig.18-19. This effect may be used for the regulation the relation between subsonic and supersonic ratios too. It is possible to provide the two-regime demands by the some more sweep angles of base wing that may be useful for decreasing of the SST-2 structure weight. The nose deflection on the outer wing parts. gives the most contribution.

The results of calculations shows, that SST-2 designed as two-regime plane will have the same values of range parameter $(L/D)V/C_e$ at subsonic ($M\sim 0,95$) and supersonic ($M\sim 2,0$) cruising flight velocities. This means that the fuel consumptions pro 1 km of flight are about the same at $M=0,95$ and $M=2,0$ and that this SST-2 is a really two-regime plane. As a result this plane will have equal ranges at $M_{cr}=0,95$ and $M_{cr}=2,0$, fig.26. The changes of flight ranges by the transition from supersonic cruise speed to subsonic one and vice versa are very small. It is very important for two-regime SST-2 which can fly on the combined routes with the subsonic segments of flight.

The take-off characteristics and wing devices

The main requirement to take-off aerodynamic characteristics SST-2 is achievement of high lifting properties and lift-to-drag ratio on take-off angles of attack.

It is known that the angle of inclination, θ , of the air rectilinear part of take-off trajectory is depended on the plane thrust-to-weight ratio $\varphi=T/W$ and the balanced lift-to drag ratio, (L/D) :

$$\sin \theta = \varphi - \frac{1}{(L / D)_{\text{bal}}} .$$

The thrust of power plant is strictly limited by community noise norms. In our case the variant of throttling the engines thrust up to $0.4T_{o,\text{max}}$ is considered. It is very difficult to satisfy to demand that the tangent of take-off flight path must be according to norms more than 0.05. It was shown than the lift coefficient C_L must be less or equal than 0.6, fig.20.

For the increase the take-off lift-to-drag ratio it is necessary to diminish the C_L values that can be reached by means of diminution the wing loading to values $W_0/S \sim 310 \text{ kg/m}^2$.

A distinctive feature of SST-2 configuration is the use of wing with relatively small angles of outer wings, that permits to increase wing aspect ratio up to 2.2 (in comparison with 1.67 at SST-1 Tu-144) and by that to increase lifting properties and lift-to-drag ratio at takeoff and landing .

The use of the leading edge flaps in a combination with a deflection downwards of the elevons along trailing edge of wing is stipulated in configuration SST-2. Such mechanization of the wing permits to increase essentially the values of C_L at $\alpha=\text{const}$ and lift-to-drag ratio at $C_L=\text{const}$, fig. 20-21. The angles of elevon deflection will be about $\delta_{ev}=10^0 \div 12^0$ on the main take-off regime. On the fig.22 the pressure distributions over upper surfaces of vortex flaps are shown (\bar{X} -is the distance from vortex flaps LE related to flap chord and measured along the perpendicular to flap LE. It is necessary to pay attention to large pressure reductions for flap section iii. This is the most effective flap part for increasing the lift-to-drag ratio.

Deflection of the elevons on the positive angles, however, gives an increment of the coefficient of pitching-down moment. For compensating of this moment and maintenance thus trim condition at the take-off values C_L various ways can be applied.

Variant of trimming with the elevons at choice of appropriate aft center of gravity position, as well as creation positive increment of a pitching moment coefficient with unflat wing mean surface was accepted. The configuration with aft c.g. position and appropriate small degree of static longitudinal instability was chosen to improve the SST-2 take-off aerodynamic characteristics .

Investigations of sonic boom levels for various SST-2 designs

Recently standard solution of a problem of sonic boom for a supersonic passenger airplane of the second generation is the full refusal of flight on supersonic speed above the occupied land. The SST-2 flights on supersonic speed will be made only above a water surface of the seas and oceans or above the not occupied parts of a land. In these conditions the small changes of sonic boom levels Δp have not basic value. It is known, for example, that in a water the phenomenon of sonic boom in general is absent, and the surface world of marine mammals in main lives in coastal areas, above which SST-2, as a rule, will fly over with subsonic speeds. At arrangement of the airport in a coastal zone, when the trip line places above a water surface, subsonic trip segments of climbing and downward flight above a water surface have the length not less than hundred kilometers. In these cases the requirement of flight above a coastal zone with subsonic speed is not the limiting factor.

The prohibition of supersonic flights above the occupied land demands that SST-2 should be two-regime plane which is capable to have the equal effectiveness of flight on supersonic and subsonic velocities. Nevertheless, for SST-2 the research of measures of sonic boom decrease is of interest, if these measures are not accompanied by deterioration of aerodynamic and weight efficiency of a plane. In particular, it would be desirable, that the levels of sonic boom from SST-2 were commensurable with Δp for SST-1 Tu-144 and Concorde, despite of essential larger (in $\sim 2,5$ times) wing area. In this connection the problem of decreasing of sonic boom levels for SST-2, in a way, remains urgent.

It is natural, that for SST-2, which is primary designed for fulfilment of supersonic flights above water surfaces or above the not occupied land, those measures and modifications of baseline configuration lowering sonic boom can be recommended only which do not render adverse effects on flight characteristics of a plane. For example, the measures leading to decreasing of the values $(L/D)_{\max}$ or to deterioration of weight efficiency of a plane are unacceptable.

It was shown that:

- the increase of cruising C_L values leads up to decrease of sonic boom level Δp ,
- the increase of cruising M number leads up to small decrease of Δp ,
- the raise of wing area reduces Δp ;
- the decrease of wing loading allows to reduce Δp .

There are a number of modifications of base configuration which reduce sonic boom levels and thus, as a minimum, do not worsen aerodynamic efficiency of the plane. To such measures it is necessary to relate:

1- optimization of the mean wing surface form raising $(L/D)_{\max}$ and lowering levels of sonic boom in comparison with a flat wing configuration;

2- applications of V-form of a wing (dihedral angle $V = 5^\circ$), which essentially reduces sonic boom intensity without deterioration of $(L/D)_{\max}$ values;

3- displacement of a wing back on length of a fuselage ($\Delta x < 5-10$ m);

4- small displacement of a wing on altitude of a fuselage, Δy ;

5- applications small foreplane in case when its installation is necessary under the requirements of maintenance of the acceptable characteristics of the airplane stability and controllability.

Comparison of relations $\Delta p = f(H)$, fig. 23 shows, that the combination of the considered modifications of base configuration results in significant reduction of sonic boom intensity from 148 up to 108 Pa at $C_y = 0,1$. This result confirms the capability of achievement for SST-2 the same sonic boom levels as for SST-1 Tu-144 and Concorde ($\Delta p \sim 120 - 130$ Pa).

The baseline variant of Russian SST-2

The baseline variant of Russian SST-2 is shown on fig. 24. For comparison on fig.25 it is shown the plan view of SST-1 Tu-144 too in the same scale.

The comparatively small sweep angle of SST-2 wing consoles is the distinctive peculiarity of the aerodynamical wing design. The diminution of sweep angle allowed to increase the wing aspect ratio to $\lambda \sim 2,5$ (SST-1 had $\lambda = 1,67$) and improve the lifting characteristic at take-off and landing regimes. It is foreseen to use the nose flaps deflection on the consoles in combination with deflection elevons along the wing TE. Such devices allow to rise the lift-to-drag ratios at take-off.

According to the Russian conception the SST-2 must have the next main data:

Maximum take-off weight, t	380
Wing area, m ²	1200
Range, kms	9200
Passenger capacity	350

The CPW has a big strake with relative span $\bar{Z}_{st}=0,5$ and optimized forms of wing mean surface and thickness distribution. This provides the high required levels of lift-to-drag ratios on cruise supersonic ($M=2$) and subsonic ($M=0,93$) regimes, fig. 25.

The SST-2 will have the maximum weight $G_0 = 380$ t; this allows to realize required passenger capacity and range of flight.

The results of preliminary estimations fulfilled on base the experimental and computational investigations show that the SST-2 will significantly exceed SST-1 in $(L/D)_{max}$ values, fig. 25.

The SST-2 will possess higher transport efficiency than subsonic passenger aeroplane and SST-1.

The SST-2 creating will allow to realize the most important ecology advantage of supersonic flights which consist in significant reduction of the flight time [7].

Reference

1. Л.Е.Васильев, С.И.Попов, Г.П.Свищев
Сверхзвуковой пассажирский самолет второго поколения
ТВФ, N1-2, 1994 г.
2. Аэродинамика, устойчивость и управляемость сверхзвуковых самолетов. (под редакцией академика РАН Г.С.Бюшгенса)
Москва, Наука, Физматлит, 1998 г.
3. В.И.Алферов, Т.И.Окерблом, А.И.Саранцев
Экспериментальные исследования вихревых течений около крыльев малого удлинения при числе $M=2,0$
Механика жидкости и газа, N5, 1967 г.
4. А.В.Воеводин, А.В.Зубцов, Г.Г.Судаков
Результаты расчета дозвукового обтекания потоком идеального газа аэродинамической компоновки СПС
Отчет НИО-2 ЦАГИ. 1998 г.
5. Л.Е.Васильев, И.В.Николаева
Экспериментальные исследования эффективности вихревых носовых щитков при малых взлетно-посадочных скоростях
Труды ЦАГИ, 1988 г.
6. Л.Е.Васильев, А.В.Климин, В.В.Коваленко
Исследование аэродинамических характеристик и уровней звукового удара для различных компоновок СПС-2
Отчет МНТЦ. 1997 г.
- 7, Л.Е.Васильев, Г.П.Свищев
Проблемы создания сверхзвукового пассажирского самолета второго поколения
“Полет”. 1998 г.

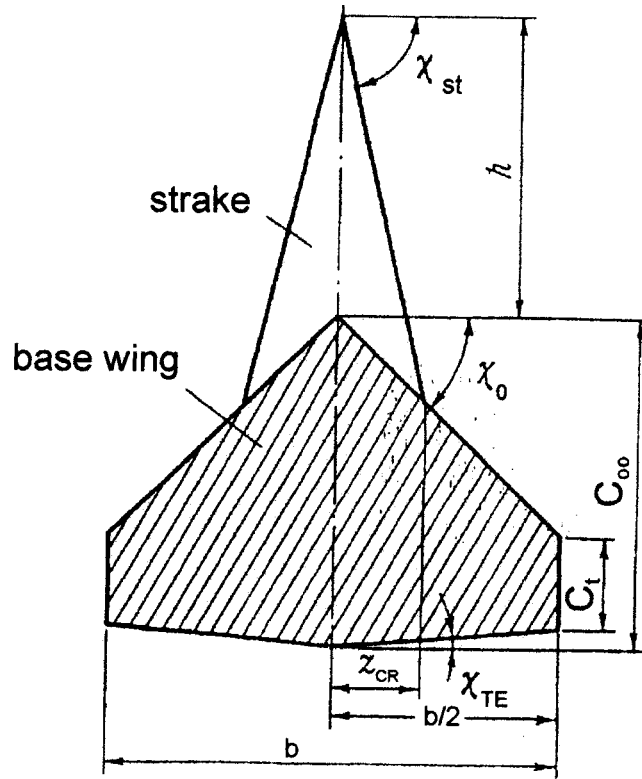


Fig. 1

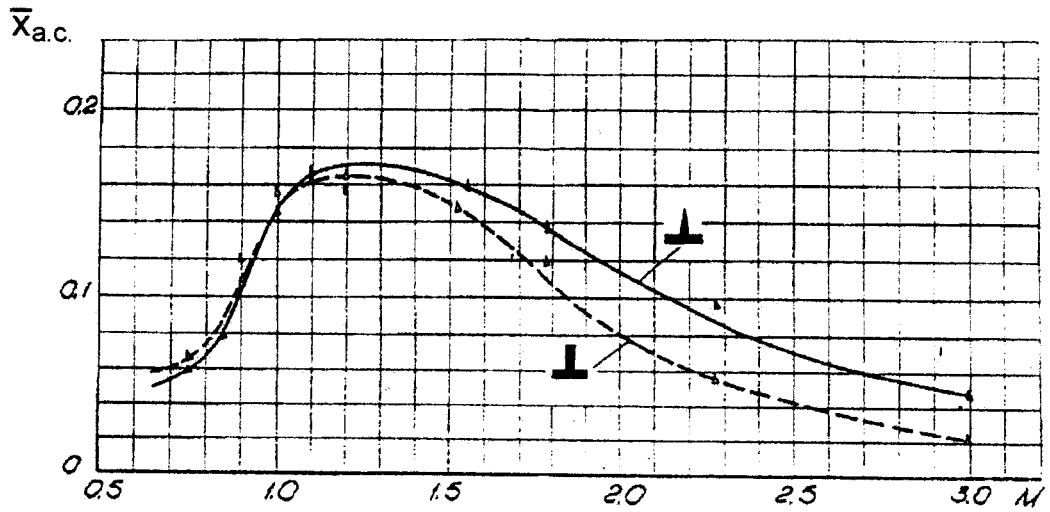


Fig. 2

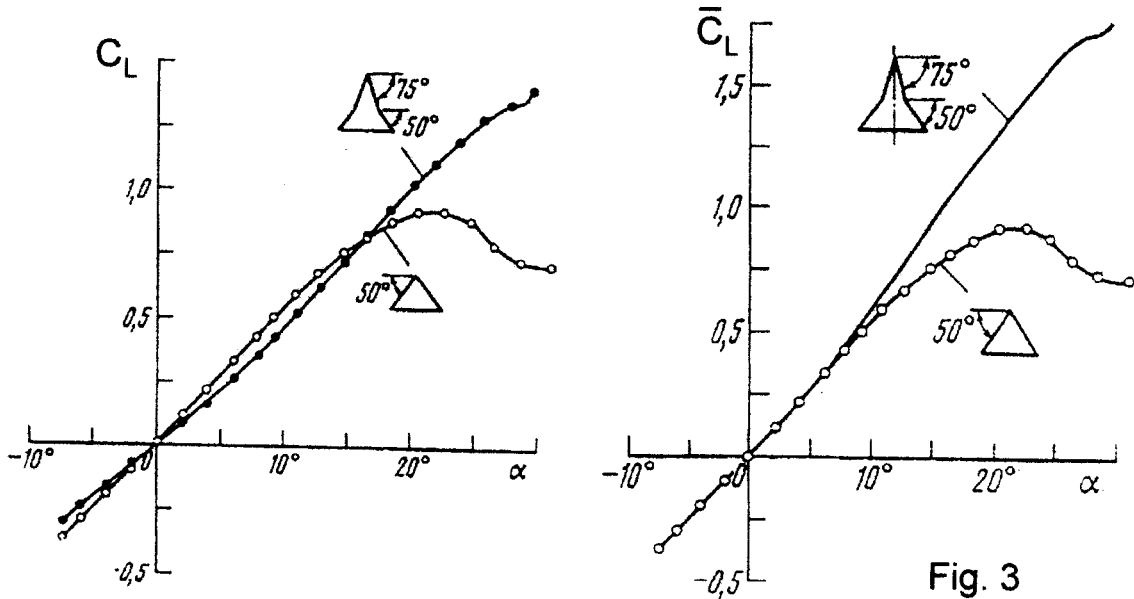


Fig. 3

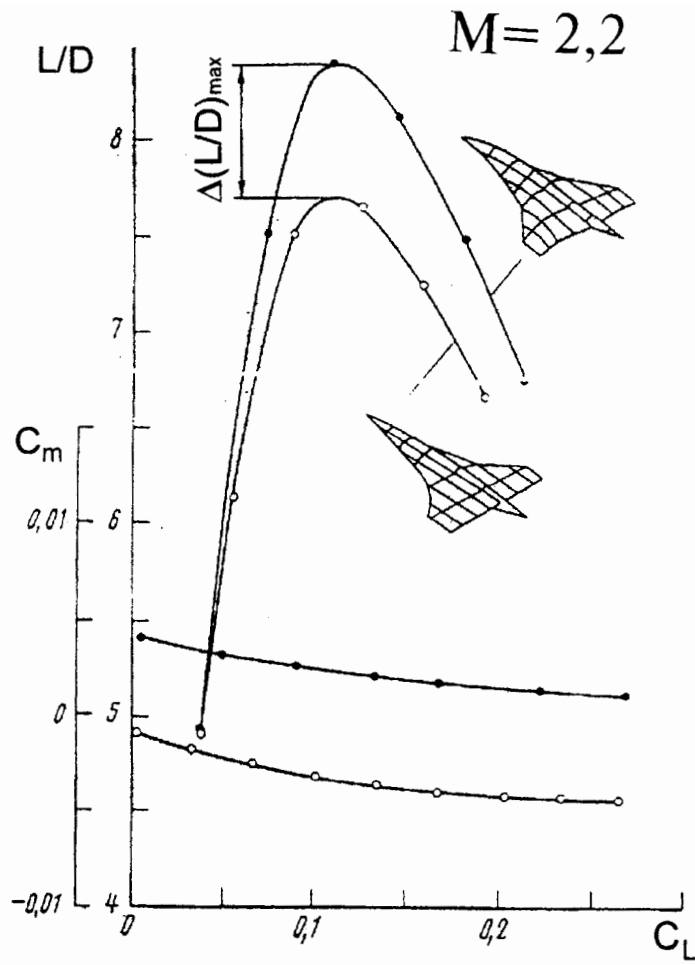


Fig. 4

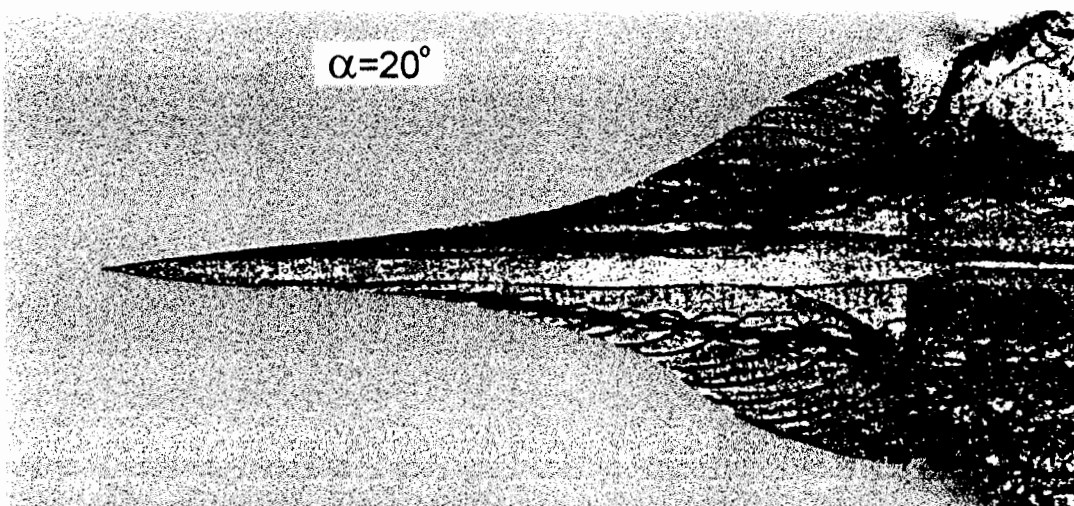


Fig. 5

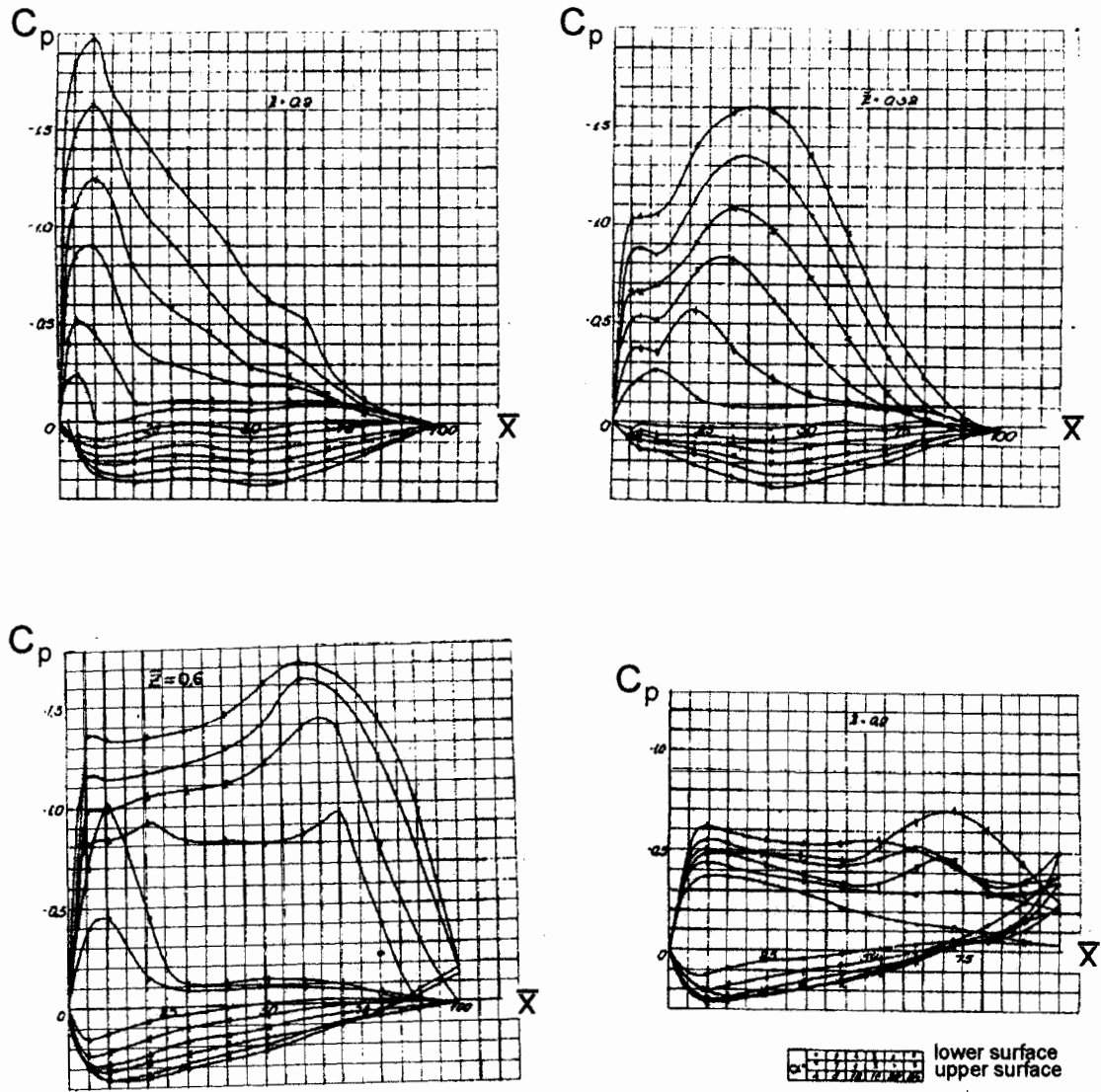


Fig. 6

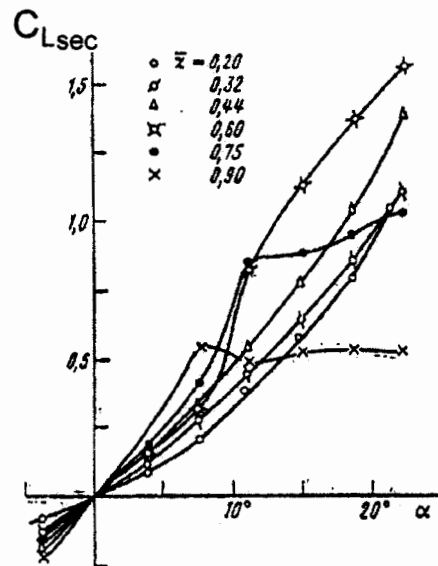
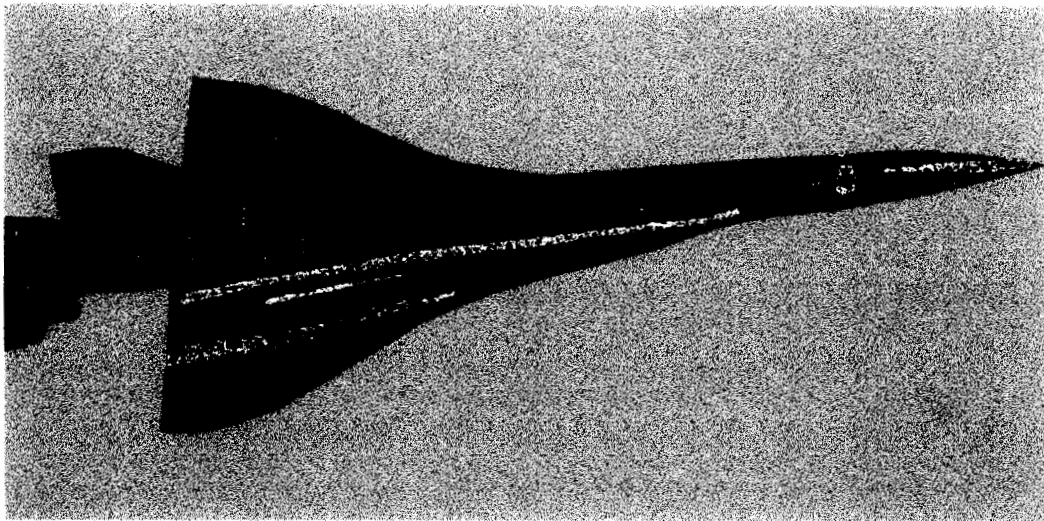


Fig. 7



$M=2.0, \alpha=10^\circ, \gamma=45^\circ$

Fig. 8

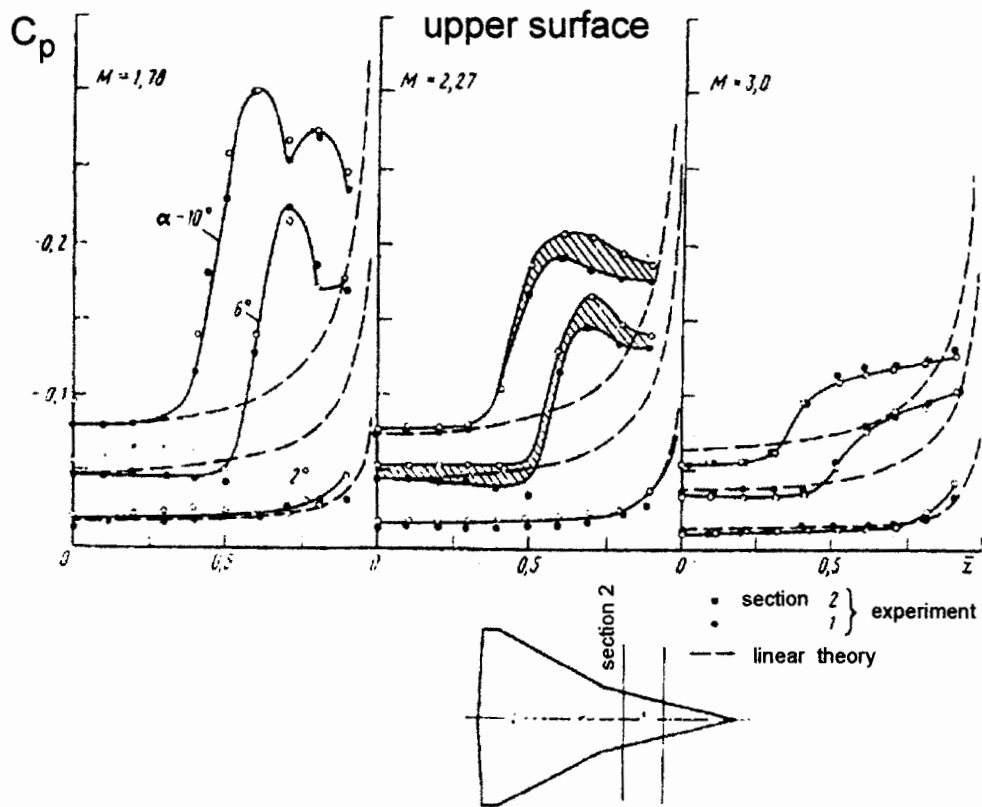
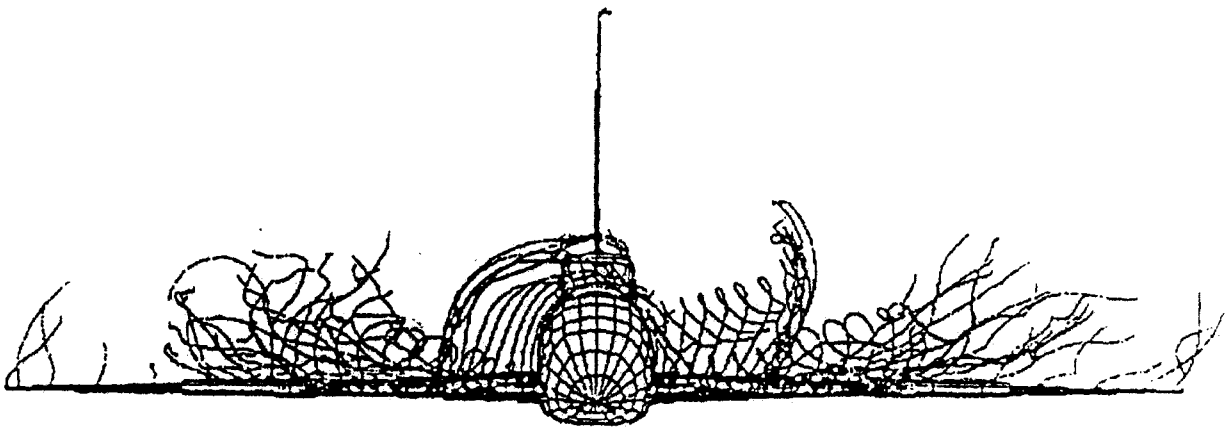
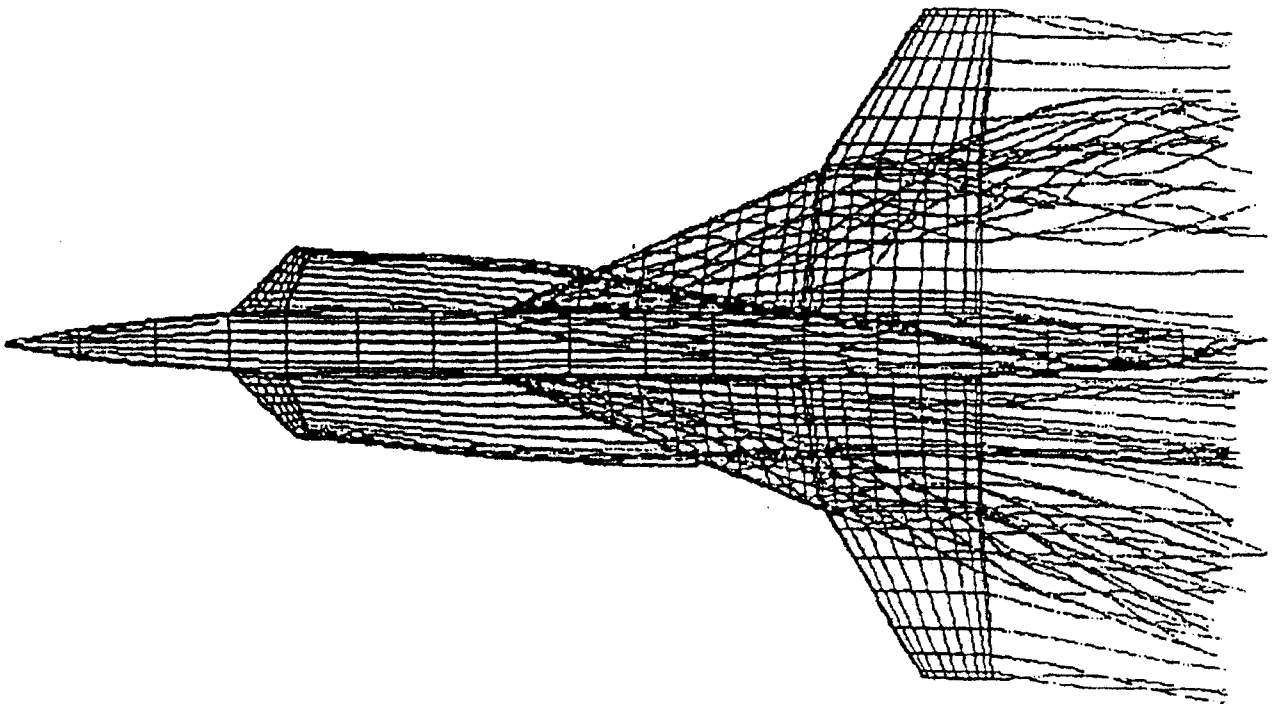


Fig. 9



$$\alpha = 10^\circ, \varphi = -8^\circ, \beta = 5^\circ.$$

Fig. 10

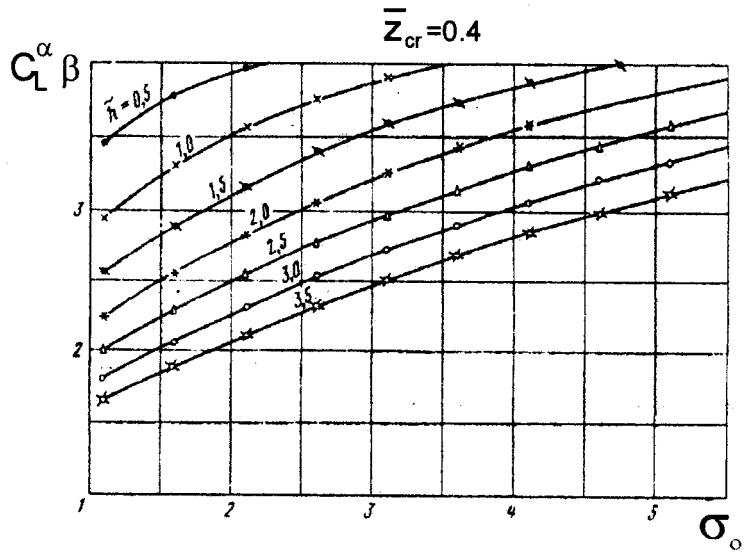


Fig. 11

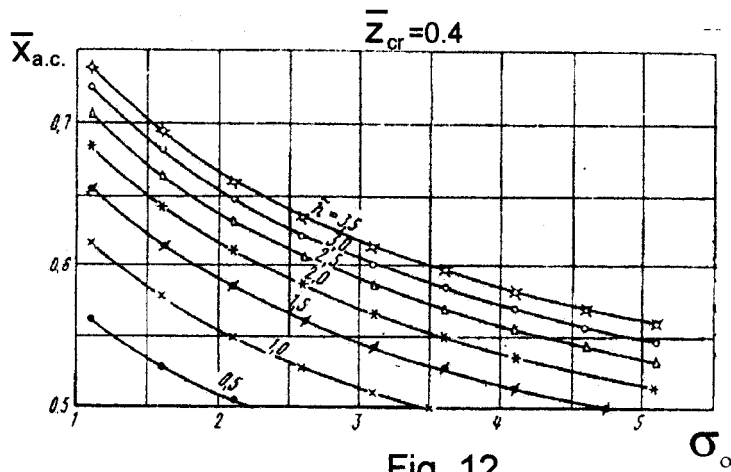


Fig. 12

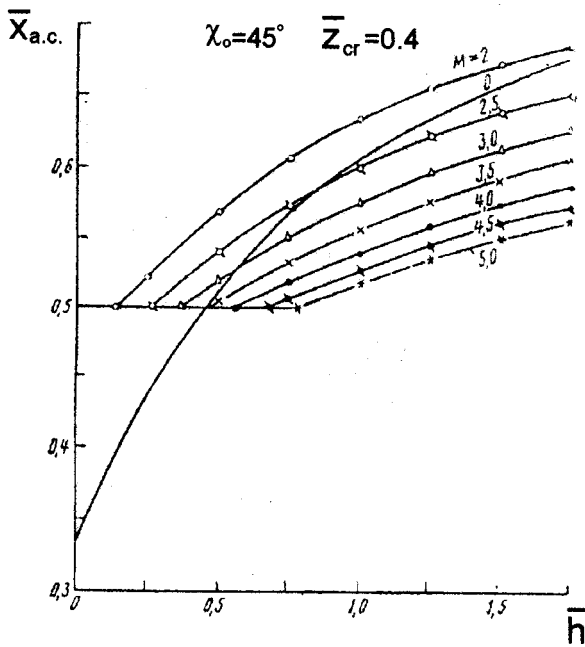


Fig. 13

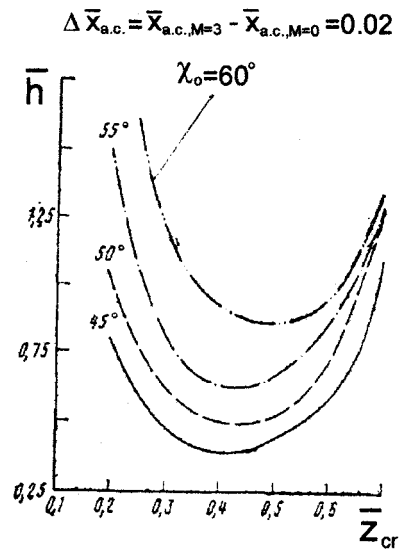


Fig. 14

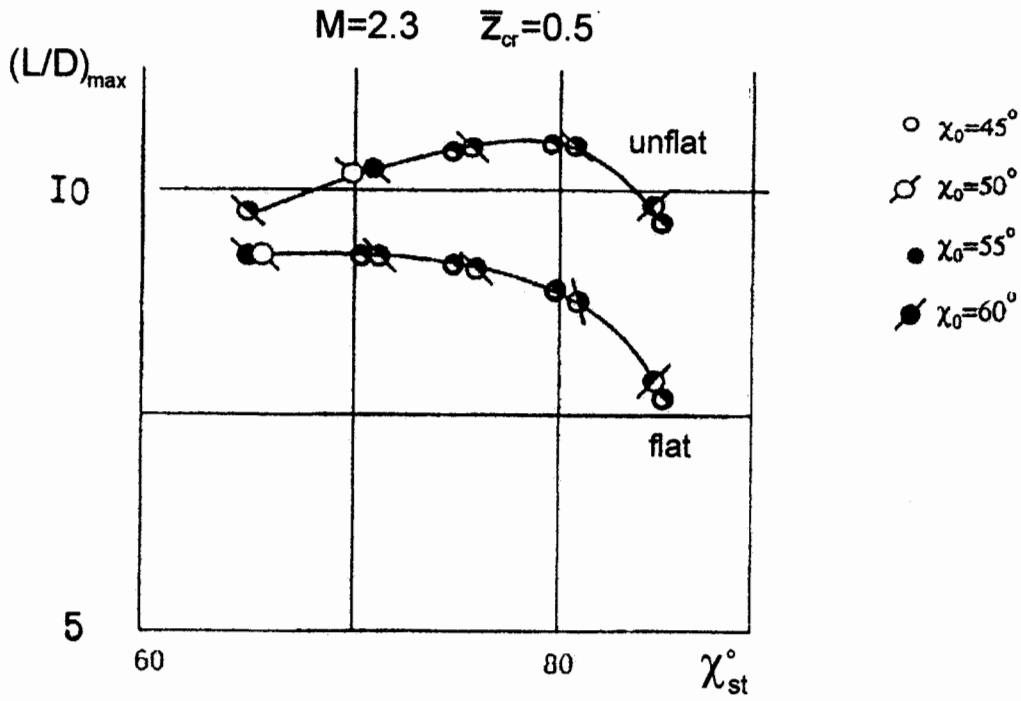


Fig. 15

$\eta_0=6; \chi_{st}=80^\circ$
 $\chi_0=50^\circ; \lambda=1.772$
 $\chi_0=55^\circ; \lambda=1.446$
 $\chi_0=60^\circ; \lambda=1.255$

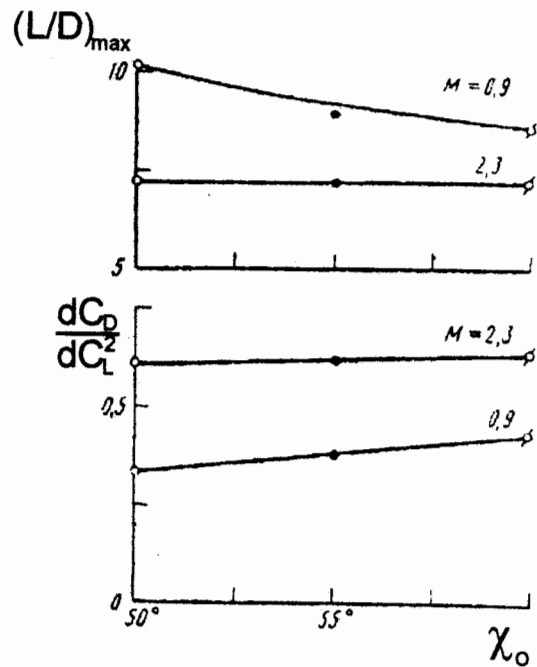
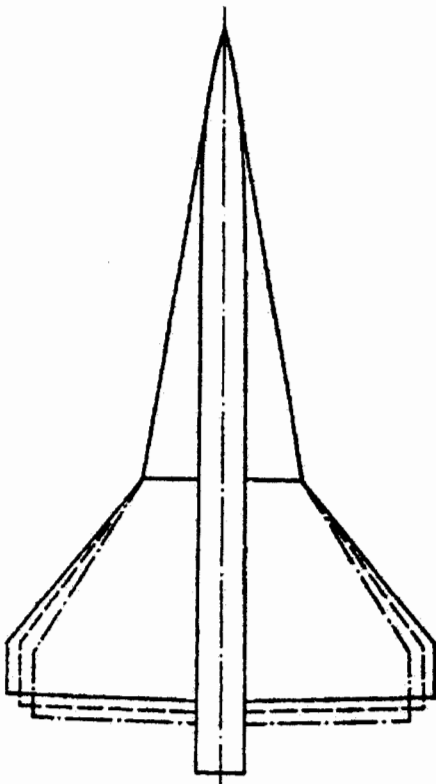


Fig. 16

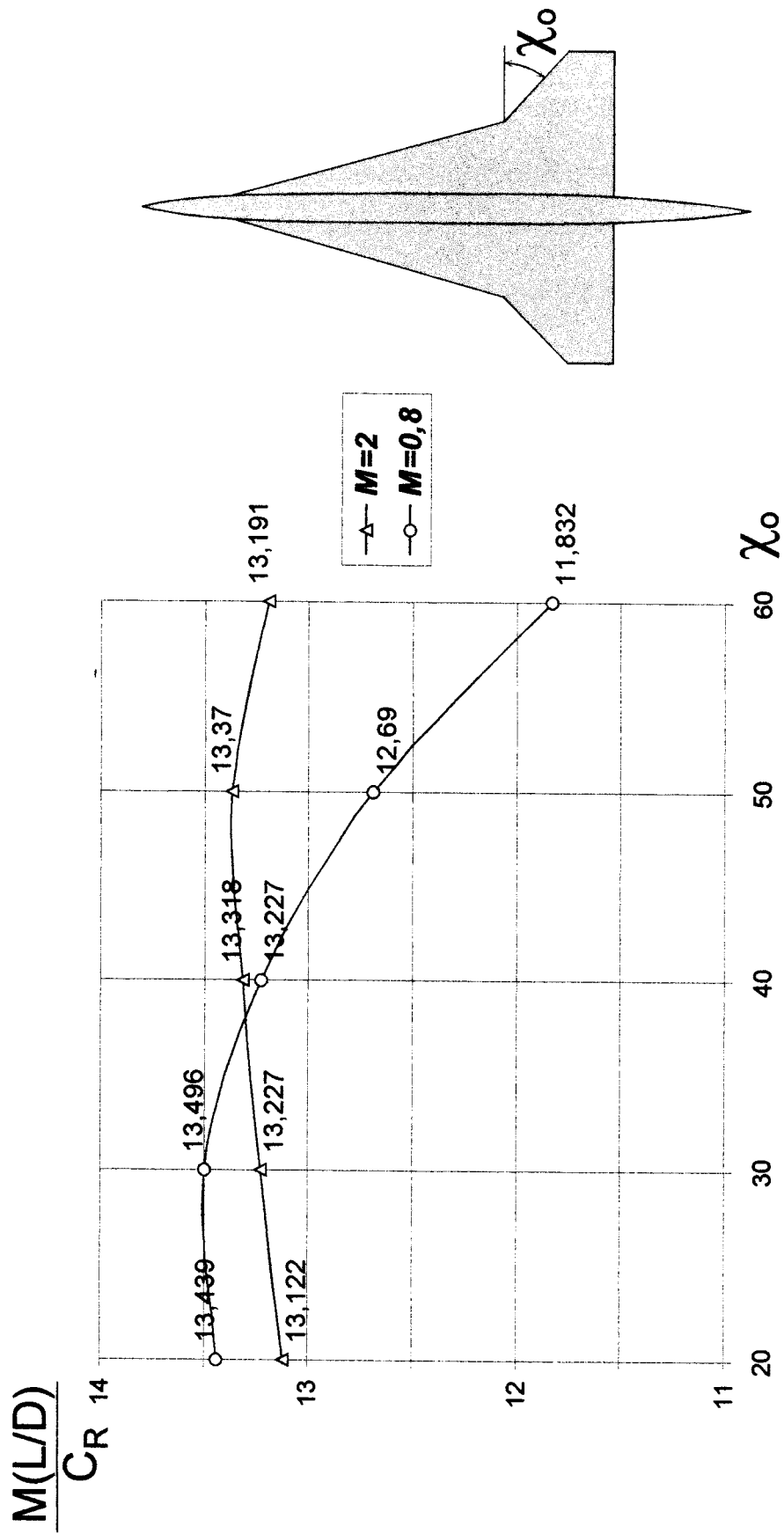


Fig. 17

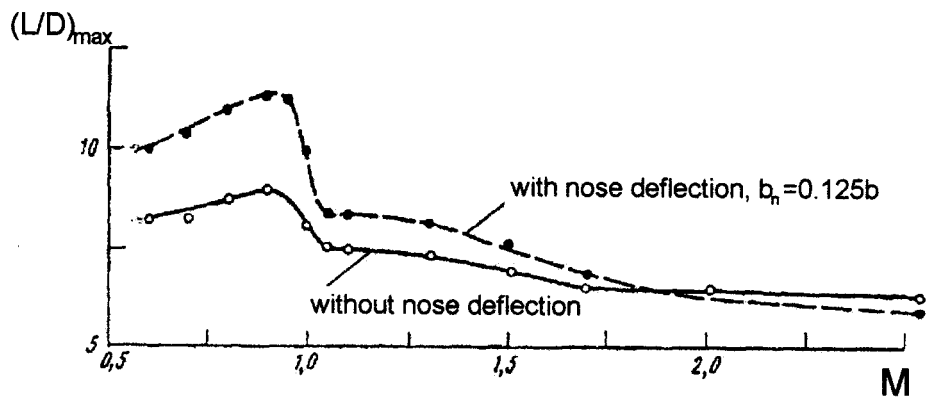
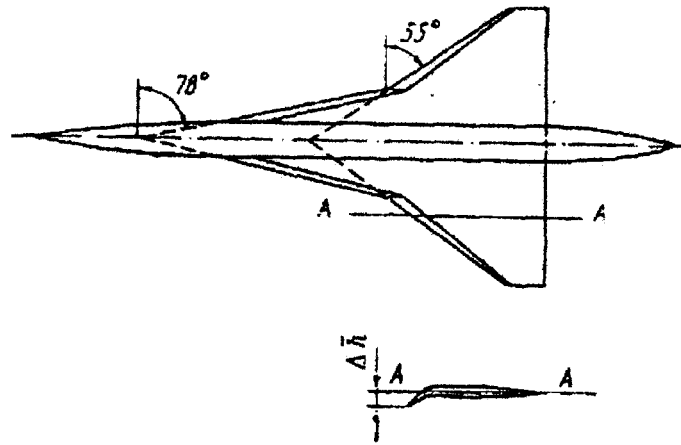


Fig. 18

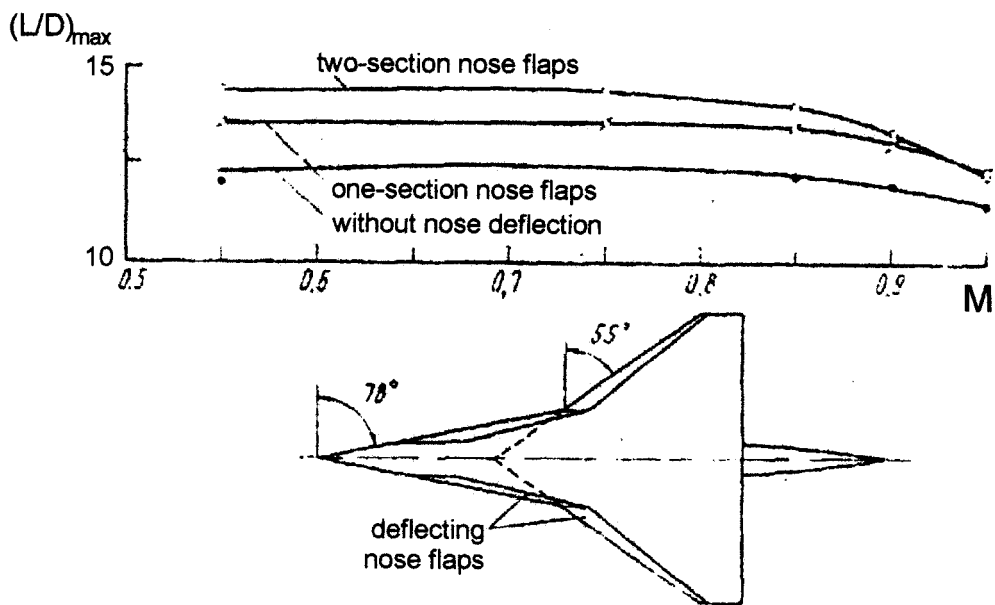


Fig. 19

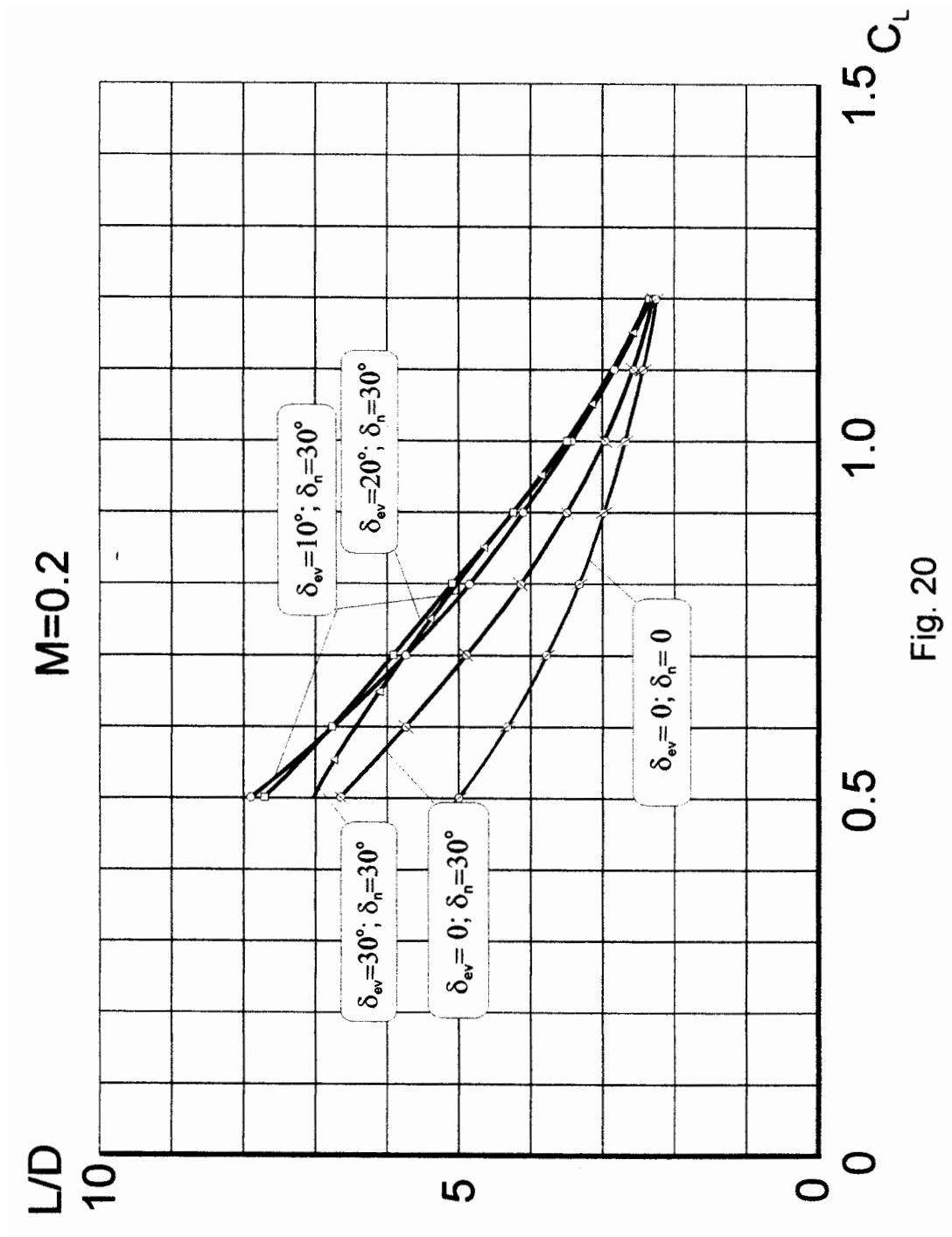


Fig. 20

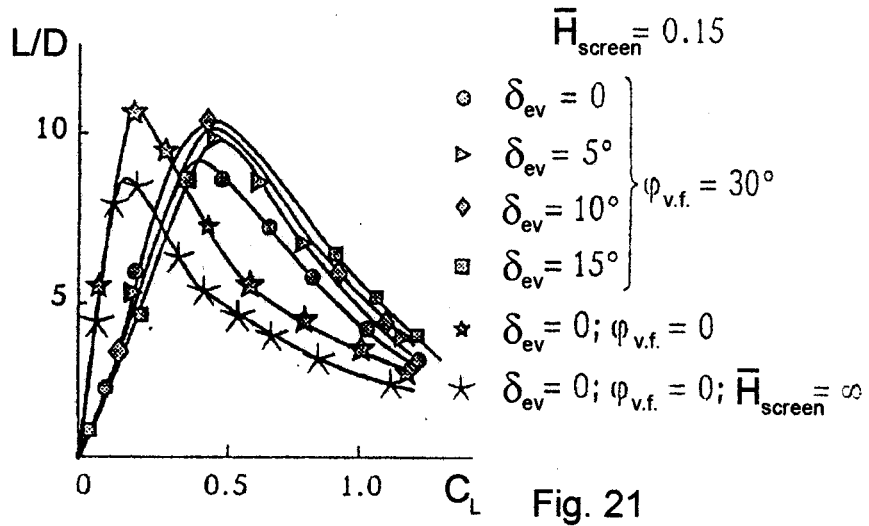
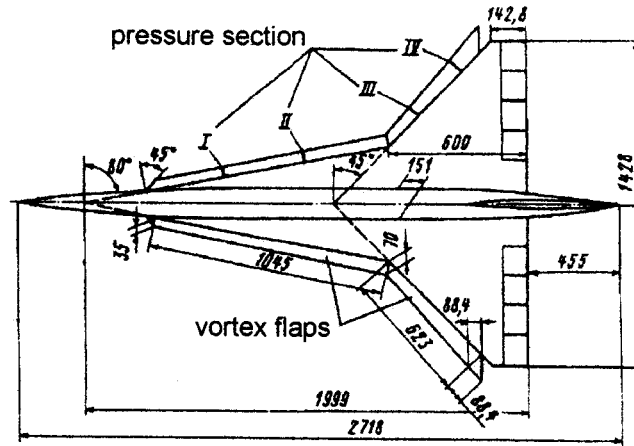


Fig. 21

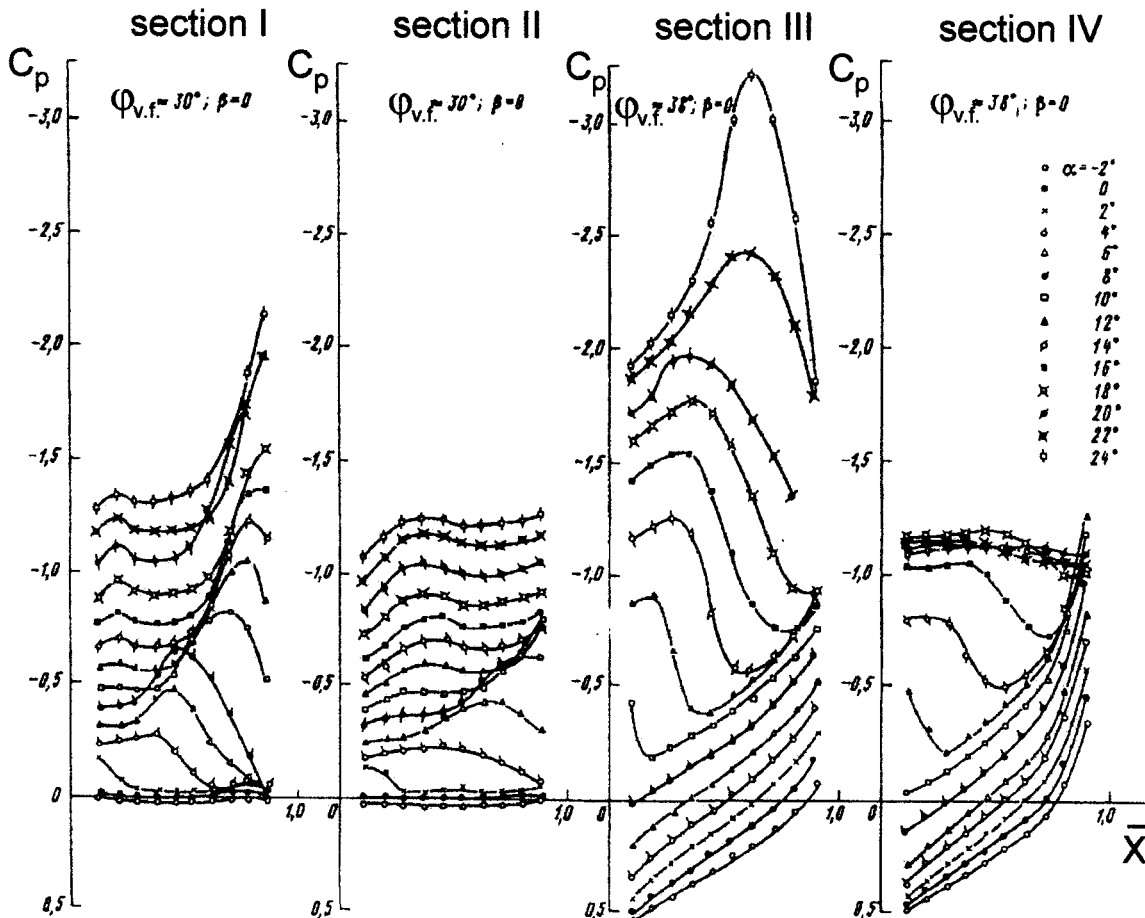


Fig. 22

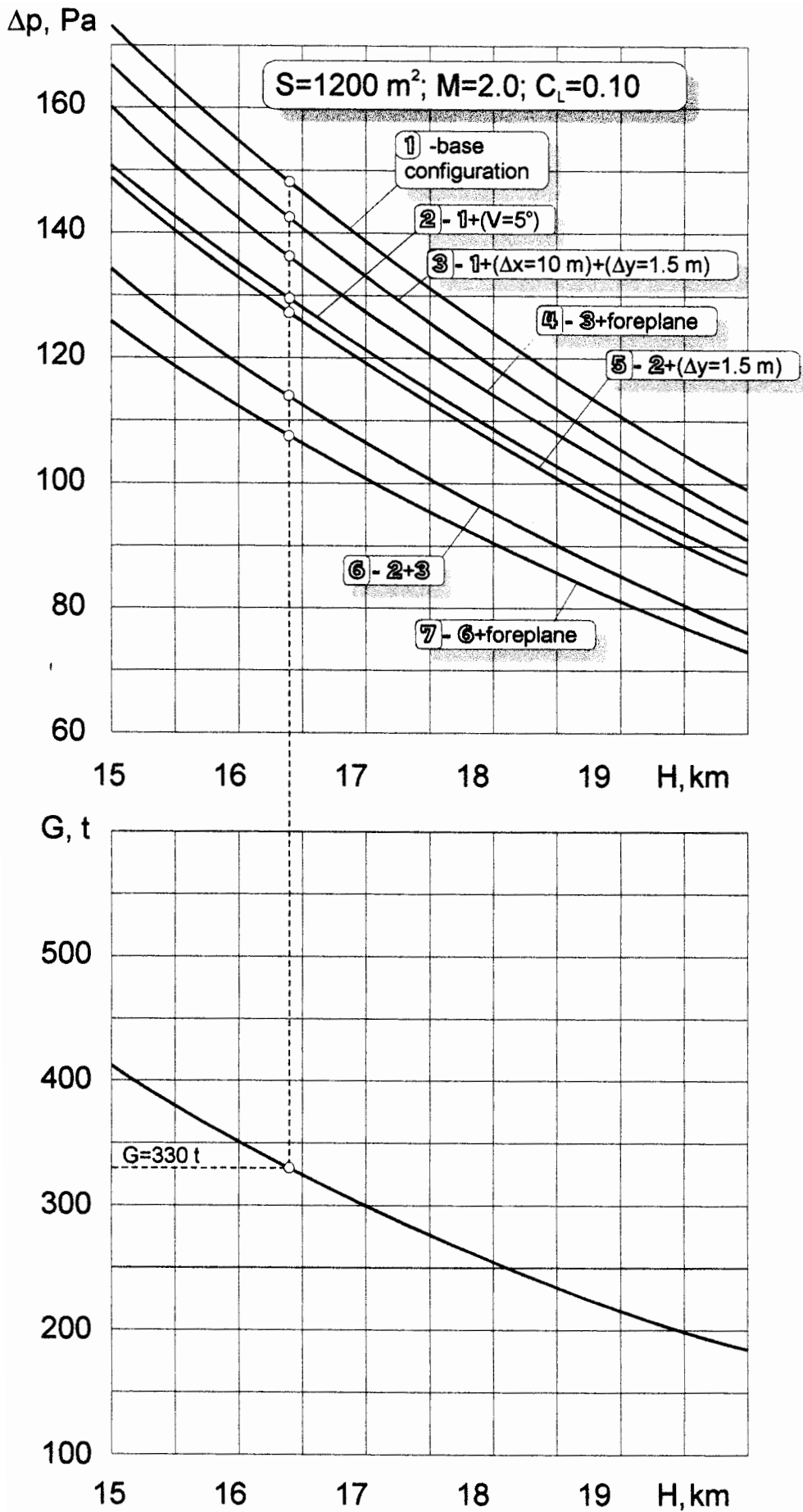


Fig. 23

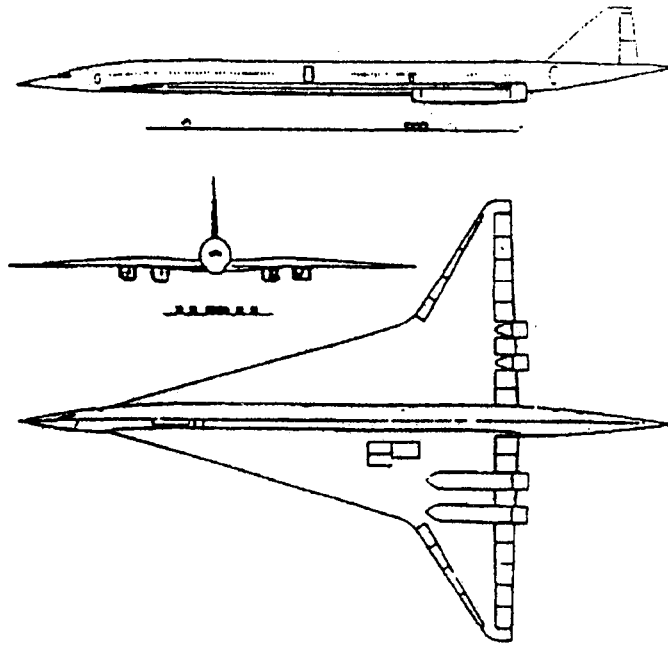


Fig. 24

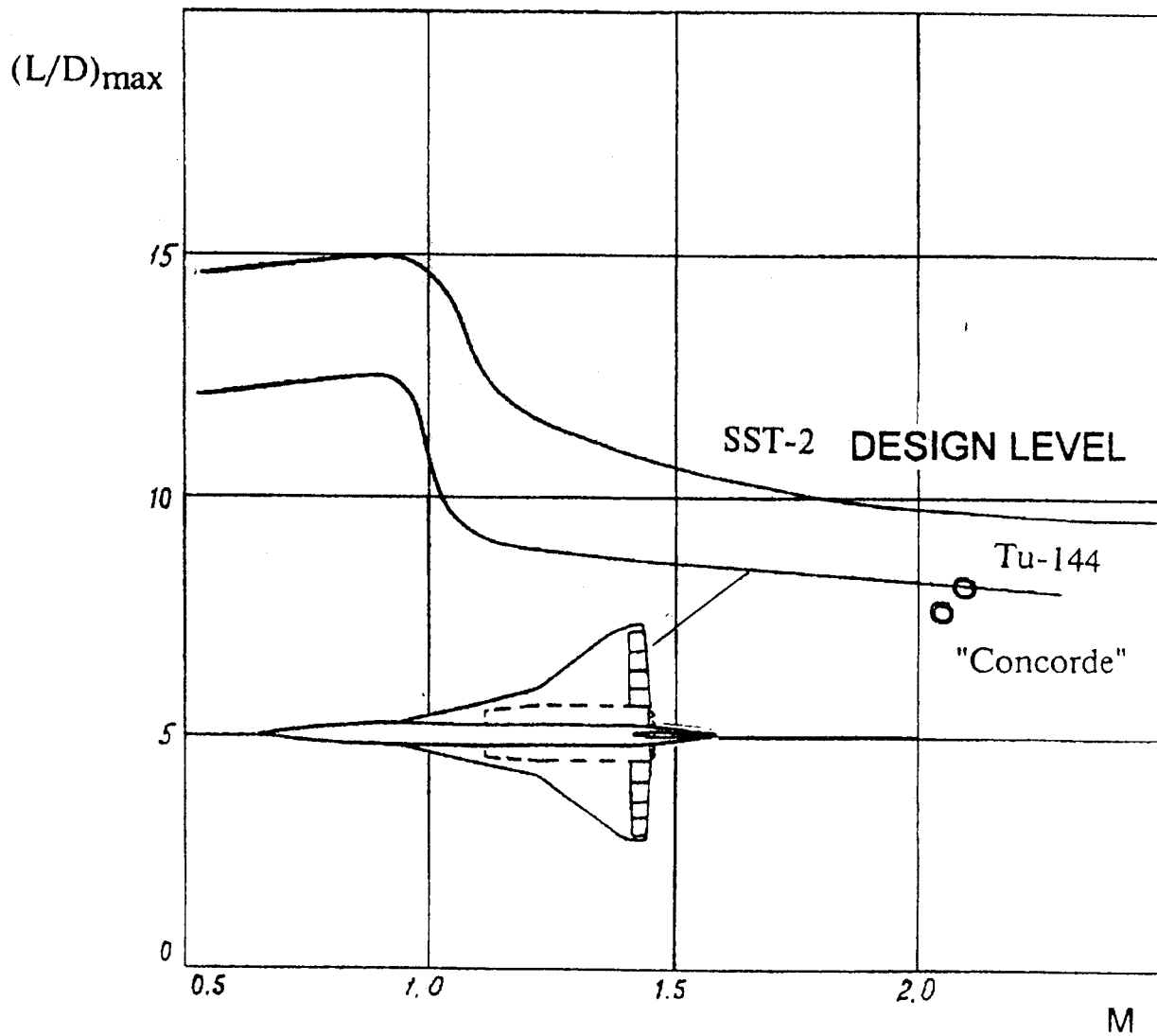


Fig. 25



“ ESCT propulsion system integration: Review and Progress”.

Authors : Thierry SURPLY , Damien PRAT

Aerodynamics department

316, route de Bayonne - 31060 Toulouse Cedex 03 - France

The three major European Aircraft Manufacturers have agreed on a common configuration for the future Supersonic Transport Aircraft: the ESCT. The economic viability of such an aircraft requires ambitious aerodynamic performances. Owing to its large impact on aircraft performances, the aerodynamic design of the future supersonic transport aircraft propulsion system is of utmost importance. The use of efficient CFD methods proves to be very helpful and powerful in designing the whole propulsion system. Through this process, AEROSPATIALE MATRA AIRBUS has developed know-how on both the internal and external parts of the propulsion system.

Although the internal component of the propulsion system, i.e. the air intake, engine and nozzle have to be studied as a whole, the internal performance of a supersonic air intake is highly dependant on overall aircraft configuration. It requires special care in the trade off between internal performance and external drag. CFD tools, which are able to simulate intake operation characteristics, added to overall expertise on intake design, were used to define and test a supersonic air intake.

The external design of the nacelles and propulsion system integration results from careful analysis of the flow pattern on the wing's lower surface. A complete propulsion system has been obtained which minimises the total aircraft drag, while considering local flow conditions and the strong interactions of the nacelles. Experimental data are presented which confirm the overall design process.

The high level of information provided by modern CFD methods is a key point for both internal and external flow analysis, while the various levels of modelling provide an appropriate cost effective answer to each type of physical phenomenon. The level of performance achieved is encouraging for a second generation supersonic transport aircraft feasibility, and AEROSPATIALE MATRA AIRBUS is continuing its research effort on supersonic aircraft.

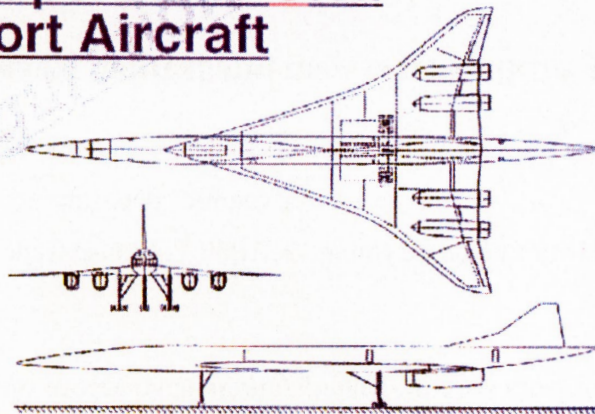
European Supersonic Civil Transport Aircraft

Wing Span : 42 m

Length : 89 m

MTOW : 340 t

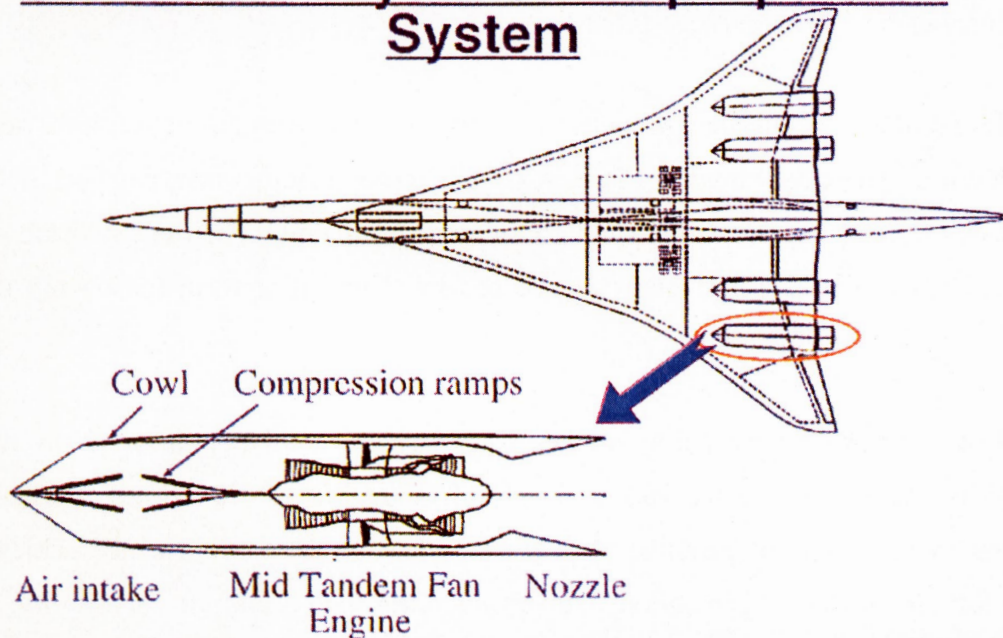
250 passengers

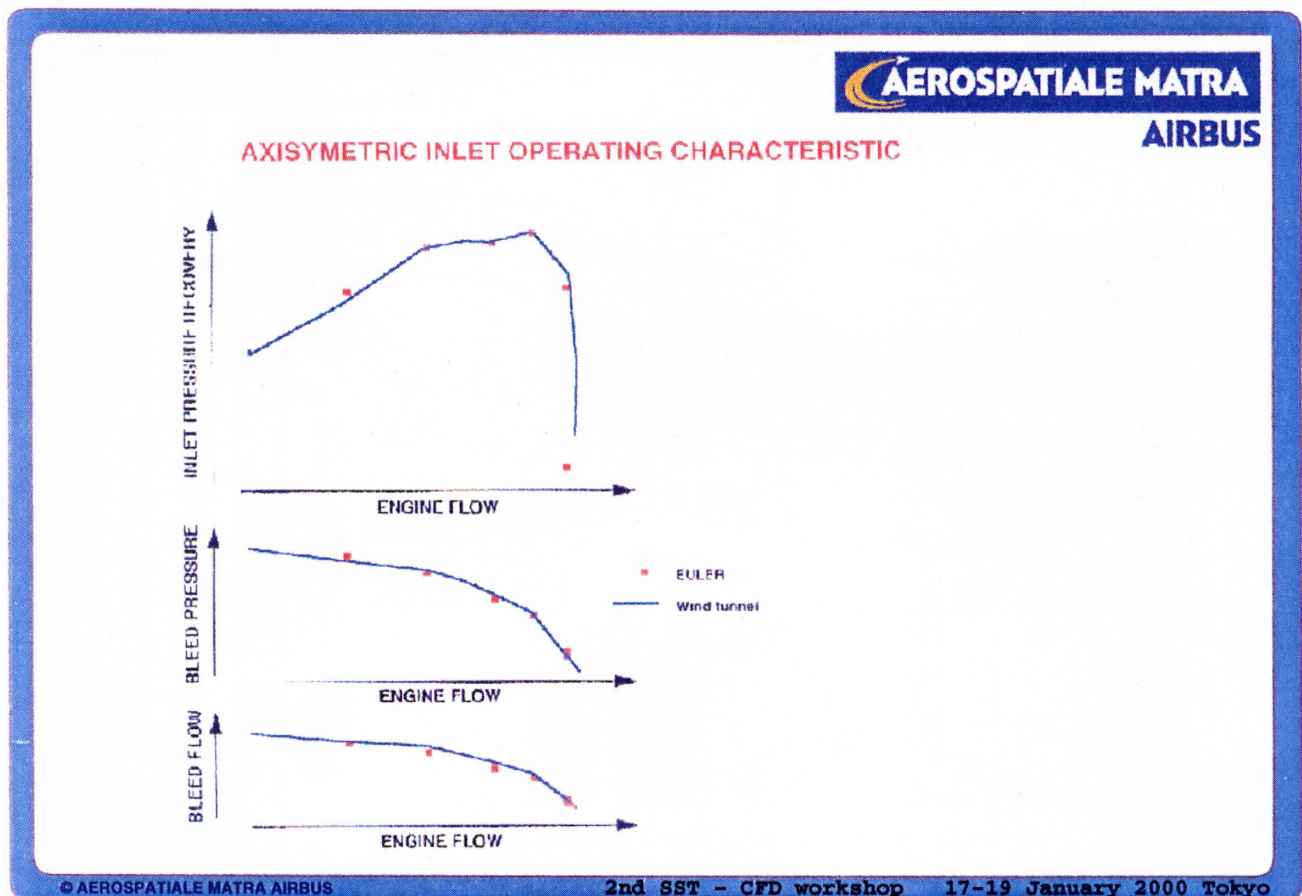
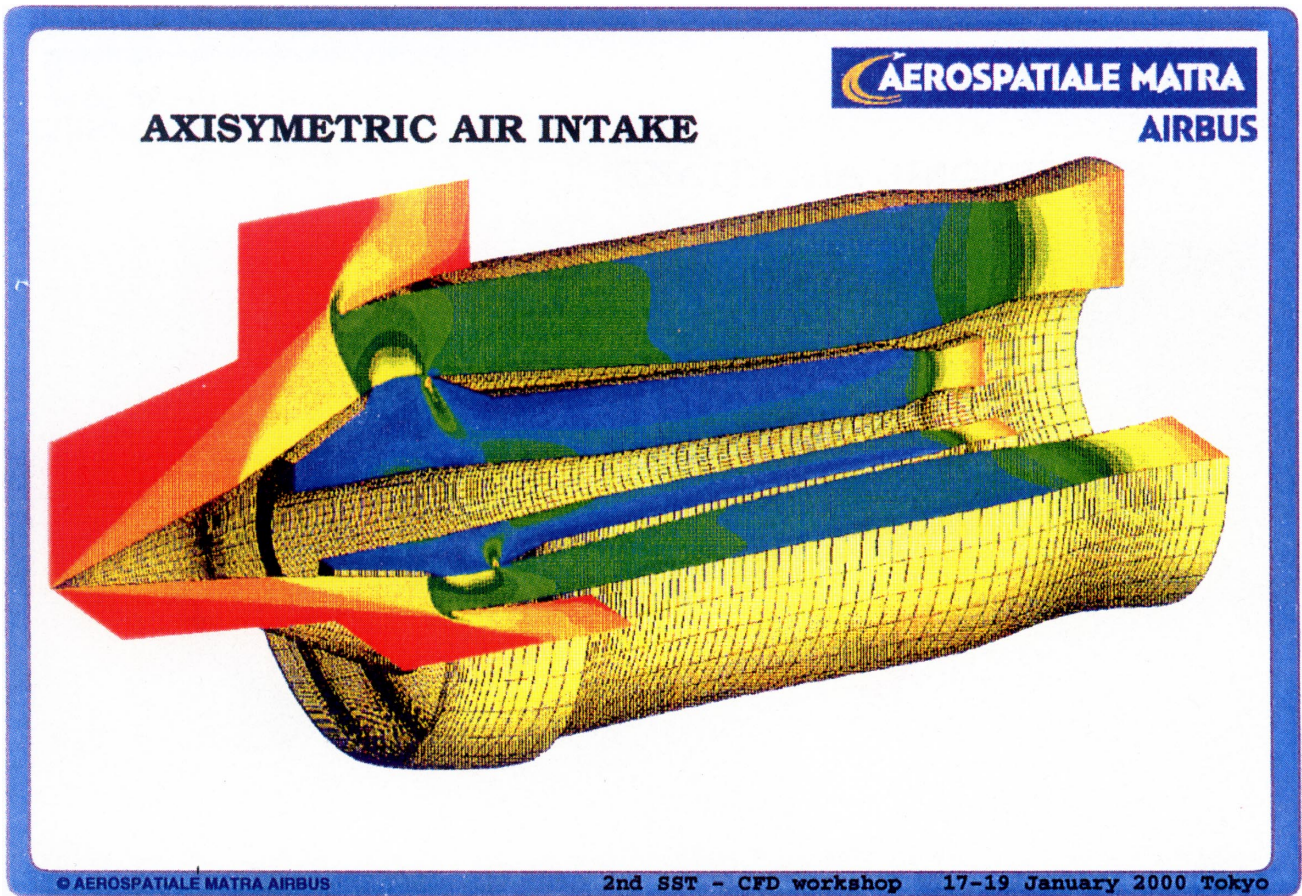


Characteristics	Concorde	ESCT
Range (km/nm)	6300 / 3400	>10000 / 5400
Cruise Mach number	2.0	2.0
MTOW (t)	185	340
Passengers	100	250
Flyover Noise (EPNdB)	119.5	105.2
Consumption kg/(seat.km)	0.1	0.05

Internal Elements Design

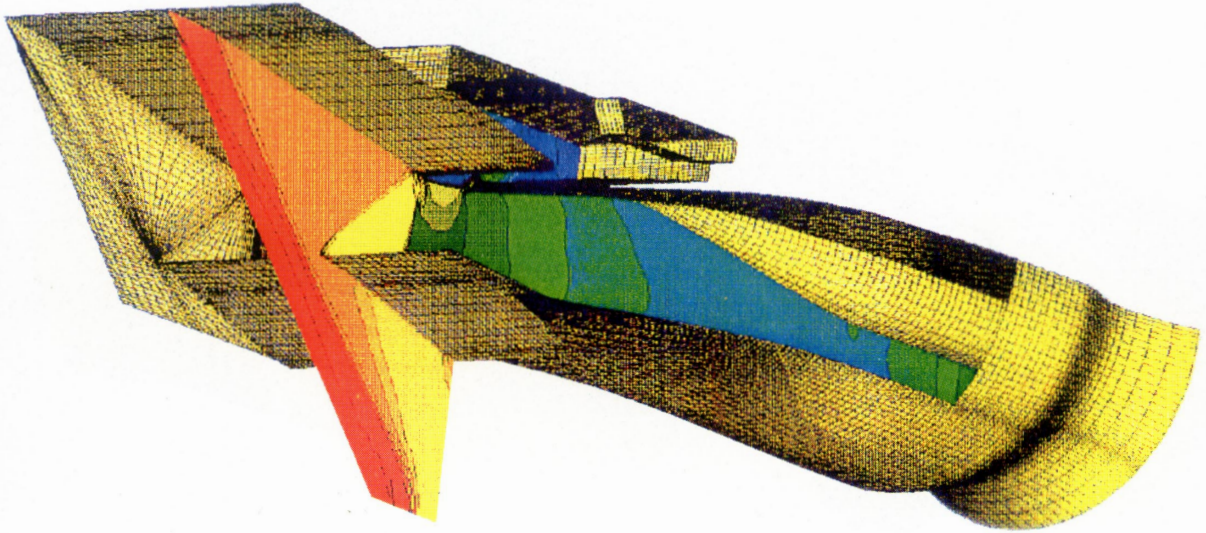
Schematic Layout of the propulsion System





AEROSPATIALE MATRA
AIRBUS

SUPERSONIC AIR INTAKE

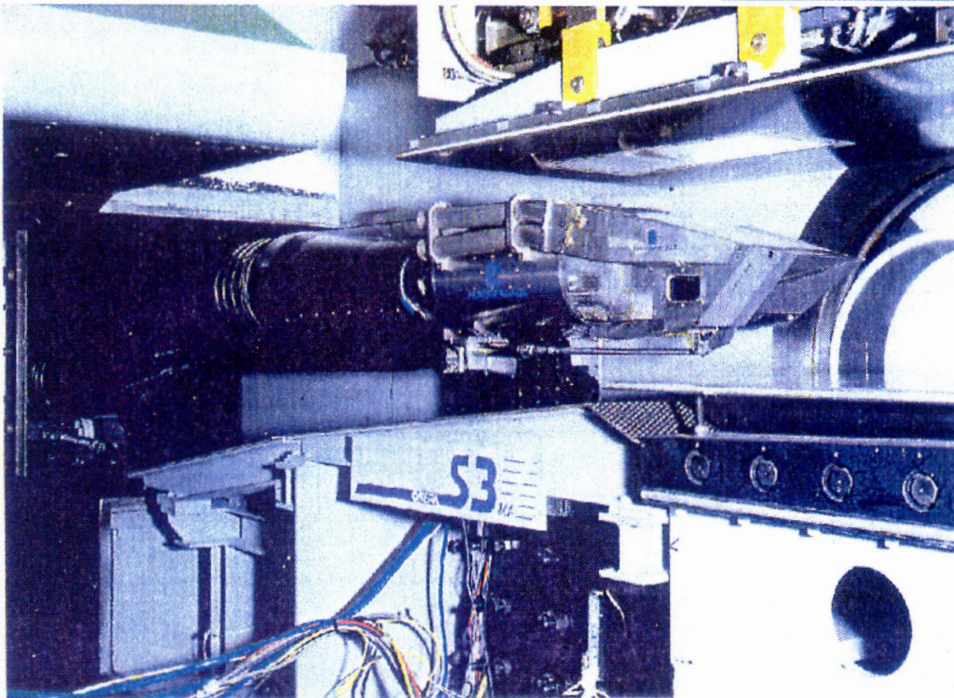


© AEROSPATIALE MATRA AIRBUS

2nd SST - CFD workshop 17-19 January 2000 Tokyo

SUPERSONIC AIR INTAKE

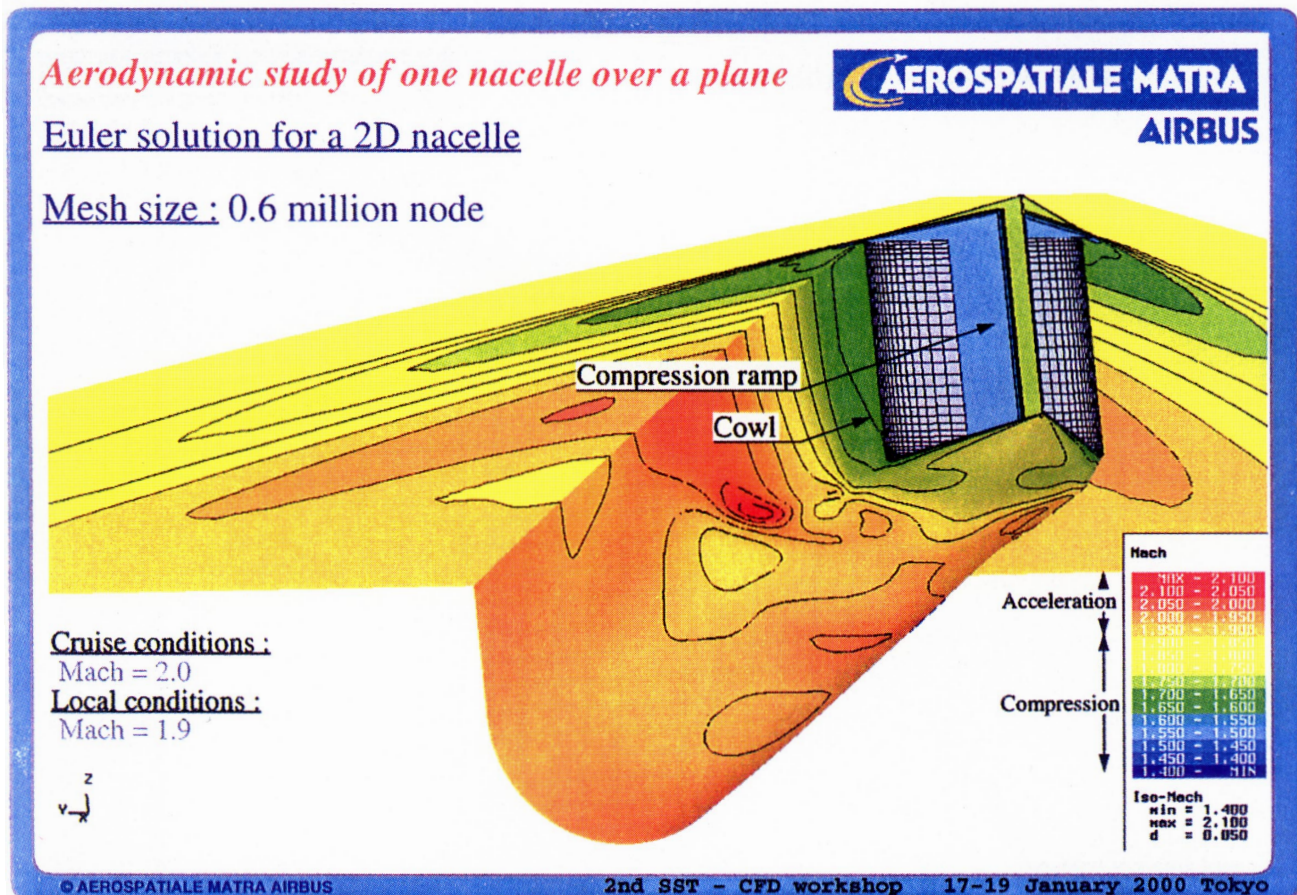
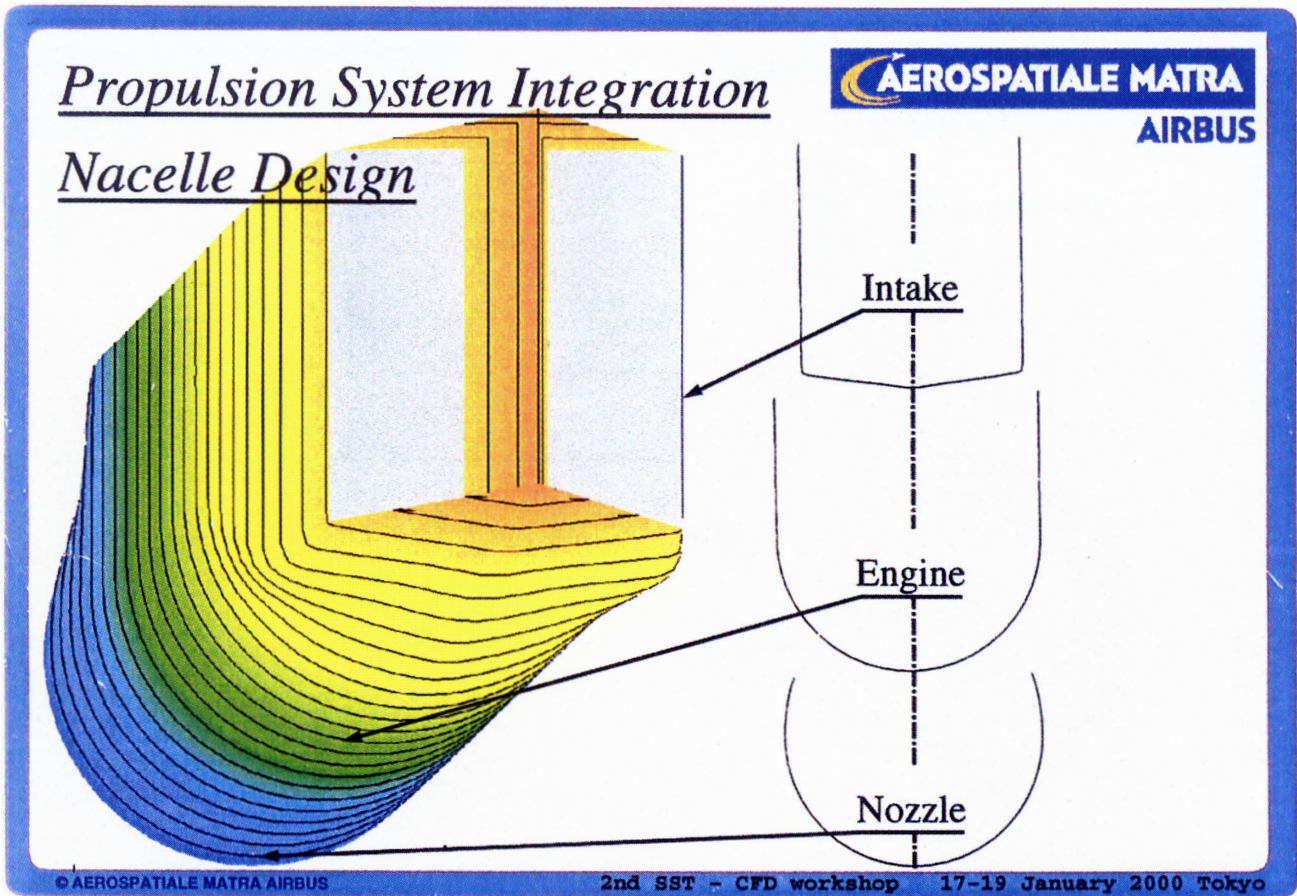
AEROSPATIALE MATRA
AIRBUS



WIND TUNNEL S3 ONERA MODANE

© AEROSPATIALE MATRA AIRBUS

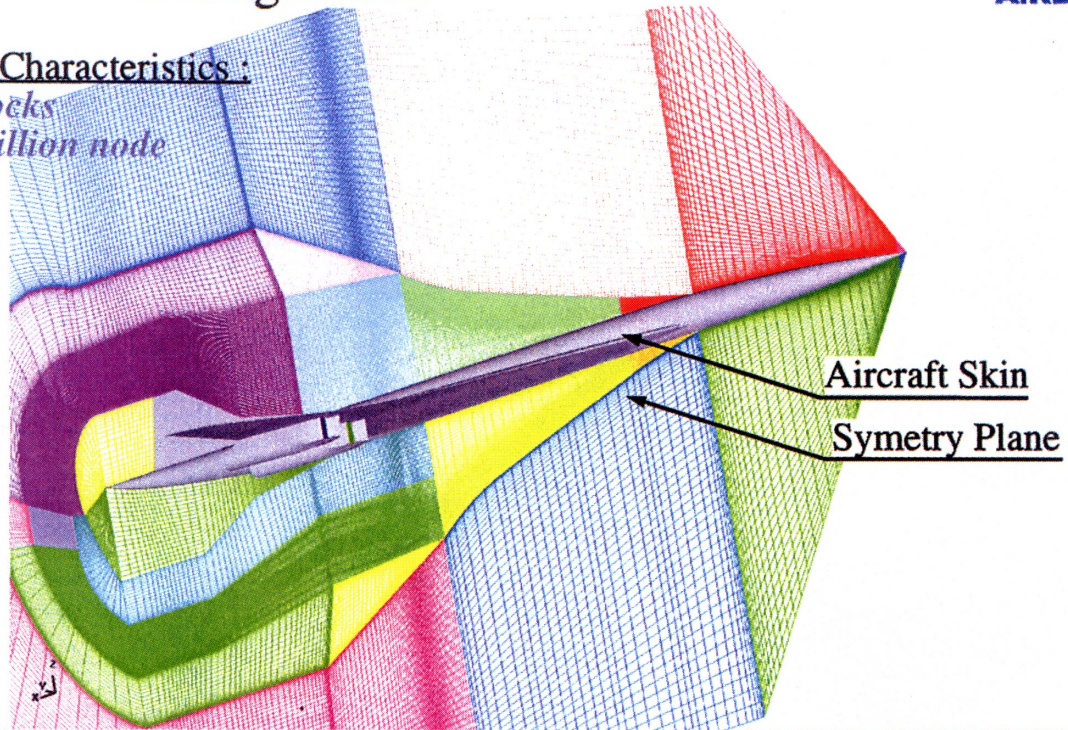
2nd SST - CFD workshop 17-19 January 2000 Tokyo



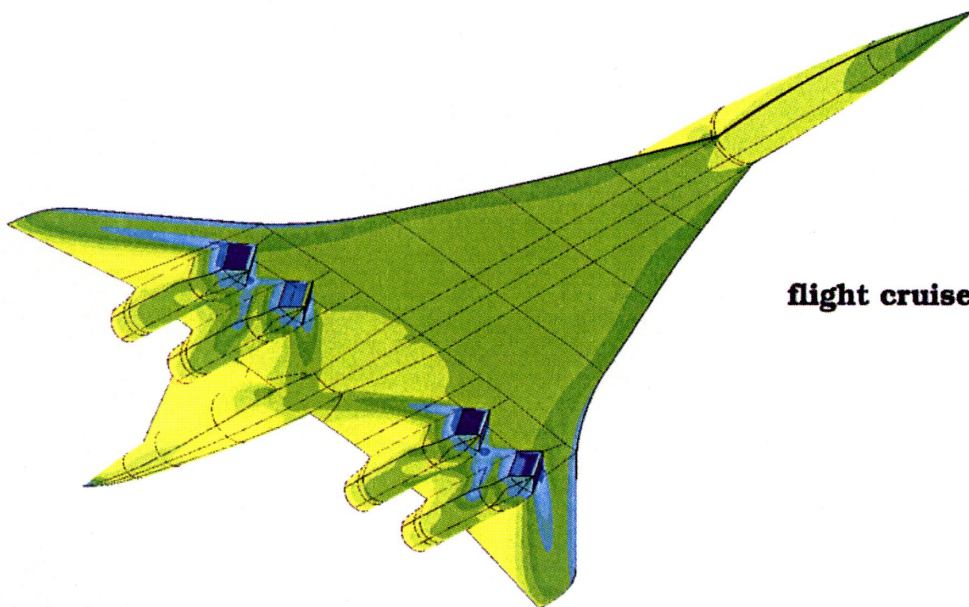
Mesh Around the Complete Aircraft Configuration



Main Characteristics :
70 blocks
1.5 million node



BIDIMENSIONAL AIR INLET



flight cruise Mach=2.0

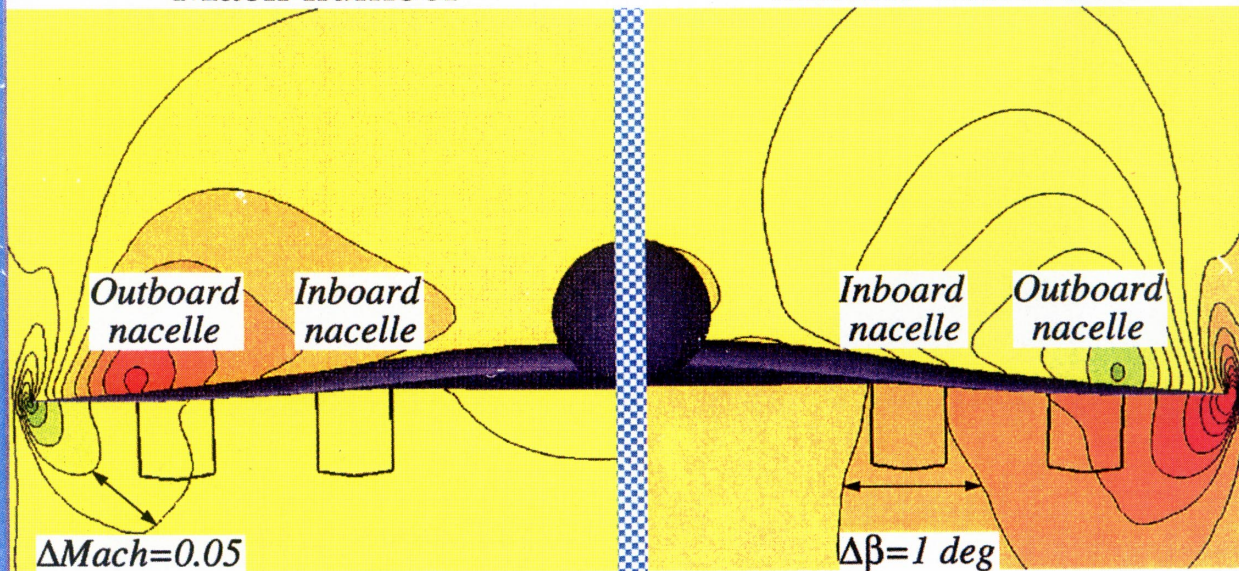
Analysis of the air intake entry plane



Supersonic cruise conditions : Mach 2.0 Incidence 4 deg

Mach number

Lateral deflection

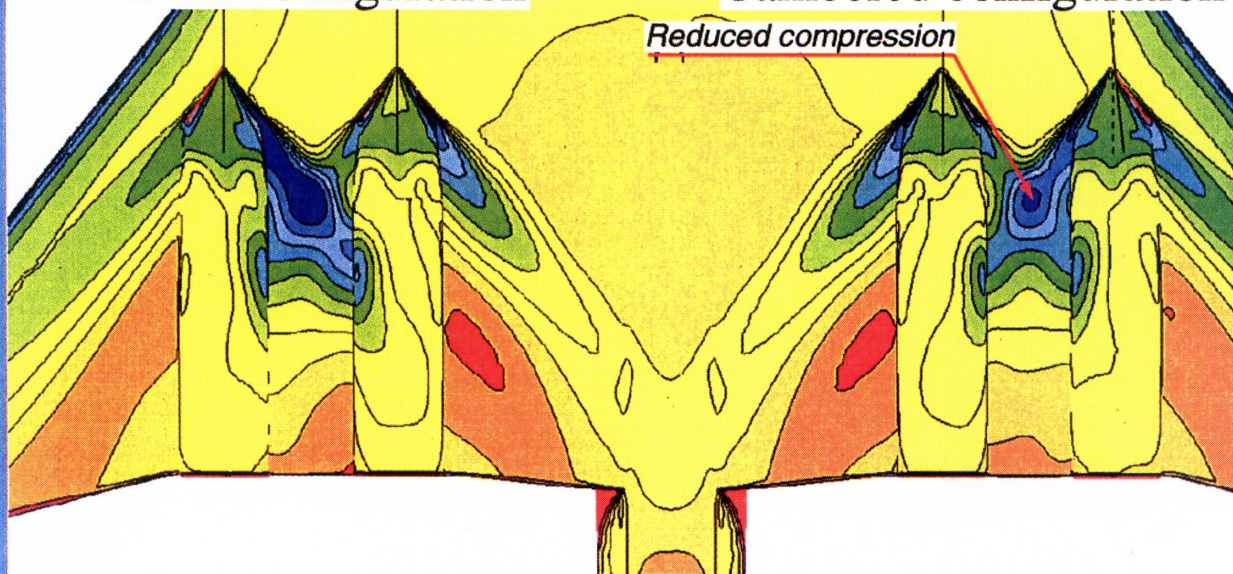


Mach number modification through the cambering process



Initial configuration

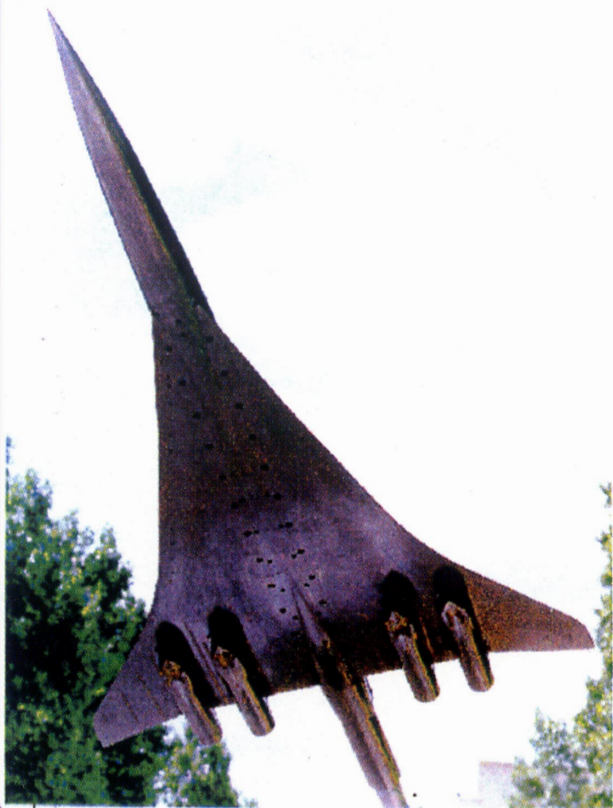
Cambered configuration



Supersonic cruise conditions : Mach 2.0 Incidence 4 deg

AEROSPATIALE MATRA
AIRBUS

WIND TUNNEL MODEL

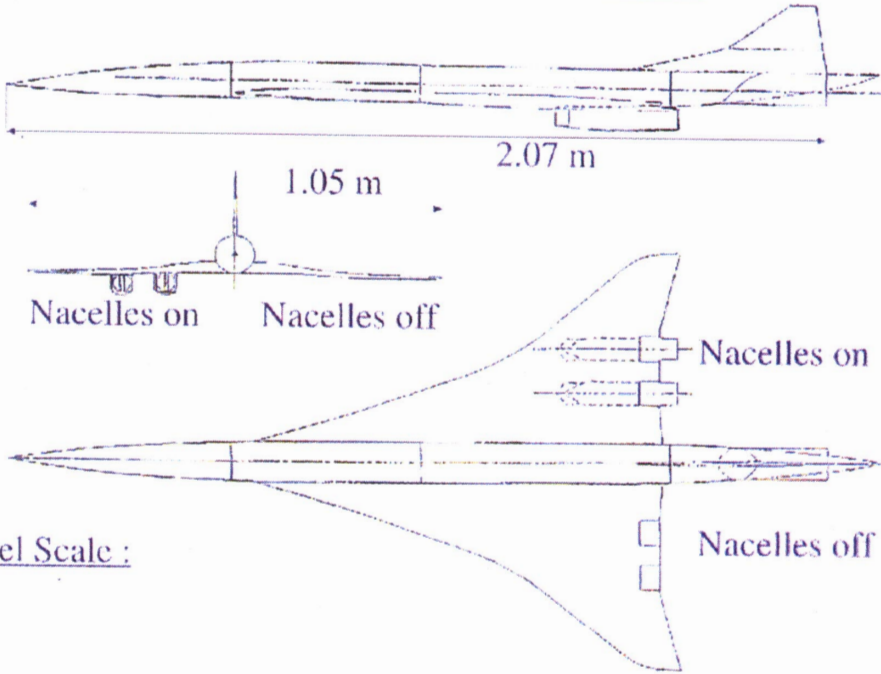


MODEL SCALE: 1/40

© AEROSPATIALE MATRA AIRBUS 2nd SST - CFD workshop 17-19 January 2000 Tokyo

AEROSPATIALE MATRA
AIRBUS

Wind Tunnel Model



1.05 m 2.07 m

Nacelles on Nacelles off

Nacelles on

Nacelles off

Model Scale :
1/40

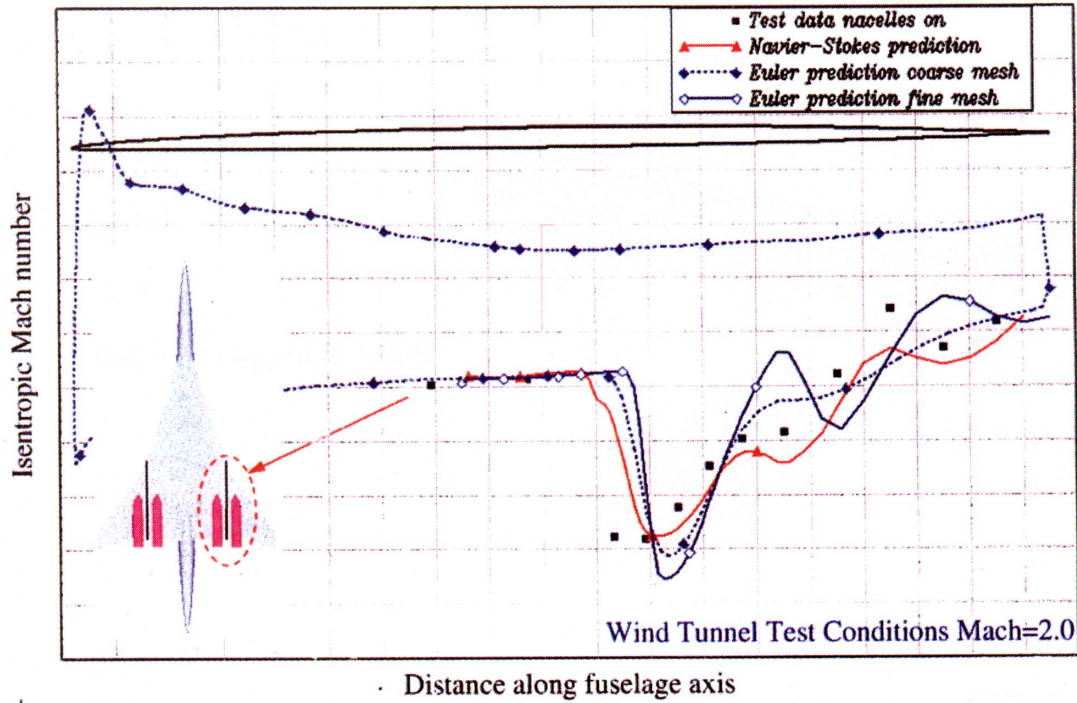
© AEROSPATIALE MATRA AIRBUS 2nd SST - CFD workshop 17-19 January 2000 Tokyo

Comparison of CFD predictions to pressure data



AIRBUS

Chordwise cut between the two nacelles

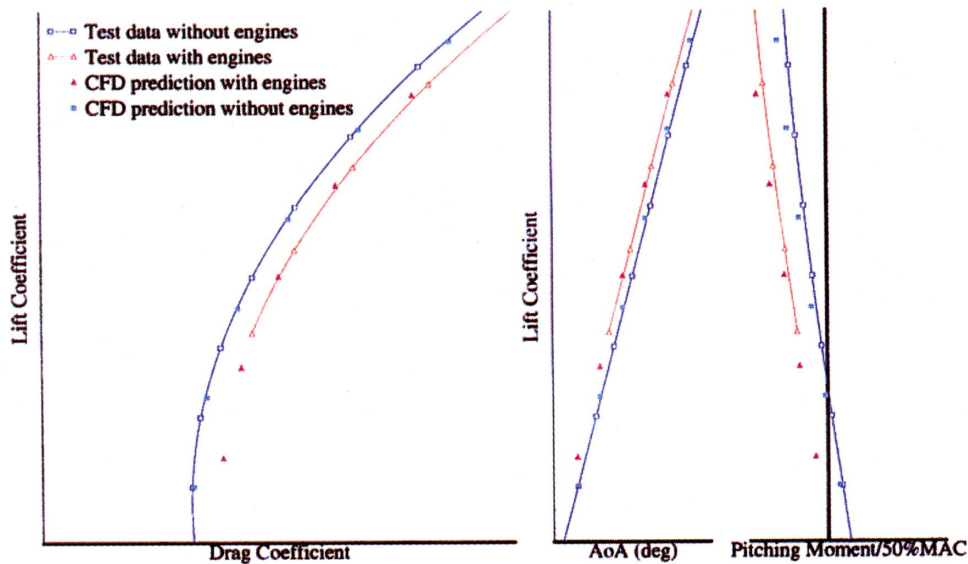


Comparison of CFD predictions to experimental data on integral coefficients



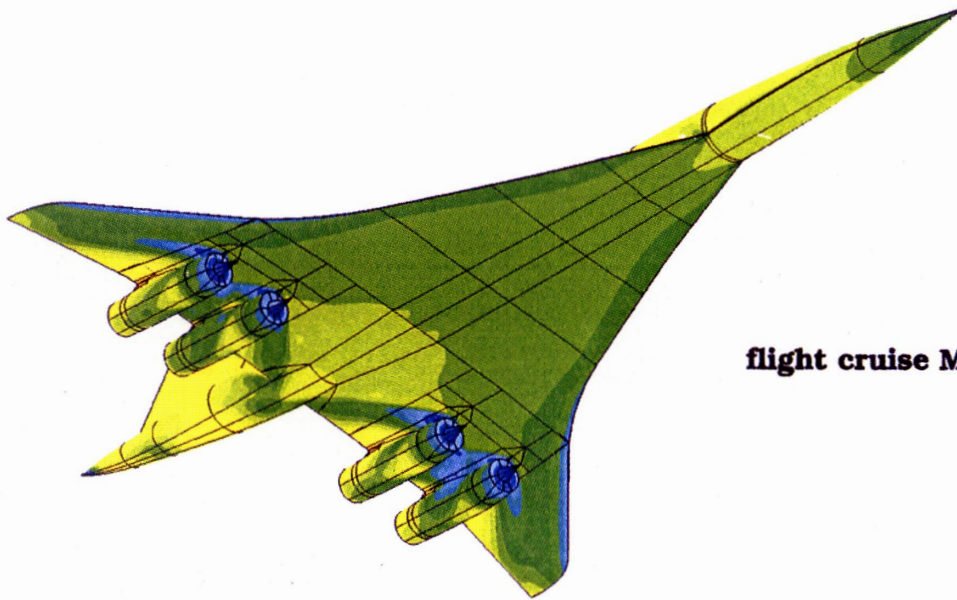
AIRBUS

Wind Tunnel Test Conditions Mach=2.0



AXISYMMETRIC AIR INLET

AEROSPATIALE MATRA
AIRBUS



flight cruise Mach=2.0



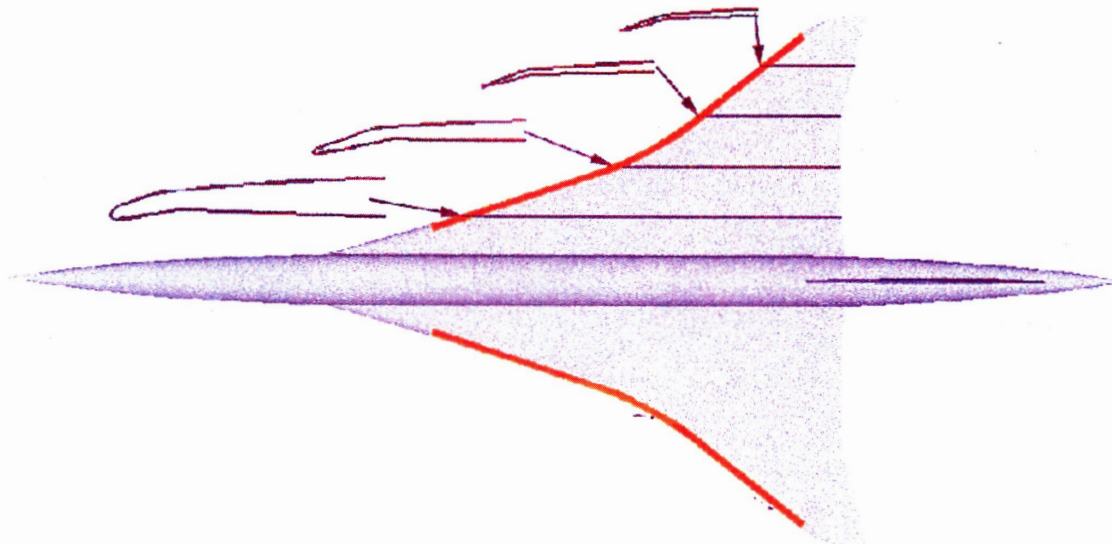
© AEROSPATIALE MATRA AIRBUS 2000

© AEROSPATIALE MATRA AIRBUS

2nd SST - CFD workshop 17-19 January 2000 Tokyo

SLATS FOR TRANSSONIC CRUISE

AEROSPATIALE MATRA
AIRBUS



© AEROSPATIALE MATRA AIRBUS

2nd SST - CFD workshop 17-19 January 2000 Tokyo

Supersonic Experimental Airplane Program in NAL (NEXST) and its CFD-Design Research Demand

SAKATA, Kimio

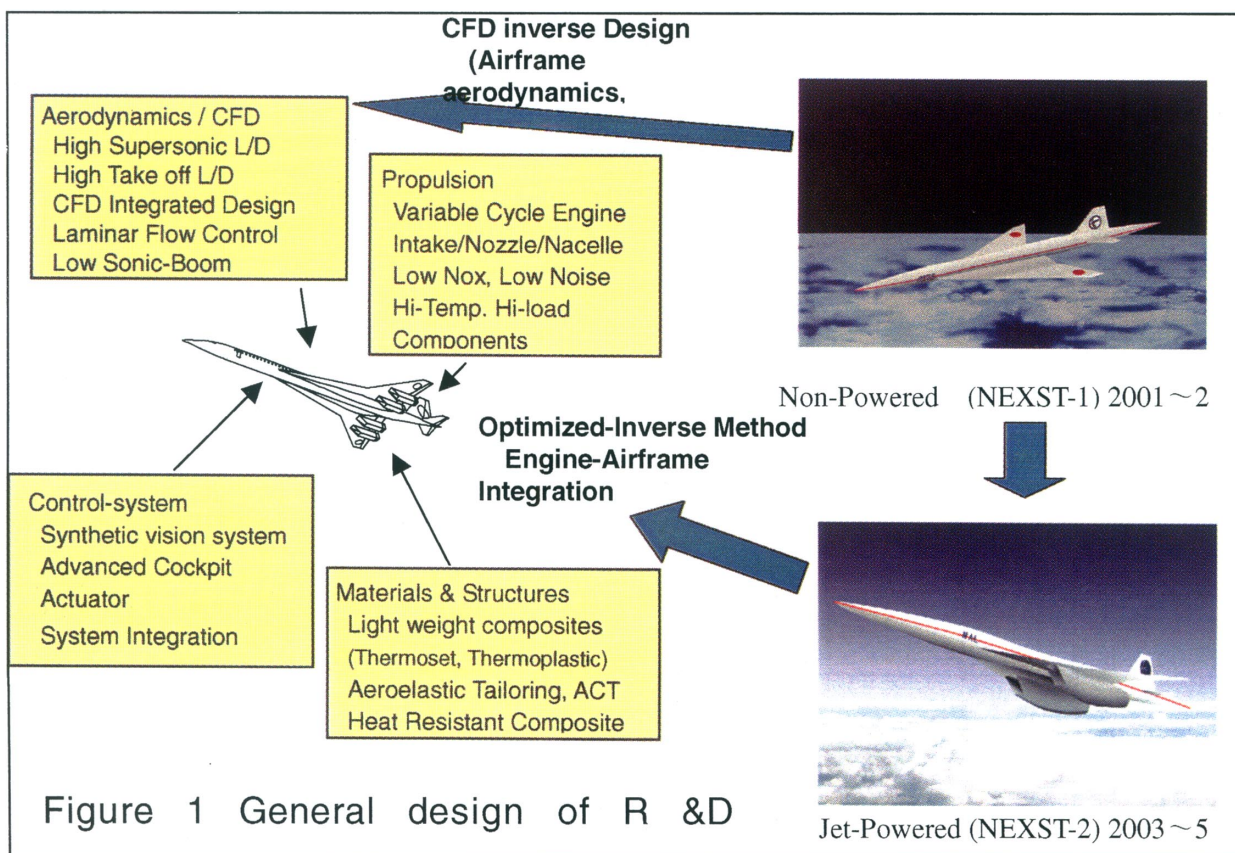
Supervising Researcher, Advanced Aircraft Project Center
National Aerospace Laboratory

ABSTRACT

In order to upgrade Japan's technological base and then to increase the chance of participation of Japanese aerospace players in collaboration for the development of the next-generation supersonic transport, being anticipated within 20 years. R&D program for the next generation supersonic transport (NEXST), being initiated in NAL of Japan in 1997 and to be completed in 2005, is aiming at establishing the advanced and emerging technologies. The program contains two types of the unmanned experimental airplanes to be developed, a non-powered and a twin-jet airplanes. The computational design system introducing NAL's original CFD (Computational Fluid Dynamics) code is the main technology to be proved by the experimental airplane. Inverse method, optimization and integration including multi-disciplinary treatment are studied and the results from those are applied to the aerodynamic design of the experimental airplanes and tested for technological proof. The program is managed by NAL's program office in cooperation with in-house collaboration and Japanese aerospace industries. Research cooperation is also encouraged with domestic and international institutions.

Table.1 Design Requirements compared with Concorde

CONCORDE		Next Generation SST	SSBJ
2.05	Cruise Mo	2.0~	1.6~
100 Pax	Payload	250 Pax	8 Pax
6,000 km	Range	11,000 km	8,000km
62.1m	Length	100m	25m
174 ton	Max Weight	360 ton	30 ton
Very large	Noise	Stage3-3dB	Equivalent
20	NOx Index(EI)	< 5	< 5



1. Program outline

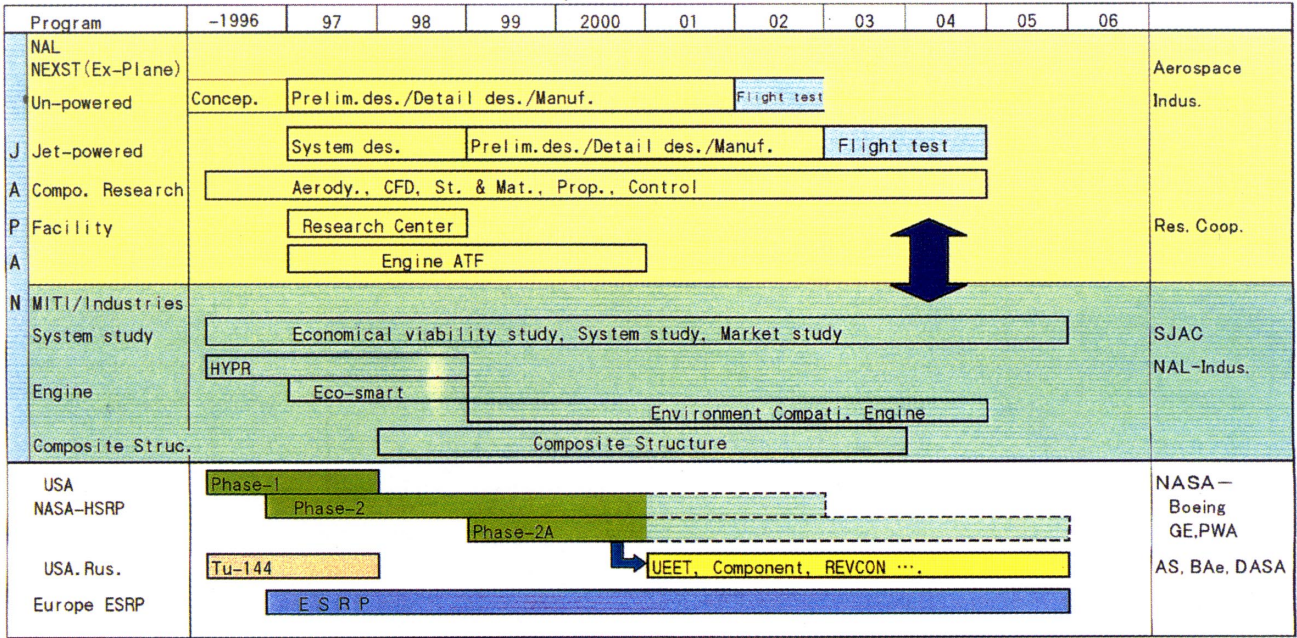


Figure 2 NEXST program schedule and related programs

NAL of Japan has her own heritage of CFD and aerodynamic design researches mainly using the large scale super-computer complex. Realization of the next generation supersonic civil transport (SST) requires many technological preparation such as high-lift drag ratio, light weight composite structures and highly efficient supersonic engine, together with environmental compatible technologies. Comparing to the Concorde, the next generation SST should be much larger and more productive as shown in Table 1. Japan thinks that her aerospace activities should be activated by establishing richer technological basis, typically to match those requirements for the future aircraft developments and productions.

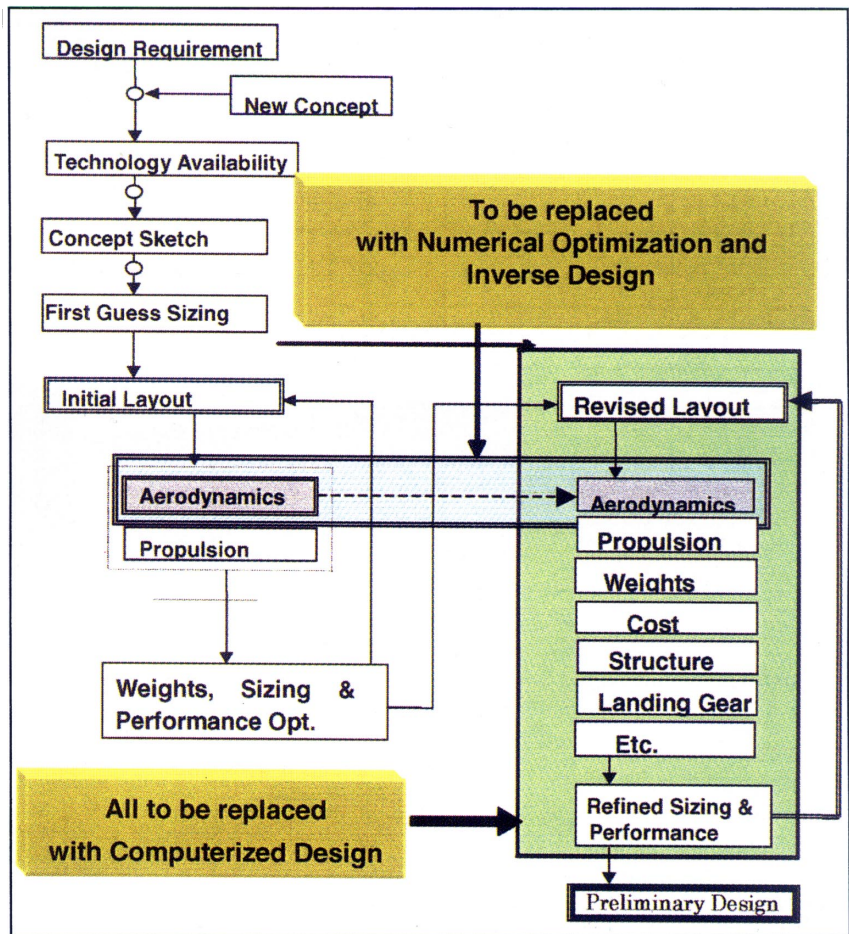


Figure 3 Conceptual design process and its modernization

As a major part of Japan's research activities, NAL conducts the NEXST project using its accumulated research achievement. The grand design of NEXST project, which consists of development and flight tests of two types of the unmanned experimental airplanes and

component researches, is shown in figure 1. The main subjects of the program are including CFD-based aerodynamic design technology so called NAL's computational optimized design system. The program also conducts the equipment of the facilities, such as the small scale supersonic engine test facility with high-altitude capability and the CFD research center. Figure 2 shows the program schedules together with ones of another National and overseas projects subjected to the SST. NEXST projects is harmonizing to other programs conducted in Japan mainly by MITI management.

Technical objectives of the NEXST program are; ① to obtain the system integration technology of the aircraft, ② to establish the CFD-based aerodynamic design system with inverse method and optimization, ③ to upgrade the emerging component technologies including composite structure and propulsion system, and so on.

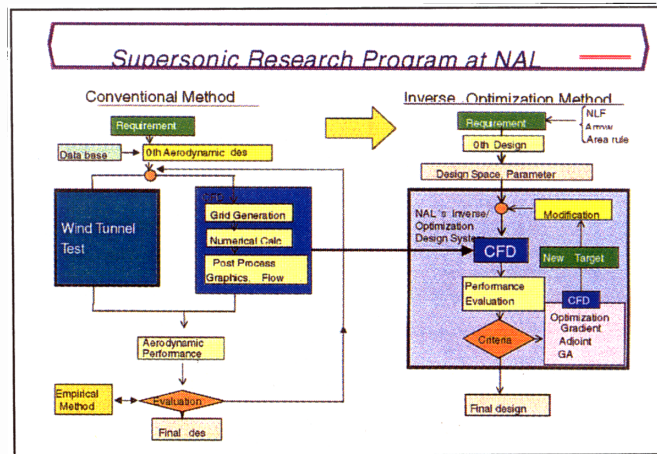


Fig.4 Inverse-Opt. design system vs. conventional

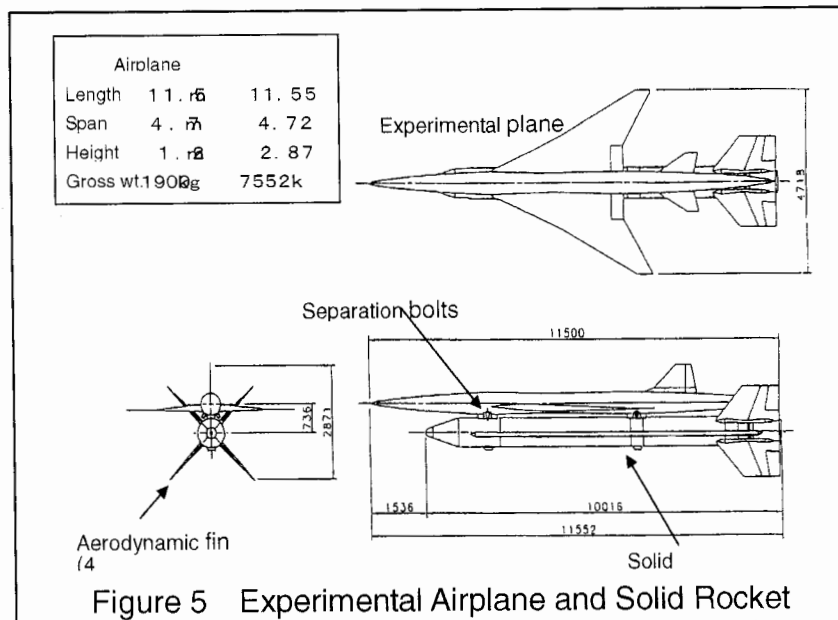


Figure 5 Experimental Airplane and Solid Rocket

2. Design system development

The reasons for choosing the CFD based design system as the technical objective are:

- (1) Importance of development of the advanced technology to be applied to the conceptual design and/or preliminary design of the new aircraft is recognized for Japanese aerospace community.
- (2) Utilization and further progress of the accumulated heritage of world class research on numerical simulation technology is very promising. So that CFD is as the first trial introducing the computerized code into the conceptual design process. The simulation of the structural dynamics, control, engine and other components may join in the future together with multidisciplinary optimization.
- (3) Cost reduction achieved by using the computerized design, manufacturing, and other process for aircraft development and production is strongly anticipated and its effect should be large.

The computerized design process introducing the inverse and optimization methods, is promising for the complex systems such as the next generation supersonic transport. Figure 3 shows the existing conceptual design process and its modernization by introducing the advanced design system being developed in the program. Figure 4 shows the conceptual diagram of the new aerodynamic design system by using CFD, comparing to the conventional aerodynamic design process which is mainly relied on the wind tunnel tests and empirical database.

The design technology will be proven by applying those to the experimental airplane designing.

Undoubtedly, the numerical simulation or modeling of the design components is necessary for the computerized design system, so that the accurate and easy-to-use CFD codes are required for the aerodynamic component. Optimization is inevitable for significantly complex system, such as engine installation to the supersonic airframe, because of its unknown factors in designing. So, a kind of non-

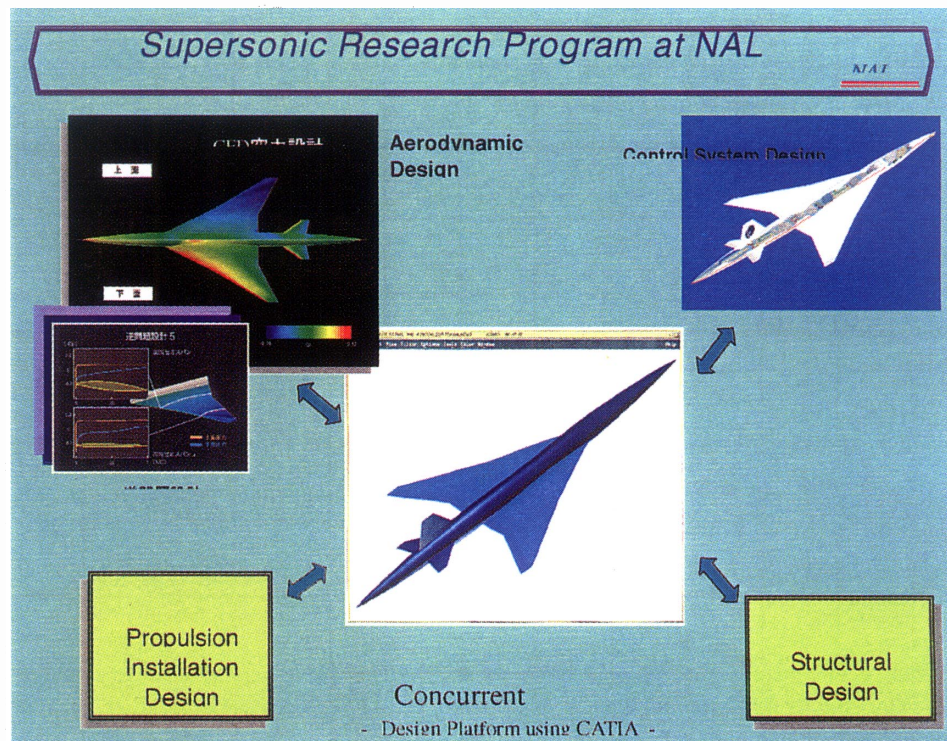


Figure 6 Concurrent designing with computational design system

deterministic design system should be introduced for the jet-powered experimental airplane. Multidisciplinary simulation and optimization, in which the numerical simulations of structure, control, heat transfer and so forth are involved simultaneously, is another technological target in the future.

3. Experimental air-planes

NAL plans to develop two types of unmanned experimental airplanes. In the first phase, the non-powered airplane is to prove the theoretical possibility of the inverse design technology aimed at an adequate target value to be achieved. Natural laminar flow concept integrated with the arrow-wing, area-rule and warp configuration is adopted in order to accomplish high lift/drag ratio at Mach 2. Figure 5 shows the 3 views of the non-powered airplane at the combined configuration with booster rocket. The scale of the airplane is about 1/10 of the actual next generation SST. The critical design of the non-powered airplane has been completed in 1999 in cooperation with the industries' design team called SSET (Super-Sonic experimental aircraft Engineering Team) in which MHI, KHI, FHI and Nissan Motors Co. are participating. Figure 6 shows the concurrent design work based on the NAL's aerodynamic design using new software in collaboration with SSET and another component engineers. NWT (Numerical Wind Tunnel) of NAL has been used as the center computer and engineering workstations are the peripheral processors. The jet-powered experimental airplane will be developed with more advanced way based on that learned through the first airplane development. Engine installation is the most important design space to be defined for the optimization.

4. CLOSURE

In 1999, design of the non-powered airplane was completed. Preliminary design of the jet-powered airplane will be initiated within a year from now (Jan. 2000) just after completion of optimization method development. The computerized design system development is going well in cooperation with the industries and universities domestically. International cooperation is also welcomed. The flight tests will be conducted from 2002 to 2005 sequentially in Australia.

Multidisciplinary Optimization Tools

Based on Manual Design Exercises

Helmut Sobieczky *

DLR German Aerospace Research Establishment
Institute for Fluid Mechanics
Dept. High Speed Aerodynamics
D-37073 Göttingen, Bunsenstr. 10
Germany

<http://www.sm.go.dlr.de/~helmut/>

Abstract

In this presentation an aerospace vehicle surface definition concept is outlined, which has been developed and applied to basically aerodynamic design and optimization, but with recent extensions, consequently using the mathematical tools of this geometry generator, some multidisciplinary optimization goals in aero-vehicle design may be reached. A key element of the approach is the definition of knowledge-based parameters which ensure a maximum of effect to an objective function, with a minimum of required and tuned input data.

In the following an outline of the presentation is given, mentioning some recent design case studies from supersonic aerodynamics and proposing their extension to be test cases for a more multidisciplinary approach.

Introduction

Geometry generation is the first and basic activity needed to define examples to obtaining starting models for early stage numerical design, analysis and experimental investigations of a high speed aerodynamic configuration. A general experience learned both at industry and applied research institutions is the fact that commercial CAD software is not suited to provide a link of the aerodynamicist's knowledge base and the variety of possible solid surface elements modeled by such software. In this situation we have compiled a set of functions subsequently incorporated in various computer codes to generate parametric surface elements. Depending on the required applications we have created software to provide 2D sections, or 3D surfaces and finally 4D (moving) surfaces which, so far, basically were applied to aerodynamic design tasks.

The concept underlying this presentation can be found in [1], where the importance of a suitable geometry preprocessing for the early phases of high speed transport aircraft design is stressed. A simple and mathematically

precise technique employing a large variety of basic functions is used to create curves of an arbitrary complexity. This basic concept subsequently is used to smoothly vary input data along a third dimension, creating surfaces with a controlled smoothness. This general method has been used in modern software development [2]. In the following some recent and additional ideas are illustrated, which may be found useful for modeling boundary conditions for more than aerodynamic purposes: A truly multidisciplinary optimization will require a coupling between aerodynamic, aeroelastic and aeroacoustic design and analysis efforts, which again interacts with the options and constraints given by structure, thermal loads and, last not least, with economic considerations directly affected by passenger cabin, cargo and tank volume.

Aerodynamic design knowledge base

Aerodynamic analysis still requires the most time-consuming numerical analysis steps in a multidisciplinary approach. It seems therefore justified to develop flexible tools to modify boundary conditions very rapidly, in a tuned procedure guided by flow physics and its application to create shapes with controlled flow quality.

Airfoils and wings

Initial work in applied aerodynamics usually involves airfoil design. Data bases were developed experimentally for families of airfoils, resulting in catalogs which provide starting data for the case study. Today we have numerical tools to compute 2D airfoil flow results, wind tunnel tests are rather needed for the 3D configuration. In this situation we propose to use analytically defined airfoils which are controlled by a set of relatively few parameters, their role in determining the geometry resulting from previous work when academic high speed flow examples were modeled by analytical solutions to model partial differential equations.

In a particular case study for this presentation, a series of thin airfoils is modeled using only 11 characteristic parameters [3], only a part of which are smoothly varied, see Fig. 1.

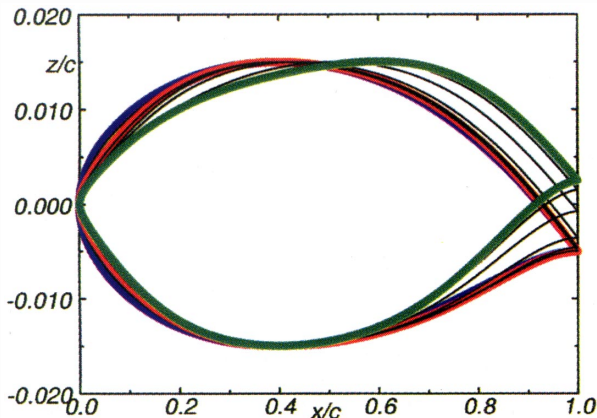


Fig. 1: Spanwise parametric variation of double-delta wing sections: root, subsonic, supersonic leading edge sections with smooth transitions

The airfoils, with a chord of unity, have been generated to be supersonic wing sections, subsequently we employ numerical methods to optimize these wing sections. A starting example providing a basic wing planform shape is the HSCT (1992) study by the US aircraft industry [4]. With leading and trailing edge geometry defined, and a twist distribution along span chosen, we have wing surface coordinates given explicitly for each arbitrary point of the wing plane, Fig. 2a. This is important for many subsequent steps of developing the wing: for instance aeroelastic analysis will need coupled results of the (outer) aerodynamic forces and the elastic deformation due to the wing (inner) structure.

Integration to a full aircraft requires mathematical modeling also for the fuselage, empennage and propulsion. This has been outlined in [1], page 146, see also Fig. 3.

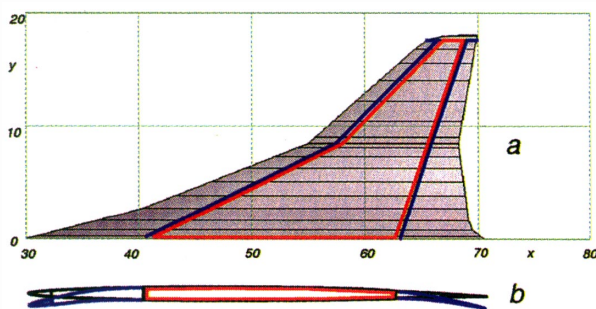


Fig. 2: Wing planform and choice of wing box model, control surfaces geometry. Sealed flap and slat modeled by rotated fixed parts and elastic connections.

Extended Geometry Generator

Control surfaces

High lift components are modeled in a similar way, cutting out parts of a clean wing and prescribing a 3D path to shift and rotate flaps and slats relative to the main fixed part of the wing. Aerodynamic optimization results for these shape variations will directly define required flap tracks.

In a simpler approach for high speed applications, so far we just model sealed flaps and slats, with simulating an elastic connection between the parts moving relatively to each other, see Fig. 2b. Depending on constraints of a chosen mechanical system which can bring the numerically optimized flap and slat positions to reality, our geometry models will successively be refined.

Internal structures

Many aspects of a multidisciplinary design process call for extending the geometry tool from a pure parametric shape generator for varying aerodynamic boundary conditions to provide also details of the model's internal structure:

Aeroelastic analysis requires definition of alternate surface grids and beam models conforming to the available space within a vehicle.

Various applications call for modeling a box or vessel within a wing: Tank volume will directly affect flight range which on the other hand is a function of fuel consumption determined by the wing's aerodynamic performance.

Spanloader configurations like Flying Wing aircraft and Blended Wing Body configurations are attractive because of their payload distributed within the wing just where lift is generated. With especially passenger space posing many constraints, pressurized vessels within a wing present another example where the external shape and the vessel within should be modeled together providing input data for rapid pre-design studies.

Another highly challenging multidisciplinary task is the layout of coolant passages within turbomachinery blades, combining the fluxes of gas, heat, forces and coolant flow outside the blade, between blade and passage, and finally within the passage.

Manual design example

Our experience in defining suitable parameters and functions is limited to providing models for aerodynamic case studies of practical transonic and supersonic configurations. No other disciplines have been coupled so far to this aerodynamic modeling. With aerodynamic shapes requir-

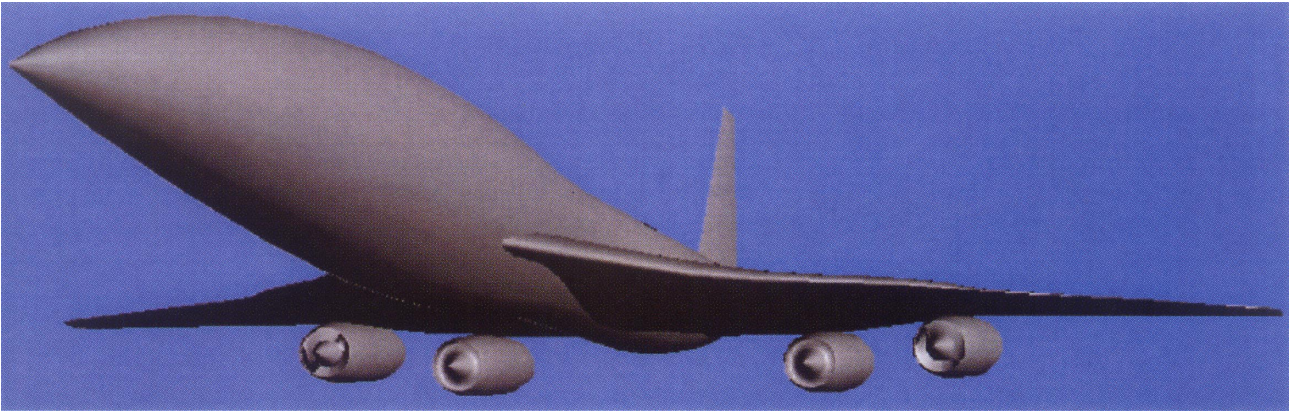


Fig. 3: Generic HSCT configuration integration by modelling, scaling and positioning components wing, body, empennage and propulsion units in 3D space.

ing the most refined definition, though, we have a sufficiently strong tool to use the available functions for internal volume distribution. This will be a challenge to extend spanloader studies like the Oblique Flying Wing (OFW), toward varying size and operation. Cruising with moderate supersonic speed, (Mach = 1.4 - 1.6), an OFW allows for thicker wing sections, compared to the formidable constraints of conventional supersonic delta wings. We use the theories of elliptic lift distribution, minimum drag bodies and transonic airfoils to acknowledge the constraints of spanwise analytical wing section definition, (Figs. 4).

For the relatively simple configuration of a clean OFW our “manual” aerodynamic optimization [5] led to remarkably high ratio of lift over drag (Fig. 5). The repeated variation of single parameters was guided by using just our knowledge of how desirable pressure distributions on a wing may be reached by shape modification, under the above constraints. This exercise, a one-time procedure intended to teach us about sensitivity of such configuration, is now carried further by application of a genetic algorithm to vary the parameters in an automated procedure [6].

Conclusion and future aspects

Conventional as well as innovative configurations for future supersonic transport are modeled to high accuracy and aerodynamic performance sensitivity. Manual design case studies guide the selection of parameters to become a set of minimum necessary input data subject to variation in automated optimization studies for cruise conditions.

Multidisciplinary aspects are addressed in a first option of providing the shapes of conformal internal structures: Various complex design goals may be formulated using configuration models with simple internal details (Fig.6)

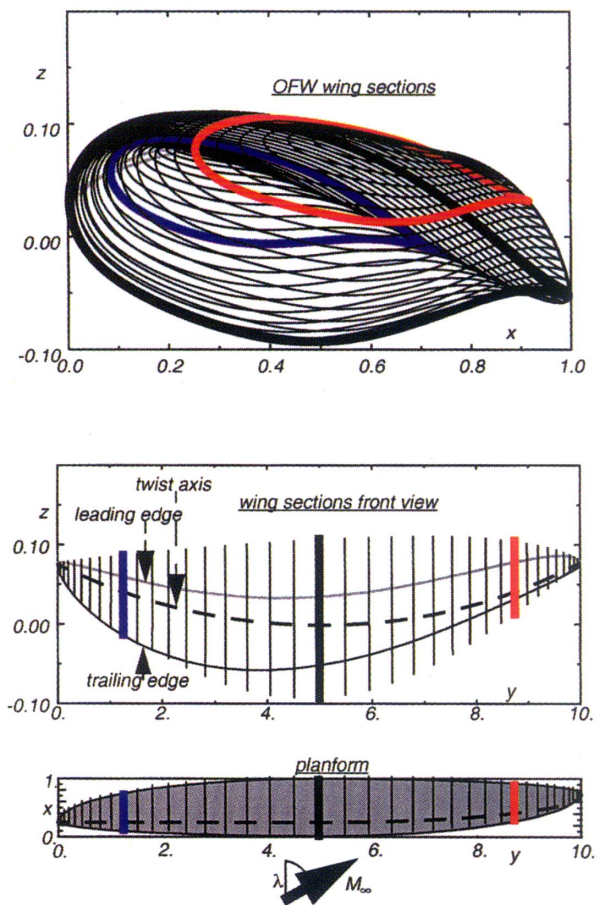
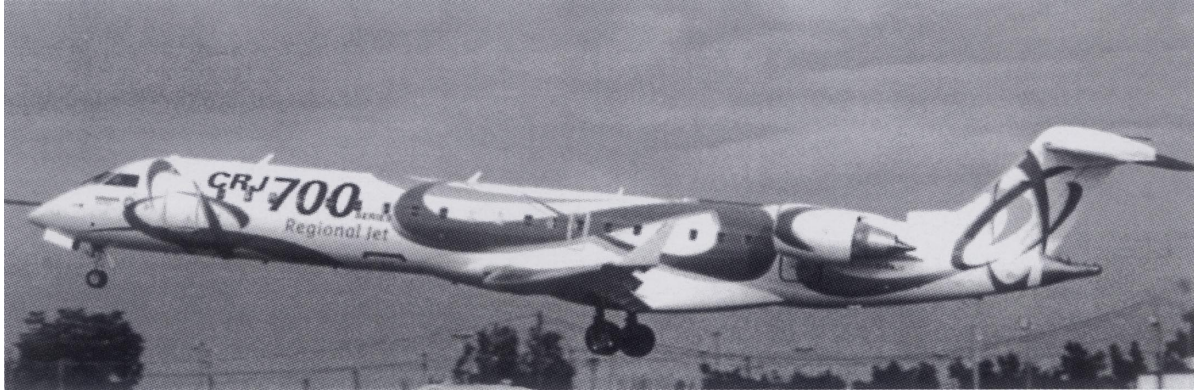


Fig. 4: Wing sections and front view in enlarged scale, planform. With airfoils of 17% maximum thickness and wing aspect ratio 10, passenger accommodation requires a wing span of 150m.

Application of Advanced CFD Methods to the Design of Modern Airplanes

Dr. Fassi Kafyeke
 Manager, Advanced Aerodynamics
 Bombardier Aerospace



Abstract

The approach to aircraft design has traditionally been based on wind tunnel testing with flight testing being used for final validation. CFD emerged in the late 1960's. Its role in aircraft design increased steadily as speed and memory of computers increased. Today CFD is a principal aerodynamic technology along with wind tunnel testing and flight-testing. State-of-the-art capabilities in each of these technologies are needed to achieve superior performance with reduced risk and low cost. This paper discusses the role of CFD in the aerodynamic development of high performance jets, as illustrated by the application to Bombardier Business and Regional Jets. Emphasis is put on the methodology, in particular the combination of CFD with targeted wind tunnel tests and flight tests to arrive at optimal configurations.

Introduction

In 1978, the Canadair Challenger became the first civil aircraft to fly with a supercritical wing designed with CFD methods; these methods included Jameson's FLO22 full potential code for transonic wings, the BGK 2D transonic airfoil code, and Canadair's MDRAG program for high-lift¹. Since then, CFD has been used as the principal tool for aerodynamic design and development of several new Bombardier jet aircraft:

- The 50-passenger CRJ-200 Regional Jet²; The CRJ-200 entered service in 1992;
- The long-range, high-speed, Global Express Business Jet³; the aircraft entered service in 1999;
- The 70-passenger regional jet CRJ-700, currently in certification flight testing;
- The BD-100 Continental Super-Midsize Business Jet, now in detailed design phase and scheduled to fly in 2001;

- Bombardier's future 100-passenger aircraft, the BRJ-X.

The New Design Environment

Figure 1 illustrates the large number of aircraft that were introduced by Bombardier over the last eight years to meet a rapidly changing market environment.

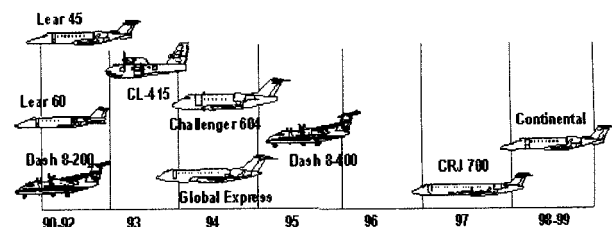


Figure 1: Bombardier aircraft launched between 1990 and 1999.

In this new competitive environment, it is no longer sufficient to produce an aircraft with the best possible quality and performance; it is also mandatory to produce such an aircraft at the lowest possible cost. This requires shortening aircraft development cycles and producing first-time quality, without changes or reworks. This is the goal pursued by engineering project plans which were introduced by aircraft manufacturers to define more clearly the phases, milestones and processes of an airplane design cycle. Bombardier's Engineering System (BES[®]) is illustrated in figure 2.

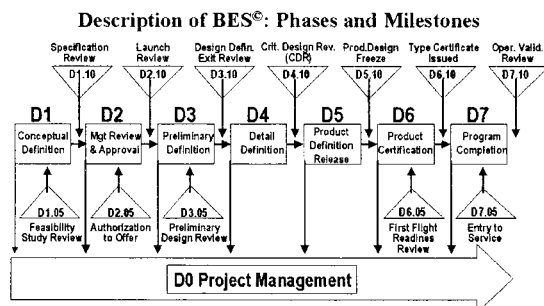


Figure 2; Phases and major milestones of the Bombardier Engineering System.

To reduce the time needed to develop an aircraft requires freezing the external aerodynamic lines as early as possible. Aerodynamic design activities occur therefore mostly in phases D1 and D2 (Figure 3). CFD methods are used in different ways in these two phases. In conceptual design, rapid methods are needed to perform parametric investigations. In preliminary and detailed design, more sophisticated methods are used for a finer optimization. Aerodynamic analysis continues through phases D3 and D4 in support of detailed product definition and first flight.

Aerodynamic Definition Process

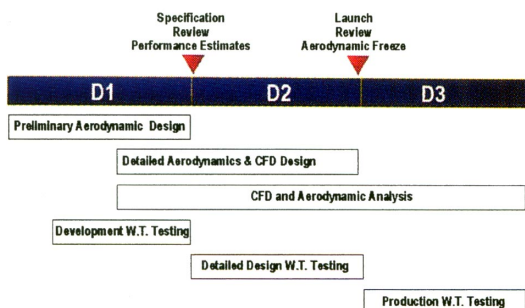


Figure 3: Bombardier CFD and experimental aerodynamic design process

The aerodynamic requirements of a new aircraft project are typically:

- The design of optimized aircraft external surfaces for efficient cruise;
- The design of optimized high lift systems for field performance;
- The prediction of airloads for the sizing of aircraft structure and systems;
- The optimization of performance and stability and control characteristics;
- The investigation of problems encountered in wind tunnel and flight tests.

The principal aerodynamic technologies used to fulfil these requirements are:

- Theoretical Aerodynamics and Handbook Methods; these methods are used most notably in the sizing of control surfaces and the evaluation of aircraft stability and control characteristics.
- Computational Fluid Dynamics (CFD); CFD provides a detailed description of complex flows and allows superior design by effective optimization; it is, however, limited by computing power and the complexity of the flow physics that the available software can model.
- Wind Tunnel Testing; testing allows the determination of performance and flow characteristics for real flow but the validity of test results is often limited by scale effects, support and wall interference and it is considerably more expensive than CFD.
- Flight-testing; it provides the most realistic environment and is used for final validation of CFD and wind tunnel test results. Flight-testing is more expensive than CFD and wind tunnel testing

The goal is to achieve a cost-effective combination of these technologies. By using advanced CFD methods for design and optimization and wind tunnel testing for verification, it is possible to minimize the drag of a new aircraft at high-speed cruise and to arrive at a configuration with good take-off and landing performance. The aerodynamic development of external lines of new Bombardier jets is accomplished using CFD extensively: design, analysis, and optimization of transonic wings, design of winglets, design of the wing leading edge fillet and wing-body fairing, design and analysis of high-lift systems, design and integration of turbofan engine

nacelles. An application of this approach to the design of the Global Express was discussed in reference 3. Figure 4 illustrates the components of the CRJ-700 designed with the assistance of CFD methods.

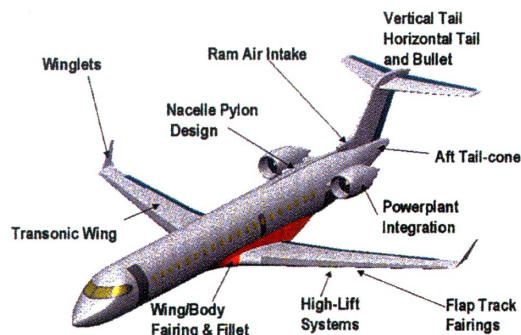


Figure 4: CRJ-700 aerodynamic components designed with CFD methods

CFD in Conceptual Design

A preliminary configuration concept is first defined for a specific cruise performance. CFD is used for the preliminary design and analysis of various wing planforms with varying thickness. Aerodynamic data from the CFD studies and empirical methods are used to establish a relevant aerodynamic data bank for the preliminary configuration. A weights data bank is also established by using empirical data based on similar types of aircraft. These two data banks are input in an Aircraft Synthesis Program (ASP) together with an engine performance deck provided by the engine manufacturer. With the aid of the ASP program, the wing and the aircraft are sized to meet the cruise-range as well as take-off and landing requirements. Several multi-disciplinary optimization strategies are being considered for this phase of the design, particularly the linking of structural sizing programs with aerodynamic load data obtained with CFD codes⁴. However, the rapid turnaround of candidate configurations required in this phase still favours a search process through pre-computed aerodynamic and weights data.

CFD in Preliminary and Detailed Design

The CFD design and experimental verification process, illustrated in figure 3, can be summarized as follows:

Preliminary CFD Design. Using existing airfoils and CFD techniques, an initial

configuration is lofted. The CFD methods used in this process are first calibrated by computing solutions on existing aircraft. They are then used in optimization loops to refine the initial configuration. This phase is also an opportunity for the first application of new, more advanced methods or methods which are better suited to the particular configuration of the new aircraft. The progression of the CFD technology used in the design of Bombardier transonic aircraft is summarized in figure 5. New CFD methods are typically matured over several years before they can be applied with confidence to the design of a new aircraft.

Year	Code	Transonic Technology	Design Application
1976	FLO22 BGK	3D Wing/Body Full Potential 2D Full Potential/B. Layer	Challenger
1989	KTRAN FLO82BL	Complete A/C TSD/B. Layer 2D Euler/B. Layer	CRJ-200
1993	MBTEC VTEC NSU2D	Complete A/C Euler Wing/Body Euler/B. Layer 2D Navier-Stokes	Global Express
1995	FANSC NSU2D	Complete A/C Euler/B. Layer 2D Navier-Stokes	CRJ-700 BD-100
1998	FANSC NSU2D	Complete A/C Navier-Stokes 2D Navier-Stokes	BRJ-X

Figure 5: Transonic CFD technology used for the design of Bombardier aircraft.

Detailed CFD Design. This phase follows the first series of development wind tunnel tests. Typically, the aerodynamic layout of the aircraft will have evolved during the period assigned to the initial test campaign. Changes to the configuration are usually made to match evolving customer requirements or as a result of continuing multi-disciplinary optimization. All components may be affected: wing planform, fuselage, empennage and powerplant. The lift, drag, moments and pressure data obtained in the initial wind tunnel tests are compared with the CFD computations and the design targets. If necessary, adjustments are made to the CFD models to insure a better match with experimental data: refined meshes, numerical scheme control parameters, convergence criteria, etc. The updated CFD codes are then used to improve the initial configuration until better aerodynamic characteristics are achieved. The best features of this configuration are then adapted to the final layout (typically a new wing planform) and further optimization is performed.

Experimental Verification

The experimental verification is made through targeted wind tunnel tests arranged in three series:

- **Initial development wind tunnel tests** are conducted in phase D1, following initial CFD design. The tests are used to validate the preliminary design, to calibrate CFD codes and to obtain initial performance figures. These tests are carried out using models of one or several promising configurations.
- **Detailed design and development wind tunnel tests** are conducted in phase D2, following detailed CFD design, on the updated, presumably final, configuration. These tests are used to support the aerodynamic freeze of the external lines.
- **Production wind tunnel tests** are conducted in phase D3, using the configuration adopted after the previous test series with small modifications that are typically due to systems installation. These tests serve to investigate all possible configurations of the aircraft and to obtain data needed before the aircraft first flight.

CFD Methods for Transonic Wing Design

Among the CFD codes developed after the Challenger design were the KTRAN⁵ transonic small disturbance code for complete aircraft configurations, the multi-block structured grid generation package MBGRID⁶, the multi-block Euler code for complete aircraft configurations MBTEC⁷ and the block-structured full aircraft Navier-Stokes code FANSC⁸.

KTRAN is a transonic small disturbance code developed at Bombardier for complete aircraft configurations. The program solves an extended version of the transonic small disturbance equation. It was originally written to predict pressure distributions on complex military aircraft configurations with multiple store carriage. KTRAN was later extensively developed for application to commercial aircraft with thicker supercritical airfoils. The code was coupled with laminar and turbulent boundary layer codes with semi-empirical treatment of the cove flow on aft-loaded airfoils found on most Bombardier aircraft. Several drag computation modules were added to the code: a semi-empirical module for fuselage

and nacelle drag, a Multhopp algorithm for induced drag, Lock's method for computation of wave drag based on shock strength⁹ and a Squire-Young module for the computation of wing and tailplane viscous drag. The latest changes made to the code are the addition of a module to compute airplane trim drag¹⁰ and the linking of the code with an algorithm to predict the aeroelastic deformation of wings with specified structural characteristics. With these improvements, KTRAN can be used for routine viscous transonic analysis of multi-component configurations. The code is ideal for parametric studies involving mutual interfering components (fuselage-nacelle, wing-nacelle and wing-winglets). It gives reliable estimates of aerodynamic loads on all aircraft components. Usage of the code is limited, because of the formulation of the equations, to a range of angles of incidence around transonic cruise conditions. The code was extensively calibrated using Challenger, CRJ-200, CRJ-700 and Global Express data. This code is a good example of how a code with many inherent limitations can be used, together with properly calibrated semi-empirical relations, to give reliable results when a fast answer is needed.

The Multi-Block Transonic Euler code MBTEC and the Full Aircraft Navier-Stokes Code FANSC were developed at Bombardier from Jameson's FLO67 and FLO97 single-grid programs for isolated wings. FANSC uses a finite volume algorithm based on multi-block structured meshes. The program uses an unstructured block topology, i.e. it allows any number of blocks to merge at the same location. To better achieve this, the program was changed from a cell-vertex stencil to a cell-centered one. The code can be run in inviscid Euler mode, in Euler mode with boundary layer coupling and in Navier-Stokes mode. Three numerical schemes are implemented for the convection terms: the CUSP (Convection Upstream Splitting Pressure) scheme of Jameson (1993), the AUSM (Advection Upstream Splitting Method) scheme of Liou-Steffen (1993) and the JST (Jameson-Schmidt-Turkel) scheme (1981). The viscous terms are discretized using a second order central difference scheme. The Navier-Stokes code uses a Spalart-Allmaras turbulence model (1992) discretized using a

first order upwind scheme for the convective term and a second order central difference for the diffusion term. The code uses a fully implicit treatment for the source terms (approximate factorization). The boundary layer scheme used for the viscous/inviscid coupling is Keller's box implicit method. The drag prediction modules previously used with KTRAN were incorporated, with the necessary adaptation to FANSC. The Euler and Navier-Stokes formulations allow additional approaches such as far-field (Trefftz plane) methods for the induced drag and the computation of wave drag from the integration of entropy variation across shock waves.

To support the block-structured Euler and Navier-Stokes computations, a suitable grid generation program was needed. MBGRID was developed progressively, starting in 1989. It uses an interactive CAD-based domain decomposition procedure, an initial grid generation by transfinite interpolation (GRID3D) and a final grid optimization using a Poisson solver (EGRID3D). Given the large number of configurations to be investigated in a design cycle, the industry's overwhelming requirement is the generation of high-quality grids in the shortest possible time. The absolute time to generate a body-fitted structured grid is always a function of the user experience and skill. However, the MBGRID package was developed with a view to reduce this time to a minimum. There are three steps in multi-block grid generation that can become, depending on the configuration, potential bottlenecks:

- Geometry definition
- Domain decomposition
- Grid quality optimization

It is our experience that any one of these steps can become the dominant factor in the time required to grid. To minimize the geometry definition time, we adopted concurrent engineering principles: MBGRID was interfaced with a state-of-the-art CAD system, Dassault Systèmes' Catia. This allowed meshes to be generated directly on the Catia workstation used to define the airplane surfaces. Meshes are visualized and optimized on the Catia screen. Only mesh points are exported at the end of the process. Several schemes were added to MBGRID to reduce

the domain decomposition time: inverted block-tree structure, automatic generation of connectivity information, automatic slaving of spacing distributions, systematic error checking, geometry adaptive decomposition wireframes and a library of decomposition wireframes. A promising development was the incorporation of automatic domain decomposition algorithms. The elliptic smoothing program was written with several features to insure grid quality: control of orthogonality conditions and variable spacing on all boundaries, control of global and local stretching functions and automatic treatment of degenerate boundaries. The grid quality optimization was automated through the implementation of new elliptic equations taking into account curvature effects for arbitrarily complex meshes¹¹. A new approach for the generation of Navier-Stokes meshes by mesh refinement was implemented. This allowed a large number of previously generated Euler meshed to be converted easily into Navier-Stokes meshes. The MBGRID package was used to develop grids for high-speed analysis for all recent Bombardier jets: Global Express, CRJ-700, Continental and BRJ-X.

KTRAN, MBGRID, MBTEC and FANSC were developed and matured over several years to satisfy the basic requirements of CFD methods for effective use in industry:

- An ability to model 3D complete aircraft configurations in viscous transonic flow.
- Accuracy and reliability that do not depend on fine-tuning and tailoring of input parameters during the design process.
- Short turnaround times for grid generation, solution set-up, execution and analysis.
- Ease of use. Attention must always be given to maintain a reasonable degree of specialization so that application engineers and not only the code developers can use them effectively.
- An ability to generate reliable component lift and drag predictions for trimmed aircraft configurations at specified lift coefficients.
- These predictions must be calibrated for a variety of applications and the margin of confidence in the results of each code documented.

The pressure distribution computed at 26% semi-span on the Challenger wing/body configuration with KTRAN and FANSC in Euler/Boundary Layer mode and Navier-Stokes mode is given in figure 6. The Navier-Stokes solution is a fully turbulent one, with a Spalart-Allmaras turbulence model. The results shown are for a high-speed cruise Mach number of 0.82 and a wind tunnel chord Reynolds number of 6 million. The figure gives in comparison the experimental pressure distribution measured in the MicroCraft Trisonic Wind Tunnel on a 7% scale full model.

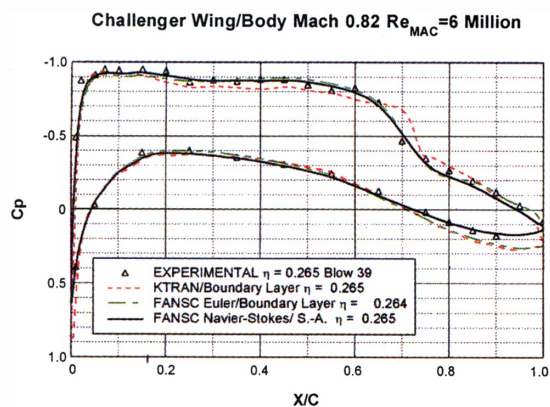


Figure 6: CFD and experimental pressures for a Challenger wing/body test case.

The improvement of the results going from the extended small disturbance formulation to the more sophisticated Navier-Stokes formulation can be clearly seen. It can also be seen that even for this off-design flight condition with a strong shock wave, the KTRAN computations give a fairly reasonable representation of the flow. The table in figure 7 illustrates the higher computing costs of the higher-fidelity codes.

	KTRAN TSD/Boundary Layer	FANSC Euler/Boundary Layer	FANSC Navier-Stokes
Mesh Points	300,000	605,000	1,340,000
RAM Memory	10 Mbytes	242 Mbytes	838 Mbytes
CPU Time	5 min 1 SGI R10000 CPU	0.5 hours 8 CPU Cray J-932	2.5 hours 8 CPU Cray J-932
Parallelization	None	6 out of 8 CPUs	6 out of 8 CPUs
Time to Mesh & Set-Up	1 hour	1 day	2 days

Figure 7: Comparison of computational costs of analyses with three CFD codes.

Drag reduction is a crucial part of the aircraft design process since the drag of an aircraft is directly related to fuel consumption and,

hence, operating costs. A vital aspect of this process is accurate drag prediction. The drag prediction techniques implemented in the KTRAN code are illustrated in figure 8 which gives total drag polars for a wing-body configuration and figure 9 which gives the drag rise curve of a typical wing-body-pylon-nacelle configuration.

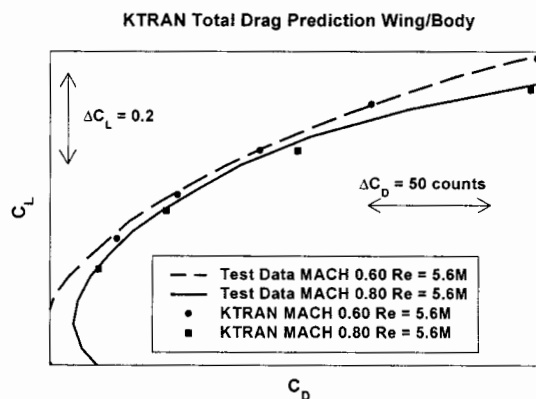


Figure 8: CFD prediction of total drag of a typical wing-body configuration

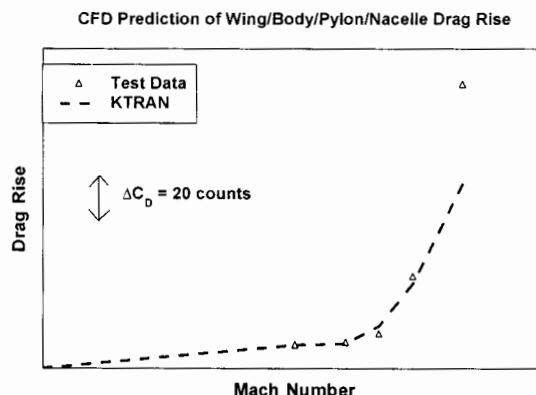


Figure 9: CFD prediction of total drag of a typical wing-body-pylon-nacelle configuration

Accurate drag prediction from the integration of pressures calculated with Navier-Stokes codes can be obtained, but that requires very large numbers of grid points. For this reason, the drag prediction modules developed for KTRAN were ported to the more accurate FANSC Euler/Navier-Stokes code. However, the prediction of viscous drag still tends to be inaccurate for cases with considerable flow separation found in some cases during the design process.

Figure 10 shows the predicted and experimentally derived buffet boundaries for the second iteration of a complete aircraft model. The CFD method used to predict the

buffet boundary of this configuration was calibrated on test data obtained on a previous configuration in a development wind tunnel test. The following test data indicated that the buffet boundary of the new configuration was close to the CFD prediction near typical cruise conditions and better than prediction elsewhere.

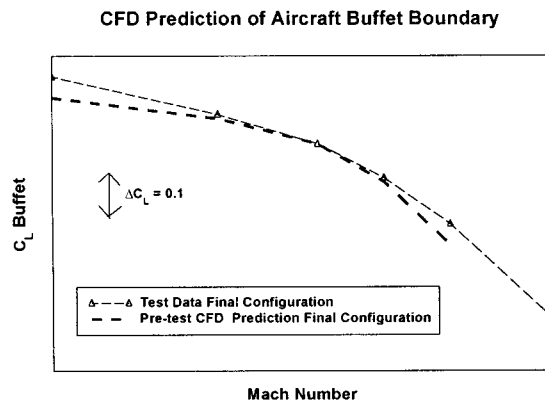


Figure 10: CFD prediction of the buffet boundary of a complete aircraft configuration.

KTRAN and FANSC are interfaced with Bombardier's ALLOP optimization program for wing design. This code was developed in-house for multi-point design optimization¹². The ALLOP program uses an unconstrained quasi-Newton minimization procedure to optimize a suitably chosen objective function. ALLOP modifies iteratively the geometric shape of a wing to minimize a specified objective function. The objective function can be the total drag, a component drag or the difference between computed and target pressure distributions. The code can use also a combination of multi-disciplinary functions, such as aerodynamic performance characteristics and wing weight. Constraints are introduced as penalty functions. The optimizer computes the sensitivity of the objective function to changes of each design parameter and then identifies the best direction for a line search. The disadvantage of an optimization method lies in the large number of flow solutions (several hundreds) that must be computed to evaluate the gradients. The computing times for the design of 3D wings can become prohibitive if the computing hardware is not powerful enough. All developments of ALLOP have therefore been geared towards the reduction of the turnaround time. The whole process has been designed to run in parallel mode over a large number of

CPU's. A load-sharing routine was also written to run the optimizer overnight on dozens of idle workstations. The traditional geometric representation of airfoils by cubic splines through co-ordinate points was replaced by more advanced Non Uniform Rational B-Splines (NURBS). The advantages of the new representation are:

- Reduction of the number of degrees of freedom necessary to model accurately an airfoil and, hence, a reduction of the number of variables required to design it.
- Faster convergence of the design process. This is because NURBS offer a more natural support for the optimization than the bump functions that were used traditionally to deform cubic splines.
- Reduced training requirements for new users of the design method, since the setting-up of the design problem is more intuitive with NURBS than with bump functions. Also, since NURBS are smooth by construction, their use does not introduce oscillations in the curves that would need to be smoothed on Catia workstations after the optimization. This step is completely obviated with the new method.

The next step is the use of NURBS to interpolate a wing 3D surface spanwise, between airfoil defining sections. The objective is to reduce the total number of parameters required to define a 3D wing while satisfying all required structural and manufacturing constraints on the wing geometry: no inflexions, minimum curvature of the wing plank, straight spars, etc. The biggest challenge here is to impose all necessary geometric constraints: straight leading and trailing edges, straight spoiler trailing edges, minimum curvature spars, etc.

It is our experience that the most complete representation of the aircraft is needed to design a wing. In particular, a model of the power-plant installation is needed since it modifies significantly the wing pressure distribution and aerodynamic characteristics. A representation of the tailplane is also needed if trim drag is to be taken into account and to minimize the induced drag of the complete, trimmed aircraft, as suggested by Munk. This immediately increases the number of grid

points required and makes the run times to convergence very large for sophisticated Euler and Navier-Stokes programs. There have been several attempts in industry to minimize this problem, such as running the codes to a lesser degree of convergence or to update only part of the flow field, but none of these solutions is really completely satisfactory. Unless high-fidelity codes are used in high-accuracy mode (complete aircraft model, fine meshes, uniform convergence), they may mislead the optimizer into what is essentially numerical noise. The optimization of a transonic wing must also be done for multiple design points. Otherwise, the wing may display good pressures at one cruise condition but have unacceptable aerodynamic characteristics at some other cruise condition or at off-design conditions. There are good examples of multi-point designs conducted with Full Potential/Boundary Layer codes reported in the literature¹³. These illustrate the trade-off that needs to be done between the complexity of the flow model and the complexity of the geometry. At Bombardier, complete aircraft KTRAN models are used for rapid investigation of the wing overall parameters: planform shape, thickness and camber distributions, spanwise load, trim conditions. The FANSC Euler/Boundary Layer code is used on tail-off configurations for section optimization including powerplant interference. The Euler/boundary layer code is also used extensively for the design of the wing-body fairing, cockpit and aft fuselage and for powerplant integration. Applications of this code to the design of the Global Express can be found in reference 3. Tail-Off FANSC Navier-Stokes models are used for final analysis at multiple design conditions and for the investigation of wing characteristics at off-design conditions. There is promising research in the area of wing design, notably the development of design methods using Control theory¹⁴. These methods promise convergence in 10 to 20 design cycles, each equivalent to 2 flow conditions; hence 20 to 40 solutions. At 10 hours on average for each solution, one design exercise would still need 200 to 400 hours of computing time and therefore require parallelization. Another promising area of research is transonic wing design by inverse optimization using a multi-objective genetic algorithm¹⁵.

CFD for Transonic Aerodynamic Analysis

CFD is also used to analyze the aerodynamic characteristics of various configurations (lift, drag, buffet boundary) and to generate distributions of pressures, forces, and moments needed for the estimation of airloads. During the detailed design phase of a project, CFD methods are used to guide the location of instrumentation (total and static pressure probes, alpha vanes, ice detectors) and to optimize the location of inlets and exhaust vents. One interesting example of the use of CFD is the application of the Euler code FANSC in qualifying Bombardier aircraft for safe flight under Reduced Vertical Separation Margins (RVSM). This supposes that the error of altitude indication on board the aircraft, including instrumentation error, is kept within tight tolerances. CFD, supported with a limited number of flight tests, was used to demonstrate that the static pressure variations due to normally expected skin waviness and instrument position tolerances do not introduce unacceptable altitude measurement errors. At 38,000 ft and Mach 0.80, a pressure variation ΔC_p of 0.01 will cause the altimeter to misread the altitude by 93 ft. It is therefore necessary to install the instrumentation with tight tolerances. FANSC was used to determine the acceptable tolerance. A multi-block grid generated for a Global Express wing-body configuration is shown in figure 11, with a large concentration of grid points in the cockpit area

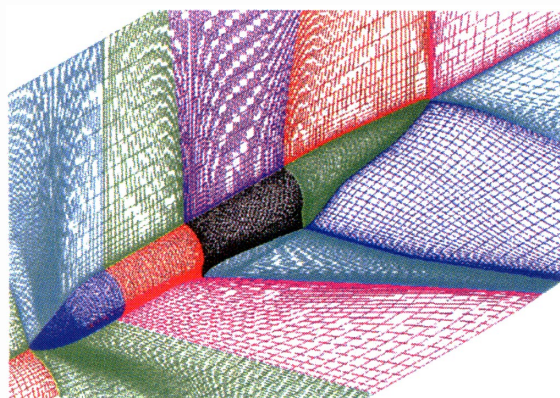


Figure 11: MBGRID multi-block Euler grid for a Global Express wing-body configuration.

Figure 12 shows pressure contours computed for the theoretical aircraft surface and for the real surface around the Pitot-Static probes as measured on one particular aircraft.

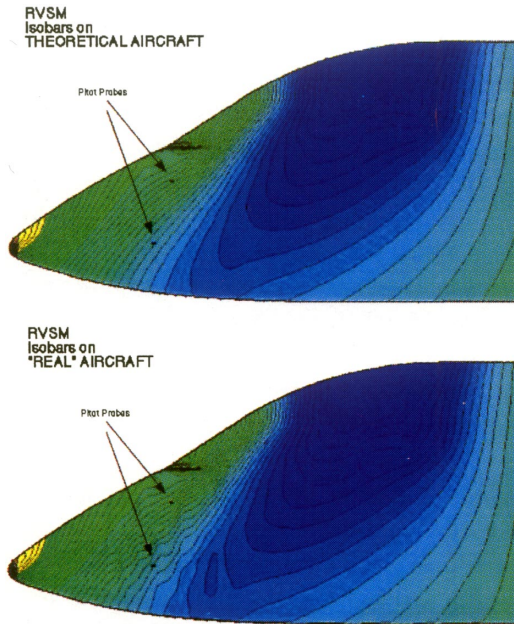


Figure 12: FANSC computed isobars on Global Express theoretical and manufactured cockpit surface.

The fine grid convergence characteristics of FANSC for this particular application are shown in Figure 13. The aircraft lift coefficient is converged for engineering purposes after 50 fine grid cycles. However, to reduce oscillations in local C_p 's at the Pitot-Static location requires 200 to 250 more cycles.

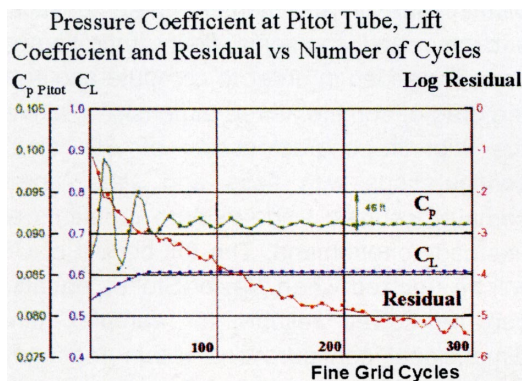


Figure 13: Convergence characteristics of FANSC computations on Global Express

CFD Methods for High-Lift

The design of high-lift systems goes through several iterations before it is finalized. The planform characteristics of flaps and slats are often determined by other considerations such as the location of the spars, the design of the actuating mechanisms, the installation of hydraulic lines, and that of the landing gear. The objective is normally to provide optimum

high-lift performance for take-off, climb, approach and landing while satisfying geometry requirements such as attitude on approach and landing. CFD is used to produce optimum contours for flaps, slats and for the fixed wing leading edge underneath the slats. It is used also to define optimum gaps and overlaps/overhangs for various deflections of flaps and slats. Two-dimensional studies of multi-element airfoils are made first on a number of sections along the wing span. Three codes are used for these studies, with increasing levels of complexity. The initial design is carried out using the CEBECI2DM panel code with viscous/inviscid interaction¹⁶. This code can model separated flows and is capable of predicting the complete (C_L, α) curve of a multi-element airfoil, up to and beyond maximum lift in a very short time. The code is used to establish baseline performance for various gaps and overlaps. The Analytical Methods Inc.'s MSES viscous Euler code for multi-element airfoils is used to study flap and slat contours. Configurations of interest are further checked with the NSU2D unstructured grid Navier-Stokes code¹⁷. The Navier-Stokes code is used in particular to investigate the flow field in the flap and slat coves. Fig. 14 shows a Navier-Stokes model of a CRJ-700 multi-element airfoil. The Analytical Methods Inc.'s VSAERO panel code is used to compute 3D loads on the wing and is used in combination with Bombardier semi-empirical methods to predict C_{Lmax} of various take-off and landing configurations. Fig.15 shows the VSAERO model used during the design of the CRJ-700 flaps and slats.

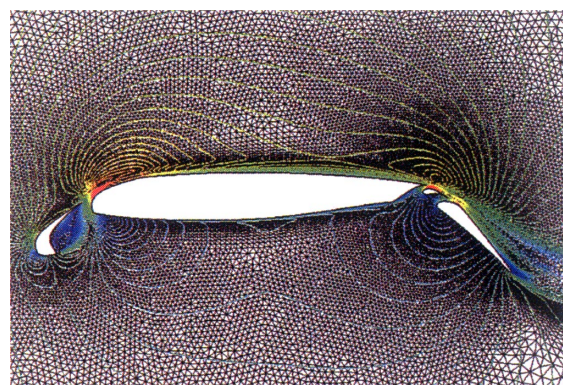


Figure 14: NSU2D Navier-Stokes model of a CRJ-700 multi-element airfoil; $\delta_{slat} = 25$ degrees, $\delta_{flap} = 40$ degrees, Mach 0.20 $\alpha = 3$ degrees.

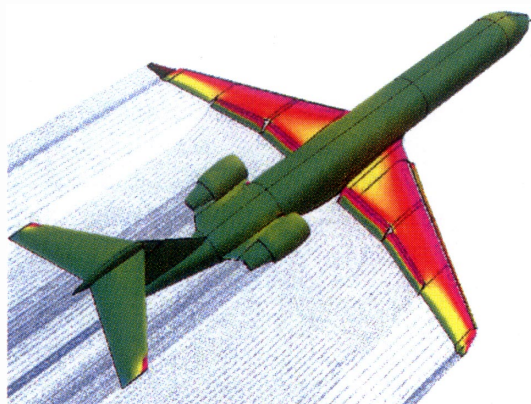


Figure 15: VSAERO model of the Bombardier CRJ-700 with landing flaps and slats; $M = 0.20$

2D Navier-Stokes codes are now used routinely for high-lift applications. 3D Navier-Stokes codes have only recently been applied to realistic high-lift configurations. Bombardier is studying the application of unstructured Navier-Stokes codes to the prediction of vortical and separated flows. The code used is D. Mavriplis' NSU3D¹⁸. Figure 16 shows an NSU3D Euler result of a Bombardier research configuration, focussing on engine installation. There are several difficulties to overcome before 3D Navier-Stokes codes can be used routinely by designers: grid quality requirements, large CPU time and memory requirements for good accuracy, convergence characteristics of solver and turbulence model, etc.

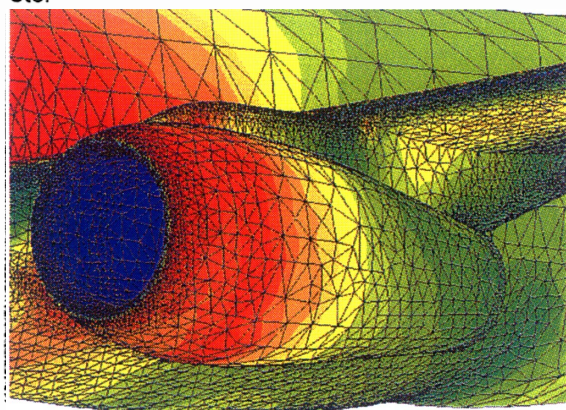


Figure 16: NSU3D Euler model of a Bombardier research configuration.

Aerodynamic Design Support Codes

Two CFD codes extensively used to support an aircraft development cycle are the CANICE ice-accretion code¹⁹ and the SCOLIC boundary layer stability and transition code²⁰. École Polytechnique de Montréal and Bombardier

developed these two codes. The first one is used to predict ice shapes on wing and tail surfaces and to obtain initial estimates of ice accretion. These estimates are used to size the anti-icing hot air system. The SCOLIC code is used to predict the location of natural transition on wings in typical flight conditions and in wind tunnel conditions. These results are used in the interpretation of wind tunnel results and in the extrapolation of the data to full-scale flight conditions. The code is also used to support studies of airfoils for hybrid laminar flow control experiments.

Conclusions

The experience of most aircraft manufacturers is that CFD methods allow the design of more efficient aircraft configurations with reduced risk and reduced cost and time. However, many codes acquired from external sources are research codes that do not meet all the requirements for design application. These codes are further developed by industry to meet the requirements of quality and acceptance with a reasonable degree of completeness. The level of effort required to develop good CFD codes into reliable industrial design and analysis tools is very large. In the absence of significant flow separation, CFD methods can provide today fairly accurate estimates of surface pressure distributions, lift and moment characteristics in subsonic and transonic flow. Improvements are still needed in order to compute accurately the drag of complex three-dimensional aircraft, the high-lift characteristics of 3D aircraft configurations with flaps and slats, and to compute coupled fluid-structure problems and unsteady phenomena. The full benefit of CFD will be realized when Navier-Stokes equations can be solved reliably for complex three-dimensional configurations within reasonable computing time.

Acknowledgement

The author would like to acknowledge the contribution of the staff of Bombardier Advanced Aerodynamics for the development of the codes, the running of the reported applications and the preparation of this document.

References

1. Mavriplis, F., "Comparison of Prediction, Wind Tunnel and Flight Test Data for the Canadair Challenger Turbofan Aircraft", AGARD CP-339, Oct. 1982
2. Mavriplis, F., "Design and Development of a Transonic Wing for the Canadair Regional Jet", CASI Journal Vol. 37, No. 4, Dec. 1991.
3. Kafyeke, F. and Mavriplis, F., "CFD for the Aerodynamic Design of Bombardier's Global Express High Performance Jet", AIAA Paper 97-2269, June 1997.
4. Murra I., "Sizing of a Regional Aircraft Wing – An Astros Application", CASI Journal, Vol. 44, No.1, March 1998.
5. Kafyeke, F., Piperni, P. and Robin, S., "Application of KTRAN Transonic Small Disturbance Code to the Challenger Business Jet Configuration with Winglets", SAE Paper 881483, October 1988.
6. Piperni, P., "Multi-Block Grid Generation with CAD-Based Domain Decomposition", Proceedings of the 4th International Conference on Numerical Grid Generation in CFD and Related Fields", 1994, pp. 109-121.
7. Kafyeke, F., Piperni, P., Mokhtarian, F., and Djilali, N., "Development of a Transonic Euler Method for Complete Aircraft Configurations", Proceedings, 3rd Canadian Symposium on Aerodynamics, Nov. 1991.
8. Laurendeau, E., Zhu, Z. and Mokhtarian, F., "Development of the FANSC Full Aircraft Navier-Stokes Code", Proceedings of the 46th Annual Conference of the Canadian Aeronautics and Space Institute, May 1999.
9. Laurendeau, E. and Thériault, M.-C., "Induced and Wave Drag Prediction Methods", Canadair memorandum MAA-000-295, January 1998.
10. Piperni, P., Patel, K. and Kafyeke, F., "The Prediction of Aircraft Trim Drag in Transonic Flight Using CFD", Proceedings of the 46th Annual Conference of the Canadian Aeronautics and Space Institute, May 1999.
11. Piperni, P., "New Elliptic Grid Generation Equations with Exact Curvature Effects", Proceedings from the 6th International Conference on Grid Generation, Greenwich, U.K., June 1998.
12. Lépine, J., Trépanier, J.Y. and Pépin, F., "Optimization of Wing Profile Geometrical Representation Using NURBS", Proceedings of the 46th Annual Conference of the Canadian Aeronautics and Space Institute, May 1999.
13. Tinoco, E.N., "The Impact of Computational Fluid Dynamics in Aircraft Design", CASI Journal, Vol. 44, No.3, September 1998.
14. Reuther, J.J. and Jameson, A., "Aerodynamic Shape Optimization of Wing and Wing-Body Configurations Using Control Theory", AIAA Paper 95-0123, Jan 1995.
15. Obayashi, S., Takahashi, S. and Fejtek, I., "Transonic Wing Design by Inverse Optimization Using MOGA", CFD98, 6th Annual Conference of the CFD Society of Canada, Quebec City, June 1998.
16. Cebeci, T., Jau, J. and Vitiello, D. "An Interactive Boundary Layer Approach to Multi-Element Airfoils at High Lift", AIAA Paper 92-0404, January 1992.
17. Mavriplis, D. J., "Turbulent Flow Calculations using Unstructured and Adaptive Meshes", International Journal for Numerical Methods in Fluids, Vol. 13, No. 9, pp. 1131-1152, Nov. 1991
18. Mavriplis, D. J., "Effective Aerodynamic Analysis Using Unstructured Meshes", CASI Journal, Vol. 44, No. 3, September 1998.
19. Tran, P., Brahim, M.T., Paraschivoiu, I., Pueyo, A. and Tezok, F., "Ice Accretion on Aircraft Wings with Thermodynamic Effects", AIAA Paper 94-0605, January 1994.
20. McDonald, P., Langlois, M. and Kafyeke, F., "Transition Prediction and Correlation on Bombardier Wings", Proceedings of the 46th Annual Conference of the Canadian Aeronautics and Space Institute, May 1999.

Sonic Boom Research: TsAGI Approach

S.L.Chernyshev, L.G.Ivanteeva, V.V.Kovalenko, L.L.Teperin
Central Aerohydrodynamic Research Institute
(TsAGI),

Due to sonic boom concern the supersonic flights are prohibited over the most populated areas. Development of future generation supersonic transport and ongoing space launch activity support interest in continuing sonic boom research. Since the flight experiment is expensive way of analysis and ground test facility does not provide full similarity in sonic boom modeling the numerical methods are the main tools in sonic boom analysis.

TsAGI has been involved in sonic boom theoretical, numerical and experimental research since 1960s. It was Prof. Zhilin who developed theory for calculating sonic boom from aircraft, flying along arbitrary trajectory with three-dimensional non-homogeneities of atmosphere. On a base of this theory the computational method of sonic boom analysis in stratified non-homogeneous atmosphere with three-dimensional wind has been developed. Computer code calculates pressure signature and ray paths both for primary and secondary sonic boom areas. It provides calculation of the sonic boom exposure areas on the ground including focusing boom, superboom, and secondary sonic boom areas.

The near field pressure distribution is used for F-function calculation on a base of panel methods or Euler equation solutions without introducing concept of equivalent body of revolution. This approach gives higher accuracy of sonic boom calculation in compared with regular quasi-linear Whitham based calculation technique.

Effects of aerodynamic configuration, flight trajectory, and atmospheric conditions on sonic boom have been investigated. Various aircraft geometry parameters, flight maneuvers, weather conditions have been considered in a sonic boom analysis.

Minimum boom concept and the main trends in SST sonic boom reduction have

been investigated. Computer code for the minimizing sonic boom due to aircraft geometry change has been developed. There are several low boom SST configurations, developed in accordance with this minimizing procedure.

Presented paper provides review of mentioned above TsAGI results in sonic boom prediction technique, analysis, and minimization. Most attention has been given to the recent results.

Dynamical Systems Approach to Optimization Problems — Optimization through Bifurcation —

Kazuo Tsuchiya

Graduate School of Engineering, Kyoto University,
Yoshida-Honmachi, Sakyo-ku, Kyoto city, Kyoto 606-8501, Japan

Abstract

This presentation introduces a heuristic method of optimization problem. The method which utilizes the successive bifurcations of replicator equations is explained. The performance of the method is demonstrated by applying to a combinatorial optimization problem, a quadratic assignment problem (Q.A.P.).

1 Introduction

One of the objectives of engineering science is to develop the methodology of system design. System design is to determine the structure of the system which realizes the given function. Here, the structure means the connections between the elements in the system. The computational theory of system design is the theory of optimization. The optimization problem is formulated as follows;

$$\text{Minimize } L(x_i) \quad (i = 1, \dots, N) \quad (1)$$

$$\text{subject to } g_k(x_i) \leq 0 \quad (k = 1, \dots, M)$$

where function $L(x_i)$ is called the objective function and variables x_i are called the decision variables. The functions g_k express the constraints on the problem. The methods of optimization are classified into two groups. One is the exact method which guarantees the optimality of the solution. The other is the heuristic method which may find a good solution

with a feasible computational cost. Now, we must deal with a complex optimization problem. Complex means that the size of the problem is large and the imposed constraints are complicated. Design of supersonic transport is one of the examples. At that time, from the practical view point, it becomes well suited to obtain an approximate solution with a feasible computational cost [1]. The heuristic methods are classified into two groups; one is the stochastic method and the other is the deterministic method. For the algorithms of the stochastic method, there are the simulated annealing algorithm and the genetic algorithm, etc.. The deterministic method was first formulated from the stochastic method by the use of the mean field approximation. The basic idea of the heuristic method is as follows; first, an energy function is composed of the objective function and the constraints,

$$E(x_i) = L(x_i) + \sum_{k=1}^M \lambda_k g_k(x_i) \quad (2)$$

where λ_k are the constants. A dynamic system of the variables x_i is constructed as a gradient vector field of the energy function $E(x_i)$

$$\dot{x}_i = -\frac{\partial}{\partial x_i} E(x_i). \quad (3)$$

The approximate solution of the problem is obtained as an equilibrium point of Eq. (3). To improve the performance of the solution, the annealing algorithm (deterministic annealing) is applied. The deterministic annealing is to

vary the parameter in the system slowly. Usually, the rate of variation (Annealing schedule) is determined empirically. We have proposed another model of the deterministic method of optimization problem. As the dynamic system, we adopt a replicator system instead of a gradient system and the annealing schedule is determined based on the bifurcation characteristics of the replicator equation.

In the following, the basic characteristics of the replicator equation is explained briefly in Sec. 2 and the proposed method of optimization proposed is explained with numerical examples in Sec. 3.

2 The Replicator Equation [2]

The replicator equation is the equation where the derivative of the variables is proportional to the state of the variable. Here, we use the following simple model,

$$U^T = (u_1, \dots, u_N) \quad (4)$$

$$\dot{u}_i = f_i(u_j; \lambda_i, \alpha)u_i$$

$$f_i(u_j; \lambda_i, \alpha) = (\lambda_i - u_i^2) - \alpha \sum_{j \neq i}^N u_j^2$$

$$\lambda_1 > \lambda_2 > \dots > \lambda_N > 0, \quad \alpha > 0$$

The proportional coefficient (growth rate) f_i is composed of two terms; the first one expresses the self activatory and inhibitory influences, and the second one expresses the mutual inhibitory interactions between elements. There are three types of equilibrium solution. The first one is the uniform solution U_{uni} where all the elements take non zero values, the second one is the transient solution $U_{\text{trans}}^{(k)}$ where the values of the last k elements are zero, and the third one is the feasible solution $U_{\text{feas}}^{(i)}$ where the only i th element has non zero value; that is,

$$U_{\text{uni}} = (*, *, \dots, *) \quad (5)$$

$$U_{\text{trans}}^{(k)} = (*, \dots, *, \overbrace{0, \dots, 0}^k)$$

$$U_{\text{feas}}^{(i)} = (0, \dots, 0, \underset{i}{*}, 0, \dots, 0)$$

where $*$ means a non zero value.

The stability of Sols. U_{uni} and $U_{\text{feas}}^{(i)}$ are as follows; in the region where α is small, Sol. U_{uni} is the only stable equilibrium solution whereas in the region where α is large, Sols. U_{feas} are the only stable equilibrium solutions. And, the bifurcation characteristics of the branch connected to Sol. U_{uni} are as follows; when parameter α increases, Sol. U_{uni} connects with Sol. $U_{\text{trans}}^{(1)}$ through the pitchfork bifurcation and then, finally, connects with Sol. $U_{\text{feas}}^{(1)}$, where Sol. $U_{\text{feas}}^{(1)}$ is the solution in which the only element with the largest value of λ has a non zero value (Fig. 1), where α_U is the point at which Sol. U_{uni} becomes unstable through the bifurcation and $\alpha_F^{(i)}$ is the point at which Sol. $U_{\text{feas}}^{(i)}$ becomes stable through the bifurcation.

It should be noted that, *from the view point of optimization, this process can be thought to be a process which searches the element with the largest value of λ .*

The optimization method which utilizes the bifurcation characteristics of the replicator equation has been proposed. It will be explained in Sec. 3.

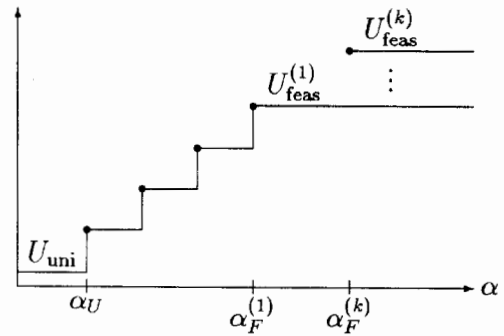


Fig. 1. Schematic diagram of bifurcation of Eq. (4)

3 Optimization Method [3, 4]

The optimization problem is classified into two groups, the nonlinear optimization problem and the combinatorial optimization problem. The former is the problem where the decision variables are continuous whereas the latter is the problem where the decision variables are discrete. Here, the optimization method which utilizes the bifurcation characteristics of a replicator equation is explained for the combinatorial optimization problem. It should be mentioned that this method can be also successfully applied to a nonlinear optimization problem. One of the examples of combinatorial optimization problem is the quadratic assignment problem (Q.A.P.). Q.A.P. is formulated as follows;

$$\text{Minimize } L(X) = \text{trace}(A^T X^T B X) \quad (6)$$

where X is a $N \times N$ permutation matrix, A, B are given $N \times N$ matrices. For the problem, we set the following replicator equation

$$U = [u_{ij}] \quad (i, j = 1, \dots, N) \quad (7)$$

$$\dot{u}_{ij} = f_{ij}(u_{i'j'}, \alpha_0, \alpha_1) u_{ij}$$

The growth rate f_{ij} is determined so that matrix U asymptotically converges to matrix X with a small value of the objective function $L(X)$. The growth rate is designed as follows;

$$f_{ij} = (1 - u_{ij}^2) - \frac{\alpha_0}{2} \left(\sum_{i' \neq i} u_{i'j}^2 + \sum_{j' \neq j} u_{ij'}^2 \right) - \frac{\alpha_1}{2} \sum_{i', j'} (a_{jj'} b_{i'i} + a_{j'j} b_{i'i}) u_{i'j'}^2 \quad (8)$$

$$(i, j = 1, \dots, N),$$

The growth rate is composed of three terms; the first one expresses a self activatory and inhibitory influence and the second one expresses mutual inhibitory interactions between the elements in the same row and column. The third one expresses the inhibitory influence due to the objective function. There are three types

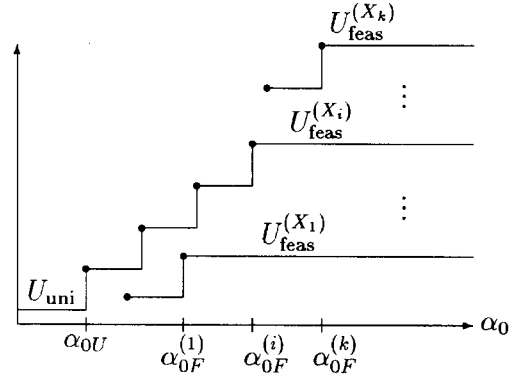


Fig. 2. Schematic diagram of bifurcation of Eq. (7)

of equilibrium solution. The first one is the uniform solution U_{uni} where all the elements take non zero values and the second one is the transient solution $U_{\text{trans}}^{(k)}$ where k elements take zero values. The third one is the feasible solution $U_{\text{feas}}^{(X)}$ where only the one element in a row and a column takes a non zero value. A feasible solution $U_{\text{feas}}^{(X)}$ corresponds to a permutation matrix X . The stabilities of Sol. U_{uni} and $U_{\text{feas}}^{(X)}$ are as follows; in the region where α_0 is small, Sol. U_{uni} is the only stable equilibrium solution whereas, in the region where α_0 is large, Sol. $U_{\text{feas}}^{(X)}$ are only the stable equilibrium solutions. And, the bifurcation characteristics of the branch connected to Sol. U_{uni} are as follows; when parameter α_0 increases, Sol. U_{uni} connects with Sol. $U_{\text{trans}}^{(1)}$ through the pitchfork bifurcation and then, finally connects with Sol. $U_{\text{feas}}^{(X_i)}$ where Sol. $U_{\text{feas}}^{(X_i)}$ corresponds to permutation matrix X_i which gives the i th smallest value of the objective function $L(X)$. Indeed, Sol. $U_{\text{feas}}^{(X_i)}$ is not the optimum solution but, in many cases, is a good approximate solution (Fig. 2), where α_{0U} is the point at which Sol. U_{uni} becomes unstable through the bifurcation and $\alpha_{0F}^{(i)}$ is the point at which Sol. $U_{\text{feas}}^{(i)}$ becomes stable through the bifurcation.

Based on the analysis, the optimization algorithm has been proposed;

1. Trace the branch of Sol. U_{uni} by increasing

α_0 slowly.

2. Accept Sol. $U_{\text{feas}}^{(X_i)}$ obtained as an approximate solution of the problem.

In order to improve the performance of the solution, the parameter α_0 must be increased very slowly near the bifurcation points. The deterministic annealing algorithm is designed as follows; Function S , the entropy over the set of the solutions, is introduced such that

$$S = -\frac{1}{N \ln N} \sum_{i,j} p_{ij} \ln p_{ij} \quad (9)$$

$$p_{ij} = \frac{u_{ij}^2}{\sum_{j'} u_{ij'}^2}$$

The annealing schedule is given as

$$\Delta\alpha_0 = \left(\frac{\Delta S^{\text{d}}}{\Delta S^{\text{old}}} \right) \Delta\alpha_0^{\text{old}} \quad (10)$$

where $\Delta\alpha_0$ is the amount of increment of parameter α_0 for the interval of time, $\Delta\alpha_0^{\text{old}}$ and ΔS^{old} are the amounts of increment of parameters α_0 and S for the previous interval of time. Since entropy S is sensitive to the variation of parameter α_0 near the bifurcation points, by the use of the annealing schedule (10), the value of parameter α_0 is increased slowly at the points where the bifurcations occur and as a result, a solution with a high performance may be obtained.

The proposed optimization algorithm is applied to the problems in QAPLIB. Some of the results are shown in Table 1. It can be seen that for many problems, the difference between the value obtained and the optimum value is less than 1%. The CPU time for the problem, $N = 20$, is about 2 min by DEC Alpha Station 500/333.

References

- [1] C. R. Reeves, editor. *Modern Heuristic Techniques for Combinatorial Problems*. Blackwell Scientific Publications, 1993.

Table 1. Performance of the proposed method

name	N	L_{opt}	L	L/L_{opt}
Had20	20	6922	6970	1.00693
Nug24	24	3488	3490	1.00057
Tho30	30	(149936)	151256	1.0088
Tho40	40	(240516)	241192	1.00281
Tai50a	50	(4941410)	5051386	1.02226
wil50	50	(48816)	48892	1.00156
Sko56	56	(34458)	34502	1.00128
Tai80a	80	(13557864)	13733524	1.01296
Tai80b	80	(818415043)	821025553	1.00319
Sko100a	100	(152002)	152502	1.00329
wil100	100	(273038)	273294	1.00094
Tho150	150	(8133484)	8158137	1.00303

- [2] A. S. Mikhailov. *Foundations of Synergetics I*, chapter 7. Springer-Verlag, 1994.
- [3] K. Tsuchiya, T. Nishiyama, and K. Tsujita. An algorithm for a combinatorial optimization problem based on bifurcation. submitted to *Neural Networks*.
- [4] K. Tsuchiya, T. Nishiyama, and K. Tsujita. A deterministic annealing algorithm for a combinatorial optimization problem using replicator equations. submitted to *Physica D*.

Aerodynamic Design of Supersonic Experimental Airplane

Toshiyuki Iwamiya, Kenji Yoshida, Yuichi Shimbo,
Yoshikazu Makino (NAL), Kisa Matsushima (Fujitsu)

Abstract

In the first stage of the NAL's experiment for supersonic transport (NEXST-1) project, the aerodynamic design has focused on the reduction of drag at a supersonic cruising speed with a clean wing-body configuration by using Computational Fluid Dynamics (CFD). In the course of design process, four aerodynamic concepts have been applied: (1) arrow-type planform design (2) warped wing (3) area-ruled body (4) a natural laminar flow (NLF) wing. (1) and (2) are effective for the reduction of drag due to lift while (3) is effective for the reduction of wave drag due to volume. They are the concepts based on the linear theory. The concept (4) is devised for the reduction of the friction drag. The application of the NLF concept to the SST configuration has no previous instance and an original trial.

For the realization of the NLF wing at supersonic cruising speed, we first designed a pressure distribution on the wing and then applied an inverse design method based on the supersonic small perturbation equation. After less than 10 design cycles, we obtained a satisfactory design result which display a good agreement with target pressure. The transition position was evaluated by an incompressible boundary layer stability code (SALLY code) and compressible boundary layer stability code (LSTAB code), the latter of which was developed in NAL. The evaluation revealed that the turbulence transition characteristics are good.

1. Introduction

National Aerospace Laboratory (NAL) initiated a supersonic research project in 1997. This is the project including two flight experiments. The configuration of the first experimental airplane was selected to be a simple wing-body configuration with no engines to easily evaluate the relation between the design intention and the design process.

The computer simulation technology for not only structure but also aerodynamics has made rapid progress in the past several decades. It seems well developed to be incorporated in the design process as a design tool as well as analysis tool. We intended to apply the CFD based aerodynamic design approach to determine the wing-body configuration as much as possible. Hence we set that one of the objectives in the project is to test the capability of CFD technologies in their application to achieve a higher lift-to-drag ratio at the design point and to validate it by flight tests of the designed vehicles.

2. Review of Design Process

We first set a target specification that is reasonable for the next generation supersonic transport. The cruising speed is Mach 2.0 and the lift coefficient is 0.1.

The aerodynamic design process of the experimental airplane followed conventional procedures based on the linear theory (Ref.1). In this stage, three aerodynamic concepts have been applied: (1) arrow-type planform design (2) warped wing and (3) area-ruled

body. See fig. 1.

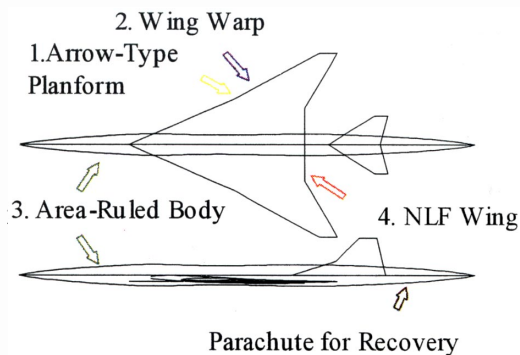


Fig. 1 Aerodynamic Concept for NEXST-1

Ninety-nine arrow wings wing with a subsonic leading edge and aspect ratio between 1.8 and 2.2 were examined by using a supersonic lifting surface theory. Among them, we chose eight planforms with the best drag-due-to-lift parameter. For each of the eight planform, a wing warp was designed with use of the Carlson's method (Ref.2). The method designed the optimal load distribution and the corresponding camber geometry that minimizes the drag due to lift at the design point. A supersonic area rule (Ref.3) was also applied to minimize a drag due to volume. The body was so designed that the cross sectional area distribution of the aircraft is the same as that of the equivalent Shears-Hack body.

For the scaled supersonic experimental airplane with a body length of 11.5m, the friction drag was estimated to occupy about a half portion of the total drag if the flow is fully turbulent over the airplane. Therefore, the fourth concept we applied to the experimental airplane is a natural laminar flow (NLF) wing concept to improve L/D.

2. Natural Laminar Flow Wing

2.1. Target Pressure Distribution

The transition from laminar to turbulent

flow on a wing with a large sweptback angle is governed by the amplification of the disturbance through cross flow instability. Pressure distributions on the upper wing surface with a steep pressure drop near the leading edge followed by an almost flat distribution toward the trailing edge might be effective for the suppression of the growth. With a certain parameterization having this feature, the transition characteristics were evaluated by an incompressible boundary layer stability code (SALLY code) based on the so-called e^N method (Ref.4), where N is the amplification factor of disturbance. One of them indicating a wide laminar flow region was selected as a target pressure distribution on the upper wing surface.

On the other hand, Navier-Stokes analysis indicated the discrepancy in load distribution from the optimum one which was derived in the warp design. The second strategy of the target pressure design on the wing is to set the pressure distribution on the lower wing surface to recover the optimum load distribution by subtracting from the upper surface pressure distribution. The target pressure distribution at the 30% semi span station is shown in fig. 2.

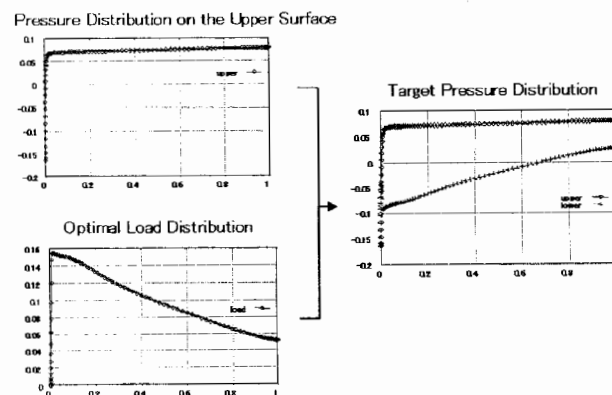


Fig. 2 Target Pressure Distribution

2.2 Inverse Design Method

In order to realize the target pressure distribution defined as above, a newly developed inverse design method was applied. The feature of the method is the utilization of linearized supersonic small disturbance equation to connect a pressure difference with an increment of the geometry. The formulation like this is originated by Takanashi (Ref.5). He treated the transonic wing design. We can say that this method is a supersonic version of Takanashi's method. The flowchart of the inverse design is shown in fig. 3. The design system consists of an inverse problem solver and a Navier-Stokes solver. The geometry is successively modified until the pressure distribution can be regarded as the target.

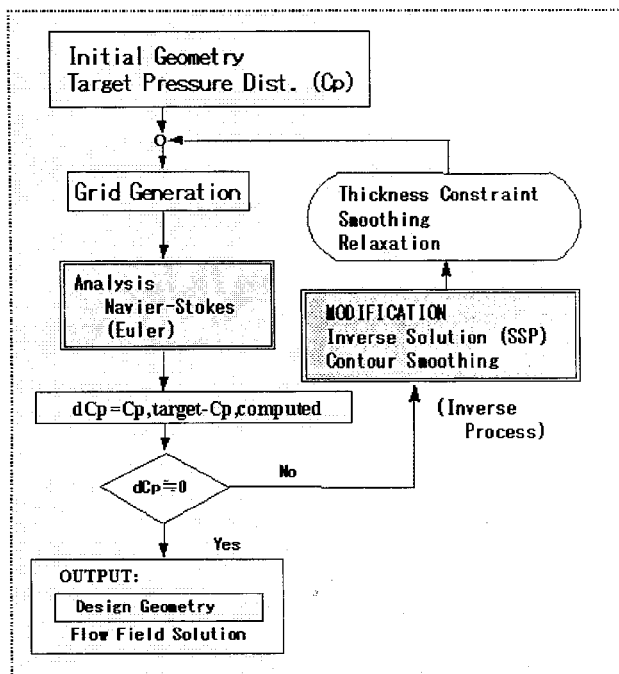


Fig.3. Flowchart of Inverse Design Method

The first version of the method was examined during 1997 and 1998 (Ref.6). We improved the way of treatment of the constraints such as wing thickness that come from structural requirements. These constraints were imposed after the geometry

modification. After the first inverse design, we found that the body volume should be increased due to the installation of equipments. Therefore, we had to change the sectional area distribution of the body. We applied the improved version of the inverse design system to the new wing-body configuration. With the geometry designed in the previous design process as the initial geometry, we executed 6 design cycles to obtain a admissible coincidence.

Figure 4 shows the target and final pressure distribution at 30% semi-span location with the wing section. The feature of the target pressure distribution is well reproduced and the good agreement can be seen. Good transition characteristics are expected. Refer to Ref.7 for more detail of the treatment of constraints.

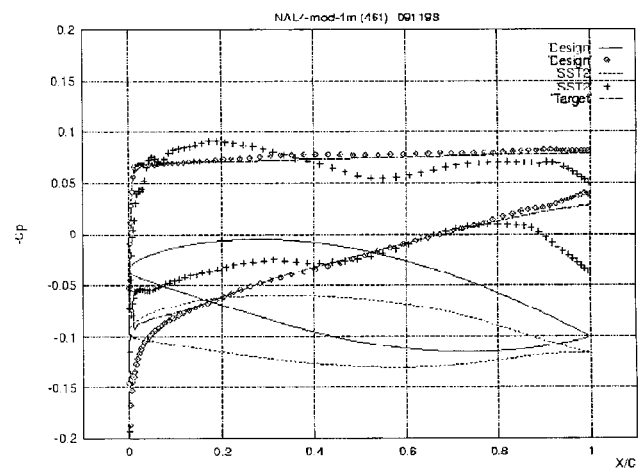


Fig.4. Comparison of Pressure Distribution at 30% semi span

2.3. Transition Characteristics

The key point in the design of the NLF wing is how the transition characteristics can be estimated correctly. The SALLY code has been utilized to estimate the transition location when the target pressure distribution was set. The SALLY code is well known but based on

the stability theory for the incompressible flow and does not take the compressibility of the flow into account. To improve this point, the LSTAB code was developed which considers the compressibility of the flow. Figure 5 and 6 display the transition locations corresponding to each N value estimated by the SALLY code and by the LSTAB code, respectively. Although the N values estimated by the LSTAB code are about a half of those estimated by the SALLY code, the qualitative tendencies are the same. Since there is no database of the N value for the transition point in the flight environment, it is difficult to predict the transition location quantitatively, but we can conclude that the application of the SALLY code that accounts for the transition in our design is turned out reasonable. Refer to Ref.8 for more detail.

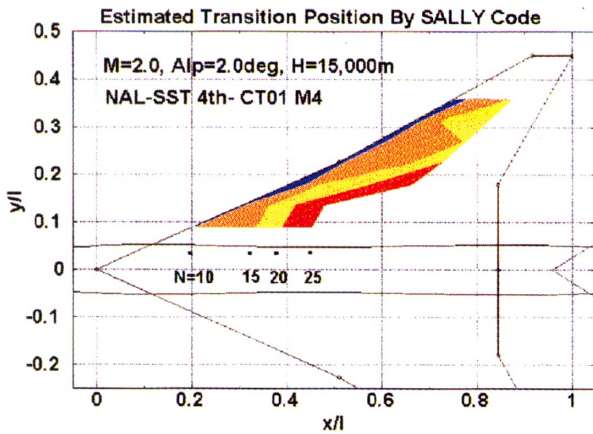


Fig. 5. Transition Location Estimated by SALLY code

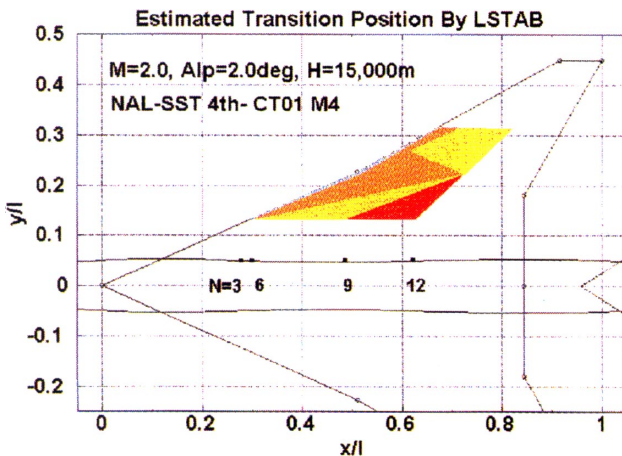


Fig. 6. Transition Location Estimated by LSTAB

3. Stability around the Design Point

Stability around the design point was also examined. Figure 7 shows the pressure distribution at the 30% semi span station with the angle of attack varied. No big change in characteristics can be seen. Estimated friction drag corresponding to the attack angle is shown in fig. 8.

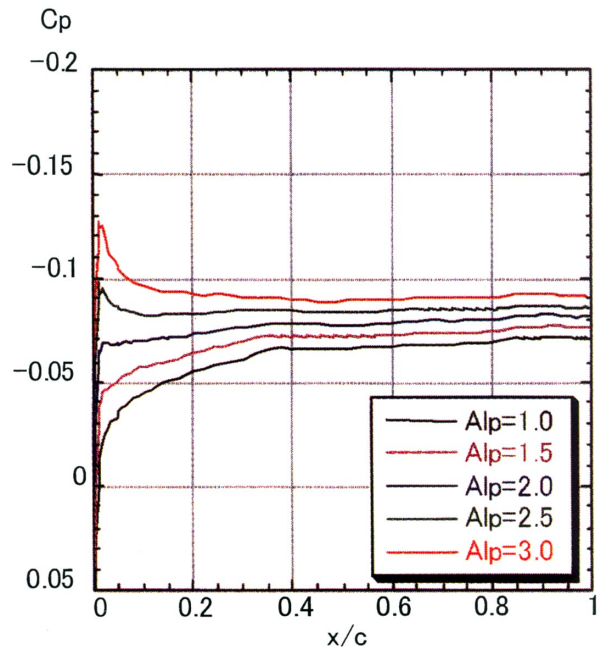


Fig. 7. Pressure Distribution at off-design points

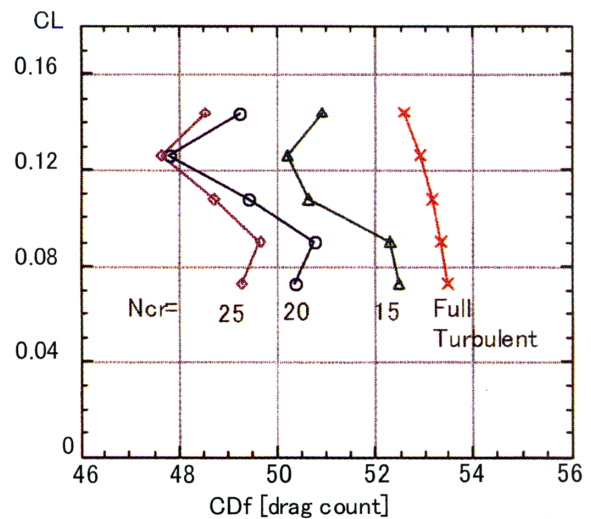


Fig. 8. Estimated Friction Drag

Several wind tunnel experiments were done and are planned by the transition

experiment team in NAL to ensure the transition characteristics of the designed configuration. Figure 9 shows a comparison of a supersonic wind tunnel test and a CFD analysis, that shows the good agreement. The detail of the experiments will be reported in the near future.

In the flight tests that will be performed in 2002, the transition location will be measured with the use of hot-films(x), thermocouples(+), unsteady pressure transducer(*), and Preston tube(*). Figure 10 shows the location of measurement points. Pressure distribution is also measured to compare with the CFD analysis.

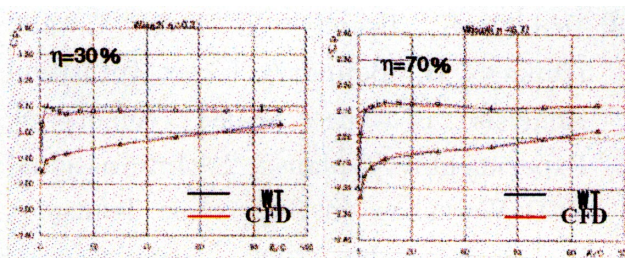


Fig. 9. Pressure Distribution ($M=2$, $\alpha=2\text{deg}$)

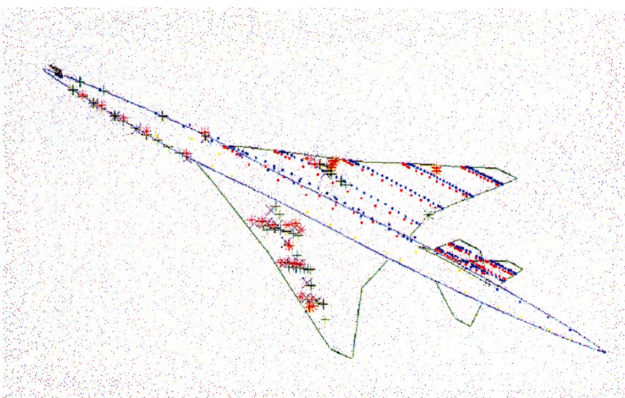


Fig. 9. Measurement points of NEXST-1

3. Toward NEXST-2

The critical design of NEXST-1 has been completed in 1999. The next target of CFD-based design is NEXST-2, which is now on the preliminary design phase. The target is the same, the reduction of the drag. For the

purpose, we are preparing both analysis and design tools and trying a preliminary design.

- CFD analysis of interaction between wings, body and nacelles.
 - Improvement of accuracy of a structured grid based CFD analysis in simulating a flow around supersonic transports, especially the interaction between wings and nacelles (fig.10).

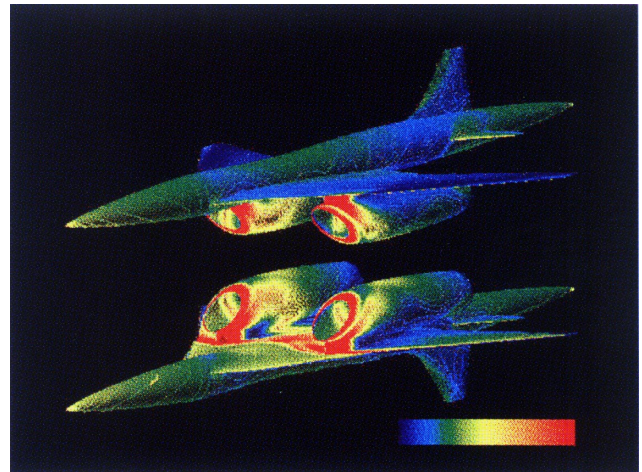


Fig. 10. Navier-Stokes Analysis with Multiblock Grid

- Try again the NLF concept on the upper surface of the wing (the prediction of transition position and widen the applicability of the inverse design method)
 - Establish the construction of target pressure distribution introducing a relaxation of wing-nacelle interaction
 - Widen the applicability of the Inverse wing design method with ensuring design constraint
 - Improve the boundary layer transition analysis to predict a precise transition location
- Use the optimization technique to attenuate the interference from the nacelle
 - Aerodynamic nacelle shape optimization (See ref. 9)
 - Wing shape optimization

4. Conclusion NAL's first supersonic experimental airplane (NEXST-1) was designed and the CFD design tools based on a supersonic inverse problem were successfully used for incorporating the NLF concept. Stability analyses show the good characteristics of transition. Wind tunnel experiments under way also support the features. A farther wind tunnel tests are planned to improve the prediction tools of transition. The flight test is planned to perform in 2002.

References

- (1) Shimbo Y., Yoshida K., Iwamiya T., Takaki R. and Matsushima K., Aerodynamic Design of the Scaled Supersonic Experimental Airplane, 1st International CFD Workshop on Supersonic Transport Design, Tokyo, Mar., 1998.
- (2) Carlson H. W. and Miller D. S., Numerical Method for the Design and Analysis of Wings at Supersonic Speeds, NASA TN D-7713, 1974.
- (3) Ashley H. and Landahl M., Aerodynamics of Wings and Bodies, Addison-Wesley Publishing Company, Inc., 1965.
- (4) Srokowski, Mass Flow Requirements for LFC Wing Design, AIAA 77-1222
- (5) Takanashi S., Iterative Three Dimensional Transonic Wing Design Using Integral Equations, J. of Aircraft, Vol. 22, No. 8, pp. 655-660, 1985.
- (6) Matsushima K., Iwamiya T., Jeong S., and Obayashi S., Aerodynamic Wing Design for NAL's SST Using Iterative Inverse Approach, 1st International CFD Workshop on Supersonic Transport Design, Tokyo, Mar., 1998.
- (7) Matsushima K., Iwamiya T., and Zhang W., Inverse Wing Design for the Scaled Supersonic Experimental Airplane with Ensuring Design Constraints, 2nd International CFD Workshop on Supersonic Transport Design, Tokyo, Jan., 2000
- (8) Yoshida K., Iwamiya T., Ueda Y., and Ishikawa H., Boundary Layer Transition Analysis of the Scaled Supersonic Experimental Airplanes, 2nd International CFD Workshop on Supersonic Transport Design, Tokyo, Jan., 2000
- (9) Makino Y., Iwamiya T., and Lei Z., Aerodynamic Nacelle Shape Optimization for NAL's Experimental Airplane, 2nd International CFD Workshop on Supersonic Transport Design, Tokyo, Jan., 2000

Boundary Layer Transition Analysis of the Scaled Supersonic Experimental Airplane

Kenji YOSHIDA (Advanced Technology Aircraft Project Center, NAL: yoshiken@nal.go.jp)
 Toshiyuki IWAMIYA (Computational Science Division, NAL: iwamiya@nal.go.jp)
 Yoshine UEDA (Supporting Staff for Priority Research, NAL: yueda@nal.go.jp)
 Hiroaki ISHIKAWA (Sankoh Software Dept. Co., LTD: hiroaki@nal.go.jp)

ABSTRACT

Boundary layer transition characteristics of the scaled supersonic experimental airplane was numerically analyzed to confirm its natural laminar flow (NLF) wing design. Using conventional incompressible and newly developed compressible transition prediction codes based on an e^N method, the NLF characteristics were well confirmed through the following results. (1) The step function type target pressure distribution applied in the NLF wing design was found to be optimum. (2) Comparing the transition N value estimated by the compressible code with experimental results obtained by NASA, wide laminar region of the NLF wing was expected. (3) Laminar boundary layer profiles estimated by a Navier-Stokes code led to smaller N value than one by the compressible boundary layer code. (4) No transition due to attachment-line contamination was predicted.

INTRODUCTION

National Aerospace Laboratory (NAL) is promoting the National Experimental Supersonic Transport (NEXST) Program¹⁾. In the aerodynamic design of the unmanned and non-powered scaled supersonic experimental airplane (NEXST-1), an original natural laminar flow (NLF) wing concept was applied to reduce its friction drag^{2, 3)}. A target pressure (C_p) distribution⁴⁾ to delay natural transition and a newly-developed CFD-based supersonic inverse method⁵⁾ were combined to design the wing geometry.

In this NLF wing design, transition analysis plays a major role. We used a well-known transition prediction code called SALLY⁶⁾ based on an e^N method as a practical tool. In general, the e^N method estimates the so-called N value defined as integrated amplification rates of small disturbances. If a critical N value corresponding to natural transition ("transition N value") is specified through wind tunnel tests or flight tests, it can estimate transition location. However, since we only have a few data for the transition N value in three-dimensional supersonic flow, we can not predict it at present. Therefore the best way

to analyze transition characteristics is to investigate the qualitative characteristics of transition locations corresponding to several typical N values.

After several iterative design processes, the desired NLF wing was designed at a design point of $M=2.0$, $C_L=0.1$ and 15,000 m in altitude^{2, 3)}. Fig.1 shows estimated chordwise N characteristics at a typical spanwise station of the NLF wing. The SALLY code estimates two kinds of N value, one is for Tollmien-Schlichting (T-S) instability and another is for crossflow (C-F) instability. As is shown in this figure, the growth of N value due to C-F instability at the front part of the wing was completely suppressed. Fig.2 shows estimated transition locations corresponding to typical transition N values. If $N=20\sim 25$ is a transition N value, we suppose a large laminar region on the upper surface at supersonic speed. The validity of this selection will be discussed later.

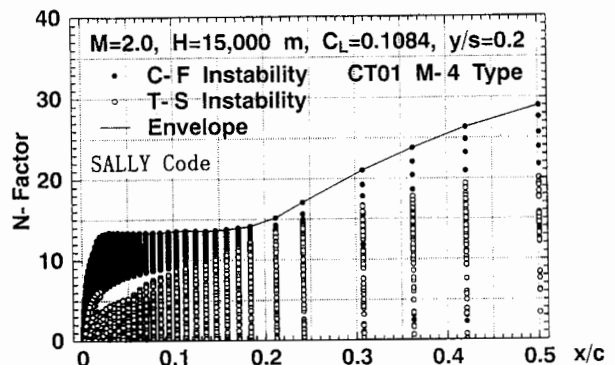


Figure 1. N characteristics estimated by SALLY code at 20% semi-spanwise station of the designed NLF wing

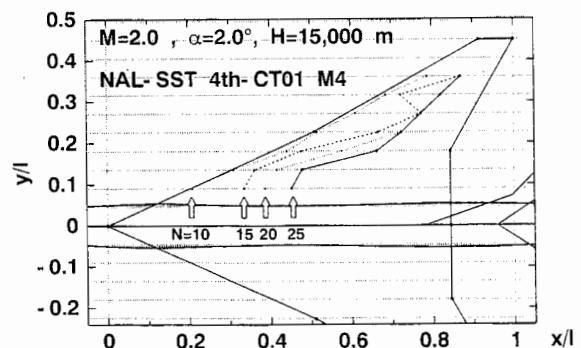


Figure 2. Estimated transition locations of the NLF wing by SALLY code

In this work, we have advanced the transition analysis to establish this NLF wing design concept completely by solving the following problems.

- (1) We have never confirmed that the step function type target Cp distribution for the NLF wing design is optimum.
- (2) Since the SALLY code was formulated on an incompressible stability theory, we must investigate the effect of compressibility.
- (3) In general, any current three-dimensional e^N method has not been completely established yet, because of the following problems, how to select the integral path of amplification rate, how to specify any relations among components of complex wave number vector, and how to understand the influence of higher mode (Mack mode) instability on transition process.
- (4) The laminar velocity profile near the leading edge estimated by boundary layer approximation is relatively inaccurate, because of the strong streamline curvature.
- (5) We have only a few experimental data on transition N value in supersonic flow.
- (6) In addition, we must also investigate the possibility of transition due to attachment-line contamination.

This paper describes some trials on them.

RECONSIDERATION OF TARGET Cp DISTRIBUTION

The present target Cp distribution³⁾ for the NLF wing was derived under the following consideration. To suppress C-F and T-S instabilities, a pressure distribution with narrow accelerated region near the leading edge and no adverse pressure gradient from mid to rear chord is very effective. Therefore we specified the target Cp distribution with a shape like "step function" shown in Fig.3 in achieving the NLF design. The detail was described in Refs.2-3.

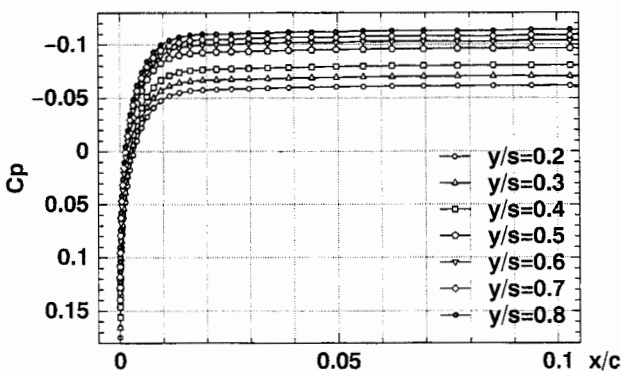


Figure 3. Target Cp distributions for supersonic NLF wing design at M=2.0, Cl=0.1

To investigate the validity of this target Cp, we made a model of Cp distribution schematically shown in Fig.4. The major parameters characterizing it are pressure gradient (m_1) between $\xi = 0$ and ξ_1 , width of the accelerated region (ξ_2), flat Cp level (Cp_2) and pressure gradient ($m_2 = \tan \phi$). The combination corresponding to the target Cp was named as "case No.0" in Fig.5 and other 20 combinations of those parameters listed in Table 1 were generated. Fig.5 shows typical candidate distributions and N characteristics of these 21 combinations were evaluated by the SALLY code.

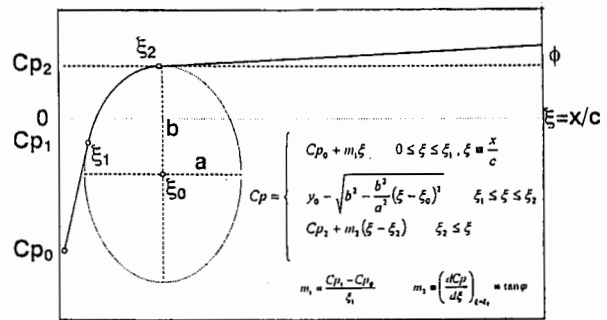


Figure 4. A model of the target Cp distribution for the NLF wing design

Table 1. Combinations of parameters on candidate target Cp distributions

No.	Parameters of Model Cp						
	Cp ₂	ξ ₁	Cp ₁	m ₁	ξ ₂	Cp ₂	φ
0	0.165	0.0010	0.030	-135.00	0.016	-0.065	-0.0595
1	0.165	0.0050	0.030	-27.00	0.016	-0.065	-0.0595
2	0.165	0.0005	0.030	-270.00	0.016	-0.065	-0.0595
3	0.165	0.0010	0.030	-135.00	0.016	-0.030	-0.0595
4	0.165	0.0010	0.030	-135.00	0.016	-0.100	-0.0595
5	0.165	0.0010	0.030	-135.00	0.008	-0.065	-0.0595
6	0.165	0.0010	0.030	-135.00	0.024	-0.065	-0.0595
7	0.165	0.0050	0.030	-27.00	0.016	-0.030	-0.0595
8	0.165	0.0050	0.030	-27.00	0.016	-0.100	-0.0595
9	0.165	0.0005	0.030	-270.00	0.016	-0.030	-0.0595
10	0.165	0.0005	0.030	-270.00	0.016	-0.100	-0.0595
11	0.165	0.0020	0.030	-67.50	0.016	-0.065	-0.0595
12	0.165	0.0020	0.030	-67.50	0.016	-0.030	-0.0595
13	0.165	0.0020	0.030	-67.50	0.010	-0.065	-0.0595
14	0.165	0.0020	0.030	-67.50	0.010	-0.030	-0.0595
15	0.165	0.0020	0.050	-57.50	0.016	-0.065	-0.0595
16	0.165	0.0020	0.050	-57.50	0.016	-0.030	-0.0595
17	0.165	0.0020	0.050	-57.50	0.010	-0.065	-0.0595
18	0.165	0.0020	0.050	-57.50	0.010	-0.030	-0.0595
19	0.165	0.0040	0.030	-33.75	0.020	-0.030	-0.0595
20	0.165	0.0040	0.030	-33.75	0.020	-0.065	-0.0595

Fig.6 shows qualitative feature of estimated transition locations corresponding to typical N values. If we pay attention to N=25 for natural transition similar to the design process, the target Cp (case No.0) is found to be nearly optimum comparing with other cases. Therefore we think present target Cp distribution is effective for the NLF wing design.

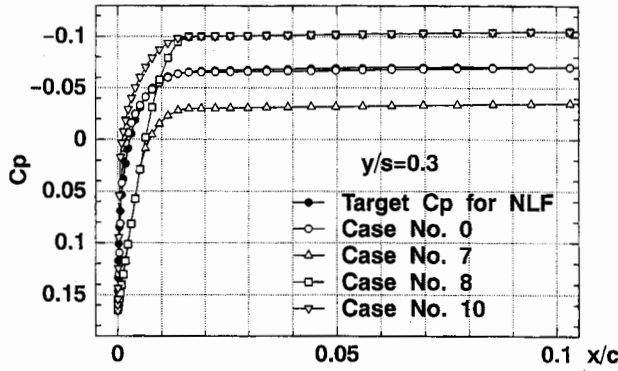


Figure 5. Some candidate target Cp distributions

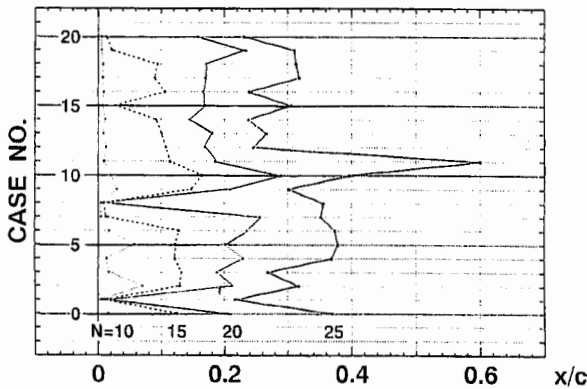


Figure 6. Estimated transition characteristics on candidate target Cp distributions

EFFECT OF COMPRESSIBILITY

Because we did not have any practical compressible code based on an e^N method, we originally developed a compressible code named "LSTAB" according to the formulation derived by El-Hady⁷⁾ and Mack⁸⁾, taking account of the problems mentioned above. The remarkable assumptions of this code are as follows.

- (1) In the formulation, simple plane wave disturbances were assumed as follows:

$$\{u, v, w, p, T, \rho, \mu\} \equiv q(x, y, z, t) = \bar{q}(y) \exp[i(\alpha x + \beta z - \omega t)]$$

Here (x, y, z) are coordinates in streamwise direction, boundary layer thickness direction and spanwise direction. (u, v, w) are velocities in (x, y, z) direction components. (p, T, ρ, μ) are pressure, temperature, density and viscosity. And ω is circular frequency (real) and (α, β) are components of wave number vector (complex).

- (2) A local streamline direction was selected as an amplification direction.
- (3) The angles of wave number vector and amplification vector $\psi, \bar{\psi}$ defined below were treated as parameters; namely any auxiliary rela-

tion on them was not specified.

$$\psi \equiv \tan^{-1} \left(\frac{\beta_r}{\alpha_r} \right), \quad \bar{\psi} \equiv \tan^{-1} \left(\frac{\beta_i}{\alpha_i} \right)$$

where $\alpha \equiv \alpha_r + i\alpha_i, \beta \equiv \beta_r + i\beta_i$

- (4) The N value corresponding to transition was assumed to be an envelope of N values at several parameter conditions as follows.

$$N = \text{Max}_{\psi} \text{Max}_{\bar{\psi}} \text{Max}_f \left[\int_{x_0}^x (-\alpha_i)_{\psi, \bar{\psi}, f} dx \right]$$

Here $-\alpha_i$ is an amplification rate, which is an eigenvalue solution of a stability equation. f is dimensional frequency of the plane wave disturbance.

The detail of the present formulation and some validations were described in Ref.9, and a few applications were mentioned in Ref.10.

In applying this code to the transition analysis of the NLF wing, a large parameter space for $\psi, \bar{\psi}$ is necessary. To reduce calculation time, first of all, we investigated an influence of $\bar{\psi}$ on the amplification rate at a typical Reynolds number and frequency. Fig.7 shows the result of eigenvalue solutions at 20% semi-spanwise station of the designed NLF wing. We can find that maximum amplification rate is realized in the condition of $\psi \cong 70^\circ$ and $\bar{\psi} = 0^\circ$ in this figure. Through the similar analysis at other Reynolds numbers and frequencies, we found the condition of $\bar{\psi} = 0^\circ$ was almost dominant and enough for estimating maximum amplification rate as an envelope. Therefore we applied this condition in all analysis.

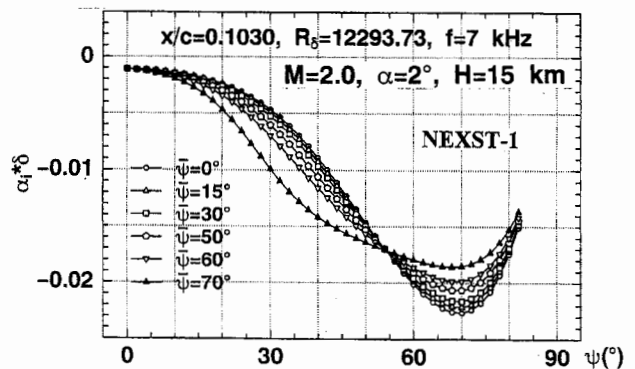


Figure 7. Influence of $\bar{\psi}$ on amplification rate

Fig.8 and 9 show some neutral stability curves and envelope of N values corresponding to each ψ at 20% semi-spanwise station. It was found in both figures that large ψ corresponding to C-F instability was dominant near the leading

edge. By taking account of compressibility effect, unstable disturbances with very high frequencies near the leading edge was obtained as shown in Fig.8. It was also found that the behavior of the N curve in Fig.9 was qualitatively similar to one in Fig.1 except the mid-chord region. Fig.9 indicates that the NLF wing completely suppresses the growth of the N value due to both C-F and T-S instabilities at the front and mid-chord.

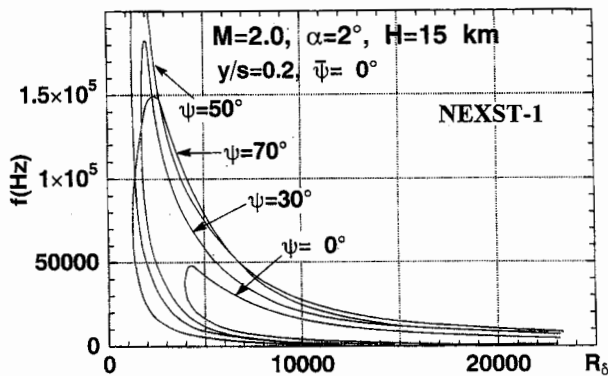


Figure 8. Neutral stability curve at 20% semi-spanwise station of the NLF wing

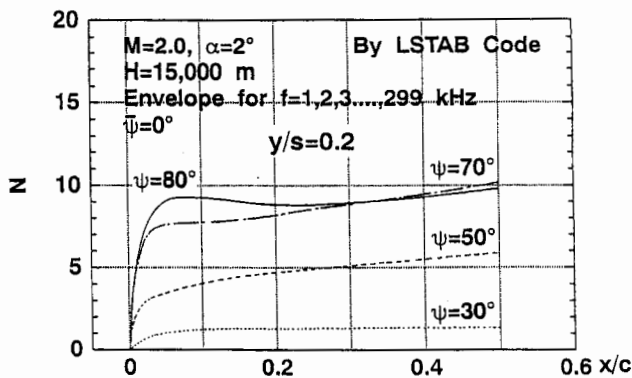


Figure 9. N characteristics estimated by LSTAB code at 20% semi-spanwise station of the designed NLF wing

Then Fig.10 shows estimated transition locations corresponding to each typical transition N value. The qualitative feature was similar to one in Fig.2 for transition N values about a half of them by the SALLY code. In general, such reduction of N value due to compressibility is well known to be valid¹¹⁾.

As was mentioned above, we do not have any clear transition N value in such a crossflow-dominant case at supersonic speed. However, NASA recently found out $N=14$ as the transition N value through the transition experiment on F-16XL airplane using supersonic low-disturbance tunnel at Langley¹²⁾. If it is assumed to be valid and universal, we can expect very large laminar region on the upper surface of the designed NLF wing. This must be verified at any future experi-

ment. Therefore we confirmed present compressible transition analysis indicated the validity of the NLF wing design. Naturally this result must be verified by any future experiment.

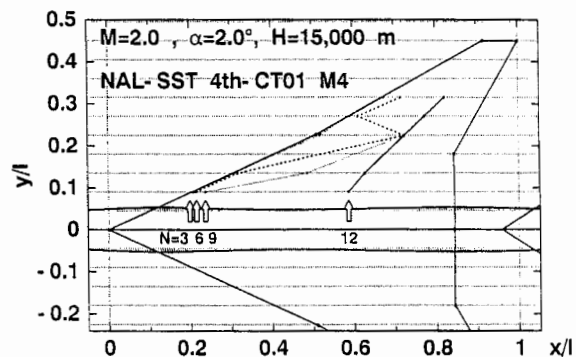


Figure 10. Estimated transition location of the NLF wing by LSTAB code

IMPROVEMENT OF LAMINAR PROFILES

In our transition prediction system, the laminar boundary layer profile was estimated by a compressible boundary layer code based on Kaups-Cebeci (K-C) method¹³⁾. Although their method is very effective as a practical tool for high aspect ratio wings, it has some errors in the flow field with strong streamline curvature such as one near the leading edge. In general, the growth rate of the C-F instability depends on the precision of estimated laminar profiles. In order to improve the transition prediction, it is very effective to use laminar boundary layer profiles computed by a Navier-Stokes (N-S) code, because it is usually formulated on a general curvilinear coordinate system.

Fig.11 shows laminar velocity profiles computed by our N-S code¹⁴⁾. We used a fine grid system that had about 50 points within a boundary layer. In general, careful selection of boundary layer edge is required in such an N-S calculation. After some trials on it, we assumed that the edge was placed in the height with 99% of maximum resultant velocity. Fig.12 shows the comparison of estimated laminar profiles computed by the N-S analysis (indicated by "CFD") and the K-C method (indicated by "BLT"). It was found that there was remarkable difference in the crossflow velocity profile (v) even though there was a little difference in the streamwise velocity (u) and temperature (T) profiles. The crossflow velocity was weakened by strong streamline curvature near the leading edge.

Fig.13 shows comparison of the N characteristics. We found that the N value based on laminar profiles computed by the N-S analysis were less than one by the K-C method. This con-

sideration also leads to further improvement in the transition characteristics of our NLF wing design.

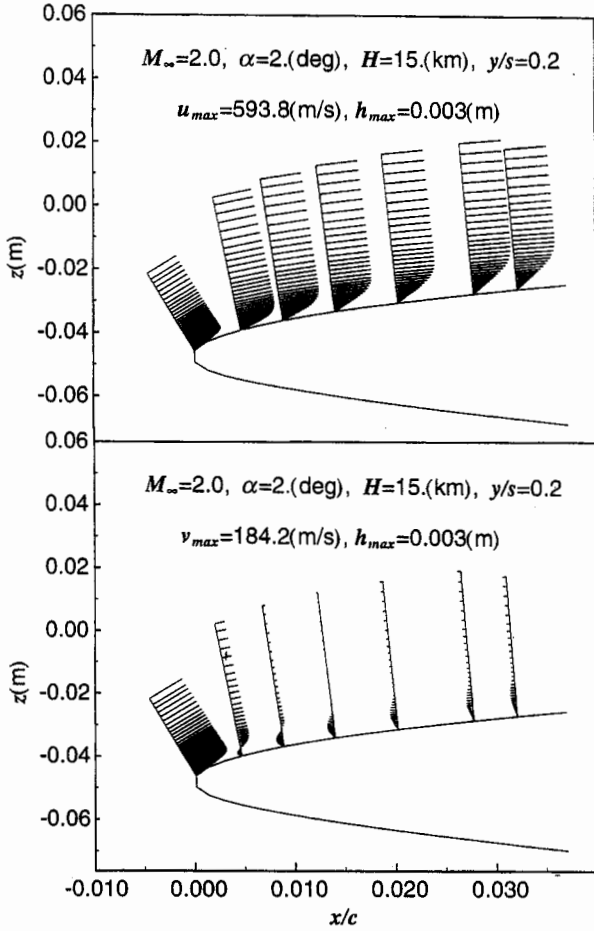


Figure 11. Laminar profiles estimated by N-S calculation

INVESTIGATION OF ATTACHMENT-LINE CONTAMINATION

In a swept wing, it is well known that there is another transition mechanism, which is different from one due to T-S and C-F instability. This is transition due to attachment-line contamination originated in a turbulent boundary layer on the fuselage surface¹⁰⁾. Although this process can not be analyzed theoretically, we well know that Poll's criterion¹⁴⁾ based on empirical database is very effective as a practical tool. Therefore we applied the criterion in this consideration.

Poll's criterion indicates that there is no possibility of transition due to attachment-line contamination if the special Reynolds number R^* is less than 245. In general, the R^* is related to the boundary layer characteristics of attachment-line flow, compressibility effect and radius of surface curvature near the leading edge.

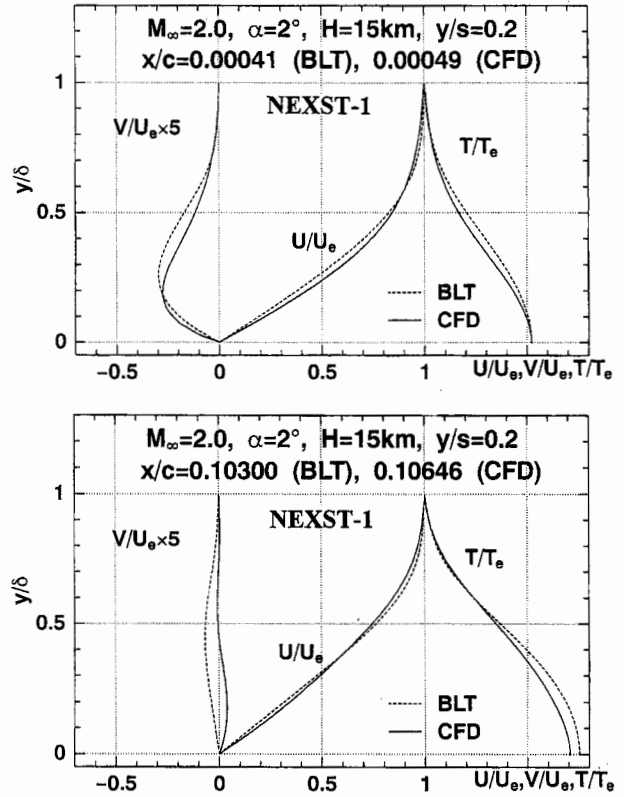


Figure 12. Comparison of laminar velocity profiles

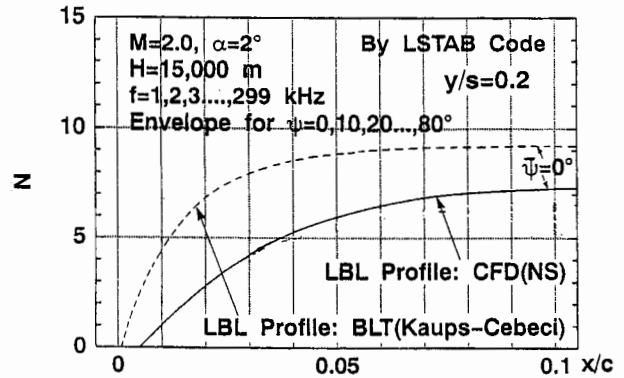


Figure 13. N characteristics estimated by LSTAB code with improved laminar profiles

Fig.14 shows spanwise distribution of estimated R^* in some wall temperature conditions. Here T_w and T_0 mean wall temperature and total temperature. It was found that all R^* was less than Poll's criterion 245, because our designed NLF wing had very small leading edge radius. Consequently we can expect no transition due to attachment-line contamination. Because this consideration is very rough, this problem must be experimentally investigated in the near future.

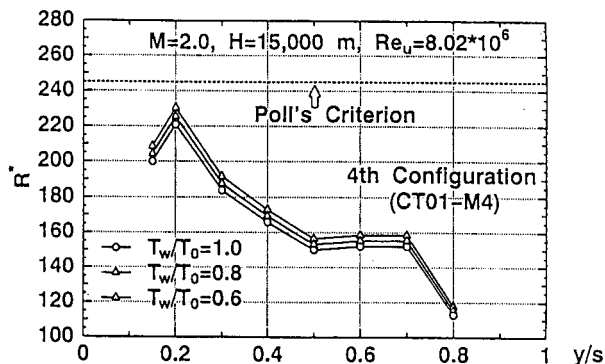


Figure 14. Result of consideration on attachment-line contamination

CONCLUDING REMARKS

We advanced transition analysis to verify the NLF wing concept incorporated in the aerodynamic design of the scaled supersonic experimental airplane. Using conventional incompressible and newly developed compressible transition prediction codes based on an e^N method, the NLF characteristics were well confirmed through the following results. (1) The step function type target C_p distribution applied in the NLF wing design was found to be optimum. (2) Comparing the transition N value estimated by the compressible code with experimental results obtained by NASA, wide laminar region of the NLF wing was expected. (3) Laminar boundary layer profiles estimated by a Navier-Stokes led to smaller N value than one by the compressible boundary layer code. (4) No transition due to attachment-line contamination was predicted. As a next step, we are planning some wind tunnel tests to validate these numerical results.

REFERENCES

1. Sakata, K., "SST Research Project at NAL", 1st International CFD Workshop on Supersonic Transport Design, Tokyo, March, 1998.
2. Shimbo, Y., Yoshida, K., Iwamiya, T., Takaki, R. and Matsushima, K., "Aerodynamic Design of the Scaled Supersonic Experimental Airplane", 1st International CFD Workshop on Supersonic Transport Design, Tokyo, March, 1998.
3. Yoshida, K., "Overview of NAL's Program Including the Aerodynamic Design of the Scaled Supersonic Experimental Airplane", Special Course on "Fluid Dynamics Research on Supersonic Aircraft" held at the VKI, RTO Educational Notes 4, 15-1~16, 1998
4. Ogoshi, H., "Aerodynamic Design of a Supersonic Aircraft Wing - Application of the Natural Laminar Flow Concept to Airfoil", Proc. of the 47th Nat. Cong. of Theoretical & Applied Mechanics, pp. 341-2, 1998 (in Japanese) / "Aerodynamic Design of Natural Laminar Flow Supersonic Aircraft Wings", 2nd SST-CFD-Workshop, IV-2, Tokyo, January, 2000
5. Matsushima, K., Iwamiya, T., Jeong, S. and Obayashi, S., "Aerodynamic Wing Design for NAL's SST Using Iterative Inverse Approach", 1st International CFD Workshop on Supersonic Transport Design, Tokyo, Japan, March 16-17, 1998.
6. Srokowski, A.J., "Mass Flow Requirements for LFC Wing Design", AIAA Paper 77-1222, 1977.
7. El-Hady, N.M., "Nonparallel Stability of Three-Dimensional Compressible Boundary Layers, Part I - Stability Analysis", NASA CR-3245, 1980
8. Mack, L.M., "Boundary-Layer Linear Stability Theory", Special Course on Stability and Transition of Laminar Flow, AGARD Report No.709, 3-1~81, 1984
9. Yoshida, K., Ogoshi, H., Ishida, Y. and Noguchi, M., "Numerical Study on Transition Prediction Method and Experimental Study on Effect of Supersonic Laminar Flow Control", Special Publication of National Aerospace Laboratory SP-31, pp. 59-79, 1996.
10. Yoshida, K., Ishida, Y., Noguchi, M., Ogoshi, H. and Inagaki, K., "Experimental and Numerical Analysis of Laminar Flow Control at Mach 1.4", AIAA Paper 99-3655, 1999.
11. Arnal, D., "Boundary layer transition: prediction based on linear theory", AGARD FDP/VKI Special Course on Progress in Transition Modeling, AGARD Report 793, 1993
12. Joslin, R. D., "Aircraft Laminar Flow Control", Annu. Rev. Fluid Mech. Vol.30, pp.1-29, 1998.
13. Kaups, K. and Cebeci, T., "Compressible Laminar Boundary Layers with Suction on Swept and Tapered Wings", J.A. Vlo.14, No.7, pp.661-667, 1977
14. Takaki, R., Iwamiya, T. and Aoki, A., "CFD Analysis Applied to the Supersonic Research Airplane", 1st International CFD workshop on Supersonic Transport Design, Tokyo, Japan, March, 1998.
15. Murakami, A., Stanewsky, E and Krogmann, P., "Boundary-Layer Transition on Swept Cylinders at Hypersonic Speeds", AIAA J. Vol.34, No.4, pp.649-654, 1996

Inverse Wing Design for the Scaled Supersonic Experimental Airplane with Ensuring Design Constraints

Kisa MATSUSHIMA¹⁾ (E-mail: kisam@nal.go.jp) Toshiyuki IWAMIYA²⁾ (iwamiya@nal.go.jp)
and Wanqiu ZHANG²⁾ (zhang@nal.go.jp)

1) FUJITSU Ltd., 1-9-3, Nakase, Mihama-ku, Chiba, 261-8588, Japan.

2) National Aerospace Laboratory, Japan.

Key Words: Aerodynamic design, Supersonic transport, Wing, Thickness constraints

ABSTRACT

Aerodynamic shape of a wing for NAL (National Aerospace Laboratory)'s first SST model has been designed by a supersonic inverse design method. This method handles wing-fuselage configurations and provides wing section's geometry at every span for Navier-Stokes flowfields. The design target is a NLF (natural laminar flow) wing at the speed of $M_\infty = 2.0$. The original system of the inverse design method has to be modified so that several design constraints can be satisfied. By means of the method, a wing section shape which has much more desirable characteristics has been designed than that by the traditional design method. In terms of aerodynamics to realize a NLF wing, the modified method works very well. The pressure distribution of the designed wing shows good agreement with the target pressure. In terms of constraints, most of them can be satisfied by using the modified design method; however, difficulty has been found during the process for thickness constraint control. The prospective strategy to cope with the thickness constraint is discussed.

1 Introduction

The scaled experimental airplane models of a Super-Sonic Transport are under development at the NAL in Japan. Unlike the traditional way, their aerodynamic shapes are being primarily designed by numerical tools such as CFD (Computational Fluid Dynamics). One of the important tools is a design method which determines the shape of a wing. We have been developing the method in which a new inverse problem has been formulated, because the NAL's SST model has a challenging design concept of an NLF wing to reduce the drag. The method provides the wing section geometry at every span station which realizes the specified target pressure distribution of an NLF wing. The method was devised and the initial (or first) version of the method was examined during 1997 and 1998^[1]. After some preliminary examinations, it was practically applied to the design of the first NAL's model which had no propulsion system. Its wing-fuselage configuration used for the first practice is shown in Fig. 1. This design has been successfully ended and the designed model is under manufacturing at present. Through the experience of the practical application of the initial version of the method, we have found that improvement is needed for the method. In this article, design results by the initial version of the method are introduced and then what to be improved and how to cope with the improvement are discussed.

2 Overview of the Design Method

This method designs wings for SST wing-fuselage configurations. It provides wing section's geometry at every span with the fixed planform. The design system of the method consists of an inverse problem solver and a Navier-Stokes simulation. Figure 2 illustrates the design system. The design procedure is iterative; the baseline shape is successively modified as the process of the inverse problem solver and Navier-Stokes simulation is iterated until the pressure distribution given by the designed wing can be regarded to converge to the target one. When a wing for the SST wing-fuselage model such as presented in Fig. 3 is designed, the target pressure distribution should be specified, as well as a baseline shape of the wing should be provided. The baseline wing is combined with the fuselage. Then the flow field around the wing and the fuselage combination is analyzed by Navier-Stokes flow simulation to get the current Cp distribution on the wing surface. Next the inverse problem is solved to obtain the geometrical correction value Δf corresponding to the difference between target and current pressure distributions ΔCp . The inverse problem is described as two integral equations^[1]. Those equations relate ΔCp (residual) to two values, Δw_s and Δw_a , which are the function of the geometrical correction Δf . This formulation is similar to the singularity source method based on the small perturbation and thin wing theory^[2]. So, we consider an isolated wing when the inverse problem is solved.

The integral equations are solved using piece-wise function approximation. The discretized wing surface is presented in Fig. 4. With the discretization, we solve a algebraic linear equation system instead of integral equations. Figures 5 and 6 are the brief explanation about the equation system and the coefficients. In Fig. 5, Δw_s indicates the x -derivative of the thickness change of a wing, where Δu_s is a function of pressure coefficients;

$$\Delta w_s == -\frac{1}{\beta^3} \left(\frac{\partial \Delta f(+0)}{\partial x} - \frac{\partial \Delta f(-0)}{\partial x} \right) \quad (2.1)$$

$$\Delta u_s == -\frac{1}{2\beta^2} (\Delta Cp(+0) + \Delta Cp(-0)) \quad (2.2)$$

+0 means the upper surface while -0 means the lower surface of a wing. In Fig. 6, Δw_a indicates the x -derivative of the change on the camber-line of a wing, where Δu_a is also a function of pressure coefficients;

$$\Delta w_a == -\frac{1}{\beta^3} \left(\frac{\partial \Delta f(+0)}{\partial x} + \frac{\partial \Delta f(-0)}{\partial x} \right) \quad (2.3)$$

$$\Delta u_a = -\frac{1}{2\beta^2} (\Delta Cp(+0) - \Delta Cp(-0)) \quad (2.4)$$

As illustrated in Fig. 2, the wing section shape at every span station is designed by modifying the baseline shape with Δf which is the solution to the inverse problem. When modifying the section shape, we impose the design constraints explicitly on Δf . Now, the current shape is updated with satisfying the design constraint. Then we joint the updated wing with the fuselage and go back to the analysis part, again.

For practical design, the consideration of design constraints is inevitable. The first version of the method adopted the simple way to apply constraints. The constraints were imposed on the geometry after the inverse problem was solved. Thus, the geometry was modified explicitly. We admit that the imposition of constraints may put the geometry off from the exact solution to the inverse problem. However, this treatment is justified because If the difference between an exact solution and an imposed one is in a proper range, the geometry will still converge with iterations.

3 Design, Results and Discussion

A wing for the SST wing-fuselage model whose planform is presented in Fig. 3 was designed in 1998^[1]. The design target was a NLF wing at the speed of $M_\infty = 2.0$. The profile of the target pressure distribution is presented by chain lines in Fig. 7. The baseline shape was the results designed by the traditional linear theory. Every wing section shape was NACA66003 airfoil geometry. The baseline wing section shape is drawn with dashed lines and its pressure distribution is presented by + lines in Fig. 7. The final (converged) wing section shape is drawn with solid lines and the realized pressure distribution is presented by \diamond lines. For the design, we used 50 (x :chord-wise) \times 80 (y :span-wise) panels on a semi-span wing surface, when solving the inverse problem. Several design constraints have been intended to be satisfied. They are 1) to assure the closed trailing edge, 2) to assure the twisting axis of every span section to be on a certain straight line, 3) thickness constraints of wing sections such as $0.03 \leq (t/c)_{max} \leq 0.037$ at each span station, and so on. As one can see from Fig. 7, the designed wing shape by the method is having the pressure distribution that almost completely agrees the target one. As a whole, the new method worked very well to design the wing section geometry except thickness control. In fact, we have encountered difficulty to enforce the thickness constraint. Sometimes the explicit enforcing of thickness control deteriorated the performance of the designed wing. For this design, we gave up controlling the thickness on the inner part of the wing than 40% semi-span station. However, without the thickness control, the largest "t/c" is still around 4.10% that is acceptable for manufacturing a real airplane. The situation of the thickness control is described in the following paragraph.

Figure 8 shows the design results of two different ways for the thickness control, at two locations of 30% and 70% semi-span stations. The plots on the left-hand side of the figure present the results designed with thickness constraint control. Those on the right-hand side are the results designed without the control. The dashed line and the solid line indicate the geometry of the baseline and designed wing section shape respectively, while + and \diamond lines do pressure distribution of the both. The target pressure is indicated by chain lines. As expected, the resulting wing designed without the thickness control realizes much closer pressure distribution to the target than the other one does. We admit the explicit enforcing of thickness control sometimes deteriorates the performance of the designed wing. The extent of the deterioration is to be verified. The deterioration does not violate the NLF concept on the outer part of the wing than 40% semi-span station. The situation at the 70% semi-span station shown in Fig. 8 is one typical example of non-violated cases. On the other hand, the situation at the 30% semi-span station in Fig. 8 is the example where the thickness control violates the concept.

From the investigation done before^[3], thickness is best controlled through careful specification of the target pressure. We are thinking there will be some range of the variation of target C_p , which does not violate the design concept for the SST. This encourages us to study a good algorithm to determine the optimized target pressure distribution. For more sophisticated thickness control, additional module to modify the target C_p to the design system of Fig. 2 is needed. In the module, investigation on target C_p will be conducted.

4 Conclusions

The inverse design method ensuring design constraints were introduced. The method is practical, efficient and accurate. It was shown through the design of an NLF wing for the wing-fuselage configuration of NAL's Scaled Supersonic Experimental Airplane. The method worked well with this practical aerodynamic design except satisfying thickness constraint for the inner part of the wing. To settle this difficulty, more sophisticated thickness control strategy and investigation

on target C_p are needed.

References

- [1] Matsushima, K., Iwamiya, T. Jeong, S., and Obayashi, S.: *1st International CFD Workshop on SST Design*, pp. 73-78, 1998.
- [2] Lomax, H., Heaslet, M. A. and Fuller, F. B.: *NACA Rep.* 1054, 1951.
- [3] Matsushima, K., Jeong, S. et. al.: Lecture Note in Physics, Vol. 515, *Proceedings 16th ICNMF*, pp. 79-84, 1998.

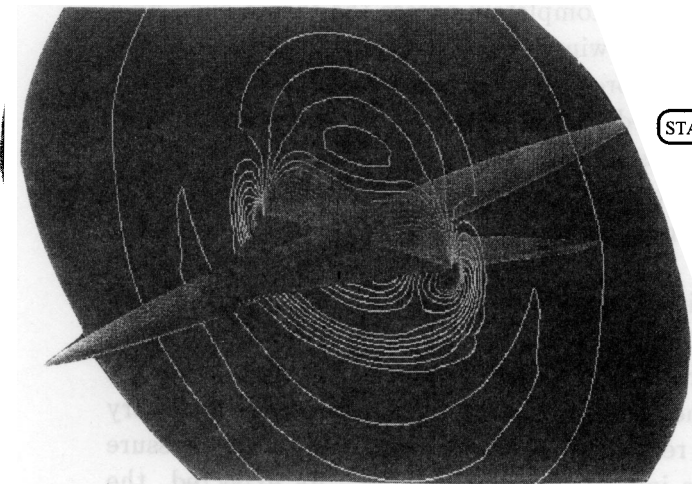


Figure 1 SST Wing-Fuselage Configuration.

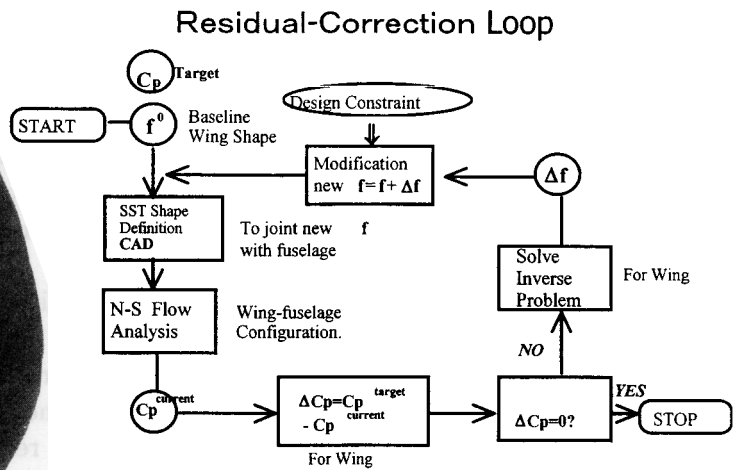


Figure 2 Design Method,(1st ver.).

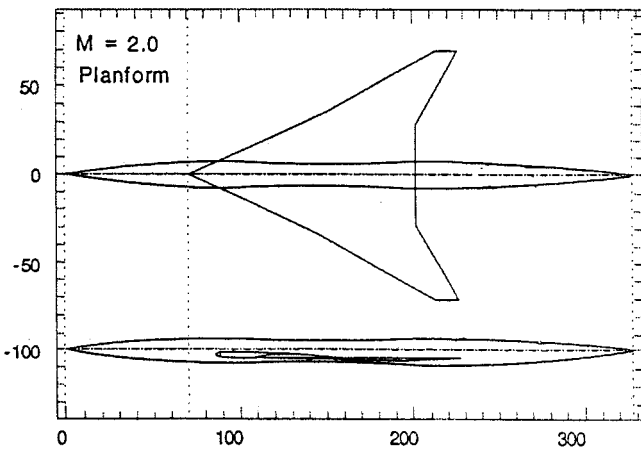


Figure 3 SST Planform.

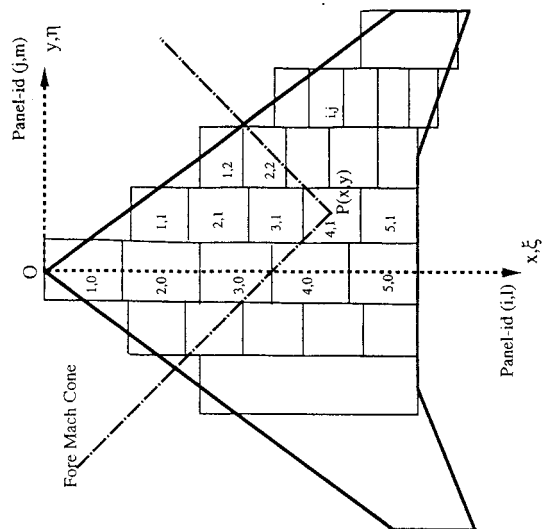


Figure 4 Discretization of Wing Surface.

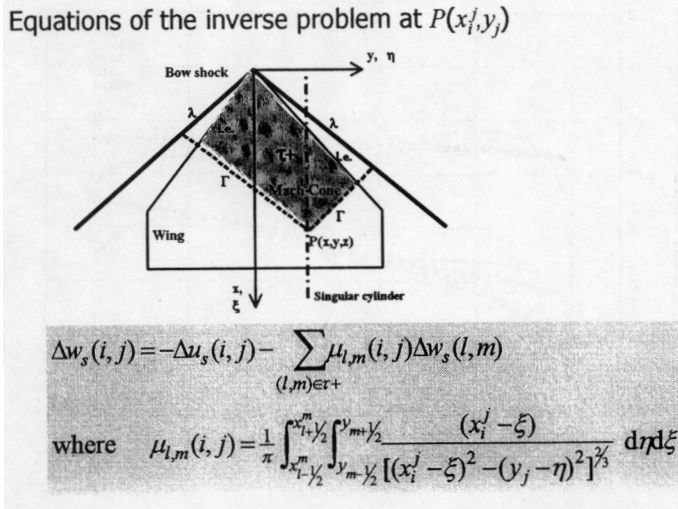


Figure 5 Discretized Equation System(1).

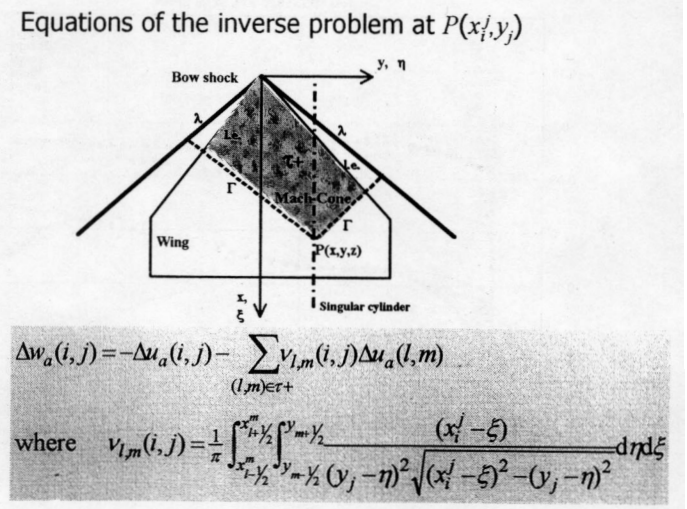


Figure 6 Discretized Equation System(2).

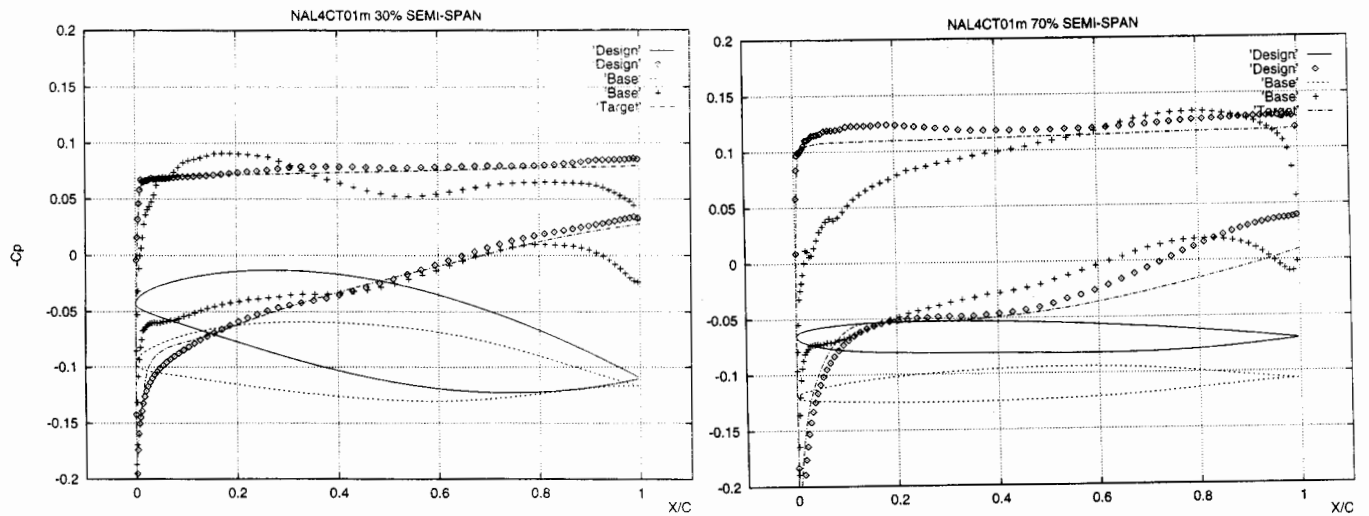


Figure 7 Final Design Results at 30% and 70% Semi-span Stations

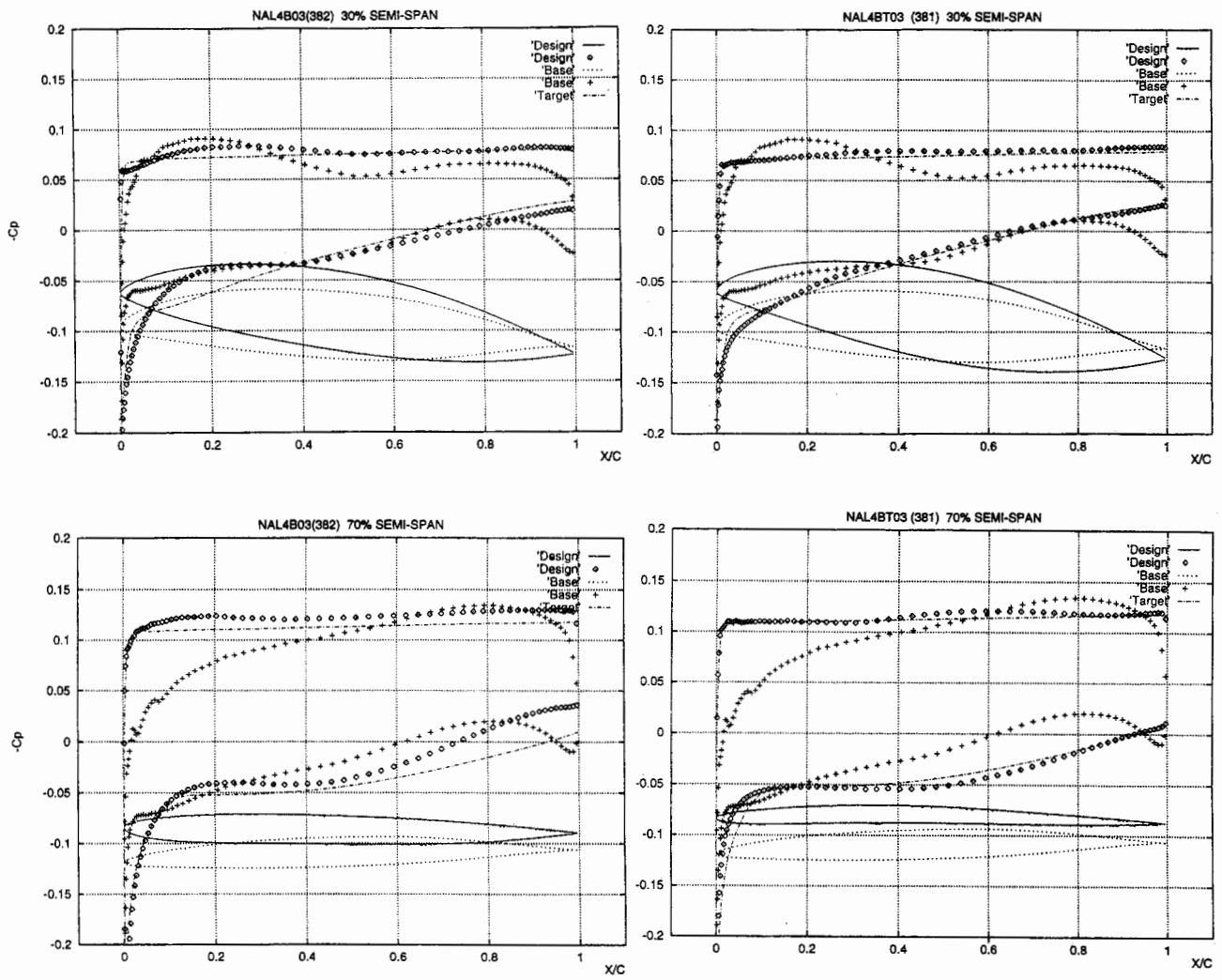


Figure 8 Design Results on 30% and 70% Semi-span Stations
 Comparison of Realized Pressures by Design Method with/without Thickness Control

Development of a Preliminary SST Planform Design Tool Using a Numerical Optimization Routine

Shin Matsumura^{*}, John P. Sullivan⁺
Purdue University
West Lafayette, IN 47906 USA

Yuichi Shimbo[⊥]
National Aerospace Laboratory
Osawa, Mitaka, Tokyo 181-0015 Japan

ABSTRACT

A preliminary SST wing planform design program was developed using the simplex downhill method for numerical optimization and lifting surface theory for aerodynamic analysis. The wing planform was restricted to an arrow wing with a constant planform area, and the geometry was represented by at most seven independent design variables. The objective function of the optimization was the inviscid drag at design condition ($M=2$, $C_L=0.1$) with penalty functions for the violation of geometry constraints. Because the program only performs aerodynamic analysis, variables were bound or held constant based on multidisciplinary considerations such as structural and manufacturing restrictions, in order to avoid unrealistic planforms.

The results showed the design variables could be grouped into a set of primary variables (aspect ratio, slenderness ratio, sweep angle of inner leading edge) which played key roles to the optimization, and a set of secondary variables, primarily used to satisfy the geometry constraints. Finally, as a preparation for the multi-point design, the optimization was performed at several design Mach numbers and corresponding design lift coefficients while keeping the flight altitude and the weight of the aircraft the same. The resulting optimum geometry changed to trade off the induced drag from the high aspect ratio with the wave drag from the high leading edge sweep.

INTRODUCTION

To prepare for commercial flight in the 21st century, National Aerospace Laboratory (NAL) of Japan is promoting a high-priority research program for the next-generation supersonic transport (SST). The objective of the program is to develop design techniques/methods that will make the next-generation SST a reality.

One of the mandatory requirements for a SST is a low drag, high efficiency wing. Today, with massively paralleled supercomputers and workstations such as the ones present at NAL, the aerodynamic design of an aircraft and/or aircraft component is possible through the use of computational fluid dynamics (CFD). Different techniques are used at different design process stages, so that computing time is efficiently used. During the preliminary design stage, a large number of iterations are done with lower level analysis methods, to find a good starting point for detailed design. For such purposes, simple methods such as linear theory are very well suited.

Codes that use Carlson's Method for aerodynamic analysis, and the design of load distributions were developed at NAL by K. Yoshida, in [1]. By using these programs, an optimization program PLANFOPT for the wing planform design was developed. The purpose of this program was to find a starting point for a CFD-based detailed design.

^{*} Student, School of Aeronautics and Astronautics

⁺ Professor, School of Aeronautics and Astronautics

[⊥] Senior Researcher, Advanced Technology Aircraft Project Center

This paper will discuss the results shown by PLANFOPT in the design of a supersonic wing planform.

OPTIMIZATION ROUTINE

As with any optimization program, an iteration routine is necessary. This work implemented the simplex downhill method from [2]. The simplex method was chosen due to the simplicity of the algorithm, and because it uses only the values of the function evaluated and not the derivatives for the iteration. This makes the method inefficient in terms of the number of function evaluations it must perform, but it offers the advantage that numerical errors resulting from computing the derivatives can be avoided.

The simplex method works by first building a simplex, a polygon in the function space, whose vertices are the initial starting point of the variable(s), and some deviation from these variable(s). For example, if the function that is to be minimized is given by $z = z(a, b)$, then the vertices are made of

$$\begin{aligned} &(a_0, b_0) \\ &(a_0 + \delta a_0, b_0) \\ &(a_0, b_0 + \delta b_0) \end{aligned}$$

where the subscript '0' denotes the initial condition, and δ is the initial perturbation percentage.

The method then evaluates the function at these vertices, and finds the maximum and minimum. The method then takes the variables that gave the maximum value, and moves it in one of the predetermined ways such as contraction. The routine is repeated until the difference between the vertex that gives the highest and lowest value of the function are within a given convergence tolerance level.

Using this method for wing design, the independent variables described the geometry of the wing such as the leading edge sweep angle, and the function to be minimized was an objective function specified by the design target. More discussion on the objective function used will be given later.

AERODYNAMIC ANALYSIS METHOD

Lifting surface theory was chosen as the analysis method to determine the aerodynamic characteristics of the wing. To be more precise, the singularity-distribution method outlined in [3] was used. The singularity-distribution method is a procedure to

solve the perturbation potential equation for supersonic flow. The numerical procedure outlined by Carlson and Middleton in [4] was used to solve the differential pressure coefficient distribution over the wing.

In addition to the planform, the camber distribution must be specified for the complete aerodynamic characterization of a lifting surface. PLANFOPT used Carlson's Method of component loading to determine the optimal warp for each planform iterated, which is also outlined in [4].

The inviscid drag polar was modeled using the quadratic equation shown below.

$$C_D = C_{D0} + K(C_L - C_{L0})^2$$

Here, C_D is the total inviscid drag, which consists of induced drag and wave drag due to lift, C_{D0} is the drag coefficient at a lift coefficient equal to C_{L0} , and K is the drag polar factor. The shift in the vertex of the drag polar is due to the warping of the wing, which is a complex distribution of twist and camber typical of SST's.

PLANFORM GEOMETRY DEFINITION

The variables of the function to be minimized are the parameters that describe the planform geometry of the wing. The arrow wing was chosen as the type of planform for two reasons. First, a wing with straight edges would have a lower manufacturing cost than a wing with curved edges due to simpler structural geometry and design. Second, the arrow wing is known to have a superior performance over simpler wings such as delta wings. Comparisons between the arrow and delta wing can be found in [5].

A schematic of an arrow wing is given in Figure 1. The arrow wing is defined by eight parameters: wing surface area (S), aspect ratio (AR), slenderness ratio (SL), taper ratio (λ), leading edge inner sweep angle (Λ_{LE}), trailing edge inner and outer sweep angle (Λ_{TEin} , Λ_{TEout}), and the trailing edge kink position (ϵ_T). The wing surface area was set constant at 9000 sq. ft. because the wing surface area is usually determined from the preliminary mission analysis. This reduced the number of variables to seven.

Given these parameters, the x and y coordinates of the six vertices can be determined. Using the surface area and the aspect ratio, the span can be found. The length of the wing is found by dividing the semi-span with the slenderness ratio, which is defined to be the ratio of the semi-span to the wing length. The geometry of the trailing edge is completely defined by the inner and outer sweep

angles and the kink location, which is normalized by the semi-span. The taper ratio will define the location where the leading edge meets the wing tip. The final point to solve is the kink location on the leading edge. This location is found so that the planform surface area will be what was specified, and from the leading edge inner sweep angle.

DESIGN CONDITION AND CONSTRAINTS/BOUNDS

The design flight condition was arbitrarily chosen as one that is typical of a SST configuration. The flight Mach number was chosen as 2.0 with a lift coefficient of 0.1. Although many of the conceptual SST studies done by various organizations call for a higher Mach number, this Mach number offers the advantage that the aerodynamic heating would be low enough that a conventional material could be used. This will also help to reduce the possible cost.

Having set the design flight condition, PLANFOPT was run for a particular case. The purpose of this first case was to verify that the results from PLANFOPT agree with the more simplified conical flow theory, and to show that additional constraints and bounds need to be specified for a realistic wing design. All seven variables were iterated in this initial trial with the objective function taken as the drag coefficient multiplied by a factor of 10^4 . If during the optimization the planform became physically unrealistic, the planforms were eliminated. The three criteria for elimination were: 1) one or more of the planform edges became less than a foot in length, 2) the leading edge kink was located behind the trailing edge, and 3) the leading edge kink was located farther out spanwise than the wing tip. The simplex method does not incorporate any methods to do this, so the objective function was manually set to 10,000. This however caused problems with the optimization. It created a wall in the variable space around some initial conditions and did not allow the optimization to proceed. In order to relax this wall, the objective function was manually set to 120% of the objective function from the previous iteration. This smoothed out the objective function, and allowed the optimization to find a path to the optimum planform.

Taken from [3], the drag coefficient for a swept rectangular wing is

$$C_D = C_{de} \cos \Lambda (1 - \sin^2 \Lambda \cos^2 \alpha)$$

Here, C_{de} is the wave drag normal to the leading edge, Λ is the leading edge sweep angle, and α is the angle of attack. Although this equation is for a

rectangular wing, the general trend of the drag coefficient as the sweep changes should be the same as that with the arrow wings. The importance of this equation can immediately be seen by observing that a wing swept to the limit of 90 degrees results in a wave drag of zero. In addition, the aspect ratio ought to approach infinity, resulting in no induced drag. This would be a good way to test PLANFOPT, to see whether the planform will approach this limit.

Figure 2 shows a typical result for the above setup. The wing is extremely slender and thin, with the leading edge sweep very close to 90 degrees. The span is relatively large, which is what causes the chord to be extremely small. If both the length and the span of the wing increase, then the chord must decrease so that the wing surface area remains constant. A planform as such may mathematically be the optimum with linear theory, but there are other considerations, such as the structural design. The structural design of this wing is impossible, and in addition there are other problems such as viscous effects, placement of ailerons, etc. The aerodynamic design of a planform using PLANFOPT requires knowledge of limits to some of the parameters, which can be used to constrain and bound the planform. For PLANFOPT, these multidisciplinary considerations were based solely on engineering judgement and intuition, which will be outlined next.

Few of the variables were set as constants from multidisciplinary considerations. First, the aileron is a critical component of a wing, and will need to be placed on the inner region of the trailing edge. The structural design of this section of the wing will be simpler if there was no sweep to the inner trailing edge. The size of the ailerons will also need to be considered. It would be advantageous to reduce the chord and increase the span, rather than vice-versa, given a required aileron surface area. This would reduce complications between the placement of the actuators and other components within the wing structure. This meant that Λ_{TEin} and ϵ_T could be held constant. The sweep was set at 0 degrees, and the kink location was set to 0.4, or 40% of the semi-span.

Aspect ratio is another important variable that not only affects the aerodynamics of the wing, but also the structural design. Aerodynamically the drag will decrease without bound as the aspect ratio is increased, but at the same time the weight of the wing will increase, and at some point will become prohibitive. Because there is no structural model in PLANFOPT if the aspect ratio is made a variable it would increase without bound until one or more of the other constraints are violated, and if a maximum aspect ratio was set, then the resulting wing would always approach the maximum possible. Therefore,

the aspect ratio was set constant at 2.2 for now, which is again, a typical value for a SST.

Bounds were placed on the leading edge sweep, taper ratio, and the trailing edge outer sweep. A minimum on the leading edge sweep was set at 60 degrees, so that the leading edge would be inside the Mach cone at Mach 2.0, resulting in a subsonic leading edge. In reality however, the SST will have to fly transonic over land, and during transonic cruise, it will be better to have a lower sweep angle. This would however add additional complexity to the problem, and a more sophisticated model for the wing and aerodynamics would be required to evaluate the transonic performance. To keep PLANFOPT to a single point design, this was not performed.

The bounds on the trailing edge outer sweep and taper ratio were chosen by structural considerations. Too much sweep and too small of a tip chord would require a heavier structure to support the loads on the wing. The taper ratio was bound to be between 0.08 and 0.2, and a maximum for the trailing edge outer sweep was set at 35 degrees.

The final constraint set was for the kink location on the leading edge. There was really no basis for the limits, except for the fact that an arrow wing is defined by a kink on the leading edge. It was thought that if the location of the kink moved too close to the tip or the root, it would be simpler not to have the kink at all. To make sure that the kink is about the half semi-span, the location was required to be between 0.4 and 0.6, or between 40 and 60% of the semi-span.

These constraints and bounds presented were implemented using penalty functions. However, the value of the penalty had to be dependent on how much the variables deviated from their maximum or minimum values, so that the penalty function will force the optimization to find a planform that satisfies the constraints. The penalty function was formulated as the sum of each constraint normalized to a specified maximum or minimum value, added onto the objective function. For example, to force the taper ratio to be between 0.08 and 0.2, if the taper ratio became less than 0.08, then a value of $z(0.08/\lambda)^2$ was added to the objective function, and if the taper ratio became greater than 0.2, then $z(\lambda/0.2)^2$ was added. The factor z is the penalty factor used to control the strength of each constraint. The same was done for the remaining constraints, and the objective function I with the penalties is shown.

$$I = C_D \times 10^4 + \sum z_i \left(\frac{k_i}{k_{\max_i}} \right)^2 + \sum z_i \left(\frac{k_{\min_i}}{k_i} \right)^2$$

Here, k is the value of the variables, and k_{\max} and k_{\min} are the maximum and minimum value for that variable. If the variable is within constraint, then the penalty is neglected. The subscript 'i' denotes that there can be as many constraints desired, and this also means that the penalty factor for each constraint can be different.

With the four components of the program (optimization routine, aerodynamic analysis, variable space, constraints/bounds) set up, it was now possible to use the code for wing design. The results will be presented in three sections; the first section will demonstrate the results from the above set up, and at the same time examine whether the final planform is dependent on the initial condition. In the second section, the constraints/bounds set on the problem will be investigated by examining how the results change as the constraints/bounds are changed. And then the final setup of the program and its results, which will be based on the results from the second part, will be presented.

DEMONSTRATION OF PLANFOPT

With any optimization problem, initial condition dependency of the converged solution is always a concern. Because the simplex method is a global optimization routine, the final planform should not depend on the initial condition, for a reasonable tolerance level. In addition, the implementation of bounds and constraints ought to guide the optimization in a common direction, regardless of the starting point.

Figures 3-6 show four initial planforms that were tested. Due to time constraints, the investigation of the initial condition dependency was limited to these cases. The initial results showed that there was some dependency on the initial condition, as shown in Figure 7. However, it was thought that these minor differences were due to numerical noise within the optimization, and could be eliminated by running the optimization a second time, with these final planforms as the initial condition, and with a smaller value for the initial deviation. It was found that repeating this routine a number of times essentially eliminated any dependency on the initial condition, as shown in Figure 8. Figures 9-12 show the histories of each variable for all four initial planforms. Again, these plots show that the final values of the variables are independent on the initial value. For the remainder of this work, it was

assumed that PLANFOPT could be used without worrying about the initial condition dependency.

The history of the optimization process for the initial planform A is shown in Figures 13 and 14. Figure 13 shows the four variables normalized to their initial values and Figure 14 shows the drag coefficient and the objective function. The planforms that were not within constraints show up as black dots above the red circles in Figure 14. The drag coefficient and the objective function decrease initially until a planform within constraints is established. From then on, only a few of the planforms violate the constraints, and the objective function decreases slowly.

Judging from this plot, it appears as if the optimization process can be divided into two steps, where the first step is not really for drag reduction, but for the search of a planform within constraints. Once that is established, a local optimization process takes place to improve the planform. Correlating the histories of the variables in Figure 13 with Figure 14 can give further insight about the optimization process. Some of the variables change very aggressively, while the others remain almost constant. Observing a different section, the passive variable will be changing quite a bit, while the one that was changing aggressively before remains about constant. This can be seen clearly with the taper ratio, slenderness ratio, and the leading edge sweep. The slenderness ratio and the leading edge sweep have an inverse relation, where if one is increasing, the other is decreasing, and vice-versa. The values for the initial and final planforms are tabulated in Tables 1 and 2.

Table 1 – Values for Initial Planforms

	Case A	Case B	Case C	Case D
SR	0.5	0.42	0.45	0.425
λ	0.15	0.12	0.35	0.5
Λ_{LE}	70.0	68.0	75.0	80.0
Λ_{TEout}	25.0	32.0	20.0	45.0
$C_D \times 10^4$	37.8	36.0	41.4	41.6

Table 2 – Values for Final Planforms

	Case A	Case B	Case C	Case D
SR	0.404	0.402	0.405	0.400
λ	0.080	0.081	0.080	0.081
Λ_{LE}	70.889	71.209	70.718	71.441
Λ_{TEout}	34.998	34.810	34.960	34.955
$C_D \times 10^4$	33.6	33.6	33.6	33.6

CHANGE CONSTRAINTS/BOUNDS

The constraints on the planform were chosen based on multidisciplinary considerations, such as the placement of the ailerons, and the feasibility of the structural design. In reality it will not be possible to design a wing based solely on aerodynamics, and compromises between the different disciplines will have to be made. With PLANFOPT it is not possible to perform these trade studies, however it is still important to understand the effects of changing the constraints.

The trailing edge kink location and the trailing edge inner sweep was held constant at an arbitrarily chosen value. These settings were examined by running cases with the kink location set at 0.2, 0.3, 0.5 and 0.6. Finally the location was made a variable.

Figure 15 compares some of the final planforms with different settings for the kink location, and Figure 16 shows the final planform for the variable kink location case. There were a few obvious trends in the solution, one being that the closer the kink was to the wing root, the lower the drag coefficient. For the case where the kink location was made a variable, the kink moved all the way to the root, until the inner trailing edge reached the minimum one foot. Figure 17 shows the trend in the drag coefficient as the kink location was changed.

A similar study was done on the effect of changing the sweep of the inner trailing edge. The sweep was set at -20, -10, 10, and 20 degrees, and then allowed to change. Some of the results are shown in Figures 18 and 19. As the sweep is increased, there is a decrease in the drag coefficient. This is shown graphically in Figure 20. When the inner trailing edge sweep was a variable, the final planform had an inner trailing edge sweep of 47 degrees. At first there seemed to be no significance to this particular value, but examining the rest of the variables, it was found that the taper ratio and the trailing edge outer sweep had reached their minimum and maximum values. This implies that if there were no bounds on the taper ratio and outer trailing edge sweep, the inner trailing edge sweep would approach 90 degrees.

These results agree with what was presented earlier in Figure 2, where the aerodynamically optimal wing had the kink location near the wing root and an extremely large trailing edge sweep. These trends can be seen in Figures 16 and 19, and if it were not for the other constraints on the taper ratio, leading edge kink location, etc., the wing would approach the one in Figure 2.

Another result that was shown in these two studies, although not obvious from looking at the

planforms, was that the taper ratio always approached 0.08, and the trailing edge outer sweep always approached 35 degrees. This was significant, because these were the minimum and maximum values set in the constraints. Like the kink location approaching 0.0, the taper ratio wanted to go to zero, and the trailing edge outer sweep wanted to go to 90 degrees. Because of this, the resulting wing should have the smallest allowed taper ratio and the largest allowed trailing edge outer sweep, regardless of the value of the bound. This was investigated by running four cases with different settings for the maximum and minimum for taper ratio and trailing edge outer sweep. The minimum taper ratio was changed to 0.06 and 0.1, and the maximum trailing edge outer sweep was changed to 30 and 40 degrees.

Some of the results are shown in Figure 21. The predicted trend did happen, and the taper ratio and trailing edge outer sweep approached their limits. This result was actually very powerful because it meant that the taper ratio and the trailing edge outer sweep should not be iterated, because they will go to their limits chosen by the user. Instead, the taper ratio and the trailing edge outer sweep should simply be chosen and kept constant, which will simplify the problem and shorten the turnaround time. The results from these cases are tabulated below in Table 3.

Table 3 – Results of Cases of Different Limits on Trailing Edge Outer Sweep and Taper Ratio

	$\lambda_{\min} = 0.06$	$\lambda_{\min} = 0.1$
$TE_{\max} = 30 \text{ deg.}$	$C_D \times 10^4 = 34.1$ $\Lambda_{LE} = 69.9 \text{ deg.}$ $SR = 0.42$	$C_D \times 10^4 = 34.7$ $\Lambda_{LE} = 69.3 \text{ deg.}$ $SR = 0.43$
$TE_{\max} = 40 \text{ deg.}$	$C_D \times 10^4 = 32.6$ $\Lambda_{LE} = 72.9 \text{ deg.}$ $SR = 0.37$	$C_D \times 10^4 = 33.1$ $\Lambda_{LE} = 71.2 \text{ deg.}$ $SR = 0.39$

These results agree with what was shown in Figure 2. The cases with the larger trailing edge sweep and the smaller taper ratio have the lower drag. Also, there is a correlation between the drag and the slenderness ratio, or the length of the wing, because the aspect ratios for all four cases are the same. The longer wing also has a larger leading edge sweep, implying a lower wave drag due to lift. Because the induced drag is dependent almost solely on the aspect ratio, the differences in the drags are due to the leading edge of the wing. This suggests that the reason why a small taper ratio and a larger trailing edge sweep is desired is because if the aspect ratio is the same, then the leading edge sweep will be allowed to be larger.

The last family of cases ran were for different values of the aspect ratio. For these cases, the result from the previous study was used, and the taper ratio and the trailing edge outer sweep were also set a constant, along with the trailing edge kink location and the trailing edge inner sweep. The taper ratio was 0.08 and the trailing edge outer sweep was 35 degrees. The aspect ratio was set from 1.4 to 2.8.

Some of the results are plotted in Figure 22. The planforms of the smaller aspect ratios are much longer because of the constraint on the surface area. Because the taper ratio and the trailing edge outer sweep are now held constant, the only parameters iterated are the leading edge sweep and the slenderness ratio. It was desired to make the aspect ratio also a variable, because the aspect ratio is a parameter that greatly influences the performance of a wing. This was however unfavorable, because it was already shown earlier that the aspect ratio wanted to be as large as it was allowed to be. Comparing the drag coefficients of the wings from the last study however provided new information, and was used for the final setup of PLANFOPT.

FINAL SETUP OF PLANFOPT

The drag coefficients as a function of the aspect ratio are plotted in Figure 23. As the aspect ratio increases, the overall drag goes down, because the induced drag is decreasing. However, at some point, aspect ratio of 2.4 for this case, there is a minimum point in the plot. If the cause of this parabolic behavior in the drag can be determined, the aspect ratio can also be made a variable, because it will no longer approach infinity, there is an optimum aspect ratio.

From elementary supersonic aerodynamics, the inviscid drag on a wing is composed of the induced drag and the wave drag due to lift. At first after seeing the result in Figure 2, it was believed that the two drags are independent of each other, in the sense that the code will change the wing in such a way that both will decrease or increase. This was what happened with the initial case run, but after the implementation of the constraints and bounds, the problem was set up in such a way that the induced drag and the wave drag could have an inverse relation with each other.

PLANFOPT, in general, changes the planform so that the span and the length increase and that is why an unconstrained optimization will result in a wing such as that in Figure 2. From Figure 22, as the aspect ratio increases the length decreases, and consequently the leading edge sweep must decrease, to maintain the constant surface area. If the aspect

ratio is too large, the planform will become too short with not enough sweep, increasing the wave drag, and if the wing is swept too much causing the planform to be long, then the aspect ratio will not be large enough and the induced drag will increase. The planform of lowest drag will be one where the aspect ratio and the leading edge sweep will be such that the induced drag and the wave drag due to lift are balanced, but not necessarily equal. Finding the planform parameters to achieve this, for a given flight condition and multidisciplinary constraints will therefore be the final setup of PLANFOPT. A description of the final structure of PLANFOPT and how it will fit into the overall design process of an aircraft will be briefly given next.

During the preliminary design stage of an aerospace system, the system parameters are determined. For transport aircraft aerodynamics, these are usually the cruise velocity and altitude, design lift coefficient, and wing surface area. The altitude can be combined with velocity to give flight Mach number. These three parameters that come from the preliminary design will be one of the two kinds of inputs to PLANFOPT, the flight condition. The second kind of inputs to PLANFOPT will be the constraints and bounds, which will be supplied by the designers of the other disciplines. These will be the trailing edge sweep, kink location, and taper ratio. PLANFOPT will then take these inputs, and find the aspect ratio, leading edge sweep, and slenderness ratio that will give a planform with the lowest inviscid drag. Higher level methods such as CFD design methods can then be used to solve for the detailed aerodynamics of the wing.

A sample study of changing the flight condition was done by varying the design Mach number. It was assumed that the weight of the aircraft and the altitude are constant, so that the product of Mach number squared and lift coefficient will be a constant. The Mach numbers were set to 1.6, 2.0, 2.6, and 3.0. Some of the results are shown in Figure 24. As the Mach number is increased the wing becomes more slender and arrow-like. As the Mach number increases, a larger leading edge sweep angle is needed, and because of the constraints, a larger length is needed. The surface area is a constant, so the aspect ratio must decrease along with the slenderness ratio. The final values of the three variables are plotted against the design Mach numbers in Figures 25-27. The plots show exactly what was stated above. And finally the drag coefficients are plotted in Figure 28, and the L/D is plotted in Figure 29. As the Mach number is increased, the lift coefficient decreases, and so does the drag coefficient. However, because the wave

drag decreases faster, the L/D increases with Mach number.

CONCLUSION

A preliminary design tool for a supersonic wing planform has been developed. The parameters that strongly influence the aerodynamic performance of the wing were made primary variables. These consisted of the aspect ratio, leading edge sweep, and the slenderness ratio. The parameters that were made constants, the trailing edge sweep, trailing edge kink location, and taper ratio, can be classified as secondary variables, because they do not directly influence the aerodynamic performance, but bound the primary variables. This classification agrees with conical theory, in that for a swept rectangular wing, the leading edge sweep and the aspect ratio are what influence the inviscid drag. Iterating only the primary variables helped to reduce the independent variables, which is always desirable because of the shorter turnaround time, especially with advanced optimization routines and aerodynamic models in the future.

The fact that the variables can be grouped into two categories shows that even a preliminary planform design is a multidisciplinary problem. If the planform is designed through aerodynamic consideration only, then the resulting planform will have the maximum aspect ratio and leading edge sweep allowed through the geometry definition. This will result in a physically unrealistic planform, which may have a very low drag, but not possible to manufacture.

Looking at the results from the final setup, the trends in the designed wings agree with the simpler theories and with actual aircraft in existence. A high Mach number results in a highly swept arrow wing, and as the Mach number is reduced, the wing becomes less swept with a larger aspect ratio. This is so that the induced drag and the wave drag due to lift are balanced, but not necessarily equal. Finally, it was shown that the L/D increases with design Mach number, if the weight of the aircraft, wing surface area, and the flight altitude are kept constant.

REFERENCES

- [1] Y. Shimbo, K. Yoshida, warpplanf,
warpdgn. National Aerospace Laboratory
FORTRAN codes.
- [2] B. Flannery, W. Press, S. Teukolsky, W.
Vetterling. Numerical Recipes in FORTRAN 2nd Ed.
Cambridge University Press Copyright 1992.
- [3] J. J. Bertin and M. L. Smith. Aerodynamics
for Engineers. Prentice Hall Copyright 1989.
- [4] D. Kuchemann. The Aerodynamic Design
of Aircraft. Pergamon Press Copyright 1978
- [5] B.R. Wright, F. Bruckman, N.A. Rodovcich.
Arrow Wings for Supersonic Cruise Aircraft. Journal
of Aircraft Vol. 15, No. 12, December 1978

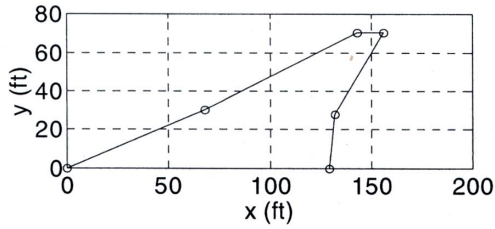


Figure 1 – Sample Arrow Wing

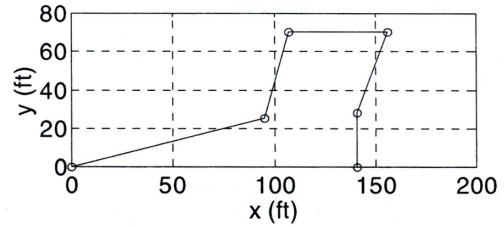


Figure 5 – Initial Condition C

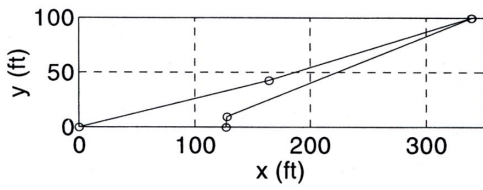


Figure 2 – Optimization with No Constraints

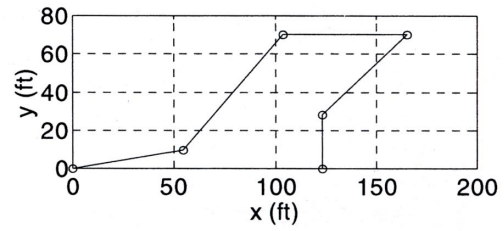


Figure 6 – Initial Condition D

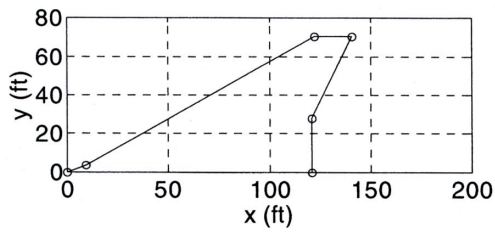


Figure 3 – Initial Condition A

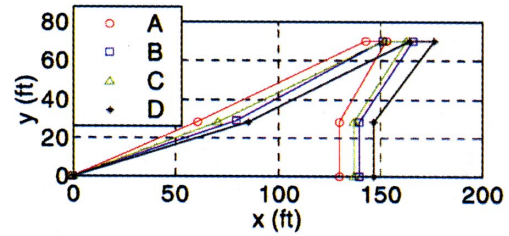


Figure 7 – Final Planforms After First Run

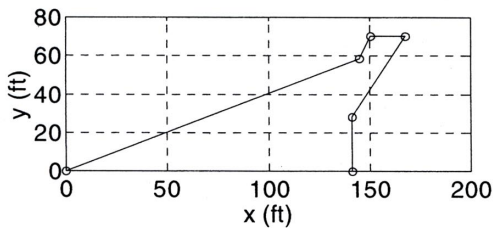


Figure 4 – Initial Condition B

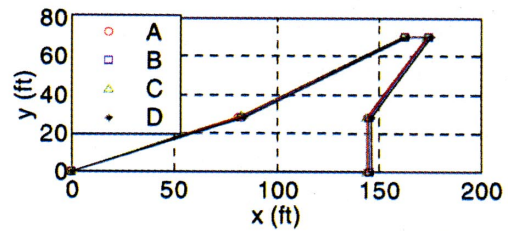


Figure 8 – Final Planforms

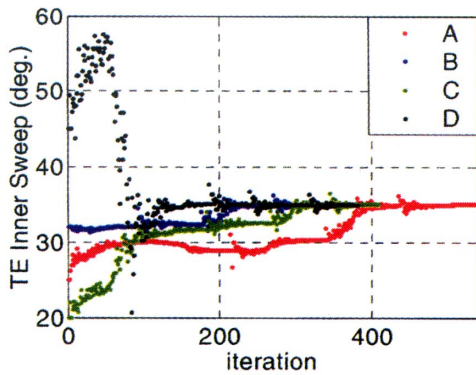


Figure 9 – Histories of Trailing Edge Outer Sweep

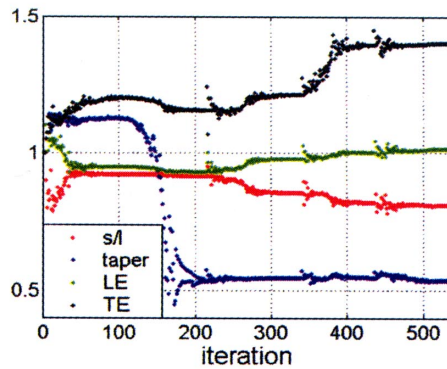


Figure 13 – Histories of Variables for Case A

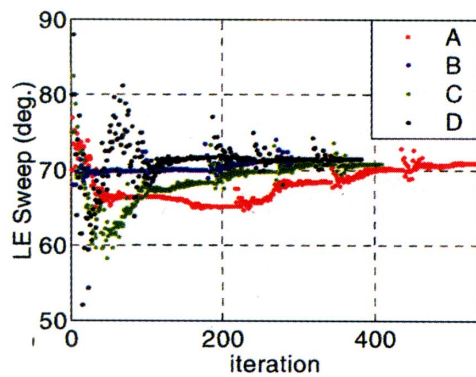


Figure 10 – Histories of Leading Edge Sweep

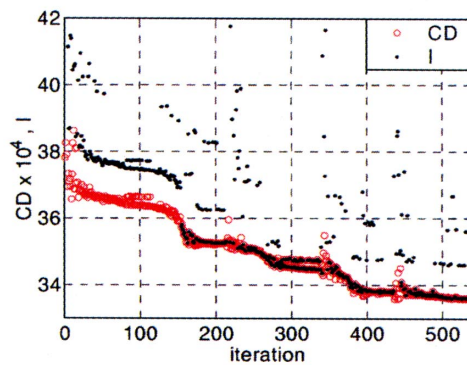


Figure 14 – History of Drag and Obj. Func. For Case A

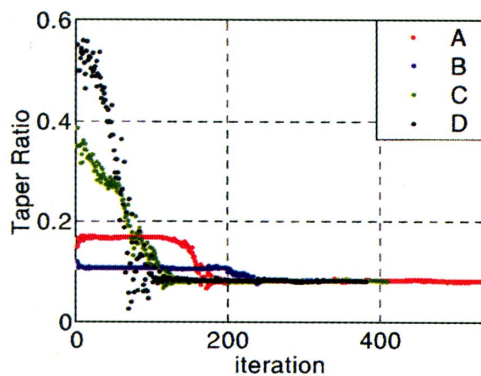


Figure 11 – Histories of Taper Ratio

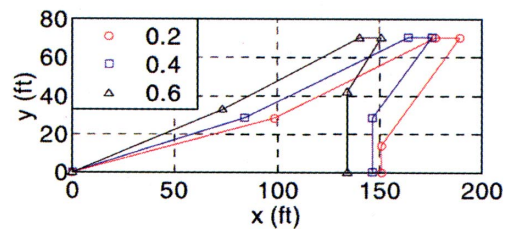


Figure 15 – Various Settings for the Trailing Edge Kink Location

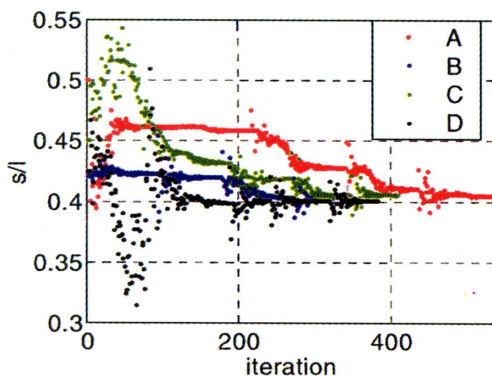


Figure 12 – Histories of Slenderness Ratio

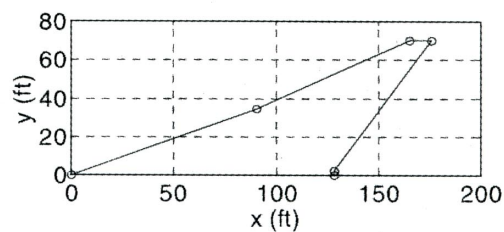


Figure 16 – Trailing Edge Kink Location is a Variable

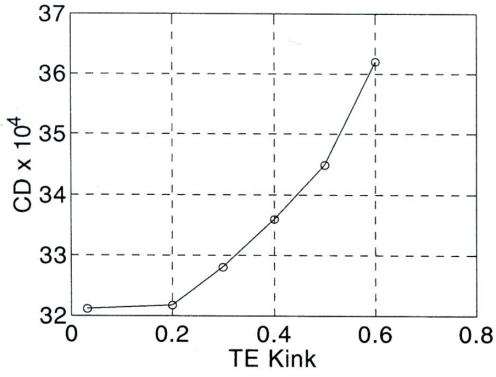


Figure 17 – C_D for Varying Trailing Edge Kink Location

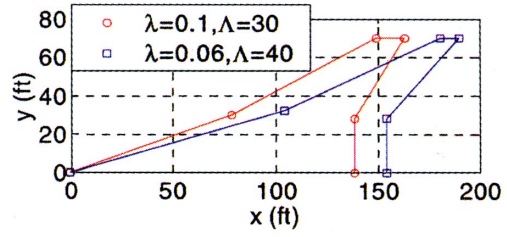


Figure 21 – Samples of Changing Maximum Trailing Edge Outer Sweep Angle and Minimum Taper Ratio

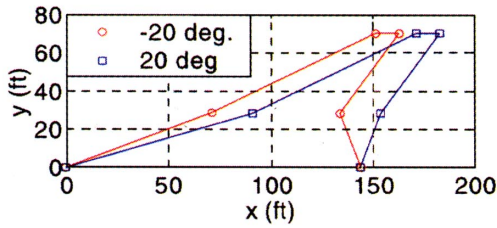


Figure 18 – Various Settings for the Trailing Edge Inner Sweep Angle

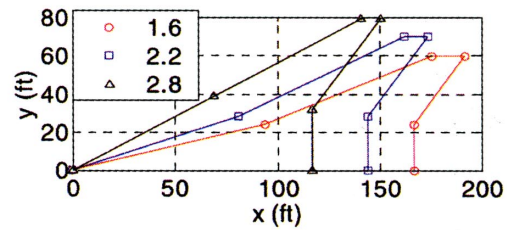


Figure 22 – Various Settings for the Aspect Ratio

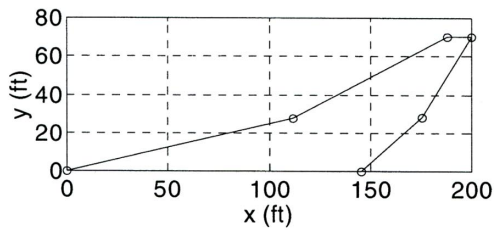


Figure 19 – Trailing Edge Inner Sweep Angle is a Variable

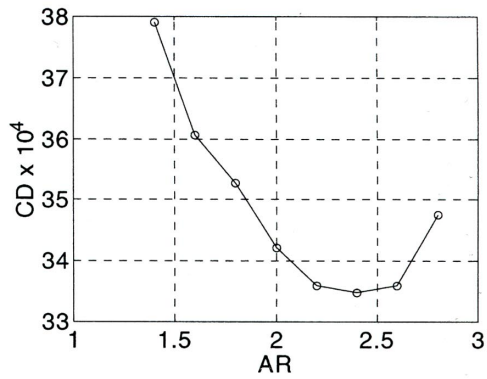


Figure 23 – C_D for Varying Aspect Ratio

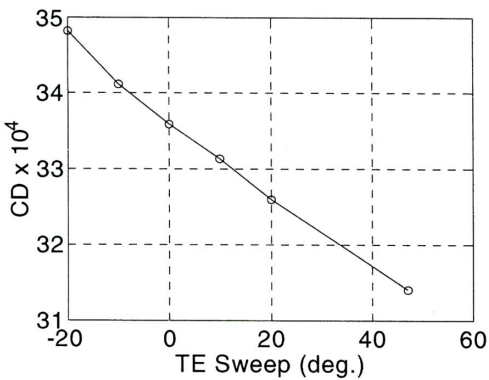


Figure 20 – C_D for Varying Trailing Edge Inner Sweep Angle

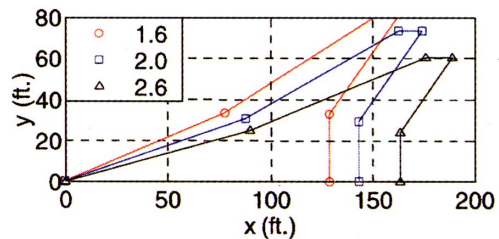


Figure 24 – Various Settings of Flight Mach Number and Corresponding C_L

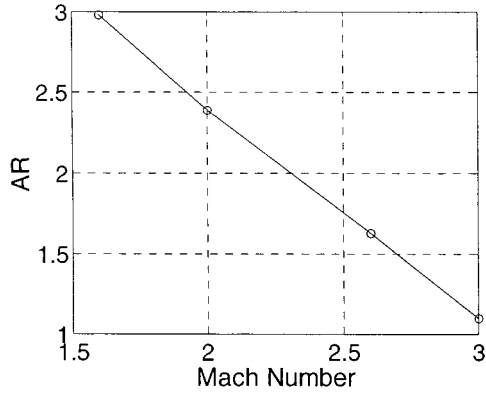


Figure 25 – Aspect Ratio for Varying Mach Number

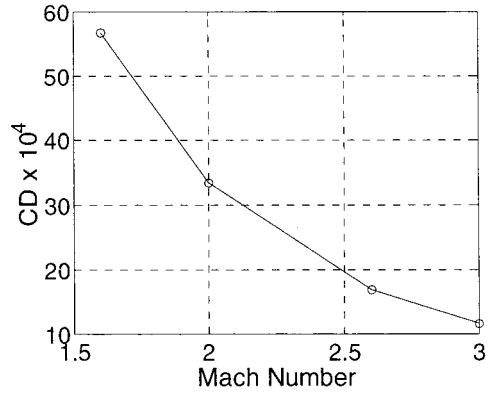


Figure 28 – C_D for Varying Mach Number

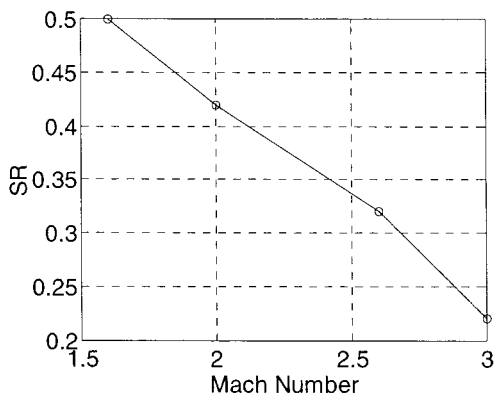


Figure 26 – Slenderness Ratio

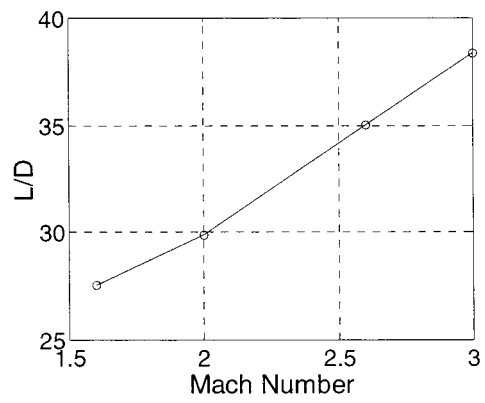


Figure 29 – L/D for Varying Mach Number

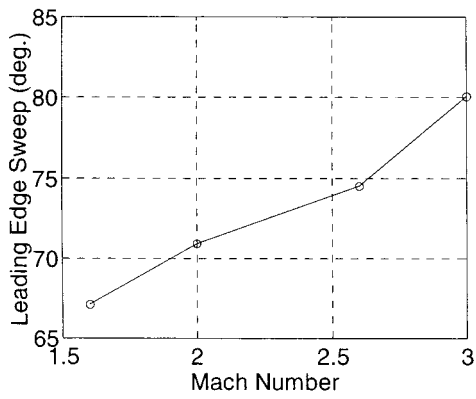


Figure 27 – Leading Edge Sweep Angle

CFD Application to SST Propulsion System

Y. Ooba and H. Kodama (Ishikawajima-Harima Heavy Industries)

O. Nozaki, K. Kikuchi, T. Nishizawa and Y. Matsuo (National Aerospace Laboratory)

Abstract

The SST propulsion system will operate in the range from takeoff to high Mach number. The high speed flight causes very high inlet air temperatures and pressures and the high inlet air temperatures and recovery pressures inside the engine make cooling for elements of the engine mandatory to keep the best available construction materials operating satisfactorily. Technology for satisfied cooling requires to understand the heat transfer in the engine, however there are many difficulties to understand detailed phenomena occurred in the engine from limited measurement.

This paper describes some CFD applications for a SST propulsion system which were carried to understand the mechanisms of flowfields and heat transfer in the engine.

Introduction

In Japan, the Hypersonic Transport Propulsion System (HYPR) Project started in 1989 to develop technologies for the propulsion system of a Mach 5 Hypersonic Transport airplane, which could be environmentally acceptable and economically viable. The engine studied is a combined-cycle engine composed of a turbo-jet engine which can operate from taking-off to Mach 3 and a ram-jet engine which can operate beyond Mach 2.5 up to Mach 5. The variable cycle engine concept is applied to the turbo engine to satisfy the conflicting requirements of low noise level at take-off and of high specific thrust at high altitude and flight speed.

In this project, a new design and analysis approach using CFD was demanded for the development of engine components. CFD was found to be extremely helpful and important to explain measured data of the tests conducted in the engine development.

This paper describes the four examples of the CFD applications which were carried out in the HYPR project; three-dimensional unsteady flow analyses of a single stage high pressure turbine including hot streaks from combustion cambers, axisymmetric steady flow analyses of disc cavities of a high pressure compressor, three-dimensional flow analyses of a rim rear cavity with exit guide vanes and three-dimensional steady flow analyses of a turbine disc cavity of a high pressure turbine.

Unsteady Stage Analysis of HP Turbine

Turbines in SST propulsion system operate near the limits of metal temperature capabilities. Temperature nonuniformity at the inlet to the turbine and their migration and redistribution through the turbine are believed to be a major cause of localized overheating of rotor airfoils and passage endwalls, resulting in reduced component life. The physics governing the temperature redistribution process is not well understood and the inability to

predict accurately the local gas temperatures in the rotor passage results in overly conservative cooling designs in order to meet turbine life goals. Difficulties in experimental measurements due to the unsteady interactions between stator and rotor prevent to understand the detailed mechanism of hot streaks. In the current study, three-dimensional unsteady stage analysis was conducted to investigate the detailed flow structure through a single stage high pressure turbine with temperature nonuniformity due to hot streaks from a combustor (see Fig.1).

Outline of Numerical method

The governing equations are the time-dependent three-dimensional Reynolds-averaged Navier-Stokes equations. An implicit finite difference scheme which is capable of using large CFD numbers is used. The convection terms are discretized using the TVD scheme developed by Chakravarthy and Osher (1985) and central differencing is used for the diffusion terms. For the implicit time integration approach, a Newton sub-iteration is performed at each time step to increase stability and reduce linearization errors. The number of sub-iterations is 4 for the present study. The turbulence viscosity is determined using Baldwin-Lomax model.

The algorithm in the present code is parallelized for NWT (Numerical Wind Tunnel) which is a parallel supercomputer developed by NAL. Each sub-domain is executed on a different processing element of NWT and exchanges boundary information with neighboring sub-domains in the same and different blade row. Further details on numerical scheme and the algorithm can be found in Matsuo (1991) and Nozaki (1999).

The single stage HP turbine is composed of 28 stator vanes and 57 rotor blades and subjected to hot streaks corresponding to 16 fuel injectors of the combustor. For the present calculation, the number of rotor was decreased to 56 in order to allow a one-hot streak / seven-stator airfoils / fourteen rotor airfoils combination to be simulated with negligible effect on the pitch-to-chord ratio.

Results and Discussions

Figure 2-(a), 2-(b) and 2-(c) show the time-averaged total temperature contours in the absolute frame of reference at the stator inlet, at the stator trailing edge and downstream of the rotor respectively. The straight lines from hub to casing represent the stator leading edge. The location of midspan are represented by a circular dotted line. At the stator trailing edge, the hot streak hit on the pressure surface of the stator is transported downwards from the midspan due to secondary flow in the stator, while other hot streaks stay at the midspan and the overall shape of the distortions are approximately the same as those of the stator inlet. It is seen that the peak values of the hot streaks are reduced through the stator passage probably due to diffusive mixing. On the other hand, the redistribution of total temperature distribution due to unsteady

effects is observed downstream of the rotor, although the cores of circular distortions are still recognized. The distortion level is significantly attenuated through the rotor.

Internal Flow in HP Compressor Disc Cavities

Due to high Mach number operations, the HP compressor discharge temperature (CDT) reaches 854K at Mach 2.5 Climb. Therefore knowledge of the heat transfer to the HP compressor disc is essential for accurate prediction of the disc stresses and thus the life of the disc.

A schematic diagram of HP compressor multiple disc arrangement of the SST engine is shown in figure 4. Coolant enters the annulus between a rotating shaft and the HP compressor drum in the upstream discs and leaves through the annulus between a rotating shaft and the last disc hub. The flow structure in the multiple rotating cavities formed by the multiple discs of the HP compressor with a rotating shaft running through the bores is considerably complex. However the detailed information on the flow structure is needed for accurate prediction of convective heat transfer in rotating disc cavities.

An axisymmetric Navier-Stokes code was applied to simulate the flow in the multiple rotating cavities, and the calculation results were used in the thermal modelling to predict the disc temperature. The calculated temperatures were compared with measured data obtained in the core engine test.

Outline of Numerical Method

A three-dimensional incompressible RANS code was used as an axisymmetric code. By assuming an incompressible flow, the buoyancy effect was ignored in the calculation. The turbulent viscosity is determined using the two-equation $k-\epsilon$ eddy viscosity turbulence model. Wall functions are used for the turbulence quantities on a solid wall.

The inflow to the annulus between a rotating shaft and the HP compressor drum in the upstream discs was given radially inward in the same way as the engine. The mass flow was obtained from one-dimensional network analyses of secondary air system using the engine test data.

In the core engine test, the HP compressor disc and the rotating shaft were connected, so the rotation speeds of those components were same.

Results and Discussions

Figure 5 shows the calculated velocity vectors in the multiple rotating cavities. Inside the cavities except near disc bores, axial and radial component of the velocities are very small.

The temperature field within the HP compressor disc was obtained through solution of heat conduction equation with finite element solver. The convective boundary conditions were specified by using the results of flow simulation in the multiple rotating cavities. The resultant temperature distribution is shown in figure 6.

Figure 7 shows the comparison between calculated and measured temperatures. The temperatures are normalized by the HP drum metal temperature measured near the coolant air injection hole (TO). A good agreement indicates that the flow structure in the multiple rotating cavities was reasonably captured

by the numerical simulation.

Overheating in the LP-turbine Rim Cavity

As for the research and development of the turbo-jet engine, the experimental engine was developed and the ground performance verification was conducted. Subsequently, the high altitude performance testing facility (ATF) was used for the running of the turbo-jet engine under a high altitude / high speed environment.

In the first ATF test, air temperature in LP-turbine rim cavity (see Fig. 8) increased beyond expectations at the Mach 2.5 climb condition. The cause of overheating was not clearly understood from the limited number of measurements.

Thus a numerical simulation was conducted to understand the flow physics behind overheating in the LP turbine rim cavity occurred in the engine test.

Outline of numerical method

A three-dimensional RANS code using unstructured grid was applied to the analyses. Full details of the numerical method are given by Ohkita et al.(1997).

The turbulent viscosity and the turbulent conductivity are determined using the two-equation $k-\epsilon$ eddy viscosity turbulence model. The current code adopts wall functions (Launder and Spalding, 1974). The wall heat transfer is also expressed using the wall functions recommended by Kays and Crawford (1980).

As the rim cavity in question was thought to be the flowfield where secondary cooling air and mainstream strongly interact, a computational grid modeling both regions was used.

The cavity inflow boundary was located at the exit of upstream labyrinth seal. The mass flow and the temperature were obtained from one-dimensional network analyses of secondary air system.

The mainstream inflow boundary was located at the trailing edge of upstream bucket. The profiles of total pressure, total temperature and flow angles obtained from data analysis using an axisymmetric throughflow calculation of LP turbine based on the engine test data, turbulent kinetic energy and dissipation rate were imposed at the boundary.

The static pressure at the outlet boundary was given such that the calculated inlet Mach number matched the data analysis result.

Considering eight EGVs located at circumferentially regular intervals, the calculation region was confined to one-eighth sector including a EGV, and periodic conditions were imposed at the circumferential boundaries.

Results and Discussions

The calculated velocity vectors in the meridional plane at the circumferential location of the EGV leading edge (Pos.1), the pressure side plane (Pos.2) and the suction side plane (Pos.3) are shown in figure 9-(a), 9-(b), 9-(c), respectively. The colors of the arrows represent the level of temperature. These calculated results indicates that the overheating occurred in the engine test was attributed to circumferentially local hot gas ingestion.

Discoloration on rear stator disk surface at cavity as sketched in Figure 11 was observed when the engine was overhauled after the test. This discoloration resulted at locations subjected to high temperature flow during the engine test. The calculated contours of

temperature at the same disk surface is compared in figure 12. The discoloration in the test and the high temperature region in the calculation generally agree in their locations. This suggests that the numerical simulation captures the overall flow structure in the cavity. Both results show that the highest temperature in the cavity may be observed at the circumferential location near the EGV leading edge.

The calculated contours of static pressure on the hub endwall in the mainstream is shown in figure 10. The figure shows that the potential pressure disturbance due to the thickness and turning of the EGV exists over the cavity entry region. This is thought to be the reason why pressure asymmetry was appeared in the cavity and hot gas ingestion was caused.

Internal Flow in HP Turbine Disc Cavity

Flows inside a turbine disc cavity tend to be very complex because of its complicated geometries (see Fig.13). Heat transfer to the turbine disc is strongly influenced by the flow structure in the cavity. Therefore it is essential to know the flowfield inside the cavity for accurate prediction of the heat transfer.

Outline of Numerical Method

In this study, a three-dimensional RANS code was applied to simulate the flows in the turbine disc cavity. Navier-Stokes equations are discretized using a finite volume method in the relative coordinate of the turbine disc. The study is focused on the effect of bolts in the cavity on the flowfield and resultant heat transfer. 30 bolts are located on the rotating wall surface of the turbine disc. One thirtieth domain of the annulus is calculated using the periodic boundary conditions at the circumferential ends. Computational domains both with bolt and without bolt are shown in figure14. Non-slip boundary condition are imposed on the surfaces for both stationary and rotating parts. Inlet and outlet secondary cooling air conditions are set at the inlet boundary of the upper side and the lower side of the cavity using data from the network calculation of the secondary air system.

Results and Discussions

Figure 15, 16 and 17 respectively show velocity vectors, distributions of temperature and swirl ratio inside the turbine disc cavity for the cases both with bolts and without bolts respectively. Swirl ratio is defined as swirl velocity of fluid divided by swirl velocity of the rotating surface at the same radial position. These figures show that flows inside the cavity are strongly influenced by existence of bolts inside the cavity.

Figure 18 compares radial distribution of heat transfer coefficient on the rotor disc. It can be seen that the averaged heat transfer coefficient for the case with bolts well agrees with the experimental results for the configuration with bolts, and the average heat transfer coefficient for the case without bolts would increase by 30%.

Conclusions

Four sets of CFD simulations focused on the prediction of flow and heat transfer applied to the engine of HYPR project were presented. It was found that CFD takes an important role in understanding the phenomena occurred in the SST propulsion

system.

References

- [1]Chakravarthy, S. R. and Osher, S., "A New Class of High Accuracy TVD Schemes for Hyperbolic Conservation Laws", AIAA 85-0363, 1985.
- [2]Baldwin, B. S. and Lomax, H., "Thin-Layer Approximation and Algebraic Model for Separated Turbulent Flows", AIAA 78-257, 1978.
- [3]Matsuo, Y., "Computations of Three-Dimensional Viscous Flows in Turbomachinery Cascades", AIAA 91-2237, 1991.
- [4]Nozaki, O. et al, "Unsteady Three-Dimensional Viscous Flow Computations of Multiple Blade-Row Interactions", ISABE 99-7032, 1999.
- [5]Yamawaki, S. et al, "CFD Contribution to Development of HYPR Engine", AIAA 99-0886, 1999.
- [6]Ohkita, Y. et al, "Numerical Simulation of Flow and Heat Transfer in 3D Complicated Geometries Using Unstructured Grids", AIAA 97-1948, 1997.
- [7]Lauder, B. E. and Spalding, D. B., "The Numerical Computation of Turbulent Flows", Computer Methods in Applied Mechanics and Engineering, Vol.3, pp.269-289, 1974.
- [8]Kays, W. M. and Crawford, M. E., "Convective Heat and Mass Transfer", McGraw-Hill, New York.

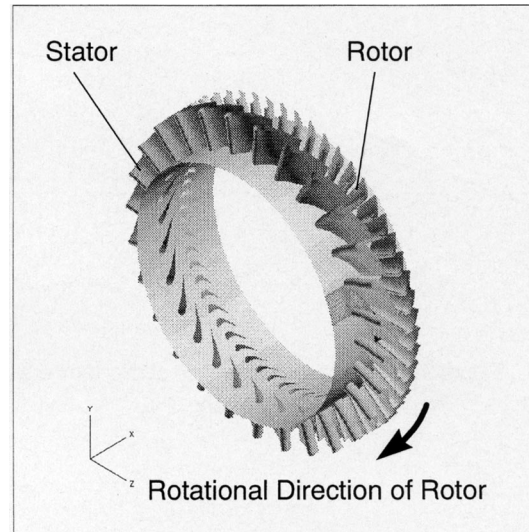
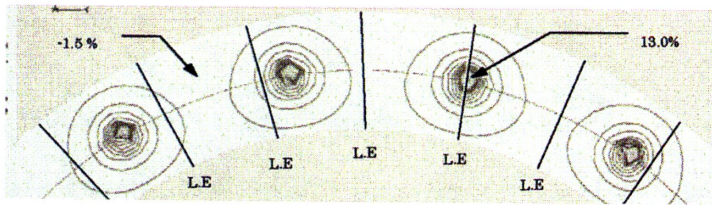
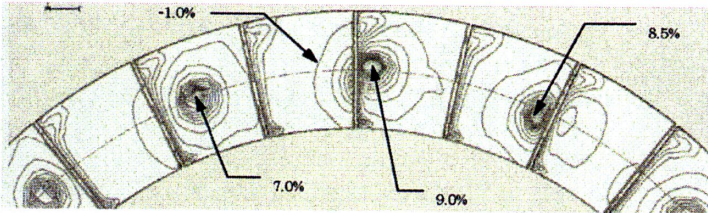


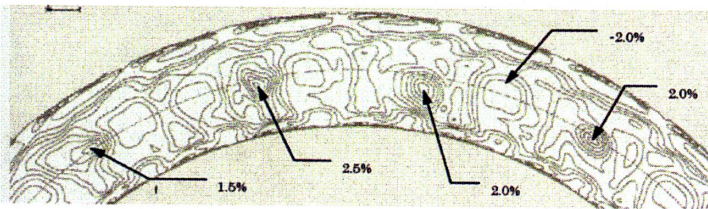
Figure 1 Schematic of single stage high pressure turbine



(a) upstream of stators



(b) stator T/E



(c) downstream of rotor T/E

Figure 2 Time averaged distribution of total temperature

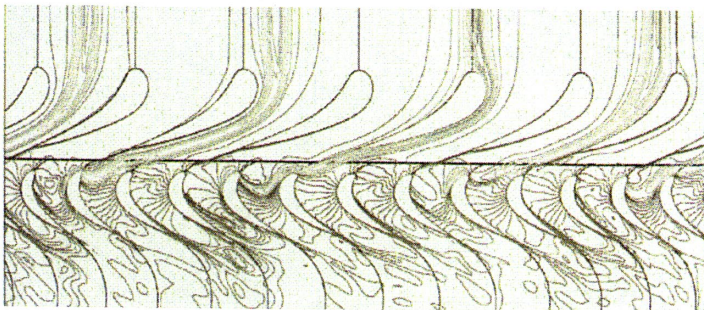


Figure 3 Instantaneous distribution of total temperature (midspan)

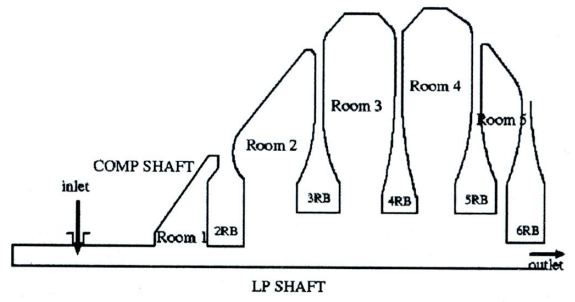


Figure 4 Schematic of high pressure compressor disc cavity

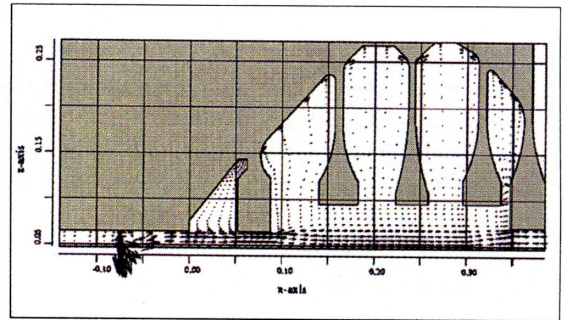


Figure 5 velocity vectors inside HPC disc cavity

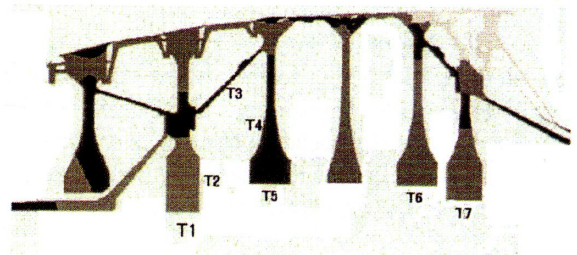


Figure 6 Temperature distribution of HPC disc

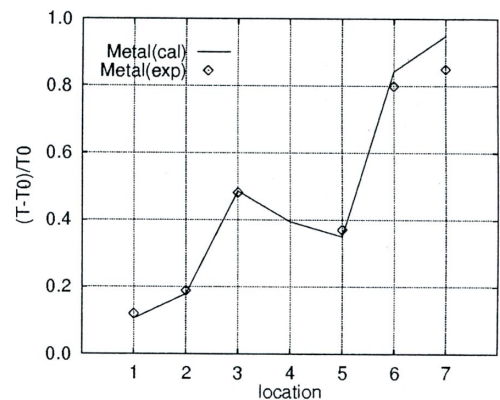


Figure 7 Comparison of distributions of wall temperature

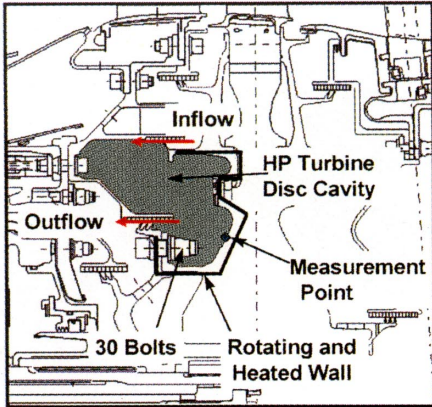
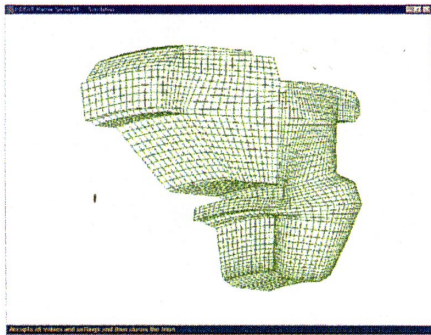
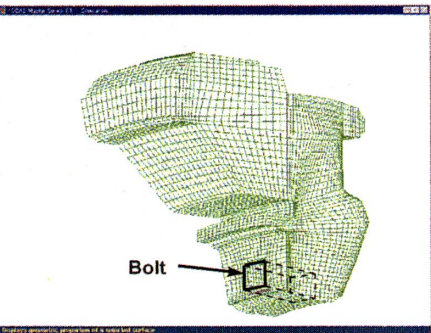


Figure 13 Schematic of high pressure turbine disc cavity

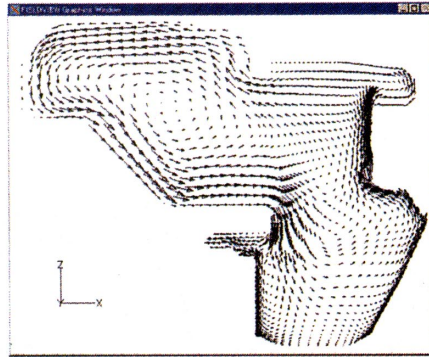


(a) without bolt

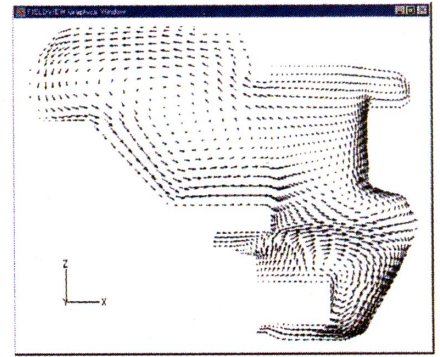


(b) with bolt

Figure 14 Numerical grid of turbine disc cavity

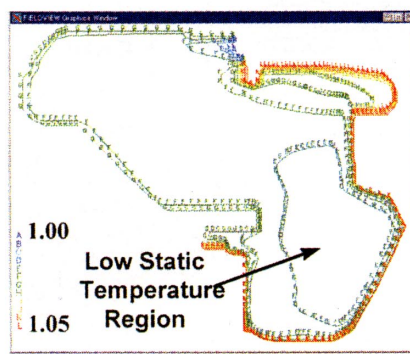


(a) without bolt

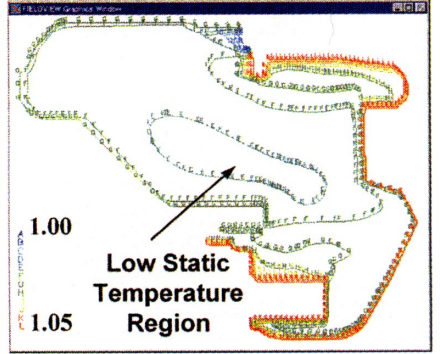


(b) with bolt

Figure 15 Velocity vectors at center of bolt

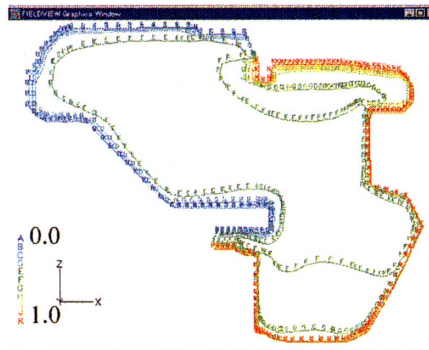


(a) without bolt

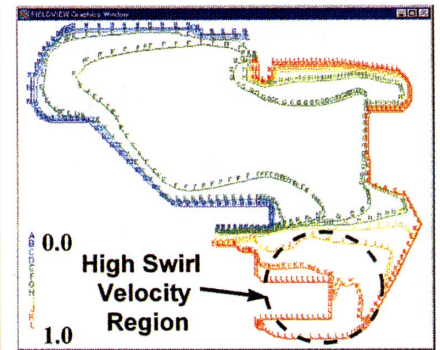


(b) with bolt

Figure 16 Distributions of normalized temperature at center of bolt



(a) without bolt



(b) with bolt

Figure 17 Distributions of swirl ratio at center of bolt

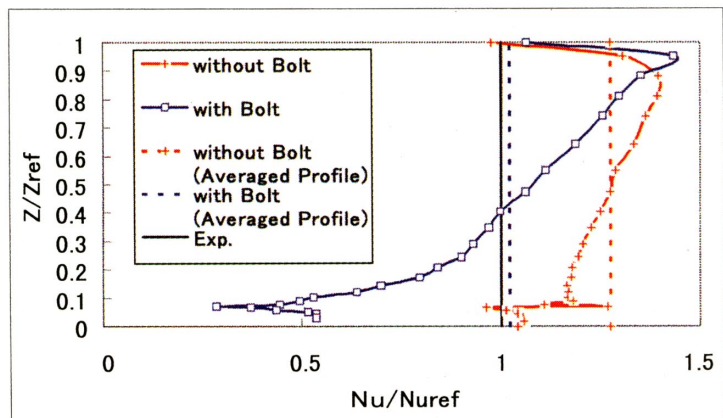


Figure 18 Distributions of circumferentially averaged normalized heat transfer ratio at measurement point

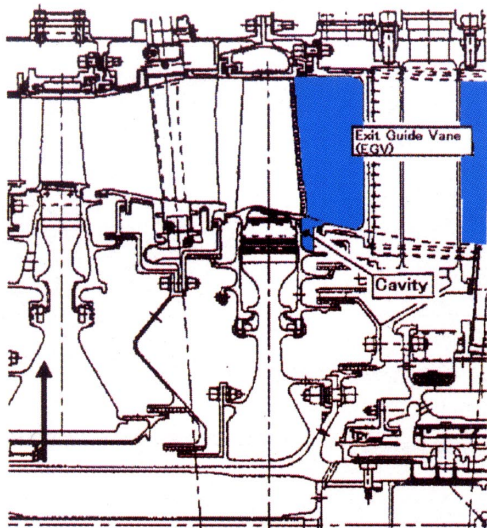


Figure 8 Schematic of EGV and Rim-rear cavity

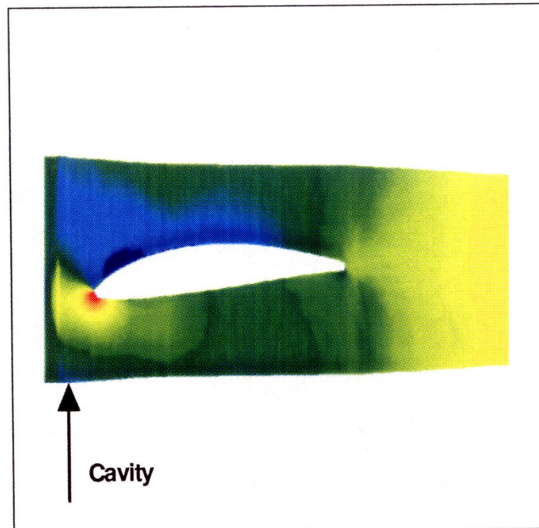
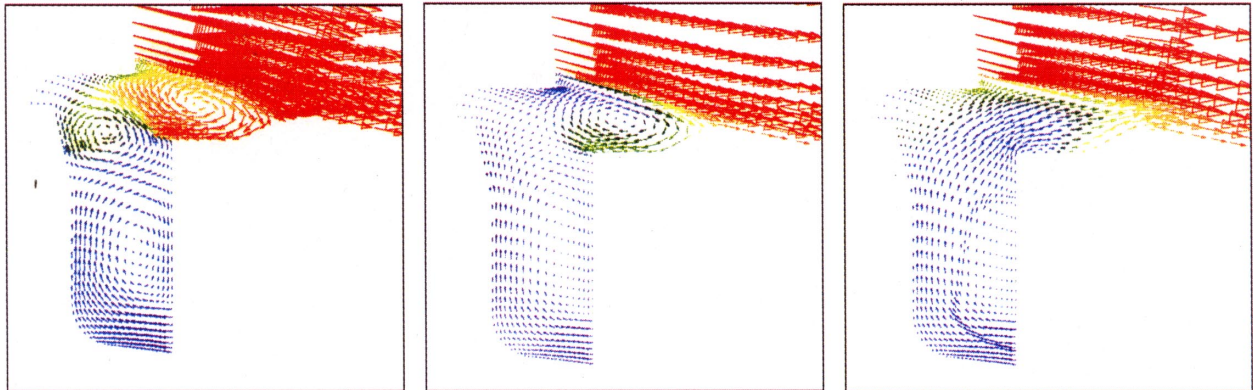


Figure 10 Distribution of static pressure on endwall surface of EGV



(a) Pos.1 (near EGV L/E) (b) Pos.2 (near EGV pressure surface) (c) Pos. 3 (near EGV suction surface)

Figure 9 Distributions of temperature and velocity vectors inside rim-rear cavity near EGV L/E

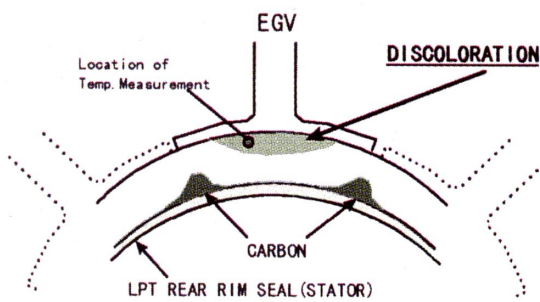


Figure 11 Schematic of discolored region on stator disc surface (Rim-rear cavity)

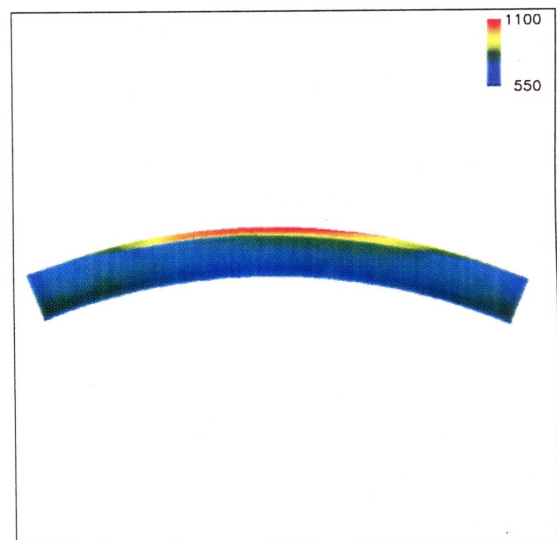


Figure 12 Distribution of temperature on stator disc surface (Rim-rear cavity)

Aerodynamic Nacelle Shape Optimization for NAL's Experimental Airplane

Yoshikazu Makino and Toshiyuki Iwamiya

National Aerospace Laboratory

7-44-1 Jindaijihigashi-machi, Chofu, Tokyo 182-8522, JAPAN

Zhong Lei

VINAS Co., Ltd.

1-18-35 Edobori, Nishi, Osaka, Osaka 550-0002, JAPAN

Abstract

The numerical simulation of a Mach 2.0 scaled supersonic experimental airplane is conducted with the consideration of the integration between airframe and engine nacelles. A three-dimensional Euler CFD code with an overset-grids technique is adopted for solving the flow-field around a complex airplane configuration. The calculated pressure distributions are compared with wind tunnel test data and show good agreement with them. The aerodynamic design tool which combines the CFD code with an optimization technique for drag minimization is developed. At first, it is applied to an axisymmetrical body in order to validate this design tool. The result shows that the optimized body geometry agrees well with the Sears-Haack body. Next, it is applied to two bodies under a wing-body configuration. The pressure drag of the optimized configurations is about 9 percent lower than that of the Sears-Haack body maintaining their final volumes.

Introduction

National Aerospace Laboratory (NAL) of Japan started a scaled supersonic experimental airplane program which we call NEXST (National Experimental Supersonic Transport)¹ in 1996 in order to establish advanced technologies including a sophisticated CFD-based total design tool for the next generation supersonic civil transport. In this program, at first we will conduct flight tests of an un-manned non-powered experimental airplane in 2002. This airplane was designed at Mach 2.0 adopting a NAL's original aerodynamic design technology together with CFD prediction². Its design concepts for a high lift/drag ratio are a cranked arrow wing, a modulated warp, an area-ruled configuration and a natural laminar flow

wing. In order to develop a CFD-based total aerodynamic design tool for a complete airplane configuration, a jet-powered experimental airplane will be designed as a successor of the non-powered airplane. Considerations of airframe/nacelle integration are important in the design process of this jet-powered airplane.

Numerical Simulation Method

In order to simulate the flow around a complex airplane configuration, an overset-grids technique is adopted in our study. The airplane configuration which is a half configuration in computational space is divided into five components; wing-body, engine nacelle, diverter, horizontal tail and vertical tail. The grids which are independently generated around each component are overlapped. Figure 1 shows the computational grids generated around the non-powered experimental airplane configuration with an axisymmetrical engine nacelle. This simple flow-through nacelle configuration is an experimental model configuration used in our wind tunnel tests. A CFD code which is based on three-dimensional Euler equations is used to solve the flow-field around the airplane. The numerical method is an implicit finite difference scheme. The diagonalized ADI scheme which utilizes an upwind flux-split technique is used for the implicit left-hand-side, and a higher-order upwind scheme based on TVD scheme by Chakravarthy and Osher³ is applied to the explicit right-hand-side. Communications among the overset-grids are accomplished by interpolations of the independent variables at grid boundaries⁴. Figure 2 shows the calculated surface pressure contours of the airplane in the case of angle-of-attack 2° at Mach 2.0. It is shown in the figure that two strong shocks are generated from the nacelles and diverters on each side of the wing. These shocks interact under the

centerline of the airplane and generate high pressure region on the lower wing surface. Figure 3(a) to 3(c) show the fuselage and wing surface pressure distributions compared with the experimental data at spanwise location $\eta=0.0$ (fuselage center line), $\eta=0.3$ (nacelle center line) and $\eta=0.5$, respectively. At $\eta=0.0$ and $\eta=0.3$, the calculated pressure distributions and the experimental data show good agreement. At $\eta=0.5$, there are two pressure peaks on the lower surface of the wing which are due to the shocks from the nacelle and diverter. The pressure rise due to the nacelle in the calculated pressure distribution is located more rearward than that in the experimental data. A grid sensitivity analysis will be necessary in order to clarify whether this discrepancy is due to the viscous effects which cannot be considered by our Euler CFD code.

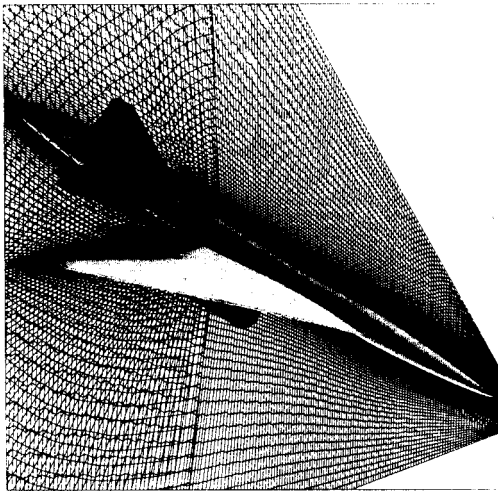


Figure 1: Overset grids.

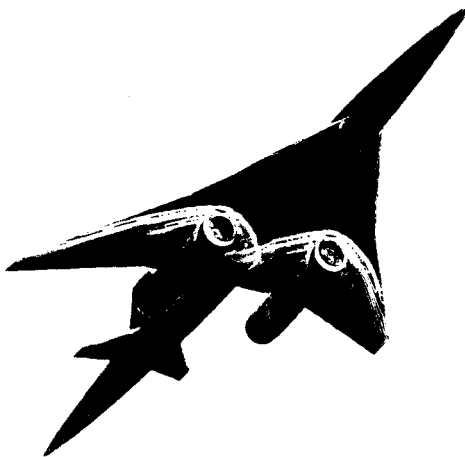
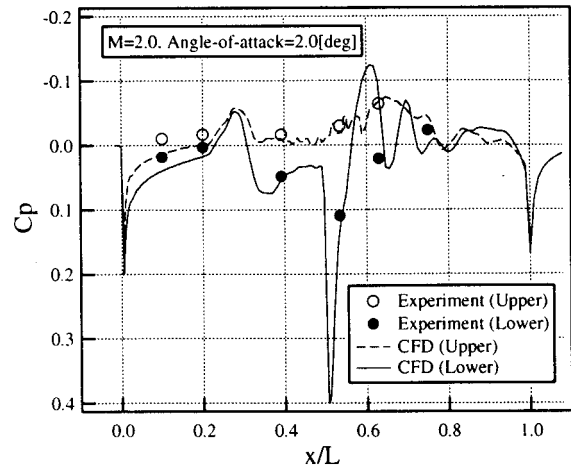
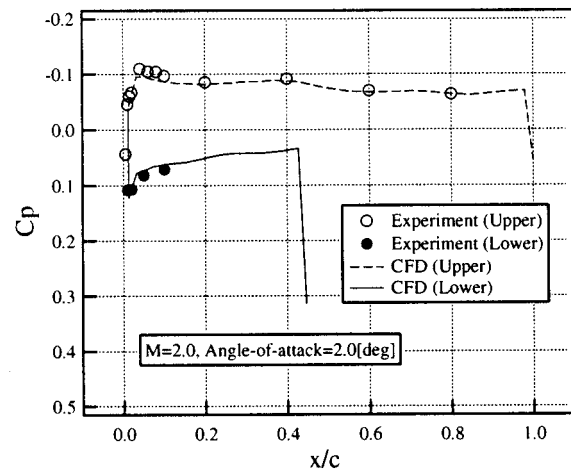


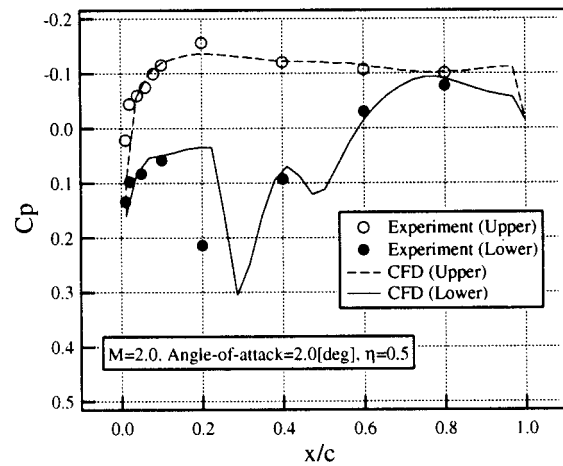
Figure 2: Surface pressure contours.



(a) $\eta = 0.0$.



(b) $\eta = 0.3$.



(c) $\eta = 0.5$.

Figure 3: Calculated pressure distributions compared with experimental data.

Aerodynamic Design Method

In order to reduce interaction drag between airframe and engine nacelles, position and shape optimization tools for designing the propulsion system are needed. The design tool which combines the CFD code with an optimization technique is developed in our study. A quasi-Newton optimization method based on a conjugate gradient method is adopted as an optimization technique. At first, it is applied to an axisymmetrical body configuration to minimize the pressure drag as a sample demonstration. The object function to be minimized through the optimization is:

$$I = \frac{C_{Dp} + K \times \left(\frac{V-V_0}{V_0}\right)^2 \times H(V_0 - V)}{C_{Dp_0}} \quad (1)$$

where C_{Dp} and V are a pressure drag coefficient and a volume of an axisymmetrical body, respectively. The subscript 0 means the initial value. The function $H(x)$ is the Heaviside step function which replies 1 when x has a positive value and replies 0 when x is less than 0. The quantity K is a coefficient of a penalty function in order to keep the body volume no less than that of an initial geometry. This penalty function coefficient K is 5 in this case. The initial axisymmetrical body geometry shown in Figure 4 is modified by adding radial perturbations whose axial distribution is defined by a Bezier curve controlled by 7 points including fixed two points at nose and tail of the body. The radial coordinates of the other 5 points are used as design variables in the optimization process.

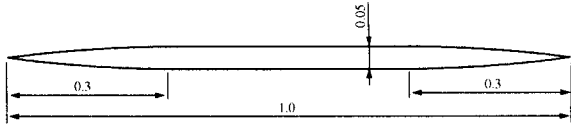


Figure 4: Initial axisymmetrical body geometry.

One design cycle of the quasi-Newton optimization method is composed of two processes: gradient calculation of the object function and line minimization in the direction which is conjugate to the calculated steepest direction. As for the gradient calculation process, two methods are used in this study. One method is a finite difference method and another is an adjoint method⁵. In the finite difference method, the gradients of the object function to all design variables are calculated by adding a small perturbation to every design variable and evaluating the object function by CFD

one by one. Therefore the number of CFD calculations is the same as that of the design variables in this process. The general formulation of the adjoint method is shown in Reference 5. The object function is defined by the aerodynamic properties which are functions of the flow-field variables(q) and the physical location of the boundary(\mathcal{F}).

$$I = I(q, \mathcal{F}) \quad (2)$$

A change in \mathcal{F} results in a change

$$\delta I = \left[\frac{\partial I}{\partial q} \right]_I^T \delta q + \left[\frac{\partial I}{\partial \mathcal{F}} \right]_{II}^T \delta \mathcal{F} \quad (3)$$

in the object function, where the subscript I represents $\delta \mathcal{F} = 0$ and the subscript II means $\delta q = 0$. The governing equations of the flow-field and their variations are

$$R(q, \mathcal{F}) = 0 \quad (4)$$

$$\delta R = \left[\frac{\partial R}{\partial q} \right]_I \delta q + \left[\frac{\partial R}{\partial \mathcal{F}} \right]_{II} \delta \mathcal{F} = 0 \quad (5)$$

Next, introducing a Lagrange Multiplier ψ , we have

$$\begin{aligned} \delta I &= \delta I - \psi^T \delta R \\ &= \left\{ \left[\frac{\partial I}{\partial q} \right]_I^T - \psi^T \frac{\partial R}{\partial q} \right\} \delta q \\ &\quad + \left\{ \left[\frac{\partial I}{\partial \mathcal{F}} \right]_{II}^T - \psi^T \frac{\partial R}{\partial \mathcal{F}} \right\} \delta \mathcal{F} \quad (6) \end{aligned}$$

Choosing ψ to satisfy the following adjoint equations

$$\left[\frac{\partial I}{\partial q} \right]_I^T = \psi^T \left[\frac{\partial R}{\partial q} \right]_I \quad (7)$$

the coefficient of δq becomes zero and we find

$$\begin{aligned} \delta I &= \mathcal{G} \delta \mathcal{F} \quad (8) \\ \mathcal{G} &\equiv \left[\frac{\partial I}{\partial \mathcal{F}} \right]_{II}^T - \psi^T \left[\frac{\partial R}{\partial \mathcal{F}} \right]_{II} \end{aligned}$$

Here, the variation of the object function δI is independent of δq . Therefore only one calculation of the adjoint equations is enough to obtain the gradients of the object function. Figure 5 shows the adjoint gradients compared with the finite difference gradients. Good agreements are shown between both methods.

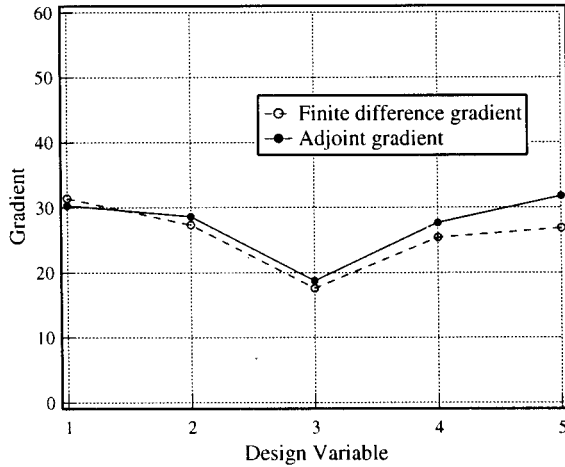
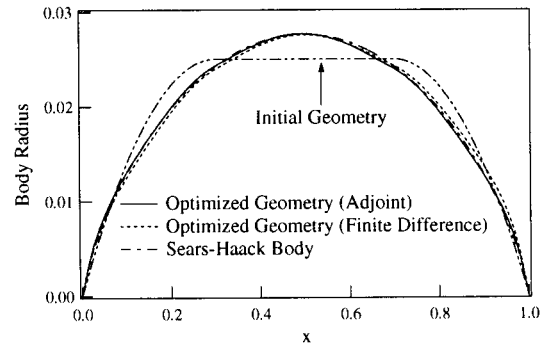
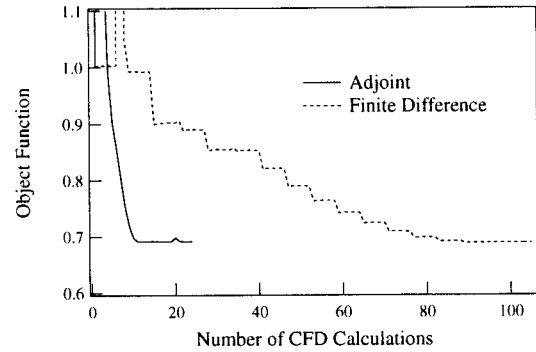


Figure 5: Comparison of gradients.

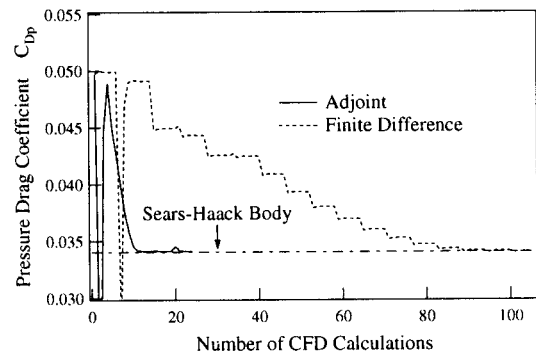
Figure 6(a) shows the optimized body shapes which are obtained by using both gradient estimation methods compared with the initial geometry. They are also compared with the Sears-Haack body whose volume equals to that of the initial geometry. Both optimized geometries agree with the Sears-Haack body. Figure 6(b) to 6(d) show the convergence histories of the object function, the pressure drag coefficient and the volume of the body with respect to the number of CFD calculations. In Figure 6(b), it is shown that the object function by the finite difference gradient goes down every step in the optimization process. This step shape represents the two processes in one design cycle: the finite difference gradients are calculated in the flat part of the step and then the object function goes down by the line minimization process. It is shown that the object function which is obtained by using the adjoint gradients converges at about 15th CFD calculation while one obtained by using the finite difference gradients converges after 90 CFD calculations. Including the computational costs for calculating the adjoint equations every design cycle, the total computational cost of the adjoint method is much smaller than that of the finite difference method. This merit of the adjoint method increases when the number of the design variables becomes large. As shown in Figure 6(c), the pressure drag coefficients of both optimized geometries are about the same as that of the Sears-Haack body. The body volume of both optimized geometries are, however, about 0.7 percent smaller than that of the Sears-Haack body. These results suggest that the penalty function coefficient K , which is 5 in this case, should be larger in order to keep the initial volume.



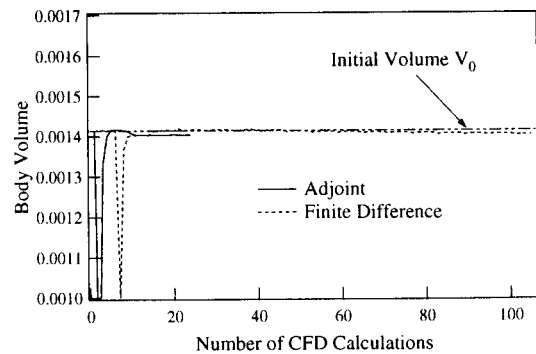
(a) Optimized geometries.



(b) Object function.



(c) Pressure drag coefficient.



(d) Body volume.

Figure 6: Optimization results for the axisymmetrical body.

Design Results

Next, the design tool which uses the adjoint gradients is extended to a complex airplane geometry. In Reference 6, the adjoint method is applied to a complex airplane geometry with a multi-block technique. In this work, it is extended to be used with an overset-grids technique and applied to two bodies under a wing-body configuration as shown in Figure 7. The object function of the design cycle is the same as stated in equation (1) in which C_{Dp} is the pressure drag coefficients of two bodies. The penalty function coefficient K is 50 in this case. The Sears-Haack body is selected as an initial geometry. The calculated pressure contours on the wing-body configuration with these initial axisymmetrical bodies are also shown in Figure 7. Figure 8 shows the calculated pressure coefficient distributions along the upper, inner, lower, outer side lines on the initial bodies. In this figure, there is a pressure rise due to the nose shock in the front part of every pressure distribution. In the upper-side line, a pressure peak is shown at about $x = 0.25$ which is due to the reflected shock from the lower surface of the wing. This reflected shock generates pressure increases in the inner and outer side lines, too. In the inner side line, another pressure peak is shown at about $x = 0.6$ which is due to the shock from another body nose. Therefore, two shape modification methods are used in this design process. The first method is axisymmetrical modification which is the same as the single body case. Another method is non-axisymmetrical modification in which only the upper and inner side radius distributions are changed while the lower and outer side ones are fixed. In this case the number of design variables are 10 in which each 5 controlling points are distributed on the upper and inner side line, respectively. These design variables control Bezier curves as stated in previous section.

The design results are shown in Figure 9. Figure 9(a) shows the body radius distributions of the optimized body geometries. In the case of non-axisymmetrical modification, the upper-side geometry becomes flatter in the front part in order to reduce the drag component of the high pressure force due to the reflected shock. Similarly, the location of the maximum radius of the inner side geometry goes forward in order to increase the thrust component of the high pressure force due to the shock from another body nose. Figure 9(b) to 9(d) show the convergence histories of the object function, the pressure drag coefficient and the volume of the body, respectively, with respect to the number

of CFD calculations. Both object functions converge after about 17 CFD calculations. The final pressure drag coefficient of the non-axisymmetrical body is about 9.4 percent lower than that of the Sears-Haack body. This drag coefficient is lower than that of the axisymmetrical optimized body which is about 6.7 percent lower than that of the Sears-Haack body. The final volumes of both optimized bodies are almost the same as the initial volume as shown in Figure 9(d).

This is just a test case for designing nacelle shapes and the design method developed here will be soon applied to the flow-through nacelles shown in Figure 2 in our future work.

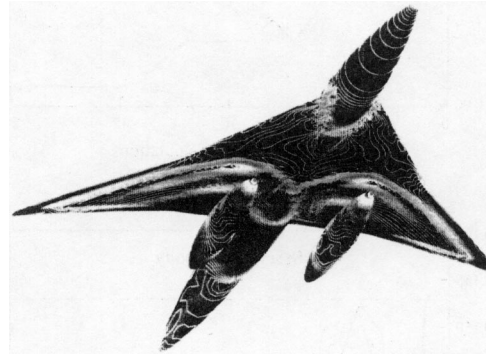


Figure 7: Two axisymmetrical bodies under the wing-body configuration.

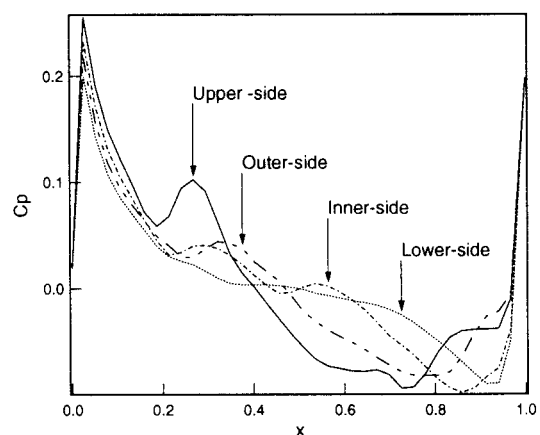
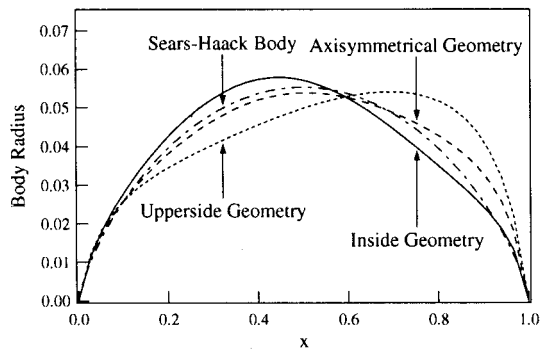
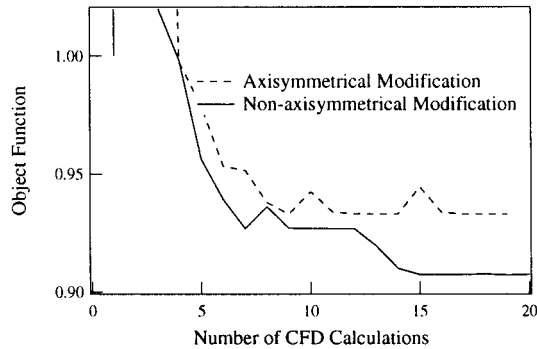


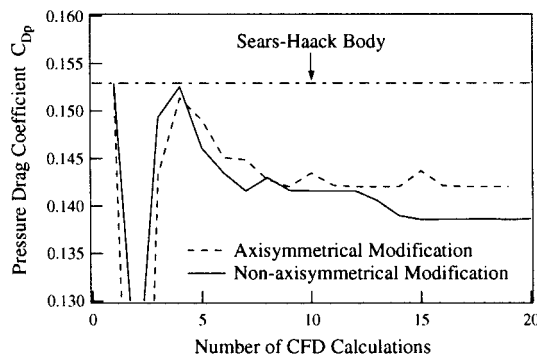
Figure 8: Pressure coefficient distributions on the Sears-Haack body.



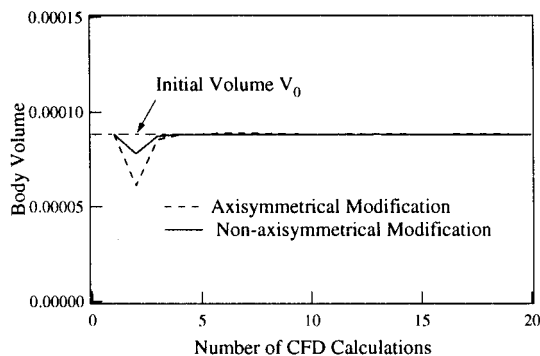
(a) Optimized geometries.



(b) Object function.



(c) Pressure drag coefficient.



(d) Body volume.

Figure 9: Optimization results for two bodies under the wing-body configuration.

Conclusions

The numerical simulation of a complex airplane geometry is conducted by using the three-dimensional Euler CFD code with an overset-grids technique. The calculated pressure distributions show good agreement with the experimental data. The aerodynamic design tool is developed by combining the CFD code with an optimization technique which utilizes either finite difference gradients or adjoint gradients. The results of its application to an axisymmetrical body show that the pressure drag coefficients of the optimized bodies are about the same as the Sears-Haack body and the convergence of the design cycle of the adjoint method is faster than that of the finite difference method. The design tool is applied to two bodies under a wing-body configuration. The results indicate that in the specific flow situation including shock interactions, the Sears-Haack body is not a minimum drag configuration. The pressure drag coefficient of the non-axisymmetrical optimized body is lower than that of the axisymmetrical optimized body in such a flow situation.

Acknowledgement

The authors express their sincere gratitude to Mr. Yuichi Shimbo and Mr. Masayoshi Noguchi for providing the experimental data.

References

1. Sakata, K., "Supersonic Research Program in NAL, Japan," 1st International CFD Workshop for Super-Sonic Transport Design, pp.1-4, 1998.
2. Shimbo, Y., Yoshida, K., Iwamiya, T., Takaki, R. and Matsushima, K., "Aerodynamic Design of the Scaled Supersonic Experimental Airplane," 1st International CFD Workshop for Super-Sonic Transport Design, pp.62-67, 1998.
3. Chakravarthy, S.R. and Osher, S., "A New Class of High Accuracy TVD Schemes for Hyperbolic Conservation Laws," AIAA paper 85-0363, 1985.
4. Benek, J.A., Buning, P.G. and Steger, J.L., "A 3-D Chimera Grid Embedding Technique," AIAA paper 85-1523, 1985.
5. Jameson, A., "Optimum Aerodynamic Design Using CFD and Control Theory," AIAA paper 95-1729-CP, 1995.
6. Reuther, J., Jameson, A., Farmer, J., Martinelli, L. and Saunders, D., "Aerodynamic Shape Optimization of Complex Aircraft Configurations via an Adjoint Formulation," AIAA paper 96-0094, 1996.

AERODYNAMIC OPTIMIZATION OF SUPERSONIC WING-NACELLE CONFIGURATION USING AN ADJOINT METHOD WITH THE UNSTRUCTURED-GRID APPROACH

Hyoung-Jin Kim^{*}, Shigeru Obayashi[†], and Kazuhiro Nakahashi[‡]
Tohoku University, Sendai, 980-8579 JAPAN

ABSTRACT

An aerodynamic design method has been developed by using a three-dimensional unstructured Euler code and an adjoint code with a discrete approach. The resulting adjoint code is applied to a wing design problem of supersonic transport with a wing-body-nacelle configuration. Hicks-Henne shape functions are adopted for the surface geometry perturbation, and the elliptic equation method is employed for the interior grid modification during the design process. Interior grid sensitivities are neglected except those for design parameters associated with nacelle translation. The Sequential Quadratic Programming method is used to minimize the drag with constraints on the lift and airfoil thickness. Successful design results confirm validity and efficiency of the present design method.

Introduction

With the advances in computational fluid dynamics (CFD) and computing power of modern computers, aerodynamic design optimization methods utilizing CFD codes are more important than ever. Among several design optimization methods applicable to aerodynamic design problems, the gradient-based method has been used most widely due to its well-developed numerical algorithms and relatively small computational burden. In the application of gradient-based methods to practical aerodynamic design problems, one of the major concerns is an accurate and efficient calculation of sensitivity derivatives of an aerodynamic objective function. The finite difference approximation is the simplest way to calculate the sensitivity information since it does not require any sensitivity code. However, the accuracy of such an approach depends critically on the perturbation size of design variables and the flow initialization.[1]

Sensitivity derivatives can be evaluated more robustly and efficiently by using a sensitivity analysis code based either on a direct method[2-4] or on an adjoint method[2,5-14]. An adjoint method is preferable in aerodynamic designs because it is more economical when the number of design variables are larger than the total number of an objective function and constraints. Reuther et al.[8,9], for example, designed aircraft configurations using a continuous adjoint method with the Euler equations in a structured multi-block grid system. Kim et al.[10] developed direct and adjoint sensitivity codes from 2-D Navier-Stokes code with an algebraic turbulence model in a structured grid system.

For complex aerodynamic configurations, the unstructured grid approach has several advantages over the structured grid approach. This approach can treat complex geometry with greater efficiency and less effort. It

also has a greater flexibility in the adaptive grid refinement/unrefinement; thus the total number of grid points can be saved. Newman et al.[4] developed a direct sensitivity code via a discrete approach for the 2-D and 3-D Euler equations in the unstructured grid framework, and demonstrated design examples of multi-element airfoil in a subsonic flow and Boeing 747-200 in a transonic regime. Elliot and Peraire[11] reported a discrete adjoint method for the Euler equations with unstructured grids, which was applied to design a 2-D multi-element airfoil, a 3-D wing, and a wing-body configuration. Recently, Nielson and Anderson [13] developed a discrete adjoint code for the 3-D Navier-Stokes equations with a one-equation turbulence model, and examined numerical effects on the accuracy of sensitivity derivatives due to the flux jacobian simplification and turbulence model differentiation. Mohammadi[14] developed an unstructured adjoint code for the 2D/3-D Navier-Stokes equations with a two-equation turbulence model using an automatic differentiation tool with the reverse mode.

In this study, direct and adjoint sensitivity codes have been developed from a 3-D unstructured Euler solver based on a cell-vertex finite volume method. With the resulting adjoint code, aerodynamic design of a Supersonic Transport (SST) wing with nacelle is conducted. Wing geometry is perturbed in an algebraic manner at five design sections. Interior grids are moved accordingly by the elliptic equation method. Grid sensitivities of interior nodes are neglected except those for design variables associated with nacelle translation in order to reduce required computational time for the mesh sensitivity calculation.

The rest of this paper presents a brief review on the flow solver and the direct and adjoint methods with a discrete approach. Sensitivity code validation is then given, followed by design methodologies including surface mesh deformation and interior mesh movement techniques. A design example utilizing the resulting design method is finally given for a supersonic transport (SST) wing in the wing-body-nacelle configuration.

^{*} Postdoctoral Research Fellow, Dep't of Aeronautics and Space Eng.

[†] Associate Professor, Dep't of Aeronautics and Space Eng.

[‡] Professor, Dep't of Aeronautics and Space Eng.

Flow Analysis

The Euler equations for compressible inviscid flows are written in an integral form as follows;

$$\frac{\partial}{\partial t} \int_{\Omega} \mathbf{Q} dV + \int_{\Omega} \mathbf{F}(\mathbf{Q}) \cdot \mathbf{n} dS = 0 \quad (1)$$

where $\mathbf{Q} = [\rho, \rho u, \rho v, \rho w, e]^T$ is the vector of conservative variables; ρ the density; u, v, w the velocity components in the x, y, z directions; and e the total energy. The vector $\mathbf{F}(\mathbf{Q})$ represents the inviscid flux vector and \mathbf{n} is the outward normal of $\partial\Omega$ which is the boundary of the control volume Ω . This system of equations is closed by the perfect gas equation of state with a constant ratio of specific heats.

The equations are solved by a finite volume cell-vertex scheme. The control volume is a non-overlapping dual cell. For a control volume, Eq.(1) can be written in an algebraic form as follows;

$$V_i \frac{\partial \mathbf{Q}_i}{\partial t} = - \sum_{j(i)} \Delta S_{ij} \mathbf{h}^{n+1} (\mathbf{Q}_j^+, \mathbf{Q}_j^-, \mathbf{n}_{ij}) \quad (2)$$

where ΔS_{ij} is a segment area of the control volume boundary associated with edge connecting points i and j . This segment area ΔS_{ij} as well as its unit normal \mathbf{n}_{ij} can be computed by summing up the contribution from each tetrahedron sharing the edge. The term \mathbf{h} is an inviscid numerical flux vector normal to the control volume boundary, and \mathbf{Q}_j^{\pm} are flow variables on both sides of the control volume boundary. The subscript of summation, $j(i)$, means all node points connected to node i .

The numerical flux \mathbf{h} is computed using an approximate Riemann solver of Harten-Lax-van Leer-Einfeldt-Wada(HLLEW)[15]. The second order spatial accuracy is realized by a linear reconstruction of the primitive gas dynamic variables $\mathbf{q} = [\rho, u, v, w, p]^T$ inside the control volume using the following equation;

$$\mathbf{q}(\mathbf{r}) = \mathbf{q}_i + \psi_i \nabla \mathbf{q}_i \cdot (\mathbf{r} - \mathbf{r}_i), \quad (0 \leq \psi \leq 1) \quad (3)$$

where \mathbf{r} is a vector pointing to point (x, y, z) , and i is the node index. The gradients associated with the control volume centroids are volume-averaged gradients computed by the surrounding grid cells. Venkatakrishnan's limiter [16] is used for the function ψ_i in Eq.(3) because of its superior convergence properties.

In order to integrate Eq. (2) in time, the Lower-Upper Symmetric Gauss-Seidel(LU-SGS) implicit method [17] is adopted. With $\Delta \mathbf{Q} = \mathbf{Q}^{n+1} - \mathbf{Q}^n$ and a linearization of numerical flux term as $\mathbf{h}_j^{n+1} = \mathbf{h}_j^n + \mathbf{A}_j^+ \Delta \mathbf{Q}_i + \mathbf{A}_j^- \Delta \mathbf{Q}_j$, Eq.(2) becomes the following equations.

$$\left(\frac{V_i}{\Delta t} \mathbf{I} + \sum_{j(i)} \Delta S_{ij} \mathbf{A}_i^+ \right) \Delta \mathbf{Q}_i + \sum_{j(i)} \Delta S_{ij} \mathbf{A}_j^- \Delta \mathbf{Q}_j = \mathbf{R}_i \quad (4)$$

where \mathbf{R} is a residual vector;

$$\mathbf{R}_i = - \sum_{j(i)} \Delta S_{ij} \mathbf{h}_j^n \quad (5)$$

The LU-SGS method on unstructured grid can be derived by splitting node points $j(i)$ into two groups, $j \in L(i)$ and $j \in U(i)$, for the second summation in LHS of Eq.(4). The final form of the LU-SGS method for the unstructured grid becomes,

Forward sweep:

$$\Delta \mathbf{Q}_i^* = \mathbf{D}^{-1} \left[\mathbf{R}_i - \sum_{j \in L(i)} \Delta S_{ij} \mathbf{A}_j^+ \Delta \mathbf{Q}_j^* \right] \quad (6a)$$

Backward sweep:

$$\Delta \mathbf{Q}_i = \Delta \mathbf{Q}_i^* - \mathbf{D}^{-1} \sum_{j \in U(i)} \Delta S_{ij} \mathbf{A}_j^- \Delta \mathbf{Q}_j \quad (6b)$$

where \mathbf{D} is a diagonal matrix derived by Yoon and Jameson[17] with Jameson-Turkel approximation of Jacobian[18] as $\mathbf{A}^{\pm} = 0.5(\mathbf{A} \pm \rho_A \mathbf{I})$, where ρ_A is a spectral radius of Jacobean \mathbf{A} .

$$\mathbf{D} = \left(\frac{V_i}{\Delta t} + 0.5 \sum_{j(i)} \Delta S_{ij} \rho_A \right) \mathbf{I} \quad (7)$$

The lower/upper splitting of Eq.(6) for the unstructured grid is realized by using a grid reordering technique [19] to vectorize the LU-SGS method and to improve the convergence.

Sensitivity Analysis

Direct Method

An aerodynamic sensitivity analysis begins with the fact that the discrete residual vector, Eq.(5) of the nonlinear flow equations is null for a converged flow field solution of steady problems, which can be written symbolically as

$$R_i[\mathbf{Q}, \mathbf{X}, \boldsymbol{\beta}] = 0, \quad (8)$$

where \mathbf{X} is the grid position vector, $\boldsymbol{\beta}$ the vector of design variables. Equation (8) can be directly differentiated via the chain rule with respect to $\boldsymbol{\beta}$ to yield the following equation.

$$\frac{dR_i}{dQ} = \left[\frac{\partial R_i}{\partial Q} \right] \left\{ \frac{dQ}{d\boldsymbol{\beta}} \right\} + \{C_i\} = 0, \quad (9)$$

where $\{C_i\} = \left[\frac{\partial R_i}{\partial X} \right] \left\{ \frac{dX}{d\boldsymbol{\beta}} \right\} + \left\{ \frac{\partial R_i}{\partial \boldsymbol{\beta}} \right\}$.

This equation is the direct sensitivity equation for the flow variable sensitivity $\{dQ/d\boldsymbol{\beta}\}$. The vector $\{C_i\}$ has no relation with the $\{dQ/d\boldsymbol{\beta}\}$, and thus, is constant throughout the solution process of the sensitivity equation for a design variable $\boldsymbol{\beta}$. $\{dX/d\boldsymbol{\beta}\}$ in the $\{C_i\}$ is a vector of grid sensitivity, which can be calculated by a finite-difference approximation or the direct differentiation of a routine for the grid generation or modification.

In order to find the solution $\{dQ/d\boldsymbol{\beta}\}$ of Eq.(9) iteratively, a pseudo time term is added as follows to obtain the incremental form;

$$V_i \frac{\partial \mathbf{Q}_i'}{\partial t} = \left[\frac{\partial R_i}{\partial Q} \right] \left\{ \frac{dQ}{d\boldsymbol{\beta}} \right\}^{n-1} + \{C_i\}, \quad (10)$$

where \mathbf{Q}' represents the solution vector $\{dQ/d\boldsymbol{\beta}\}$. The above system of equations is solved with the LU-SGS scheme that is used for the flow solver. By comparing Eqs.(2) and (10), it is noted that one can obtain a direct

sensitivity code by directly differentiating the right-hand side of the flow solver.

The Jacobian matrices $[\partial R/\partial Q]$ and $[\partial R/\partial X]$ in Eq.(9) are very large banded matrices. Even for a two-dimensional grid system, if its banded structure is not considered, the memory requirement easily exceeds several Gbytes. In order to circumvent this problem Newman et al.[4] adopted an efficient matrix-vector product method. In the present direct sensitivity analysis, however, the terms $[\partial R/\partial Q] \{dQ/d\beta\}$ and $[\partial R/\partial X] \{dX/d\beta\}$ in Eq.(9) was calculated without any 'matrix-vector product'. [10] This could be done by directly differentiating those terms in the residual vector R that are explicit functions of the flow variable Q with respect to β for the $[\partial R/\partial Q] \{dQ/d\beta\}$ calculation. The same procedure is applied to $[\partial R/\partial X] \{dX/d\beta\}$; those terms in the residual vector R explicitly related with the grid position vector X are differentiated with respect to β .

When the flow variable sensitivity vector $\{dQ/d\beta\}$ is obtained, the total derivative of the objective function F can be calculated. The objective function F is usually aerodynamic coefficients such as C_D , C_L , C_M , or differences of surface pressures with specified target pressures. F is a function of flow variables Q , grid position X , and design variables β , i.e.,

$$F = F(Q(\beta), X(\beta), \beta). \quad (11)$$

The sensitivity derivative of the cost function F with respect to a design variable β is given by

$$\left\{ \frac{dF}{d\beta} \right\} = \left\{ \frac{\partial F}{\partial Q} \right\}^T \left\{ \frac{dQ}{d\beta} \right\} + \left\{ \frac{\partial F}{\partial X} \right\}^T \left\{ \frac{dX}{d\beta} \right\} + \left\{ \frac{\partial F}{\partial \beta} \right\}. \quad (12)$$

Adjoint Method

Since the total derivative of the flow equations in the steady state is null as can be seen in Eq.(9), we can introduce adjoint variables and combine Eqs. (9) and (11) to obtain

$$\left\{ \frac{dF}{d\beta} \right\} = \left\{ \frac{\partial F}{\partial Q} \right\}^T \left\{ \frac{dQ}{d\beta} \right\} + \left\{ \frac{\partial F}{\partial X} \right\}^T \left\{ \frac{dX}{d\beta} \right\} + \left\{ \frac{\partial F}{\partial \beta} \right\} + \{\lambda\}^T \left[\left\{ \frac{\partial R}{\partial Q} \right\} \left\{ \frac{dQ}{d\beta} \right\} + \{C\} \right]. \quad (13)$$

Coefficients of the flow variable sensitivity vector $\{dQ/d\beta\}$ form the following adjoint equation.

$$\left[\frac{\partial R}{\partial Q} \right]^T \{\lambda\} + \left\{ \frac{\partial F}{\partial Q} \right\} = 0. \quad (14)$$

If one finds the adjoint variable vector $\{\lambda\}$ which satisfies the above adjoint equation, one can obtain the sensitivity derivative of F with respect to β without any information about the flow variable sensitivity vector $\{dQ/d\beta\}$. This makes the computational cost for the sensitivity analysis independent of the number of design variables. Eq.(13) eventually becomes to the following form,

$$\left\{ \frac{dF}{d\beta} \right\} = \left\{ \frac{\partial F}{\partial X} \right\}^T \left\{ \frac{dX}{d\beta} \right\} + \left\{ \frac{\partial F}{\partial \beta} \right\} + \{\lambda\}^T \{C\} \quad (15)$$

As Eqs.(2) and (10), the adjoint equation (11) is

also converted to the following system of linear algebraic equations with a pseudo time term added and is solved with the LU-SGS scheme.

$$\left(\frac{I}{\Delta t} + \sum_{j \neq i} \Delta S_{ij} A_i^{+j} \right) \Delta \lambda_i - \sum_{j \neq i} \Delta S_{ij} A_i^{-j} \Delta \lambda_j = R_{_adj_i}, \quad (16)$$

where $R_{_adj_i}$ is the adjoint residual defined as

$$R_{_adj_i} = \left[\frac{\partial R}{\partial Q_i} \right]^T \{\lambda\} + \left\{ \frac{\partial F}{\partial Q_i} \right\}.$$

Flux Jacobian matrix A^* in the second summation is calculated at node i instead of node j and of negative sign. This shows that wave propagation direction of the adjoint equations is opposite to that of the flow equations. However, the information on grid reordering used in the LU-SGS routine of the flow solver for the convergence improvement and vectorization is still valid here for the adjoint equations.

As mentioned earlier, the flux Jacobian $[\partial R/\partial Q]^T$ in the RHS of Eq.(16) is a very large banded matrix. In the adjoint method, unlike the direct method, all the elements of the Jacobian matrix should be calculated explicitly. If all of the calculated elements are stored in memory, computational time can be drastically reduced, but the memory requirement would prohibitively large for three dimensional problems. On the other hand, if the elements are not stored but recalculated every iteration repetitively, the memory requirement can be remarkably reduced with increased computational costs. This demands a compromise which should be made considering available computer resources.[11] In this study, among the elements of $[\partial R/\partial Q]^T$, stored in memory are those calculated by the differentiation of $\psi_i \nabla \mathbf{q}_i$, the reconstruction and limiter terms (see Eq.(3)). Other parts obtained by the differentiated HLLW flux are recalculated every iterations of the adjoint analysis instead of being stored in memory.

Figure 1 compares a two-dimensional example of flux accumulation for the flow solver and the adjoint method. In the flow solver, primitive flow variables are reconstructed at the control volume surface using surrounding node point values. Then the flux \mathbf{h} through the control volume surface is calculated and accumulated at both nodes 1 and 2. This is repeated for all edges to obtain flux residual for the control volume. On the other hand, in the adjoint method, the adjoint flux $\left[\frac{\partial R_i}{\partial Q} \right]^T \{\lambda\}$ is

accumulated at all the node points that have effects on the reconstructed flow variables at the control volume surface. For example, if we set the flux for the edge connecting node 1 and node 2 as $R_{12} (= -\Delta S_{12} \mathbf{h}_{12})$, accumulation of the adjoint residual $R_{_adj}$ is made at nodes related with node 1 as follows.

$$R_{_adj_j} \leftarrow R_{_adj_j} + \left[\frac{\partial R_{12}}{\partial Q_j} \right]^T \lambda_j, \quad j = 1, 2, 3, \dots, 7 \quad (17)$$

For nodes surrounding node 2,

$$R_{_adj_j} \leftarrow R_{_adj_j} - \left[\frac{\partial R_{12}}{\partial Q_j} \right]^T \lambda_j, \quad j = 1, 2, 3, 7, 8, 9, 10.$$

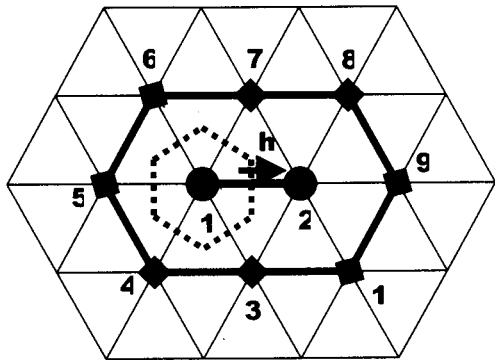


Fig.1 A 2-D example of flux accumulation for the flow solver and the adjoint method

This causes small loops for the neighboring nodes to be inserted into the big loop for all edges. The length of the small loop was usually from 5 to 25 around a node point for a three dimensional Euler grid depending on the grid structure. If the adjoint code is run on a vector machine, it would hamper the flux calculation routine of the adjoint code to be vectorized with the big loop of edges.

In order to simplify the differentiation process of $[\partial R/\partial Q]^T$, the residual vector R is differentiated by primitive variables $\mathbf{q} = [\rho, u, v, w, p]^T$ rather than by the conservative variables Q . [6] Then, the flux Jacobian via the conservative variable can be obtained introducing the transformation matrix $M = \partial Q/\partial \mathbf{q}$;

$$\left[\frac{\partial R}{\partial Q} \right]^T = \left(\left[\frac{\partial R}{\partial \mathbf{q}} \right] \left[\frac{\partial \mathbf{q}}{\partial Q} \right] \right)^T = \left[\frac{\partial \mathbf{q}}{\partial Q} \right]^T \left[\frac{\partial R}{\partial \mathbf{q}} \right]^T = M^{-T} \left[\frac{\partial R}{\partial \mathbf{q}} \right]^T. \quad (18)$$

The transformation matrices in a transposed form are given as

$$M^T = \begin{bmatrix} 1 & u & v & w & \frac{(u^2 + v^2 + w^2)}{2} \\ 0 & \rho & 0 & 0 & \rho u \\ 0 & 0 & \rho & 0 & \rho v \\ 0 & 0 & 0 & \rho & \rho w \\ 0 & 0 & 0 & 0 & 1/(\gamma - 1) \end{bmatrix},$$

$$M^{-T} = \begin{bmatrix} 1 & -u/\rho & -v/\rho & -w/\rho & \frac{(\gamma - 1)(u^2 + v^2 + w^2)}{2} \\ 0 & 1/\rho & 0 & 0 & -(\gamma - 1)u \\ 0 & 0 & 1/\rho & 0 & -(\gamma - 1)v \\ 0 & 0 & 0 & 1/\rho & -(\gamma - 1)w \\ 0 & 0 & 0 & 0 & (\gamma - 1) \end{bmatrix} \quad (19)$$

In this study, the required differentiation process is conducted by human hand. Hand differentiation of a modern CFD code is somewhat a tedious job to do. However, if once done carefully, it provides an efficient sensitivity analysis tool. [10]

Boundary Conditions for the Sensitivity Analysis

Boundary conditions for the direct method can be simply imposed by differentiating the boundary

conditions for the flow equations. This section is thus mainly devoted to the boundary conditions for the discrete adjoint method. The adjoint equation (14) can be written in a more detail form containing boundary conditions as follows.

$$\begin{bmatrix} \left[\frac{\partial R^i}{\partial Q^i} \right]^T & \left[\frac{\partial R^b}{\partial Q^b} \right]^T \end{bmatrix} \begin{Bmatrix} \{\lambda^i\} \\ \{\lambda^b\} \end{Bmatrix} + \begin{Bmatrix} \left\{ \frac{\partial F}{\partial Q^i} \right\} \\ \left\{ \frac{\partial F}{\partial Q^b} \right\} \end{Bmatrix} = \begin{Bmatrix} \{0\} \\ \{0\} \end{Bmatrix}. \quad (20)$$

or

$$\left[\frac{\partial R^i}{\partial Q^i} \right]^T \{\lambda^i\} + \left[\frac{\partial R^b}{\partial Q^i} \right]^T \{\lambda^b\} + \left\{ \frac{\partial F}{\partial Q^i} \right\} = \{0\}, \quad (21a)$$

$$\left[\frac{\partial R^i}{\partial Q^b} \right]^T \{\lambda^i\} + \left[\frac{\partial R^b}{\partial Q^b} \right]^T \{\lambda^b\} + \left\{ \frac{\partial F}{\partial Q^b} \right\} = \{0\}, \quad (21b)$$

where the superscript i presents values of inner node, and b values of boundary nodes. For example, R^i is the residual at nodes in computational domain, and R^b is the residual of the boundary conditions at boundary nodes. Equation (21a) is solved in an incremental form of Eq.(16). The adjoint variable vector at boundary nodes, $\{\lambda^b\}$ is calculated from Eq.(21b) with the adjoint variable vector at the interior nodes $\{\lambda^i\}$ of the previous time level and the flux Jacobian $[\partial R^i/\partial Q^b]^T$.

An alternative way to impose boundary conditions of the discrete adjoint equations is to treat boundary conditions of a flow solver as an implicit manner. A discrete adjoint code developed from the flow solver with implicit boundary conditions would then automatically satisfy the boundary conditions for the adjoint equations. [4,11]

Sensitivity Code Validation

In order to validate the direct and adjoint sensitivity codes developed in this study, sensitivity analyses are conducted for a typical Supersonic Transport (SST) immersed in a supersonic flow. Flow conditions are $M_\infty = 2.0$ and $\alpha = 2.0$ degree. All the computations for the code validation were conducted with a single processor of a NEC SX-4 vector computer.

We used the following design parameter β for the purpose of test.

$$\beta : y_{\text{new}} = y - \Delta\beta * x, \quad (22)$$

where x and y are coordinates of longitudinal and normal direction, respectively. The sensitivity derivatives are compared with those computed by the forward finite-difference approximation with a step size $\Delta\beta$ of 10^{-7} . The residual of the flow solver is reduced to nearly machine zero for the finite difference calculation. Table 1 compares the sensitivity derivatives by the adjoint, direct, and finite-difference method. They compare very well with one another with errors less than 0.004 %.

Figure 2 shows a comparison of convergence histories of the Euler solver, adjoint and direct sensitivity codes. All of them show similar convergence properties

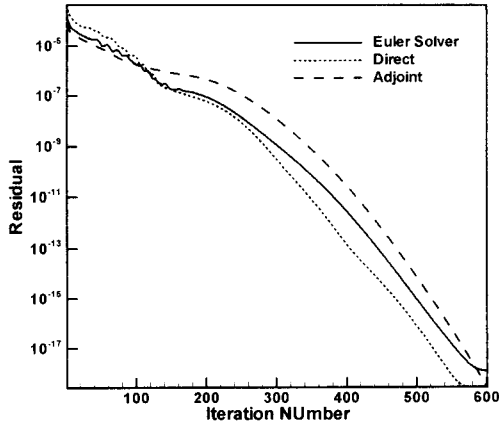


Fig.2 Convergence histories of flow solver and sensitivity codes

since they all have the same flux Jacobian matrices, and also they adopt the same implicit time marching algorithm of LU-SGS scheme. The initial values of the sensitivity derivative $\{dQ/d\beta\}$ are obtained by differentiating those of the flow solver, and the initial adjoint variables $\{\lambda\}$ are set to zero. Table 2 compares required memory and computational time for the Euler solver and its sensitivity codes. The required memory for both direct and adjoint codes seems to be reasonable. The adjoint code costs somewhat large computational time per iteration due to the poor vectorization performance of the adjoint residual accumulation routine as mentioned in the previous section. We also tested the ratio of computational time of the flow solver over the adjoint code at a Compaq α workstation, a scalar machine, and found that the adjoint code costs only 1.5 times the CPU time of the flow solver per iteration.

Figure 3 shows convergence history of the C_D gradient as the adjoint code converges. It should be noted that even only one-order reduction of the adjoint residual gives accurate gradient value within 1 % error for the present design parameter.

Table 1 Comparison of sensitivity derivatives: errors are with respect to the values of FD

	Finite Difference	Direct code (%error)	Adjoint code (%error)
$dC_L/d\beta$	1.308065	1.308050 (0.00115)	1.308056 (0.00069)
$dC_D/d\beta$	0.0983594	0.0983587 (0.000712)	0.0983557 (0.00376)

Table 2 Comparison of memory and CPU time; numbers in the parentheses are relative ratios to the flow solver

	Flow Solver	Direct code	Adjoint code
Required Memory(MB)	160	222 (1.39)	360 (2.25)
Time per Iteration (sec.)	3.75	5.7 (1.52)	26.5 (7.07)

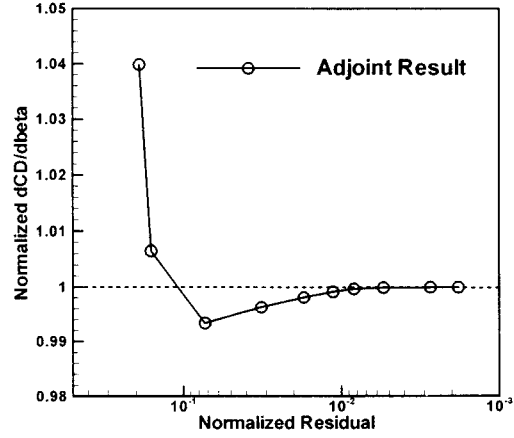


Fig.3 Convergence trends of sensitivity derivative with respect to residual of the adjoint code

Design Methodology

Design Objective

The present design method using the unstructured Euler solver and the adjoint method is applied to an experimental SST wing with a flow-through type engine nacelle attached on its lower surface, which is under development by National Aerospace Laboratory of Japan as a basic study for the next generation supersonic transport.[20]

The objective of the present design study is defined as follows.

$$\begin{aligned} &\text{Minimize } C_D \\ &\text{Subject to } C_L = C_L^* \end{aligned} \quad (23)$$

where C_D and C_L are drag and lift coefficients, respectively, and C_L^* is specified. If the lift constraint is dealt as an explicit constraint in an optimizer, it requires an additional adjoint code computation for the C_L derivatives. In this study, therefore, the lift constraint is satisfied running the flow solver in a fixed-lift mode, in which the incidence angle α is adjusted based on $C_{L\alpha}$. The incidence angle is modified every 20 iteration of the LU-SGS time integration after the residual is reduced by 2 orders of magnitude to obtain a lift coefficient satisfying the following inequality conditions.

$$C_L^* \leq C_L \leq 1.003 C_L^*$$

Since we would like to minimize drag when $C_L = C_L^*$, i.e. at an adjusted incidence angle, the objective function $F = C_D$ should be modified as follows to consider the lift constraint consistently,

$$F = C_D^* = C_D + \frac{\partial C_D}{\partial \alpha} \Delta\alpha, \quad (24)$$

where C_D is a drag coefficient without any incidence angle modification, and $\Delta\alpha$ is a required incidence angle variation to match the lift with a target one. Similar relation can be written for the lift.

$$C_L^* = C_L + \frac{\partial C_L}{\partial \alpha} \Delta\alpha, \quad (25)$$

where C_L is a lift coefficient without any incidence angle variation, and C_L^* is the target lift coefficient, which is 0.100 for this case. If we arrange the above equation for

$\Delta\alpha$ and input to Eq.(24), we obtain a modified objective function

$$F = C_D - \frac{\left(\frac{\partial C_D}{\partial \alpha}\right)}{\left(\frac{\partial C_L}{\partial \alpha}\right)} (C_L - C_L^*) \quad (26)$$

where the second term of lift acts as a penalty term, which prevents the design from reducing the drag by simply reducing the lift. The same expression for the modified objective function was suggested in a variational form by Reuther et al.[8].

Design Parameters and Grid Modification Method

The wing section geometry is modified adding a linear combination of Hicks and Henne shape functions[21], f_k as follows.

$$y_{new} = y_{initial} + \sum_{k=1}^{n_s} \beta_k \cdot f_k \quad (27)$$

$$f_k = \sin^3[\pi x^{e(k)}], \quad e(k) = \frac{\ln(0.5)}{\ln(x_k)}$$

where β_k are design variables, n_s the number of design variables, and x_k represents the peak location of f_k . Although this Hicks-Henne shape functions are not orthogonal, they have been widely used for aerodynamic design optimization problems with successful results.[3,8]

We used five design sections along the SST wing span and defined 20 Hicks-Henne design variables and one twist angle per a design section. Figure 4 shows ten Hicks-Henne functions used for upper and lower surface perturbation. In addition to the 105 design variables, the height of diverter is also considered as a design parameter. With the new geometry of the design sections, node points on the wing surface are linearly interpolated.

When the surface grid is modified, the interior grid points should be moved accordingly. In the structured grid approach, the interior grid positions can be moved with a relative ease using an algebraic mesh movement strategy which modifies the grid point coordinates along a grid line of the same index. In the unstructured grid method, however, such a simple grid modification method cannot be applied, and a more sophisticated grid movement method is needed.

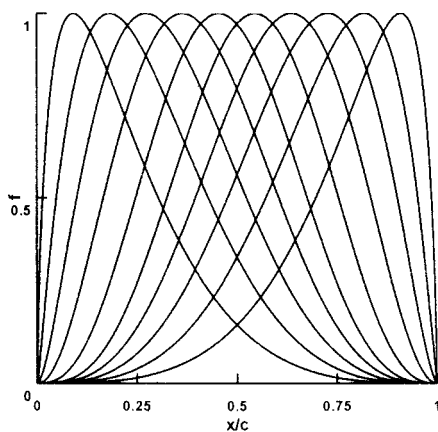


Fig.4 Adopted ten Hicks-Henne Shape Functions

For the movement of the grid points with the perturbed surface grid, we used the elliptic partial differential equation method proposed by Crumpton and Giles[22]. In the method, the displacement δx from initial grid point x_θ is prescribed by the following equation with Dirichlet boundary conditions

$$\nabla \cdot (k \nabla \delta x) = 0 \quad (28)$$

Diffusion coefficient k is constant in each cell and is given by

$$k = \frac{1}{\max(Vol, \varepsilon)} \quad (29)$$

where Vol is a control volume of each grid point and ε is a small positive number to prevent k from becoming negative. In the original form of the method in Ref.22, Vol is obtained from deformed grid system $x_\theta + \delta x$. In this study, however, the cell volume is calculated from initial grid x_θ with an assumption that the cell volumes (or at least their relative ratios) do not change much through one iteration of the optimization process, which is often the case for aircraft wing section design problems. With this assumption, the nonlinear elliptic equation becomes a linear one, which is much simpler and thus can be solved with a less computational time since the control volumes of the grid points do not need to be calculated during the iteration step. Although this caused no problem in the present design study, it might need to consider the original nonlinear equation for a robust grid modification if the geometry changes much throughout the design process. The elliptic equation (28) is discretized by a finite volume method, and subsequent linear algebraic equations are solved by the conjugate gradient method[23]. Required computational time to obtain converged solution δx was same with that of a few iterations of the Euler solver.

Grid Sensitivity

The elliptic equation method for the interior grid movement is differentiated to be applied to the grid sensitivity calculation for the vector $\{C\}$ in Eq.(9) with respect to each geometric design variable. Since this requires almost the same computational cost with the grid movement procedure, the total computational burden would be a substantial amount if the number of design variables becomes large; say, more than one hundred.

One possible way to reduce the computational burden of the grid sensitivity calculation is to neglect the grid sensitivity of interior node points. Eyi and Lee[3] defined grid sensitivities on the body surface only by ignoring the movement of interior grid points in their study on direct sensitivity analysis with 2-D Euler equations. Although they did not present an explicit accuracy comparison, they reported that the simplification approach does not affect the accuracy of the resulting sensitivity.

In this study, we made a comparison between the derivatives with and without the interior grid sensitivities in order to evaluate the accuracy of the simplification approach ignoring the interior grid movement. Figure 5 compares the derivatives of the objective function ob-

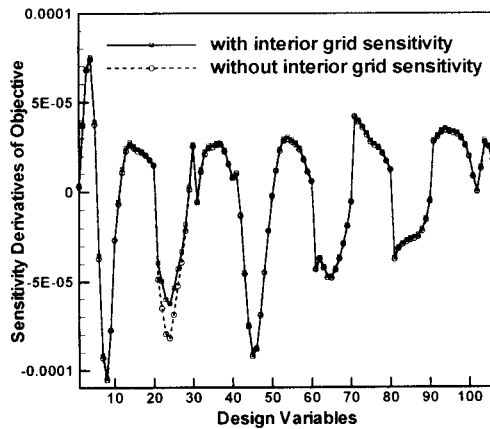


Fig.5 Comparison of sensitivity derivatives with and without interior grid sensitivity information

tained with and without the interior grid sensitivity information. Derivatives with respect to the design variables have little difference between the two values except those of 21 ~ 30 in the design variables. The design variables with indices from 21 to 30 are defined on the lower surface of the second design section, which is located at the centerline of the diverter. Thus, they cause the nacelle to be translated vertically because of the constraint on the leading edge height which will be mentioned in a following section. It has been shown in Ref.7 that for geometries with singularity such as sharp trailing edges, interior mesh sensitivities must be included for the calculation of the derivatives associated with translation. In this case, the nacelle inlet and outlet have sharp edges, which causes the derivatives calculated without interior mesh sensitivities to be deviated from those values obtained with the mesh sensitivities. It can be noted here that the interior grid sensitivities are required for design variables associated with translation of the nacelle, and, on the other hand, the grid sensitivities can be ignored for other ordinary design variables, i.e. coefficients of shape function or twist angles, without major accuracy degradation.

Recently, on the other hand, Anderson and Bonhaus[12] compared the accuracy of sensitivity derivatives with and without interior grid sensitivities with an adjoint code for Navier-Stokes equations with a one equation turbulence model. In their work, it was reported that derivatives with and without the grid sensitivities differ significantly, and therefore, the design could fail if the grid sensitivity terms were not included. Reminding that the present study deals with the Euler equations, this disagreement seems to be caused by the effects of the viscosity and/or turbulence model considered in the reference. However, further research is required to reveal the exact reason of the disagreement.

In this study, interior grid sensitivities for the ten design variables (21~30) are calculated by the elliptic equation method, while for other design variables, only the surface grid sensitivities are defined. This simplification approach required only a quarter of the computational time for the approach computing all the interior grid sensitivities.

Optimization Method

For the minimization of the objective function with specified constraints, the ADS(Automated Design Synthesis) program[24] was used as an optimizer. The Sequential Quadratic Programming (SQP) method[25] is adopted in which the objective is approximated by a quadratic Taylor series expansion to create a direction-finding problem. This subproblem is solved using the Modified Method of Feasible Directions. Lagrangian multipliers are calculated at the optimum of the subproblem. Then one-dimensional search is conducted using quadratic polynomial interpolation. When the one design iteration is complete, the approximated Hessian matrix is updated by the Broydon-Fletcher-Goldfarb-Shanno formula. Detailed algorithms and methodologies of the SQP method is described in Ref.25.

Design Results

Design conditions are a freestream Mach number of 2.0 and C_L of 0.100. Figure 6 shows the wing-nacelle configuration and surface grids of initial geometry. The number of nodes and cell for the adopted volume grid are about 270,000 and 1,500,000, respectively. The initial geometry has a drag coefficient of 0.02051 and L/D of 4.883, which is much smaller than general SST configurations. This is because the size of NAL experimental aircraft is roughly 10% scale of the assumed actual size SST, and thus the relative size of an engine nacelle is comparatively larger than that of the actual SST.

In the present optimization the diverter leading edge height is also constrained to be larger than the initial value. This lower side constraint is to prevent the boundary layer flow from being entrained into the engine, which might occur if the height of the diverter leading edge becomes smaller than the initial value. Additional constraints are imposed so that wing section thickness values at front (5%chord), rear (80%chord) spar position and maximum thickness position (50 % chord) should be larger than those of initial geometry.

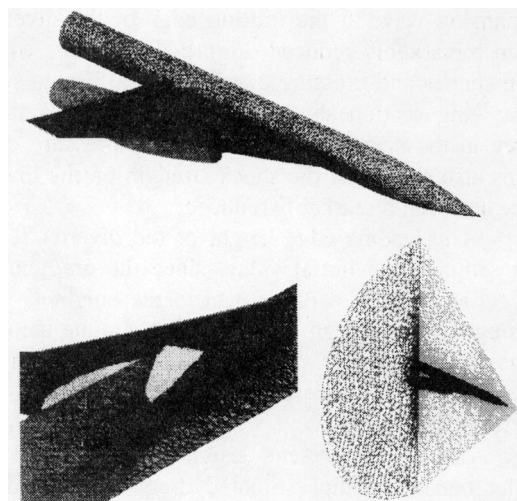


Fig.6 Surface grids of NAL experimental supersonic aircraft with nacelles

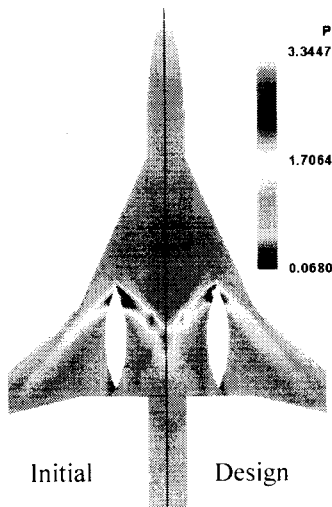


Fig.7 Comparison of lower surface pressure contours

Table 3 Design results: SST wing-nacelle configuration

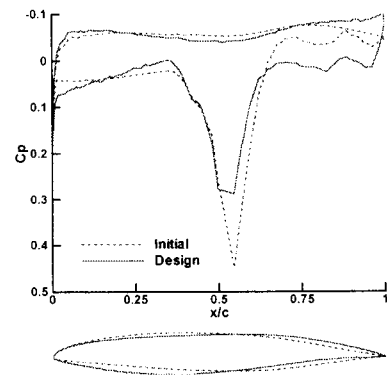
	Initial	Design	Δ (%)
C_L	0.10017	0.10020	+0.03
C_D	0.020513	0.018918	+7.78
L/D	4.883	5.297	+8.48

The density residual of the Euler solver was reduced by four orders from the initial value, and that of the adjoint code by two orders. The SQP optimization iterations converged with three iterations to obtain a drag coefficient reduced by 16 counts from 0.0205 to 0.0189 retaining the lift coefficient as the specified value and satisfying imposed thickness constraints. Table 3 summarizes the design results. During the design process, the Euler solver was run three times and the adjoint code also three times, which is equivalent to about less than six analyses of the Euler solver in computational time.

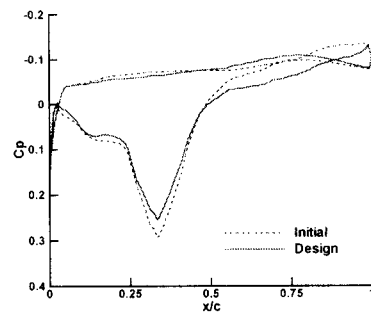
Figure 7 shows the surface pressure contours on the wing lower surface. It can be noted that the strength of the impinging shock wave on the wing lower surface generated by the diverter leading edge is greatly reduced through the design procedure. Also the strength of the expansion wave at the trailing edge of the diverter has been remarkably reduced. Figure 8 compares wing section shapes and pressure distributions at design sections. The wing section shapes are elongated by a factor of three in the normal direction. Section pressure distributions also show that the shock strength on the lower surface has been remarkably reduced.

The leading-edge height of the diverter remained the same as the initial value, since the gradient of the objective function with respect to the height is positive throughout the design iteration. This is quite natural in a sense that the volume of the aircraft will be increased and therefore the pressure drag will be increased if the diverter height increases.

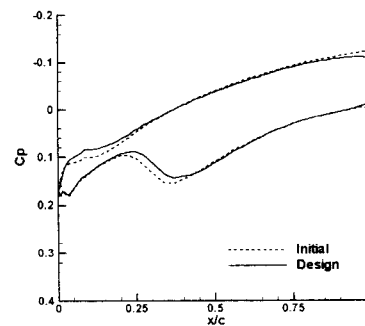
Since the present design study is based on the Euler equations, the estimated drag might be deviated from the realistic value, especially for this kind of cases with a strong interaction between shock wave and boundary layer. In order to consider the viscous effects in the design process, employment of the Navier-Stokes



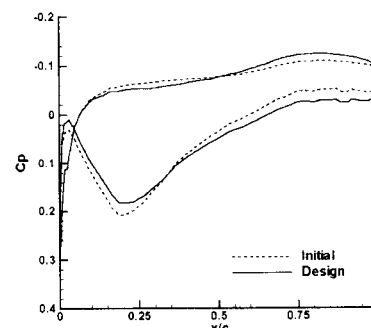
(a) $\eta = 0.232$



(b) $\eta = 0.430$



(c) $\eta = 0.561$



(d) $\eta = 0.762$

Fig.7 Design results: section shapes and pressure distributions at design sections; ---- initial, — design.

equations would be necessary, and also, development of a discrete adjoint code for a 3-D unstructured Navier-Stokes solver with a turbulence model would be required.

Concluding Remarks

An aerodynamic design optimization system is developed using the unstructured Euler solver and the discrete adjoint method. Surface geometry is perturbed by simple algebraic shape functions and a twist angle variation. The interior grid position movement is made by the elliptic equation method. For an efficient calculation of terms related with the grid sensitivities, grid sensitivities of interior node points are ignored except those for the design variables associated with nacelle translation. The present method is successfully applied to design a SST wing with nacelles. The impinging shock wave from the diverter on the wing lower surface has been greatly reduced, and as a consequence, drag is remarkably reduced by three iterations of the SQP optimizer.

Acknowledgement

The first author was supported by the Japan Society for Promotion of Science (JSPS). The authors also wish to thank Mr. Itoh, a graduate student of Tohoku University, for his help to generate the surface grid.

References

1. Eyi, S. and Lee, K. D., "Effect of Sensitivity Calculation on Navier-Stokes Design Optimization," AIAA 94-0060, Jan. 1994.
2. Sherman, L. L., Taylor, III, A. C., Green, L. L., Newman, P. A., Hou, G. J., and Korivi, V. M., "First- and Second-Order Aerodynamic Sensitivity Derivatives via Automatic Differentiation with Incremental Iterative Methods," AIAA94-4262, Sep. 1994.
3. Eyi, S. and Lee, K. D., "Effect of Sensitivity Analysis on Aerodynamic Design Optimization," FED-Vol.232, CFD for Design and Optimization, ASME 1995.
4. Newman III, J. C., Taylor III, A. C., and Barnwell, R. W., "Aerodynamic Shape Sensitivity Analysis and Design Optimization of Complex Configuration Using Unstructured Grids," AIAA 97-2275, Jan. 1997.
5. Eleshaky, M. E. and Baysal, O., "Aerodynamic Shape Optimization Using Sensitivity Analysis on Viscous Flow Equations," *Journal of Fluid Engineering*, Vol.115, No.3, pp75-84, 1993.
6. Jameson, A., Pierce, N. A., Martinelli, L., "Optimum Aerodynamic Design using the Navier-Stokes Equations," AIAA 97-0101, Jan. 1997.
7. Anderson, W. K., and Venkatakrishnan, V., "Aerodynamic Design Optimization on Unstructured Grids with a Continuous Adjoint Formulation," AIAA 97-0643, 1997.
8. Reuther, J. J., Jameson, A., Alonso, J. J., Rimlinger, M. J., and Saunders, D., "Constrained Multipoint Aerodynamic Shape Optimization Using an Adjoint Formulation and Parallel Computers, Part 1," *J. of Aircraft*, vol. 36, No.1, pp51-60, 1999.
9. Reuther, J. J., Jameson, A., Alonso, J. J., Rimlinger, M. J., and Saunders, D., "Constrained Multipoint Aerodynamic Shape Optimization Using an Adjoint Formulation and Parallel Computers, Part 2," *J. of Aircraft*, vol. 36, No.1, pp61-74, 1999.
10. Kim, H. J., Kim, C., Rho, O. H., and Lee, K., "Aerodynamic Sensitivity Analysis for Navier-Stokes Equations," AIAA 99-0402, Jan. 1999.
11. Elliot, J. and Peraire, J., "Aerodynamic Optimization on Unstructured Meshes with Viscous Effects," AIAA 97-1849, June 1997.
12. Anderson, W. K. and Bonhaus, D. L., "Airfoil Design on Unstructured Grids for Turbulent Flows," AIAA J. Vol.37, No.2, pp185-1191, 1999.
13. Nielson, E. J., and Anderson, W. K., "Aerodynamic Design Optimization on Unstructured Meshes Using the Navier-Stokes Equations," AIAA J. Vol.37, No.11, pp1411-1419, 1999.
14. Mohammadi, B. "Optimal Shape Design, Reverse Mode of Automatic Differentiation and Turbulence," AIAA 97-0099, Jan. 1997.
15. Obayashi, S., and Guruswamy, G. P., "Convergence Acceleration of an Aeroelastic Navier-Stokes Solver", AIAA J. Vol.33, No.6, pp.1134-1141, 1995.
16. Venkatakrishnan, V., "On the Accuracy of Limiters and Convergence to Steady State Solutions," AIAA Paper 93-0880, January 1993.
17. Yoon, S. and Jameson, A., "Lower-Upper Symmetric-Gauss-Seidel Method for the Euler and Navier-Stokes Equations," AIAA J., Vol.26, No.9 pp. 1025-1026, 1988.
18. Jameson, A., and Turkel, E., "Implicit Schemes and LU Decompositions," *Mathematics of Computation*, Vol.37, No.156, pp.385-397, 1981.
19. Sharov, D., and Nakahashi, K., "Reordering of Hybrid Unstructured Grids for Lower-Upper Symmetric Gauss-Seidel Computations," AIAA J., Vol.36, No.3, pp.484-486, 1998.
20. Iwamiya, T., "NAL SST Project and Aerodynamic Design of Experimental Aircraft," *Proc. Computational Fluid Dynamics '98*, Vol.2, ECCOMAS 98, John Wiley & Sons, Ltd. pp.580-585, 1998.
21. Hicks, R. M. and Henne, P. A., "Wing Design by Numerical Optimization," *J. of Aircraft*, Vol.15, No.7, pp. 407-412. 1978.
22. Crumpton, P. I. and Giles, M. B. "Implicit Time Accurate Solutions on Unstructured Dynamic Grids," AIAA 95-1671, June, 1995.
23. Press, W. H., Teukolsky, S. A., Vetterling, W. T., and Flannery, B. P., "Numerical Recipes in Fortran," 2nd ed. Cambridge Univ. Press, Cambridge, England, UK, 1992.
24. Vanderplaats, G. N., "ADS - A Fortran Program For Automated Design Synthesis version 3.00," *Engineering Design Optimization, INC.*, 1987.
25. Vanderplaats, G. N., "Numerical Optimization Techniques for Engineering Design: With Applications," McGraw Hill, N.Y., 1984.

An Application of Numerical Optimization to a Wing Twist of SST Wing-Nacelle Configuration

Tetsuo Yamazaki and Mitsuru Saito

Aerodynamics Research Section, Aerospace Division, Fuji Heavy Industries Ltd.

In designing an aircraft it is necessary to evaluate the characteristics of various configurations by wind tunnel tests, CFD methods, and other estimation methods. So far it took too much time because of many design parameters. But improvements in numerical algorithms and computer hardware have made it possible to design an optimized configuration automatically. Therefore in this paper we have applied numerical optimization methods to the wing twist distribution of SST wing-nacelle configuration that maximizes the lift to drag ratio at a constant lift coefficient.

In order to improve the lift to drag ratio it is important to reduce the drag due to the wing-nacelle interference. The wing twist, the wing camber, and the nacelle position affect the flow field in the region between the wing and the nacelle. So we selected the wing twist as a design parameter, because the design process is simplified.

The analyzed model is given in figure 1. It has a cranked arrow wing and two nacelles which have two dimensional intakes.

The conditions of the numerical optimization are below.

Initial configuration: Wing-nacelle configuration

Initial wing twist: 0deg

CFD method: Panel method

Optimization method: Sequential quadratic programming, Modified feasible directions algorithm, Genetic algorithm

Objective: Maximize the lift to drag ratio

Constraint: $CL=0.10$

Variables: Wing twist angle at 5 sections.

$$\eta (=2y/b)=0.1,0.4,0.5045,0.75,1.0$$

Center of twist: $0.70x/c$

Design point: Mach2.0

Surface pressure distributions of the initial configuration and the optimized one are shown in figure 2. At the optimized the interference between the lower surface and the nacelle is reduced, and the drag coefficient of the optimized is lower than that of the initial(see figure 3). And we have examined the dependence of the result on the optimization method, but the results of three methods are the same(see figure 4). Therefore the designing by numerical optimization methods is effective for SST wing-nacelle configuration.

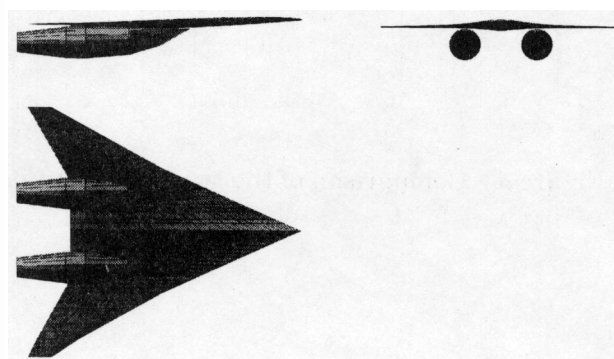


Figure 1 Analyzed model

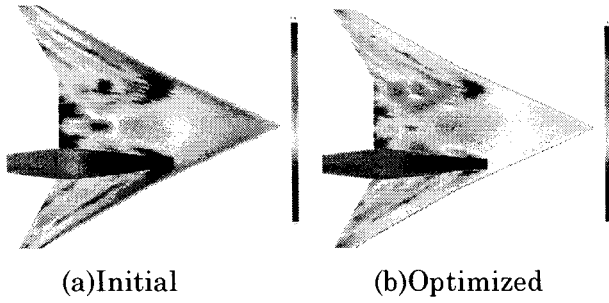


Figure 2 Lower surface pressure distribution

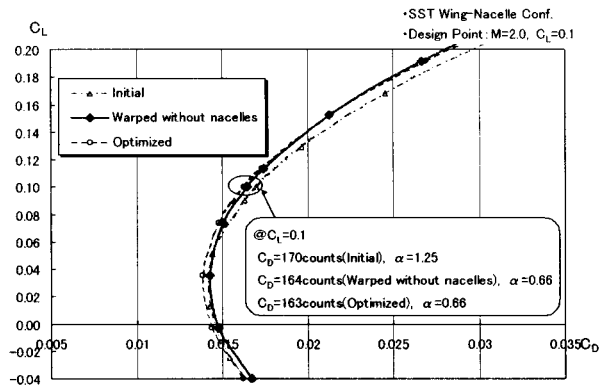


Figure 3 Drag polar

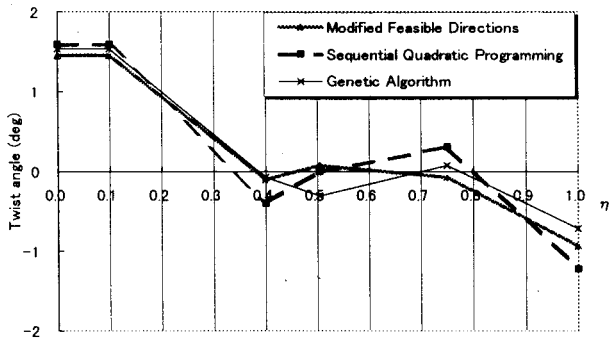


Figure 4 Comparison of the twist distribution

A Coupled Aero-Structural Optimization Method For Complete Aircraft Configurations

James J. Reuther
Research Scientist
MCAT Institute
(650) 604-1516
reuther@ra-iris.arc.nasa.gov

Juan J. Alonso
Assistant Professor
Stanford University
(650) 723-9954
jjalonso@stanford.edu

Joaquim R. R. A. Martins
Graduate Student
Stanford University
(650) 723-9564
kmartins@stanford.edu

Stephen C. Smith
Research Scientist
NASA Ames Research Center
(650) 604-5856
scsmith@mail.arc.nasa.gov

Abstract

This paper presents a new framework for the coupled optimization of aero-structural systems. The framework permits the use of high-fidelity modeling of both the aerodynamics and the structures and represents our first step in an effort towards the development of a high-fidelity multidisciplinary optimization capability. The approach is based on efficient analysis methodologies for the solution of the aerodynamics and structures subproblems, an adjoint solver to obtain aerodynamic sensitivities, and a multiprocessor parallel implementation. We have placed a geometry database representing the outer mold line (OML) of the configuration of interest at the core of our framework. Using this geometry description, the information exchange between aerodynamics and structures is accomplished through an independent coupling of each discipline with the OML database. The framework permits the later inclusion of other disciplines, such as heat transfer and radar signatures, with relative ease. Specific results from the coupling of a finite volume flow solver for the Euler and Reynolds Averaged Navier-Stokes equations with two different linear finite element structural models are explored. Care is taken in the treatment of the coupling of the disciplines such that a consistent and conservative scheme is achieved. Direct comparisons with wind-tunnel data are presented to demonstrate the importance of aeroelastic solutions. In addition, simplified design examples are presented to illustrate the possible advantages of the new aero-structural design methodology in evaluating trade-offs between aerodynamic performance and structural weight for complete aircraft configurations.

1 Introduction

Considerable research has already been conducted on the multidisciplinary optimization (MDO) of flight vehicles. The survey paper by Sobieski [1] provides a comprehensive discussion of much of the work completed to date. These efforts have ranged from the development of techniques for discipline coupling to actual demonstrations on real-world design problems. In most cases, these research efforts have shown the importance of interdisciplinary coupling, as well as the inability of sequential disciplinary optimization to achieve the true global optimum of a coupled system. For example, Wakayama [2, 3] has shown that in order to obtain realistic planform shapes in the design of aircraft configurations it is necessary to include both multiple disciplines and a complete set of real-

world constraints. Meanwhile, in the design of novel configurations such as a joined-wing aircraft, Gallman [4] demonstrated that only multidisciplinary methods are capable of revealing the relevant design trade-offs; single-discipline optimization often leads to incorrect design choices. Unfortunately, the fidelity in the modeling of the various component disciplines in these preliminary design tools has remained at a relatively low level. Therefore, while useful at the conceptual design stage, these tools cannot accurately represent a variety of nonlinear phenomena, such as wave drag, which can play a key role during the detailed design phase.

On the other hand, recent applications of aerodynamic shape optimization using high-fidelity CFD methods have resulted in substantial improvements in the aerodynamic performance of complex aircraft configurations [5, 6, 7, 8, 9]. Jameson, et

al. [10, 11, 12, 13, 14] have developed a mathematical framework for the control of systems governed by the Euler and Navier-Stokes equations that has resulted in significant reductions in the computational cost of aerodynamic shape optimization (ASO). Despite the broad possibilities that these new ASO methods have brought about, they also have had their share of problems. In the case of aerodynamic wing design, planform and thickness constraints have often been artificially imposed so that structural weight, fuel volume, and takeoff/landing requirements would not be adversely affected by the changes in the wing shape. These constraints were typically guided by the result of low-fidelity multidisciplinary models and individual decisions made by experts from selected disciplines. By neglecting the coupling between various disciplines, design constraints have often been too restrictive to permit significant performance improvements, or not restrictive enough, thus allowing ASO to produce infeasible designs. In addition, improvements in aerodynamic performance resulting from span load changes cannot be accurately quantified in view of their unknown impact on the structural weight.

Enabled by recent advances in single-discipline optimization, novel restructuring of the multidisciplinary design process [15, 16], and affordable supercomputing alternatives [17, 9], the opportunity now exists to develop an MDO framework which allows the participation of various relevant disciplines with high-fidelity modeling. The goal here is not to use high-fidelity modeling to construct a response surface [18] or train a neural network [19] but to use it directly during design. This kind of MDO environment has yet to be developed, but promises to improve upon existing design methodologies by increasing the level of confidence in the final results from preliminary design. A higher confidence level at an earlier stage in the design process holds out the possibility of dramatically reducing the development costs of the detailed design phase. Furthermore, the overall quality and performance of the resulting design will be improved when compared with traditional sequential design strategies.

The goal of the current research is to establish a new framework for high-fidelity MDO. The important contributions presented to support such a framework are:

- The use of high-fidelity modeling of two disciplines (RANS aerodynamics and linear FEM structures).
- An OML geometry database which serves as both an interface to the optimization algo-

rithm and an interface for communication between disciplines.

- Sophisticated coupling algorithms that link each discipline to the OML such that information transfer between the disciplines is consistent and conservative.
- A framework for the computation of coupled sensitivities.

An excellent demonstration problem which illustrates the strong coupling that can occur between disciplines is the case of aeroelastic wing design. The optimized shape and structure are the result of compromises among numerous requirements and constraints. Changes in the span load may lead to improvements in induced drag but they can also incur a structural weight penalty. Similarly, an increase in the thickness-to-chord ratio of the wing sections may substantially improve the structural efficiency of the configuration, but it may also lead to an undesirable increase in compressibility drag. Moreover, design constraints are often set by off-design conditions, such as protection from high-speed pitch-up, leading to the need to simulate these conditions as well.

The complete aero-structural design problem involves the simultaneous optimization of the aerodynamic shape of a configuration and the structure that is built to support its loads. The cost function to be optimized requires a combination of aerodynamic performance and structural weight, in order to address two of the main components of the Breguet range equation. Design variables are set up to parameterize the external aerodynamic shape of the configuration and the shape and material properties of the underlying structure (spar cap areas, skin thicknesses, etc.). The design problem must also impose various constraints on the details of the structure, such as the yield stress criterion (the maximum stress in any part of the structure may not exceed the yield stress of the material at a number of critical load conditions with the appropriate safety margin), minimum skin thickness constraints, and fuel volume requirements. On the aerodynamics side, equality and inequality constraints may be imposed on both the total lift and pitching moment. Details of the pressure distribution for a transonic wing design problem, such as the location of the upper surface shock, the slope of the pressure recovery, and the amount of aft loading, may also be imposed as design constraints.

The desired high-fidelity MDO framework for flight vehicle design suggested by this work must address the following issues:

1. Level of accuracy of disciplinary models.
2. Coupling between disciplines.
3. Computation of sensitivities.

In order to obtain the necessary level of accuracy, we intend to use high-fidelity modeling for both the aerodynamic and structural subsystems. For this purpose, an Euler and Reynolds Averaged Navier-Stokes (RANS) flow solver has been used to model the aerodynamics. The details of the multiblock solver, FLO107-MB, can be found in Ref. [7] and its parallel implementation on a variety of computing platforms has been described in Ref. [9, 17]. Two different Finite Element Methods (FEM) have been used for the description of the behavior of the structure. The first is a linear FEM model that uses brick elements which are appropriate for solid wind tunnel configurations. The second is a linear FEM that uses truss and triangular plate elements to model the structural components of aircraft configurations. Given these choices of the physical models for the disciplines involved, it will be possible to capture all of the key trade-offs present in the aero-structural design problem.

In our work, the inter-disciplinary coupling is performed using a geometry database of the outer mold lines (OML). All exchanges of information between disciplines are accomplished by independent communication with this OML database. This has the advantage of standardizing the communication process and facilitates the inclusion of other disciplines. For the specific case of aero-structural coupling, we have chosen to follow the work of Brown [20] in order to carry out the bidirectional transfer of loads and displacements between the structure and the CFD mesh via the OML database. Careful attention has been paid to the consistency and conservativeness of the load transfer, to the point that we believe the current setup will be suitable even for unsteady aeroelastic flutter analysis. A consistent transfer is one that preserves the resultant forces and moments. If, in addition, the total work and energy are conserved, the transfer method is said to be conservative.

The strong interdependence between aerodynamics and structures makes the computation of sensitivities of cost functions and constraints a difficult task. In our past works, we have obtained the sensitivities of aerodynamic cost functions using the solution of an adjoint equation. This technique produced aerodynamic sensitivities at a fraction of the cost of traditional methods such as the finite-difference approach. The advantage of using the

adjoint approach was due, in large part, to the fact that the number of design variables was much larger than the number of functions for which sensitivities were needed.

In the case of combined aero-structural design, a similar approach can be pursued: a set of aero-structural adjoint equations can be formulated which considerably reduce the cost of coupled sensitivity analysis. However, the nature of the aero-structural design problem is such that the number of design variables is not always larger than the number of cost functions and constraints. In particular, this problem is often characterized by a large number of structural stress constraints (one per element in the complete finite element model). Thus, by using a coupled adjoint approach directly it will be necessary to calculate a separate adjoint system for each of these structural constraints. The straightforward alternative to the adjoint approach is to use finite differencing. For cases in which the number of design parameters is relatively small, this alternative may indeed prove more cost-effective. However, the desired goal of admitting a large number of design variables makes the computational cost of the finite-difference approach unaffordable. Similarly problematic is the use of the "direct" approach often used efficiently in structural optimization. A prefactored CFD Jacobian matrix is simply too large to compute with reasonable resources. Given these constraints, the sensitivity analysis aspect of high-fidelity MDO will require much further future research. Details of the simplified sensitivity analysis used here, as well as a framework to obtain coupled sensitivities, are presented in Section 4.3.

2 Structural Finite Element Models

In order to allow for the possibility of utilizing an arbitrary finite element model for the description of the structure, a detailed Application Programming Interface (API) has been developed. This API explicitly outlines both the content and format of the information that must be provided by a Computational Structural Mechanics (CSM) solver intended for aeroelastic design. The API definition has also been kept general enough to allow for a variety of element types within the same model.

The integration of existing and future structural solvers with the design code is therefore accomplished through the use of this API. A typical sequence of calls to the structural model is as follows: the first function call in the API consists of an ini-

tialization process that builds the structural model and all ancillary arrays, matrices, and matrix decompositions. Additional functions in the API provide the design algorithm with the complete geometry description of the external surface of the structural model and the interpolation functions for both the coordinates and displacements at any point of the structural model surface. Simple function calls exist in the API to obtain the structural displacement vector and a list of element principal stresses. Finally, since the design module continuously updates the OML geometry, an additional API call is used to update the structural model geometry and its stiffness matrix such that they conform to the OML.

For the results presented in this paper, we chose to develop our own CSM solvers so that any necessary changes to the source code could be made readily. Retrospectively, it became clear that once a coupling interface was defined, no source code for the CSM solver needed to be examined. The only adaptation to existing CSM methods that will be required is the creation of a conforming interface (see Section 3). Thus, in future works we intend to couple the same MDO framework with commercially available CSM codes such as ANSYS and MSC-NASTRAN. The two CSM solvers developed here use different finite element types and meshing strategies. They were built to reflect accurately the behavior of the types of wing structures present both in wind tunnel models and in real aircraft. Both solvers require the solution of the classical structural equilibrium equation,

$$\mathbf{K}\mathbf{q} = \mathbf{f}. \quad (1)$$

Here, \mathbf{K} is the global stiffness matrix of the structure, \mathbf{q} is the vector of nodal displacements, and \mathbf{f} is the vector of applied nodal forces. With the appropriate boundary conditions, matrix \mathbf{K} is symmetric and non-singular. For the problem sizes of interest here, a Cholesky factorization is appropriate. This factorization can be stored and used multiple times with changing load vectors during an aeroelastic calculation. The stresses in each element can then be related to the displacements by the following equation:

$$\sigma = \mathbf{S}\mathbf{q}, \quad (2)$$

where \mathbf{S} represents the product of the constitutive law matrix, the nodal displacement-strain matrix and the local-to-global coordinate transformation matrix.

2.1 Wind Tunnel Model CSM Solver

A simple CSM solver was developed to compute deflections of wind tunnel model wings. Because wind tunnel models are typically machined from a single billet, 8-node isoparametric hexahedral solid elements were chosen to represent this type of solid structure. These “brick” elements have 24 degrees of freedom, representing the 3 components of the displacement at each node. The stiffness matrix for each element is found using an 8-point (2 points in each coordinate direction) Gauss quadrature of the strain energy distribution within the element. These elements are called “isoparametric” because the same interpolation functions are used to describe the displacement field and the metric Jacobians used for the global coordinate transformation.

The CSM solver was designed to exploit the convenience of an ordered arrangement of elements; element connectivity is implied by the point ordering of the input CSM mesh. This approach greatly simplifies input, and allows the flexibility of modeling the channels typically cut in the wing surface to install pressure orifices and route pressure tubing. For this purpose, finite element nodes can be located along the channel edges, so that distinct brick elements occupy the volume of the pressure channels. The modulus of elasticity is then set to zero for these elements, thus simulating the missing material.

For this study, the geometries of two typical business jets were chosen since wind tunnel measurements and CFD computational meshes were already available in both cases. For each of the wings, a finite element model was constructed using 8-node brick elements. To avoid zero-height elements at the leading and trailing edges, the wing surface definition was truncated at 4% and 96% of the wing chord. The motion of all nodes at the side of the fuselage is fully constrained. The remaining enclosed volume was modeled by an ordered mesh of 4 nodes through the wing thickness, 6 nodes in the chordwise direction, and 44 nodes spanwise from the side of the fuselage to the wing tip. For both cases, this results in 645 elements and 3,168 degrees of freedom. A typical wing CSM mesh is shown in Figure 1 together with the location of the points on the surface of the OML and short segments indicating the points on the CSM surface from which the OML derives its displacements.

2.2 Aircraft Structure CSM Solver

A different CSM solver was used to model the behavior of realistic aircraft structures. This solver models a wing with multiple spars, shear webs, and

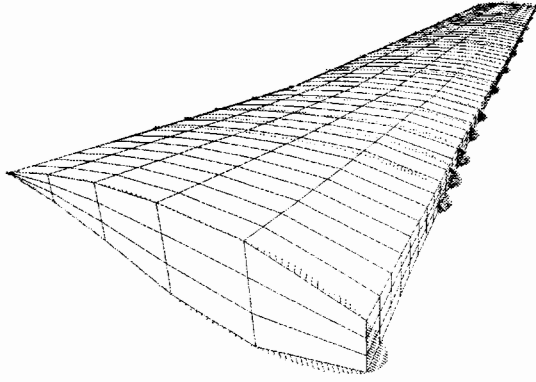


Figure 1: Brick-element mesh of wind tunnel model wing.

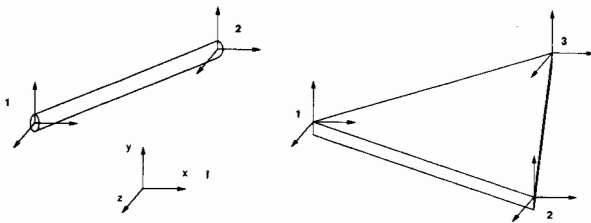


Figure 2: Truss and Triangular Plane Stress Plate elements

ribs located at various spanwise stations, and the skins of the upper and lower surfaces of the wing box. The structural solver is based on a finite element code, *FESMEH*, developed by Holden [21] at Stanford.

Two types of finite elements are used: truss and triangular plane-stress plate elements. Both element types have 3 translational degrees of freedom per node, so the truss has a total of 6 degrees of freedom and the plate has 9 degrees of freedom. Figure 2 shows a graphical representation of these two element types. Neither of these elements can carry a bending moment, since their nodes do not have rotational degrees of freedom. The wing bending, however, is still well-captured since the contributions of the second moments of inertia for the plates and trusses due to their displacement from the wing neutral axis is dominant when compared to their individual moments of inertia about their own neutral axes. The only limitation when using these kinds of elements is that each of the nodes must be simply supported, implying that we can have only one set of plate elements between any two spars.

In the modeling of a typical wing structure, trian-

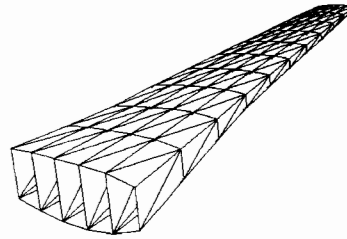


Figure 3: Wing Structural Model

gular plates are used to model the wing skins. Plates are also used for the shear webs of spars and ribs, while the upper and lower spar caps are modeled using trusses. The wing model in our case consisted of 6 spars and 10 ribs, adding up to a total of 132 nodes and 640 elements. Figure 3 shows the geometry of the finite element discretization used.

3 Aero-Structural Coupling Techniques

Within the framework described previously, the optimization of aero-structural systems requires, at least, the solution of the coupled aeroelastic analysis problem. The interaction between these two disciplines, aerodynamics and structures, is quite strong since the former provides the necessary loads to the latter in order to determine the displacement field of the structure. In return, the structure provides surface deflections that change the aerodynamic properties of the initial configuration.

Two issues in this transfer of information between disciplines are of utmost importance to the success of an automatic design technique: first, the level of fidelity in the coupling of both disciplines has to be carefully considered in order to guarantee that the accuracy of the individual disciplines is not jeopardized, and second, the evolving disciplinary designs must have exact geometric agreement by the end of the design process.

In order to tackle the fidelity of the coupling, we have chosen to ensure that the transfer of the distributed pressure forces and moments from the CFD calculation to the CSM nodal load vector is both consistent and conservative as defined in the approach developed by Brown [20]. The property of consistency implies that the resultant forces and moments imparted by the distributed pressure field, p , must be equal to the sum of the nodal forces and moments in the CSM load vector, f . Conservation addresses the important issue that the virtual work

performed by the load vector, \mathbf{f} , undergoing a virtual displacement of the structural model (represented by $\delta\mathbf{q}$) must be equal to the associated work performed by the distributed pressure field, p , undergoing the associated displacement of the CFD mesh surface, $\delta\mathbf{r}$. Thus, a procedure is devised that describes the motion of every surface point in the CFD mesh as a function of the nodal displacements of the structural model,

$$\delta\mathbf{r} = [\eta]^T \cdot \delta\mathbf{q}, \quad (3)$$

where $[\eta]$ is a matrix of linear weights on the displacement vector that is a combination of interpolations within the CSM mesh and extrapolations to the OML as described by Brown [20]. The virtual work in the CSM model can be represented as

$$\delta W_{CSM} = \mathbf{f}^T \cdot \delta\mathbf{q},$$

while the virtual work performed by the fluid acting on the surface of the CFD mesh is given by

$$\delta W_{CFD} = \int_{\partial\Omega} p \mathbf{n}^T \cdot \delta\mathbf{r} dS + \int_{\Omega} \mathbf{b}^T \cdot \delta\mathbf{r} dV.$$

Here, \mathbf{b} represents a distributed body force per unit mass, if it exists, and $\partial\Omega$ is the CFD mesh surface that describes the interface between the fluid and the structure. For a conservative scheme, $\delta W_{CFD} = \delta W_{CSM}$, and the consistent and conservative load vector is given by:

$$\mathbf{F}^T = \int_{\partial\Omega} p \mathbf{n}^T \cdot [\eta]^T dS + \int_{\Omega} \mathbf{b}^T \cdot [\eta]^T dV. \quad (4)$$

For the two different structural models used in this work, the procedure used to obtain the relation in Eq. 3 is implemented in a preprocessing step following Brown's approach. The matrix $[\eta]$ is thus pre-computed and stored for later use during the aeroelastic iteration procedure and plays a key role in both the transfer of displacements and the computation of the conservative and consistent load vector.

In order to enable communication between the aerodynamic and structural solvers, a standardized OML surface representation of the configuration of interest is required. Solutions from each of the disciplines (aerodynamics and structures) are interpolated onto this OML database so that they may be accessed as needed by the other disciplines.

For this purpose, the OML geometry produced by *AeroSurf* has been used as the central database. *AeroSurf* is a geometry generation system that has been specifically created for the analysis and design of aircraft configurations including fuselage,

wings, pylons, nacelles, and empennage [5, 6]. *AeroSurf* preserves an aerodynamic geometry component view of the complete configuration. These geometry components are stored un-intersected in three-dimensional space. Typically, aerodynamic shape changes are applied to these un-intersected components, and, once all modifications are completed, a new configuration is created by finding the intersection(s) of the resulting surfaces. The intersected geometry is then decomposed into a series of well-defined parametric patches that constitute the OML of the complete configuration. These patches (or the points they are composed of) serve as the interface between aerodynamic and structural calculations. It is our intention to expand the capability of this geometry-based interface to include additional disciplines in the future.

Each *AeroSurf* point is associated with a point on the surface of the CSM model in a preprocessing step. During optimization, the displacements of each *AeroSurf* point are calculated by first using the CSM basis functions to interpolate the CSM nodal displacements at the projected *AeroSurf* point. Then extrapolation functions are used to carry the displacements from the CSM mesh to the OML. When the CSM solver dictates a new position for the structure, the locations in three-dimensional space of all the *AeroSurf* points are updated by adding the deflections to the jig-shape points. This update process effectively constructs new parametric patches to represent the surface of the perturbed configuration. In a similar fashion, during a preprocessing step, every point on the surface of the CFD mesh is associated with an *AeroSurf* patch and a parametric location within that patch. The CFD points are assumed to be "tied" to these parametric locations, and, when the *AeroSurf* database is altered, the location of the CFD surface mesh points can be obtained by straightforward evaluation of their parametric locations on the corresponding *AeroSurf* patches. As can be seen, *AeroSurf* plays a central role in the transfer of displacements from CSM to CFD.

Furthermore, the *AeroSurf* database also plays a similar role in the transfer of pressure information from the CFD calculation to the structural load vector. The transfer of surface pressure information to the *AeroSurf* database is achieved by identifying the "donor" cells from the CFD mesh that contain the desired information. The pressure integrations in Eq. 4 are then performed with the same accuracy as can be achieved if the integration were to occur directly on the surface of the CFD mesh. The underlying assumption is that the mesh resolution of

the *AeroSurf* database is comparable to, if not better than, that of the CFD surface mesh. This has always been the case in our design efforts. The coupling between aerodynamic and structural solvers in order to obtain an aeroelastic solution is achieved in an explicit, sequential, iterative fashion by exchanging information at regular intervals during the convergence process. This coupling is greatly simplified by the fact that only static aeroelastic solutions are considered in this work, and the issue of time accuracy is inconsequential. For a typical complete, rigid configuration at fixed lift, an Euler solution requires in the neighborhood of 120 multigrid cycles to reduce the average density residual by 5 orders of magnitude. It has been found that, for fixed-lift aeroelastic calculations, the number of multigrid iterations required increases by at most 10% if information is exchanged between the structural model and the aerodynamics every 10 multigrid cycles. Of course, in addition to the larger number of iterations required, the cost of the structural solution has to be accounted for. However, most of this cost is incurred in the decomposition of the stiffness matrix, and, as mentioned above, this can be accomplished in a pre-processing step. During the process of an update to the structures, all that remains to be done is the creation of a load vector and a back-solve operation with the already factored stiffness matrix.

The *AeroSurf* geometry database is currently a set of subroutines which are compiled together with the main optimization program. As the number of disciplines increases, a desirable development would be to make the OML database a stand-alone program that communicates directly with all the participating disciplines. The *AeroSurf* OML can then take the form of a daemon, and all communication can be made via sockets.

Finally, although the current implementation of *AeroSurf* relies on geometry creation and manipulation routines that we have developed, the ultimate goal is to use *AeroSurf* as a front-end to a Computer Aided Design (CAD) geometry kernel. This would greatly facilitate the transfer of information back to the working engineering model once the objectives of the design have been met. An interesting possibility is to use the Computational Analysis PRogramming Interface (CAPRI) developed by Haimes [22] which enables individual discipline programs to interact *directly* with a CAD solid model representation of the geometry in question. However, even in this CAD-oriented scenario, the process of component-based design with the necessary re-intersections will still form the core of the methodology.

4 Sensitivity Analysis

The proposed high-fidelity MDO framework will also need a strategy to perform design changes in a way that will minimize the need for expensive function evaluations. Detailed shape optimization of aerodynamic surfaces for transonic wing design problems requires a parameter space of $\mathcal{O}(100)$ or larger [23, 24]. This requirement combined with the enormous cost of each function evaluation renders the use of zeroth-order methods, such as random searches and genetic algorithms, inefficient for this problem. The alternative of using a response surface whereby a polynomial fit of the design space is constructed prior to optimization is also plagued with intractable computational costs since the number of function evaluations required is proportional to the square of the number of design variables.

If we assume that the basic topology of the structure (i.e., the number of spars, the number of ribs, the choice of materials, etc.) is not altered during the design, the design space should be smooth. Although many alternative global optimization strategies exist, for the aero-structural problem of interest, a gradient-based procedure holds the most promise. Gradient-based optimization algorithms can be shown to converge only to a local optimum. If the cost function of the aero-structural problem is sufficiently multi-modal, these algorithms can fail to achieve the global optimum. Nevertheless, when used in conjunction with lower-fidelity MDO tools that provide a reasonable starting point for the optimization, they can yield significant and credible improvements in the design.

When compared with zeroth-order methods, gradient-based algorithms shift the computational burden from evaluating the cost function to calculating values of its gradient. The most direct way to estimate gradients is the finite-difference approach in which a separate function evaluation is required for each design variable in the problem. By using gradient information, the total number of function evaluations is greatly reduced. However, given the large computational cost involved in each function evaluation, the finite-difference method has proven to be unaffordable for the aerodynamic design of complete configurations. This limitation of the finite-difference method has provided the motivation to develop new methods of obtaining sensitivity information for aerodynamic design problems. In particular, the control theory adjoint technique has proven extremely valuable in making these kinds of calculations possible.

4.1 Aerodynamic Sensitivities

The ground-breaking development of the adjoint methodology for both the Euler and Navier-Stokes equations was pioneered by Jameson [13, 14, 12, 10]. Its extensions to treat complex configurations including the treatment of linear and non-linear constraints and mesh deformations has been demonstrated by the first author [5, 6, 9].

In essence, the adjoint approach is able to obtain the gradient of a cost function with respect to an arbitrary number of design variables through the solution of a co-state equation. Given an aerodynamic cost function, I , which depends on both the flow field variables, \mathbf{w} , and the physical location of the OML boundary, \mathcal{F} ,

$$I = I(\mathbf{w}, \mathcal{F}),$$

a change in \mathcal{F} results in a change

$$\delta I = \frac{\partial I^T}{\partial \mathbf{w}} \delta \mathbf{w} + \frac{\partial I^T}{\partial \mathcal{F}} \delta \mathcal{F} \quad (5)$$

in the cost function. The governing equation, R , and its first variation express the dependence of \mathbf{w} and \mathcal{F} within the flow field domain:

$$R(\mathbf{w}, \mathcal{F}) = 0, \quad \delta R = \left[\frac{\partial R}{\partial \mathbf{w}} \right] \delta \mathbf{w} + \left[\frac{\partial R}{\partial \mathcal{F}} \right] \delta \mathcal{F} = 0. \quad (6)$$

Next, introducing a Lagrange multiplier, ψ , we have

$$\begin{aligned} \delta I &= \frac{\partial I^T}{\partial \mathbf{w}} \delta \mathbf{w} + \frac{\partial I^T}{\partial \mathcal{F}} \delta \mathcal{F} - \psi^T \left(\left[\frac{\partial R}{\partial \mathbf{w}} \right] \delta \mathbf{w} + \left[\frac{\partial R}{\partial \mathcal{F}} \right] \delta \mathcal{F} \right) \\ &= \left\{ \frac{\partial I^T}{\partial \mathbf{w}} - \psi^T \left[\frac{\partial R}{\partial \mathbf{w}} \right] \right\} \delta \mathbf{w} + \left\{ \frac{\partial I^T}{\partial \mathcal{F}} - \psi^T \left[\frac{\partial R}{\partial \mathcal{F}} \right] \right\} \delta \mathcal{F}. \end{aligned} \quad (7)$$

Choosing ψ to satisfy the adjoint or co-state equation

$$\left[\frac{\partial R}{\partial \mathbf{w}} \right]^T \psi = \frac{\partial I}{\partial \mathbf{w}}, \quad (8)$$

the first term in Eq. (7) is eliminated, and we find that the desired gradient is given by

$$\mathcal{G}^T = \frac{\partial I^T}{\partial \mathcal{F}} - \psi^T \left[\frac{\partial R}{\partial \mathcal{F}} \right]. \quad (9)$$

Since Eq. (9) is independent of $\delta \mathbf{w}$, the gradient of I with respect to an arbitrary number of design variables can be determined without the need for additional flow field evaluations. The main cost incurred is in solving the adjoint equation. In general, the complexity of the adjoint problem is similar to that of the flow solution. If the number of design variables is large, it becomes compelling to take advantage of the cost differential between one

adjoint solution and the large number of flow field evaluations required to determine the gradient using finite differences. Once the gradient is obtained, any descent procedure can be used to obtain design improvements. At the end of each optimization iteration, new flow and adjoint calculations are performed to obtain an updated gradient, and the process is repeated until the cost function reaches a minimum.

It must be noted that in the case of aerodynamic design it is often the case that the problems are characterized by a large number of design variables and a small number of independent aerodynamic cost functions and constraints. This ratio of design variables to cost functions and constraints is often the opposite in structural optimization problems. If an aerodynamic problem were characterized by having a larger number of aerodynamic constraints compared with the number of design variables, the finite difference approach may be more suitable. The alternative *direct* approach, often used for structures, requires the solution of

$$\left[\frac{\partial R}{\partial \mathbf{w}} \right] \delta \mathbf{w} = - \left[\frac{\partial R}{\partial \mathcal{F}} \right] \delta \mathcal{F} \quad (10)$$

for $\delta \mathbf{w}$, followed by a substitution into Eq. (5). It is noted that $\delta \mathbf{w}$ must be calculated for each design variable independently. For small problems, it is possible to factor and store $\frac{\partial R}{\partial \mathbf{w}}$ and obtain all the $\delta \mathbf{w}$ vectors by a series of back-substitutions [25]. Unfortunately, for large three-dimensional Euler and Navier-Stokes problems, the cost of factoring $\frac{\partial R}{\partial \mathbf{w}}$ is not acceptable, leaving the advantage of the direct approach difficult to obtain. For many flow regimes of interest, the linearization of the CFD Jacobian matrix introduced in Eq. (10) is an unacceptable approximation. Most aerodynamic solvers make no attempt to compute the Jacobian matrix; it is simply too large and prefactoring it does not yield the advantage seen for linear systems. Thus, without prefactoring, the cost of solving Eq. (10) for each design variable is not too different from the cost of finite differencing.

The reader is referred to our earlier works for the detailed derivation of the adjoint equations specific to either the Euler or Navier-Stokes equations as well as the other elements necessary to create an overall design algorithm [5, 6, 9].

4.2 Structural Sensitivities

In the structural optimization subproblem, typical design variables include the cross-sectional areas of the truss elements that are used to model the spar

caps, and the thicknesses of the plate elements that model the shear webs and skins.

The functions for which we require sensitivity information will typically be the total weight of the structure and the maximum stress on a given element. These are used as part of the overall cost function (aerodynamic performance plus structural weight) and to impose constraints on the problem. The sensitivities of the total weight with respect to the element size are trivial, since the weight of a given element is proportional to a given dimension. The sensitivities of the element stresses can be calculated in a straightforward fashion using finite differences. However, this approach is not very cost-effective since it requires the assembly and factorization of the global stiffness matrix, along with the solution of the structural equilibrium equation for each of the design variables. Although the finite-difference method was used in the results presented in this work, the method of choice is the *direct method* which is more efficient for cases where the number of cost functions and constraints is larger than the number of design variables [26]. For cases in which the number of design variables dominates the problem, a structural adjoint method analogous to the aerodynamic adjoint method can be used.

In the following, we are interested in obtaining the sensitivity of a vector-valued function g_i , ($i = 1, \dots, n_{elems}$) to the design parameters \mathcal{P} . In other words, we are seeking the values for all the entries in the matrix $\left[\frac{dg_i}{d\mathcal{P}}\right]$, where the cost function, say structural weight, is but a single component of g_i .

The *direct method* is derived by taking the first variation of Eq. (1):

$$\mathbf{K} \delta \mathbf{q} = \frac{\partial \mathbf{f}}{\partial \mathbf{q}} \delta \mathbf{q} - \frac{\partial \mathbf{K}}{\partial \mathcal{P}} \mathbf{q} \delta \mathcal{P} + \frac{\partial \mathbf{f}}{\partial \mathcal{P}} \delta \mathcal{P}. \quad (11)$$

It must be noted that for static load conditions, where the load vector is assumed to be independent of the structural design variables and deflections, as is often the case for structural optimization as a single discipline,

$$\frac{\partial \mathbf{f}}{\partial \mathcal{P}} = 0, \quad \text{and} \quad \frac{\partial \mathbf{f}}{\partial \mathbf{q}} = 0. \quad (12)$$

This reduces Eq. (11) to

$$\mathbf{K} \delta \mathbf{q} = - \frac{\partial \mathbf{K}}{\partial \mathcal{P}} \mathbf{q} \delta \mathcal{P}. \quad (13)$$

As is shown later, the assumption of a constant load vector does not hold in the more general problem of coupled aeroelastic design.

To find $\delta \mathbf{q}$, Eq. (13) can be solved using the previously factorized stiffness matrix by the same method used for the solution of Eq. (1). This procedure needs to be repeated for each design variable.

To obtain the sensitivity of a vector of functionals g_i (where g_i could represent the stress in an element in addition to any cost functions), we write the total variation with respect to the design variables as follows:

$$\delta g_i = \frac{\partial g_i}{\partial \mathcal{P}} \delta \mathcal{P} + \frac{\partial g_i}{\partial \mathbf{q}} \delta \mathbf{q}. \quad (14)$$

Note that $\delta \mathbf{q}$ is valid for the evaluation of the sensitivity of any functional.

It is seen that the prefactored stiffness matrix renders the solution with respect to a significant number of design variables relatively inexpensive. In the work presented for this paper, where the cost of the aerodynamic state and co-state analyses are at least 2 orders of magnitude more than that of the structural analyses, the benefit of using the direct approach has not as yet been pursued.

4.3 Coupled Sensitivities

The computation of sensitivities for the aero-structural problem has components of both ASO and structural optimization techniques. However, if the true sensitivities of the design problem are needed, the coupling terms cannot be neglected. For example, the sensitivity of the stress in a given element of the CSM model to an aerodynamic twist variable has a component that depends on the change to the geometry of the structural model and a second component that depends on the changing load vector applied to the structure. Both of these contributions are significant and must be accounted for. Although in the results presented in this paper a simplified penalty function is used to obtain a first cut at the aero-structural design problem, we feel it is important to place the mathematical framework for coupled sensitivities on more solid footing. It will inevitably turn out that the choice of the use of an adjoint approach will depend upon the problem at hand. Since we propose to establish a flexible design environment, the possibility of using a coupled adjoint must be considered. The remainder of this section has been developed in collaboration with Lessoine [27].

Consider, for example, a cost function where both aircraft weight and drag are included. Then, if \mathbf{q} and \mathcal{P} denote respectively the structural displacement field and structural parameters of the structural model, \mathbf{w} denotes the flow solution, and \mathcal{F} represents the design parameters of the undeformed air-

craft shape, the aeroelastic objective function whose sensitivity we are looking for becomes $I(\mathbf{w}, \mathbf{q}, \mathcal{F}, \mathcal{P})$. The variations in I are subject to the constraint

$$R_{as}(\mathbf{w}, \mathbf{q}, \mathcal{F}, \mathcal{P}) = 0, \quad (15)$$

where R_{as} designates the set of aero-structural equations and can be partitioned as

$$R_{as} = \begin{pmatrix} R(\mathbf{w}, \mathbf{q}, \mathcal{F}, \mathcal{P}) \\ S(\mathbf{w}, \mathbf{q}, \mathcal{F}, \mathcal{P}) \end{pmatrix}. \quad (16)$$

Here, R denotes the set of fluid equations and S the set of structural equations. The variation δI can be expressed as

$$\delta I = \frac{\partial I^T}{\partial \mathbf{w}} \delta \mathbf{w} + \frac{\partial I^T}{\partial \mathbf{q}} \delta \mathbf{q} + \frac{\partial I^T}{\partial \mathcal{F}} \delta \mathcal{F} + \frac{\partial I^T}{\partial \mathcal{P}} \delta \mathcal{P}. \quad (17)$$

In order to eliminate $\delta \mathbf{w}$ and $\delta \mathbf{q}$ from the above equation, the following constraint can be introduced:

$$\begin{aligned} \delta R_{as} &= \left[\frac{\partial R_{as}}{\partial \mathbf{w}} \right] \delta \mathbf{w} + \left[\frac{\partial R_{as}}{\partial \mathbf{q}} \right] \delta \mathbf{q} \\ &+ \left[\frac{\partial R_{as}}{\partial \mathcal{F}} \right] \delta \mathcal{F} + \left[\frac{\partial R_{as}}{\partial \mathcal{P}} \right] \delta \mathcal{P} = 0, \end{aligned}$$

which calls for the partitioned Lagrange Multiplier

$$\psi_{as} = \begin{pmatrix} \psi_a \\ \psi_s \end{pmatrix}, \quad (18)$$

where ψ_a is the portion of the adjoint associated with the fluid, and ψ_s is the portion of the adjoint associated with the structure. It follows that the first expression of δI can be replaced by

$$\begin{aligned} \delta I &= \frac{\partial I^T}{\partial \mathbf{w}} \delta \mathbf{w} + \frac{\partial I^T}{\partial \mathbf{q}} \delta \mathbf{q} + \frac{\partial I^T}{\partial \mathcal{F}} \delta \mathcal{F} + \frac{\partial I^T}{\partial \mathcal{P}} \delta \mathcal{P} \\ &- \psi_{as}^T \left(\left[\frac{\partial R_{as}}{\partial \mathbf{w}} \right] \delta \mathbf{w} + \left[\frac{\partial R_{as}}{\partial \mathbf{q}} \right] \delta \mathbf{q} + \left[\frac{\partial R_{as}}{\partial \mathcal{F}} \right] \delta \mathcal{F} + \left[\frac{\partial R_{as}}{\partial \mathcal{P}} \right] \delta \mathcal{P} \right) \\ &= \left\{ \frac{\partial I^T}{\partial \mathbf{w}} - \psi_{as}^T \left[\frac{\partial R_{as}}{\partial \mathbf{w}} \right] \right\} \delta \mathbf{w} + \left\{ \frac{\partial I^T}{\partial \mathbf{q}} - \psi_{as}^T \left[\frac{\partial R_{as}}{\partial \mathbf{q}} \right] \right\} \delta \mathbf{q} \\ &+ \left\{ \frac{\partial I^T}{\partial \mathcal{F}} - \psi_{as}^T \left[\frac{\partial R_{as}}{\partial \mathcal{F}} \right] \right\} \delta \mathcal{F} + \left\{ \frac{\partial I^T}{\partial \mathcal{P}} - \psi_{as}^T \left[\frac{\partial R_{as}}{\partial \mathcal{P}} \right] \right\} \delta \mathcal{P}. \end{aligned}$$

Now, if ψ is chosen as the solution of the aero-structural adjoint equation

$$\begin{pmatrix} \left(\frac{\partial R_{as}}{\partial \mathbf{w}} \right)^T \\ \left(\frac{\partial R_{as}}{\partial \mathbf{q}} \right)^T \end{pmatrix} \begin{pmatrix} \psi_a \\ \psi_s \end{pmatrix} = \begin{pmatrix} \frac{\partial I}{\partial \mathbf{w}} \\ \frac{\partial I}{\partial \mathbf{q}} \end{pmatrix}, \quad (19)$$

the expression for δI simplifies to

$$\delta I = \mathcal{G}_{\mathcal{F}} \delta \mathcal{F} + \mathcal{G}_{\mathcal{P}} \delta \mathcal{P}, \quad (20)$$

where

$$\mathcal{G}_{\mathcal{F}} = \frac{\partial I^T}{\partial \mathcal{F}} - \psi_{as}^T \left[\frac{\partial R_{as}}{\partial \mathcal{F}} \right], \quad (21)$$

and

$$\mathcal{G}_{\mathcal{P}} = \frac{\partial I^T}{\partial \mathcal{P}} - \psi_{as}^T \left[\frac{\partial R_{as}}{\partial \mathcal{P}} \right]. \quad (22)$$

Hence, the sought-after objective, which is the elimination of $\delta \mathbf{w}$ and $\delta \mathbf{q}$ from the expression for δI , is attainable but requires the solution of the adjoint *coupled aero-structural* problem

$$\begin{pmatrix} \left(\frac{\partial R}{\partial \mathbf{w}} \right)^T & \left(\frac{\partial S}{\partial \mathbf{w}} \right)^T \\ \left(\frac{\partial R}{\partial \mathbf{q}} \right)^T & \left(\frac{\partial S}{\partial \mathbf{q}} \right)^T \end{pmatrix} \begin{pmatrix} \psi_a \\ \psi_s \end{pmatrix} = \begin{pmatrix} \frac{\partial I}{\partial \mathbf{w}} \\ \frac{\partial I}{\partial \mathbf{q}} \end{pmatrix}. \quad (23)$$

Now, since the creation of a completely coupled aero-structural adjoint would compromise our objective of developing a flexible MDO framework, we can rewrite Eq. (23) as

$$\begin{aligned} \left(\frac{\partial R}{\partial \mathbf{w}} \right)^T \psi_a &= \frac{\partial I}{\partial \mathbf{w}} - \left(\frac{\partial S}{\partial \mathbf{w}} \right)^T \tilde{\psi}_s \\ \left(\frac{\partial S}{\partial \mathbf{q}} \right)^T \psi_s &= \frac{\partial I}{\partial \mathbf{q}} - \left(\frac{\partial R}{\partial \mathbf{q}} \right)^T \tilde{\psi}_a, \end{aligned}$$

where $\tilde{\psi}_s$ and $\tilde{\psi}_a$ are lagged values which are updated via outer iterations. This implies that existing adjoint solvers for both the aerodynamics and structures can be used subject to convergence of the iteration. The additional right-hand-side forcing terms can then be updated in the same way as has been done here with the state equations. Thus, the OML geometry can serve to couple both the state and co-state equations.

Beyond employing a coupled adjoint, the alternative of using a coupled direct approach also exists. The development follows the one above very closely in terms of the coupling. The terms in Eq. (12) which were assumed to be zero become the coupling variables. However, since prefactoring of the CFD Jacobian matrix is problematic, the approach will not be much cheaper than using finite differencing. An alternative to either the adjoint or the direct approaches is the use of a decomposed optimization strategy such as multi-level optimization [28] or collaborative optimization [15]. Exploring all of these various possibilities will form the basis of our future work.

For the purposes of the present paper where a coupled adjoint has yet to be implemented, the sensitivities are obtained without coupling. The aerodynamic adjoint is used to obtain aerodynamic sensitivities and finite differences are used to obtain the structural sensitivities. This approximation inherently implies that gradient information for a combined aerodynamic plus structural objective function will not be completely accurate. The earlier

example of exploring how wing twist affects structural stress levels highlights our current limitation. Without the coupling, we will capture only the portions of the sensitivities that result from structural changes. The loading will act as if it were frozen just as in Eq. (12). Future works will address this limitation by implementing the coupled adjoint as outlined above. Finally, for a detailed treatment of the overall design process, we refer to references [5, 6].

5 Results

The results of the application of our aero-structural design methodology are presented in this section. These results are divided into two parts: results of aeroelastic analysis of existing complete configuration wind tunnel models, and results of aeroelastic design for flight configurations. The two sets of results use two different structural models. In addition, some of the results presented used the Euler equations, while others used the Reynolds Averaged Navier-Stokes equations to model the fluid flow. The results are intended to showcase the current capabilities of the design method.

5.1 Navier-Stokes Aeroelastic Analysis of Complete Configuration Wind Tunnel Models

In this section, results of the rigid and aeroelastic analysis of two different wind tunnel models representing typical complete configuration business jets are presented and compared with the available experimental data. The CFD meshes used for each of the two models contain the wing, body, pylon, nacelle, and empennage components. The mesh for the first model (model A) uses 240 blocks with a total of 5.8 million cells while the second mesh (model B) contains 360 blocks and a total of 9 million cells. The large mesh sizes are required for adequate resolution of all the geometric features for each of the configurations and the high Reynolds number boundary layers on their wings. It should be mentioned that viscous and structural effects are resolved only on the wing surface; all other surfaces in the model are assumed to be inviscid and rigid. All calculations were run using 48 processors of an SGI Origin2000 parallel computer. A total of 1.3 hours (model A) and 2.0 hours (model B) of wall clock time were required for the rigid-geometry solutions, while 1.4 hours and 2.1 hours were required for the aeroelastic calculations. The structural model is the one described in Section 2.1 since the proper-

ties of its elements more closely approximate the behavior of the wind tunnel model structure. Experimental wind tunnel data are available for the two models at flight conditions as follows: Model A, $M_\infty = 0.80$, $Re = 2.5$ million and cruise C_L , and Model B, $M_\infty = 0.80$, $Re = 2.4$ million and cruise C_L . Aeroelastic updates are performed every 10 multigrid iterations of the flow solver. A total of 400 iterations were used to ensure an aeroelastically converged solution. All solutions were calculated at a fixed C_L by incrementally adjusting the angle of attack.

A view of model A shaded by C_p appears in Figure 4 showing the wing, body, pylon, nacelle, and empennage present in the calculation. Figure 5 shows a comparison of the pressure distributions for the rigid wing, the aeroelastic wing, and the wind tunnel data for model A. The sectional cut is near mid-span where wind tunnel measurements were available. The figure shows that for this case the aeroelastic deformation of the wing is so small that virtually no difference between the two computed results exists. In fact, the maximum tip deflection of the model was calculated to be only 0.3% of the wing span. Agreement with the sparse wind tunnel data indicates that the CFD is capturing the right trends present in the tested configuration. The fact that the differences between the computed rigid and elastic wings are so small leads to the conclusion that the wind tunnel data from this test probably need not be corrected for aeroelastic deflections. In retrospect, it can be noted that the model A configuration has low sweep so there is very little twist due to bending. Thus, since the outboard wing tip is not twisting much, large differences in the pressure distribution do not appear. If these calculations had been performed before test entry, the confidence level on the tunnel data could have been increased. Figure 6 shows the difference in the spanload of the two computed solutions.

Figure 7 shows a similar comparison of pressure distributions for rigid, aeroelastic, and wind tunnel data from model B. It is immediately clear that the deflections predicted by the aeroelastic calculation have a much larger impact on the pressure distributions than in the case of model A. The changes in the pressure distributions show all the typical signs of aeroelastic relief in swept-back wings: a decrease in the twist of the outboard sections of the wing with the consequent forward motion of the shock location and alterations in the spanload distribution.

Although the aeroelastic solution does not agree fully with the experimental data for model B, it is clear that the aerolastic effects change the solution

in the correct direction to improve the agreement. Additional discrepancies are believed to be caused by inaccuracies in the Baldwin-Lomax turbulence model. It is also evident that this wind tunnel model is flexible enough that significant aeroelastic effects are present in the wind tunnel data. In view of the small increase in cost of the aeroelastic solutions, it is clear that this type of analysis is preferable for the comparison between experimental and wind tunnel data in order to eliminate some of the uncertainties causing the differences.

5.2 Aerodynamic Shape Optimization of a Flight Wing-Alone Geometry

The results presented in this section correspond to a typical aerodynamic shape optimization calculation on a rigid geometry. The structural model is completely inactive. This calculation is representative of many of our earlier works [5, 6] and is intended to present a baseline for comparison with the aeroelastic design in the following sections.

The geometry to be optimized is the wing of a typical business jet having the same planform as that of the airplane shown in Figure 4. The flow field is computed using the Euler equations. A multi-block mesh following a C-H topology is constructed around the configuration with a total of 32 blocks and 750,000 cells. A total of 133 design variables are used to parametrize the surface of the wing. Hicks-Henne perturbation functions combined with exponential functions at the wing trailing edges were distributed across the entire span of the wing to provide full geometric flexibility. Thickness constraints typical of our previous works are imposed in order to maintain the structural soundness of the final outcome of the design process. These constraints include spar depth constraints at 10% and 80% chord, a leading edge radius constraint ahead of the 2% location, a trailing edge included angle constraint behind the 95% chord location, and an additional thickness constraint to maintain maximum thickness and fuel volume at 40% chord. Note once more that these thickness constraints are the results of low-fidelity analyses and are derived from years of accumulated experience by aerodynamic and structural designers. The objective function is the wing coefficient of drag, C_D , at a fixed cruise $C_L = 0.35$ and a fixed Mach number of $M = 0.82$. It must be said that these flight conditions represent a significant increase in both Mach number and lift coefficient over those for which the original baseline wing was designed. It is therefore expected that improved

aerodynamic designs should be attainable with the use of optimization. All wing-alone design calculations presented hereafter were carried out on an SGI Origin2000 parallel computer using 16 processors.

The results of this single-point shape optimization process can be seen in Figure 8 which shows the initial and final pressure distributions for several span stations along the wing. Similar results have been presented in [12]. Notable features are the decrease in induced drag due to the shifting of the spanload towards the tip (Figure 9) and the decrease of wave drag that results from the weakening or disappearance of the shock waves on the upper and lower surfaces. Note that at the location of the front spar (10% chord) where the thickness constraint is active, the lower surface pressure distribution at some of the stations exhibits an oscillation and a loss of lift due to the requirement of maintaining thickness. The changes in airfoil shape are rather small, but the overall effect on the C_D of the configuration is drastic: after 20 design iterations, the total value of C_D is reduced by 31%, or from 95.6 counts to 65.6 counts.

As shown in Figure 10, a comparison of aeroelastic analyses of the baseline and resulting designs reveals that the maximum stress levels for the rear spar have increased substantially in the inboard wing region, especially near the crank point. Figure 9 shows that the reason for the increase in stress in the rear spar is that the span loading has been shifted outboard substantially for this rigid-wing design in an effort to reduce the induced drag. Since the optimization algorithm can not see a structural penalty in this outboard shift of the spanload, it simply maintains the required thickness constraints and redistributes the load as it sees fit.

5.3 Aero-Structural Shape Optimization of a Flight Wing-Alone Geometry

The idea in this wing-alone design case is to incorporate some basic elements of the aero-structural interaction present in the existing design methodology. Despite the fact that development of the complete coupled sensitivity analysis is not yet implemented, several results of interest can be shown which establish the soundness of the procedure. In this particular case, we utilize the geometry of the previous section, the same CFD mesh and structural model, and the same set of aerodynamic shape variables. The artificial thickness constraints are removed, leaving only the leading edge radius and included trailing edge angle constraints. The design is now set up

with both the coefficient of drag and the \mathcal{L}^2 norm of the stress in the structure as a combined cost function. This combined penalty function method can be thought of as a first cut approach to minimizing total drag in the presence of structural constraints. The ASO adjoint system is used to calculate the gradient of the aerodynamic cost function (C_D) and finite differencing is used to calculate the gradient contribution from the structural changes. Despite the fact that these sensitivities are not fully accurate because of the lack of coupling, they provide our first approximation for solving the AESO (AeroElastic Shape Optimization) problem. The weights between the two components of the objective function were arbitrarily chosen such that the stress penalty was equal to about 40% of the drag penalty. This choice resulted in an optimized design where the \mathcal{L}^2 norm of the stress in the structure remained largely unchanged.

Figure 11 depicts the pressure distributions before and after the design process. Once more, the resulting pressure distributions and changes to the sections look similar to those from the previous design case. However, there are some noteworthy differences. The oscillation in the lower surface pressure distribution seen in the earlier solution near the 10% span chord location is not present. Since we are no longer imposing artificial thickness constraints, the resulting design was able to thin this region with some benefit to the aerodynamics and without a significant increase in the structural stress distributions. The more clearly observable difference between this solution and the previous one is the dramatic thickening of the airfoil section near the crank point. This is the location where the highest stress level is recorded in the rear spar. Figure 12 shows that the design has again dramatically changed the loading distributions by moving part of the load outboard. This has a corresponding tendency to increase the load at the critical crank point rear spar location. The design algorithm has chosen to increase the airfoil thickness at this station to compensate for the shift in load outboard. It is worth remembering that changes to the wing thickness can have an effect on wave drag. Indeed a re-examination of Figure 11 reveals that the shock strength on the lower surface has been increased from the original design. However, since the final design in this case is less than one count higher in drag than that achieved in the previous case, this weak lower surface shock must not be incurring a significant drag penalty. Figure 13 illustrates the benefit of adding the stress penalty function to the design problem. The spanwise stress on the rear

spar at the planform break has been reduced slightly in the optimized configuration. Assuming that no other constraints were placed on the problem, it would then be possible to shift the load on the wing outboard, while thickening the inboard sections so as to keep the wing weight approximately constant. With a more accurate description of the cost functions and constraints in the problem, these kinds of trade studies will allow the designer to make better-informed choices about the development of the configuration.

6 Conclusions

The work presented in this paper represents our first step towards the establishment of a high-fidelity multidisciplinary environment for the design of aerospace vehicles. The environment is in its infancy and will continue to evolve during the coming year(s). At its core, it consists of the following key elements:

- High-fidelity modeling of the participating disciplines (RANS flow models for the aerodynamics and linear finite element model for the structure).
- An OML geometry database which serves as the interface between disciplines. This database contains information regarding the current shape of the configuration and the physical solutions from the participating disciplines.
- A force- and work-equivalent coupling algorithm designed to preserve a high level of accuracy in the transfer of loads and displacements between aerodynamics and structures.
- A framework for the computation of coupled sensitivities of the aero-structural design problem.

This design environment has been used to perform RANS aeroelastic analysis of complete configuration flight and wind-tunnel models with an additional cost which is less than 10% of the cost of a traditional rigid-geometry CFD solution. These solutions can be used to determine *a priori* whether significant aeroelastic corrections will or will not be needed for the resulting wind tunnel data.

In addition, simplified design cases have been presented that include the effect of aeroelastic deformations in the design process. These cases have

shown that our design methodology is able to predict the correct trades between aerodynamic performance and structural properties present in these types of wing design problems.

Finally, a structural stress penalty function was added to the coefficient of drag of the complete configuration to allow elimination of artificial thickness constraints that are typically imposed in aerodynamic shape optimization methods. This rudimentary coupling of aerodynamics and structures in the design not only eliminates the necessity to impose artificial constraints, but also produces designs where trade-offs between aerodynamic and structural performance are considered.

Further work will focus on the continued development of the proposed MDO framework. Topics requiring significant research include sensitivity analysis, optimization strategy, Navier-Stokes based design, use of commercially available CSM codes, multipoint design, and CAD integration.

7 Acknowledgments

This research has been made possible by the support of the MCAT Institute, the Integrated Systems Technologies Branch of the NASA Ames Research Center under Cooperative Agreement No. NCC2-5226, and the David and Lucille Packard Foundation. Raytheon Aircraft is acknowledged for providing relevant aircraft configurations and wind tunnel data as well as guiding the overall research effort. The authors would like to acknowledge the assistance of David Saunders in the review of the final manuscript and the help of Mark Rimlinger in the preparation of CFD meshes and figures.

References

- [1] J. Sobieszczanski-Sobieski and R. T. Haftka. Multidisciplinary aerospace design optimization: Survey of recent developments. *AIAA paper 96-0711*, 34th Aerospace Sciences Meeting and Exhibit, Reno, NV, January 1996.
- [2] S. Wakayama. Lifting surface design using multidisciplinary optimization. *Ph. D. Dissertation*, Stanford University, Stanford, CA, December 1994.
- [3] S. R. Wakayama and I. M. Kroo. A method for lifting surface design using nonlinear optimization. Dayton, OH, Sept. 1990. AIAA Paper 90-3120. AIAA/AHS/ASEE Aircraft Design Systems and Operations Conference.
- [4] J. W. Gallman. *Structural and Aerodynamic Optimization of Joined-Wing Aircraft*. Ph.d. dissertation, Department of Aeronautics and Astronautics, Stanford University, Stanford, CA, June 1992.
- [5] J. J. Reuther, A. Jameson, J. J. Alonso, M. Rimlinger, and D. Saunders. Constrained multipoint aerodynamic shape optimization using an adjoint formulation and parallel computers: Part I. *Journal of Aircraft*, 1998. Accepted for publication.
- [6] J. J. Reuther, A. Jameson, J. J. Alonso, M. Rimlinger, and D. Saunders. Constrained multipoint aerodynamic shape optimization using an adjoint formulation and parallel computers: Part II. *Journal of Aircraft*, 1998. Accepted for publication.
- [7] J. Reuther, A. Jameson, J. Farmer, L. Martinelli, and D. Saunders. Aerodynamic shape optimization of complex aircraft configurations via an adjoint formulation. *AIAA paper 96-0094*, 34th Aerospace Sciences Meeting and Exhibit, Reno, Nevada, January 1996.
- [8] J. Reuther, A. Jameson, J. J. Alonso, M. J. Rimlinger, and D. Saunders. Constrained multipoint aerodynamic shape optimization using an adjoint formulation and parallel computers. *AIAA paper 97-0103*, 35th Aerospace Sciences Meeting and Exhibit, Reno, Nevada, January 1997.
- [9] J. Reuther, J. J. Alonso, J. C. Vassberg, A. Jameson, and L. Martinelli. An efficient multiblock method for aerodynamic analysis and design on distributed memory systems. *AIAA paper 97-1893*, June 1997.
- [10] A. Jameson, N. Pierce, and L. Martinelli. Optimum aerodynamic design using the Navier-Stokes equations. *AIAA paper 97-0101*, 35th Aerospace Sciences Meeting and Exhibit, Reno, Nevada, January 1997.
- [11] A. Jameson. Re-engineering the design process through computation. *AIAA paper 97-0641*, 35th Aerospace Sciences Meeting and Exhibit, Reno, Nevada, January 1997.
- [12] J. Reuther and A. Jameson. Aerodynamic shape optimization of wing and wing-body configurations using control theory. *AIAA paper 95-0123*, 33rd Aerospace Sciences Meeting and Exhibit, Reno, Nevada, January 1995.

- [13] A. Jameson. Automatic design of transonic airfoils to reduce the shock induced pressure drag. In *Proceedings of the 31st Israel Annual Conference on Aviation and Aeronautics, Tel Aviv*, pages 5–17, February 1990.
- [14] A. Jameson. Aerodynamic design via control theory. *Journal of Scientific Computing*, 3:233–260, 1988.
- [15] I. M. Kroo. Decomposition and collaborative optimization for large scale aerospace design. In N. Alexandrov and M. Y. Hussaini, editors, *Multidisciplinary Design Optimization: State of the Art*. SIAM, 1996.
- [16] R. Braun, P. Gage, I. Kroo, and I. Sobieski. Implementation and performance issues in collaborative optimization. *AIAA paper 96-4017*, 6th AIAA/USAF/NASA/ISSMO Symposium on Multidisciplinary Analysis and Optimization, Bellevue, WA, September 1996.
- [17] A. Jameson and J.J. Alonso. Automatic aerodynamic optimization on distributed memory architectures. *AIAA paper 96-0409*, 34th Aerospace Sciences Meeting and Exhibit, Reno, Nevada, January 1996.
- [18] A. A. Giunta, V. Balabanov, D. Haim, B. Grossman W. H. Mason, and L. T. Watson. Wing design for a high-speed civil transport using a design of experiments methodology. *AIAA paper 96-4001*, 6th AIAA/NASA/ISSMO Symposium on Multidisciplinary Analysis and Optimization, Bellevue, WA, September 1996.
- [19] R. S. Sellar and S. M. Batill. Concurrent subspace optimization using gradient-enhanced neural network approximations. *AIAA paper 96-4019*, 6th AIAA/NASA/ISSMO Symposium on Multidisciplinary Analysis and Optimization, Bellevue, WA, September 1996.
- [20] S. A. Brown. Displacement extrapolation for CFD+CSM aeroelastic analysis. *AIAA paper 97-1090*, 35th Aerospace Sciences Meeting and Exhibit, Reno, NV, January 1997.
- [21] M. Holden. Optimization of dynamic systems using collocation methods. *Ph. D. Dissertation*, Stanford University, Stanford, CA, February 1999.
- [22] R. Haimes. *CAPRI: Computational Analysis Programming Interface*. Massachusetts Institute of Technology, March 1998.
- [23] R. M. Hicks and P. A. Henne. Wing design by numerical optimization. *Journal of Aircraft*, 15:407–412, 1978.
- [24] R. Kennelly. Improved method for transonic airfoil design-by-optimization. *AIAA paper 83-1864*, AIAA Applied Aerodynamics Conference, Danvers, Massachusetts, July 1983.
- [25] G. W. Burgreen and O. Baysal. Three-dimensional aerodynamic shape optimization of wings using sensitivity analysis. *AIAA paper 94-0094*, 32nd Aerospace Sciences Meeting and Exhibit, Reno, Nevada, January 1994.
- [26] H. M. Adelman and Raphael T. Haftka. Sensitivity analysis of discrete structural systems. *AIAA Journal*, 24:823–832, 1986.
- [27] J. Gallman, J. J. Alonso, J. Reuther, and M. Lessoine. Multi-disciplinary optimization using computational fluid dynamics (cf). Topic Area Number 29: BAA 98-04-PRK, Research Proposal Submitted to the Air Force Research Laboratory, Wright-Patterson Airforce Base, Dayton, Ohio, 1998.
- [28] M. Baker and J. Giesing. A practical approach to mdo and its application to an hscst aircraft. *AIAA paper 95-3885*, 1st AIAA Aircraft Engineering, Technology, and Operations Congress, Los Angeles, CA, September 1995.



Figure 4: Typical business jet configuration. FLO107-MB: Navier-Stokes, Baldwin-Lomax, $M = 0.80$, $Re = 2.5$ million, 5.8. million mesh cells. C_p contours.

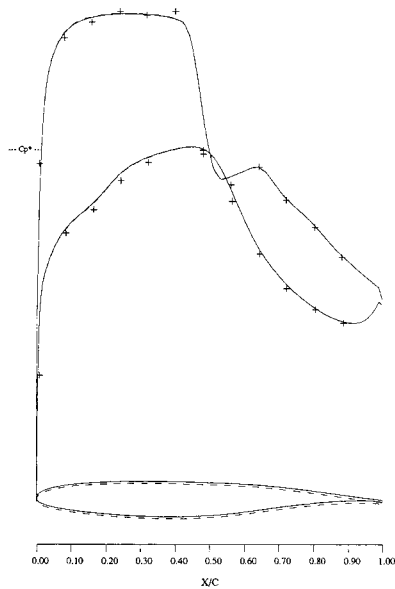


Figure 5: C_p distribution at near wing tip station. Navier-Stokes calculations, $M = 0.80$, $Re = 2.5$ million
 —, Aeroelastic solution
 - - -, Solid geometry solution
 + + +, Wind tunnel data

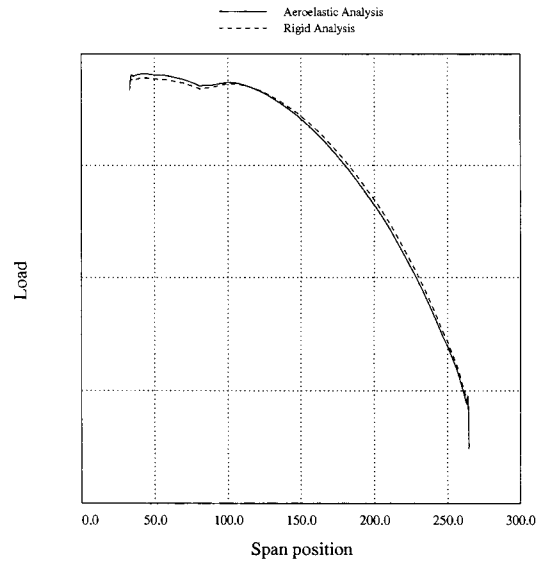


Figure 6: Spanwise Load Distribution. Comparison of the Rigid Analysis and Aeroelastic Analysis. Complete Configuration Navier-Stokes Solution.

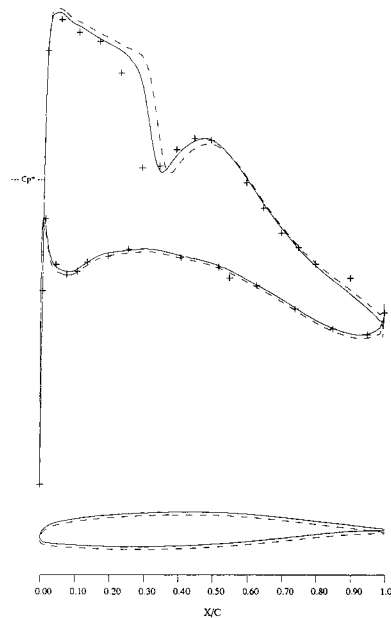


Figure 7: C_p distribution at near wing tip station. Navier-Stokes calculations, $M = 0.80$, $Re = 2.4$ million
 —, Aeroelastic solution
 - - -, Solid geometry solution
 + + +, Wind tunnel data

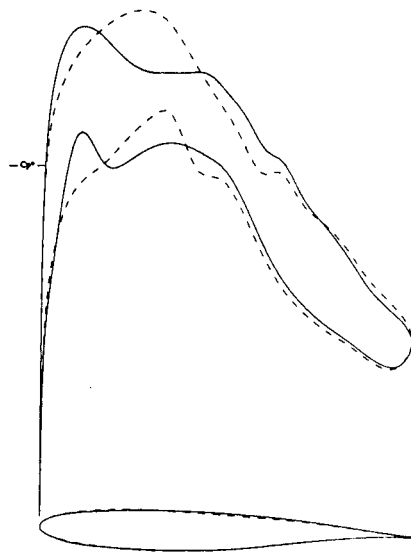
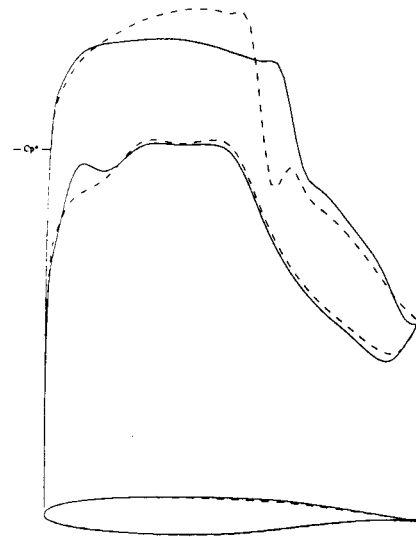
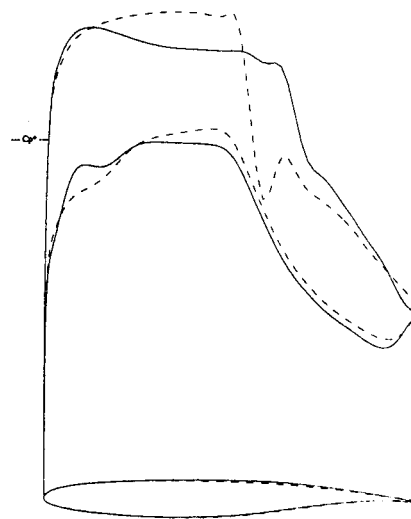
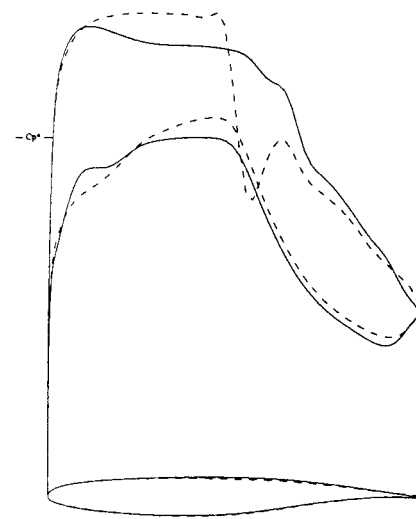
8a: span station $z = 0.194$ 8b: span station $z = 0.387$ 8c: span station $z = 0.581$ 8d: span station $z = 0.775$

Figure 8: Typical Business Jet Configuration. Drag Minimization at Fixed C_L .
 Rigid Design, $M = 0.82$, $C_L = 0.35$, 133 Hicks-Henne variables. Spar Constraints Active.
 Rigid Analysis at Fixed C_L .
 - - -, Initial Pressures
 —, Pressures After 20 Design Cycles.

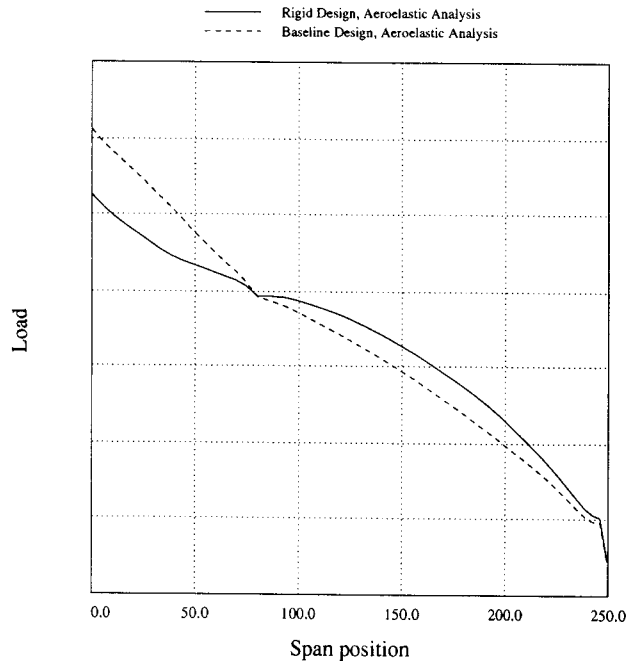


Figure 9: Spanwise Load Distribution. Comparison of the Rigid Design and the Baseline Design. Wing Alone Configuration. Rigid Design, Drag Minimization at Fixed C_L . Aeroelastic Analysis at Fixed C_L .

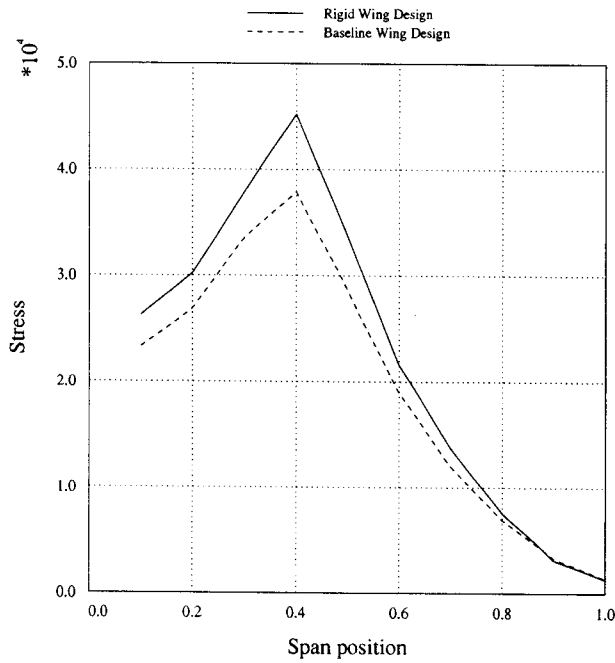


Figure 10: Spanwise Stress Distribution for the Rear Spar. Comparison of the Rigid Design and the Baseline Design. Wing Alone Configuration. Rigid Design, Drag Minimization at Fixed C_L . Aeroelastic Analysis at Fixed C_L .

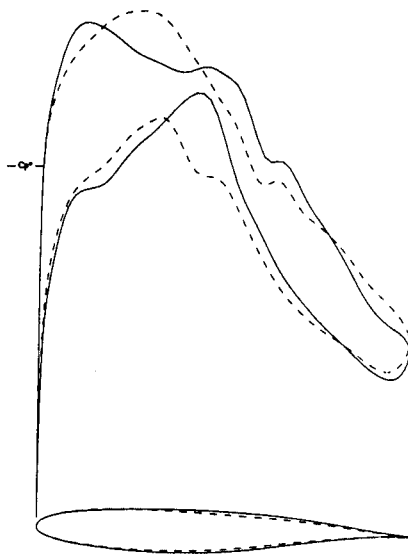
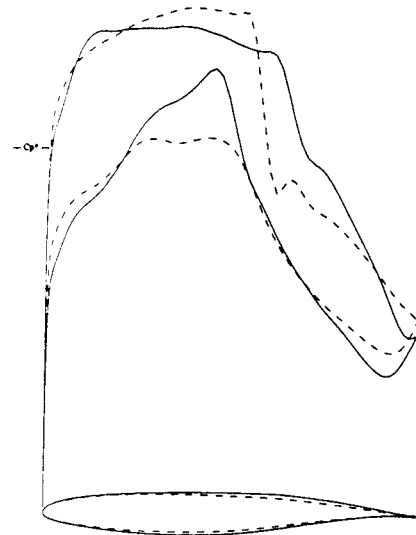
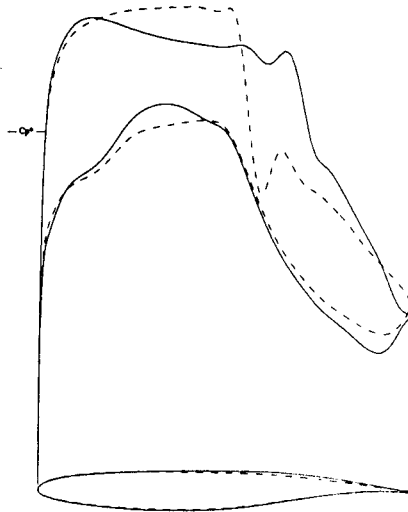
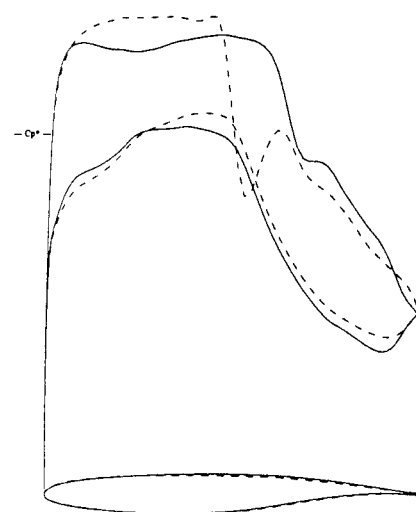
11a: span station $z = 0.194$ 11b: span station $z = 0.387$ 11c: span station $z = 0.581$ 11d: span station $z = 0.775$

Figure 11: Typical Business Jet Wing Configuration. Drag + Stress Minimization at Fixed C_L .
 Aeroelastic Design with Stress Penalty Function. $M = 0.82$, $C_L = 0.35$
 133 Hicks-Henne variables. Spar Constraints Inactive.
 Aeroelastic Analysis at Fixed C_L .
 - - -, Initial Pressures
 ———, Pressures After 13 Design Cycles.

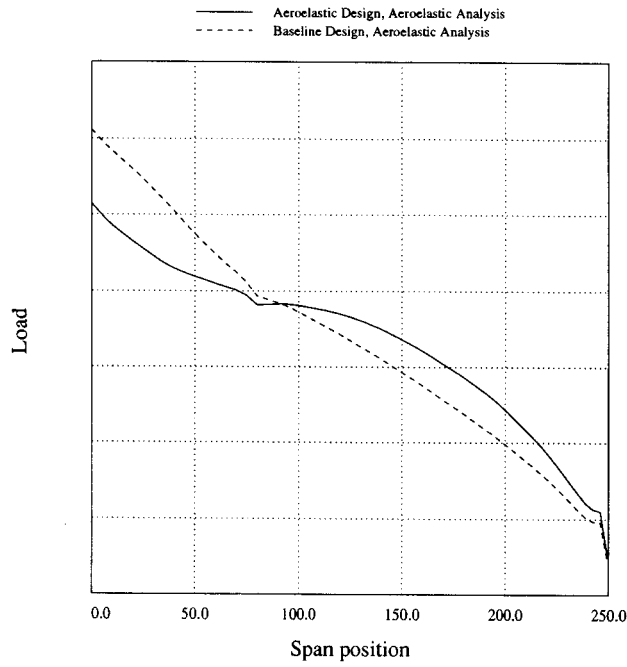


Figure 12: Spanwise Load Distribution. Comparison of the Aeroelastic Design and the Rigid Design. Wing Alone Configuration. Aeroelastic Design, Drag + Stress Minimization at Fixed C_L . Aeroelastic Analysis at Fixed C_L .

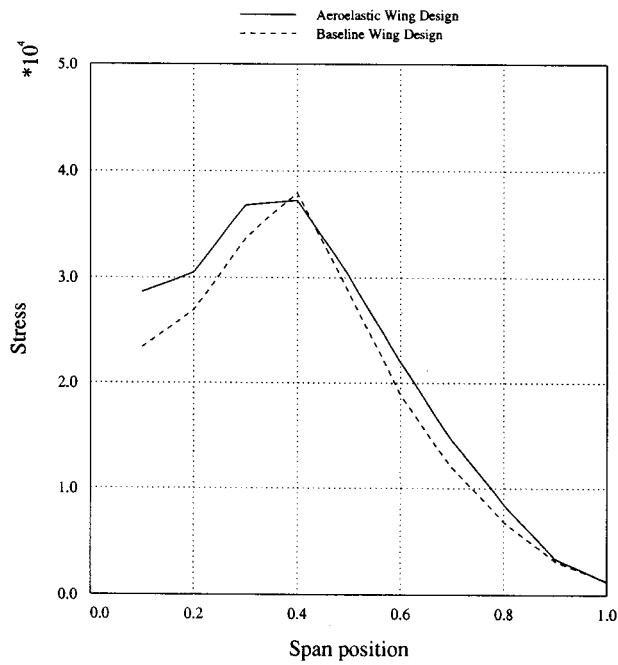


Figure 13: Spanwise Stress Distribution for the Rear Spar. Comparison of the Aeroelastic Design and the Rigid Design. Wing Alone Configuration. Aeroelastic Design, Drag + Stress Minimization at Fixed C_L . Aeroelastic Analysis at Fixed C_L .

Supersonic Civil Transport Design Using Collaborative Optimization

NAL Workshop on Numerical Simulation Technology for The Design of Next Generation Supersonic Civil Transport

**Prof. Ilan Kroo
Stanford University
Stanford, California, USA**

Abstract

This paper describes the application of collaborative optimization, a strategy for distributed design, to the optimization of two supersonic civil aircraft concepts. This design approach permits tasks to be decomposed into domain-specific subproblems, and coordinated to achieve an optimal system. Developed over the past few years by researchers at Stanford, NASA, and Boeing, the methodology is now being applied to large-scale problems requiring high-fidelity modeling. The paper describes one of these applications, the preliminary design of supersonic transports, and provides preliminary results for both a conventional design and a novel natural laminar flow concept. A summary of the laminar flow design concept is complemented by some initial flight test results demonstrating the feasibility of the idea.

Introduction

This paper is divided into two parts: a description of the methodology used for high fidelity multidisciplinary optimization together with some results, and further details on one of the applications, the supersonic natural laminar flow concept. Because of the strong interactions between wing structure and aerodynamics, and because of the complexity of transition prediction, the MDO technique described in the first part is an important part of the laminar flow concept development. The work described here is a brief summary of work at Stanford, NASA, and industry over the past several years. It should be regarded only as a survey of the more complete body of work discussed in references 1-5. The application of new multidisciplinary design approaches to supersonic aircraft began was undertaken to examine how such methods performed using industry-standard analysis methods on a problem that was too large to integrate each of the disciplines into a single analysis methods. It was the first large scale test of the use of approximation methods with collaborative optimization and proved quite successful [1]. We are currently extending this approach to the design of natural laminar flow supersonic aircraft, based on some of the ideas described in [6]. This paper describes the basic structure used to solve these multidisciplinary design problems, some of the details concerning its implementation, and current work in developing the natural laminar flow concept.

High Fidelity MDO Using Collaborative Optimization

Collaborative optimization is a strategy for multidisciplinary optimization that permits decomposition of the design problem into disciplinary subproblems, coordinated with a system-level optimization problem. This approach permits the local disciplines to choose appropriate design variables and satisfy local constraints using a design method appropriate for that discipline. Interdisciplinary variables (those that are required in multiple subproblems) are specified by the system optimizer and each the goal of each subproblem is to minimize the discrepancies between these targets and the values that are required in order to satisfy the local constraints. The system is charged with minimizing the global objective while making sure that the targets are compatible with all of the subproblems. This two-level strategy is attractive in many ways, reducing the need for tight integration of multiple disciplines, allowing disciplinary experts to make design decisions, and minimizing the complexity of the system level problem. Like many multilevel optimization methods, however, the system can be sensitive to noise in the subspace optimization results and the system optimizer must be capable of dealing with the constraints in a reasonably efficient manner. Several publications describe some of the motivation and results of the basic concept applied to problems ranging from analytic test problems to more complex engineering tasks. [2-4]. In the present application the architecture is used to divide the supersonic aircraft design problem into three disciplines as shown in figure 1. Aerodynamics, structures, and mission analysis subproblems are posed to minimize the take-off gross weight of a commercial supersonic transport.

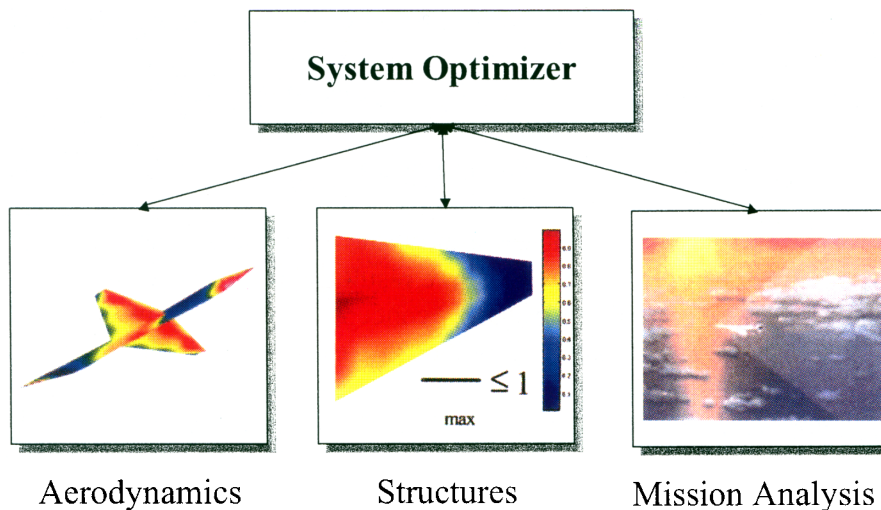


Figure 1. Basic decomposition of supersonic transport design problem.

In these design problems, a fully aeroelastic optimal solution was obtained using high fidelity industry codes for aerodynamics, a finite element structural analysis, and a mission simulation. Each of these disciplines accomplishes design tasks in parallel, at geographically distributed locations on heterogeneous computing platforms. Results are synthesized by the system optimizer that is able to reduce take-off weight using 14 system-level design variables, while the subspace optimization includes dozens of additional variables used to satisfy local constraints. Further details on the decomposition are shown in figure 2.

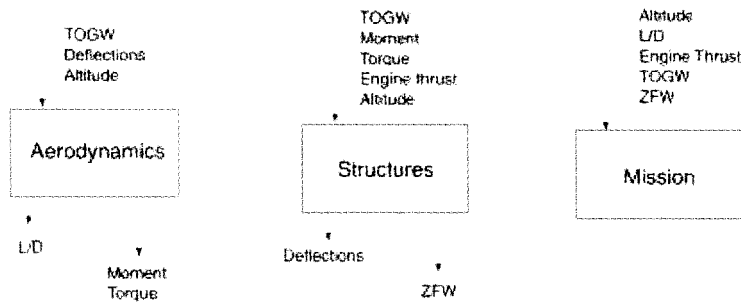


Figure 2. Decomposition of subproblems in collaborative design of SST.

To expedite the system optimization, subspace design results are modeled with a response surface technique described in [3]. Iterative updates to a low order fit are accomplished using the trust region method of [7]. The system optimization in each fitting cycle is therefore fast and insensitive to subspace noise.

The entire process is implemented within a framework that makes the construction of such problems relatively simple. This framework is an API and a collection of networked applications that manage the communication among the analyses, optimizers, and fitting routines. Using Java for socket-based communications, XML for representing shared information, and collection of distributed applets that comprise the user interface, this Collaborative Application Framework For Engineering (Caffe) simplifies the construction of complex enterprise design problems.

Initial work on the collaborative optimization of a high speed civil transport is described in [1] and involved the disciplinary models described below.

Aerodynamics

Pressure distributions on the wing/fuselage combination were computed using Boeing's high order, potential-based surface panel method A502. More recent computations employ Euler solvers, but for the cases studied in [1] the linear method provided acceptable results. Surface pressures were computed at a typical cruise point as well as at a single structural design point. These pressures were modeled with a reduced basis set that reflected the basic character of the pressures and faithfully reproduced the wing bending moment and torsion distributions as well as the vehicle forces and moments. The aerodynamics discipline was permitted to adjust angles of attack and wing twist distributions, satisfying load factor constraints at the specified cruise and maneuver conditions. Typical results for the conventional configuration are illustrated in figure 3.

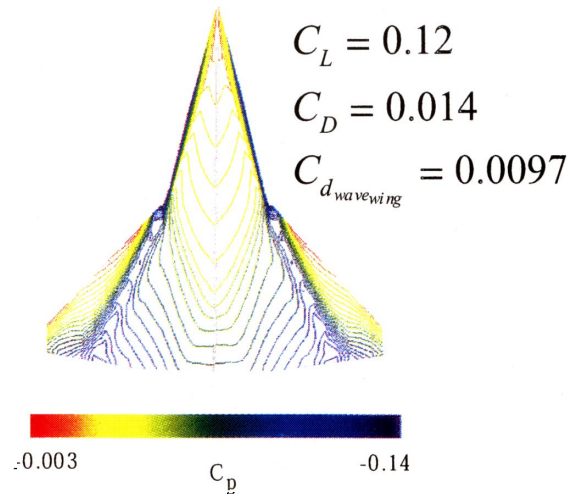


Figure 3. Sample results from aerodynamics subproblem: wing pressures and overall force coefficients at cruise.

Structures

Structural analysis was done using a finite element code developed by NASA Langley. The structural design problem involved element thickness design variables and stress constraints with the objective of matching targets that included deflections, applied loads, and weights. The finite element code was combined with the NPSOL optimizer [8], which was also used for the system level design problem. Typical results are depicted in figure 4.

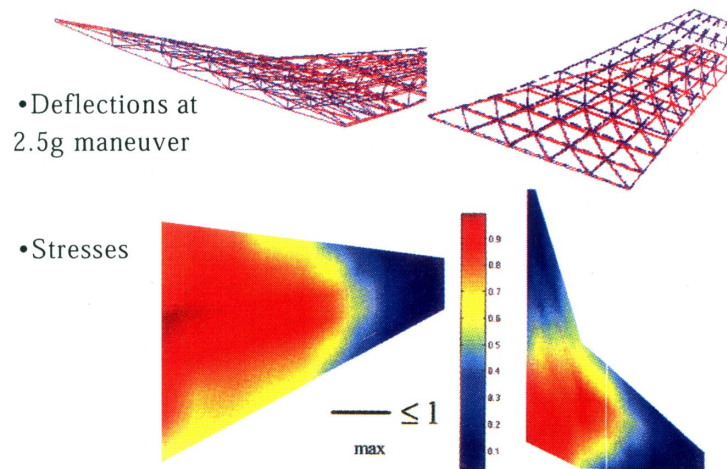


Figure 4. Sample results from structures subproblem including deflections and stresses.

Mission Analysis

The mission analysis subproblem enforced range and field length constraints and included simple mission models along with a propulsion deck. This discipline involved little analysis and served as a stand-in for a more complex mission model that might involve trajectory optimization.

The problem was to minimize take-off weight (another stand-in for a more refined objective that would involve economic modeling) for a 200 passenger SST with a 5000 n.mi. range.

Figure 5 shows how the system converged as the fitting cycles proceeded. After about 10 cycles the system succeeded in satisfying disciplinary constraints and interdisciplinary compatibility. Based on the subspace design fits, at the end of this process, we verified that the solution was indeed optimal. The process was then applied to the design of a low-sweep supersonic laminar flow configuration with similar success. The basic concept and configuration are discussed in the following section.

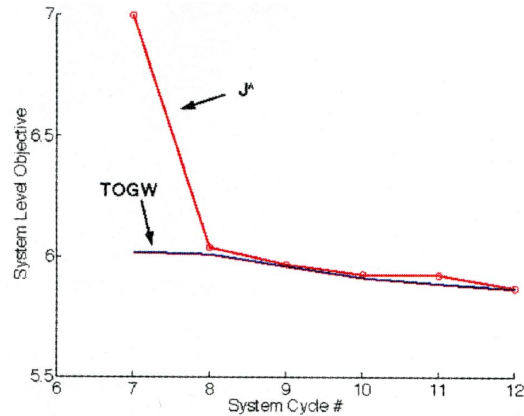


Figure 5. Convergence history of SST design problem: Cycles indicate response surface fitting updates. J^* denotes system objective that includes interdisciplinary discrepancies as penalties.

Supersonic Natural Laminar Flow Concept

The conventional approach to supersonic wing design for transport aircraft involves the use of a highly swept wing to reduce wave drag due to lift and volume. It has long been noted that wing skin friction contributes substantially more drag than the wing wave drag and a variety of attempts have been reported to reduce skin friction by modification of the turbulent boundary layer and by active control to maintain a laminar boundary layer. Tracy [6] noted that by adopting a wing planform with low sweep, the wing pressure distributions would be favorable for extensive laminar flow (see figure 5). The present work is based on that concept which has been studied for possible application to an unmanned reconnaissance aircraft and a supersonic business jet (figure 6).

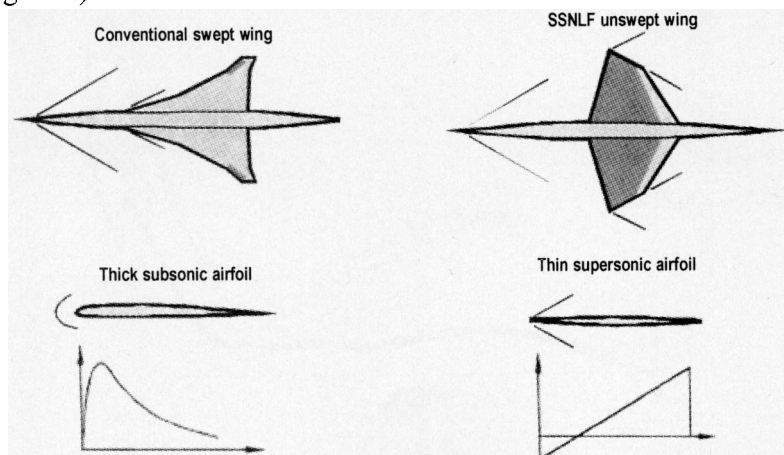


Figure 5. Exploiting favorable pressure gradients for supersonic laminar flow. Low sweep wing provides favorable pressure gradient over entire chord.

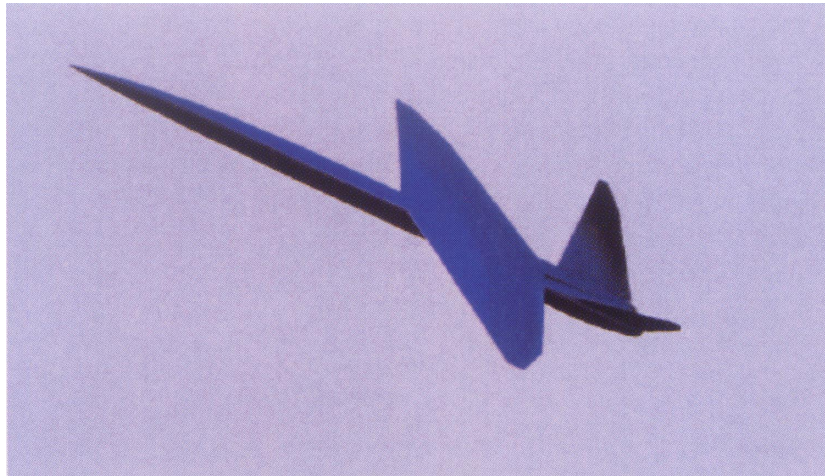


Figure 6. Example configuration: supersonic reconnaissance UAV with NLF wing.

The design problem is challenging because the penalty for the low sweep wing is a potentially large wave drag. This can be mitigated by adopting a very thin wing, but with significant implications for structural design. So the problem is strongly multidisciplinary. In addition, the computation of transition is difficult, requiring high fidelity aerodynamic simulation.

Much of the current work (partly described in [9]) has focused on the development of a method for rapidly predicting transition due to Tollmein-Schlichting instability or boundary layer cross-flow. The basic approach involves computation of the inviscid pressure distribution (using an Euler solver), estimation of boundary layer properties using a modified sweep-taper approximation described in [9], and estimation of a transition location based on cross flow Reynolds number and a correlation with more detailed compressible linear stability calculations. Figure 7 shows how the combined Euler and sweep-taper method compares with Navier-Stokes calculations for a thin supersonic wing with little sweep.

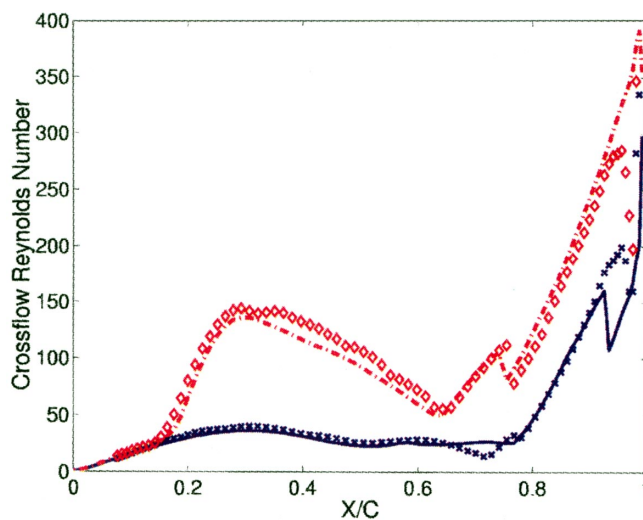


Figure 7. Validation of the sweep-taper method: Lines are Navier Stokes computations, symbols are sweep-taper method. Results at two spanwise locations on wing.

Figure 8 shows the estimated transition location for a thin wing on the basis of a composite amplification factor that reaches a value of 1.0 when transition is forecast. Results suggest that at the flight condition under consideration extensive laminar flow would be possible.

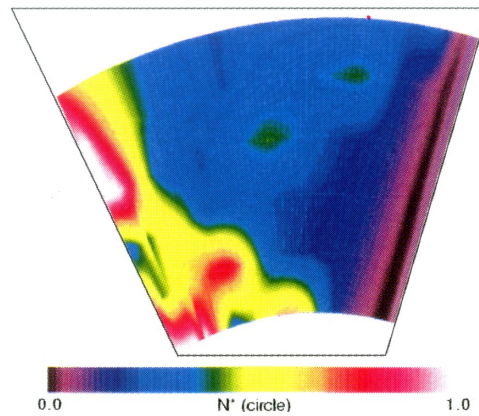


Figure 8. Composite amplification factor for supersonic natural laminar flow wing design: white areas indicate predicted transition.

In cooperation with Tracy, NASA Dryden, Stanford, University of California at Davis, and DARPA, a test of this configuration was conducted. Since a quiet supersonic wind tunnel with high Reynolds number capability was not available, the wing was mounted on an F-15 as shown in figure 9 and flown on a series of tests in late 1999. Transition location was indicated by an on-board infrared video camera. A typical result is shown in figure 10, which compares very well with the predictions and shows almost full chord laminar flow over much of the wing.

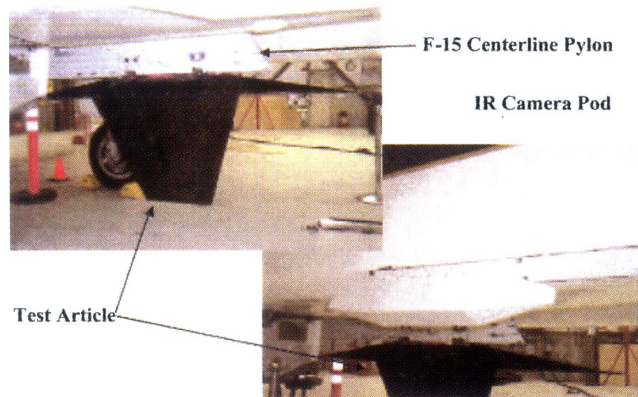


Figure 9. Test Wing and infrared camera mounted on NASA Dryden F-15



Figure 10. In-Flight infrared image of test wing showing extensive laminar flow.

Conclusions and Future Work

The work summarized here suggests that high fidelity multidisciplinary optimization is an essential component of supersonic aircraft design. The collaborative optimization approach was applied successfully to conventional and natural laminar flow SST designs. It provides a means of combining design tools in various disciplines without extensive integration efforts. The response surface version of the method avoided some difficulties that might have been experienced with a direct approach. The Caffe framework, still in development, promises to simplify the implementation of such complex design strategies.

The use of a mildly swept wing with carefully-designed pressure distributions to achieve natural laminar flow appears very promising. Initial flight tests agree well with predicted 3D transition locations and show that extensive runs of natural laminar flow are indeed achievable in flight.

The application of this concept to unmanned air vehicles or business aircraft is particularly attractive since the wings of these vehicles operate at lower Reynolds numbers than would be typical of a large supersonic transport and hence lead to more stable boundary layers.

Future work will involve continued development of an easily deployed framework for distributed design and collaborative optimization, continued flight tests of the supersonic natural laminar flow wing, and application studies based on these concepts.

References

1. Manning, V., Large-Scale Design of Supersonic Aircraft Via Collaborative Optimization, Stanford Ph.D. Thesis, 1999.
2. Kroo, I., "MDO for Large-Scale Design," in Multidisciplinary Optimization: State of the Art, Alexandrov, N., Hussaini, eds., SIAM 1997.
3. Sobieski, I., Manning, V., Kroo, I., "Response Surface Estimation and Refinement in Collaborative Optimization," AIAA 98-4753, 1998.
4. Braun, R., Collaborative Optimization: An Architecture for Large-Scale Distributed Design, Ph.D. Thesis, Stanford University.
5. Alexandrov, N., Lewis, R. M., "Comparative Properties of Collaborative Optimization and Other Approaches to MDO," in Engineering Design Optimization, MCB Univ. Press, 1999.
6. Tracy, R., Kroo, I., Chase, J., Viken, J., "Exploiting Natural Laminar Flow for Economical Supersonic Transport," SAE Paper 952040, SAE Aerotech '95, 21 Sept. 1995.
7. Dennis, J., Torczon, V., "Managing Approximation Models in MDO," in Multidisciplinary Optimization: State of the Art, Alexandrov, N., Hussaini, eds., SIAM 1997.
8. Gill, P., Murray, W., Saunders, M., Wright, M., User's Guide for NPSOL: A Fortran Package for Nonlinear Programming, Stanford University 1995.
9. Sturdza, P. et al. "Boundary Layer Calculations for Preliminary Design of Wings in Supersonic Flow," AIAA 99-3104, June 1999.

SIMULTANEOUS SHAPE AND FLIGHT TRAJECTORY OPTIMIZATION OF A SPACEPLANE USING PARALLEL OPTIMIZATION METHOD

Shinji Suzuki and Takeshi Tsuchiya

Graduate School of Engineering, the University of Tokyo
tshinji@mail.ecc.u-tokyo.ac.jp

Key Words: Guidance and Control, Optimization Technique, Spaceplane, Parallel Computation

ABSTRACT

This paper presents a parallel optimization method to solve large-scale optimization problems and apply the method to the simultaneous vehicle design and flight trajectory optimization problems of a spaceplane. Generally, to obtain an accurate optimal solution, a large-scale problem has to be solved, and it takes much computing load and time. Therefore, the new method divides the problem into several sub-problems which can be solved in parallel. In the first half of the paper, we describe the way to decompose the problem and the fundamental algorithm to solve it. We introduce the conjunctive constraints among the sub-problems and define Lagrange multipliers for each conjunctive constraint. Each sub-problem can be solved in a parallel manner by updating both the Lagrange multipliers and design variables. In the latter half of the paper, the parallel optimization method is applied to obtain the optimal shape and optimal flight trajectory of a spaceplane.

INTRODUCTION

This paper considers an optimization design problem of a spaceplane in which design parameters of a vehicle and its ascent trajectory are optimized simultaneously. A new parallel optimization technique is introduced to solve the large-scale simultaneous design. The method decomposes an original problem into multiple sub-problems by using the Lagrange variables which can be solved in parallel, and this process is iterated by updating Lagrange variables until converged solutions are obtained.

This method is applied to the design problem of a spaceplane which takes off horizontally, climbs up to a space station and returns to the earth airport with horizontal landing. The vehicle is intended to be fully reusable by installing the different type of propulsion system, e.g., air-breathing engines and a rocket engine. Since the mission requirements of this vehicle is highly severe for the present technological level, optimization design techniques must be introduced to obtain the most efficient design. It must be noted that the vehicle shape and its flight trajectory must be optimized simultaneously since these two designs have strong coupling.

The main emphasis of this paper is to develop the parallel multi-disciplinary optimization techniques, thus simplified models are used to estimate the aerodynamic and engine characteristics, and structural design is represented as structural weight estimation from statistical data. Flight trajectories are calculated by a point mass model where the angle of attack is selected as a control variable and the engine keeps the maximum

thrust. In a total design problem, the design variables to be optimized are the design parameters in the vehicle design and the control parameters in the trajectory design. The former variables are the body length, the wing area, the size of engine, the body diameter and so on. The latter variables are the time history of the angle of attack, the burn out time and the altitude, and the timing of engine selection.

As a numerical optimization method, we are using the Sequential Quadratic Programming which approximates a nonlinear optimization problem as a quadratic problem using derivative information of a Lagrange function. Whereas the optimal trajectory problem is a dynamic problem where the time history of control variable is a design variable and the time differential equations are the state equations to be satisfied as constraints in the optimization process, the direct collocation method can convert the dynamic optimization problem to a static optimization problem. Therefore, we can formulate this design problem as a conventional optimization problem. However, it should be noted that this problem has a large number of design variables in different disciplines. This is a main reason why we try to introduce a parallel optimization technique.

PARALLEL OPTIMIZATION METHOD

The parallel optimization method usually decomposes the original problem into sub-problems, and solves each sub-problem in a parallel manner. The program manager must be introduced to iterate this sequence and to update information in each sub-problem so as to obtain the total optimization solutions.

Dantzig-Wolfe originally presented decomposition algorithm¹⁾ for linear programming problem. For nonlinear programming problem, two methods called model coordination method and goal coordination method which are reviewed by Kirsch²⁾ has been well accepted. In addition, a hybrid method³⁾ combining these two methods has been studied in recent years. However, these decomposition algorithms have not been widely applied. Recently Braun et al. have proposed numerical methods called Collaborative Optimization⁴⁾ for more practical multidisciplinary optimization problems. Whereas those practical methods have robustness for practical design environment, they do not have strict mathematical background.

In our study, we try to develop mathematically well defined formulation which can be applied to practical

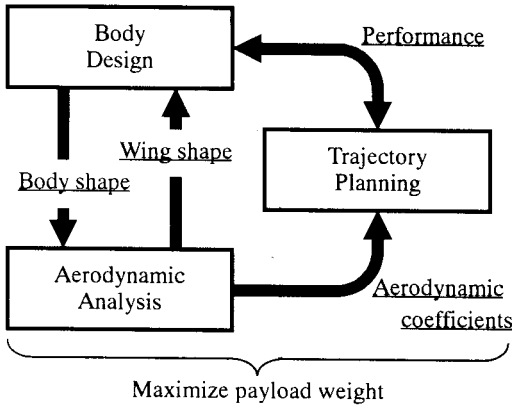


Fig. 2 Three technical fields

design problems with a large number of design variables. We consider the total model divided into three sub-system as shown in Fig.1. The total problem can be written as

$$\text{minimize: } f(x_1, x_2, x_3) \quad (1a)$$

$$\text{subject to: } g_E(x) = \begin{bmatrix} g_{E1}(x_1) \\ g_{E2}(x_2) \\ g_{E3}(x_3) \end{bmatrix} = 0 \quad (1b)$$

$$g_I(x) = \begin{bmatrix} g_{I1}(x_1) \\ g_{I2}(x_2) \\ g_{I3}(x_3) \end{bmatrix} \leq 0 \quad (1c)$$

$$h(x) = \begin{bmatrix} h_{12}(x_1, x_2) \\ h_{21}(x_1, x_2) \\ h_{13}(x_1, x_3) \\ h_{31}(x_1, x_3) \\ h_{23}(x_2, x_3) \\ h_{32}(x_2, x_3) \end{bmatrix} = 0 \quad (1d)$$

where an equality constraint h_{ij} and $h_{ij} = 0$ is respectively called a conjunctive function which connects two subsystems i and j .

In order to solve the sub-problem independently, conjunctive functions in connecting sub-problem and its Lagrange variables are incorporated in an objective function. This process can define the following sub-optimization problem.

$$\text{variable: } x_i \quad (2a)$$

$$\text{minimize } f(x_1, x_2, x_3) + \sum_{j=(i \neq j)}^3 v_{ij}^T h_{ij}(x_i, x_j) \quad (2b)$$

$$\text{subject to } g_{Ei}(x_i) = 0 \quad (2c)$$

$$g_{Ii}(x_i) \leq 0 \quad (2d)$$

$$h_{ji}(x_j, x_i) = 0 \quad (j = 1, 2, 3 \text{ and } i \neq j) \quad (2e)$$

Note that the optimized variables in the sub-problem i are x_i and v_{ji} , and the others are dealt with as constants those are updated in each iteration process.

A Fundamental algorithm to solve the

sub-problems is summarized as follows:

- (1) Determine proper initial solutions of all the variables x_i and Lagrange multipliers v_i .
- (2) Solve all sub-problems in parallel with optimization methods by which not only the variables but also the Lagrange multipliers can be computed, e.g. a sequential quadratic programming (SQP) method⁵⁾.
- (3) Exchange the obtained variables and multipliers among the sub-problems as shown in Fig. 2, and return to (2).

SPACEPLANE DESIGN STUDY

In this section, a shape design and an ascent trajectory design a spaceplane is formulated. Figure 1 indicates three technical fields, body design field, aerodynamic analysis field and trajectory planning field. These three fields are not independent but have the interactions of design variables and design specifications, i.e., some variables of body shape, wing shape, performance and aerodynamic coefficients are used in each design field. Conjunctive conditions represent the equality constraints of the design variables and design specifications commonly used in each subsystem.

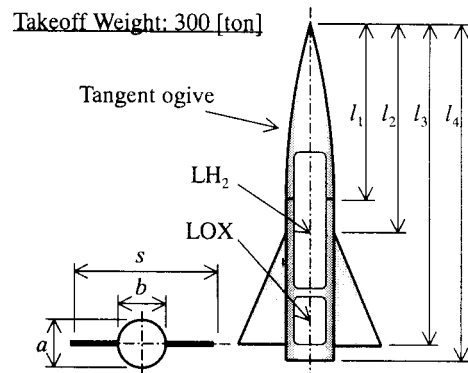


Fig. 1 Spaceplane model

(1) Body Design

The spaceplane shape model adopted in this paper is illustrated in Fig. 2. Takeoff Weight is assumed to be 300 ton and the body is composed of an elliptical cylinder body, a tangent ogive nose and a delta wing. The design variables in this field are the geometrical data and design specifications, e.g., maximum dynamic pressure $q_{max} (\leq 100 \text{ kPa})$, and maximum load factor $n_{max} (\leq 4 \text{ G})$. Note that the tank volume of fuel compounded from liquid hydrogen (LH₂) and liquid oxygen (LOX) must be less than 70 % of the total body volume.

The vehicle weight is estimated by using WAATS⁶⁾ program in which some parameters are modified for a spaceplane, structural weight W_{STR} can be estimated from the body and wing size. Considering the fuel weight W_{fuel} obtained in the trajectory planning fields together, payload weight $W_{payload}$ is defined as

$$W_{\text{payload}} = 300 - W_{\text{STR}} - W_{\text{fuel}} \text{ [ton]} \quad (3)$$

(2) Aerodynamic Analysis

The aerodynamic characteristics of the model are analytically computed by CRSFLW method in Ref. 7 and 8. Five sampling points are selected from low speed to hypersonic speed, where aerodynamic parameters related to lift coefficient and drag coefficient are calculated. Three variables, l_2 , l_3 and s ($\geq b$), representing the wing size are decided in this field. The aerodynamic coefficients are used to compute trajectories in the following field and the wing size is needed to estimate the structural weight in the body design field.

(3) Trajectory Planning

The spaceplane takes off, rises and is accelerated by ATR (up to Mach 6), SCR (switched from ATR and useable to Mach 12) and ROC (useable with ATR and SCR at the same time). Then, after the engine is cut-off above 90 km, it zooms up to 400 km with no thrust in an elliptical orbit. Finally, it is put into a 400 km circular orbit at the apogee in the elliptical orbit (Fig. 3).

In the flight trajectory design, state variables are altitude h , velocity v , flight-path angle γ and weight m . A control variable is defined as the angle of attack α . Motion equations⁸⁾ of the spaceplane are expressed as

$$\frac{dh}{dt} = v \sin \gamma \quad (4a)$$

$$\frac{dv}{dt} = \frac{(T_{\text{ATR}} + T_{\text{SCR}} + T_{\text{ROC}}) \cos \alpha - D}{m} - \frac{\mu \sin \gamma}{r^2} \quad (4b)$$

$$\frac{d\gamma}{dt} = \frac{(T_{\text{ATR}} + T_{\text{SCR}} + T_{\text{ROC}}) \sin \alpha + L}{mv} + \left(\frac{v}{r} - \frac{\mu}{vr^2} \right) \cos \gamma \quad (4c)$$

$$\frac{dm}{dt} = - \left(\frac{T_{\text{ATR}}}{I_{\text{SPATR}}} + \frac{T_{\text{SCR}}}{I_{\text{SPSCR}}} + \frac{T_{\text{ROC}}}{I_{\text{SPROC}}} \right) \frac{1}{g_0} \quad (4d)$$

where μ is the gravity constant, g_0 is the gravity acceleration at the ground level, and D and L are the lift and drag respectively, which are computed by the aerodynamic coefficients obtained in the above field. T_{ATR} , T_{SCR} and T_{ROC} are the thrust of air-turboramjet (ATR) engine, scramjet (SCR) engine and rocket (ROC) engine, I_{SPATR} , I_{SPSCR} and I_{SPROC} are specific impulse of each engine, which are represented in Ref. 8.

Initial conditions at time $t=0$ are specified as

$$h(0) = 0 \text{ [km]} \quad (5a)$$

$$\gamma(0) = 0 \text{ [deg]} \quad (5b)$$

$$m(0) = 300 \times 10^3 \text{ [kg]} \quad (5c)$$

$$L \cos \alpha + (T - D) \sin \alpha \geq m(0)g_0 \quad (5d)$$

$$v(0) \leq 150 \text{ [m/sec]} \quad (5e)$$

Terminal conditions at the engine cut-off time $t=t_f$ is expressed as

$$h(t_f) \geq 90 \text{ [km]} \quad (6a)$$

$$\gamma(t_f) \geq 0 \text{ [deg]} \quad (6b)$$

and the apogee altitude computed by the terminal states, $h(t_f)$, $\gamma(t_f)$ and $v(t_f)$, needs to be 400 km.

In addition, the following path constraints are defined.

$$h \geq 0 \text{ [km]} \quad (7a)$$

$$q \leq q_{\text{max}} \quad (7b)$$

$$\alpha \leq 20 \text{ [deg]} \quad (7c)$$

$$n \leq n_{\text{max}} \quad (7d)$$

where q is dynamic pressure and n is load factor.

It should be noted that the motion equations change discontinuously since the operating engines are switched according to the flight conditions. Therefore the trajectory planning field is subdivided into four stages, that is, ATR, SCR SCR+ROC and ROC stage, which provide four sub-problems.

(4) Optimization Process

The flight trajectory can be optimized by solving the conventional optimal control problem in which an objective function is minimization of required fuels. In this study, the state variables and constraints are discretized to 200 elements, and the state equations (Eqs. 4) are approximated as equality constraints by using the collocation method⁸⁾. These procedures transform an optimal control problem into nonlinear programming problem with static variables.

The trajectory optimization problem can be integrated with vehicle design problems in which the accent trajectory, the vehicle shape and the engine size are optimized simultaneously. The objective function in the integrated problem is maximization of the payload in Eq. (3). The parallel optimization method manages each sub-problem, i.e., the body design, the aerodynamic analysis and the trajectory planning which is divided into four problems according the engine type.

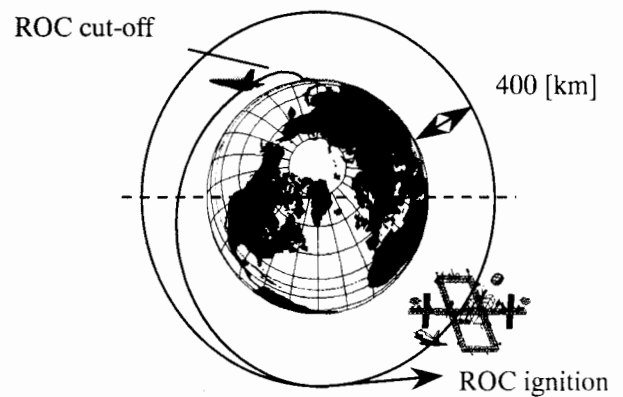


Fig.3 Flight Trajectory

NUMERICAL RESULTS

The numerical solutions are shown in Fig. 4–6 and Table 1. The maximized payload weight is negative value, -13.75 ton, and the spaceplane cannot reach the

orbit even without the payload. This indicates that the present technological level cannot launch the spaceplane to the spacestation and that the weight reduction more than 5 % is required to realize it.

Figure 4 and table 1 show the optimized wing area and the intake area of ATR are very small, and the intake area of SCR is 0 m², which means that SCR is unnecessary in this study. It can be considered that the wing area and ATR are respectively the limit size in order to take off and fly the vehicle against the aerodynamic drag, and that the volume of LH₂ is reduced because SCR isn't used.

CONCLUSIONS

The new parallel optimization method for a large-scale system design with a huge number of variables and constraint conditions is proposed in this paper. This method divides the problem into some small optimization sub-problems based on subsystems constituting the system, which are solved in parallel. This method is successfully applied to a shape and ascent trajectory optimization for a spaceplane. While the obtained payload is minus, the effectiveness and the need of multidisciplinary optimization are demonstrated.

REFERENCE

1. Lasdon, L. S., "Optimization Theory for Large Systems", The Macmillan Company, 1970.
2. Kirsch, U., "Optimum Structural Design", McGraw-Hill, 1981.
3. Suzuki, K. and Ohtsubo, H. "The Constraints between Subsystems in the Distributed Structural Optimization", Proceedings of the Conference on Computational Engineering and Science, 2-2, pp. 613-616, 1997.
4. Braun, R. D., Moore, A. A. and Kroo, I. M. "Collaborative Approach to Launch Vehicle Design", J. Spacecraft and Rockets, 34-4, pp. 478-486, 1997.
5. Ibaragi, H. and Fukushima, M. "FORTRAN77 Optimization Programming", Iwanami Shoten, 1991, (in Japanese).
6. Glatt, G. R., "WAATS-A Computer Program for Weights Analysis of Advanced Transportation Systems", NASA CR-2420, 1974.
7. Mendenhall, M. R., Goodwin, F. K., Dillenius, M. F. E. and Kline, D. M. "Computer Program for Calculating the Static Longitudinal Aerodynamic Characteristics of Wing-Body-Tail Configurations", NASA CR-2474, 1975.
8. Tsuchiya, T. and Suzuki, S. "A Study on the Numerical Method for Simultaneous Optimization for Spaceplane Design and its Flight Trajectory", J. the Japan Society for Aeronautical and Space Sciences, 46-533, pp. 346-353, 1998.

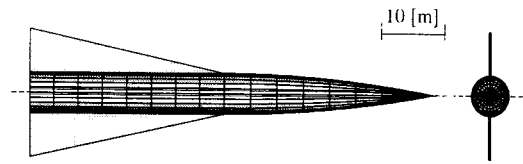


Fig.3 Optimal shape

Table 1 Characteristics of optimal spaceplane

Characteristics		Optimal values
Body length	l_4 [m]	63.48
Body height	a [m]	6.00
Body width	b [m]	6.36
Wing span	s [m]	10.02
Intake area of ATR	S_{ATR} [m ²]	12.59
Intake area of SCR	S_{SCR} [m ²]	0.00
Thrust of ROC	T_{ROC} [ton]	226.6
Max. thrust	T_{max} [ton]	226.6
Max. dynamic pressure	q_{max} [kPa]	100.0
Max. load factor	n_{max} [G]	3.82
Payload weight	$W_{payload}$ [ton]	-13.75

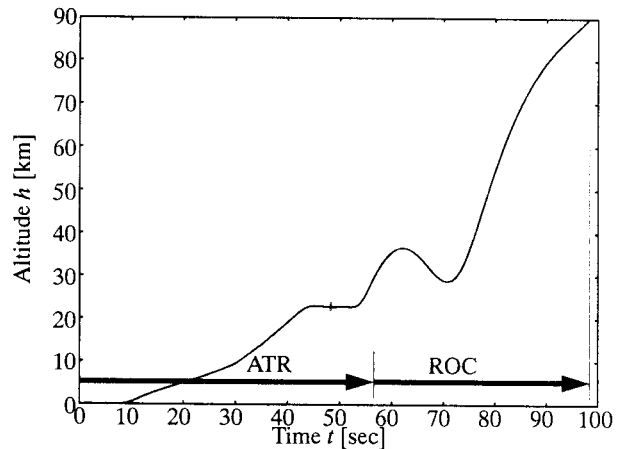


Fig.4 Time history of altitude

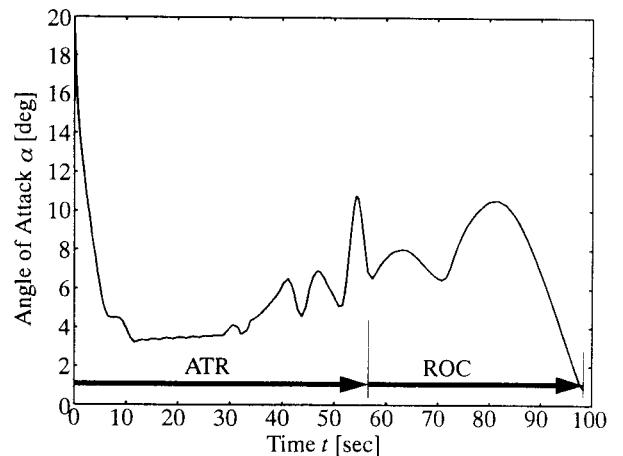


Fig. 3 Time history of angle of attack

Application of Direct Search Method to Aeroelastic Tailoring of an Arrow Wing Configuration

Koji Isogai

Department of Aeronautics and Astronautics

Kyushu University

6-10-1 Hakozaki Higasiku Fukuoka 812-8581, Japan

E-mail: isogai@aero.kyushu-u.ac.jp

Abstract. A computer code for aeroelastic tailoring of an arrow wing supersonic cruise configuration is developed. A direct search method is employed to find the optimum fiber orientation angles and thickness distributions of the upper and lower skin panels of the wing box for the minimum weight design under the multiple constraints. The static strength, symmetric and antisymmetric flutter velocities are taken into account at the same time as the constraints. The code is applied to a typical arrow wing configuration to demonstrate its capabilities.

Key words: Aeroelasticity, SST, Arrow wing, Aeroelastic tailoring, Composite, Optimization

1. Introduction

The flutter characteristics, especially in the transonic regime, play the critical role in structural design of an arrow wing supersonic cruise configuration¹⁾. For example, the design studies performed by Turner and Grande²⁾ of the early Boeing Supersonic Transport (SST) Model 969-512B disclosed that the strength designed configuration does not meet the flutter requirement and an unrealistically high mass penalty was expected to achieve the flutter clearance ($1.2V_D=259$ m/s EAS at $M=0.90$ which was initially set. In order to improve the flutter characteristics of an arrow wing configuration without mass penalty, the application of the aeroelastic tailoring technology might be one of the most promising approaches. However, its effectiveness for the arrow wing configuration has not yet been well examined, though it has been shown that it is highly effective for the high aspect-ratio transport type wings^{3)~5)}.

In order to perform the trend study on the effectiveness of the aeroelastic tailoring for the structural design of an arrow wing supersonic cruise configuration, a preliminary design code is developed. In the present code, a direct search method (the Complex Method^{5), 6)}), which does not depend on the derivatives of the objective and constraint functions, is employed to find the optimum fiber orientation angles and the thickness distributions of the upper and lower skin panels and the thickness of the spar and rib materials of the wing box for the minimum weight design under the multiple constraints. One of the characteristics of the code is that it can treat the static strength, the symmetric/antisymmetric flutter velocities and the minimum gauges at the same time as the constraints. In the next sections, the outline of the code and the results obtained by applying the present code to a typical arrow wing configuration will be presented.

2. The Outline of the Optimum Design Code

In order to perform the aeroelastic tailoring, we need several analysis codes as the elements of the optimization code. For the strength and vibration analyses, the in-house Finite Element Method (FEM) code is developed since we should know the fine-details of the FEM code to develop the aeroelastic optimization code by combining it with the aeroelastic analysis code. The in-house FEM code, in which the membrane elements are employed, is specialized to an arbitrary arrow wing configuration. That is, only a few parameters can generate, automatically, the FEM grids for the wing box of an arbitrary double delta type wing planform. For aeroelastic analyses, the modal approach is taken by using the symmetric/antisymmetric natural vibration

modes (16 mode shapes including rigid body modes are employed) obtained by the FEM code. The unsteady aerodynamic forces are calculated by Doublet Lattice Method (DLM)⁷⁾ code in which the 100 panels (10 chordwise by 10 spanwise) are employed. In order that the aeroelastic analysis code is integrated effectively in the optimization code, the symmetric/antisymmetric flutter velocities should be calculated automatically.

As to the optimization algorithm, the Complex Method which is originally proposed by Box⁶⁾ is employed. Applicability of the complex method to the aeroelastic tailoring of the high aspect-ratio transport type wings are extensively examined in Ref. 5. The complex method can handle multiple (inequality type) constraints without recourse to gradients. According to our experiences⁵⁾ in the aeroelastic tailoring study of the high aspect-ratio transport type wings, the complex method is very effective and robust in finding the optimum fiber orientation angles and the thickness distributions of the upper/lower skin panels of the wing box, while the deficiency of the method is that the rate of convergence of the objective function degrades rapidly with increasing number of design variables. Therefore, it is indispensable to reduce the number of design variables as small as possible when we apply the complex method to the aeroelastic tailoring. (See Refs. (5), (6), (8) for the detailed procedure of the complex method.)

In Fig. 1, the planform of the arrow wing model, for which the present design study is performed, is shown. (The further details of the model specification will be given in the next section.) The hatched part of the planform shown in Fig. 1 indicates the wing box location. Fig. 2 shows the arrangement of ribs and spars, and it also shows the FEM grids on the upper and lower skin panels. The total 670 triangular elements are used for the present FEM analyses. In order to reduce the number of the design variables in the optimization process, the upper/lower skin panels are divided into 7 blocks for each panels, respectively, as shown in Fig. 3, and the thickness of the skin within each block is assumed to be the same. It is also assumed that the laminate construction of the upper/lower skin panels is symmetric and the thickness of each layer having different fiber orientation angle is the

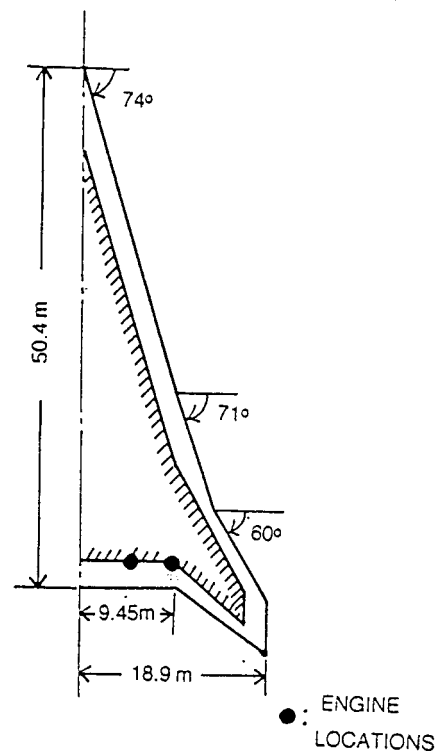


Fig. 1 Planform of Arrow Wing Model

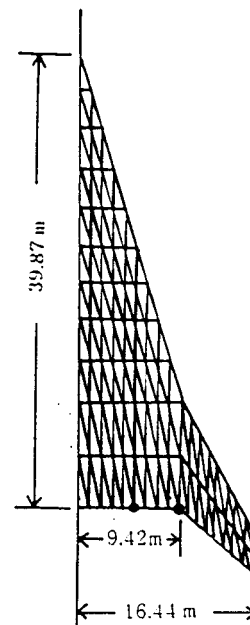


Fig. 2 Finite Element Grid

same for each other. As to the spars and ribs, the several elements which seems to be sensitive to the static strength and stiffness are selected as the design variables as shown later. In addition to this, the laminate constructions of the spars and ribs are assumed to be quasi-isotropic.

Thus, the following 25 design variables are selected:

- (a) The thickness of each block of the upper/lower skin panels (the number of design variable: $7 \times 2 = 14$)
- (b) The fiber orientation angles of the upper/lower skin panels (2)
- (c) The thickness of the fore- and hind-spars of the inboard wing (2)
- (d) The thickness of the fore- and hind-spars of the outboard wing (2)
- (e) The thickness of the spars other than (c) and (d) (1)
- (f) The thickness of the rib at the span station where the inboard engine is located (1)
- (g) The thickness of the rib at the span station where the outboard engine is located (1)
- (h) The thickness of the rib at the tip station of the wing box (1)
- (i) The thickness of the rib other than (f), (g) and (h) (1)

Although the total 25 design variables mentioned above is employed for the present study, the design variables up to 34 (the maximum number of blocks up to 10 for each upper/lower skin panels and the maximum number of fiber orientation angle up to 5) can be taken in the present optimization code.

The objective function is the structural weight of the wing box, namely, the total sum of the weights of the upper/lower skin panels, spar materials and ribs.

The constraints are the static strength, the symmetric/antisymmetric flutter velocities and the minimum gauges for the upper/lower skin panels,

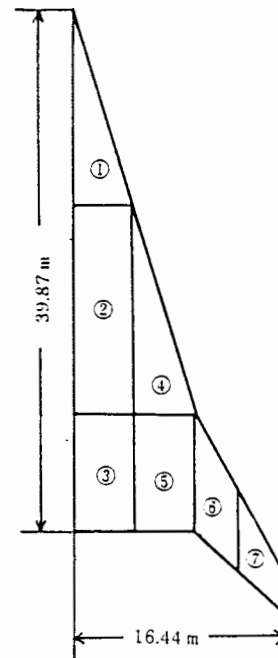


Fig. 3 Zoning of Upper/Lower Skin Panels

the spars and ribs. Tasi-Wu failure criterion⁹⁾ is employed to identify the structural failure.

3. Results and Discussions

As an example of the application of the present optimization code, the design study has been performed of an arrow wing configuration shown in Fig. 1. The length of the root chord is 50.4 m and the semispan length is 18.9 m. The leading edge sweep angles of the inner and outer wings are 74° and 60° , respectively. The full-span wing area is about 830 m^2 and the aspect ratio is 1.61. The airfoil section is 3 percent thick circular-arc. The engine mass is assumed to be 6,500 Kg for each of the four engines. The engines are expressed by the concentrated masses at the locations indicated in Fig. 1. For the full fuel condition, which is the most critical for flutter, 200,000 Kg of the fuel mass is assumed. The maximum gross take-off mass is assumed to be 374,500 Kg. Therefore the zero fuel mass becomes 174,500 Kg. The structural materials used in the present study is Graphite/PEEK (APC2), whose material properties are $E_L = 134 \text{ GPa}$, $E_T = 8.90 \text{ GPa}$, $\nu_{LT} = 0.28$, and $G_{LT} = 5.10 \text{ GPa}$.

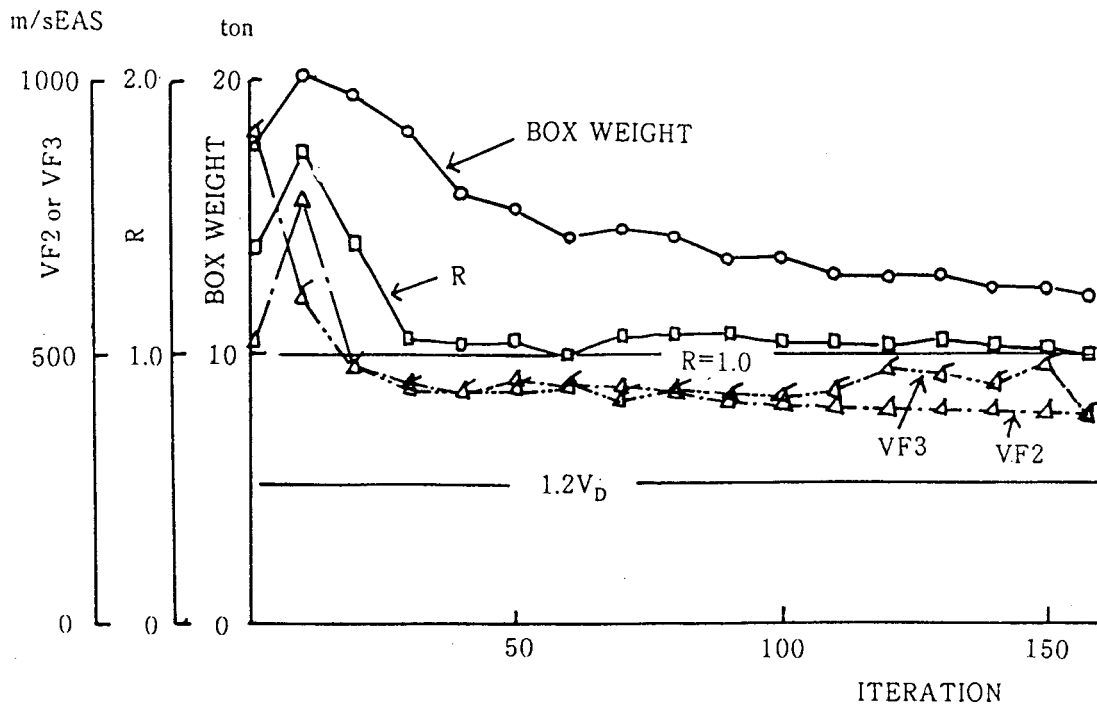


Fig. 4 Convergence Histories of the Box Weight, Strength Ratio and Symmetric/Antisymmetric Flutter Velocities during Optimization Process

The minimum weight design is performed under the following design conditions (inequality constraints):

a) Static Strength

The strength requirement is to sustain 2.5g load of the maximum take off gross weight which corresponds with 9.175×10^6 N. This static load can be realized at $M=0.90$ and $\alpha=5.1^\circ$. The load distributions calculated by using DLM is applied at each node point of the FEM grid.

b) Flutter Velocity Requirement

The symmetric/antisymmetric flutter velocities should clear $1.2 V_D=259$ m/s EAS at $M=0.90$.

c) Minimum Gauges

Since the laminate construction of the upper/lower skin panels of the present model is assumed to be $(\beta_1:50\%; \beta_2:50\%)_S$ where β_1 and β_2 are the fiber orientation angles (design variables), the minimum gauge for the upper/lower skin panels is taken to be 0.52 mm.

As to the minimum gauge for the spars and ribs, 1.04 mm is assumed since the laminate constructions of them are quasi-isotropic.

In Fig. 4, the convergence histories of the wing box structural weight (the objective function), the strength ratio R , the symmetric (VF2) and antisymmetric (VF3) flutter velocities during optimization process are plotted. The value of the wing box weight has converged to 12.148 ton after 158 iterations. As seen from the figure, the strength ratio R has reached to 1.0 at the optimum point, while the flutter velocities at the optimum point are $VF_2=387$ m/s EAS and $VF_3=388$ m/s EAS, that are considerably higher than $1.2 V_D=259$ m/s EAS. This fact suggests that the structure obtained by the present optimum design is strength critical rather than flutter critical.

The total wing box structural weight of 12.148 ton is composed from 3.656 ton of the upper/lower skin panels, 6.604 ton of the spar materials and 1.888 ton of the ribs. The optimum fiber orientation angles and the thickness distributions of the upper/lower skin panels are shown in Fig. 5. The 12.148 ton of the wing box

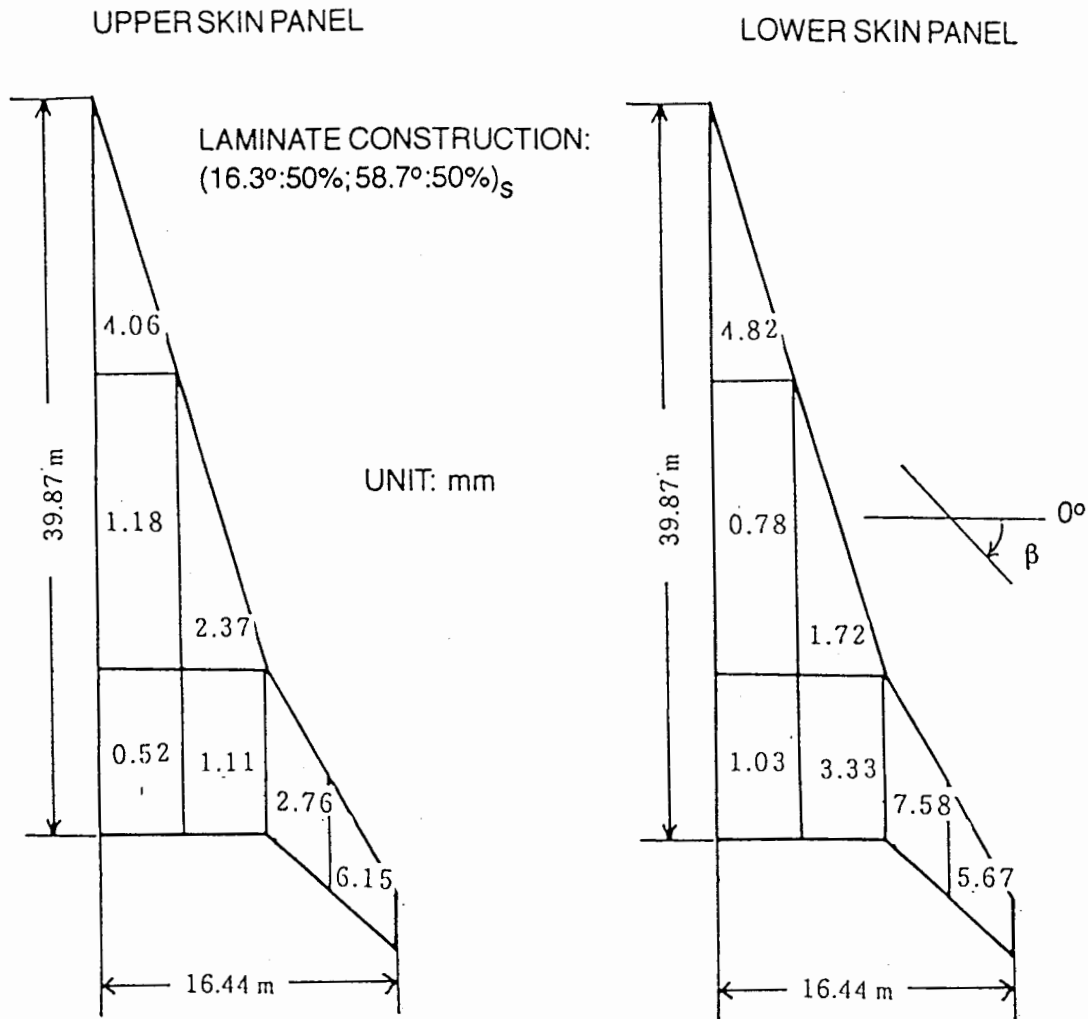


Fig. 5 Fiber Orientation Angles and Thickness Distributions of Upper/Lower Skin Panels

structural weight obtained by the present optimum design is about 19% reduction of the corresponding wing box structural weight of our previous design¹⁰), which was obtained by the trial and error design under the same design conditions.

In Figs. 6a and 6b, the symmetric and antisymmetric natural vibration mode shapes and frequencies of the present optimized structure are shown, respectively. It should be noted that the first three modes are the rigid body modes, namely, $f_1=f_2=f_3=0$ and that only the elastic modes are shown in the figures.

As already mentioned, the structural weight reduction attained by the present optimization is about 19% compared with our previous trial and error design. When we notice that the present

optimized model is strength critical rather than flutter critical, it could be said that the aeroelastic tailoring might be more effective than the present example if we apply the present code to the arrow wing model which is flutter critical rather than strength critical.

4. Concluding Remarks

A preliminary design code for aeroelastic tailoring of an arrow wing supersonic cruise configuration has been developed. A direct search method, which does not depend on the derivatives of the objective and constraint functions, is employed to find the optimum fiber orientation angles and thickness distributions of the upper and lower skin panels, and to find the optimum thickness of the spar and rib materials of the wing box structure for the minimum weight design under the multiple constraints. The static

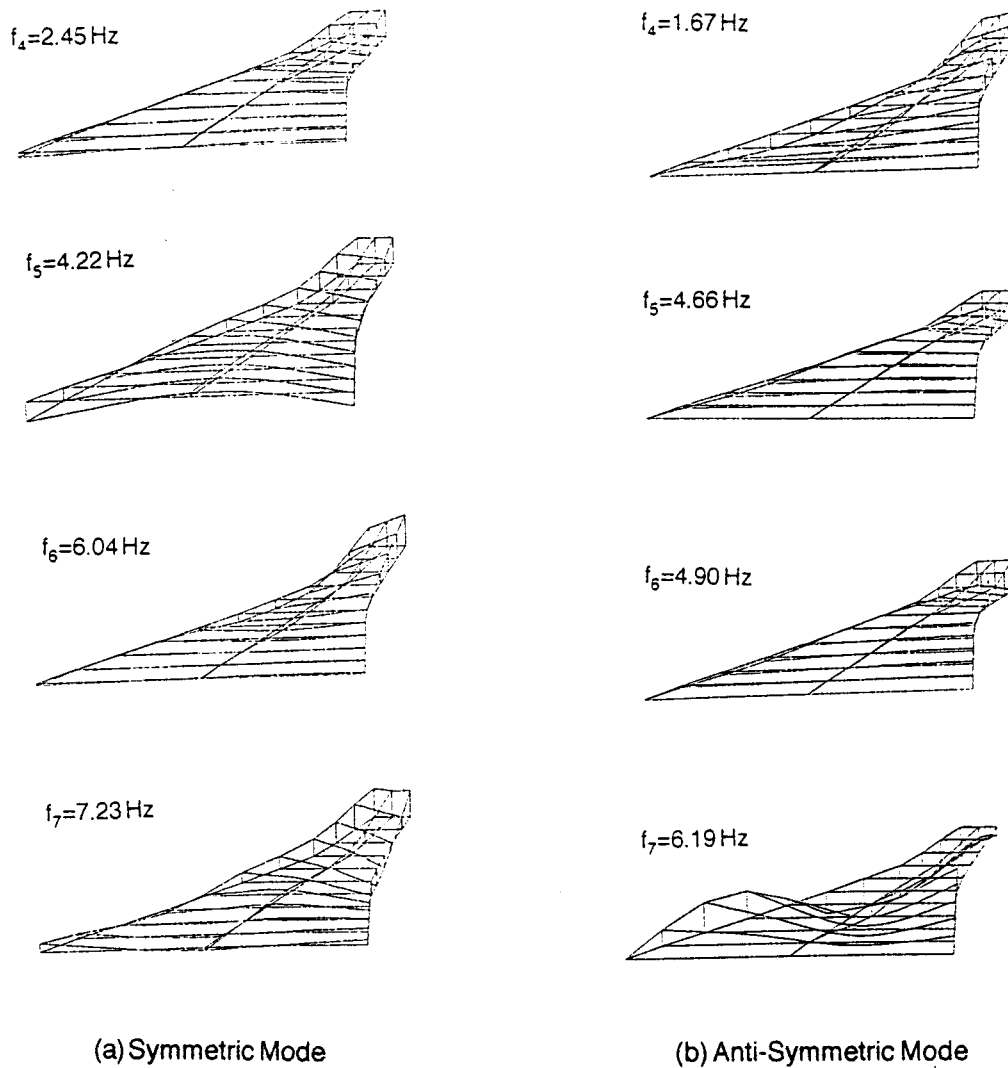


Fig. 6 Natural Vibration Mode Shapes and Frequencies of Optimum Designed Structure

strength, symmetric and antisymmetric flutter velocities are taken into account at the same time as the constraints. The code is applied to a typical arrow wing configuration to demonstrate its capabilities. It has been shown that the 19% reduction of the structural weight can be attained by the optimization compared with our previous trial and error design obtained under the same design conditions.

References

1. Bhatia, K. G. and Wertheimer, J., "Aeroelastic Challenges for a High Speed Civil Transport," AIAA-93-1478-CP, 1993.

2. Turner, M. J. and Grande, D. L., "Study of Metallic Structural Design Concepts for an Arrow Wing Supersonic Cruise Configuration," NASA Contractor Report 2743, Dec. 1977.

3. Isogai, K., Ejiri, H., Kukuchi, T., Yamane, K., Kumakura, I., Sotozaki, T., Minegishi, M., and Noguchi, Y., "Effects of an Optimized Fiber Orientation on Transonic Flutter Characteristics of a High-Aspect-Ratio Composite Wing," TR-930, National Aerospace Laboratory, Japan, May 1987.

4. Isogai, K., "Transonic Flutter/Divergence Characteristics of Aeroelastically Tailored and Non-Tailored High Aspect-Ratio Forward Swept Wings," *Journal of Fluids and Structures*, 6, 1992, pp. 525-537.
5. Isogai, K., "Direct Search Method to Aeroelastic Tailoring of a Composite Wing under Multiple Constraints," *Journal of Aircraft*, Vol.26, No. 12, Dec. 1989. pp. 1076-1080.
6. Box, M.J., "A New Method of Constrained Optimization and a Comparison with Other Methods," *Computer Journal*, Vol. 8, 1965, pp. 42-52.
7. Albano, E. and Rodden, W. P., "A Doublet-Lattice Method for Calculating Lift Distributions on Oscillating Surfaces in Subsonic Flows," *AIAA Journal* Vol. 7, Feb. 1969, pp.279 ~ 285.
8. Beveridge, G.S.G. and Schechter, R.S. *Optimization, Theory, and Practice*, Chemical Engineering Series, McGraw-Hill, New York, 1970, pp. 453-456.
9. Tasi, S. W. and Wu, E. M., "A General Theory of Strength for Anisotropic Materials," *Journal of Composite Materials*, Vol. 5, Jan. 1971, pp. 58-80.
10. Isogai, K., "Study on Transonic Flutter Characteristics of an Arrow Wing Configuration," *Proceedings of CEAS International Forum on Aeroelasticity and Structural Dynamics*, June 1997, pp. 87-95.

Evolutionary Computation of Supersonic Wing Shape Optimization

Shigeru Obayashi

Department of Aeronautics and Space
Engineering, Tohoku University

Aoba-yama 01, Sendai, Japan 980-8579

Daisuke Sasaki

Yukihiro Takeguchi

Abstract

This paper discusses design optimization of a wing for supersonic transport (SST) using Multiple Objective Genetic Algorithm (MOGA). Three objective functions are used to minimize the drag for supersonic cruise, the drag for transonic cruise and the bending moment at the wing root for supersonic cruise. The wing shape is defined by in total of 66 design variables. An Euler flow code is used to evaluate supersonic performance, and a potential flow code is used to evaluate transonic performance. To reduce the total computational time, flow calculations are parallelized on NEC SX-4 computer using 32 PE's. The detailed analysis of the resulting Pareto front suggests a renewed interest in the arrow wing planform for the supersonic wing.

1 INTRODUCTION

To respond future increase of air traffic demand, development of next generation supersonic transport is considered worldwide. Aerodynamic design of such aircraft must account for drag reduction as well as sonic boom minimization. However, drag reduction is in conflict with sonic boom minimization. Since acceptability of supersonic transport is very sensitive to the sonic boom over populated areas, one of the design choices is to limit supersonic flight over sea and to have transonic flight over land. Although such decision excludes the sonic boom from the design consideration, the design is now faced with transonic performance of the aircraft.

This paper considers multipoint aerodynamic optimization of a wing shape for supersonic aircraft both at a supersonic cruise condition and at a transonic cruise condition. Aerodynamic drag will be minimized at both cruise conditions under lift constraints. Aerodynamic optimization of the wing planform, however, drives the wing to have an impracticably large aspect ratio. Therefore, minimization of the wing root bending moment is added as a third design objective.

The present multipoint design problem can be regarded as multiobjective (MO) optimization. Solutions to MO

problems are often computed by combining multiple criteria into a single criterion according to some utility function. In many cases, however, the utility function is not well known prior to the optimization process. The whole problem should then be treated with non-commensurable objectives. MO optimization seeks to optimize the components of a vector-valued objective function. Unlike single objective optimization, the solution to this problem is not a single point, but a family of points known as the Pareto-optimal set.

By maintaining a population of solutions, Genetic Algorithms (GA) can search for many Pareto-optimal solutions in parallel. This characteristic makes GAs very attractive for solving MO problems. As a solver for MO problems, the following two features are desired: 1) the solutions obtained are Pareto-optimal and 2) they are uniformly sampled from the Pareto-optimal set. To achieve these, MOGAs have successfully been introduced by Fonseca and Fleming, 1993.

Furthermore, it was shown that the so-called best- N selection helps to find the extreme Pareto solutions (Obayashi, Takahashi and Takeguchi, 1998). The best- N selection picks up the best N individuals among N parents and N children for the next generation similar to CHC (Eshelman, 1991). The extreme Pareto solutions are the optimal solutions of the single objectives. By examining the extreme Pareto solutions, quality of Pareto solutions can be measured. The present MO problem will be solved by using MOGA coupled with the best- N selection.

2 APPROACH

In GAs, the natural parameter set of the optimization problem is coded as a finite-length string. Traditionally, GAs use binary numbers to represent such strings: a string has a finite length and each bit of a string can be either 0 or 1. For real function optimization, however, it is more natural to use real numbers. The length of the real-number string corresponds to the number of design variables.

2.1 CROSSOVER AND MUTATION

A simple crossover operator for real number strings is the average crossover (Davis, 1990) which computes the

arithmetic average of two real numbers provided by the mated pair. In this paper, a weighted average is used as

$$\begin{aligned} \text{Child1} &= \text{ran1} \cdot \text{Parent1} + (1 - \text{ran1}) \cdot \text{Parent2} \\ \text{Child2} &= (1 - \text{ran1}) \cdot \text{Parent1} + \text{ran1} \cdot \text{Parent2} \end{aligned} \quad (1)$$

where Child1,2 and Parent1,2 denote encoded design variables of the children (members of the new population) and parents (a mated pair of the old generation), respectively. The uniform random number ran1 in $[0,1]$ is regenerated for every design variable.

Mutation takes place at a probability of 20% (when a random number satisfies $\text{ran2} < 0.2$) initially and the rate is going to decline linearly during the evolution. Equations (1) will then be replaced by

$$\begin{aligned} \text{Child1} &= \text{ran1} \cdot \text{Parent1} + (1 - \text{ran1}) \cdot \text{Parent2} + m \cdot (\text{ran3} - 0.5) \\ \text{Child2} &= (1 - \text{ran1}) \cdot \text{Parent1} + \text{ran1} \cdot \text{Parent2} + m \cdot (\text{ran3} - 0.5) \end{aligned} \quad (2)$$

where ran2 and ran3 are also uniform random numbers in $[0,1]$ and m determines the range of possible mutation.

2.2 MULTIOBJECTIVE PARETO RANKING

To search Pareto-optimal solutions by using MOGA, the ranking selection method (Goldberg, 1989) can be extended to identify the near-Pareto-optimal set within the population of GA. To do this, the following definitions are used: suppose \mathbf{x}_i and \mathbf{x}_j are in the current population and $\mathbf{f} = (f_1, f_2, \dots, f_q)$ is the set of objective functions to be maximized,

1. \mathbf{x}_i is said to be dominated by (or inferior to) \mathbf{x}_j , if $\mathbf{f}(\mathbf{x}_i)$ is partially less than $\mathbf{f}(\mathbf{x}_j)$, i.e., $f_1(\mathbf{x}_i) \leq f_1(\mathbf{x}_j) \wedge f_2(\mathbf{x}_i) \leq f_2(\mathbf{x}_j) \wedge \dots \wedge f_q(\mathbf{x}_i) \leq f_q(\mathbf{x}_j)$ and $\mathbf{f}(\mathbf{x}_i) \neq \mathbf{f}(\mathbf{x}_j)$.
2. \mathbf{x}_i is said to be non-dominated if there doesn't exist any \mathbf{x}_j in the population that dominates \mathbf{x}_i .

Non-dominated solutions within the feasible region in the objective function space give the Pareto-optimal set.

Let's consider the following optimization:

$$\begin{aligned} \text{Maximize:} \quad & f_1 = x, \quad f_2 = y \\ \text{Subject to:} \quad & x^2 + y^2 \leq 1 \quad \text{and} \quad 0 \leq x, y \leq 1 \end{aligned}$$

The Pareto front of the present test case becomes a quarter arc of the circle $x^2 + y^2 = 1$ at $0 \leq x, y \leq 1$.

Consider an individual \mathbf{x}_i at generation t (Fig. 1) which is dominated by p_i^t individuals in the current population. Following Fonseca and Fleming (1993), its current position in the individuals' rank can be given by

$$\text{rank}(\mathbf{x}_i, t) = 1 + p_i^t \quad (3)$$

All non-dominated individuals are assigned rank 1 as shown in Fig. 1. The fitness values are reassigned

according to rank as an inverse of their rank values. Then the SUS method (Baker, 1987) takes over with the reassigned values.

2.3 FITNESS SHARING

To sample Pareto-optimal solutions from the Pareto-optimal set uniformly, it is important to maintain genetic diversity. It is known that the genetic diversity of the population can be lost due to the stochastic selection process. This phenomenon is called the random genetic drift. To avoid such phenomena, the niching method has been introduced (Goldberg, 1989).

The model used here is called fitness sharing (FS). A typical sharing function is given by Goldberg (1989). The sharing function depends on the distance between individuals. The distance can be measured with respect to a metric in either genotypic or phenotypic space. A genotypic sharing measures the interchromosomal Hamming distance. A phenotypic sharing can further be classified into two types. One measures the distance between the decoded design variables. The other, on the other hand, measures the distance between the designs' objective function values. Here, the latter phenotypic sharing is employed since we seek a global tradeoff surface in the objective function space.

This scheme introduces new GA parameters, the niche size σ_{share} . The choice of σ_{share} has a significant impact on the performance of MOGAs. Fonseca and Fleming (1993) gave a simple estimation of σ_{share} in the objective function space as

$$N \sigma_{\text{share}}^{q-1} = \frac{\prod_{i=1}^q (M_i - m_i + \sigma_{\text{share}}) - \prod_{i=1}^q (M_i - m_i)}{\sigma_{\text{share}}} = 0 \quad (4)$$

where N is a population size, q is a dimension of the objective vector, and M_i and m_i are maximum and minimum values of each objective, respectively. This formula has been successfully adapted here. Since this formula is applied at every generation, the resulting σ_{share} is adaptive to the population during the evolution process. Niche counts can be consistently incorporated into the fitness assignment according to rank by using them to scale individual fitness within each rank.

3 RESULTS

Flow conditions are $M_\infty = 2.0$ and $C_L = 0.1$ for supersonic cruise and $M_\infty = 0.9$ and $C_L = 0.15$ for transonic cruise. The supersonic inviscid drag to be minimized is evaluated by using an Euler flow solver (Obayashi et al. 1998). The transonic inviscid drag is evaluated by using a full potential flow solver (Jameson and Caughey, 1977). The bending moment is evaluated by directly integrating the pressure load at the supersonic cruise condition.

Design variables are illustrated in Figs. 2-5. The wing planform is determined by six design variables as shown in Fig. 2. The variable ranges are summarized in Table 1. A wing area is fixed at $S = 60$. A chord length at the wing tip is automatically determined due to the given wing area. An airfoil shape is defined by its thickness distribution and camber line. The thickness distribution is given by a Bezier curve shown in Fig. 3. The maximum thickness is constrained from 3 % to 4 % chord lengths. The location of the maximum thickness is also constrained from 15 % to 70 % chordwise locations. The thickness distributions are defined at the wing root, kink and tip. They are linearly interpolated in the spanwise direction. The camber surfaces are defined at the inboard and outboard of the wing separately. Each surface is given by the Bezier surface using four polygons in the chordwise direction and three polygons in the spanwise direction. The resulting camber line at the wing root is shown in Fig. 4. It is concave only at the root and it becomes convex at the other spanwise locations similar to the linearized theory. Finally, the wing twist is defined by a B-spline curve as shown in Fig. 5. A monotonic variation is enforced by rearranging the polygons in numerical order in the spanwise direction. In total, 66 design variables are used.

MOGA is used as a design optimizer. Flow calculations were parallelized on 32 PE's of NEC SX-4 computer at Computer Center of Tohoku University, using the simple *Master-Slave* concept. The population size was set to 64 and 70 generations were run. To constrain the lift coefficient, three flow calculations were used per drag evaluation. The total computational time was roughly 100 hours.

Figure 6 shows the resulting Pareto solutions in the three dimensional objective function space. They form an approximate tradeoff surface. Typical planform shapes are also plotted in the figure. The extreme Pareto solutions (denoted as bending moment minimum, C_D (supersonic) minimum, C_D (transonic) minimum) have physically reasonable shapes: a very short span length (corresponding to a large taper ratio as well as a low aspect ratio) for minimizing bending moment, high aspect ratios for minimizing induced drag and larger sweep angles for minimizing wave drag. These results indicate the validity of the present optimization.

Tradeoffs between the objectives can be observed more easily in the two-dimensional projections as shown in Figs. 7 and 8. Figure 7 presents the tradeoffs between supersonic and transonic drag coefficients. The Pareto solutions are plotted in different symbols according to the aspect ratio. Lower drag coefficients are obtained from larger aspect ratios in general as suggested by the standard aerodynamic theory.

In Fig. 7, the edge of the projected Pareto surface I indicates purely aerodynamic tradeoffs between supersonic and transonic flights. This curve would be the Pareto front if only these two objectives are used. However, as shown in Fig. 6, the extreme Pareto solutions

for supersonic and transonic drag have too large aspect ratios, and thus they are impossible to be built within a reasonable structural weight. This is true for all solutions on the edge I. The other edge of the projected Pareto surface II indicates the tradeoffs between the supersonic drag and the bending moment. (Note that the bending moment is evaluated at the supersonic flight condition.) A practical wing shape is expected to appear in this region.

Figure 8 illustrates the tradeoffs between the bending moment and the supersonic drag. The edge of the projected Pareto surface forms a simple convex curve toward the lower left corner of the figure, representing the pure tradeoffs between these two objectives. The edge IV may be less interesting to aircraft designers because it indicates severe penalties in the drag with little improvements in the bending moment. On the other hand, the edge III represents more reasonable tradeoffs. The Pareto solutions are plotted in different symbols according to the taper ratio. To be on the edge III, the taper ratio of the wing should roughly be less than 0.4.

To evaluate the present Pareto solutions further, they are compared with the aerodynamic design of the supersonic wing for National Aerospace Laboratory's Scaled Supersonic Experimental Airplane (Iwamiya, 1998). NAL SST Design Team has performed the following four aerodynamic designs. The first design was a selection of a planform shape among 99 different shapes by direct comparisons. The second design was performed by the warp optimization based on the linearized theory. The third design was obtained from an inverse design to yield a natural laminar flow based on the Navier-Stokes code. The fourth design was then performed for a wing-fuselage configuration. Since the present optimization is based on the inviscid flow codes, NAL's second design is chosen for the comparison here. Its performance was evaluated by using the same codes in this study.

Figure 9 and Table 2 summarize the comparisons of six Pareto solutions with NAL's second design. It should be noted that NAL's design appears close to the edge II in Fig. 7. This indicates that the edge II represents practical solution area as well as that the warp optimization of NAL's design has a good accuracy. Six solutions were picked up so as to represent the sensitivity of the Pareto surface. The solutions A, B and C have transonic drag similar to NAL's design but their supersonic drag is in order of $A < B < C$. (The solution C and NAL's design perform alike.) To improve the supersonic performance over NAL's design, the taper ratio of the wing becomes larger and the root chord length becomes smaller. However, there is an upper limit for the taper ratio from the observation in Fig. 8.

The solutions C, D and E have supersonic drag similar to NAL's design and transonic drag in order of $E < D < C$. To improve the transonic performance over NAL's design, the aspect ratio of the wing becomes larger and the root chord length becomes smaller. However, the increase of the aspect ratio also results in the increase of the bending moment as indicated in Table 2.

Finally, the solution F is found to outperform NAL's design in all three objectives. A common geometric feature among the three solutions A, E and F is their root chord lengths shorter than the root of NAL's design. This means that they have larger taper ratios. Aerodynamic theory generally suggests an increase of the aspect ratio to improve the aerodynamic performance as mentioned before. However, the present solution A, E and F all have smaller aspect ratios than NAL's design does. The resulting shape is somehow similar to the "arrow wing" planform rather than the conventional "delta wing" planform.

The arrow wing shape was originally derived from research in the late 1950's indicating that the optimum wing planform would be a highly swept, highly tapered, arrowhead shape (Nelson, 1992). Attempts to incorporate such arrow wing shapes eventually failed due to design integration difficulties, aeroelastic problems and high structural weight. Studies from 1970 to 80's then resulted in the "cranked arrow" wing. The cranked arrow retains the original arrow on inboard wing only. The "cranked" forward outboard wing provides more span and higher effective aspect ratio (Fig. 10). The main interest in the supersonic wing development has been an increase of the aspect ratio in compromise with the highly swept planform.

The present results suggest a new type of the arrow wing planform having a larger taper ratio instead of a larger aspect ratio. This means a less tapered arrow wing in contrast to the original, highly tapered arrow wing as compared in Fig. 10. In the present MOGA result, either the cranked arrow or the modified delta did not survive as a Pareto solution. The original arrow wing was abandoned due to the structural problems. After 40 years of the development in the structural dynamics and materials, the present arrow wing may be interesting for further studies.

4 CONCLUSIONS

The multipoint design optimization of a wing for SST has been performed by using MOGA. The three objective functions are used to minimize the drag for supersonic cruise, the drag for transonic cruise and the bending moment at the wing root for supersonic cruise. The wing shape is defined by in total of 66 design variables.

Physically reasonable extreme Pareto solutions were obtained from the present formulation. This indicates the validity of the present optimization. One of the Pareto solutions was found to outperform the existing design in all design objectives. The detailed analysis of the Pareto solutions suggests a new type of the arrow wing with a larger taper ratio and a smaller aspect ratio compared with the existing planform shapes.

Acknowledgments

This research was funded by Japanese Government's Grants-in-Aid for Scientific Research, No. 10305071. The

first author's research has been partly supported by Bombardier Aerospace, Toronto, Canada. The computational time was provided by Computer Center, Tohoku University. The authors would like to thank National Aerospace Laboratory's SST Design Team for providing many useful data.

References

- Baker, J. E. (1987) Reducing bias and inefficiency in the selection algorithm. *Proceedings of the Second International Conference on Genetic Algorithms*, 14-21. San Mateo, Calif.: Morgan Kaufmann Publishers.
- Davis, L. (1990) *Handbook of Genetic Algorithms*, Reinhold, New York: Van Nostrand.
- Eshelman, L. J. (1991) The CHC Adaptive Search Algorithm: How to Have Safe Search When Engaging in Nontraditional Genetic Recombination. *Foundations of Genetic Algorithms*, 265-283. San Mateo, Calif.: Morgan Kaufmann Publishers.
- Fonseca, C. M. and Fleming, P. J. (1993) Genetic algorithms for multiobjective optimization: formulation, discussion and generalization. *Proceedings of the 5th International Conference on Genetic Algorithms*, 416-423. San Mateo, Calif.: Morgan Kaufmann Publishers.
- Goldberg, D. E. (1989) *Genetic Algorithms in Search, Optimization & Machine Learning*. Reading, Mass.: Addison-Wesley.
- Iwamiya, T. (1998) NAL SST Project and Aerodynamic Design of Experimental Aircraft, *Proceedings of the Fourth ECCOMAS Computational Fluid Dynamics Conference*, Vol. 2, 580-585. Chichester, UK: John Wiley & Sons.
- Jameson, A. and Caughey, D. A. (1977) A Finite Volume Method For Transonic Potential Flow Calculations. AIAA paper 77-677. Reston, VA: American Institute of Aeronautics and Astronautics.
- Nelson, C. P. (1992) Effects of Wing Planform on HSCT Off-Design Aerodynamics. AIAA paper 92-2629-CP. Reston, VA: American Institute of Aeronautics and Astronautics.
- Obayashi, S., Nakahashi, K., Oyama, A. and Yoshino, N. (1998) Design Optimization of Supersonic Wings Using Evolutionary Algorithms. *Proceedings of the Fourth ECCOMAS Computational Fluid Dynamics Conference*, 575-579. Chichester, UK: John Wiley & Sons.
- Obayashi, S., Takahashi, S. and Takeguchi, Y. (1998) Niching and Elitist Models for MOGAs. *Parallel Problem Solving from Nature - PPSN V*, 260-269, Lecture Notes in Computer Science. Berlin, Germany: Springer.

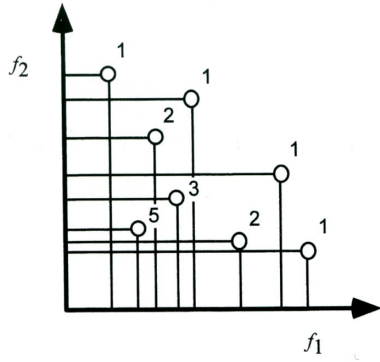


Figure 1: Pareto Ranking Method

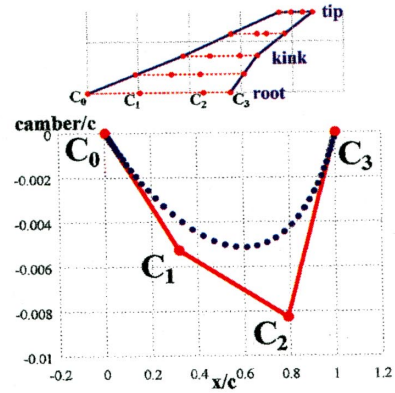


Figure 4: Wing Camber Definition

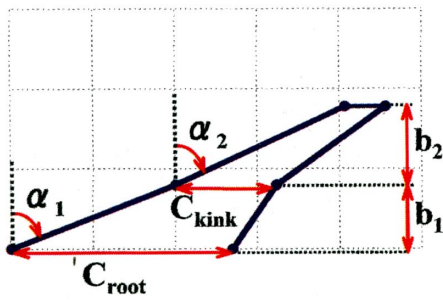


Figure 2: Wing Planform Definition

Table 1: Variable Domain for Planform Definition

Variable	Range
α_1	35 - 70 deg
α_2	35 - 70 deg
C_{root}	10 - 20
C_{kink}	3 - 5
b_1	2 - 7
b_2	2 - 7

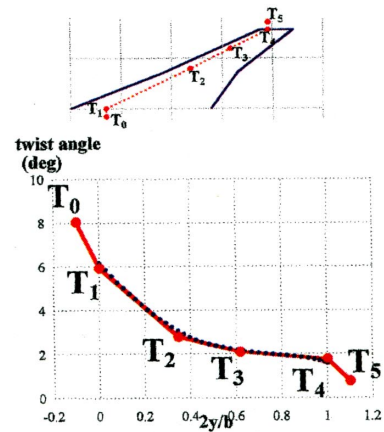


Figure 5: Wing Twist Definition

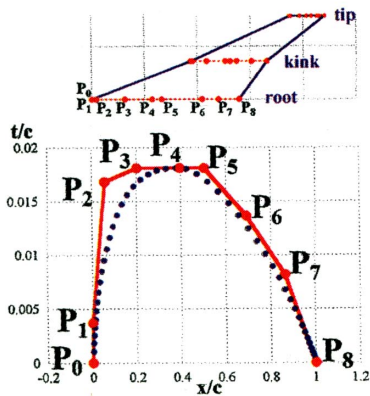


Figure 3: Wing Thickness Definition

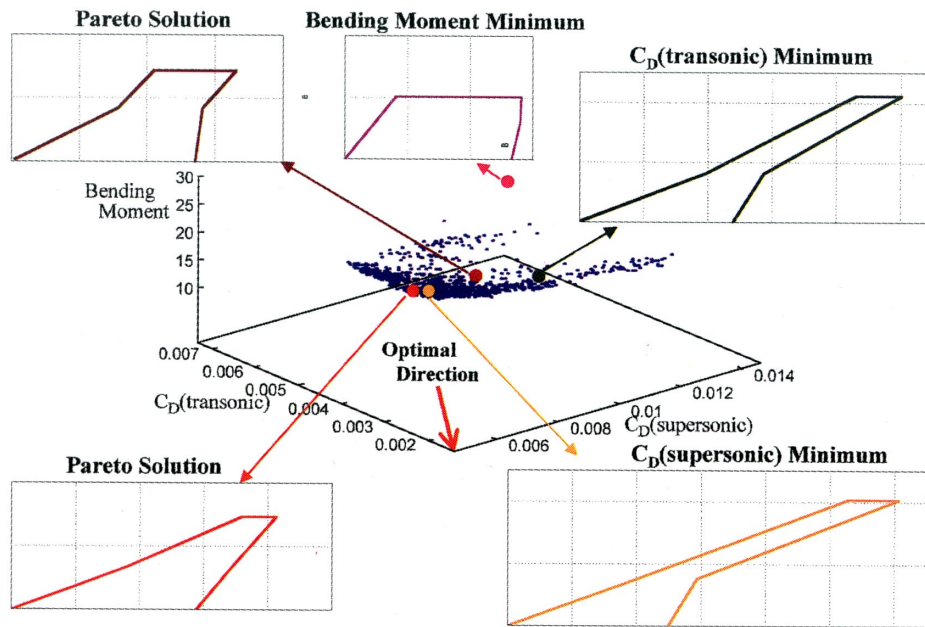


Figure 6: Pareto Front in the Objective Function Space and Typical Planform Shapes

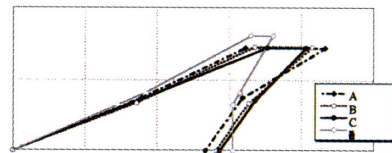
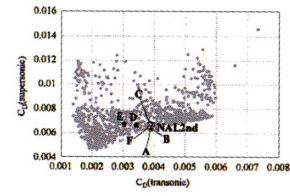
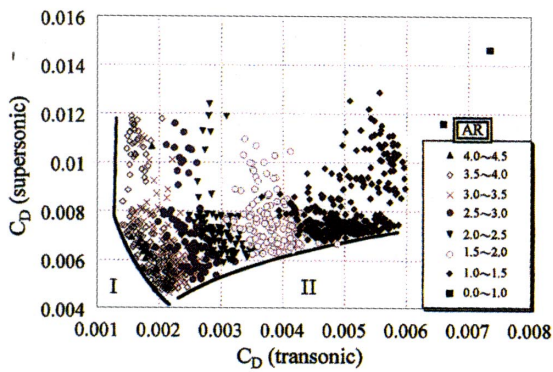
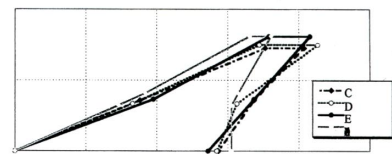
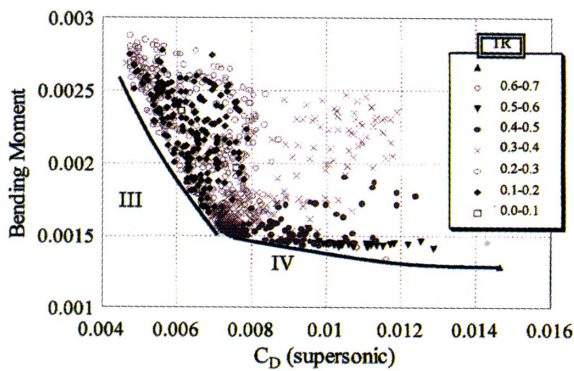
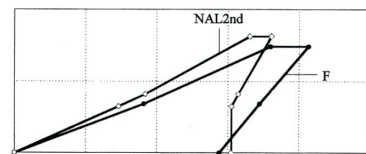


Figure 7: Projection of Pareto Front to Supersonic and Transonic Drag Tradeoffs

a) Pareto Solutions at Nearly Constant Transonic Drag



b) Pareto Solutions at Nearly Constant Supersonic Drag



c) Pareto Solution Better Than NAL Design in All Three Objectives

Figure 8: Projection of Pareto Front to Bending Moment and Supersonic Drag Tradeoffs

Figure 9: Comparison of Pareto Solutions with NAL Inviscid Design

Numerical Flutter Simulation -Application to Structural Design of Main Surface of SST Experimental Aircraft-

Jiro NAKAMICHI¹ and Hamid Reza KHEIRANDISH²

¹National Aerospace Laboratory, Tokyo, Japan jiro@nal.go.jp

²Research Center of Computational Mechanics, Inc, Tokyo, Japan hamid@rccm.co.jp

Introduction

The estimation of flutter boundary of high-speed aircraft plays an essential role in the structural design concepts and parameters. Its role gets more importance in the case of supersonic transport because relatively thin wing-sections or control surfaces are necessarily used for these configurations. Therefore an interactive relation between design parameters and flutter boundary suggested by experiment or CFD is highly requested at primarily steps of structural design. With remarkable progresses in computing speed and numerical methods, the CFD is now of much current interest to do this request. Linear methods can predict the flutter boundary with relatively high accuracy in all the flows except for transonic region where the flow is highly nonlinear or when the flow is highly separated. In these regions the nonlinear methods should be employed for accurate prediction.

The authors have developed a CFD Code to numerically simulate unsteady coupled fluid-structure problems based on Navier-Stokes/Euler equations. This code has been used and verified in several large scale problems such as 3-D high aspect ratio wings^{1,2}, and Arrow wing configuration³. This report describes numerical simulation of aeroelastic responses of the NAL Supersonic Transport(SST) experimental aircraft around transonic region. The unsteady Euler equations coupled with structural equations were solved to obtain flutter boundary of SST. The results were obtained either with and without structural damping and were compared with linear theory results when available. The aileron flutter, like the linear theory, was found the most critical one for this configuration. The flutter boundaries are estimated lower than those obtained by the linear theory for the range of Mach number 0.6-1.0

Governing Equations

The computation is based on unsteady Euler equations for governing flow field and a modal approach form of equations for structural side(Eqs. 1). These equations can be described in non-dimensional form as

$$\frac{\partial \hat{Q}}{\partial \bar{a}} + \frac{\partial \hat{r}}{\partial \bar{\xi}} + \frac{\partial \hat{g}}{\partial \bar{\eta}} + \frac{\partial \hat{e}}{\partial \bar{\zeta}} = 0$$

$$m_i \ddot{q}_i + k_i^2 m_i q_i = \bar{Q} \iint_S (-C_p n_z) \Phi_i dS \quad (1)$$

where q_i are generalized coordinates: Φ_i , m_i and k_i are the natural modes, generalized masses and natural reduced frequencies corresponding to the i 'th mode, respectively. \bar{Q} is the nondimensionalized dynamic pressure and n_z is the z-direction component of normal vector to the wing surface. The double integration symbol implies the integration over the whole aircraft surface. The structural equations of motion are derived by the assumption that the deformation of the body under consideration can be described by superposing the orthogonal natural vibration modes weighted with generalized displacements. For more information on obtaining governing equations see Ref 4-5. The integration of governing equations are implemented using a second order upwind TVD scheme^{6,7} for the flow equations and Wilson's θ implicit method⁸ for the structural ones. The procedure of unsteady computations can be carried out as follows:

1. Compute steady state solution at a given Mach number
2. Assume dynamic pressure
3. Assume initial value for some of generalized velocities
4. Solve structural equations and update surface geometry and corresponding surfaces and internal grids
5. Update flow field solution
6. Repeat steps 4 and 5 for many cycles and save time history of generalized coordinates.

To find flutter boundary at a given Mach number, repeat steps 3 to 6 for a range of dynamic pressures and find stable and unstable regions by analyzing mode responses.

Characteristics of Experimental Model

A plan-view of this model is given in Figure 1. The dimensions and typical parameters of the are as follows; Fuselage length 11.5m, wing root chord-length 4.2m, span length 4.72m, aspect ratio 2.1. Swept-back angles of inner and outer boards are 24° and 28.8°. The structural dynamic characteristics, natural mode shapes and frequencies of this model were found, using NASTRAN, by FHI. The flutter boundary, except at transonic regions, was also determined using linear theory. They found that the aileron flutter is the most critical one. The first 24 symmetric and anti-symmetric modes of fuselage and wings are shown in Table 1. The modes which contain aileron motion are marked by '*'.

¹Lead, Aeroelasticity, Structures Division

²Senior Eng., Technical Development

Table 1. Vibration Characteristic of Experimental Model

Mode No.	Frequency Hz	Dominant Mode Shape
1	0.0	Rigid Pitching
2	0.0	Rigid Heaving
3	0.0	Rigid Rolling
*4	8.7	FLaB, WB
5	11.5	FLaB
*6	16.5	WB-s
*7	26.0	FLaB, Aileron T-s
*8	27.4	WB-s
*9	29.8	Aileron T-s
10	30.2	Aileron T-s
11	34.1	FLaB
12	38.1	FLaB T
13	42.4	V
14	42.9	FLoB
15	47.7	H-a
16	48.7	H-s
17	56.3	W-s
18	62.5	W-a
19	67.9	W-s
20	71.0	W-a, V
21	72.2	W-s, Aileron B
22	76.9	W-s, Aileron T
23	83.0	V
24	89.1	V

F:Fuselage W:Main Surface H:Horizontal Tail V:Vertical Tail
 B:Bending T:Torsion
 Lo: Longitudinal La: Lateral -s: Symmetric -a: Anti-symmetric
 * : Mode indicated in Figures

in normal direction is of order of .005 based on the wing root chord length. The outer boundaries are put at least 15 times the wing root chord length away from the surfaces in the stream-wise and normal directions and 3 times the half-span length in span-wise direction. A schematic view of grids around the half-span of SST is shown in Fig 3.

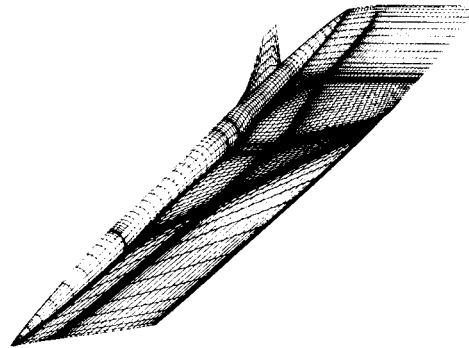


Fig 3. Grid Distributions on SST

The first 24 modes, which were found by NASTRAN, were considered in the computations. These modes contain symmetric modes as well as anti-symmetric modes. The SST responses in Mach number range 0.6 to 1.2 at several dynamic pressures with or without structural damping were found. The results are illustrated as selected generalized modes(dominant modes) vs. non-dimensional time at each Mach number and dynamic pressure to investigate the SST responses. For the sake of convenience modes marked by "*" in table 1 are only illustrated in this paper. They are mode 4: fuselage and main surface bending, mode 6: main surface symmetric bending, mode 7: fuselage bending and aileron torsion-symmetric, mode8: main surface bending-anti-symmetric, and mode 9: aileron torsion-anti-symmetric modes. The first three rigid modes are not considered here.

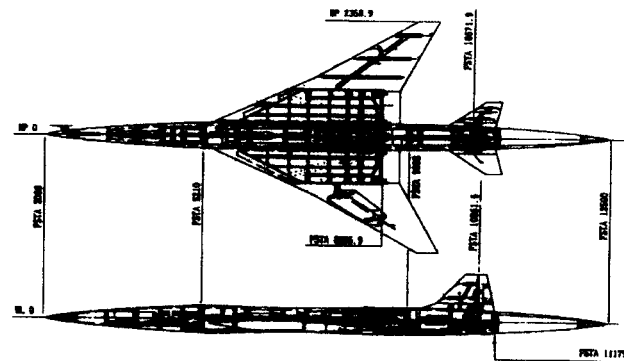


Fig 1. Plan-View of SST Experimental Model

The flight envelope of SST experimental aircraft in a frame of Altitude vs. Equivalent Air Speed (EAS) is illustrated in figure 2. This figure shows the rocket launching path and also free flight path. Our objective is to investigate that the flight path is free of flutter especially in transonic region.

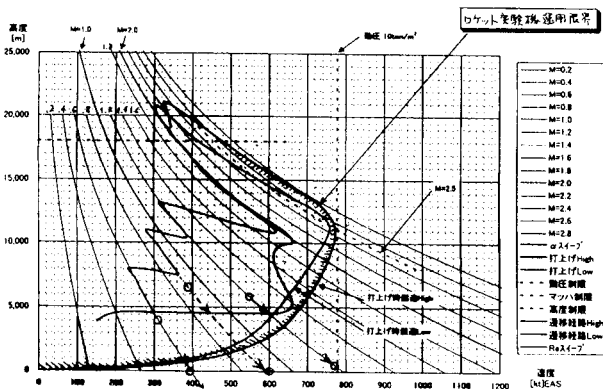


Fig 2. Flight Envelope of SST

Numerical Results and Discussions

A H-H type mesh with 126x121x80 grid points was generated around full SST configuration for these computations. The mesh generator is based on elliptic methods. The minimum size of grid

An example of steady state pressure distributions on four different semi-span stations(0.0%, 30%, 50%, 70%) at Mach number 0.9, obtained by present computation and linear theory, are given in Figure 4. The 0.0% semi-span stations, corresponds to body-symmetric line.

Hereunder unsteady numerical computation results will be shown and discussed. At all the numerical simulations, structural damping is set to 0.0 unless mentioned.

The results at Mach number 0.6, where dynamic pressures are 100kPa and 80kPa, respectively are given in figures 5-6. This figures show the time histories of some dominant generalized coordinates. It can be seen from figure 6 that only those modes which contain aileron mode(ie; mode7 and 8) will be diverged first by a 20kPa increase in dynamic pressure. Other modes show positive damping at this range of dynamic pressure.

Figure 7-9 show simulation results at Mach number 0.9. The dynamic pressures are set at 90kPa, 60kPa and 25kPa. At this Mach number simulations with structural damping equal to 0.02 were also carried out. These results are given in figures 10-11. As the previous case, modes 7 and 8 are the modes which show instability first by an increase in dynamic pressure. The inclination is similar for the case with structural damping 0.02, too. The critical dynamic pressure(the dynamic pressure at which flutter occurs) is about less than 60kPa without structural damping while it increases to 70kPa when structural damping is 0.02.

The SST response at Mach number 1.0 and dynamic pressure 90kPa is shown in figure 12. The modes 7 and 8 are already diverged at this dynamic pressure. Other modes are still show convergence.

The results at Mach number 1.2, dynamic pressures 130kPa and 100kPa are given in figures 13-14. The response is stable at 100kPa while some modes(ie; mode 7 and 8) seems to be unstable at 130kPa. The tendency of modes are similar to the previous cases..

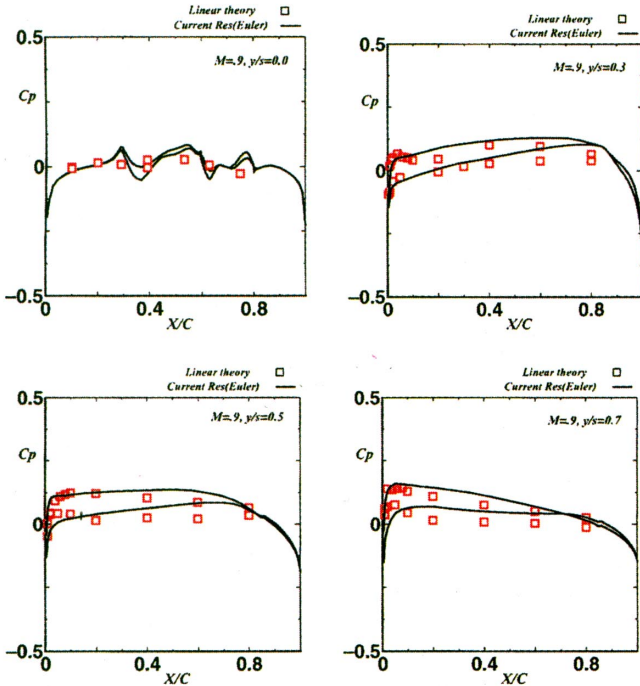


Fig 4. Steady State Pressure Distributions, M=0.9, A=0.0

Figure 15 shows the main surface flutter boundary obtained by present method and linear-theory. The vertical and horizontal axes are: equivalent air speed(EAS) and Mach number, respectively. In this figure main surface and aileron flutter boundaries obtained by linear theory are illustrated by dashed line. The triangles show the data computed by present method. The results are agreed together only at Mach number 1.2. The flutter speed obtained by present simulations are lower than those estimated by linear-theory for Mach numbers less than 0.9 A dip-like curve is obtained by present method although no shock waves were seen in all the computations.

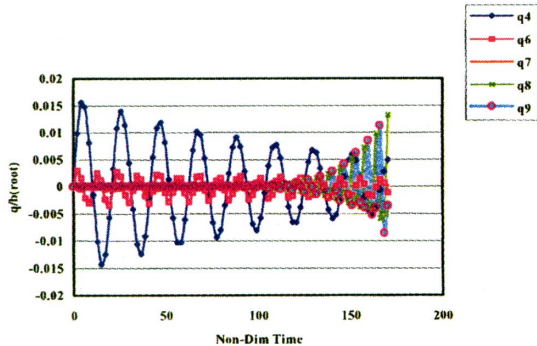


Fig.5 SST Response at Dp=100kPa, M=0.6

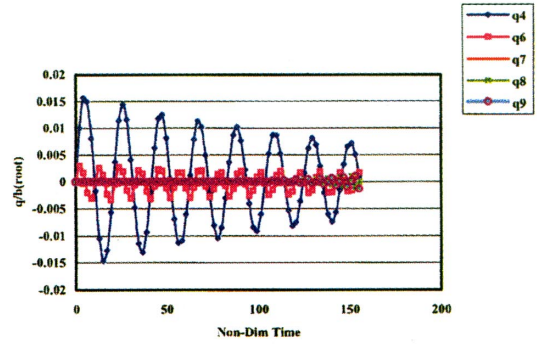


Fig.6 SST Response at Dp=80kPa, M=0.6

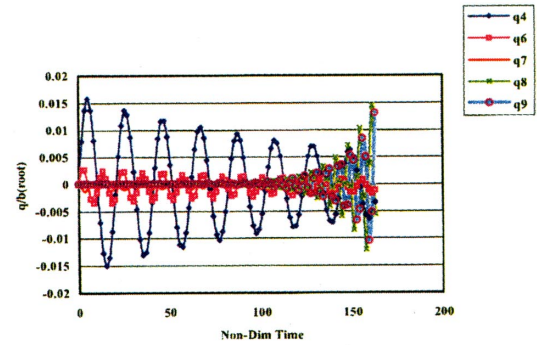


Fig. 7 SST Response at Dp=90kPa, M=0.9

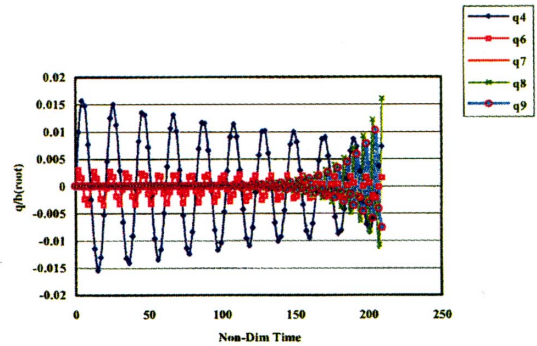


Fig. 8 SST Response at Dp=60kPa, M=0.9

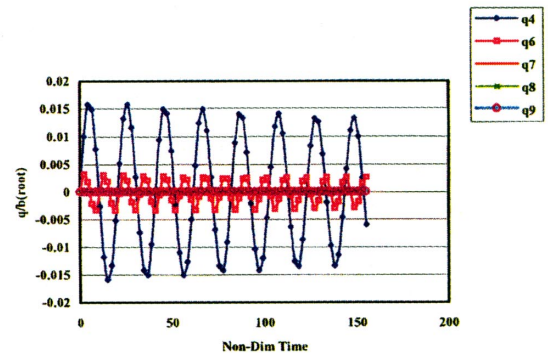


Fig.9 SST Response at Dp=25kPa, M=0.9

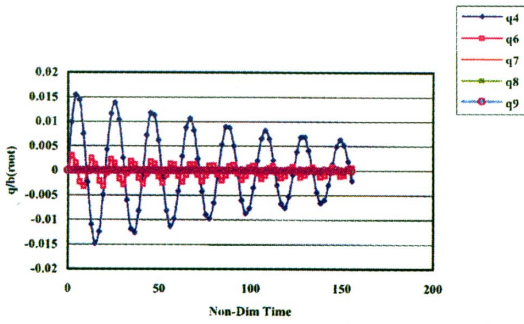


Fig.10 SST Response at $D_p=60\text{kPa}$, $M=0.9$, $g=.02$

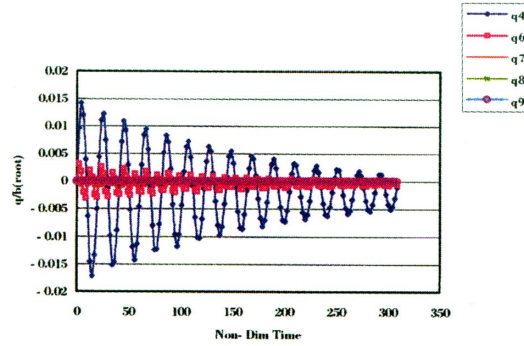


Fig.14 SST Response at $D_p=100\text{kPa}$, $M=1.2$

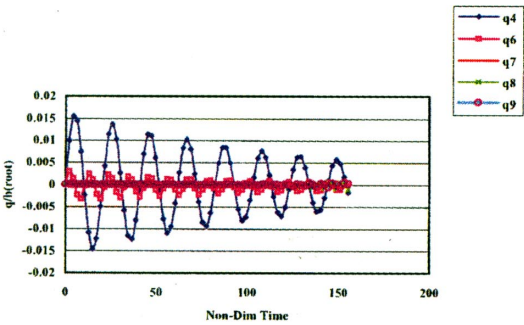


Fig. 11 SST Response at $D_p=70\text{kPa}$, $M=0.9$, $g=.02$

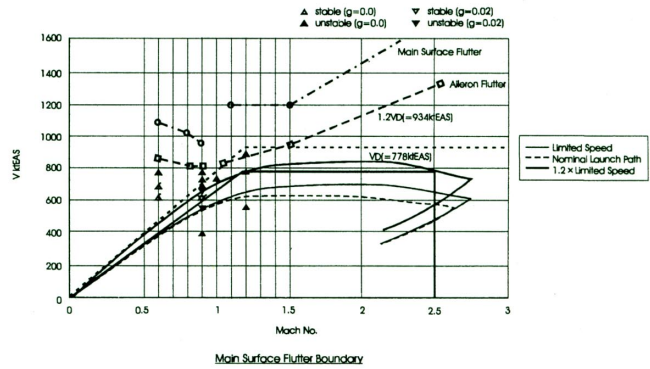


Fig 15. Main surfaces Flutter Boundaries

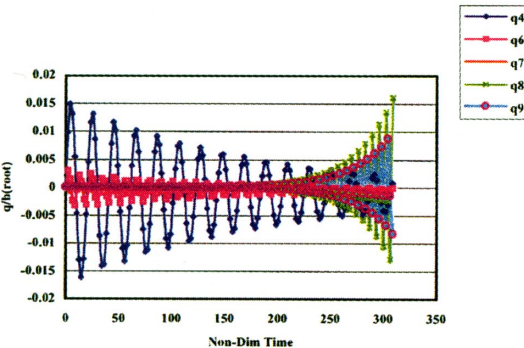


Fig. 12 SST Response at $D_p=90\text{kPa}$, $M=1.0$

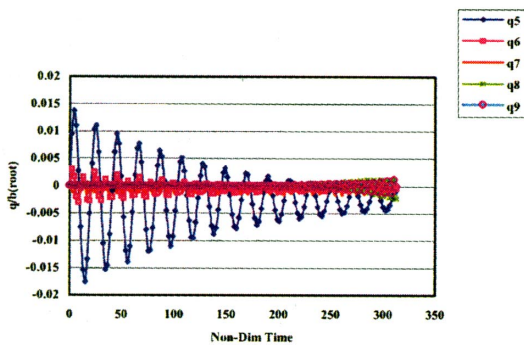


Fig. 13 SST Response at $D_p=130\text{kPa}$, $M=1.2$

Conclusion

Numerical flutter simulation of full-SST configuration has been carried out using Euler solution at transonic region. The aileron flutter was found as the most critical one. The flutter speeds obtained by the present code do not agree well with those of linear-theory except at Mach number 1.2.

The authors thank Fuji Heavy Industries for their offering the results of vibration analysis for the present studies.

REFERENCES

- [1] H. Kheirandish, G. Beppu and J. Nakamichi, Numerical Simulation of Viscous Unsteady Flow around Wings Oscillation in Elastic Modes, JSCE Symposium, Tokyo, Japan (1996)
- [2] H. Kheirandish, G. Beppu and J. Nakamichi, Computational Investigation of Wings Flutter To be published in "International Journal of Computational Fluid Dynamics, 99/10
- [3] H. Kheirandish, and J. Nakamichi, Inter-Code Validation between NAL and DLR in the Aeroelastic Simulation for SST Configuration, CEAS/ICAS/AIAA/NASA Langley International forum on Aeroelasticity and structural Dynamics (Virginia-Williamsburg), 1999/6/21-25
- [4] T.H. Pulliam and J.L. Steger, Recent Improvements in Efficiency, Accuracy, and Convergence for Implicit Approximate Factorization Algorithms, AIAA Paper 85-0360, (1985)
- [5] R.L. Bisplinghoff, H. Ashley, Principles of Aeroelasticity, Dover Pubs (1975)
- [6] H. Yee and A. Harten, Implicit TVD Schemes for Hyperbolic Conservation Law in Curvilinear Coordinates, AIAA paper 85-1513 also AIAA Journal, Vol.25, No.2,(1987), pp.266-274
- [7] H. Yee and G.H. Klopfer and J.L. Montagne, High-Resolution Shock-Capturing Schemes for Inviscid and Viscous Hypersonic Flows, NASA TM-100097 (1988).
- [8] K.J. Bate and E.L. Wilson, Numerical Methods in Finite Element Analysis, Prentice-Hall (1976)

CFD Activity for Future Winged Space Transport System

Yukimitsu Yamamoto (National Aerospace Laboratory yukimitu@nal.go.jp)
 Takuji Kurotaki (National Aerospace Laboratory kurotaki@nal.go.jp)

Numerical Simulation for aerodynamic study of atmospheric space transport vehicles has been conducted at NAL (National Aerospace Laboratory) as the cooperative research work with NASDA (National Space Development Agency). CFD technology enlarges its application area with the progress of the computer hardware systems and now CFD has been developed as the strong aerodynamic design tool which covers flight range of space transport vehicle from the launching to the re-entry phase. Here, recent progress of numerical simulations at NAL are introduced.

Parametric Design Study of New HOPE-X Configuration

HOPE-X (H-II Orbiting Plane Experiment) is scheduled for launch in 2004. For several years, systematic aerodynamic study has been conducted by the wind tunnel experiments and CFD simulations from low to hypersonic speeds.

Recently, in order to reduce vehicle weight and get high performance, configuration of HOPE-X is changed from tip-fin type to two-vertical fin type geometry.

For this new aerodynamic configuration design, CFD has been mainly used and Navier-Stokes calculations have been performed from low ($M_\infty=0.2$) to hypersonic speed ($M_\infty=26$), using NAL NWT(Numerical Wind Tunnel) system. Totally, 250 computations were conducted for 10 candidate configurations of new HOPE-X and the geometry and control surface effects on aerodynamic characteristics were investigated in detail. In Fig.2, pressure contours around HOPE-X improved baseline configuration are plotted in symmetry plane at typical Mach numbers. In Fig.3, oil flow patterns of HOPE-X improved model are shown at $M_\infty=3.0$ and an angle of attack $\alpha=25^\circ$. The control

efficiency of The vertical fins with 10 deg deflection are investigated.

Through these systematic CFD applications, the demand from the design side is satisfied in time schedule as well as in number of test cases needed for design process. Also, through the rapid response to the design work, which is one of useful advantages of CFD, the concept of numerical wind tunnel is almost realized. In Fig.4, are shown the new HOPE-X basic design model which is determined by parametric CFD studies. In Fig.5, are shown a series of geometries investigated for the design of HOPE-X basic design model in Fig.4.

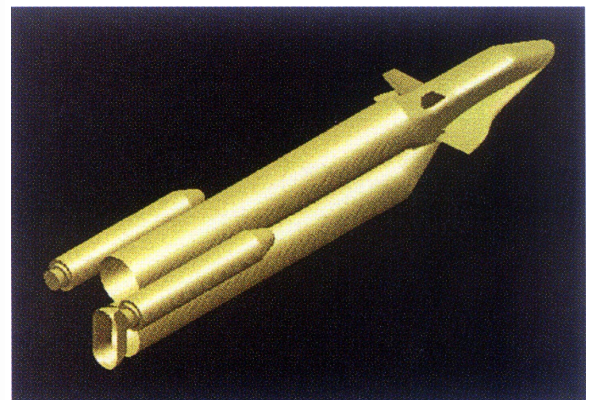


Fig.1 HOPE-X with H-IIA Rocket

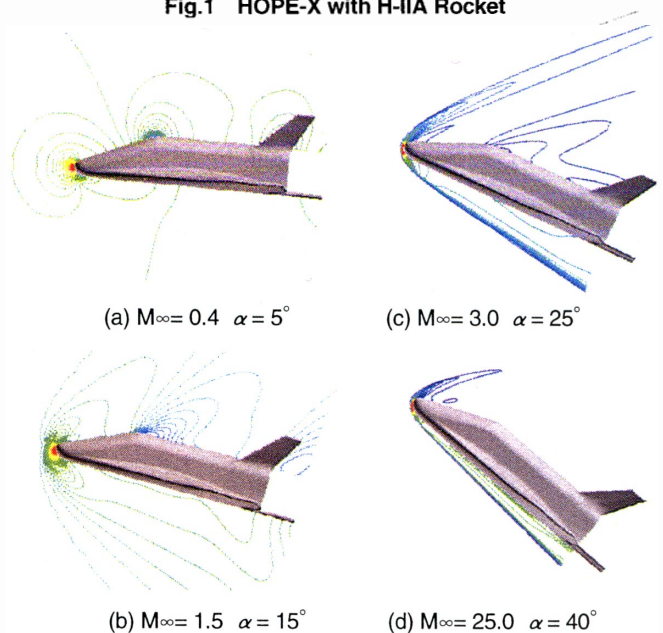


Fig.2 Pressure Contours around Two Vertical Fin Model at Various Mach Numbers

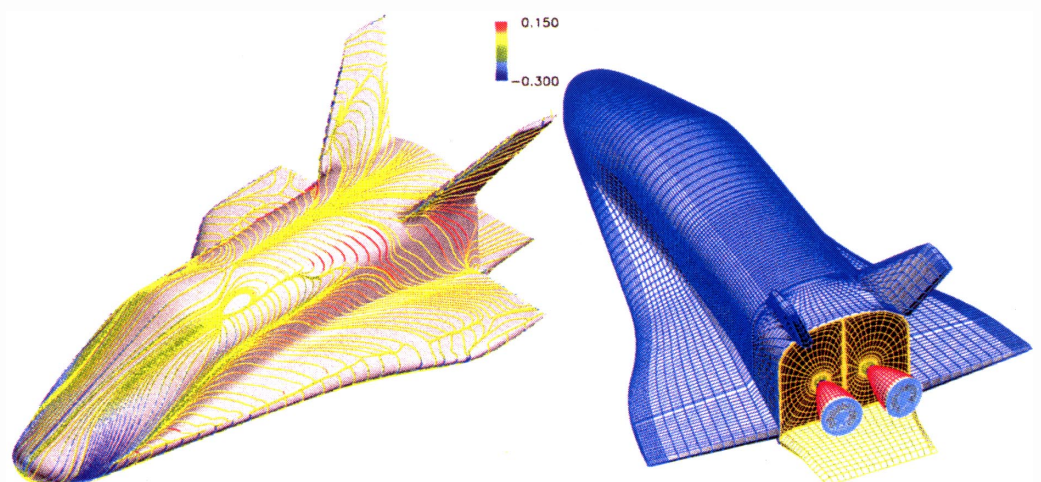


Fig.3 Oil Flow Patterns of Two Vertical Fin Model ($M_\infty=3.0, \alpha=25^\circ$)

Fig.4 Surface Grid of New HOPE-X Basic Design Model

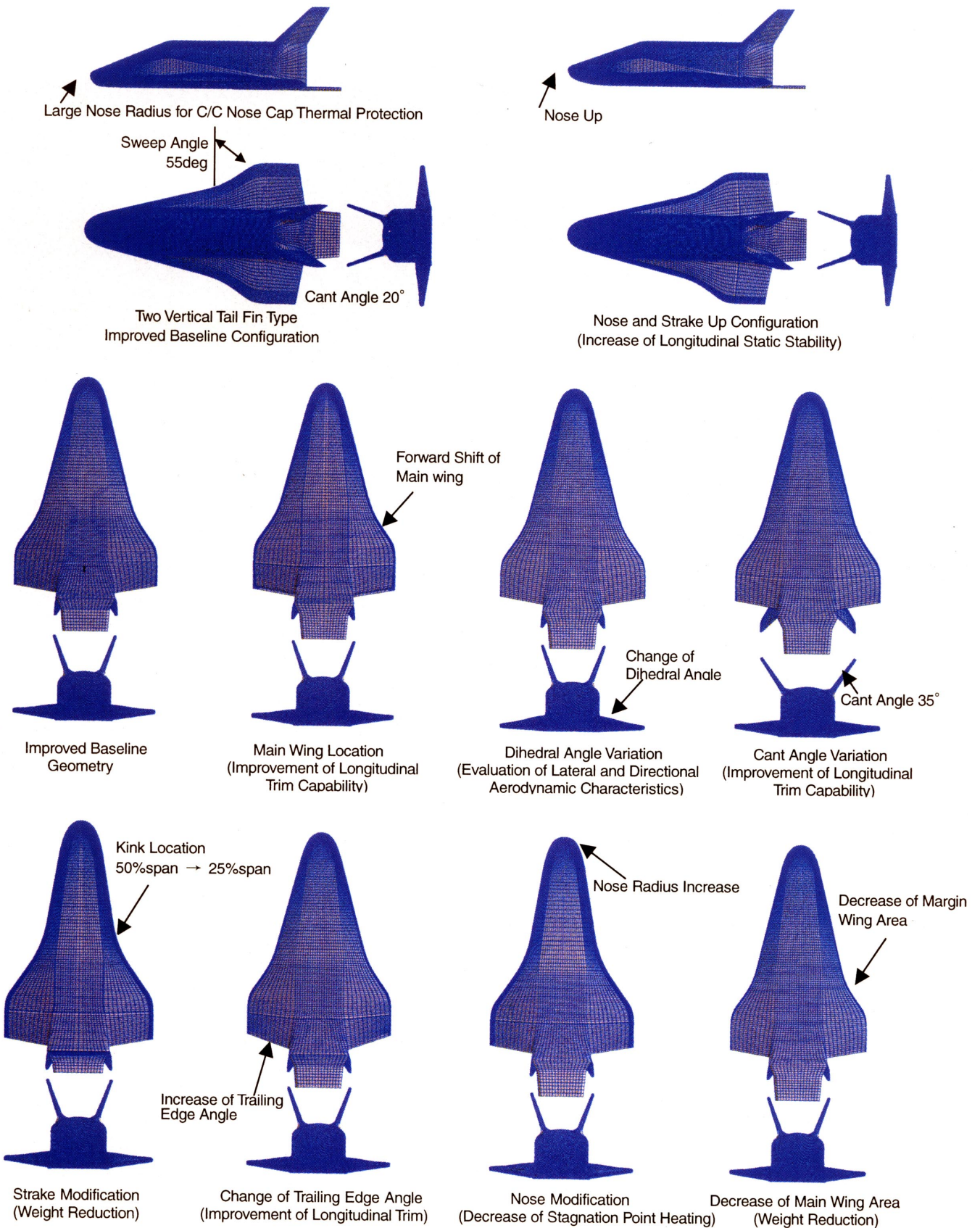


Fig.5 New HOPE-X Configurations

Transonic Flow Analysis for Detailed Design Phase of HOPE-X

CFD analysis using multi-block grids is developed to get more precise aerodynamic data, such as hinge moments of deflected flaps or base flow effects. In Fig.6, are shown multi-block surface grid of HOPE07 model with 20 deg elevon deflections. In order to investigate gap flows between the wing and elevon, 42 multi-block grids are generated and total number of grid points are 350 millions. Figure 7 shows pressure contours at $M_\infty = 0.7$ and $\alpha = 0^\circ$. Total Reynolds number is 1×10^8 based on the body length. By this

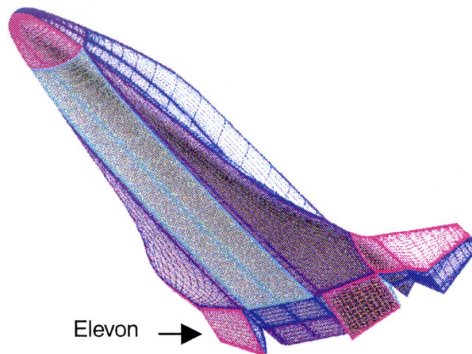


Fig.6 Multiblock Surface Grid for Deflected Elevon Analysis

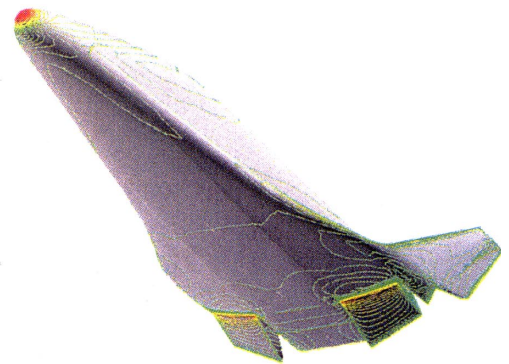


Fig.7 Surface Pressure Contours
 $M_\infty = 0.7 \quad \alpha = 0^\circ \quad Re_\infty = 1 \times 10^8$

CFD analysis, hinge moment of deflected control surfaces can be evaluated more exactly.

On the other hand, evaluation of base flow effects on aerodynamic characteristics are very important and data correlation between wind tunnel results and flight is studied. Figure 8 shows of pressure contours of new HOPE-X configuration containing base flow regions by using the multi-block grids. CFD now plays an important role for the detailed design phase and complicated flow can be evaluated exactly.

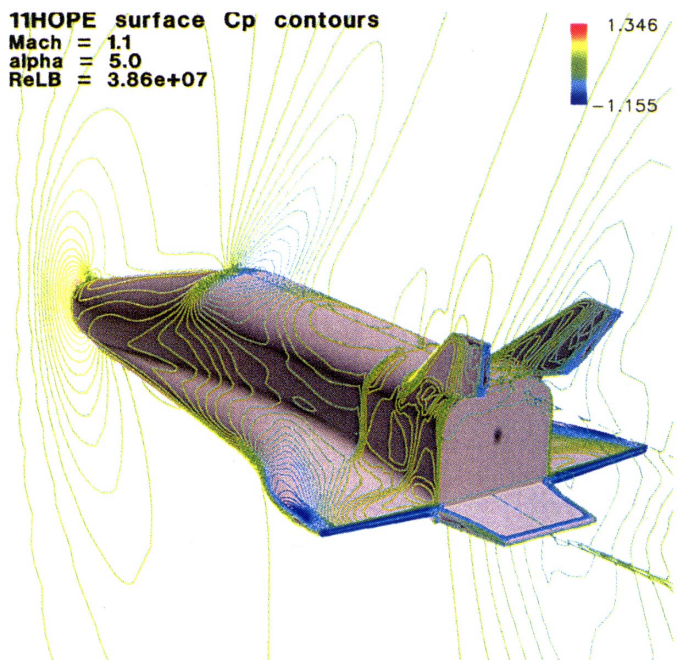
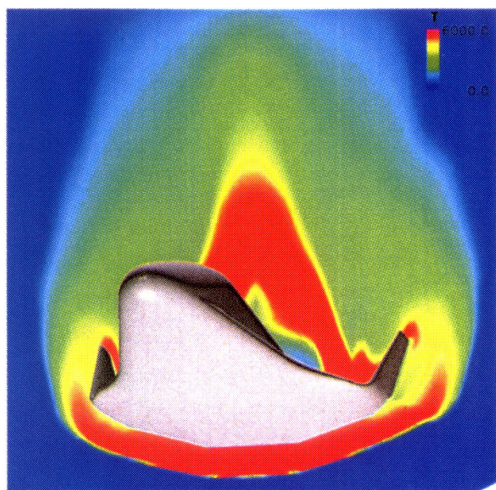


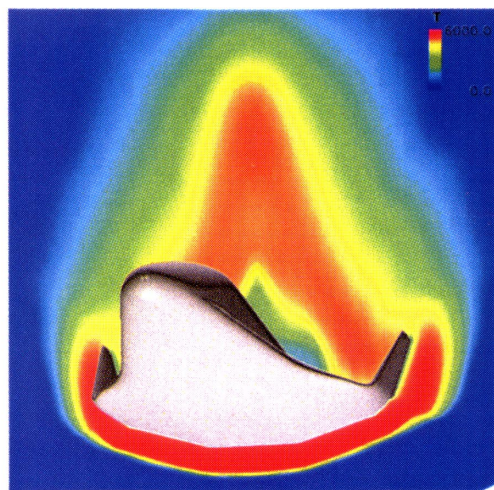
Fig.8 Pressure Contours around New HOPE-X Including Base Flows
 $M_\infty = 1.1, \alpha = 5^\circ \quad Re_\infty = 3.86 \times 10^7$

HOPE-X High Temperature Real Gas Analysis

In high temperature environments of re-entry flight of HOPE-X, chemical reactions, in which air molecules are dissociated and ionized, must be solved. Figure 9 shows cross sectional temperature contours around HOPE07 model at $M_\infty = 26$, $\alpha = 40^\circ$. Flow analysis is made by using two-temperature chemically non-equilibrium Navier-Stokes code. In the figure, translational / rotational temperature are shown with the vibrational one. At present, finite rate catalycity effects are investigated by using flight data and developments of catalycity models are underway. Validation of the real gas CFD code are progressed by the comparisons of experimental data from NAL HIEST and ONERA F4 shock tunnels.



(a) Translational and Rotational Temperature



(b) Vibrational Temperature

Fig. 9 HOPE07 Real Gas Flow Analysis $M_\infty = 26, \alpha = 40^\circ$

Aero-Thermal Structural Analysis and Application of Multi-Disciplinary Simulations to the Future Space Transport Systems

HYFLEX flight experiment was conducted in Feb. 1996. In this hypersonic flight, aerodynamic data and temperature data on TPS materials and internal structure parts were obtained. Figure 10 shows surface temperature history of HYFLEX flight, simulated by CFD-FEM coupling analysis. This type of multi-disciplinary simulation demonstrated its usefulness for high quality evaluation of aerothermal environments of re-entry flight.

In order to develop the present method to the total thermal-structural analysis, FEM mesh is generated including internal structures, such as frames and stringers as shown in Fig.11. In Fig.12, are shown typical temperature contours of TPS and internal aluminium frames. Flow-thermal analysis are made to the flight time of 300 sec and good agreements with flight data are obtained for temperature increase of HYFLEX vehicle.

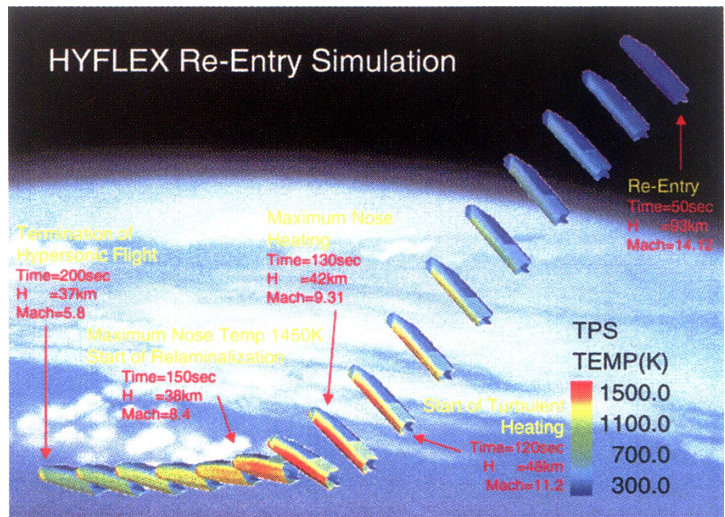


Fig.10 HYFLEX Re-Entry Flight History and TPS Surface Temperature Simulation

Finally, in Fig.13, pressure contours and oil flow patterns are shown on the X-33 type reusable rocket. In the developments of the future space transport systems, re-usability and weight reductions are the most important technological breakthrough points and CFD oriented multi-disciplinary simulations are needed for these optimum and precise design process. This study is progressed at NAL.

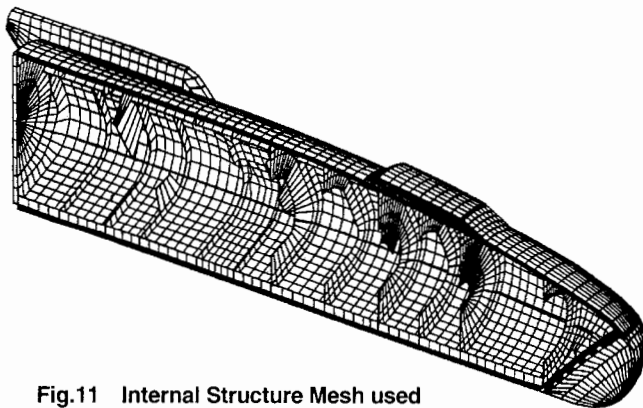
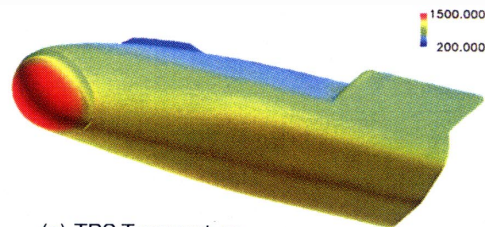


Fig.11 Internal Structure Mesh used for FEM Thermal Analysis



(a) TPS Temperature Contours at Flight Time 150 sec.

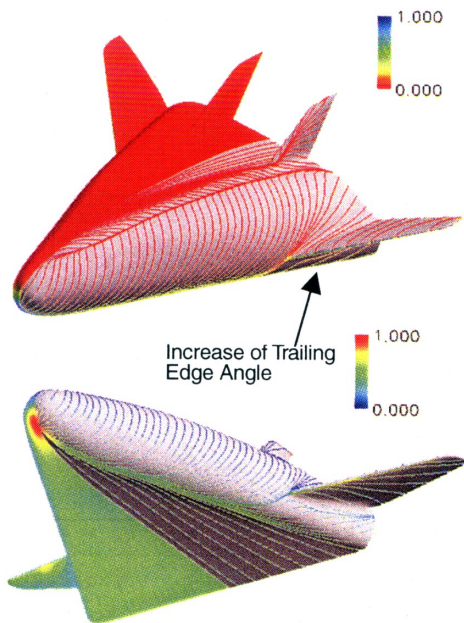
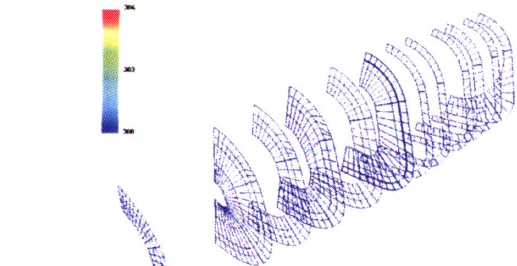


Fig.13 Pressure and Oil Flow Patterns around Future Re-usable X-33 type Vehicle $M_\infty=20.0$ $\alpha=40^\circ$



(b) Temperature Contours of Internal Frame Structure at Flight Time 300sec

Fig.12 Aero-Thermal Analysis of HYFLEX Flight by CFD/FEM Coupling

Computational Aerodynamics Research Group

E-mail : aerocarg@nal.go.jp

Numerical Wind Tunnel; Concept and Requirements

Yuichi Matsuo (matsuo@nal.go.jp)
National Aerospace Laboratory, JAPAN

National Aerospace Laboratory (NAL) has long led the aerospace research and development activities in Japan by introducing the most advanced computer system of the age. In 1993, NAL introduced a very high performance distributed parallel-vector supercomputer called Numerical Wind Tunnel (NWT-I) whose name comes from the wish that numerical simulations will be able to take the place of wind tunnel experiments in the near future. Seven years have already past since the NWT-I system was established and many achievements have been made particularly in the Computational Fluid Dynamics (CFD) applications in NAL. However, the capabilities that we originally expected to the NWT-I system e.g. high data-productivity comparable to wind tunnel test have not yet been satisfied. In the next generation NWT *i.e.* NWT-II, we are aiming at:

- realizing the NWT concept (high data-productivity and increased system-operability) both in name and reality,
- applying CFD techniques to design process through multidisciplinary analysis and design optimization;

and we focus on:

- 1) high computing performance for use in multidisciplinary analysis and optimization,
- 2) total system integration including data storage, visualization and storage-area-network,
- 3) seamless software developing environment which makes user-friendly usage possible.

Developing a CFD-based aerodynamic design method using an inverse technique is one of the major goals in the NAL SST project, and NWT-II is considered to play an important role as the computing infrastructure.

UPACS project in NAL

Kazuomi Yamamoto (kazuomi@nal.go.jp), Shunji Enomoto (eno@nal.go.jp),
Takashi Yamane (yamane@nal.go.jp), Hiroyuki Yamazaki (yamazaki@nal.go.jp),
Ryoji Takaki (ryo@nal.go.jp), Toshiyuki Iwamiya (iwamiya@nal.go.jp)

National Aerospace Laboratory

Introduction

The progress of computational fluid dynamics (CFD) and parallel computers in 1990s enables massive computation of flow around realistic complicated aircraft configuration, direct optimization of aerodynamic design including structure analysis or heat transfer, complicated unsteady flow in jet engines, and so on. This means, however, the computer program increases its complexity as well for the adaptation to the complex configuration, the parallel computation and the multi-physics coupling. Although the programming has been accomplished by great efforts of a few researchers and engineers for each specific application areas, we know it is actually inefficient not only for writing programs but also for the code validation and the accumulation of know-how.

In order to overcome the difficulty in such complicated programming and to accelerate the code development, NAL has started a pilot project UPACS (Unified Platform for Aerospace Computer Simulation) in 1998. The project aims development of common CFD codes that can be shared among researchers and code developers. The basic concept of the code design, the parallel computational method, the multi-block method and its programming are shown in the presentation.

Concept of the UPACS code

After several conceptual studies we determined the following design concept and approaches.

- (1) Multi-block methods: Concerning the adaptation to complex configuration, we chose multi-block structured grid methods as the first step. Extension to unstructured grid methods is also under consideration.
- (2) Separation of multi-block multi-processor procedures: The parallel computation and multi-block data

control processes are clearly separated from the CFD solver modules so that one can modify the solver modules without concerning the parallel techniques and multi-block data handling.

(3) Portability: The parallelization based on domain-decomposition using the communication library, MPI, is used to minimize the dependency on the hardware architecture.

(4) Structure and capsulation: Clear data and program structure and capsulation of modules are used to make the code sharing easier among CFD researchers and developers.

There are several key features in the UPACS code design to realize these concepts. For example, one of them is shown in Fig. 1, the hierarchical structure of the UPACS code. The lower layer consists of the CFD solver modules for a single block, which can be easily prepared for several numerical models. The middle layer has to handle the complicated multi-block data controls for the multi-processor hardware and the data transfer between the blocks. This layer is generalized and prepared as a library so that one can achieve complicated calculations without getting into the detail of data handling algorithms. The upper layer, which is also prepared for code extensions, determines the framework of iteration algorithm that would be dependent on the solution methods or numerical models.

Current status

The UPACS code is now under development through discussion on the detail design and validation of the CFD solver and the multi-block multi-processor procedures. The target in 2000 is practical applications in the several projects and extension to the interdisciplinary (multi-physics) problems.

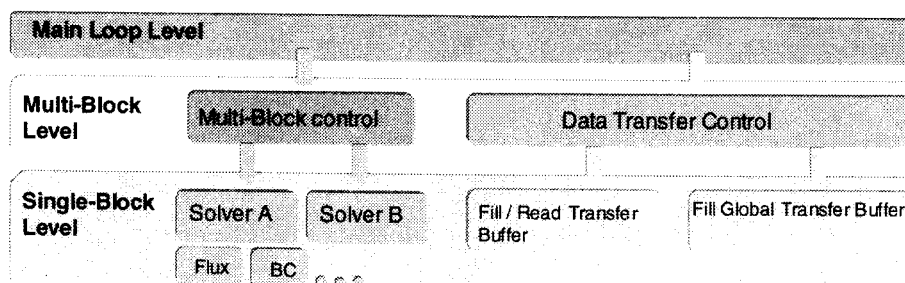


Fig.1 Hierarchical code structure of UPACS

Information and Communication Technology enabling engineering in the Virtual Enterprise

W. Loeve(loeve@nlr.nl)
NLR, The Netherlands

Customers of industry require ever more product functionality to be delivered in shorter time. Examples are civil and military aircraft products. To cope with the requirements industries assemble temporary consortia of independent member companies to quickly exploit fast changing worldwide opportunities. Sharing of cost, skills and core competencies by partners shall be possible in the consortia without regard of size, geographic location, computing environments, deployed technologies or implemented processes of the partners. Key process areas in this type of consortia are collaborative engineering and integrated management, control, access and exchange of technical and management data. Information and Communication Technology has to be and can be used to create integrated Virtual Enterprises in which the key process areas are supported economically. The set up of a Virtual Enterprise requires changes in contributing conventional companies. To effectuate the changes management and workforce have to cooperate intensively. Technological institutes in many countries are put under pressure to improve knowledge transfer to other organizations including industry. For this reason it can be recommended for technological institutes to prepare themselves to participate in Virtual Enterprises. Along these lines it is possible to facilitate knowledge transfer to industry and to facilitate use by industry of computer based facilities and facilities for experiments. Workflow Management, Data Management and Query Management shall be possible for all personnel in the Virtual Enterprise according to their authorization. A feasible way to realize the required seamless information flow in the Virtual Enterprise is to make use of middleware on the distributed computers with dissimilar operating systems of the participating companies. Furthermore the participants in the Virtual Enterprise have to consolidate and properly manage know-how in data, software and electronic documents. The consolidated and managed know-how has to be made transparent for application in multi-discipline, multi-company environments in combination with proper security measures. Know-how will only be made transparent by the owners if it is made rewarding for them. In the paper several aspects of the Virtual Enterprise will be discussed based on experiences in the Netherlands.

①

Nationaal Lucht- en Ruimtevaartlaboratorium
National Aerospace Laboratory NLR



Information and Communication Technology enabling engineering in the Virtual Enterprise

W. Loeve

National Aerospace Laboratory NLR

2nd SST Workshop Tokyo 19 January 2000

②

Nationaal Lucht- en Ruimtevaartlaboratorium
National Aerospace Laboratory NLR



NLR and the ICT Division

- NLR is not-for-profit foundation with 950 people
- NLR annual turnover ECU 70M of which ca 75% under contract
- Focus is on support of use and development of aircraft and spacecraft
- ICT systems developed by NLR serve to transfer NLR knowledge to customers (e.g. CFD, tracking with radar, control algorithms)
- ICT consultancy especially on facilitating collaboration in the virtual and extended enterprise
- ISO 9001 and AQAP-110 certificate for ICT Division since 1993

③

Nationaal Lucht- en Ruimtevaartlaboratorium
National Aerospace Laboratory NLR



Industry needs collaboration

- Customers such as of aerospace and automotive industry buy world-wide and require more product functionality delivered in shorter time at minimal cost (first time right)
- Industry has to create temporary consortia of independent member companies to exploit the world-wide opportunities
- Sharing of cost, skills, and core competencies in the consortia is needed for accessing global markets with world class solutions that could not be provided individually
- Assembly of consortia without regard for organisation size, geographic location, computing environments, technologies deployed, or processes implemented is required by industry

④

Nationaal Lucht- en Ruimtevaartlaboratorium
National Aerospace Laboratory NLR



Collaboration in a consortium requires use of ICT to create Virtual Enterprises

- A key process area in a consortium of dissimilar industries is collaborative engineering
- Collaborative engineering requires:
 - integrated management, control, access and exchange of technical and management data
 - sharing of competence consisting of know-how, know-why and the ability to apply know-how (in software and documents)
- Industries create Virtual Enterprises consisting of several companies that together behave as one enterprise for specific purposes
- ICT has to be used for management, control and seamless access to data, software and documents in Virtual Enterprises

⑤

ICT in Virtual Enterprises

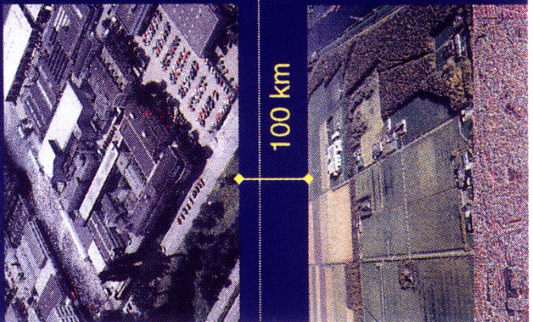
- Management, control and access to information (structured data, documents and software) with ICT requires contributions from management and engineers
- Contributing to information sharing has to be rewarding for all concerned
 - reward for management is survival of the organisation, controllability and increased continuity in availability of information
 - reward for engineers is creation of a forum via intranet to show what they can do and possible prizes for exceptional contributions
- Information management and application requires from ICT:
 - support of flexibility in information structuring according to each different process for which the information is required
 - intuitive human interaction with information independent of location

Technological Institutes and the Virtual Enterprise

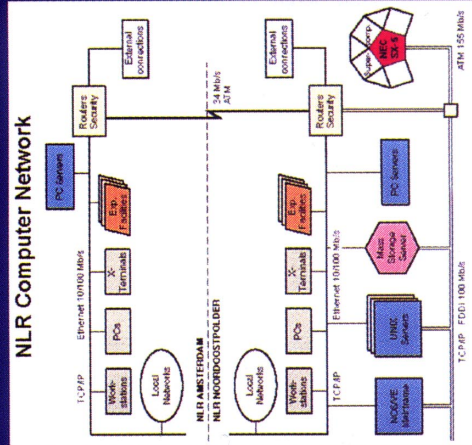
- Situation of Technological Institutes
 - Technological Institutes are forced to earn part of their income from contracts and are losing their monopoly in the home market
 - Customers of Technological Institutes require continuous improvement of efficiency and more integrated approach
 - Information in Technological Institutes has to be structured, conserved and made accessible for re-use in multi-disciplinary approach of ever more complex problems
- Possibilities for Technological Institutes to cope with the situation
 - Technological institutes can prepare for participation in Virtual Enterprises with industry and other institutes
 - Technological Institutes can prepare to become Application Service Providers for tools in engineering and decision processes

⑦

NLR operates as Virtual Institute with network of dissimilar computers



NLR
National Lucht- en Ruimtevaartlaboratorium
National Aerospace Laboratory NLR



⑥

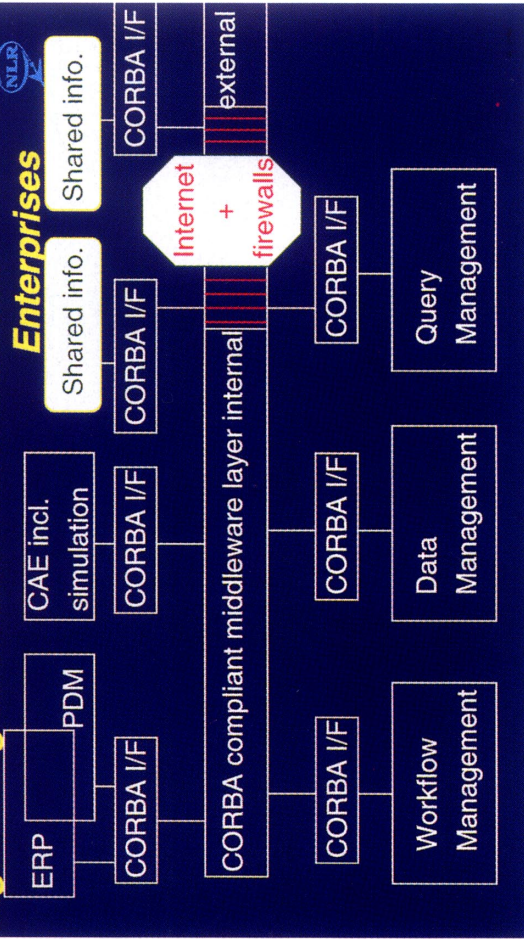
⑧

NLR applies NEC middleware as backbone for Virtual Institutes

- Realisation of seamless information flows in networks with dissimilar computers (UNIX and Windows)
 - Structuring of information tailored for particular applications in engineering or decision support for:
 - single user
 - group of users
 - application area
 - department
 - company
 - group of companies in virtual enterprise
- CORBA compliant, applied in national and international projects for conservation, accumulation and (remote) application of information

10

Middleware for seamless engineering information flow in Virtual Enterprises



9

Virtual working environments for mono- and multi-disciplinary analysis in engineering with NEC SPINEware



11

Concluding remarks

- ICT can be used to create Virtual Enterprises in which information is managed, controlled and shared
- Specialists and management have to co-operate in development of Virtual Enterprises and this has to be rewarding for both
- Technically existing middleware can be used as backbone of the Virtual Enterprise to integrate networks of dissimilar computers
- Technical Institutes shall prepare for participation in Virtual Enterprises and to become Application Service Providers
- The next generation computer system (and CFD software) for engineering will be determined by requirements from Virtual Enterprises and from Application Service Providers

Some Practical Applications of CFD Analysis to Aerodynamic Design Of the Supersonic Experimental Airplane

Naoki Futatsudera (Mitsubishi Heavy Industries, Ltd., naoki_futatsudera@mx.nasw.mhi.co.jp)

Takeshi Kaiden (Mitsubishi Heavy Industries, Ltd., takeshi_kaiden@mx.nasw.mhi.co.jp)

Abstract

In 1997, National Aerospace Laboratory (NAL) started a program to develop a scaled supersonic experimental airplane to establish the technological basis for the development of the next generation supersonic transport. A non-powered experimental airplane is being developed for the first experimental flight in 2002. The airplane is launched by a rocket-booster. After the rocket-booster is separated, the airplane starts the measurement flight at Mach 2.0 and altitude 18.5km.

In the aerodynamic design of the experimental airplane, Mitsubishi Heavy Industries, Ltd. (MHI) is in charge of the overall design and NAL mainly conducted the wing and wing-body aerodynamic integration design with their sophisticated CFD code. MHI is also in charge of the launch configuration aerodynamic design.

In the MHI design' work, wind tunnel test data were mainly used. Some experimental data were checked and corrected using the CFD analysis.

CFD analysis also played an important role in understanding physical phenomena of the complicated flow field of the experimental airplane and the rocket-booster.

1. Introduction

In 1997, NAL started the program called NEXST (National Experimental Supersonic Transport) to establish the technological basis for the development of the next generation supersonic transport ⁽¹⁾. Two types of unmanned airplanes, i.e., a non-powered and a jet-powered airplane, will be built.

A non-powered experimental airplane (Fig.1) is being developed for the first experimental flight in 2002. The main purpose of the experimental flight with this airplane is to verify the aerodynamic design methodology with CFD, especially the supersonic natural laminar flow wing design. The airplane is launched by a rocket-booster (Fig.2) to the separation point (altitude 19.5km, Mach number 2.1). After the separation of the rocket-booster, the airplane starts the measurement flight at Mach 2.0 and at altitude 18.5km and descends to altitude 12km maintaining Mach number constant. In the measurement flight, surface pressure distribution and boundary layer transition are measured. After decelerating and descending to the recovery point, the experimental airplane lands on the ground using a parachute and

airbags (Fig.3).

In the aerodynamic design of the experimental airplane, MHI is in charge of overall design (wing location and tail sizing, etc.) and NAL mainly conducted the wing and wing-body aerodynamic integration design with their sophisticated CFD code. And MHI is also in charge of the design of the launch configuration (airplane connected to the rocket-booster).

This paper describes the role of CFD analysis and four practical applications in our aerodynamic design work.

2. CFD Analysis in the Aerodynamic Design

In this MHI aerodynamic design, we used several aerodynamic analysis methods according to the design phase.

In the basic design phase, design handbook and the linear aerodynamic theory were mainly used for the design of an initial configuration and its modification. They do not take much time and are very easy to use. They also have enough

accuracy in this design phase.

And the basic wind tunnel tests were conducted for verification.

CFD analysis was mainly used to understand the physical phenomena of the complicated flow field. Some CFD analyses were also conducted for estimation of aerodynamic difference caused by configuration change, and also for complement of the wind tunnel test results. CFD analysis was used mainly for the launch configuration design. Aerodynamic coefficients of launch configuration include much interference effect and which is difficult to estimate by the other simpler methods.

In the detail design phase, the aerodynamic configuration was almost fixed. The detail wind tunnel tests were conducted and final aerodynamic data were developed based on that complete wind tunnel test data. So CFD analysis was mainly used in understanding the local physical phenomena and checking and correcting the experimental data.

In the design work, design tools are always chosen based on the trade-off between accuracy and time and cost for efficiency in design work. Applications of CFD analysis were restricted in our design work because of the following reasons:

- Taking time for modeling and calculation
- Less accurate in detail design
- Difficult in the detail modeling
- Not easy to use (Specialists are needed)

3. CFD Method

CFD method used in following examples is as follows.

(Grid Generation)

Chimera technique ⁽²⁾⁻⁽³⁾ is applied to this computation. The grids used in this method are generated independently for the each component, i.e., the experimental airplane (wing / fuselage / vertical tail), horizontal tail, rocket-booster. The number of the grids for half model used here is shown in the Tab.1. These grids are generated by the algebraic interpolation method.

The differences between CFD model and wind tunnel model are as follows. First, CFD model does not simulate many protuberances (antennas, connection parts between the experimental airplane and the rocket-booster etc. shown in Fig.1 and Fig.2). Secondly, space-gaps between

the rocket-booster fin and the deflected control surface are not simulated.

The grid for the isolated airplane computation is shown in Fig.4. The grid of the horizontal tail is overset in this computation. Fig.5 shows the grid for computation of the launch configuration and configuration in the separation procedure. In these configurations, the grid of the rocket-booster is overset.

(Flow Solver)

The governing equations are three-dimensional thin layer Reynolds-averaged Navier-Stokes equations. The convective term is discretized using Roe's flux difference splitting with MUSCL ⁽⁴⁾. LU-ADI implicit method is adopted in time integration. The local time stepping is used to accelerate the convergence of the iteration. The turbulence model used here is an algebraic model of Baldwin-Lomax type.

The solution process of Chimera technique is described in Fig.6. First, physical properties of the hole on the mother grid are interpolated from those of the child grid (Process A). The hole stated here is defined as the location where the flow properties are set from those of the other grids. After the interpolation, the flow computation on the mother grid is performed (Process B). At this time, flow computation is not performed on the hole of mother side. At the next step, physical properties of the hole on the child grid are interpolated from those of the mother grid (Process C). Finally, the flow computation on the child grid is done (Process D). The hole is treated in the same manner of the mother computation. This process is repeated until the residual is less than the designated value.

4. Practical Applications of CFD Analysis

The following four examples show the important role of the CFD analysis in our design work.

4.1 Stabilizer Hinge-moment

The basic wind tunnel test was conducted for the 3rd experimental airplane configuration and the detail wind tunnel test was conducted for the 4th experimental airplane configuration. The stabilizer hinge-moments measured by both wind tunnel tests were far different from each other against the prediction (Fig.7).

By the review of the experimental data, it was

found that difference partly resulted from the measurement errors and which were corrected with the CFD results.

The stabilizer hinge-moment was measured by the one-component internal (hinge-moment) balance. It would be under the interference of stabilizer lift and bending moment to some extent (Fig. 8). That means some lift force and bending moment are measured as hinge-moment. By detailed balance calibration of internal balances of 3rd and 4th configuration wind tunnel model, the interference factors were measured.

Both wind tunnel hinge-moment data were corrected with these interference factors and stabilizer lift and bending moment calculated by CFD. Filled symbols in Fig.7 represent the corrected data. Corrected data of 3rd and 4th configuration are almost same each other in supersonic region.

Corrected data seemed more reasonable, but the latter wind tunnel test data (○) are used as the design nominal considering more aerodynamic design margin.

This hinge-moment increment reduced the design margin of an actuator performance, but margin is still enough.

4.2 Rocket-booster Control Surface

Hinge-moment

Launch configuration controls maneuvers with conventional rudder type control surfaces at four rocket fins.

The basic wind tunnel test was conducted for the 1st launch configuration and the detail wind tunnel test was conducted for the 3rd launch configuration. The fin control surface hinge-moments data measured by both wind tunnel tests were far different from each other at transonic speed (Fig.9). Both test data show good agreement under Mach 0.9 and over Mach 1.6, and no measurement failures were found at every test Mach numbers. So it had been supposed that difference would be caused by an aerodynamic phenomenon.

By review with the CFD analysis, it was found that configuration difference of the rocket-booster body-end of both launch configurations was the trigger of the hinge-moment difference (Fig.10). The 1st launch configuration wind tunnel model had the gimbal base. De-touched shock from gimbal base was supposed to make difference of fin control surface hinge-moment at the transonic speed (Fig.11).

CFD calculations of both launch configurations were conducted at three Mach numbers. Fig.12 shows comparison of the surface pressure distributions of the rocket-booster aft-body of both 1st and 3rd launch.

It shows that flow fields near the fin control surfaces of the former and latter configuration are similar at Mach 0.6 and Mach 2.0, but different at Mach 1.2. The control surfaces are affected by high-pressure region caused by the gimbal base. This will be the reason of difference in fin control surfaces hinge-moment.

Fig.13 shows comparison of CFD result with wind tunnel test data of the latter configuration (3rd). The test data and CFD results show good agreement at every Mach numbers. The wind tunnel test data for the 3rd configuration were used as the design nominal for the final launch configuration.

4.3 Launch Configuration C_{m_0} at Mach 2.0

Wind tunnel test data showed that the 3rd launch configuration has large amount of negative C_{m_0} (moment coefficient at zero degree angle of attack) around Mach 2.0 (Fig.14). And it was also shown that the rocket-booster had negative C_{m_0} by the component-force measurement of the airplane of the launch configuration in the wind tunnel test.

The control authority would be short so as to keep the launching maneuver profile because of this large negative C_{m_0} and small fin control surface effectiveness around Mach 2.0.

CFD calculation was conducted at Mach 2.0, zero degree angle of attack so as to make this phenomenon clear. Fig. 15 shows the ΔC_{m_0} per unit length of both the experimental airplane and the rocket-booster. This figure shows which part makes negative C_{m_0} . It is found that the rocket fins mainly make large negative ΔC_{m_0} of the launch configuration. It is supposed that expansion waves between the fuselage of the experimental airplane and the rocket body affects the aerodynamic characteristics of the rocket fins.

So large negative C_{m_0} was understood as reasonable, launching maneuver profile was revised from the initial one.

4.4 Interference Force at the Separation

The safety separation is the final step for the successful measurement flight. But it was predicted that wing and large rocket fins made

large amount of aerodynamic interference force and which resulted in complicated separation maneuver.

Separation flight simulations were conducted so as to establish the requirement for the separation without re-contacts.

The aerodynamic characteristics used in the separation flight simulation were based on the grid wind tunnel test ⁽⁵⁾ data.

Although wind tunnel test was useful for preparing the large number of aerodynamic characteristic data with enough accuracy, it was often difficult to understand the physical phenomena of the interference force. In these cases, CFD analysis was very helpful.

With CFD results, mechanism of aerodynamic interference force at the separation is analyzed as follows.

Fig.16(1) shows the aerodynamic interference component of pitching moment (ΔC_m) of the experimental airplane (wind tunnel test data).

$$\Delta C_m = C_{m_grid} - C_{m_isolated}$$

where C_{m_grid} means C_m including the aerodynamic interference, and $C_{m_isolated}$ means C_m of the isolated airplane.

It is noticed that this graph shows just ΔC_m variation versus ΔZ of the grid wind tunnel test, not of the actual separation maneuver. ΔZ means the normal distance between the experimental airplane and the booster-rocket (Fig.17).

Four projections are found in the ΔC_m variation according to ΔZ . The oblique shock from the rocket-booster nose strikes the airplane, and that results in ΔC_m of the airplane. Fig.18 is the schlieren photographs of same grid wind tunnel test case as that shown in Fig.16. The strike point on the airplane moves backward as ΔZ increases. That makes ΔC_m variation. Four projections successively occur when the oblique shock strikes the fore-body, wing (the front part), wing (the rear part) and horizontal tail of the airplane.

This mechanism of aerodynamic interference can be easily understood with Fig.19. Fig. 19 shows the pressure distribution on the surface and X-Z plane estimated by CFD corresponding to the grid wind tunnel test case shown in Fig.16 and Fig.18. Fig.19 (1) is at $\Delta Z = 1m$, where the oblique shock from the rocket-booster nose is about to strike the wing. And Fig. 19 (2) is at $\Delta Z = 2m$, where the oblique shock strikes the middle of the wing and the large compression region can be found on the wing lower surface.

As mentioned above, the aerodynamic interference on the experimental airplane mainly results from the oblique shock from the rocket-booster nose.

Fig.16(2) shows the aerodynamic interference on pitching moment (ΔC_m) of the rocket-booster (wind tunnel test data).

One peak can be found in the ΔC_m variation according to ΔZ increasing. This variation is simpler than for the experimental airplane, but the mechanism of the interference is more complicated. ΔC_m consists of effect of the experimental airplane and effect of the reflected oblique shock from its own nose. The oblique shock from the rocket-booster nose strikes the airplane, and that is reflected. The reflected shock strikes the rocket-booster.

This mechanism can be easily found in Fig.19. In Fig.19 (1), the oblique shock from the rocket-booster nose strikes the intersection part of wing and fuselage, and the reflected shock strikes the rocket-booster mid-body.

In Fig. 19 (2), oblique shock strikes mid part of the wing, and the reflected shock strikes the rocket-booster aft-body and large fins. The reflected shock can be vaguely observed in the schlieren photograph (Fig.18, center). High-pressured region can be found on the lower fins. When the oblique shock strikes the wing, reflected shock is distinct. And when that distinct shock strikes the rocket-booster fins, large amount of interference on pitch-up moment makes peak in ΔC_m variation (at $\Delta Z=2m$ in Fig.16(2)).

Fig. 16 also shows ΔC_m estimated by CFD compared to wind tunnel test data.

For the interference on the experimental airplane, CFD result shows quite good agreement with wind tunnel test data. But for the rocket-booster, large error can be found at small ΔZ . The rocket-booster has several protuberances on its surface. But CFD model does not have these because of difficulty in the detail modeling as mentioned in the section 3.1. This is supposed to mainly cause the error.

CFD analysis could be used to estimate aerodynamic interference on the airplane but not the rocket-booster.

5. Conclusion

Four practical applications of CFD analysis to

the aerodynamic design of the experimental airplane and its launch configuration are presented.

Wind tunnel test data were mainly used for the design but the experimental data were checked and corrected by the CFD.

CFD analysis also played an important role in understanding physical phenomena of the complicated flow field of the experimental airplane and the rocket-booster.

Acknowledgments

The authors are very grateful for the assistance, support and efforts of researchers in NAL working for National Experimental Supersonic Transport (NEXST) program.

Reference

1. Sakata, K., "Supersonic Research Program in NAL, Japan," International CFD Workshop on Super-Sonic Transport Design, Tokyo, Mar. 1998.
2. NASA Ames Space Shuttle Flow Simulation Group, Buning, P., Chiu, I., Martin, F., Meakin, R., Obayashi, S., Rizk, Y., Steger, J., and Yarrow, M., "Numerical Simulation of the Integrated Space Shuttle Vehicle in Ascent," 4th internat. Conf. on Super Computing, Santa Clara, Calif., Apr. 1989.
3. Kaiden, T., Shibata, M. and Iwamiya, T., "Numerical Simulation with Bleed and Bypass Effects of Nacelles on SST," International CFD Workshop for Super-Sonic Transport Design, NAL, March, 1998
4. Fujii, K. and Obayashi, S., "High-Resolution Upwind Scheme for Vortical Flow Simulations," *J. Aircraft*, Vol.26, No.12, Dec., 1989 pp.1123-1130.
5. Ohyama, K., Kaiden, T., Futatsudera, N. and Shimbo, Y., "Rocket-Booster Separation Wind Tunnel Test of Scaled Supersonic Experimental Airplane," 37th Aircraft Symposium, Tokyo, Oct. 1999.

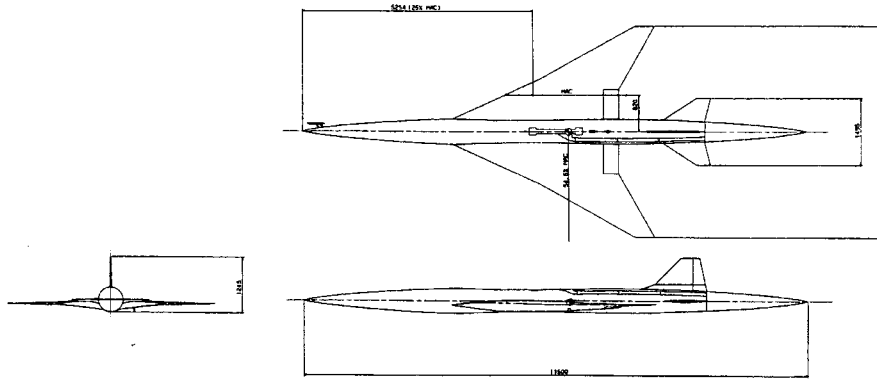


Fig.1 Non-powered experimental airplane

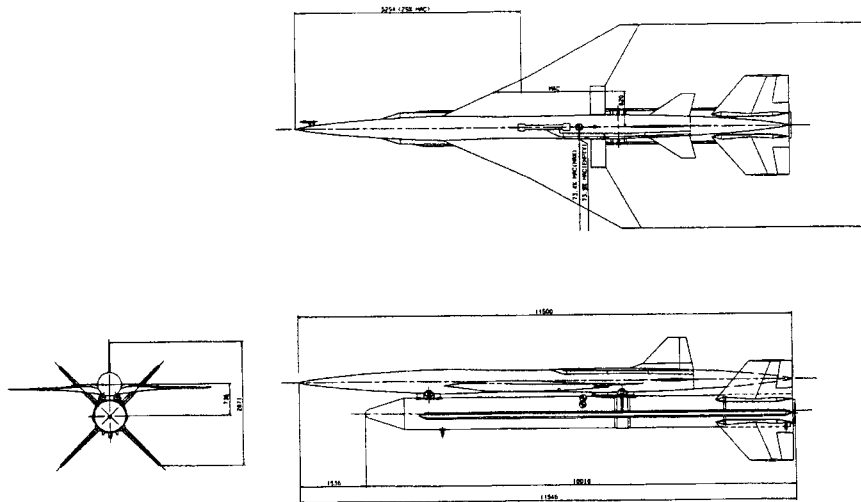


Fig.2 Launch configuration
(combination of experimental airplane and rocket-booster)

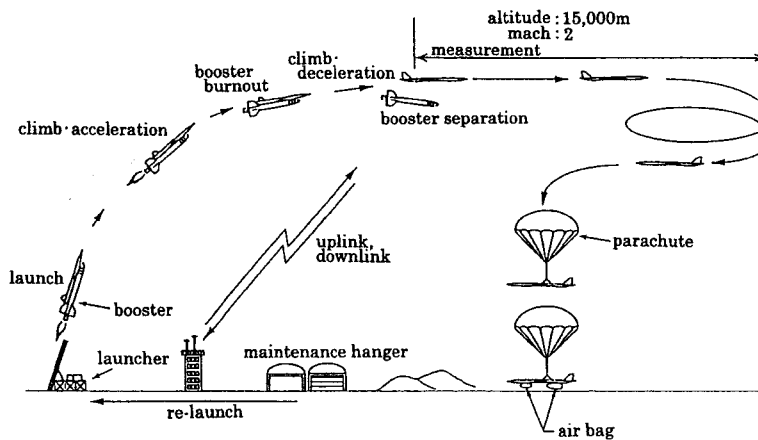


Fig.3 Experimental flight profile

Table.1 The number of the grids

	Experimental Airplane (isolated)	Launch Configuration
Experimental Airplane (*) Grid	1,642,200	2,326,450
Horizontal Stabilizer Grid	323,400	
Rocket-booster Grid	-	1,334,550
Total	1,965,600	3,661,000

(*) horizontal stabilizer less configuration

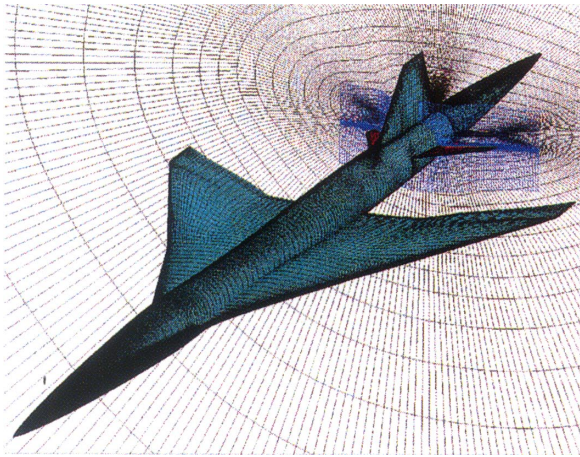


Fig.4 Grid for the computation of the isolated airplane

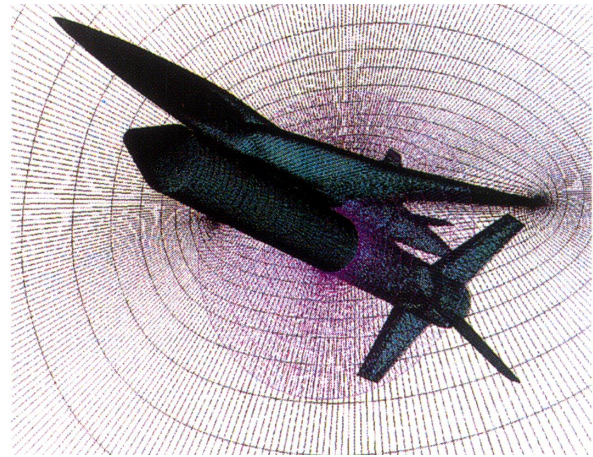


Fig.5 Grid for the computation of the launch configuration

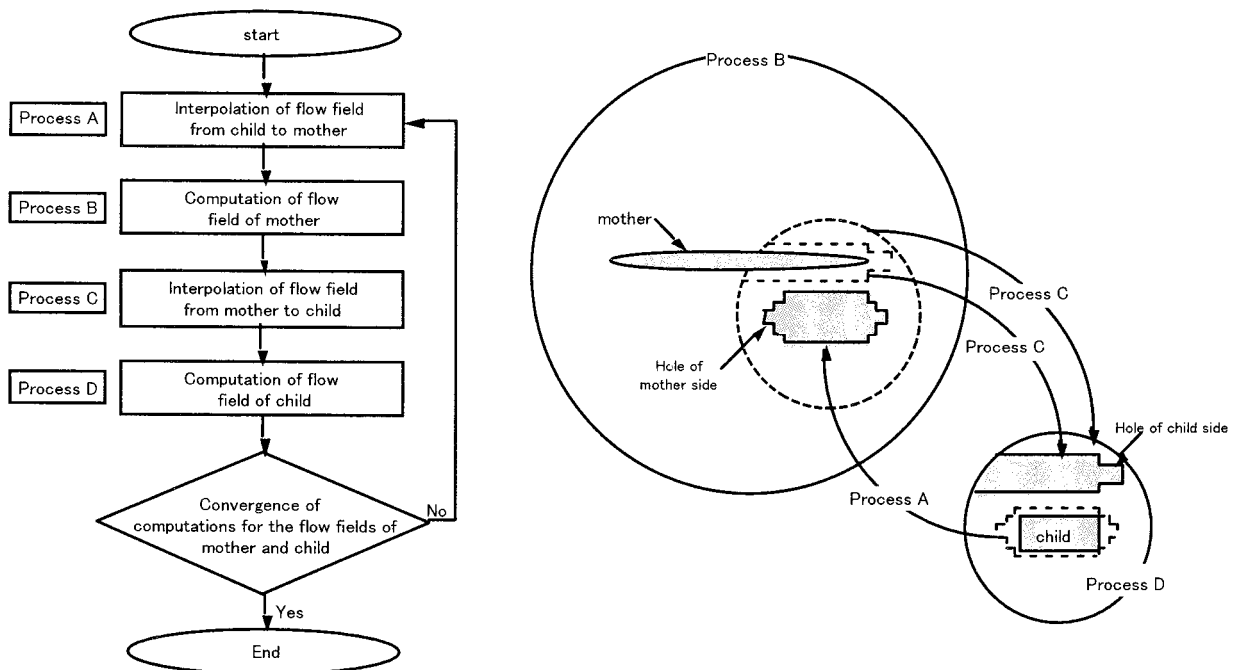


Fig.6 Flow chart of computation

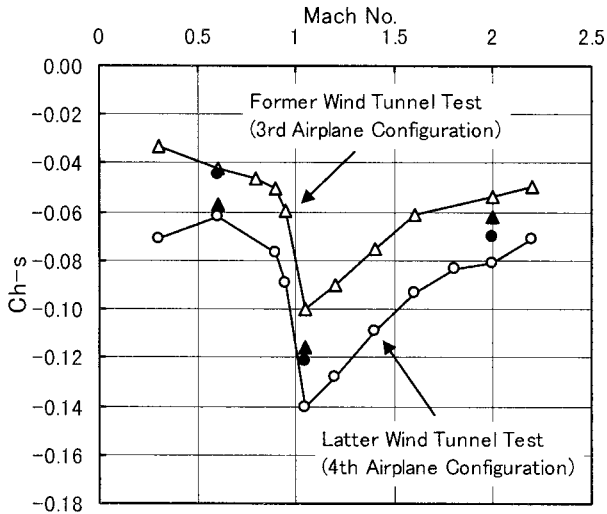


Fig.7 Hinge moment coefficients of horizontal stabilizer (pitch-up 10° , $\alpha=0^\circ$)

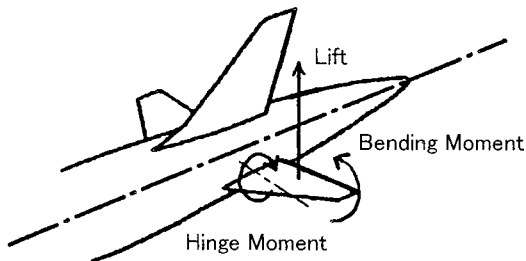


Fig.8 Horizontal stabilizer hinge moment and its interference sources

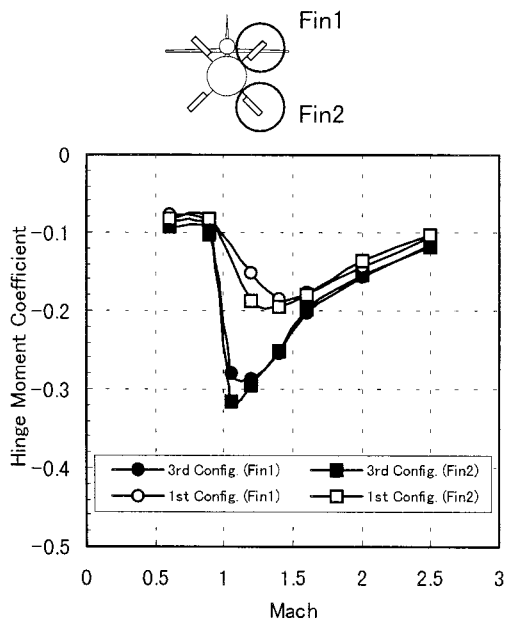


Fig.9 Comparison of hinge moment coefficients (roll 10° , $\alpha=0^\circ$)

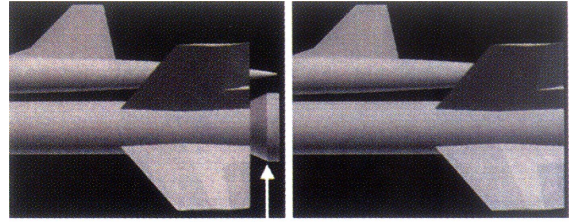


Fig.10 Difference of the rocket-booster aft-body configuration

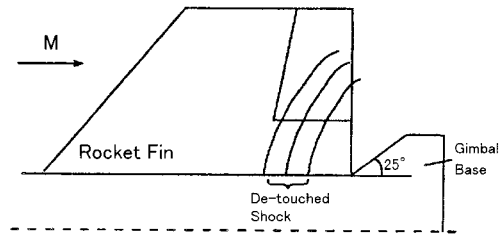
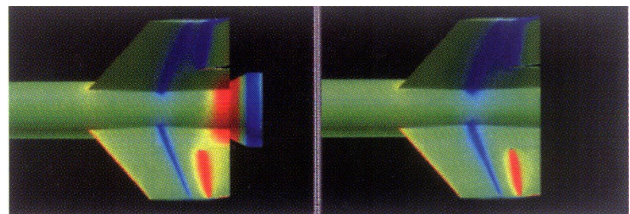
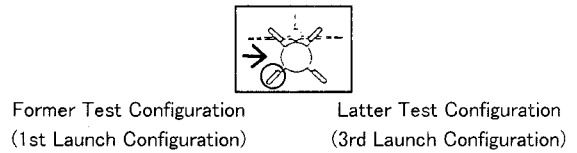
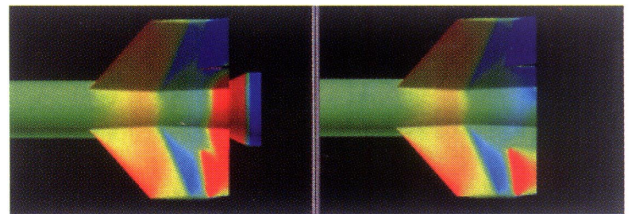


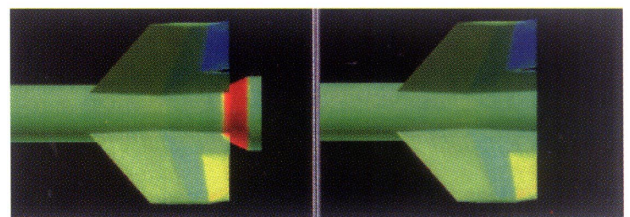
Fig.11 Schema of de-touched shock from the gimbal base at M1.2



(a) M=0.6



(b) M=1.2



(c) M=2.0

Fig.12 Surface pressure distribution by CFD (The rocket-booster aft-body)

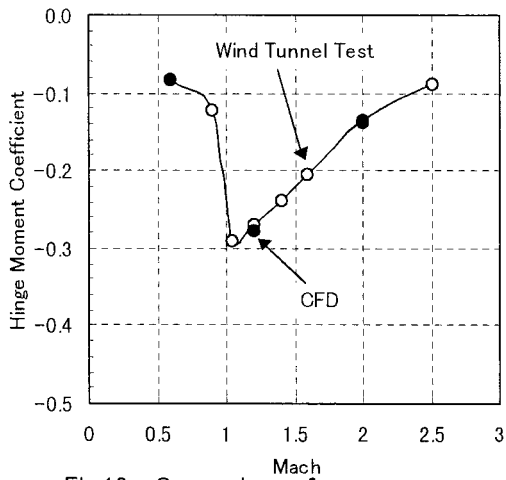
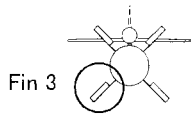


Fig.13 Comparison of CFD with wind tunnel test

(Reference Point : Experimental Airplane 25%MAC)

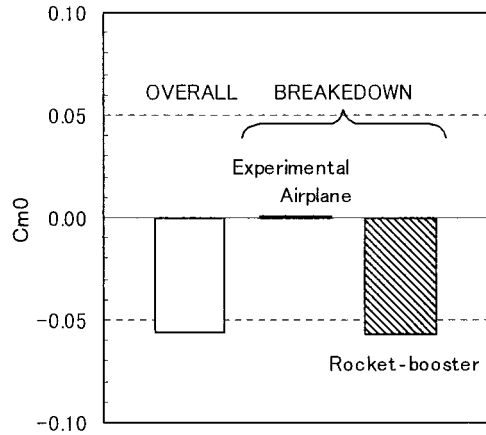


Fig.14 Pitching moment coefficient of launch configuration ($M=2.0, \alpha=0^\circ$)

(Reference Point : Experimental Airplane 25%MAC)

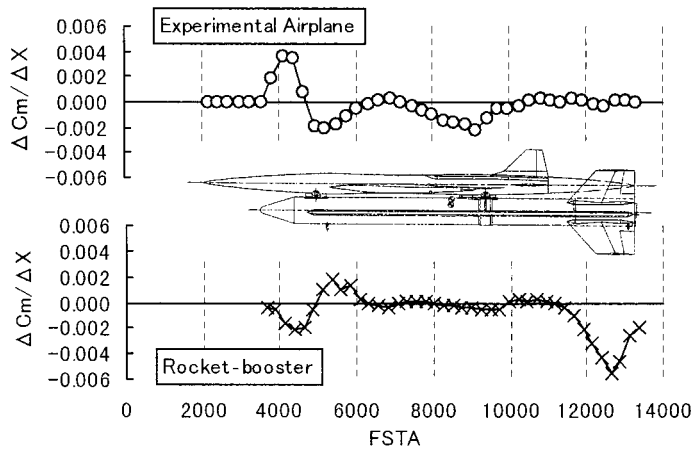
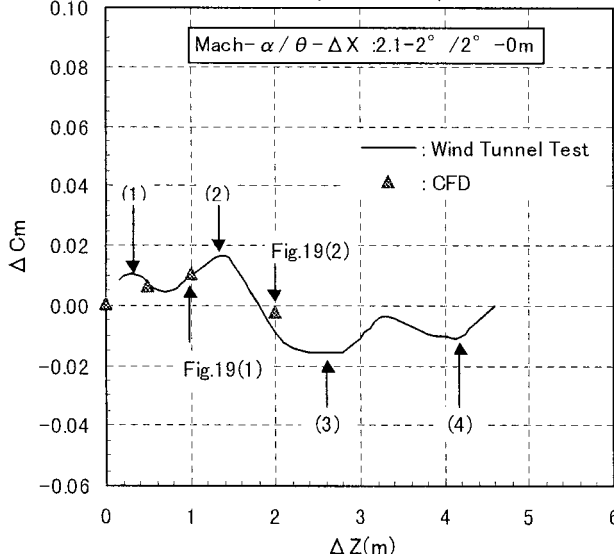


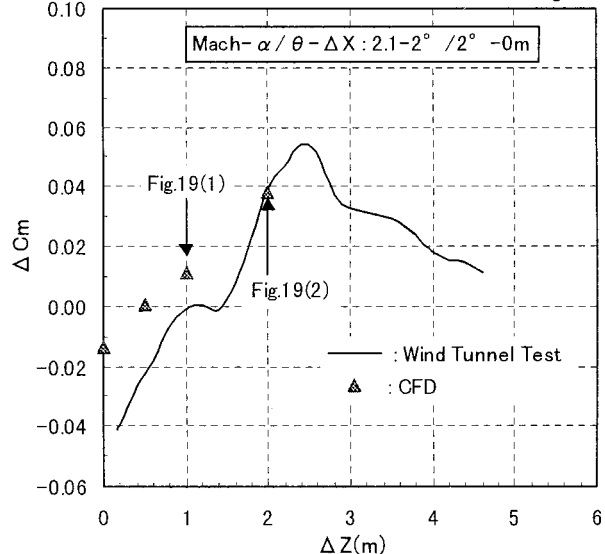
Fig.15 Pitching moment distribution of the launch configuration ($M=2.0, \alpha=0^\circ$)

(Reference Point : Experimental airplane 25%MAC)



(1) Experimental airplane

(Reference Point : 37.18% rocket-booster overall length)



(2) Rocket-booster

Fig.16 Interference component of pitching moment

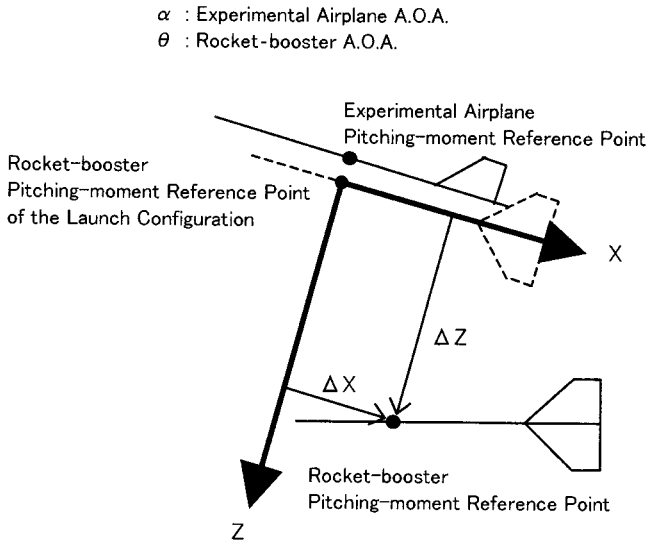


Fig.17 Definition of parameters

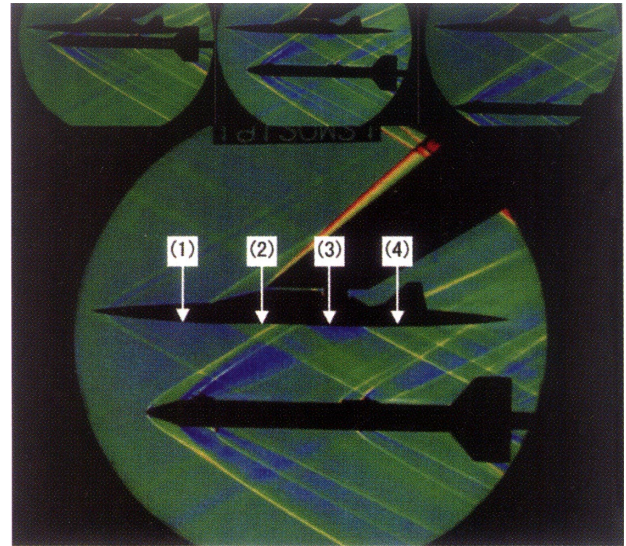


Fig.18 Schlieren photograph of grid wind tunnel test (Mach- $\alpha / \theta - \Delta X$: 2.1-2° / 2° -0m)

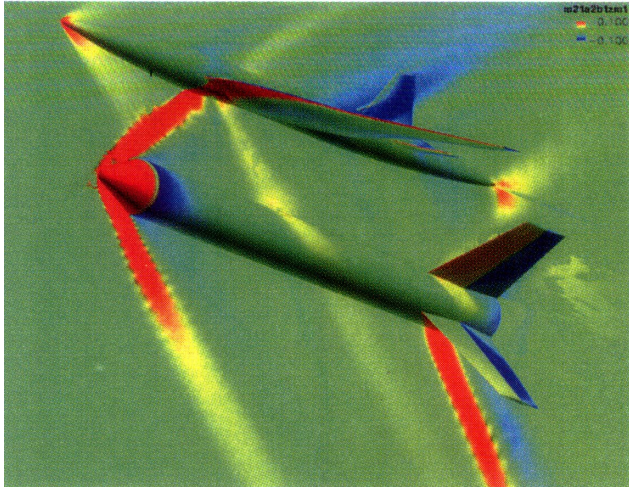


Fig.19(1) Pressure distribution by CFD (Mach- $\alpha / \theta - \Delta X / \Delta Z$: 2.1-2° / 2° -0m/1m)

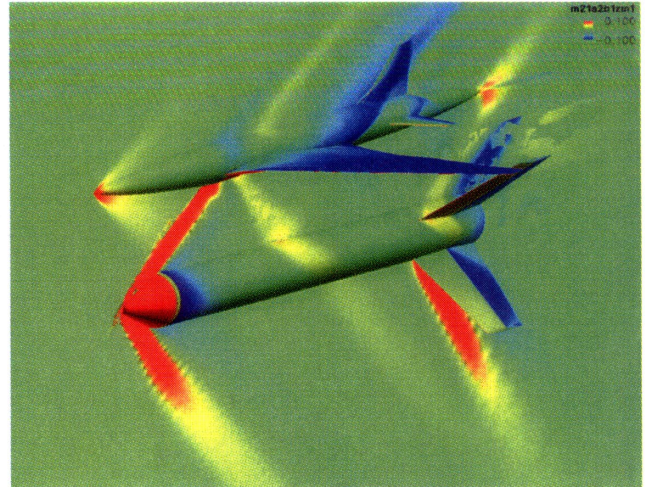
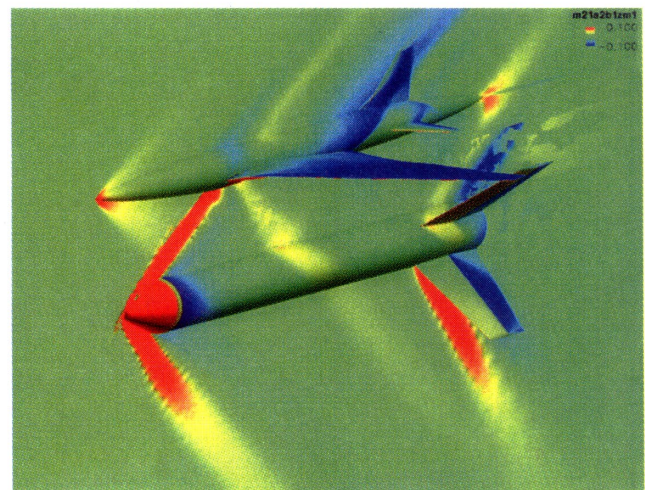
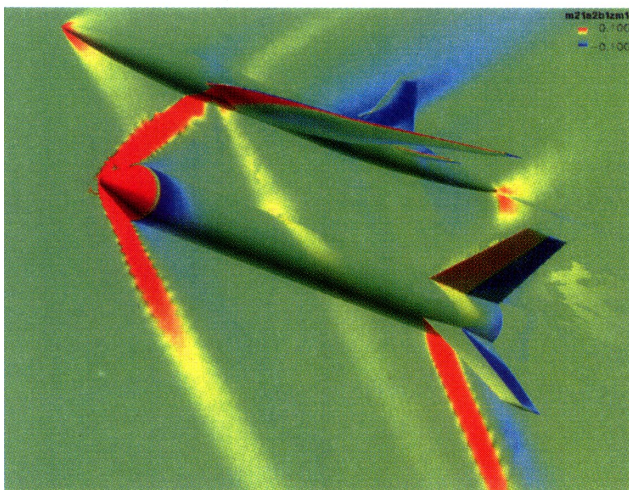


Fig.19(2) Pressure distribution by CFD (Mach- $\alpha / \theta - \Delta X / \Delta Z$: 2.1-2° / 2° -0m/2m)



Aerodynamic Design of Natural Laminar Flow Supersonic Aircraft Wings

Hirokage OGOSHI
Gifu Technology Institute
Kawasaki Heavy Industries, LTD.

Abstract

Aerodynamic design of Natural Laminar Flow (NLF) for supersonic aircraft wings was conducted by using 3-D CFD analysis and boundary layer stability analysis. There are two main subjects for NLF wing design. One is that the wing of the sub-scaled unmanned supersonic experimental aircraft of National Aerospace Laboratory¹⁾ (NAL) was designed to improve the L/D ratio. This wing sections were designed especially to reduce skin friction drag which amounts to nearly half of the total drag. For this purpose, we designed the wing sections to remain laminar flow as far as possible using 3-D CFD solver and 3-D laminar boundary layer stability analysis code and 2-D inverse design method. The other is that the simple sweep-back wing was designed to delay a transition due to cross flow instability in consideration of spanwise pressure distribution. (This design concept of NLF is patented.)

1. Introduction

A project led by NAL in Science and Technology Agency is underway to fly sub-scaled, unmanned supersonic aircraft(Fig.1). Kawasaki Heavy Industries participates in the program by designing aircraft with CFD analysis which is important in this project for aerodynamic design and evaluation. For conventional aircraft, the flight efficiency is dependent on L/D (lift to drag) ratio, so the drag should be reduced to improve the efficiency. For this purpose the following three technologies are usually applied:

- 1) reduction of wave drag due to volume (supersonic area rule, etc.)
- 2) reduction of induced drag (wing planform and warp-design, etc.)
- 3) reduction of friction drag (natural laminar flow, laminar flow control, riblets, etc.)

The first two technologies are mainly applied to the sub-scaled supersonic aircraft. Since the aircraft is nearly 12 meters long (about 10% scale of real future Supersonic Transport), friction drag amounts to about half of the total drag. To improve L/D ratio, we tried to apply friction drag reduction technology "Natural Laminar Flow" concept to wing by using "UG3²⁾" (KHI's 3-D unstructured grid CFD solver) and "SALLY³⁾" (incompressible 3-D laminar boundary layer stability analysis code).

2. Results of wing design for NLF

2.1. Set the target pressure distribution of NAL' experimental aircraft for NLF

We studied a wing without body to understand the relation between airfoil thickness distribution on wing and boundary layer transition characteristics at supersonic cruising condition, $M=2.0$, $CL=0.1$. CFD analyses were conducted with five different thickness distributions (NACA0003, 63003, 64003, 65003, 66003)⁴⁾ to obtain pressure distributions on wing surface, where the wing planform and the camber line were fixed.

The results of chordwise pressure distribution on the wing were used to perform compressive 3-D laminar boundary layer calculation to get velocity profile in boundary layer. Based on this velocity profile, we conducted 3-D laminar boundary layer stability analysis to get amplification rate of disturbance "N-factor". As an "N-factor" becomes large, the transition occurs earlier. Therefore, we judged a transition characteristics by the "N-factor". From these analyses, a transition point of NACA66003 was found closest to trailing edge. This leads to the conclusion that to optimize chordwise pressure distribution to delay the transition; the pressure distribution should be steep at leading edge and then has a slight acceleration gradient.

Therefore, we studied effects of pressure gradient change at three regions for a transition (Fig.2). After stability analysis of several pressure distributions, we achieved to obtain the optimized chordwise pressure distributions at each wing section for NLF (Fig.3).

To put that into practice, we designed a 3-D wing which realized these target pressure distributions using an inverse design method based on the 2-D Busemann's approximation. We then analyzed the 3-D wing by using UG3 and SALLY (Fig.4). The result was that the designed wing could make the "N-factor" smaller than a conventional wing section (NACA66003), which demonstrated the validity of the optimized chordwise pressure distribution that we proposed. (The increase of the N-factor at $0.05 < x/c < 0.15$ appeared because the pressure distribution of the designed wing was slightly different from the target distribution). These pressure distributions were adopted as the target distributions of NAL's experimental aircraft wing for NLF.

2.2. Considerations of Spanwise pressure distribution for NLF

When a wing has a large sweep-back angle, the cross flow instability in the boundary layer plays a dominant role in transition. To reduce cross-flow instability, we observed how the optimized chordwise pressure distribution developed spanwise. The cross flow instability is caused by the presence of cross flow velocity. To reduce cross flow velocity due to spanwise pressure difference, the pressure gradient has to be zero. To achieve such spanwise pressure distribution for NLF, we made two assumptions. One is the flow is supersonic and the other is the lift coefficient is not so large. From these assumptions, the stream line at boundary layer edge of wing upper surface matches with the mean stream, which means cross flow direction is perpendicular to the mean stream. Consequently, the design process was simplified.

Fig.5 shows surface pressure distribution on a simple sweep-back wing. In general, spanwise pressure gradient causes the cross flow velocity in boundary layer, then transition occurs due to cross-flow instability.

On the other hand, Fig.6 shows surface pressure distribution with no pressure gradient along with cross flow direction. That is, when pressure distributions at any section are on one line looking from the side, there is no pressure gradient to the cross flow direction. Consequently, a transition due to cross flow instability doesn't occur. (This wing design method is patented. (No.3005526))

Then, we designed a sweep-back wing by applying the above concept with inverse design method, and observed stream line around boundary layer edge and sublayer of both the initial and the designed configurations at $M=2.0$

(Fig.7, 8). The tip of the designed wing was twisted up because of applying large acceleration gradient to reduce T-S wave instability (Fig.8). Fig.9 shows that the stream lines on the surface of the designed wing are more straightforward than those of the initial wing, which means the cross-flow velocity in the boundary layer is reduced. (Fig.9, 10)

3. Conclusion

From a research on the application of Natural Laminar Flow to supersonic aircraft wings,

- The boundary layer transition is delayed by the optimized chordwise pressure distribution. This chordwise distribution was adopted as the target pressure distribution of NAL's experimental aircraft wing to achieve NLF.
- The optimized spanwise pressure distribution is proposed considering chordwise distribution which reduces cross-flow velocity in the boundary layer.

Acknowledgment

A part of the work was performed under contract of National Aerospace Laboratory in Science and Technology Agency.

Reference

- 1) Sakata, K., : "Supersonic Research Program in NAL, Japan", International CFD Workshop for Super-Sonic Transport Design, pp.1-4, 1998
- 2) Shima, E., : "Unstructured Grid CFD on Numerical Wind Tunnel", Parallel Computational Fluid Dynamic, North Holland, pp.475-482, 1999
- 3) Srokowski, A.J. : AIAA Paper 77-1222
- 4) I.H. Abbott, A.E. von Doenhoff : "Theory of wing sections", Dover

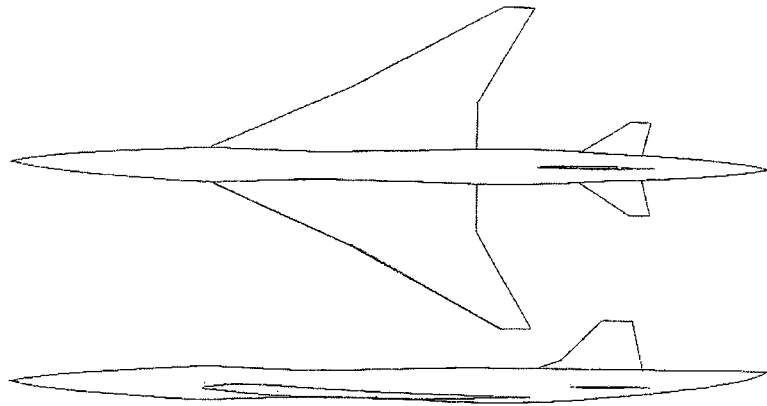


Fig.1 Supersonic sub-scaled experimental aircraft of NAL (1st Baseline)

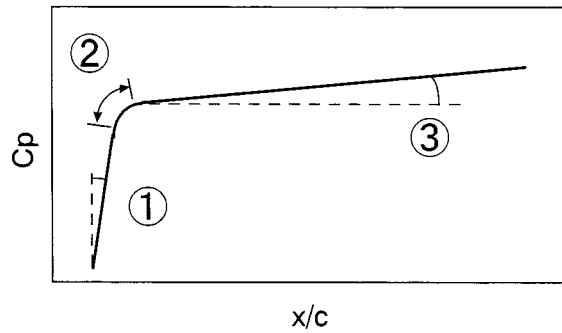


Fig.2 A model of chordwise target pressure distribution for NLF

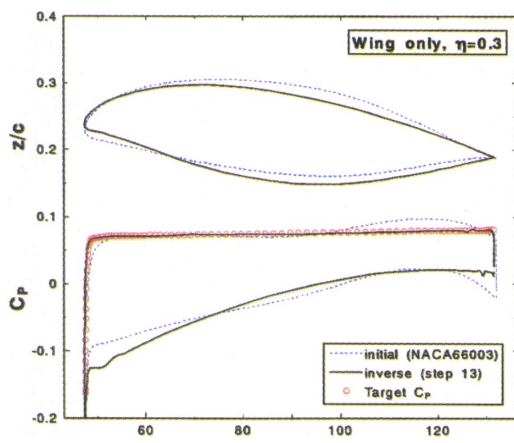


Fig.3 Optimized target pressure distribution for NLF and inverse designed wing of NAL's aircraft ($\eta = 0.3$)

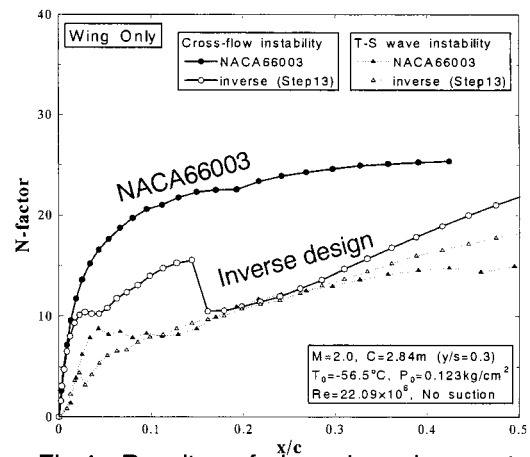


Fig.4 Results of boundary layer stability analysis.

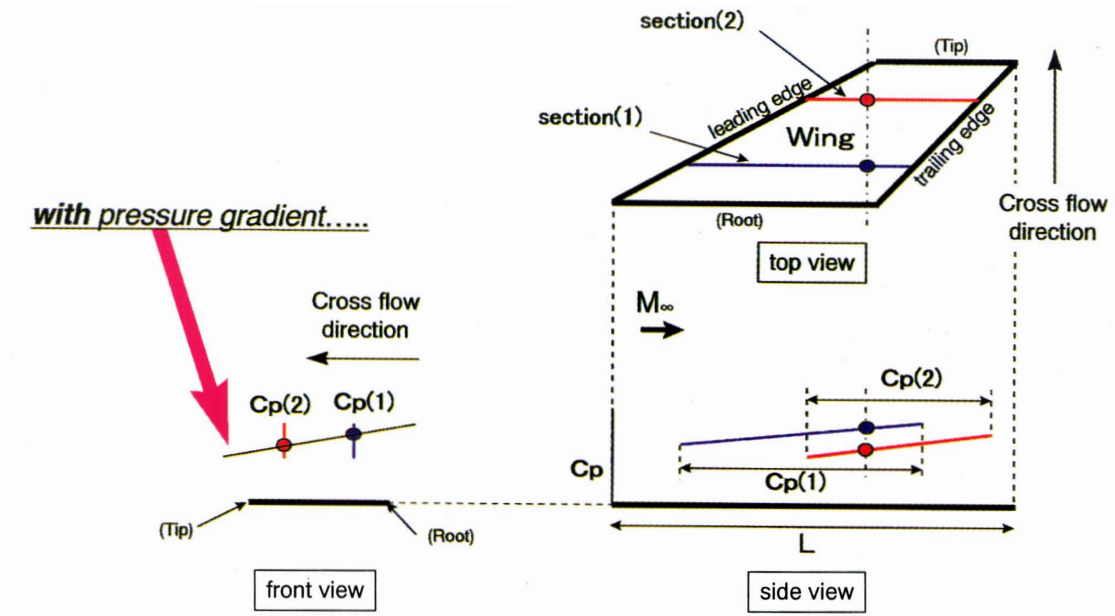


Fig.5 A model of spanwise pressure distribution of a simple sweep-back wing

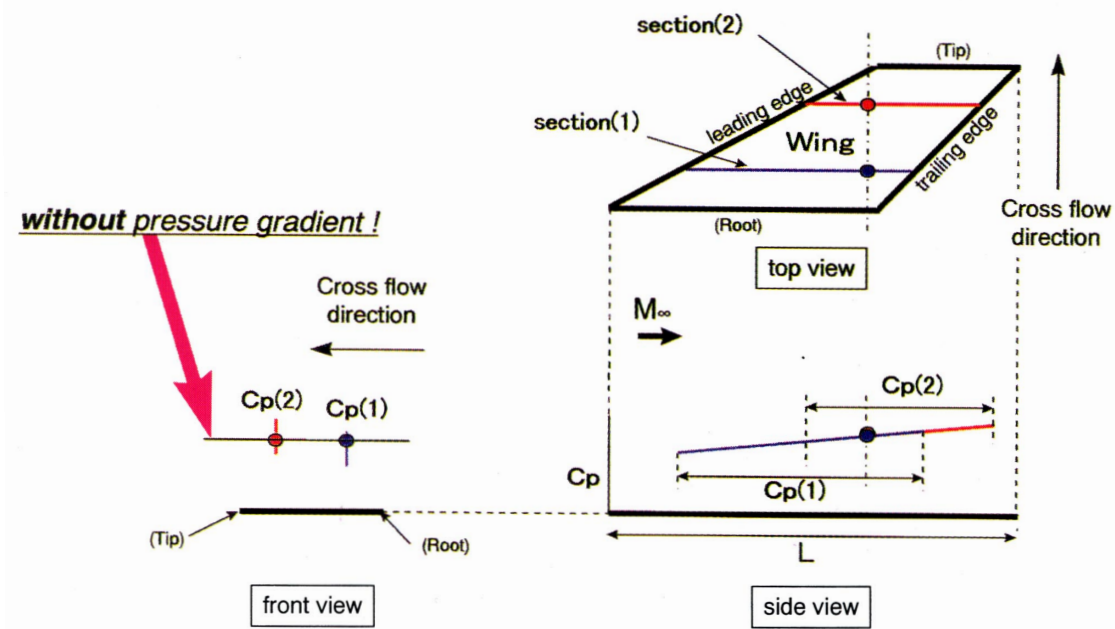


Fig.6 A model of spanwise pressure distribution of new NLF concept wing

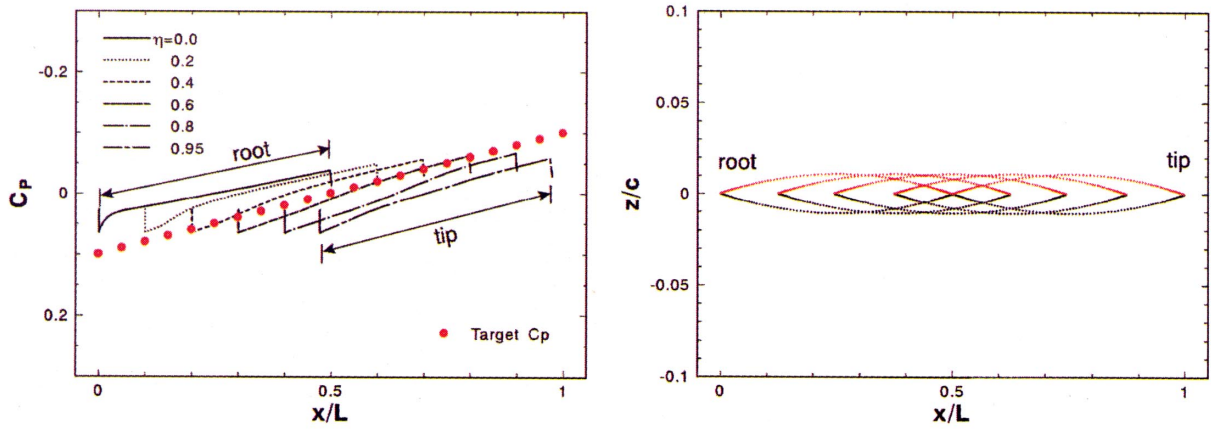


Fig.7 Pressure distributions and wing sections of an initial sweep-back wing

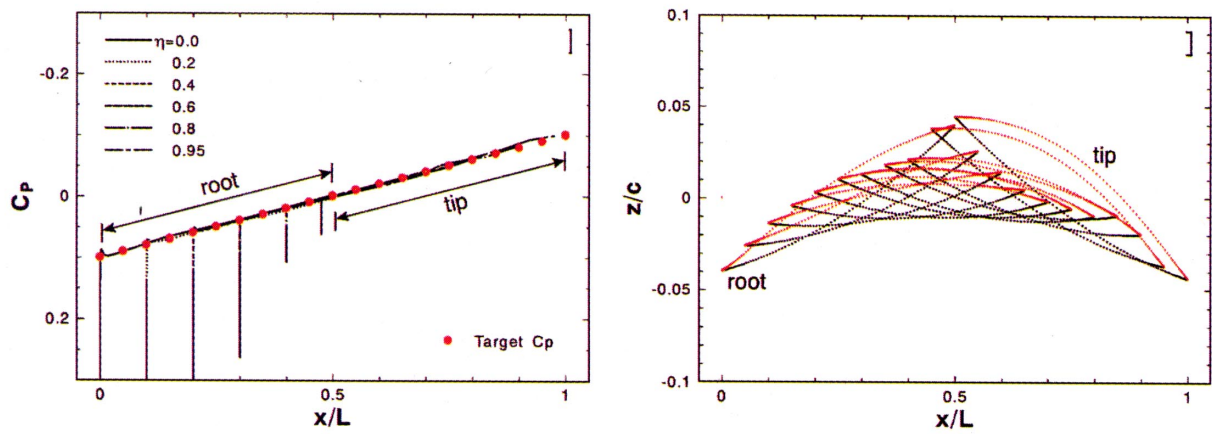


Fig.8 Pressure distributions and wing sections of a designed sweep-back wing by applying the optimized spanwise pressure distribution

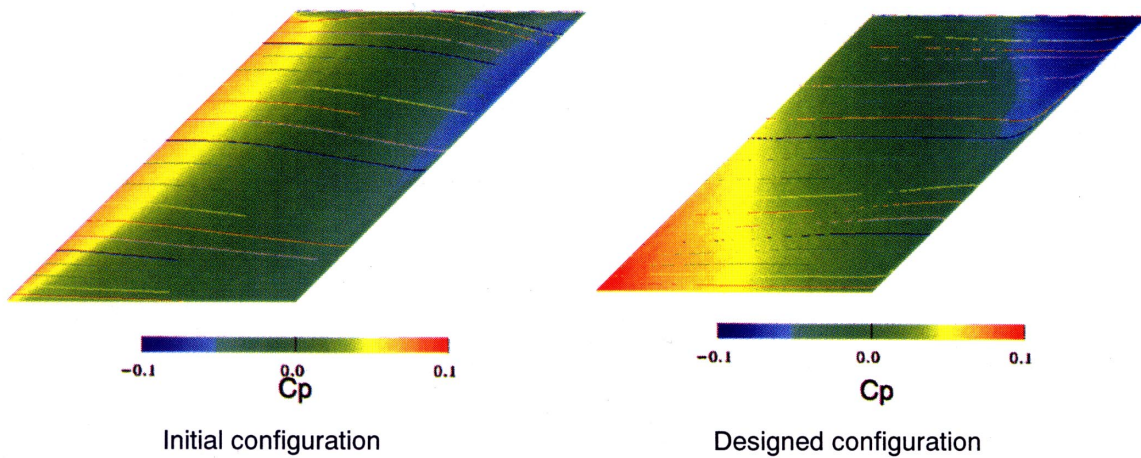


Fig.9 Surface pressure distributions and stream line in sublayer

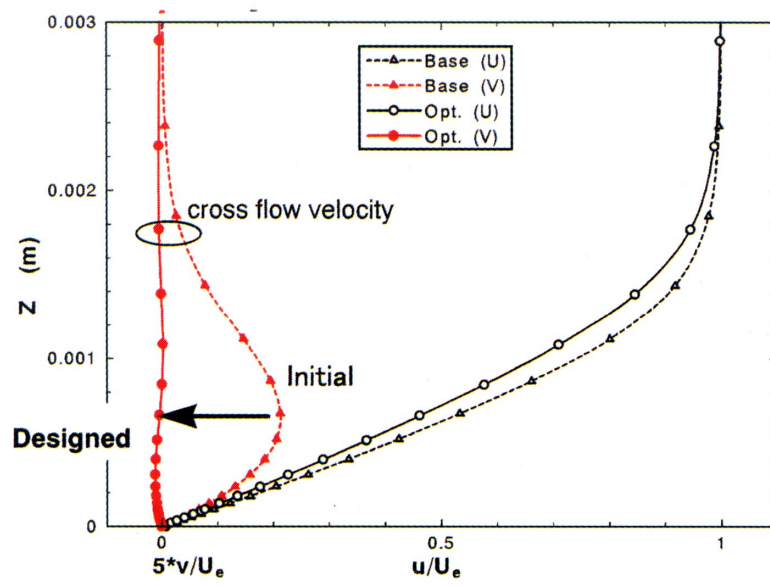


Fig.10 Boundary layer velocity profiles of initial and designed configuration (inverse) at $\eta = 0.5, x/c = 0.8$

CFD Application to SST Propulsion System

Y.Ooba and H.Kodama (Ishikawajima-Harima Heavy Industries)

O.Nozaki, K.Kikuchi, T. Nishizawa and Y.Matsuo (NAL)

Introduction

The SST propulsion system will operate in the range from takeoff to high Mach number. The high speed flight causes very high inlet air temperatures and pressures and the high inlet air temperatures and recovery pressures inside the engine make cooling for elements of the engine mandatory to keep the best available construction materials operating satisfactorily. Technology for satisfied cooling requires to understand the heat transfer in the engine, however there are many difficulties to understand detail phenomena occurred in the engine from limited measurement.

In order to understand the mechanisms of heat transfer in the engine and to explain test data results, CFD was found to be extremely helpful and important. CFD has also contributed to some new technical innovations. This paper describes some CFD applications in a SST engine development.

Analysis of secondary flowfields

inside turbine disc cavities

Flows inside a turbine disc cavity tend to be very complex because of its complicated geometries (see Fig.1). Heat transfer to the turbine disc is strongly influenced by the flow structure in the cavity. Therefore it is essential to know the flowfield inside the cavity for accurate prediction of the heat transfer.

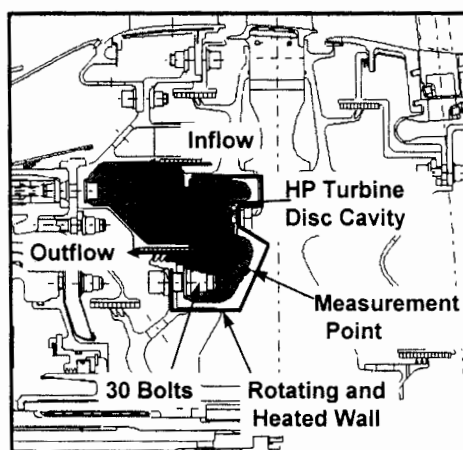


Fig. 1 Schematic of a HP turbine disc cavity

In this study, a three-dimensional Reynolds-averaged Navier-Stokes code was applied to simulate the flows in the turbine disc cavity. The study is focused on the effect of bolts in the cavity on the flowfield and resultant heat transfer.

30 bolts are located on the rotating wall surface of the turbine disc. One thirtieth domain of the annulus is calculated using the periodic boundary conditions at the circumferential ends. Only one bolt exits in the computational domain (see Fig.2).

Figure 3, 4 and 5 respectively show velocity vectors, distributions of temperature and swirl ratio inside the turbine disc cavity for the cases both with bolts and without bolts respectively. These figures show that flows inside the cavity are strongly influenced by existence of bolts inside the cavity. Swirl ratio is defined as swirl velocity of fluid divided by swirl velocity of the rotating surface at the same radial position. In the case with bolts, large differences of temperature and swirl velocity between the fluid and the heated surface of the cavity exist at the measurement point in figure 1. On the other hand, the differences of temperature and swirl velocity become smaller in the case with bolts there.

Comparing thermal conductivity calculated using numerical results between both cases, value of the case with bolts becomes 1.3 times of the case without bolts. Considering heat transfer at that region, smaller thermal conductivity for the case with bolts is explained for the reason that differences of temperature and velocity become smaller. These results indicate that heat transfer is strongly influenced by the detail shape of the surface inside the cavity.

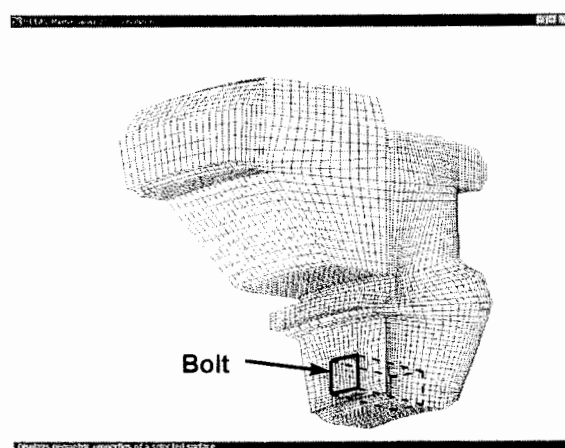


Fig.2 Numerical grid of turbine disc cavity (configuration with bolt shape)

Conclusion

The three-dimensional viscous numerical simulations of flowfield inside a turbine disc cavity including heat transfer are shown in this paper. The results indicate that the heat transfer to the turbine disc is affected by the detail shape of the surface inside the cavity like bolts and the correct modeling of the shape of the cavity must be considered in order to predict the flowfield and resultant heat transfer accurately.

References

[1] Yamawaki, S., Ohkita, Y. and Kodama, H., "CFD Contribution to Development of HYPR engine", AIAA Paper 99-0886

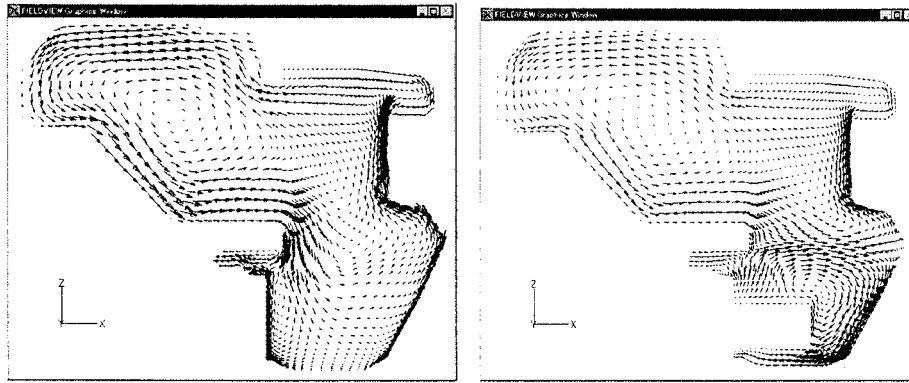


Fig. 3 Velocity vectors inside turbine disc cavity

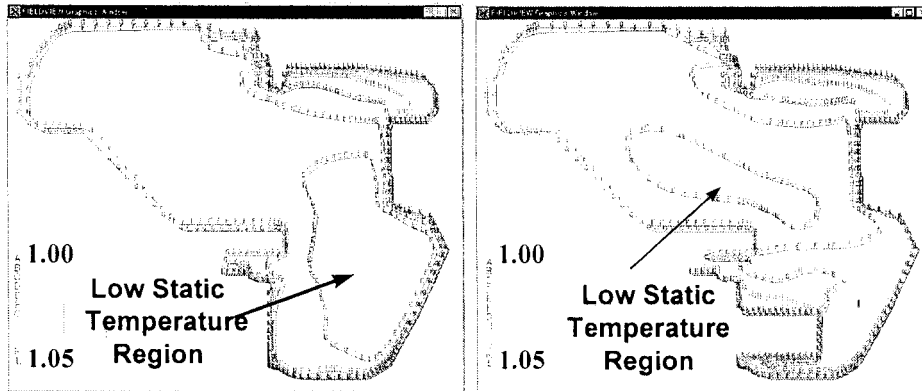


Fig. 4 Distributions of temperature inside turbine disc cavity

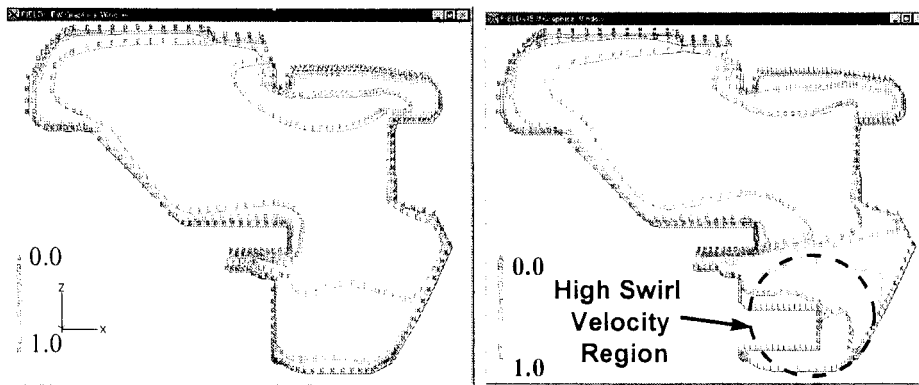


Fig. 5 Distributions of swirl angle ratio inside turbine disc cavity

A Structured Grid Method in Simulating a Flow Around Supersonic Transports

Shunji ENOMOTO

Aeroengine Division
National Aerospace Laboratory

eno@nal.go.jp

Introduction

In the SST development project, it is expected to perform numerical simulations of the configuration of the airframe and the engine (Fig.1). But it is not easy task to solve these flow field using existing CFD codes, because the geometry of the flow passage is very complicated. Development of a CFD code that makes easy to solve complex flowfield is expected.

UPACS is a CFD code development project, which is performed in National Aerospace Laboratory since 1997. A structured grid, multiblock, multiprocessor CFD solver is under development as the first CFD solver of this project. The basic idea of the code and some points of issue will be discussed in this report.

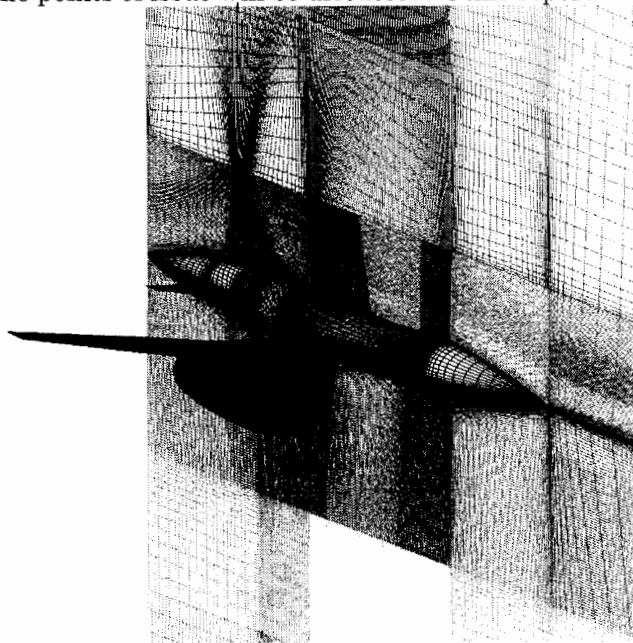


Fig. 1 Computational Grids of the SST configuration.

Numerical methods for complex topologies

The topologies of flow passages in practical problems are often very complicated. The task of making body-fitted structured grids and computational programs for them is often very troublesome. Today, the most difficult problem is the grid generation. Making body-fitted structured grid will not be automated in the near future. There are some good commercial grid generation tools, but it is

still not very easy task to make grids using these tools.

Unstructured or overset grid methods are expected to be the solution for the problem, and they seem promising. Using these methods, it will be easy to make a body-fitted grid around the complex configuration, a solution adapted grid, and a moving grid.

However, comparing to these other methods, structured grid methods still possess some advantages. It is easier to implement higher order differential schemes and turbulence models in structured grid systems. It also has the advantage of efficiency and accuracy, especially for the case that the grid has good orthogonality, since most of higher order differential schemes and turbulence models are originally developed on a structured grid.

When the accuracy of the solution has the first priority, a structured grid method may be a good choice. But we have to devise some way to solve the problem of geometry complexity.

Multiblock

To apply body-fitted structured grids to a complicated flow passage, a multi-block decomposition method has to be used. A single-block skewed grid may be converted into multi-block grids that have good orthogonality. It also provides us a straightforward way to use multi processor computers. The disadvantage is that we have to transfer data between blocks, so the programming for the multiblock grid system is not very simple.

In order to maintain the accuracy on block boundaries, grid points on the block boundary have to be one by one. The orthogonality of the grids has to be good, too. To achieve these requirements, we have to use unstructured block connection. Figure 2 shows the examples of structured connections and unstructured connections.

Structured connection

The connection between blocks categorized into two types, structured and unstructured (Fig.2).

The structured connection can be defined as the connection where four blocks meet at one point. The unstructured connection can be defined as the connection other than the structured connection, for example, the connection where three or five blocks meet at one point.

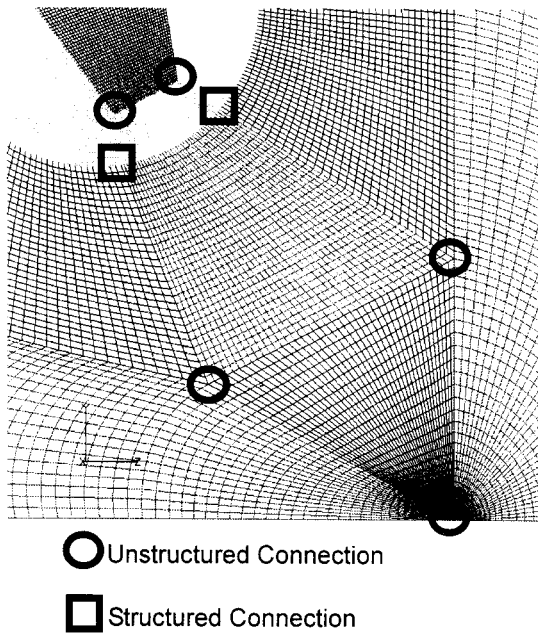


Fig.2 Structured connection and unstructured connection

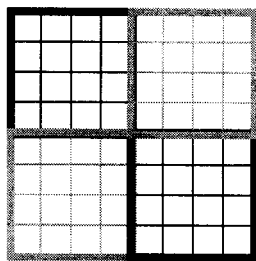


Fig.3 Structured connection

Figure 3 shows the typical example of structured block connections. Since the accuracy of the solution has the first priority, we do not want to let the block connection deteriorate the accuracy of the solution. In order to maintain the accuracy on the boundary, some overlapped region are defined and the data on that are transferred each other. The width of the overlapped region depends on the length of the stencil of the numerical scheme.

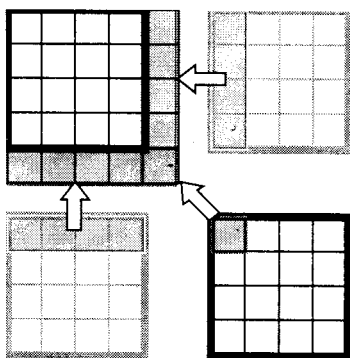


Fig.4 Overlapped region and data transfer

In order to maintain the accuracy near the block connection, each block have some overlapped points,

and data of the adjacent block are transferred each other. For the accuracy of viscous terms, corner data have to be transferred, too(Fig.4). In three dimension, there are three type data transfer such as , 6 faces, 12 edges and 8 corners.

Unstructured connection

Figure 5 shows the typical example of unstructured block connections.

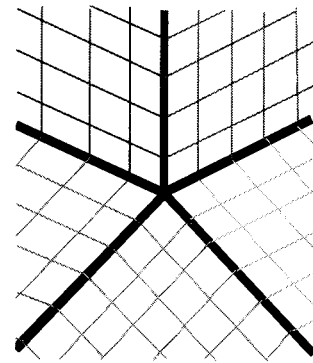


Fig.5 Unstructured connection

For the unstructured connection case, we cannot define the value of the corner point of the overlapped region. So we have to use some interpolation, and it makes the accuracy of viscous term a little worse.

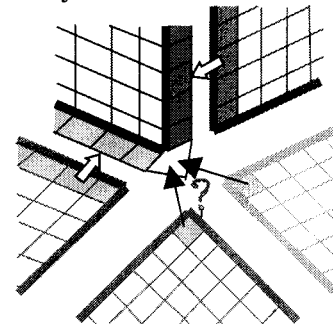


Fig.6 Data transfer for unstructured-like connections

Unstructured-like block

For some cases, we may not be able to fill all geometry with hexahedron blocks. For such case, the unstructured-like block are used. Figure 7 shows an example of such blocks.

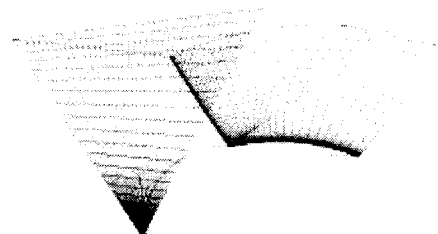


Fig.7 Unstructured-like block

In unstructured-like block, an edge line may

degenerate into a point, or a surface plain may degenerate into a line. The concentrated grid might limit the time step and the accuracy of the computation.

Requirement for a multiblock solver

The requirement for a multiblock solver is that the result is not deteriorated by the block decomposition.

1. The accuracy is not affected on the structured connections, no matter how long the length of the stencil of the numerical scheme.
2. The accuracy around the unstructured connection should be maintained as much as possible.
3. The time accuracy of the unsteady calculation is not affected by the block decomposition.

In order to satisfy these requirements, data transfer between adjacent blocks has to be performed frequently. Since we may use multi processor computers, the programming of data transfer have to be written in some multi-processing library, such as MPI. Compared with traditional single processor programming, the multi processor programming is not very easy and flexible task

Data transfer

Basic equation of a conservation law can be written in this generalized form:

$$\frac{\partial}{\partial t} \int QdV + \int FdA = 0$$

The discretized form of the basic equation can be written as like this form:

$$\Delta Q = \Delta t \cdot RHS(Q)$$

Generally, the flow chart of the CFD solver can be written like figure 8.

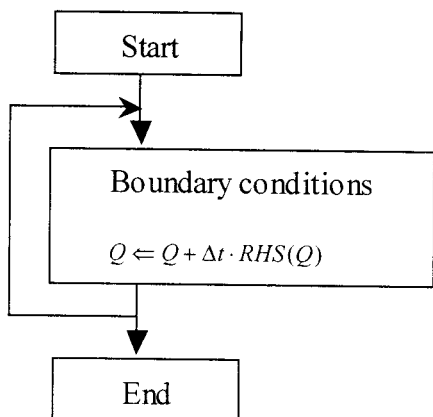


Fig. 8 Flow chart of CFD solver

For multiblock program, data transfer between blocks have to be performed somewhere in the flow chart. First, we thought that all we have to do is to transfer data between blocks one time per one iteration (Fig.9).

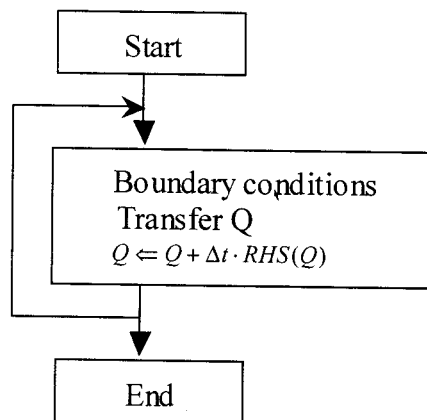


Fig.9 Flow chart of simple multiblock program

But soon we found that was not enough. We need transfer not only flow data(Q), but also grid metrics. If we use Runge-Kutta method, we need to transfer physical variables several times in one iteration. When we use a turbulence model, some other data have to be transferred between blocks, too.

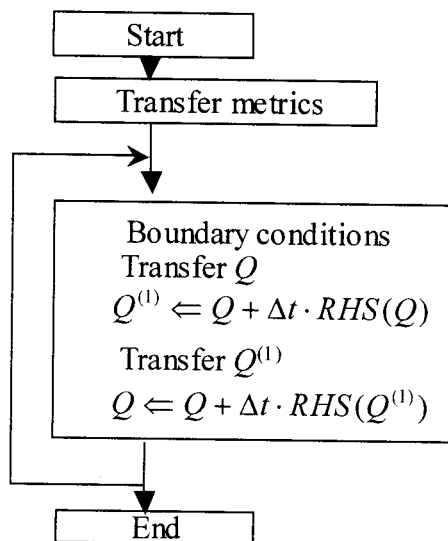


Fig.10 Flow chart of practical multiblock program

UPACS

Under these circumstances, UPACS has been developing. We think that there are two requirements for UPACS. One is that it to be a tool for CFD researchers. The other is to be a general-purpose flow solver for fluid-machine designers.

Multi-block, multi-processor programs tend to be very complicated. On the other hand, computer programs for researchers need to be simple, because the programs are continuously modified in order to try new ideas. To satisfy these requirements, UPACS has been developing as a platform or an environment for CFD tools. It has following features:

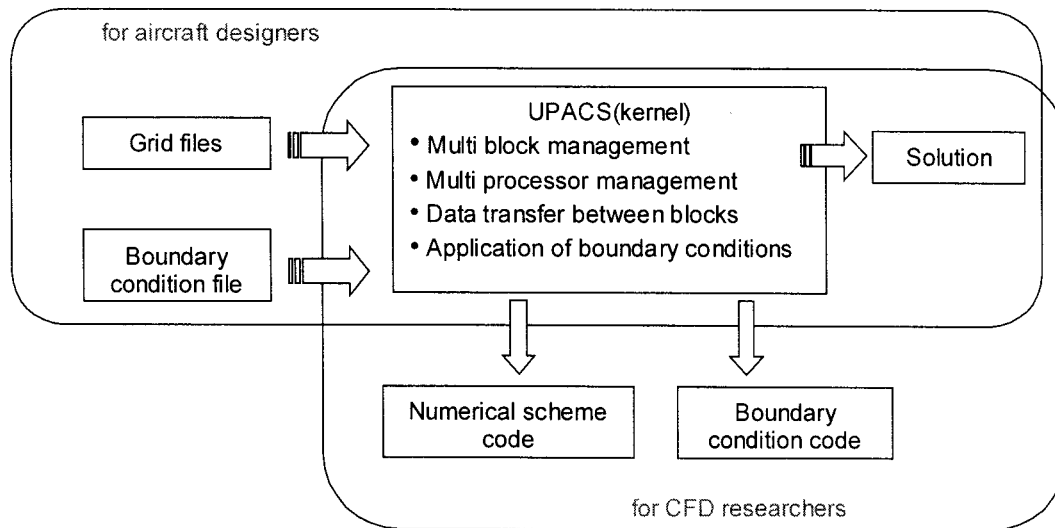


Fig. 10 UPACS environment

1. The multi-block, multi-processor part of the program and the CFD part are separated from each other. It makes easier for CFD researchers to modify and improve CFD part.
2. Existing single-block CFD solvers can be introduced into the program easily. In other words, CFD researcher writes CFD solvers for a single block and do not have to care about multiblocks. UPACS will apply the solver for all blocks.
3. CFD researcher writes generalized boundary condition routines. UPACS will apply the boundary condition to appropriate boundary.
4. Data transfer between blocks is performed automatically. CFD researcher only has to specify the data name. UPACS will transfer data between blocks.

Current CFD solver in UPACS is originally from already existed single block CFD solver. It is based on compressible Navier-Stokes equation, and has some options.

- Convective term: Roe scheme, AUSMDV, etc.
- Time integral: Runge-Kutta, MFGS, etc.
- Turbulence model: Baldwin-Lomax, Spalart-Allmaras

The program is made for general-purpose as much as possible. Many control parameters and control files made it possible. Since these control files are generated automatically, CFD designers are free from complicated tasks to apply the program to new flow geometry. Therefore, UPACS for aircraft designers is easy to use, like commercial CFD codes. Users do not need to make or edit a program to apply each problem. Computational grid and some parameter files are only required to perform CFD analysis.

Conclusion

In the SST project, UPACS is going to be used to simulate complicated flow phenomena around airframe and engine integration with higher-order

turbulence models. It will be used to evaluate the configuration of SST experimental models. Through these activities, we have many opportunities to compare experimental results and the simulations. So it also will be a test bed of turbulence models.

The latest version of UPACS has succeeded inviscid calculation around a SST configuration with 105 blocks.

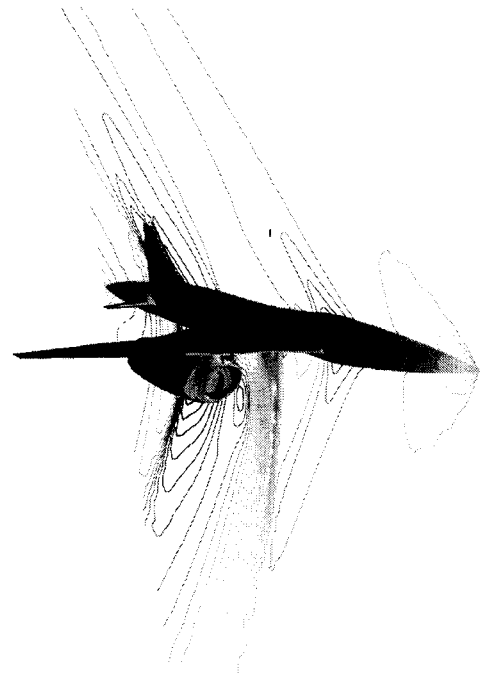


Fig. 11 Pressure contour

Simple Algorithms of CFD for Compressible Flows

Eiji Shima

Gifu Technical Institute, Kawasaki Heavy Industries LTD.

shima_e@khi.co.jp

Abstract

Upwind scheme is one of the most important components of modern numerical scheme for gas dynamics. No scheme, however, is perfect on accuracy, robustness and efficiency. Among a lot of schemes, AUSM developed by Liou et al. satisfies many requirements. Today, there are many practical schemes which can be written in the same form with AUSM. We call these schemes as AUSM type schemes. In order to investigate the key of favorable feature of AUSM type schemes, three new simple schemes are presented and numerically tested. It is shown that a new scheme (ST-AUSM) is simpler than other schemes, however, it exhibits better results.

1. Introduction

Robust and accurate numerical algorithms are required for the viscous supersonic flow analysis of an SST (Super Sonic Transport). Although Mach number of the flow around an SST is not so high, complex flows due to the realistic aircraft shape sometimes blow up computations. In order to stabilize the computation, increasing numerical viscosity is effective, it, however, degrades the accuracy of viscous boundary layer. The boundary layer must be carefully computed, because approximately 50% of total drag is generated by skin friction due to the turbulent boundary layer. A numerical inviscid flux has significant influence on both robustness and accuracy, therefore its selection is vital to the computation.

In order to give the numerical flux in a robust and accurate way, upwind schemes for gas dynamics have been widely used as the basis of high resolution schemes. FDS (Flux Difference Splitting) [1][2] schemes and FVS (Flux Vector Splitting) [3][4][5] schemes were developed as extensions of an upwind scheme for a linear equation and have achieved great successes. It is known that FDS and FVS schemes, however, have some weak points. FDS schemes sometimes give unphysical flux at high Mach number and suffer from the violent carbuncle phenomenon. Numerical diffusion of FVS schemes are too big for the viscous flow problems. HLLE (Harten-Lax-van Leer) scheme and HLLEM (HLLE Modified) scheme were developed [6] to improve FDS, but HLLE's numerical viscosity is as large as FVS and HLLEM is more complex than FDS and suffers from the carbuncle too.

On the other hand, by simplifying FVS, Liou & Steffen [7] invented AUSM (Advection Upstream Splitting Method). AUSM is very simple, robust for strong shock and accurate for boundary layer, however, shows overshoot at a shock front. Inspired by AUSM, many schemes have been proposed. Jameson [8][9] showed CUSP (Convective Upstream Split Pressure) which is similar to AUSM but is expressed in combination of central difference and numerical diffusion. Jounouchi et al. [10] showed SFS (Simplified Flux vector Splitting method) in the similar form with AUSM but using mass flux of van Leer's FVS and improved overshoot at a shock. Wada and Liou [11] showed AUSMDV (AUSM with flux Difference splitting and flux Vector splitting) as an improvement from AUSM and showed precise research on

their scheme and others. Shima and Jounouchi [12] showed that many schemes can be made which should be called AUSM type schemes in the common form with AUSM and introduced uni-particle upwind schemes in AUSM type schemes and exhibited SHUS (Simple High-resolution Upwind Scheme). Jounouchi et al. [13] pointed out the physical interpretation and theoretical background of AUSM type schemes and then showed that SFS is applicable to the two-phase flow. On the other hand, Nakamori and Nakamura proposed new FVS (NNFVS hereafter) as the improvement of Steger-Warming's FVS in order to improve the accuracy of viscous flow. [14] Liou [15] also presented AUSM+ and AUSM+-W to improve AUSM.

Although some of these schemes have been developed independently, these schemes can be written in the common form. These schemes can be called as AUSM type schemes. Since AUSM type schemes are simple, robust and accurate enough for practical application, they have been used for many applications especially for hypersonic viscous problems already.

High resolution schemes using AUSM type schemes have already been used successfully for many applications as mentioned above, however, there are other high resolution schemes which are completely different from AUSM type schemes. For example, multi-dimensional upwind schemes use multi-dimensional splitting of characteristic waves and show better performance for oblique discontinuity. [16]-[23] CIP (Cubic Interpolated Polynomial) scheme uses non-conservative semi-Lagrange scheme and von Neuman's numerical viscosity and achieves great success in computation of multiphase flows containing strong shock waves. [24][25]

It is expected that the way in which AUSM type schemes simplified one-dimensional Riemann solver will be effective for simplifying multidimensional upwind schemes. And also, upwind schemes are interpreted as non-diffusive scheme with numerical diffusion, therefore it may be possible to apply numerical diffusion working in AUSM type scheme to non-conservative scheme.

In this study, first, we show a common form for AUSM type schemes and introduce several AUSM type schemes. Second, a new member of AUSM type scheme, which may be the simplest one, is introduced in order to investigate key feature of AUSM type schemes. In order to check this feature, two more schemes are demonstrated.

2. Formulation of AUSM type schemes

2.1. The common form of AUSM type schemes

We show the formulation of AUSM type schemes for three dimensional Euler equation. The equation can be written in the integral form as follows.

$$\int \mathbf{Q} dv + \int \bar{\mathbf{F}} ds = 0 \quad (1)$$

$$\mathbf{Q} = \begin{pmatrix} \rho \\ \rho u \\ \rho v \\ \rho w \\ e \end{pmatrix} \quad (2)$$

$$\bar{\mathbf{F}} = m\Phi + p\mathbf{N}, \quad \Phi = \begin{pmatrix} u \\ v \\ w \\ h \end{pmatrix}, \quad \mathbf{N} = \begin{pmatrix} 0 \\ x_n \\ y_n \\ z_n \\ 0 \end{pmatrix} \quad (3)$$

$$m = \rho V_n, \quad V_n = x_n u + y_n v + z_n w \quad (4)$$

where ρ, u, v, w, e, p and $h = (e + p)/\rho$ represent density, velocity in x,y,z direction, total energy per unit volume and total enthalpy respectively. (x_n, y_n, z_n) is a unit normal of a surface. The variable m denotes mass flux. This form indicates that Euler flux can be divided into the convective term and the pressure term.

AUSM is based on the fact that the convective term and the pressure term can be upwinded separately. The original AUSM and all other AUSM type schemes can be written in a following form,

$$\bar{\mathbf{F}} = \frac{m + |m|}{2} \Phi_+ + \frac{m - |m|}{2} \Phi_- + \bar{p}\mathbf{N} \quad (5)$$

where subscript \pm denote physical values at the left(+) and right(-) sides of cell boundaries suggesting directions of propagation. And \bar{p} is mixing of left and right pressures using functions of Mach number of left and right state which is defined by,

$$p = \beta_+ p_+ + \beta_- p_- + p' \quad (6)$$

$$\beta_{\pm} = \begin{cases} \frac{1}{4}(2 \mp M_{\pm})(M_{\pm} \pm 1)^2, & \text{if } |M_{\pm}| < 1 \\ \max(0, \min(1, \frac{1 \pm M_{\pm}}{2})), & \text{if } |M_{\pm}| \geq 1 \end{cases} \quad (7)$$

These functions are the simplest smooth polynomial functions that satisfy consistency and upwind nature, however other selections are possible. The symbol p' is a pressure correction term mentioned in section 2.3.

2.2 Selection of mass flux

In original AUSM, the mass flux is calculated using simple switches of Mach number, as

$$m = \frac{\bar{M} + |\bar{M}|}{2} \rho_+ c_+ + \frac{\bar{M} - |\bar{M}|}{2} \rho_- c_- \quad (8)$$

$$\bar{M} = M_+ + M_- \quad (9)$$

$$M_{\pm} = \begin{cases} \pm \frac{1}{4} \left(\frac{V_{n\pm}}{c_{\pm}} \pm 1 \right)^2, & \text{if } \left| \frac{V_{n\pm}}{c_{\pm}} \right| < 1 \\ \frac{V_{n\pm} \pm |V_{n\pm}|}{c_{\pm}}, & \text{if } \frac{V_{n\pm}}{c_{\pm}} \geq 1 \end{cases} \quad (10)$$

Various schemes can be made replacing mass flux. Formulations of several AUSM type schemes are shown in

Appendix. SFS and AUSMDV use variations of van Leer's FVS for their mass flux. Shima and Jounouchi [12] showed that mass fluxes of any Riemann solvers can be applied for that of AUSM type scheme and showed improvements when those mass fluxes are used. They derived SHUS (Simple High Resolution Upwind Scheme) using mass flux of Roe scheme, such as,

$$m = \frac{1}{2} \{ (\rho V_n)_+ + (\rho V_n)_- - |\bar{V}_n| \Delta \rho - \frac{|\bar{M} + 1| - |\bar{M} - 1|}{2} \bar{\rho} \bar{V}_n - \frac{|\bar{M} + 1| + |\bar{M} - 1| - 2|\bar{M}|}{2|\bar{M}|} \Delta p \} \quad (11)$$

$$\bar{M} = \frac{1}{\theta} \frac{\bar{V}_n}{\bar{c}} \quad (12)$$

$$\theta = \max(1, \frac{1}{2\rho_+} (\frac{\bar{\rho} \Delta V_n}{\bar{c}} - \frac{\Delta p}{\bar{c}^2}), \frac{1}{2\rho_-} (\frac{\bar{\rho} \Delta V_n}{\bar{c}} + \frac{\Delta p}{\bar{c}^2})) \quad (13)$$

$$\Delta q = q_- - q_+ \quad (14)$$

$$\rho = (\rho_+ + \rho_-)/2 \quad (15)$$

$$\bar{V}_n = (V_{n+} + V_{n-})/2 \quad (16)$$

$$c = (c_+ + c_-)/2 \quad (17)$$

Note that there is no need for Roe averaged value for this scheme. A parameter θ is introduced for measure against low density. This scheme looks a little complex than original AUSM, however, the computation is simpler because no conditional branch is necessary.

The result of shock tube problem (Sod's standard problem) by second order Roe scheme, original AUSM and SHUS are shown in Fig.1-3. Second order accuracy is achieved by MUSCL using van Albada's differentiable limiter. As shown in figures original AUSM exhibit small overshoot. On the other hand SHUS shows no overshoot and almost identical result with Roe scheme. SHUS has been already applied for wide range of practical computations including three-dimensional Navier-Stokes analysis of the super sonic flyable demonstrator of NAL.

2.3 Pressure correction term

Wada and Liou^[11] showed that the pressure term without the pressure correction is sufficient for an usual case, therefore, over shoots are found at a strong propagating shock like a supersonic colliding jet without it. Note that they include this correction as a modification of normal component of momentum flux, not in the pressure correction. They pointed out that the use of normal momentum flux of Hänel's FVS, which is equivalent to van Leer's one, improve this problem. They use this momentum flux for their AUSMDV scheme. Nakamori and Nakamura^[13] used similar method in their FVS (NNFVS). These modifications can also be written as pressure corrections as follows and this way is more convenient to explain various AUSM type schemes in a unified manner.

Let $\bar{\mathbf{F}}$ be an uncorrected flux and $\bar{\mathbf{F}}_{\text{FVS}}$ be a flux whose normal momentum flux is replaced by that of a FVS scheme. This correction can be written in the form of pressure correction as,

$$\bar{\mathbf{F}}_{\text{corrected}} = \bar{\mathbf{F}} + p'\mathbf{N} \quad (18)$$

$$p' = (\bar{\mathbf{F}}_{\text{FVS}} - \bar{\mathbf{F}}) \cdot \mathbf{N} \quad (19)$$

If the mass flux of Hänel's FVS, which is same as van Leer's, is used, p' is written as,

$$p' = \frac{1}{2}(m_+ + m_- - |m|)(V_{n+} - V_{n-}), \quad (20)$$

where mass flux of Hänel's FVS is given by

$$m = m_+ + m_- \quad (21)$$

$$m_{\pm} = \begin{cases} \pm(\rho c)_{\pm}(M_{\pm} \pm 1)^2, & \text{if } |M_{\pm}| < 1 \\ \frac{(\rho V)_{n\pm} \pm |(\rho V)_{n\pm}|}{2}, & \text{if } |M_{\pm}| \geq 1 \end{cases} \quad (22)$$

Because Hänel's FVS is given by,

$$\mathbf{F}_{\text{FVS}} = m_+ \mathbf{F}_+ + m_- \mathbf{F}_- + (\beta_+ p_+ + \beta_- p_-) \mathbf{N} \quad (23)$$

See Appendix for actual form of this term for AUSMDV and NNFVS.

Note that, these corrections are only needed for a strong propagating shock and that these are not used in numerical examples of this report.

3. New simple AUSM type schemes

3.1 ST-AUSM (Simplest-AUSM): Use simpler mass flux

It has been shown in some reports that variations of AUSM type scheme works well. Let us think simpler scheme in order to investigate the key of the favorable nature of AUSM type schemes. We use a simple upwind mass flux using just convective velocity, such as,

$$m = \frac{1}{2}((\rho V_n)_+ + (\rho V_n)_- - |\bar{V}_n|(\rho_- - \rho_+)) \quad (24)$$

Several methods can be used for computing average velocity, we use mass averaged one here.

$$\bar{V}_n = \frac{(\rho V_n)_+ + (\rho V_n)_-}{\rho_+ + \rho_-} \quad (25)$$

In this case, mass flux can be also written in following form.

$$m = \frac{\rho_+ + \rho_-}{2} \bar{V}_n + \frac{\rho_+ - \rho_-}{2} |\bar{V}_n| \quad (26)$$

Numerical experiments showed that other averaging of velocity, such as arithmetic average or maximum of two, worked also well for equation (26). Although this scheme is very simple, the solution have much smaller overshoot than original AUSM (Fig.4) and give best result among Roe, AUSM, SHUS and ST-AUSM for supersonic flow before cylinder(Fig.5). In latter case, Roe scheme exhibits violent carbuncle, AUSM does overshoot at shock, SHUS does slight unnatural concave around stagnation point but ST-AUSM has no problem.

ST-AUSM is robust enough for usual subsonic and supersonic flows, because it gives only small overshoot at shock and correct flux (i.e. no flux) for strong, which means vacuum is found in expansion region, symmetric expansion, and which occurs behind body in initial stage of computation. However, computation breaks at strong, asymmetric expansion problem in one-dimensional test case.

3.2 SCHEME2: Consideration on Split pressure Term

It has been shown that various AUSM type schemes including new simple scheme work fairly well. Now we consider the common nature of AUSM type schemes. The success of new scheme (ST-AUSM) shows that even a simple upwind method based on convective velocity works well as a mass flux term. Thus it is considered that selection of mass flux has merely minor influence on the favorable nature of AUSM type schemes. Although various methods are used for mass fluxes, all AUSM type schemes use similar split pressure terms. Therefore it is easily expected that this pressure term

will be the key for favorable character of these schemes. The split pressure term looks just a smooth upwind switch, however, the Taylor expansion of this term in subsonic case shows that this term work as numerical diffusion too, as follows.

$$\begin{aligned} \bar{p} &= \beta_+ p_L + \beta_- p_R \\ &= \frac{p_L + p_R}{2} \left\{ 1 - \frac{3}{4c} (1 - M^2) \Delta V_n \right\} - \frac{1}{4} (3M - M^3) \Delta p + O(\Delta^2), |M| < 1 \end{aligned} \quad (27)$$

The second term in first blanket works as diffusion term for velocity when Mach number is smaller than unity, because first derivative of velocity in pressure term become a second order derivative in momentum equations. The Δp term works as smooth upwind switch of pressure.

Here, let us think about the origin of the split pressure term. The split pressure term comes from momentum term of van Leer's FVS scheme. van Leer's FVS is essentially a first order accurate upwind scheme for Euler equation using smooth swithing functions. An upwind scheme consists of central difference and diffusion term, thus, it is natural that the split pressure term have also diffusive effect.

In order to see the effectiveness of this term as numerical diffusion, new scheme (SCHEME2) using a slightly modified split pressure derived from equation (27). The mass flux and split pressure is given by,

$$m = \frac{1}{2} \{ (\rho V_n)_L + (\rho V_n)_R - |\bar{V}_n| (\rho_R - \rho_L) \} \quad (28)$$

$$\bar{p} = \frac{p_L + p_R}{2} \left(1 - \frac{3}{4c} \Delta V_n \right) - \frac{1}{4} (3\bar{M} - \bar{M}^3) \Delta p \quad (29)$$

This scheme works well in one-dimensional test case. (Fig.6) However, a multidimensional code that uses numerical diffusion shown above is not robust enough for general cases. In addition, this scheme only with upwind switch term but without the diffusion term could not proceed computation in stable even in one-dimensional case. Thus we can conclude that the split pressure term in AUSM type scheme works as sophisticated numerical diffusion and that nonlinear form of the split pressure term inherited from van Leer's FVS is superior to numerical diffusion form in robustness.

3.3 SCHEME3: Application to non-conservative semi-Lagrange scheme

As shown in the previous section, the split pressure term plays important part in AUSM type schemes. The split pressure term is similar to von Newman's numerical viscosity in the sense that it works in pressure term.

We try to apply the split pressure term for one-dimensional Euler equation in non-conservative primitive variable form.

$$\frac{\partial}{\partial t} \begin{pmatrix} \rho \\ u \\ p \end{pmatrix} + u \frac{\partial}{\partial x} \begin{pmatrix} \rho \\ u \\ p \end{pmatrix} = \begin{pmatrix} -\rho u_x \\ -p_x / \rho \\ -\tau p u_x \end{pmatrix} \quad (30)$$

The numerical scheme is explained as follows. See also Fig.7.

step1: Gradient at each point is approximated using van Albada's differentiable slope limiter.

step2: Profile of each variable between point is reconstructed using Third order polynomial using values and slope on both ends.

step3: Left hand side of equation is evaluated by Lagrange step.

step4: Pressure gradient term in RHS is evaluated using split pressure as AUSM.

step4: Velocity gradient terms in RHS are evaluated using central difference.

Since this scheme is not conservative, shock speed is not accurate. However, no significant oscillation is found, (Fig.8) thus the split pressure terms also works well as numerical diffusion for this scheme.

4. Conclusion

Several AUSM type schemes are presented, and three new schemes are introduced in order to indicate the nature of AUSM type schemes. These schemes, ST-AUSM, SCHEME2 and SCHEME 3 are initially developed merely for demonstration, however, ST-AUSM, in which simple upwind mass flux and split pressure are used, have also practical benefit. It shows best solution for supersonic flow around cylinder among several upwind schemes including original AUSM and Roe scheme.

It is shown that the split pressure term that is inherited from van Leer's FVS works as sophisticated numerical diffusion. SCHEME2, which utilize the same mass flux with ST-AUSM and the numerical diffusion term derived from the Taylor expansion of the split pressure, works also well, however, it is not so robust as ST-AUSM which use split pressure itself. In addition, the split pressure term can be used to stabilize non-conservative semi Lagrange scheme in SCHEME3.

It can be concluded that the key feature of AUSM type scheme is its split pressure term through research using these schemes. The split pressure term works as sophisticated numerical diffusion term and its nonlinear form does better job for strong shock and expansion than a numerical diffusion form.

When we consider simple multidimensional upwind schemes, it is thought that a key is the design of split pressure term bearing multidimensional nature, since a multidimensional upwind convective term can be constructed in a relatively easy way. It is expected that we will get simple multidimensional upwind schemes in the similar way in which we have got simple approximated Riemann fluxes by AUSM type schemes.

References

- [1]Roe,P.L., *J.Comp.Phys.*, Vol.43, pp.357-372., 1981
- [2]Chakravarthy,S.R. and Osher,S., AIAA Paper 82-0975, 1982
- [3]Steger,J.L. and Warming,R.F., *J.Comp.Phys.* vol.40, pp.263-293, 1981
- [4]van Leer,B., *Lecture Note in Physics*, vol.170, pp.507-512, 1982
- [5]Hänel,D. and Schwane,R., AIAA Paper 89-0274, 1989
- [6]Einfeldt,B., Munz,C.C., Roe,P.L. and Sjogreen,B., *J.Comp.Phys.* vol.92, pp.273-275, 1991
- [7]Liou,M.S. and Steffen,C.J., *J. Comp. Phys.* vol.107, pp.23-39, 1993
- [7]Jameson,A., AIAA Paper 93-3359, 1993
- [8]Tatsumi,S., Martinelli,L. and Jameson,A., AIAA Paper 95-0466, 1995
- [9]Jounouchi,T., Kitagawa, Sakasita, Yasuhara, *Proceedings of 7th CFD Symposium*, 1993, in Japanese
- [10]Wada,Y and Liou,M.S., AIAA Paper 94-0083,1994
- [11]Shima,E. and Jounouchi,T., NAL-SP27, *Proceedings of 12th NAL symposium on Aircraft Computational Aerodynamics*, pp.255-260, 1994, in Japanese
- [12]Jounouchi,T., Shima,E., Kitagawa,I., Yasue,T. and Yasuhara,M., *Proceedings of 8th CFD Symposium*, pp.5-8, 1994, in Japanese
- [13]Nakamori,I. and Nakamura,Y., *Proceedings of 8th CFD Symposium*, pp.9-12, 1994, in Japanese
- [14]Liou, M.S., AIAA Paper 95-1701-CP, 1995
- [15]Shima,E., NAL-SP30, *Proceedings of 13th NAL symposium on Aircraft Computational Aerodynamics*, pp.41-46, 1996, in Japanese
- [16]Roe, P.L., *J.Comp.Phys.*, vol.63, pp.458-476, 1986
- [17]Hirsch,Ch., et al., AIAA Paper87-1163-CP, 1987
- [18]Rice,J. and Schnipke, R.J., *Comp.Methods Appl.Mech.Eng.*, vol 48, pp.313-327
- [19]Deconick,H. et.al., AIAA Paper 91-1532-CP, 1991
- [20]Parpia,I.H., AIAA Paper 91-1545-CP, 1991
- [21]Hirsh, Ch. and Lacor,C., AIAA Paper 89-1958-CP, 1989
- [22]Tamura, Y. and Fujii, K., *Computer & Fluids*, vol 22, 2/3, pp.125-137, 1993
- [23]Deconick,H. and Koren,B. (ed), "*Euler and Navier-Stokes Solvers Using Multi-Dimensional Upwind Schemes and Multigrid Acceleration*", *NNFM 57*, Vieweg, 1997
- [24]Takewaki,H., Nishiguchi,A. and Yabe,T., *J.Comp.Phys.* vol 61, pp.261-268, 1985
- [25]Yabe,T. et al., *Comput.Phys.Commun.* vol 66, pp.219-242, 1991

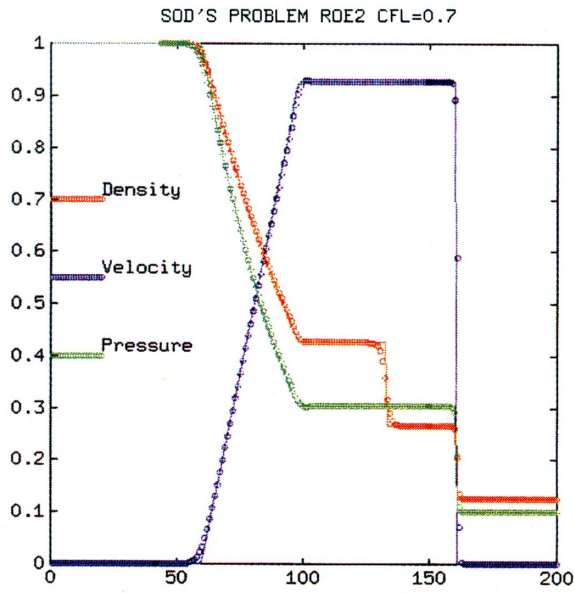


Fig.1 Sod's problem by second order Roe scheme

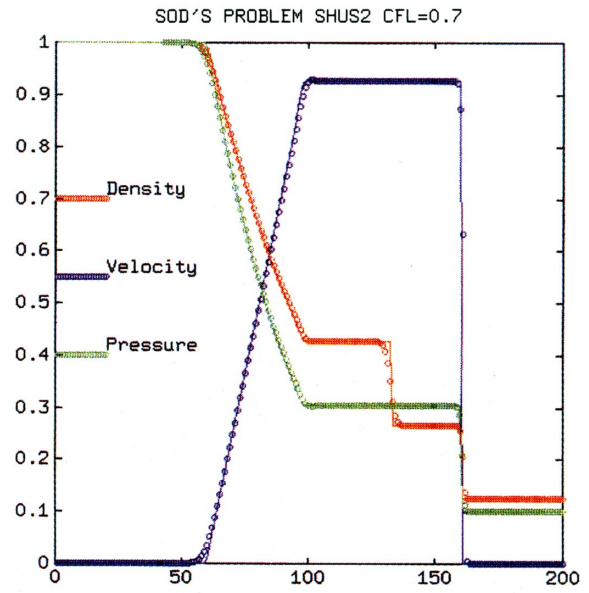


Fig.3 Sod's problem by second order SHUS

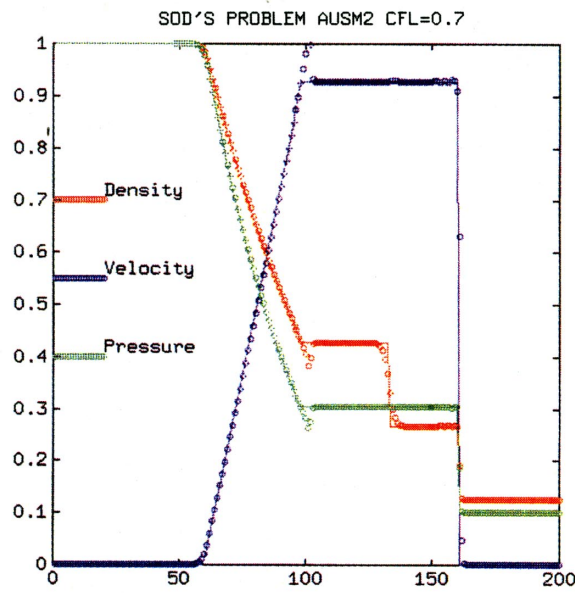


Fig.2 Sod's problem by second order AUSM

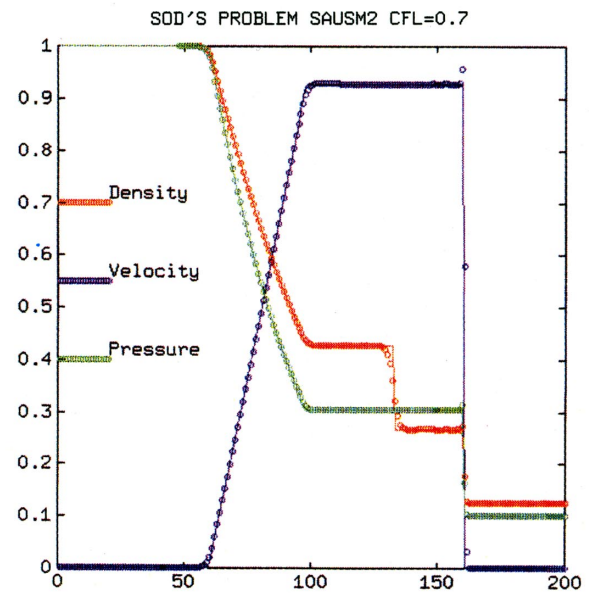


Fig.4 Sod's problem by second order ST-AUSM

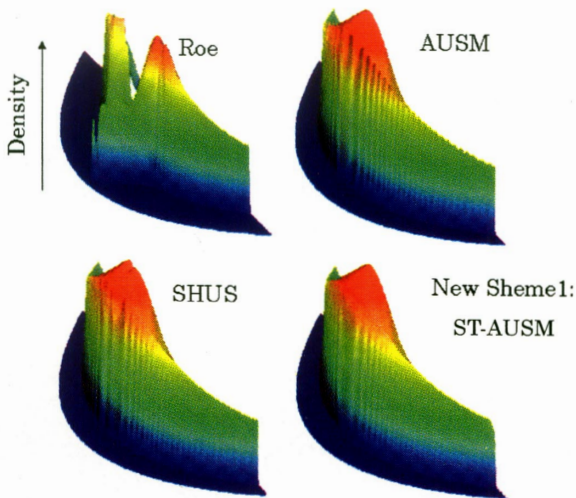


Fig.5 3D plot of density profile of supersonic flow at Mach 6 before cylinder. Violent carbuncle is found in result of Roe scheme, over shoot is found in AUSM's result and slight unnatural concave is found in SHUS's result but no problem is found in ST-AUSM's result.

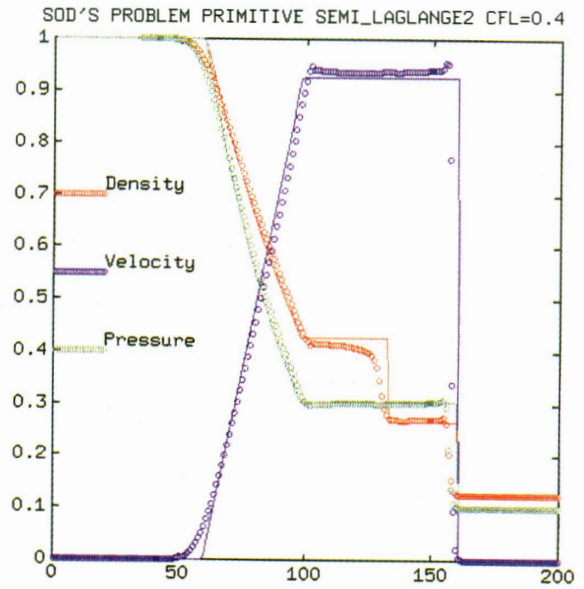


Fig.8 Sod's problem by second order, non-conservative, semi-Lagrange scheme.

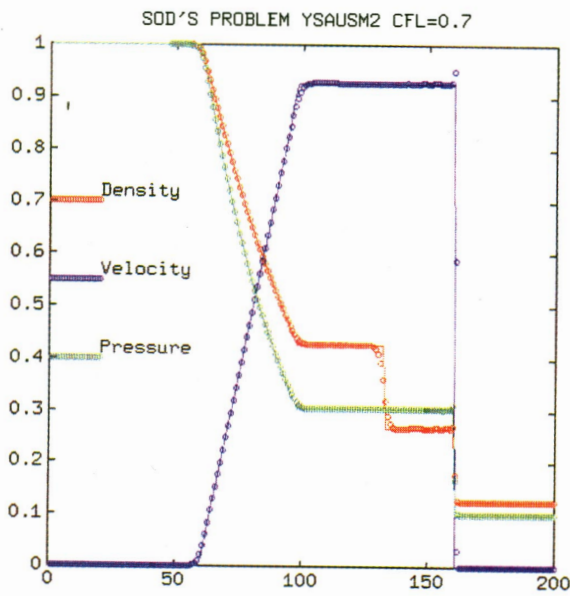


Fig.6 Sod's problem by second order scheme using upwind flux SCHEME2 .

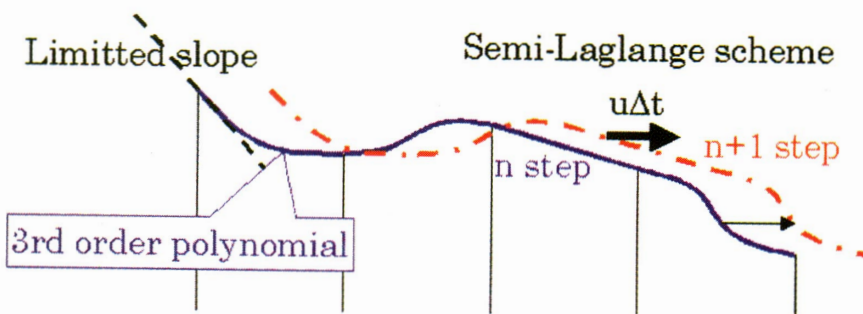


Fig.7 Illustration of Semi-Lagrange step in SCHEME3

Appendix: Formulation of AUSM type schemes

List of mass fluxes of several AUSM type scheme is presented. On the split pressure term, which is another essential component of AUSM type scheme, see Eq.(6) (7) in this paper. This term is same for all AUSM type schemes except for AUSM+.

AUSM

$$m = \frac{\bar{M} + |\bar{M}|}{2} \rho_+ c_+ + \frac{\bar{M} - |\bar{M}|}{2} \rho_- c_-$$

$$\bar{M} = M_+ + M_-$$

$$M_{\pm} = \begin{cases} \pm \frac{1}{4} \left(\frac{V_{nz} \pm 1}{c_{\pm}} \right)^2, & \text{if } \left| \frac{V_{nz}}{c_{\pm}} \right| < 1 \\ \frac{M_{\pm} \pm |M_{\pm}|}{2}, & \text{if } \left| \frac{V_{nz}}{c_{\pm}} \right| \geq 1 \end{cases}$$

AUSM+

AUSM+ is very similar to AUSM, but smooth splitting function for average Mach number and pressure are different.

$$M_{\pm} = \begin{cases} \pm \frac{1}{4} \left(\frac{V_{nz} \pm 1}{c_{\pm}} \right)^2 \pm \frac{1}{8} \left(\left(\frac{V_{nz}}{c_{\pm}} \right)^2 - 1 \right), & \text{if } \left| \frac{V_{nz}}{c_{\pm}} \right| < 1 \\ \frac{M_{\pm} \pm |M_{\pm}|}{2}, & \text{if } \left| \frac{V_{nz}}{c_{\pm}} \right| \geq 1 \end{cases}$$

Pressure splitting coefficients are also changed as,

$$\beta_{\pm} = \begin{cases} \frac{1}{4} \left(2 \mp \frac{V_{nz}}{c_{\pm}} \right) \left(\frac{V_{nz} \pm 1}{c_{\pm}} \right)^2 \pm \frac{3}{16} \left(\left(\frac{V_{nz}}{c_{\pm}} \right)^2 - 1 \right), & \text{if } \left| \frac{V_{nz}}{c_{\pm}} \right| < 1 \\ \max \left(0, 1, \left(\frac{1 \pm \frac{V_{nz}}{c_{\pm}}}{2} \right) \right), & \text{if } |M_{\pm}| \geq 1 \end{cases}$$

SFS

Mass flux of SFS is that of FVS using modified Mach number in order to satisfy zero mass flux at contact surface.

$$m = m_+ + m_-$$

$$m_{\pm} = \begin{cases} \pm \frac{\rho_{\pm} c_{\pm}^2}{4\bar{c}} (M_{\pm} \pm 1)^2, & \text{if } |M_{\pm}| < 1 \\ \frac{(\rho V_n)_{\pm} \pm |(\rho V_n)_{\pm}|}{2}, & \text{if } |M_{\pm}| \geq 1 \end{cases}$$

$$M_{\pm} = \frac{V_{nz}}{\bar{c}}, c_{\pm} = \frac{c_{\pm}^2}{\bar{c}}, c_{\pm} = \sqrt{\frac{p_{\pm}}{\rho_{\pm}}}, \bar{c} = \frac{c_+ + c_-}{2}$$

The common sound speed \bar{c} is also used for split pressure term.

AUSMDV

$$m = (\rho \tilde{V}_n)_+ + (\rho \tilde{V}_n)_-$$

$$\tilde{V}_{nz} = \begin{cases} \alpha \pm \left(\pm \bar{c} \frac{(M_{\pm} \pm 1)^2}{4} - \frac{V_{nz} \pm |V_{nz}|}{2} \right) + \frac{V_{nz} \pm |V_{nz}|}{2}, & \text{if } |M_{\pm}| < 1 \\ \frac{V_{nz} \pm |V_{nz}|}{2}, & \text{if } |M_{\pm}| \geq 1 \end{cases}$$

$$\alpha_{\pm} = \frac{2(p/\rho)_{\pm}}{(p/\rho)_+ + (p/\rho)_-}, M_{\pm} = \frac{V_{nz}}{\bar{c}}, \bar{c} = \max(c_+, c_-)$$

The common sound speed \bar{c} is also used for split pressure term. The pressure correction term is introduced as,

$$p' = \frac{1}{2} \left(\frac{1}{2} + s \right) \left((\rho V_n)_+ - (\rho V_n)_- - |m| (V_{n+} - V_{n-}) \right)$$

$$s = \frac{1}{2} \min \left(1, 10 \frac{|p_+ - p_-|}{\min(p_+, p_-)} \right)$$

SHUS

$$m = \frac{1}{2} \{ (\rho V_n)_+ + (\rho V_n)_- - |\bar{V}_n| \Delta \rho - \frac{|\bar{M} + 1| - |\bar{M} - 1|}{2} \bar{\rho} \bar{V}_n - \frac{|\bar{M} + 1| + |\bar{M} - 1| - 2|\bar{M}|}{2|\bar{M}|} \Delta p \}$$

$$\bar{M} = \frac{1}{\theta} \frac{\bar{V}_n}{\bar{c}}$$

$$\theta = \max \left(1, \frac{1}{2\rho_+} \left(\frac{\bar{\rho} \Delta V_n}{\bar{c}} - \frac{\Delta p}{\bar{c}^2} \right), \frac{1}{2\rho_-} \left(\frac{\bar{\rho} \Delta V_n}{\bar{c}} + \frac{\Delta p}{\bar{c}^2} \right) \right)$$

$$\Delta q = q_- - q_+$$

$$\bar{\rho} = (\rho_+ + \rho_-) / 2$$

$$\bar{V}_n = (V_{n+} + V_{n-}) / 2$$

$$\bar{c} = (c_+ + c_-) / 2$$

The common sound speed \bar{c} is also used for split pressure term.

NNFVS

$$m = m_+ + m_-$$

$$m_{\pm} = \rho_{\pm} \lambda_{1\pm} + \frac{p_{\pm}}{c^2} (-2\lambda_{1\pm} + \lambda_{2\pm} + \lambda_{3\pm})$$

with average sound velocity, modified Mach number and smoothed eigen values such as,

$$\bar{c} = \frac{c_+ + c_-}{2}, \bar{M}_{\pm} = \frac{V_{nz}}{\bar{c}}$$

$$\lambda_{1\pm} = \begin{cases} \frac{\bar{c} (\bar{M}_{\pm} \pm |\bar{M}_{\pm}|)}{2}, & \text{if } |\bar{M}_{\pm}| > \epsilon \\ \frac{\bar{c} (\bar{M}_{\pm} \pm \epsilon)^2}{2}, & \text{if } |\bar{M}_{\pm}| \leq \epsilon \end{cases}$$

$$\epsilon = 0.2 \frac{\min(p_+, p_-)}{\max(p_+, p_-)}$$

$$\lambda_{2+} = \lambda_{2+}(\bar{M}_+) = \begin{cases} \frac{\bar{c}}{8} (\bar{M}_+ + 1)^2 (\bar{M}_+^2 - 4\bar{M}_+ + 7), & \text{if } |\bar{M}_+| < 1 \\ \frac{\bar{c}}{2} (\bar{M}_+ + 1 + |\bar{M}_+|), & \text{if } |\bar{M}_+| \geq 1 \end{cases}$$

$$\lambda_{3+} = \lambda_{3+}(\bar{M}_+) = \begin{cases} \frac{\bar{c}}{8} (\bar{M}_+ - 1) (\bar{M}_+ + 1)^3, & \text{if } |\bar{M}_+| < 1 \\ \frac{\bar{c}}{2} (\bar{M}_+ - 1 + |\bar{M}_+|), & \text{if } |\bar{M}_+| \geq 1 \end{cases}$$

$$\lambda_{2-} = \lambda_{2-}(\bar{M}_-) = \lambda_{3+}(-\bar{M}_-)$$

$$\lambda_{3-} = \lambda_{3-}(\bar{M}_-) = \lambda_{2+}(-\bar{M}_-)$$

The common sound speed \bar{c} is also used for split pressure term. The use of one side upwind density is recommended if $|\bar{M}| < \epsilon$. The pressure correction term is given by,

$$p' = \frac{1}{2} (m_+ - m_- - |m|) (V_{n+} - V_{n-})$$

It is expected that pressure correction term is not necessary in usual condition judging from experiences with other AUSM type schemes, although it has not been tested.

ST-AUSM (New Scheme1)

$$m = \frac{1}{2} \{ (\rho V_n)_+ + (\rho V_n)_- - |\bar{V}_n| (\rho_+ - \rho_-) \}$$

$$\bar{V}_n = \frac{(\rho V_n)_+ + (\rho V_n)_-}{\rho_+ + \rho_-}$$

Anisotropic Cartesian Grid Adaptation

Paulus R. Lahur, School of Engineering, Nagoya University, E-mail: lahur@aero4.nuae.nagoya-u.ac.jp
 Yoshiaki Nakamura, Dept. of Aerospace Eng., Nagoya University, E-mail: nakamura@nuae.nagoya-u.ac.jp
 Furo-cho, Chikusa-ku, Nagoya 464-8603, Japan

Key Words: Anisotropic Cartesian Grid, Grid Adaptation

A grid adaptation method using anisotropic Cartesian grid in three dimensions has been developed to improve the efficiency of an existing Cartesian grid adaptation by reducing the total number of cells needed to resolve flow features. The method is capable of coarsening and refining a grid in such a way that the cell aspect ratio can take an arbitrary value. Flow computations with the present method for a supersonic flow around a cylinder and a transonic flow around an ONERA M6 wing are presented here, which show good agreement with experiment. For the case of cylinder, the present method produces about 67 times fewer cells than the isotropic approach. This dramatic saving is due to the ability of the three-dimensional code employed here to treat cells without any limitation on their aspect ratio. For the case of ONERA M6, the ratio of saving is about 2.5. Though the amount of memory per cell is higher than that of the isotropic approach, the overall memory requirement becomes lower, due to reduction in the number of cells. This means that the present method can make flow computation more efficient.

1. Introduction

Recently, Cartesian grids have become popular in computing the flow around a complex geometry due to their fast and automatic grid generation. Furthermore, they allow for simple local clustering of grid cells, which is particularly advantageous in performing solution adaptive for a realistic geometry. Grid refinement on a Cartesian grid is usually achieved by dividing a cell isotropically into eight sub-cells of equal size in 3D.

However, isotropic refinement results in an excessive number of cells because flow features are usually anisotropic in nature, as in the case of shock wave. To overcome this weakness, a grid that allows for anisotropic grid refinement should be employed.

Anisotropic Cartesian grid adaptation consists of two main processes: grid refinement and coarsening. At present, other researches in this particular area consider either grid refinement, as in Refs. [1], [2], and [3], or coarsening only, as in Ref. [4]. In the present study both processes are carried out, where no restrictions are imposed on the cell aspect ratio. The only restriction is concerning the minimum length of cell side. Calculated results of supersonic flow around a cylinder and transonic flow around a standard ONERA M6 wing will be described to evaluate the present algorithm.

2. Anisotropic Grid Adaptation

The main steps of the present method are shown in Fig. 1. The procedure starts with a rough grid distribution, which is generated isotropically around a body. First, on this grid the flow is solved up to a certain degree of convergence, and then the grid is improved based on the calculated result. Thus, one adaptation cycle is completed. The grid adaptation process consists of grid coarsening, refinement, and smoothing. The following sub-sections discuss the main aspects of the anisotropic grid adaptation method proposed here.

2.1. Adaptation Parameter

The adaptation parameter employed here is a modified second difference of selected components of the flow solution vector, which is calculated for each cell in the x , y and z directions. The computation is actually carried out as in Eqs. 1 and 2b, where only x direction is shown for simplicity. Incidentally, Eq. 2a is a common formula to compute second derivative.

However, for our purpose, Eq. 2a is modified to Eq. 2b. The first modification is the use of length scale L . Increasing its value will refine a large cell, but if its value is too high, it will create too many cells in smooth flow regions without sufficient cell clustering around important flow features. On the other hand, decreasing the value of L will refine a small cell, but its too low value will create a grid with abrupt spatial change in cell's relative size, which degrades solution accuracy. It is found that the value of L between around 2 and 3 gives satisfactory results for the test cases presented here.

The second modification is the use of a maximum of first solution derivatives at the cell face. It is necessary to increase the value of G for a cell with many neighbors, so that it is more likely to be refined.

$$(Q'_{ij})_x^* = (Q_j - Q_i) / (x_j - x_i) \quad (1)$$

$$(G_i)_x = (\Delta x_i)^2 \left[(Q'_{ij})_{x,\text{right}}^* - (Q'_{ij})_{x,\text{left}}^* \right] / \Delta x_i \quad (2a)$$

$$(G_i)_x = (\Delta x_i)^L \left[(Q'_{ij})_{x,\text{max}}^* - (Q'_{ij})_{x,\text{min}}^* \right] / \Delta x_i \quad (2b)$$

where Q is the flow solution, x and Δx are the coordinate of centroid and the cell size in a given direction, respectively. Subscript i indicates the cell under consideration, and j its neighboring cell. The asterisk indicates cell face. L is a length scale that

determines the balance of refinement between small and large cells.

Having obtained adaptation parameter G for all cells, its mean value and standard deviation (sdev) are calculated to determine threshold values for grid coarsening and refinement, T_{low} and T_{high} , respectively, as shown in Eqs. 3 and 4. A cell with $G < T_{low}$ in a certain direction is a candidate for coarsening in that direction, while that with $G > T_{high}$ is a candidate for refinement.

$$T_{low} = \text{mean}(G) - R_{low} \cdot \text{sdev}(G) \quad (3)$$

$$T_{high} = \text{mean}(G) + R_{high} \cdot \text{sdev}(G) \quad (4)$$

where R_{low} and R_{high} are the parameters defined by users.

2.2. Grid Coarsening

Grid coarsening is performed by removing the interface between cell i and its neighbor j if the following conditions are satisfied.

$$(G_i)_n < T_{low} \quad \text{and} \quad (G_j)_n < T_{low} \quad (5)$$

where n is the direction normal to the interface.

In general, a cell may also be a candidate for coarsening in several directions, in which case priority is given to the direction where the value of G is the lowest. It should be noted that the actual coarsening is carried out only when the two faces match exactly with each other. This is necessary to preserve the concept of Cartesian grid cell.

2.3. Grid Refinement

A cell is refined by dividing it into two parts in a direction where the value of G is higher than the upper threshold value, T_{high} in that direction. As a result, a cell can be refined in several directions, as shown in Fig. 2. For practical reasons, there are limitations on the minimum cell size and the maximum number of cells in this study.

2.4. Grid Smoothness

After the coarsening and refinement mentioned above, the cell size and orientation are not smoothly distributed. Of particular concern is the cell size relative to its neighbors, because large variation in size may degrade solution accuracy. Hence, it is necessary to smooth out the grid. The smoothing process, however, is rather time-consuming, due to the problem of neighbor searching in unstructured grid. Thus, it is preferred that the grid is already reasonably smooth before implementing the smoothing process, so that computational effort is kept to minimum. This is obtained by setting R_{low} and R_{high} in Eqs. 3 and 4 to high values, so that

only cells which definitely have to be refined or coarsened are modified. However, setting the parameter to a too high value may cause insufficient grid adaptation, which requires more adaptation cycles. A reasonable balance is found when the values of R_{low} and R_{high} is set to 0.5.

The grid smoothness is defined in this study that the number of neighboring cells is limited to a maximum of two in each of two directions along the cell face. If this condition is violated, the cell is divided into two cells in the direction with too many neighbors. The division is made in such a way that the cell boundary matches that of its neighbors. Thus, this method can successfully generate a reasonably smooth grid.

2.5. Data Structure

In generating a grid, where its cell has an arbitrary value of the aspect ratio, an unstructured approach is adopted in this study. Here each cell stores the integer coordinates to locate its vertices. Unlike floating point value, the integer representation is accurate, so that a cell can find its neighbors easily.

A problem of this approach is that the cell searching process is linear, which takes excessive time for the case of a large number of cells. To overcome this problem, an ADT (Alternating Digital Tree) is employed at grid generation and adaptation.⁵ ADT is particularly suitable for storing and searching a finite-sized object in multi-dimensional space. A well-balanced ADT can reduce the searching task to a log N process, where N is the number of cells

3. Grid Generation and Flow Solver

The Cartesian grid generation and the flow solver employed here are basically the same as those reported previously by the authors (see Ref. [6]). The Euler equations are solved to calculate inviscid, compressible flows. The flow solver is based on a cell-centered finite volume scheme, where the numerical flux is computed using Hännel's flux-vector-splitting scheme.⁷ The MUSCL method is used to compute the flux with second order accuracy. Time integration is carried out with a 3-stage Runge-Kutta method, where local time stepping is applied to accelerate the convergence rate. To make the time step size as large as possible, an extremely small cell at the solid boundary is merged with the largest of its neighbors.

4. Test Cases

4.1 Cylinder in Supersonic Flow

The first test case is a circular cylinder with a unit radius in a supersonic flow of $M=3.0$. The objective is two-fold. The first is to test applicability of the present 3D method to a 2D flow problem, since such 2D flow corresponds to a kind of anisotropic grid, where it is uniform in the spanwise direction. That is, all cells extend to the whole span region. The second objective is to examine whether the method can efficiently capture flow features of shocks and wake, as well as smooth

flow regions.

First, an isotropic grid is generated around half of the cylinder, which contains 46,480 cells. This is quite a large number for this kind of 2D computations. The initial grid used in this test case is obtained by merging all cells of the isotropic grid in the spanwise direction, which results in 1,643 cells. The upstream, downstream and upper boundary conditions are set to free flow, whereas at the left, right and lower boundaries conditions are imposed.

The anisotropic grid adaptation is carried out using density and mach number as sensor parameters. The length scale L in Eq. 2b is set to 0.3. The initial, intermediate and final grids are shown in Fig. 3, and the corresponding flow solutions are shown in Fig. 4. The number of adaptation cycle is 9, beyond which the grid and solution change little.

It is observed that the grid adaptation quickly and sharply captures flow features such as shocks by refining the cells in these regions. At the 6th adaptation cycle, the finest cells at the main shock already stretch all the way to the downstream computational boundary, which is placed at a distance 10 times as large as the radius from the center of the cylinder. Cell refinement also takes place in the regions of small variation, such as behind the main shock, but at a slower pace, i.e. at the 9th adaptation cycle in this study. It is observed that no grid modifications are made in the spanwise direction throughout the whole adaptation process. This means that the grid and flow solution remains two-dimensional. Grid coarsening in the constant flow region upstream of the bow shock is carried out in one cycle. All grids show a reasonably smooth transition between large and small cells, which can be seen clearly in the regions around the shocks.

Figure 4c shows the final result, where the main shock, the shear flow behind the cylinder, and the shocks interacting with the wake are sharply captured. The main shock standoff distance is 0.7 for the unit radius, which is quite reasonable when compared with the empirical data of 0.65 for a wedge with a cylindrical head.⁸ Moreover, the density jump across the shock is 3.878, which compares well with a theoretical value of 3.857.

Comparison of the number of cells between anisotropic and isotropic grids shows that even the final anisotropic grid contains considerably fewer cells than the initial isotropic grid. As the grid becomes more refined, the ratio of the number of cells in the isotropic grid to that in the anisotropic grid becomes even larger. In the final grid with 14,431 cells, the ratio reaches 67, which means that the equivalent isotropic grid contains about 970,000 cells.

The advantage of the anisotropic grid is evident in the requirement of the total memory, which in this study consists mainly of solution vector, flux vector, cell volume, cell face area, and face-based database. Even though the amount of memory per cell is 400 bytes for the anisotropic grid, the total memory is only 5.8MB for

the final grid. On the other hand, the isotropic grid requires only 344 bytes per cell, but the total memory is 333MB, which is about 57 times larger. Thus, the 3D anisotropic grid adaptation method can compute a 2D flow far more efficiently than the isotropic approach.

4.2 ONERA M6 Wing in Transonic Flow

The second test case is transonic flow over ONERA M6 wing.⁹ The objective is to apply the present method to a 3D transonic flow. The wing has ONERA D profile, with an aspect ratio of 3.8 and a taper ratio of 0.562. The leading and trailing edges sweep back at an angle of 30° and 15.8°, respectively. The flow condition is $M=0.84$ and $\alpha=3.06^\circ$, which is widely used for CFD validation.

Density is used to compute the adaptation parameter. The length scale L in Eq. 2b is set to 2.0, which enables us to capture two shocks on the upper surface of the wing quickly. Setting L to 3.0 as in the cylinder case will take more adaptation cycles to capture the shocks. As mentioned before, an isotropic grid is used as a starting grid. The adaptation is carried out twice, beyond which the solution on the wing changes little. The initial and adapted grids are shown in Figs. 6 and 7, where the grid is clustered in the regions of shocks on the upper surface and the leading and trailing edge regions.

The pressure distribution on the upper surface of the wing for each grid is shown in Fig. 9, which clearly depicts a lambda pattern of the shock. As the grid adaptation cycle is repeated, the pattern becomes more distinct. A more detailed view of the pressure distribution on the wing is shown in Fig. 8 at selected cross sections. It is evident here that the pressure distribution changes little after the second adaptation cycle. The final solution shows a good agreement with the experimental data, except for differences in shock locations and sharpness, due to the inviscid nature of the flow solver employed here.

As an additional comment, it is observed that when an anisotropic Cartesian grid is coupled with a first order flow solver, as in our previous study, the shock near the leading edge fails to appear, even on a fine grid. Therefore, it seems that at least a second-order scheme is required to capture the pressure jump near the leading edge.

The change in the number of cells during the adaptation process is shown in Fig. 10. The final anisotropic grid contains 171,753 cells, which is equivalent to an isotropic grid with 430,260 cells. This is 2.5 times as large as that of the anisotropic grid.

In terms of the total memory required, although not as dramatic as the cylinder test case, the anisotropic grid is still significantly better than the isotropic grid. For the final grid, the total memory for the case of anisotropic grid is 68.7MB, whereas that of the isotropic grid is 148MB, which is 2.2 times as large as that of the anisotropic grid.

5. Concluding Remarks

An anisotropic Cartesian grid adaptation method has been developed in this study to improve the efficiency of an existing Cartesian grid adaptation. It has capabilities to both coarsen and refine a Cartesian grid in any direction without any limitation on cell aspect ratio, while keeping the grid smooth.

The present method was validated for 2D and 3D test cases: a supersonic flow around a cylinder and a transonic flow around ONERA M6, respectively. The method successfully captured the flow features and improved the solution with significantly less number of grid cells, as compared to the corresponding isotropic grid. The 2D flow was computed with very high relative efficiency, since the number of cells are as few as those needed by a 2D method. This is achieved by imposing no limitations on cell aspect ratio, so that a cell can span the whole computational domain in the spanwise direction. In the final grid, the number of cells in the isotropic grid is 67 times as large as that of the anisotropic grid, whereas the total memory is 57 times.

For the ONERA M6 test case, the number of isotropic cells is 2.5 times as large as that of the anisotropic grid, whereas the total memory is 2.2 times. From the above-mentioned, a flow containing more anisotropic features will benefit more from the anisotropic adaptation.

For future research, extension of the current method to more complicated situation such as moving boundary is being considered. For this purpose, the adaptation strategy as well as the data structure will have to be reorganized to improve their efficiencies.

References

- (1) Aftosmis, M.J., "Solution Adaptive Cartesian Grid Methods for Aerodynamic Flows with Complex Geometries," von Karman Institute for Fluid Dynamics, Lecture Series 1997-02 (1997).
- (2) Welterlen, T.J., "Store Release Simulation on the F/A-18C using Splitflow," AIAA paper 99-0124 (1999).
- (3) Wang, Z.J., Cphen, R.F., Hariharan, N., Przekwas, A.J., and Grove, D., "A 2^N Tree Based Automated Viscous Cartesian Grid Methodology for Feature Capturing," AIAA paper 99-3300 (1999).
- (4) Deister, F., Rocher, D., Hirschel, E.H., and Monnoyer F., "Three-dimensional Adaptively Refined Cartesian Grid Generation and Euler Flow Solutions for Arbitrary Geometries," Proceeding of the 4th European CFD Conference, Vol. 1, Part 1 (1998), pp. 96-101.
- (5) Bonet, J. and Peraire, J., "An Alternating Digital Tree (ADT) Algorithm for 3D Geometric Searching and Intersection Problems," Int. J. for Num. Methods in Eng., Vol. 31 (1991), pp. 1-17.
- (6) Lahur, P.R., and Nakamura, Y., "A New Method for Thin Body Problem in Cartesian Grid Generation," AIAA paper 99-0919 (1999).
- (7) Hännel, D., Schwane, R., Seider, G., "On the Accuracy of Upwind Schemes for the Solution of the Navier-Stokes Equations," AIAA 87-1105, Proc. AIAA 8th Computational Fluid Dynamics Conference (1987), pp. 42-46.
- (8) Ambrosio, A. and Wortman, A., "Stagnation Point Shock Detachment Distance for Flow around Spheres and Cylinders," ARS J. 32, 281 (1962).
- (9) Schmitt, V. and Charpin, F., "Pressure Distributions on The ONERA-M6-Wing at Transonic Mach Numbers," Experiment Data Base for Computer Program Assessment, AGARD AR-138 (1979).

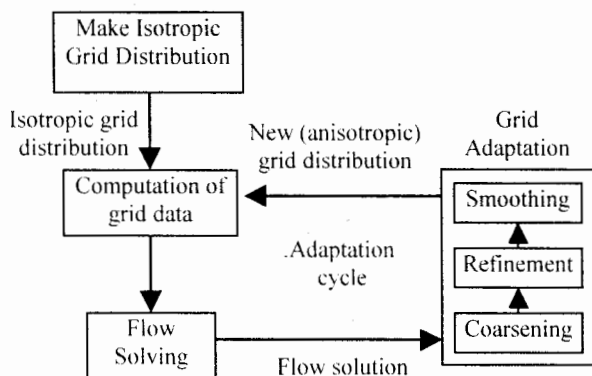


Fig. 1 Grid adaptation cycle.

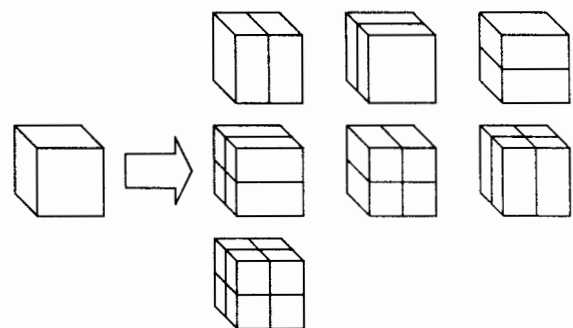


Fig. 2 Possibilities of grid refinement.

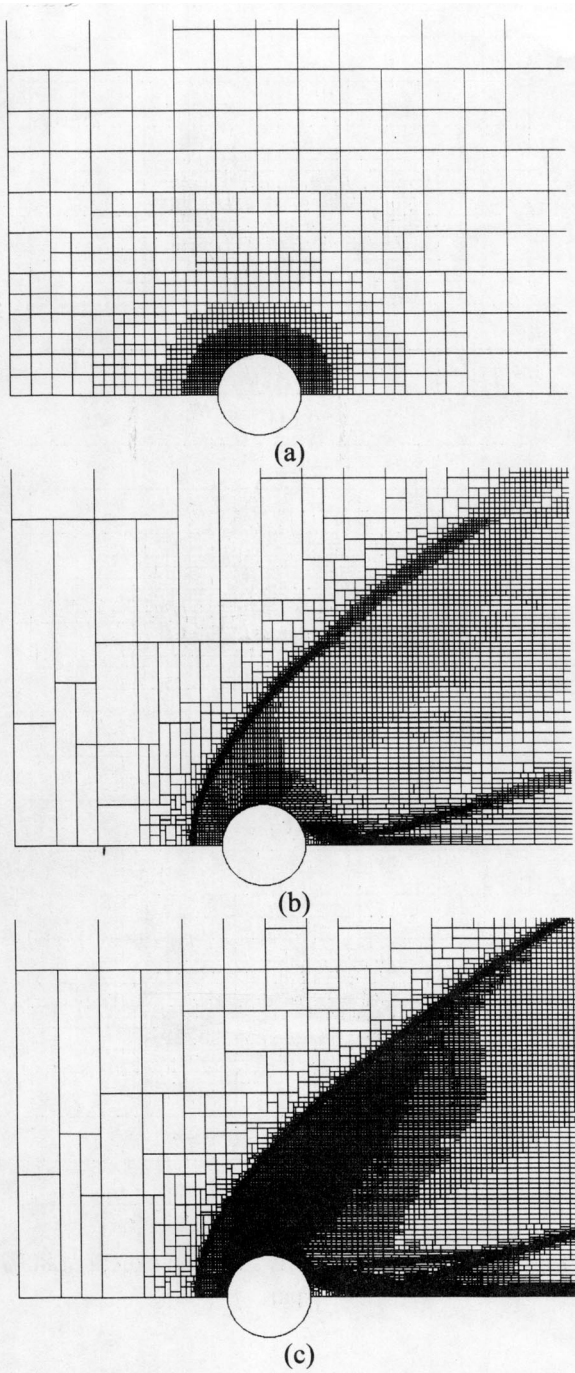


Fig. 3 Grid around cylinder: (a) at initial, (b) 4th adaptation cycle, (c) 9th.

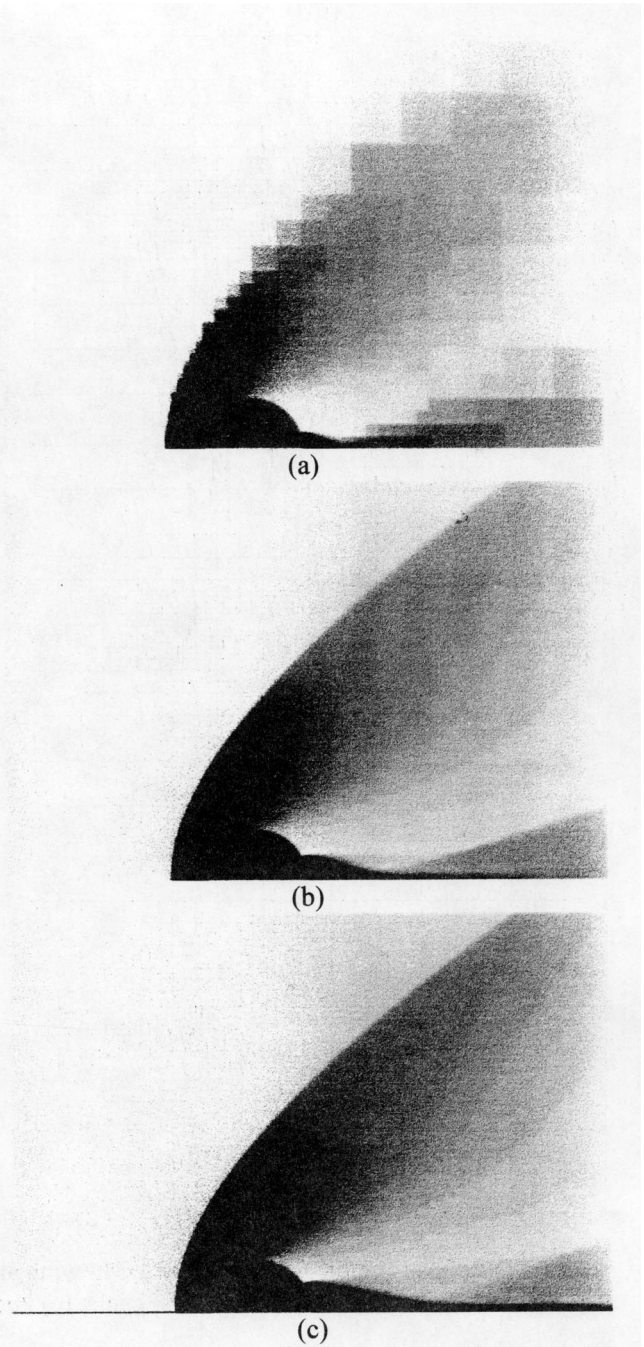


Fig. 4 Mach number distribution around cylinder: (a) at initial, (b) 4th adaptation cycle, (c) 9th.

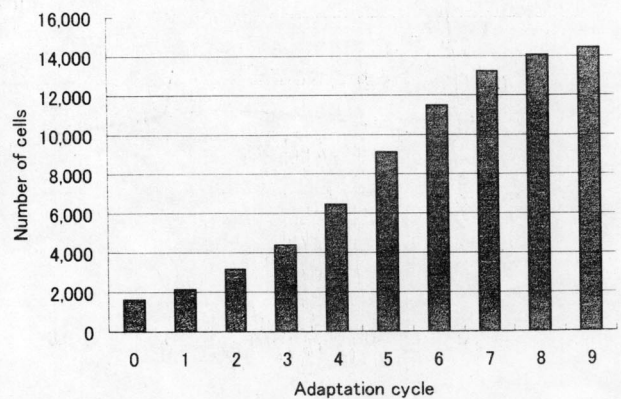


Fig. 5 Change in the number of cells with adaptation cycle for flow around cylinder.

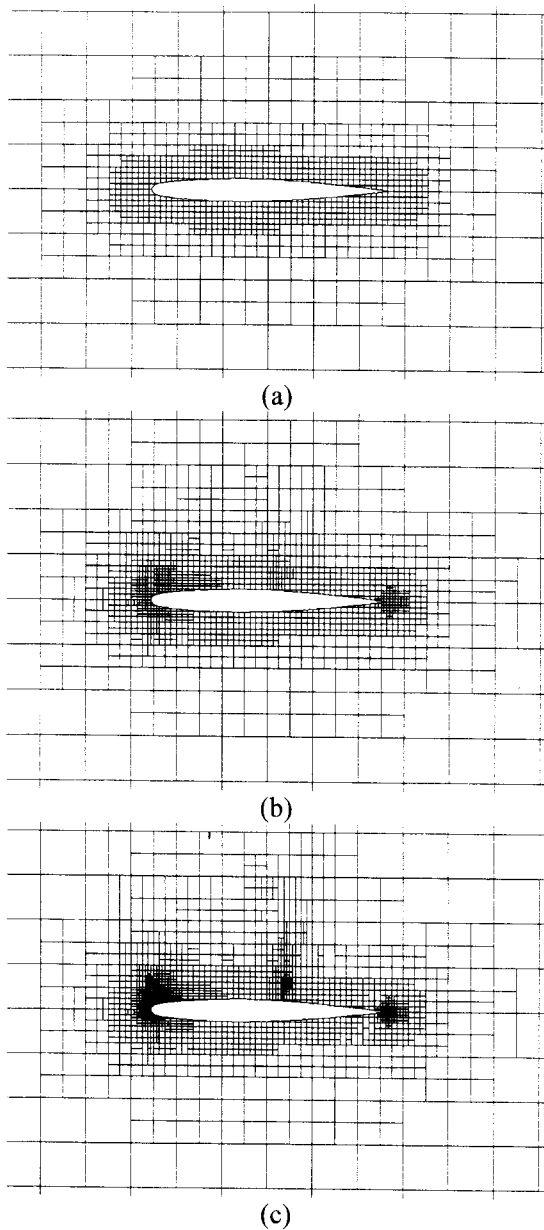


Fig. 6 Grid distribution around ONERA M6 wing at 44% span: (a) at initial, (b) 1st adaptation cycle, (c) 2nd.

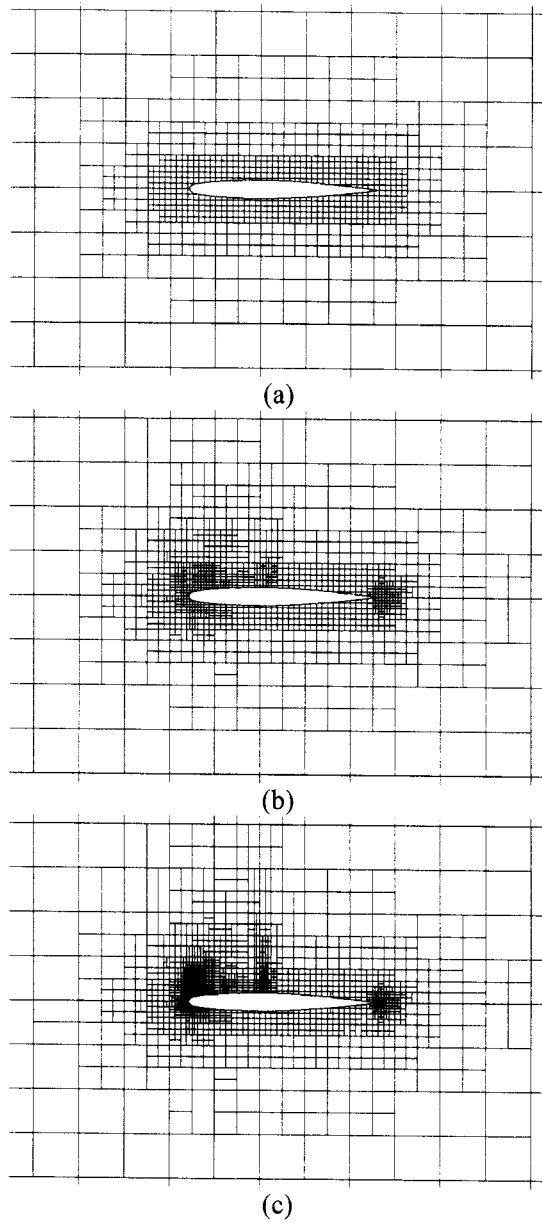


Fig. 7 The same captions as Fig. 6 except at 80% span.

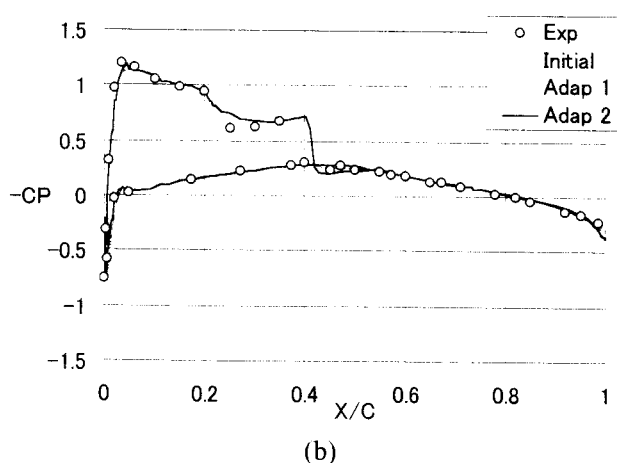
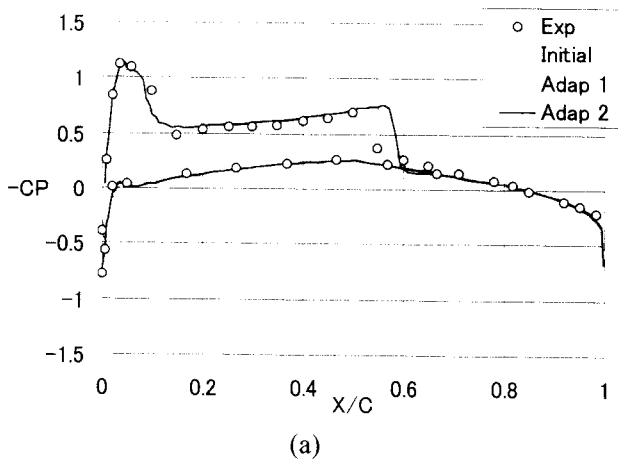


Fig. 8 Pressure distribution around ONERA M6 wing: (a) 44% span, (b) 80%.

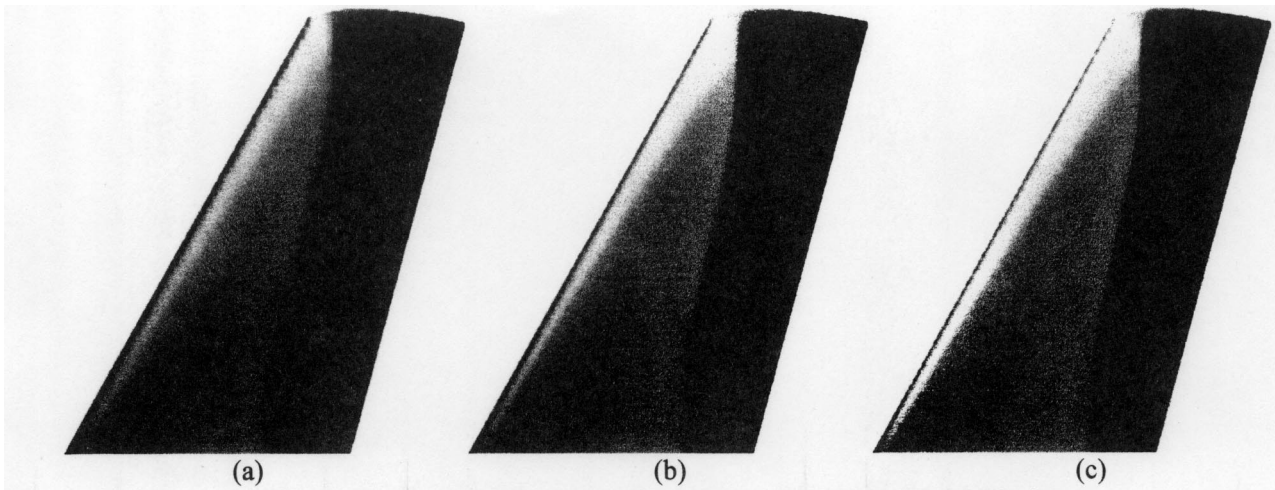


Fig. 9 Pressure distribution on the upper surface of ONERA M6 wing: (a) at initial, (b) 1st adaptation cycle, (c) 2nd.

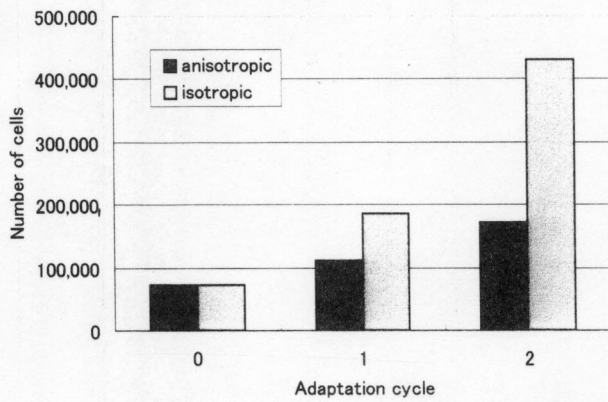


Fig. 10 Change in the number of cells with adaptation cycle for flow around ONERA M6.

A Study on Improvement of Aerodynamic Characteristic of next generation SST by Active Flow Control

Shigeru ASO

Department of Aeronautics and Astronautics, Kyushu University,
Fukuoka 812-8581, JAPAN

Keiichi KARASHIMA

Nishinippon Institute of Technology, Fukuoka, JAPAN

Recently fundamental studies on high speed transportation system (HST or next generation SST) has been studied around the world for better technology breakthrough.. One of the most important problems for designs of such vehicles is the aerodynamic characteristic improvement, especially for high L/D at any flight speed.. There are many ways to improve the aerodynamic characteristic of the main wing of SST. One of the suggested proposal of better aerodynamic characteristic improvement is active flow control. In this paper the present authors would like to explain our experimental efforts and try to offer the possibility for simulating our cases for better understanding of flow physics in the active control of the present flow conditions.

A experimental study on the improvement of aerodynamic characteristics of an arrow wing by lateral blowing in low speed flow has been conducted¹⁾. A modified arrow wing, which is one of the baseline configurations of the proto-type of next-generation SST, is selected for the experiments as shown Fig. 1. The testing model is the combination of a body of a circular cylinder and conical apex and a modified arrow wing with aspect ratio of 1.91. The lateral blowing is realized by injecting a pair of sonic jets in parallel to the trailing edge of the wing. The schematic diagram of the testing set-up is shown in the Fig. 2. The experiments have been performed in ISAS's transonic wind tunnel under the testing conditions of $M_{\infty} = 0.3 \sim 2.3$, $Re = 1.1 \times 10^7 \sim 1.6 \times 10^7$, $\alpha = -15 \text{ deg} \sim 15 \text{ deg}$ and C_j (jet momentum coefficient) = 0.0084 – 0.0211. The global features of active control by using lateral blowing are shown in Fig. 3. The results show that the C_l and L/D is increased by lateral blowing while C_d slightly increases at subsonic flows and C_d slightly increases at supersonic flows. The results suggest that the lateral blowing can be useful for the improvement of aerodynamic characteristics of the arrow wing at transonic flows as well as subsonic flows.

References

- 1) M. Kamishita, S.Aso, K. Karashima and K. Sato: Active Control of Aerodynamic Characteristics of Next-Generation SST Wing by Lateral Blowing, AIAA Paper 2000-0516.

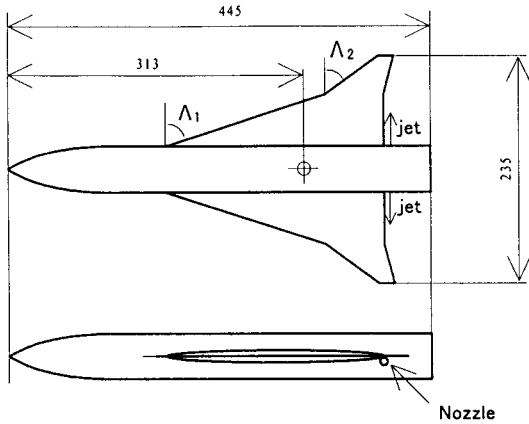


Fig.1 Model geometry

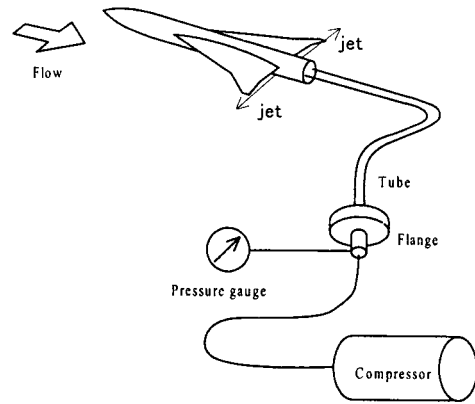


Fig.2 Schematic diagram

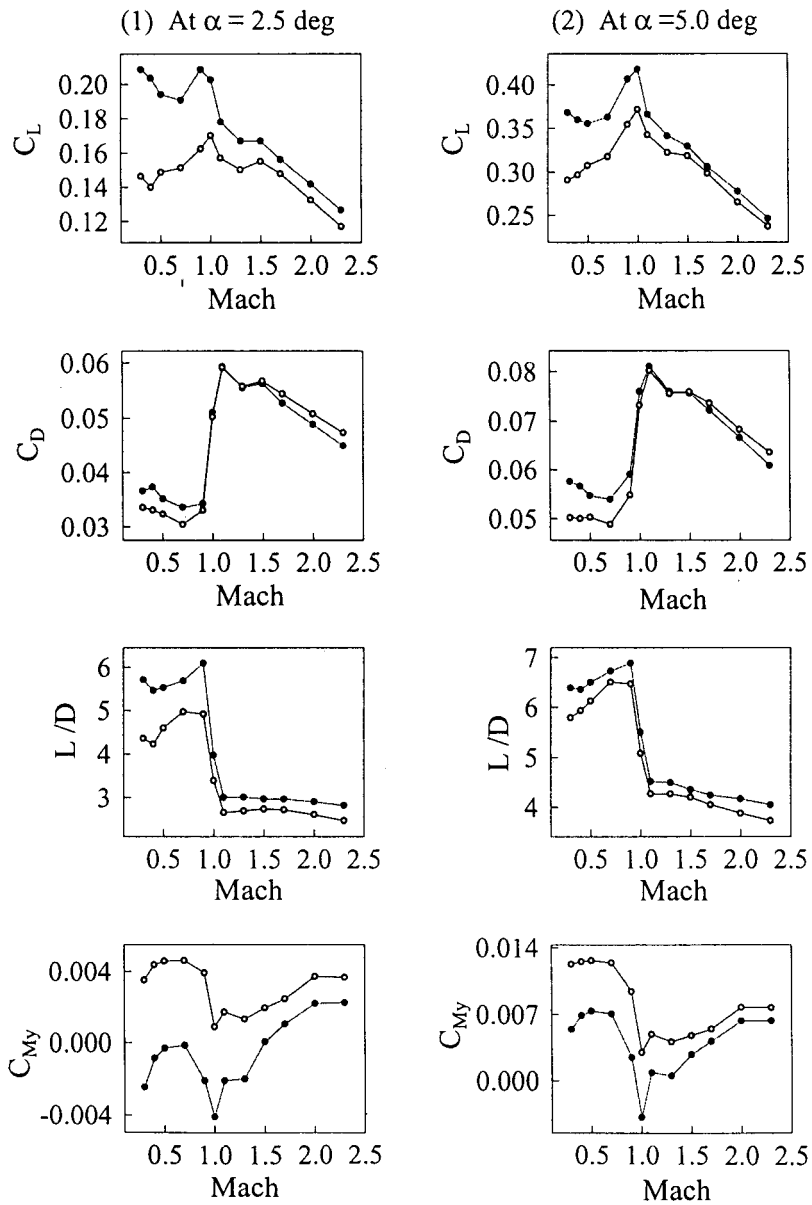


Fig.3 C_L , C_D , C_{My} and L/D vs Mach number

- Lateral blowing
- No blowing

SPECIAL PUBLICATION OF NATIONAL
AEROSPACE LABORATORY
SP-49T

航空宇宙技術研究所特別資料SP-49T号(欧文)

平成12年12月発行

発行所 科学技術庁航空宇宙技術研究所
東京都調布市深大寺東町7-44-1
電話(0422)40-3075 ㊦182-8522
印刷所 株式会社 東京プレス
東京都板橋区桜川2-27-12

Published by
NATIONAL AEROSPACE LABORATORY
7-44-1 Jindaijihigashi-Machi, Chofu, Tokyo
JANAPN

©禁無断複写転載

本書(誌)からの複写、転載を希望される場合は、管理部
研究支援課資料係にご連絡下さい。

